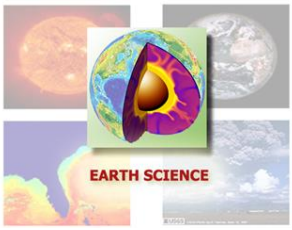

UNIVERSITÀ DEGLI STUDI DI TORINO

Doctoral School of Sciences and Innovative Technologies

Dottorato di Ricerca in Scienze della Terra XXXII ciclo

EXHUMATION OF CRUSTAL ROCKS IN A TRANSPRESSIONAL REGIME

TUTOR: Prof. Rodolfo Carosi **CANDIDATE: Matteo Simonetti**

CO-TUTOR: Prof.ssa Chiara Montomoli

Ringraziamenti

Alla fine di un percorso lungo e così tanto sfaccettato i ringraziamenti da fare sarebbero davvero tanti, chiunque io abbia incontrato ha contribuito in qualche modo a questo percorso…

Un primo grande ringraziamento va al Prof. Rodolfo Carosi e alla Prof.ssa Chiara Montomoli per la fiducia che mi hanno dato accettando di seguirmi durante questo progetto di dottorato e per avermi sempre dato grande supporto, sia dal punto di vista lavorativo che dal punto di vista umano, in ogni situazione. Desidero anche ringraziarli per avermi coinvolto in diversi progetti di grande interesse e di grande valore lavorativo e personale. È grazie a voi se ho potuto vivere esperienze che alcuni anni fa, da studente, vedevo come dei sogni quasi impossibili da realizzare!

Ringrazio molto il Dott. Salvatore Iaccarino per il grosso aiuto e supporto che mi ha fornito durante questi tre anni di lavoro, sempre con grande disponibilità e pazienza. Lo ringrazio anche per le numerose e sempre utili discussioni ricche di spunti interessanti, per avermi dato una mano con i tanti dubbi che spesso venivano fuori e per avermi sempre ascoltato quando ero in cerca di un confronto.

I really wish to thank Professor Richard D. Law for his great support to my training and my research and for his great hospitality and courtesy during my stay in Blacksburg. It was a great time and I really hope to have the chance to visit Virginia tech again in the future. I thank Professor John M. Cottle for his help with petrochronology and lab work in UCSB and Professor Michel Corsini for the helpful discussions about geology of the Maures Massif.

Ringrazio molto Luca con cui ho condiviso per tutto questo tempo la stanza in "Alcatraz" tra momenti difficili ma anche, e soprattutto, tra grandi soddisfazioni, grasse risate e speranze per il futuro! Ringrazio Nico che anche se da "Alcatraz" è andato via e ha scoperto le finestre, dentro è sempre rimasto uno di noi! Ringrazio Fra, Michele e Andre per le tante e piacevolissime pause insieme e le raffinatissime degustazioni di caffè! Un ringraziamento va anche a tutti gli altri dottorandi del dipartimento e non, colleghi e ormai amici, con i quali ho condiviso questo percorso. Questi tre anni di lavoro sono davvero volati soprattutto grazie a voi!

Arrivato ormai alla terza tesi è anche il momento di fare un doveroso e grande ringraziamento a tutti i cari amici della L.I.U.T. per i tanti momenti di gioco, hobby e svago che ormai da anni trascorriamo insieme. Il tempo passa e la vita cambia ma condividere un po' di hobby con voi, per qualche ora alla settimana, "viaggiando" nella storia e in universi fantasiosi è un piacere che ci sarà sempre!

Un ringraziamento davvero di cuore ai miei genitori per il loro grandissimo supporto e aiuto che in tanti anni non mi hanno mai fatto mancare. È grazie al vostro prezioso sostegno e grande incoraggiamento che sono riuscito a raggiungere un nuovo traguardo.

Infine ringrazio davvero tanto Giorgia per aver un giorno cominciato a salutarmi nei corridoi del dipartimento… e per tutto quello che da li è cominciato… davvero grazie…

1. Introduction

The Wilson Cycle well-explains that after convergence and oceanic subduction continents collide giving rise to mountain belts. W-directed subductions undergo back-arc extension (Doglioni *et al.* 1999) competing with the vertical growth of a belt (e.g. Appennines), whereas E or NE directed subductions are able to substain higher mountains belts (e.g. Alps and Himalaya). The subsequent fate of collisional orogens varies due to several factors such as the occurrence of erosion and isostatic equilibration, post-collisional extensional tectonics, both indentation and transpressional tectonics. Indentation tectonics (Tapponier and Molnar, 1977; Tapponier *et al.*, 1982; Davy and Cobbold, 1988) caused by continuing convergence after collision, strongly affects the tectonic evolution of the lateral portions of the indented belt. A classical example of indentation tectonics is the collision between India and Asia. In the Himalaya the Chaman Fault, on the West, and the Sagaing Fault, on the East, act as tracks allowing the northward indentation of India into Eurasia (Tapponier and Molnar, 1977; Tapponier *et al.*, 1982).

Fundamental parameters that controls this phenomena are: the rheology of the colliding blocks, their dimension and their state of confinement. Kinematic and deformation along the main regional-scale structures is very variable depending on the sector of the indented belt in which they are developed. Typically, faults and shear zones, developed at the two lateral margins of the indenter, are characterized by transpressional deformation and opposite sense of shear. The consequence of this process can be the formation of large-scale curvatures known as oroclines (Carey, 1955; Rumelhart *et al*., 1999; Bajolet *et al*., 2013). Several mountain belts, such as the New England Orogen (Glen and Roberts, 2012; Li *et al.*, 2012; Li and Rosenbaum, 2014) in the Tasmanides (Australia), the Wyoming Salient (Johnston *et al.*, 2013) in the Sevier thrust belt (United states), the Carpathian-Balkan segment (Shaw and Johnstow, 2012) of the Alpine orogeny (south eastern Europe) and the European Variscides (Matte, 1986a; Matte, 1986b; García-Navarro and Fernández, 2004; Pereira *et al.*, 2008; Pastor-Galán *et al.*, 2015a; Pastor-Galán *et al.*, 2015b) among the others, show large-scale curvatures. The overall shape of the Variscan Belt in Europe, the result of a Devonian–Carboniferous continent-continent collision between Laurentia-Baltica and Gondwana (Arthaud and Matte, 1977; Burg and Matte, 1978; Tollmann, 1982; Matte, 1986b; Matte, 2001), is characterized by a composite orocline showing two large scale arcs (Matte and Ribeiro, 1975; Matte, 1986b): a western branch

known as the Ibero–Armorican arc (Matte and Ribeiro, 1975; Brun and Burg, 1982; Dias and Ribeiro, 1995; Dias *et al.*, 2016; Fernández-Lozano *et al.*, 2016) and a smaller eastern branch (Matte, 2001; Bellot, 2005; Ballèvre *et al.*, 2018) that is delimited by a regional-scale dextral transpressive shear zone, known as the East Variscan Shear Zone (EVSZ; Corsini and Rolland, 2009; Carosi *et al.*, 2012; Padovano *et al.*, 2012; Padovano *et al.*, 2014; Simonetti *et al.*, 2018). This led some authors (Matte, 2001; Kroner and Romer, 2013; Dias *et al.*, 2016; Simonetti *et al.*, 2018) to hypothesize that Variscan Belt in Europe developed and evolved in a manner analogous to the indentation model proposed by Tapponier and Molnar (1977) and Tapponier *et al.* (1982).

The EVSZ is actually not completely understood, expecially in those sectors of the Variscan Belt that are now part of the Alps, and its role during the Variscan and post-Variscan time is still debated. According to some authors shear deformation along the EVSZ in the Variscan basement of the Western Alps is related to the transition between Pangea B to Pangea A that started during the Permian (Muttoni *et al.*, 2003; Muttoni *et al.*, 2009).

The Wegenerian confguration of Pangea, also known as Pangea A, is the widely accepted paleogeographic scenario in the Early Jurassic (Van der Voo, 1993) but paleomagnetic analysis concluded that, with this reconstruction, overlap of continental crust between Gondwana and Laurasia occurred in the Early Permian. In order to solve this problem, Muttoni et al. (1996) proposed to slide Gondwana to the east with respect to Laurasia, maintaining the coherence of the paleomagnetic poles and in agreement with the Irvinian Pangea B configuration. According to this model Pangea B finally transformed into Pangea A by the end of Permian and the movement of Gondwana was accomodate by a nearly 3000 km-long system of crustal-scale dextral strike-slip structures.

However it is not clear which structures would have allowed the movement of Gondwana, and if their remnants are still recognizable. Some authors proposed as evidence in support of this model the extensive presence of pre-Alpine dextral shear in the fragments of the Variscan Belt in the Mediterranean Area (such as the Alpine External Crystalline Massifs) coupled with the formation of Early Permian basins.

However, geochronological data from pre-Alpine shear zones in the Western Alps point out to an older deformation still related to the Variscan orogeny (Simonetti *et al.*, 2018; Pohl *et al.*, 2018), suggesting that the activity on the EVSZ is not related to the post-Variscan events. A detailed structural and

geochronological analysis of the shear zones in the Variscan basement of the Western Alps is therefore necessary to address this problem.

Another unclear question concerns the lateral relationships between the Corsica-Sardinia block, the Maures-Tanneron Massif and the Variscan basement of the Western Alps (External Crystalline Massifs). The correlation between those sectors is still debated and is mostly based on lithological and stratigraphic affinities and paleomagnetic data. In particular, it is not clear if the Corsica-Sardinia Block was connected to Iberia (Stampfli *et al.*, 2002; Turco *et al.*, 2012) or to southern France (Rosenbaum *et al.*, 2002; Advokaat *et al.*, 2014) during the Late Carboniferous times.

A deeper knowledge of the different phases of Variscan deformation, and their ages, is therefore of fundamental importance for improving correlation between the dispersed fragments of the Variscan belt in the Mediterranean area within the context of the tectonic evolution of the Southern Variscan Belt. In this thesis we focus on three fragments of the Variscan belt: the Argentera Massif and the Aiguilles Rouges Massif that belongs to the Alpine External Crystalline Massifs and the Maures Massif in southern France.

In the Argentera Massif the aim is to clarify the kinematics of the flow, the age of activity and the deformation temperature of the Ferriere-Mollières Shear Zone (Malaroda *et al.*, 1970; Faure-Muret, 1955; Carosi *et al.*, 2016), a major ductile shear zone cross-cutting the Massif, in order to check if Variscan deformation is still preserved and if dextral shear deformation affecting the Alpine External Crystalline Massifs can be linked to the activity of other similar transpressional shear zones in the Southern European Variscan Belt. To verify this hypothesis, we carried out a kinematic vorticity analysis, a study of quartz fabric in sheared rocks and a U-Th-Pb petrochronological study on syn-kinematic monazites, combined with structural and microstructural analyses on different types of mylonites. A preliminary quartz-based palaeopiezometry study was also performed in order to investigate the rheology of the shear zone.

In the Aiguilles Rouge Massif we focused on two areas where rocks are strongly sheared along a thick belt of mylonites (Von Raumer and Bussy, 2004) and Alpine deformation is very weak and developed under brittle conditions (Pilloud, 1991; Dobmeier and Von Raumer, 1995). The aim is to clarify the kinematics of the flow, the deformation temperature and to directly constrain the age of the deformation in order to verify if they are similar to the ones proposed in the literature for the Argentera Massif and for the other fragments of the belt in the Mediterranean area. We carried out a kinematic vorticity analysis, a study of quartz fabric and

a U-Th-Pb petrochronological study on syn-kinematic monazites, combined with structural and microstructural analyses of sheared rocks already recognized by Von Raumer and Bussy (2004) and Genier *et al.* (2008).

In the Maures Massif we investigated the Cavalaire Fault (CF; Schneider *et al.*, 2014; Oliot *et al.*, 2015), a major ductile shear zone that is located at the contact between the internal and external sectors of the Variscan belt. Its evolution is currently poorly understood because the current model relies mainly on field observations not integrated with data obtained using other analytical methods. The aim is to clarify both the kinematics of the flow, the deformation temperature and the age of shear deformation. In order to do that we present the results of structural and micro-structural analyses of key areas of the Maures Massif combined, for the first time, with an analysis of the kinematics of the flow, finite strain analysis, a study of quartz fabric and U-Th-Pb petrochronological study on mylonites within this shear zone.

The new data, obtained by applying systematically the same combination of analytical methods in different Variscan fragments, allow us to better contrain the complex evolution and the role of a long-lasting major shear zone and demonstrate that the same approach should always be applied when dealing with regional-scale structures.

2. Analytical Methods

2.1 Methods for structural analysis

Structural and microstructural analyses were all performed on field oriented samples cut along the XZ section of the finite strain ellipsoid.

Kinematics of the flow, i.e. components of pure and simple shear acting simultaneously during the deformation (see Xypolias, 2010 and Fossen and Cavalcante, 2017 for a review) in the high-strain zone, expressed by the kinematic vorticity number Wk, was estimated using independent kinematic vorticity gauges. In the case of pure shear (i.e. with two orthogonal flow apophyses) Wk is 0, whereas Wk is 1 in the case of simple shear (flow apophyses are coincident). Simple and pure shear equally contribute to flow at a value of Wk = 0.71. Vorticity is nearly independent of volume loss (Fossen and Cavalcante, 2017). Indeed,

in most shear zones developed in both magmatic and metamorphic rocks (excluding slates and phyllites) compaction is limited and the uncertainties related to volume loss are small with respect to the intrinsic error associated with a specific vorticity gouge (Fossen and Cavalcante, 2017). In order to check the type of deformation we calculated the angle θ between the maximum ISA in the horizontal plane and the shear zone boundary. This parameter is useful to distinguish between transpression and transtension (Fossen *et al.*, 1994; Fossen and Tikoff, 1993). The calculation was performed using the formula $\theta = (\arcsin Wk)/2$ (Xypolias, 2010). Geometry of the finite strain ellipsoid is the result of the interaction between the simple shear and the coaxial component of deformation. Finite strain and kinematic vorticity are therefore linked and can be used to distinguish between different types of deformation (Fossen and Tikoff, 1998).

2.1.1 C' shear band method for vorticity analysis

In a flow regime, two flow apophyses can be recognized, separating different domains of particle paths (Passchier, 1986). The kinematic vorticity number (Wk) is defined as the cosine of the angle between the two apophyses (Passchier, 1986).

The first applied method (Kurz and Northrup, 2008; Gillam *et al.*, 2013) is based on the measurement of the orientation of C' planes with respect to the shear zone boundaries. C' planes nucleate as the bisector of the angle (ν) between the two flow apophyses (fig. 2.1). The component of simple shear is inversely proportional to the size of this angle (Platt and Vissers, 1980; Simpson and De Paor, 1993; Kurz and Northrup, 2008). We derive the kinematic vorticity with the relation $Wk = \cos 2\nu$ (Kurz and Northrup, 2008). Some variations in the ν angles exist because during progressive deformation C' planes tend to be passively rotated towards the fabric attractor apophysis (A2). For this reason we select the maximum value of ν for the calculation since this is regarded as the closest approximation of the initial nucleation angle of C' plane (Kurz and Northrup, 2008).

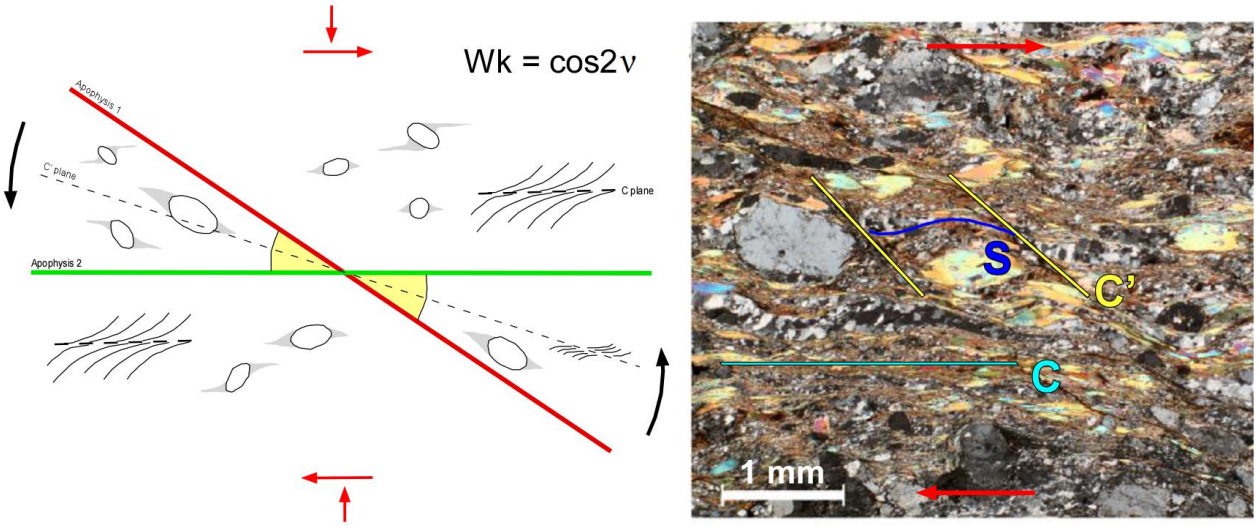

Figure 2.1 – Left: schematic diagram of possible microstructures developed under general flow conditions in a mylonite with dextral sense of shear and their appearance in thin section (right). The flow apophyses A1 and A2 are indicated in red and green, respectively. The angle 2ν between the two apophyses (yellow) is bisected by the C' shear plane (dotted line). The equation to calculate Wk is also shown (modified after Kurz and Northrup, 2008). Right: micrograph (crossed polars) showing C' planes in mylonite of the FMSZ (the short and the long borders of the micrograph are parallel to Z and X axes of the finite strain ellipsoid, respectively)

2.1.2 Stable porphyroclasts method for vorticity analysis

The second applied vorticity gauge consists in measuring the axial ratio of porphyroclasts (R) and the angles between their major axis with respect to the mylonitic foliation (Passchier, 1987; Wallis *et al.*, 1993). These data are plotted on a graph in order to estimate a critical axial ratio, Rc (Wallis *et al*. 1993), which discriminates the field where porphyroclasts reach a stable position from a field where they continue to rotate (fig. 2.2). To minimize the uncertainties, two Rc values have been chosen (Rc minimum and Rc maximum) and an average vorticity has been calculated using the relation $Wm = (Rc^2 - 1)/ (Rc^2 + 1)$. The stable porphyroclasts method is based on three main assumptions (Jeffery, 1922; Iacopini *et al.*, 2011 and references therein): 1) porphyroclasts behave as rigid objects floating in a Newtonian viscous matrix at constant deformation; 2) there is no interaction and slip between clasts and matrix; 3) there is no interference between the particles. The first condition has been assessed by verifying that the porphyroclasts do not show internal deformation and they are harder to deform compared to the matrix (Iacopini *et al*. 2011). The second condition was tested by plotting porphyroclast distribution against theoretical curves of Mulchrone (2007a) and Mulchrone (2007b), as suggested by Iacopini *et al*. (2011). The third condition is satisfied if the porphyroclasts are sufficiently far away one from each other so that they can freely rotate. To avoid mutual interference the distance between porphyroclasts should be larger than their maximum long axis (Ildefonse *et*

al. 1992). The quoted uncertainty on vorticity estimates is ± 0.1 (Tikoff and Fossen, 1995). According to Iacopini *et al*. (2011) the propagation of systematic errors indicates that for medium to low vorticity numbers (Wm<0.8), vorticity data are strongly biased and more realistic systematic error is ± 0.2.

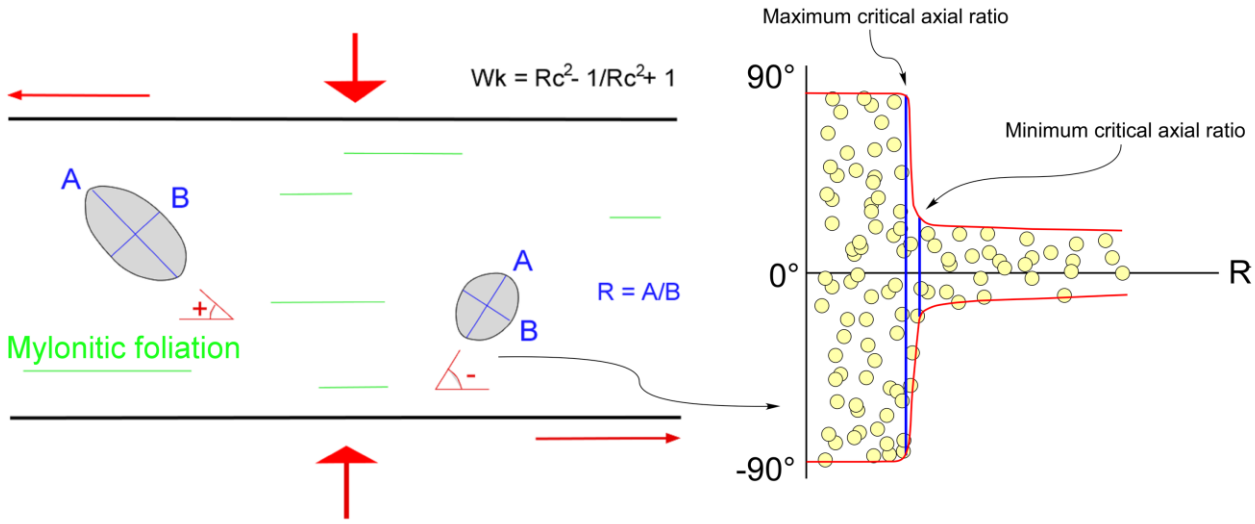

Figure 2.2 – Schematic illustration of stable porphyroclasts method for vorticity analysis. R = axial ratio of porphyroclasts; α = orientation of long axis of poprphyroclasts respect to foliation

2.1.3 Quartz fabric for vorticity analysis and deformation temperature

Quartz-rich tectonites are often characterized by single- or crossed-girdle quartz c-axis fabrics, their shape is the result of a combination of deformation temperature, chemical activity of water (hydrolytic weakening), 3D finite strain and recrystallization processes. Fabrics may either be symmetric, or exhibit varying degrees of asymmetry, with respect to the trace of trace of foliation in the XZ plane (Law, 1990). The degree of asymmetry (obliquity) of the central girdle segment of such fabrics is controlled by Wk and the finite strain (Platt and Behrmann, 1986). The central segment of quartz c-axis fabric, as indicated by Taylor-Bishop-Hill fabric modelling (Lister and Hobbs, 1980) is oriented orthogonal to the flow plane thus allowing us to identify the angle between the main foliation and the flow plane itself (fig. 2.3) that is usually not clearly visible in the field or in samples. Because of the theoretical relationship between vorticity and the orientation of the flow aphophyses and instantaneous stretching axes (ISA; Passchier, 1988), the kinematic vorticity number Wk can be estimated using the equation:

$$Wk = \sin 2\varepsilon$$

Where ε is the angle between apophysis A_2 and the maximun instantaneous stretching axes ISA_2. Wallis (1995) has argued that the orientation of the long axis of quartz neoblasts within an oblique foliation delineates the direction of the ISA_2 (fig. 2.3). This was also supported by experimental studies (Dell'Angelo and Tullis, 1989; Ree, 1991; Herwegh and Handy, 1998). Therefore, the greatest recorded angle between the oblique foliation and the shear zone boundaries should theoretically be equal to the angle between ISA_2 and the flow apophysis A_2 (Wallis,1995).

Oblique grain-shape fabrics are instantaneously sensitive features and thus such estimates possibly record the Wk at the final increment of ductile deformation rather than Wm (Wallis, 1995). In quartz-rich tectonites, the maximum recorded angle α between the oblique and the main foliation in combination with the angle β between the flow plane and main foliation determined from the quartz c-axis fabrics can be used to calculate vorticity (fig. 2.3) with the equation:

$$Wk = \sin 2(\alpha + \beta)$$

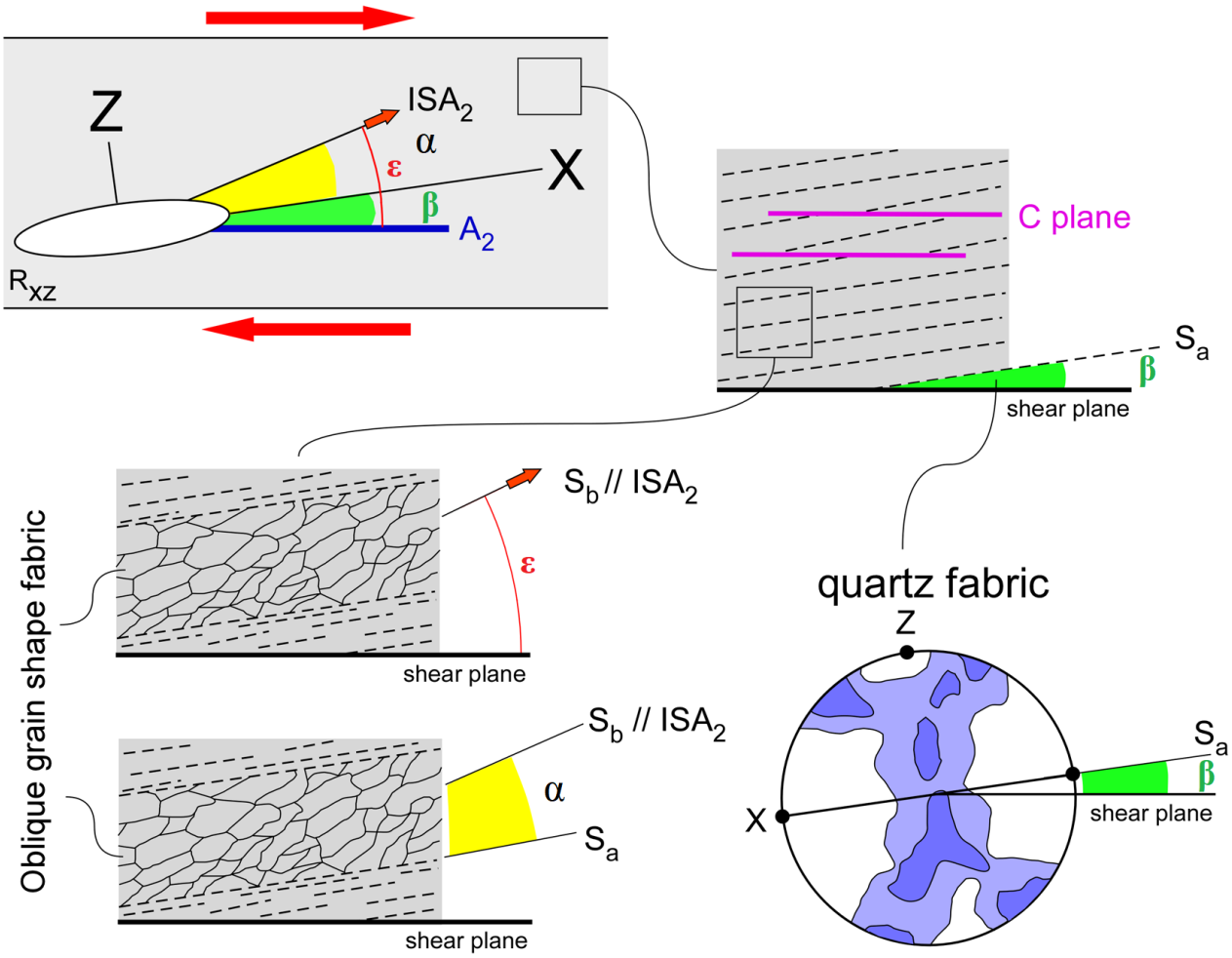

Figure 2.3 – Schematic illustration of quartz c-axis method for vorticity analysis (modified after Xypolias, 2010); A_2 = flow apophysis 2; ISA_2 = istantaneous stratching axis 2; S_a = macroscopic foliation; S_b = quartz oblique foliation; α = angle between ISA_2 and x axis of finite strain; β = angle between x axis of finite strain and flow apophysis 2; ε = angle between ISA_2 and flow apophysis 2

Quartz fabric have also been used to estimate the deformation temperature. Experimental (Tullis *et al.*, 1973) and numerical simulation studies (Lister and Hobbs, 1980; Lister and Dornisiepen, 1982) indicate that during plastic deformation and dynamic recrystallization the opening angle of quartz c-axis fabrics increases with increasing deformation temperature and hydrolytic weakening, and decreasing strain rate. The opening angle is defined as the angle between the two c-axes girdles measured in the plane perpendicular to foliation and parallel to lineation and passing through the pole to foliation (Kruhl, 1998; see review by Law 2014). At natural strain rates there is an approximately linear increase in opening angle with temperature between c. 300° and 650° C, with a nominal uncertainty usually stated at ± 50° C (Kruhl, 1998). Recently Faleiros *et al.* (2016) proposed a new calibration of the thermometer which extends the correlation between opening angle and temperature above 650° C.

Quartz fabrics where obtained by manual measuraments with the universal stage at the *Università degli Studi di Torino* of no less than ~500 grains for each thin section. Measurement was combined with a detailed study of quartz microstructures. In cases where quartz microstructures show an overprint of lower T microstruttures, even if only partial, it is more likely to consider the temperature obtained with the opening angle thermometer as a minimum estimate.

2.1.4 Center-to-center method for strain analysis

Finite strain analysis, using the center-to-center method (Fry, 1979), was performed on the XZ section and, where possible, on the YZ section in order to obtain the shape of the 3D strain ellipsoid.

We used an adequate number of porphyroclasts, with similar grain size, as strain markers. The center-to-center method is based on the redistribution of the centers of the strain markers caused by deformation, assuming an original homogeneous distribution in the undeformed state (see Genier and Epard, 2007 for a critical review). The Fry method is independent of the shape of the strain markers since the result is only a function of the distribution and the mutual distance of the objects centers. The analysis consists in the choice of a reference point that is moved on the centers of the markers in order to project the nearest centers to the

analysed marker center. Repeating this procedure a dozen times, a blank area (or an area with low density of points) representative of the finite strain ellipse and surrounded by an area with higher density of points, appears. The center-to-center analysis was carried out using the software EllipseFit 3.2 (Vollomer, 2015). Strain and vorticity pairs from the same sample were combined to calculate the percentage of shortening and stretching perpendicular and parallel to the flow plane, respectively (Wallis *et al.*, 1993; Law *et al.*, 2004; Law, 2010) by using the equation:

$$S = \left\{ \frac{1}{2} \left(1 - W_m^2\right)^{1/2} \left[\left(R_{xz} + R_{xz}^{-1} + 2 \frac{\left(1 + W_m^2\right)}{\left(1 - W_m^2\right)} \right)^{1/2} + \left(R_{xz} + R_{xz}^{-1} - 2 \right)^{1/2} \right] \right\}^{-1}$$

Where S is the shortening perpendicular to flow plane, W_m is the mean kinematic vorticity number and R_{xz} is the strain ratio on the XZ section. This relation provides reliable stretching values only in the case of plane strain where, for a given amount of shortening, all of the elongation is transport-parallel and accommodated along the X axis of the strain ellipsoid (Law, 2010). In cases of general flattening 3D finite strain we applied the correction of Law (2010), accounting for deviations from plane strain.

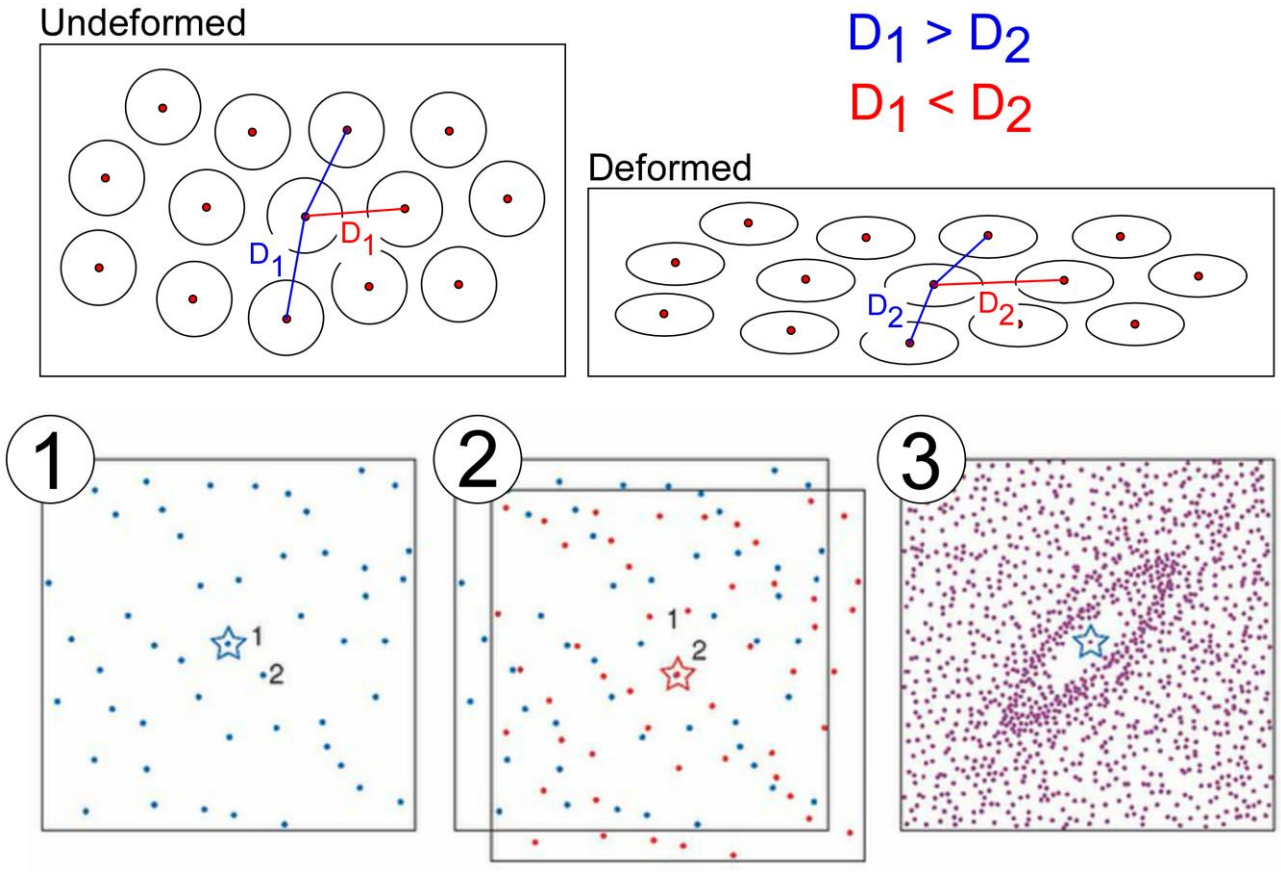

Figure 2.4 – Schematic illustration of the center-to-center method and of the relative procedure to obtain finite strain. The center of a strain marker is selected as reference point and the other centers are projected (1); the reference point is moved on another center and the other centers are projected again (2); the procedure is repeated several times and a blank area around the reference point will appear (3); D = distance between neighbouring centers

2.1.5 Convergence angle

The convergence angle between the wall-rocks of a shear zone can be calculated with the relation proposed by (Fossen and Tikoff, 1998):

$$\alpha = \tan^{-1}[\ln \frac{Kx/Kz}{\gamma}]$$

Where α is the convergence angle, Kx is the X axis of finite strain, Kz is the Z axis of the finite strain and γ is the shear strain. Shear strain can be calculated with the software *strain calculator* by combining the vorticity number and the amount of shortening.

2.2 Quartz palaeopiezometry

Deformation experiments have shown a close relationship between the dynamically recrystallized grain size and the differential stress during deformation within the Earth's crust and mantle (e.g. Stipp and Tullis, 2003; Stipp *et al*., 2006; Stipp *et al.*, 2010; Stipp, 2012) that represents the theoretical basis of palaeopiezometry.

A preliminary study was performed in this work. The average grain size (expressed as arithmetic mean, after Ghosh *et al.*, 2016) of recrystallized quartz, needed for palaeopiezometry, has been obtained starting from high-resolution images (crossed polarized light with gypsum plate inserted) of two equivalent areas in thin section) at the optical microscope. With the aid of manual contouring and of image-analysis with the software ImageJ (Abramoff *et al.*, 2004) we obtained a grain-boundary map for each analyzed area and from these maps, the corresponding area of recrystallized quartz grains. Each area of a recrystallized quartz grain has been converted to the diameter of the equivalent circle. Following Stipp and Tullis (2003), no correction has been made for the cut-effect or for non-equidimensional grain shape.

Different palaeopiezometer calibrations for quartz in the dislocation creep regime are present in the literature (Twiss, 1977; Stipp and Tullis, 2003; Shimizu, 2008; Holyoke and Kronenberg, 2010). Particularly, we estimated flow stresses using Stipp and Tullis (2003) calibration for regime (2/3) both in its original form

(fig. 2.5) and as revised by Holyoke and Kronenberg (2010) (fig. 2.5) and the following relation proposed by Shimizu (2008):

$$\sigma = 2.17 \times 10^2 \times d^{-0.8} \exp\left(\frac{1.19 \times 10^3}{T}\right)$$

were σ is the differential stress, *d* is the measured grainsize, T is the temperature (in K). The temperature derived from the quartz c-axis opening angle termometer in the same studied sample was used for the calculation.

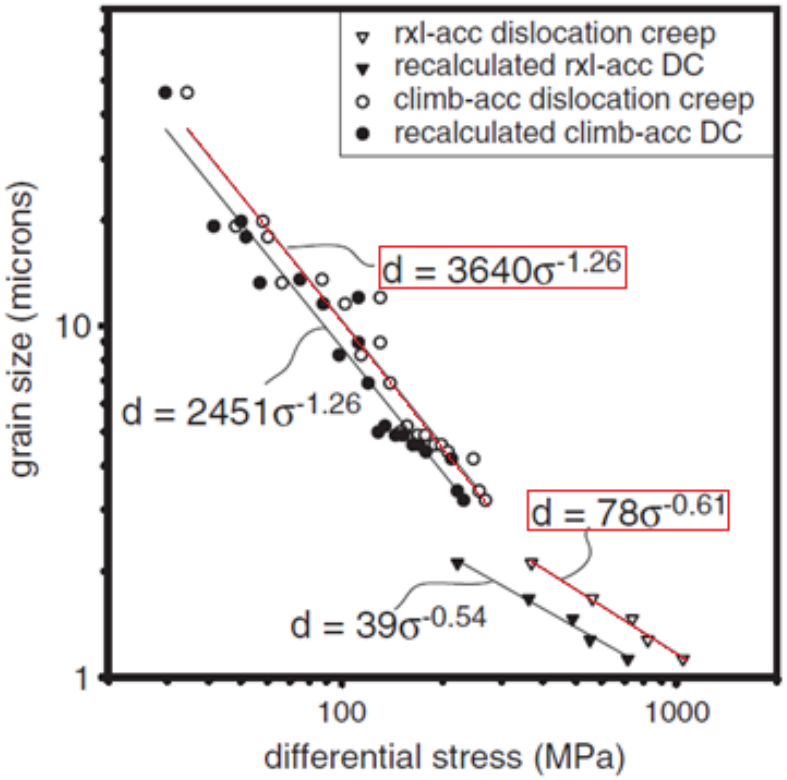

Figure 2.5 – Recrystallized grain size–differential stress relations (modified after Holyoke and Kronenberg, 2010) for dislocation creep regime 1, regimes 2 and 3 as corrected by Holyoke and Kronenberg (2010) after the original relations (in red) proposed by Stipp and Tullis (2003).

Results obtained with the quartz-based palaeopiezometers were combined with the Gleason and Tullis (1995) flow law:

$$\varepsilon = A\sigma^n e^{-\frac{Q}{RT}}$$

Where ε is the strain rate, A is a material constant ($MPa^{-n}s^{-1}$), σ is the differential stress (MPa), n is the (power-law) stress exponent, Q is the activation energy ($KJmol^{-1}$), T is the absolute temperature, R is the molar gas constant. Calculation taking into account the Holyoke and Kronenberg (2010) correction for the value A were also made. It is worth mentioning that Gleason and Tullis (1995) flow law is independent of the $f(H_2O)$, we have not used other flow law where water fugacity is considered because we do not have a precise estimate of metamorphic conditions during deformation needed to calculate this parameter.

2.3 Petrochronological tecniques for U-Th-Pb method on monazite

Petrochronological data were obtained following the analytical procedure reported in Braden et al. (2017 and references therein). Selected samples were polished, C-coated and inspected using a Scanning Electron Microscope (JEOL JSM IT300LV) hosted at the University of Torino (Italy), in order to observe monazite microstructural position, internal features and zoning in back-scattered electron (BSE). X-Ray compositional maps (for Y, Ce, Pr, Th, La, P, Ca, U) and chemical analyses were acquired with an electron microprobe (JEOL 8200 Super Probe) hosted at the University of Milano (Italy), following the procedure given in Montomoli *et al.* (2013), in order to highlight compositional zoning in monazite grains.

2.3.1 Monazite characterization

Monazite belongs to the family of orthophosphates with general formula $A(PO_4)$ and is an anhydrous rare earth phosphate (Williams *et al.*, 2007). Monazite is ideal for recording the progress of geological processes, because with its extremely variable composition it reflects the chemical and physical changes of the host rocks and preserves the age of crystallization or growth over long geological periods (Williams *et al*., 2007). It is ideal for the U-Th-Pb method because it can have large concentrations of U and Th but does not incorporate Pb during its formation.

The analysis of the microstructural position and the chemical composition of the monazites in a system in which they are associated with garnet, as in the analysed samples, allows us to understand at what time in the tectono-metamorphic history the two phases have grown.

Garnet has a major control on the heavy rare earth elements (HREE) and Y budget in the system (fig. 2.6; Engi *et al*. 2017 and references therein). In a closed system, garnet growth will fractionate HREE and Y from

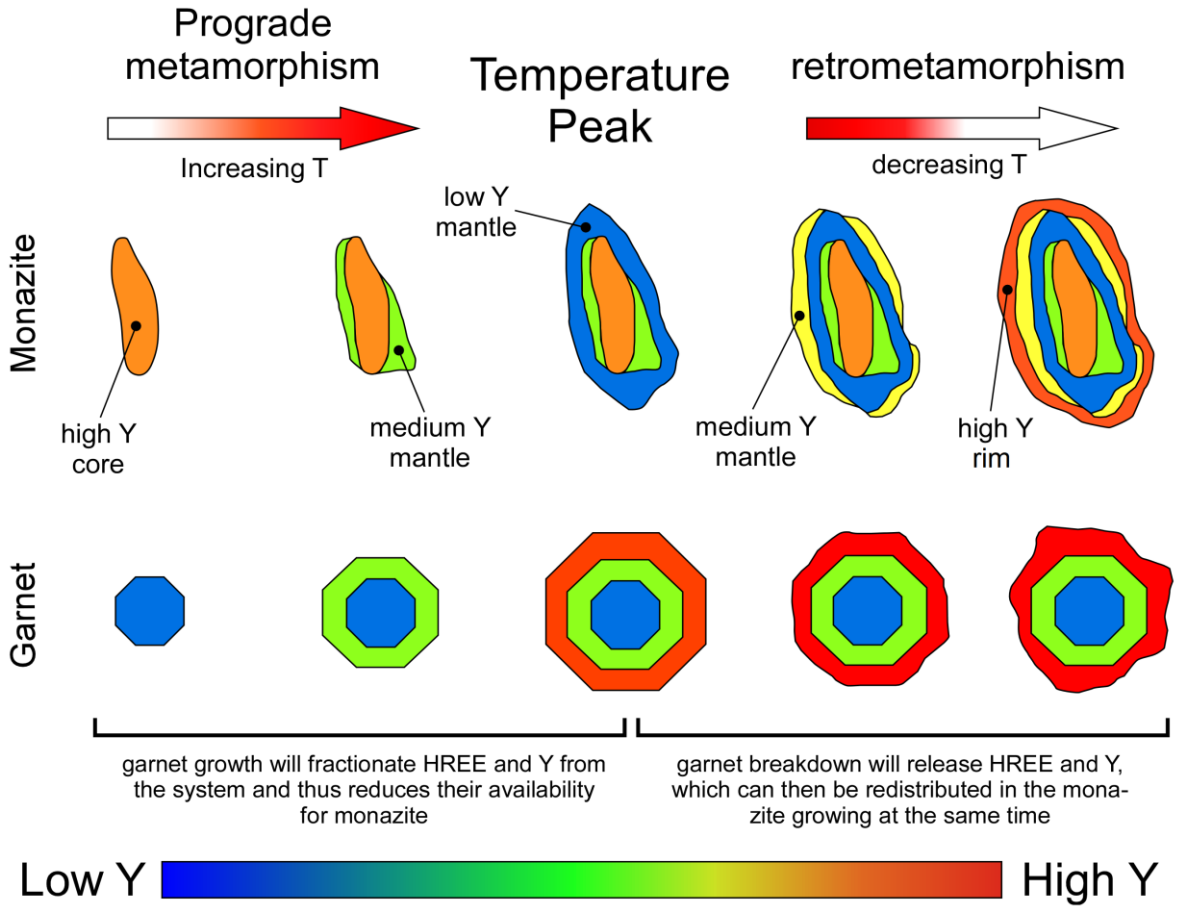

Figure 2.6 – Schematic sketch of the theoretical evolution during prograde metamorphism, temperature peak and retrometamorphism of a monazite and garnet association

the system and thus reduces their availability for monazite (Foster et al. 2002; Hermann and Rubatto 2003; Buick et al. 2006; Rubatto et al. 2006). In contrast, garnet breakdown will release HREE and Y, which can then be redistributed in the monazite growing at the same time. So, during retro-metamorphism, monazite showing increasing values of HREE and Y is expected (Pyle and Spear, 1999; Pyle *et al.*, 2001; Williams *et al.*, 2007; Iaccarino et al. 2017). The ratio of Gd to Yb is also useful to approximate the behavior of HREE: a decreasing Gd/Yb indicates garnet breakdown whereas an increasing Gd/Yb indicates garnet growth or growth of monazite in the presence of stable garnet (Braden *et al*. 2017). Moreover, Eu anomaly can be used as a proxy for monitoring the timing of melt crystallization and abundance of K-feldspar (Braden *et al*. 2017; Rubatto *et al.*, 2013). Since the mylonitic foliation in the studied shear zones developed during decreasing temperature conditions, after a prograde metamorphism, all these chemical proxies (e.g. Y+HREE zoning, the Gd/Yb ratio, REE patterns) coupled with grain textural position and zoning, guided the interpretation of monazite data with respect to the prograde and/or retrograde stages.

2.3.2 LA-ICP-MS

Monazite grains were analyzed in situ by laser-ablation inductively coupled plasma mass spectrometry (LA–ICP-MS) on 30-μm-thick sections at the CNR–Istituto di Geoscienze e Georisorse U.O. Pavia (Italy) using an Ar–F 193-nm excimer laser (GeolLas 102 from Micro-Las) coupled with a magnetic sector ICP-MS (Element I from Thermo-Finnigan). The full description of the analytical procedures is reported in Paquette and Tiepolo (2007) and Tiepolo (2003). Single analyses were performed by a one-minute acquisition of the background signal followed by recording, for at least 30 seconds, the ablation signal of the masses: 202Hg, 204(Hg+Pb), 206Pb, 207Pb, 208Pb, 232Th and 238U. The presence of common Pb was evaluated in each analysis on the basis of the net signal of 204Pb (i.e. subtracted for the interference of 204Hg and background). None of the samples gave 204Pb counts above the background level. However the relatively high Hg signal in the gas blank does not exclude the effective presence of common Pb in the analyzed monazites. Analytical conditions were 10 μm diameter of spot size, 8 J/cm2 of energy density, and 3 Hz of repetition rate. Time-resolved signals were carefully inspected to verify the presence of perturbations related to inclusions, fractures or mixing of different age domains. Laser-induced elemental fractionation and mass bias were corrected using matrix-matched external monazite standard (Moacir monazite: Cruz *et al*., 1996; Seydoux-Guillaume *et al*., 2002a, 2002b) considering the values, re-calibrated for isotopic disequilibrium, reported by Gasquet *et al.* (2010). Eight to nine external standards were analyzed in each analytical run and only those close to the reference values (at least 4 in each run) were considered in order to reduce errors related to the standard reproducibility (tab 2.1). The relative standard deviation of the analyses was mostly within 2 % – 4 %. External standards and unknowns were integrated over the same time intervals to ensure the efficient correction of fractionation effects. Data reduction was carried out with the GLITTER® software (van Achterbergh *et al*., 2001). In order to better estimate the uncertainty affecting the 206Pb/238U, 207Pb/235U and 208Pb/232Th isotope ratios, the external reproducibility of the standard was propagated relative to individual uncertainties for the isotope ratios. This procedure was carried out for each analytical run as reported in Horstwood *et al.* (2003). After this error propagation each analysis is accurate within the quoted errors. Data processing and plotting was done with the macro ISOPLOT/Ex (Ludwig, 2003).

2.3.3 LASS

Monazite was analyzed directly in thin section using the Laser Ablation Split Stream (LASS) method at the University of California Santa Barbara. Spot location was guided with the aid of X-ray compositional maps. Instrumentation consists of a Photon Machines 193 nm ArF Excimer laser and 'HelEx' ablation cell coupled to a Nu Instruments HR Plasma high-resolution multi-collector MC-ICP-MS (U, Th, and Pb isotopes) and an Agilent 7700S Quadrupole ICP-MS (major and trace elements). Methods in this study follow those outlined in Kylander-Clark *et al.* (2013) with modifications outlined in McKinney *et al*. (2015). Monazite was ablated using a 7 μm diameter spot at 3 Hz repetition rate at a laser fluence of 1.5 J/cm2, resulting in craters that are ~4 μm deep.

Data reduction, including corrections for baseline, instrumental drift, mass bias, down-hole fractionation as well as age calculations were carried out using Iolite v. 2.5 (Paton *et al*. 2010). Background intensities and changes in instrumental bias were interpolated using a smoothed cubic spline while down-hole inter-element fractionation was modeled using an exponential function. Statistics for baselines, on peak intensities and isotopic ratios were calculated using the mean with a 2.S.D. outlier rejection. Concordia and weighted mean date plots were calculated in Isoplot v.3 (Ludwig, 2003) using the 238U and 235U decay constants of Jaffey *et al*. (1971) and the 232Th decay constant of Amelin and Zaitsev (2002). All uncertainties are quoted at 2σ and include contributions from the external reproducibility of the primary reference material for the 206Pb/238U ratios and 208Pb/232Th ratios. The full dataset is presented in table 2.2.

Monazite U-Th/Pb data was normalized to '44069' (424 Ma 207Pb/235U ID-TIMS age, Aleinikoff *et al*., 2006), employed to monitor and correct for mass bias as well as Pb/U and Pb/Th down-hole fractionation. To monitor data accuracy, two a reference monazite FC-1 (55.7 Ma 206Pb/238U ID-TIMS age, Horstwood *et al*., 2003) was analyzed concurrently (once every ~7 unknowns) and mass bias- and fractionation-corrected based on measured isotopic ratios of the primary reference material. During the analytical period, 11 analyses of FC-1 gave a weighted mean 206Pb/238U date of 57.5 ± 0.4 Ma, MSWD = 1.1, and a weighted mean 208Pb/232Th date of 54.7 ± 0.5 Ma, MSWD = 0.96 (2σ). Based on the long-term reproducibility of multiple secondary reference minerals, trace element concentrations are accurate to 3–5% (2σ).

3. The European Variscan Belt

The Variscan Belt is the result of a continent-continent collision between Laurentia-Baltica and Gondwana (fig. 3.1) that occurred between 380 Ma and 280 Ma (Arthaud and Matte, 1977; Burg and Matte, 1978; Tollmann, 1982; Matte, 1986b; Matte, 2001; Di Vincenzo *et al.*, 2004). This collision led to the final assemblage of Pangea and to the formation of a 1000 km wide and 8000 km long mountain system, which extended from the Caucasus to the Appalachian and Ouachita mountains of northern America at the end of the Carboniferous (Matte, 2001).

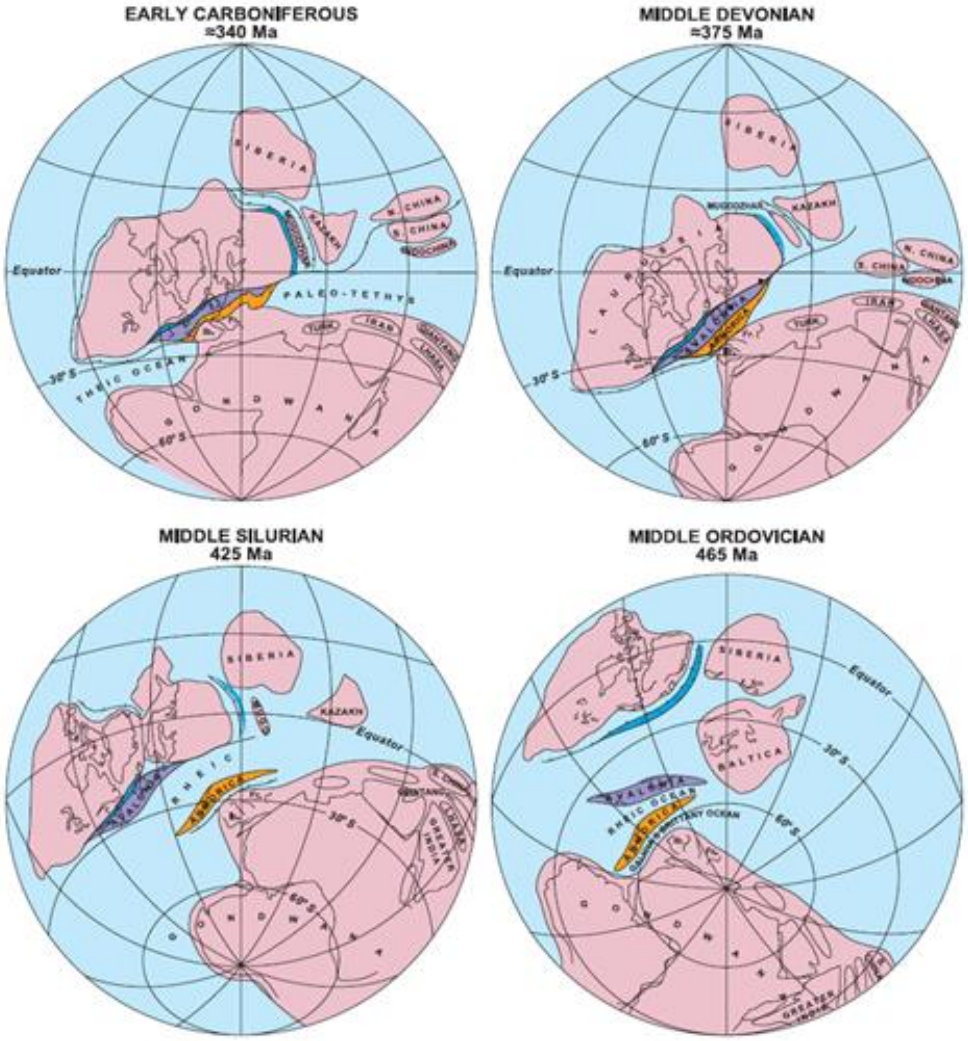

Figure 3.1 - Palaeozoic reconstructions from middle Ordovician (465 Ma) to Lower Carboniferous (340 Ma) (from Matte, 2001)

The Variscan belt is characterized by the complex juxtaposition of low strain and high strain domains (Kroner and Romer, 2009), the former contain most of the pre-Variscan, the latter the Variscan information.

The main debate concerning the Variscan collision in Europe is about the presence or absence of microplates between Laurentia-Baltica and Gondwana. According to the microplates model, between the two involved continents small microplates, defined essentially on the basis of palaeomagnetism and palaeobiostratigraphy (Scotese and McKerrow, 1990; Franke *et al*., 2017, with references therein), existed. The main microplates are known as Avalonia and Armorica (fig. 3.1; Matte, 2001). They broke away from Gondwana during the early Palaeozoic, prior to docking against Baltica and Laurentia before the Devonian-Carboniferous collision (Matte, 2001).

A contemporaneous system of transpressive shear zones with opposite kinematics in the western and eastern sector of the belt were present and suggests that, as proposed by Matte (2001), García-Navarro and Fernández (2004) and Pereira *et al.* (2008), the European Variscan Belt formed and evolved in a manner analogous to the indentation model proposed for the Himalaya by Tapponier and Molnar (1977) and Tapponier *et al*. (1982).

According to the two plates model the European Variscan belt is the result of the exclusive interaction of Gondwana and Laurentia-Baltica (Kroner and Romer, 2013) and its complexity is the result of the distribution of crustal domains of contrasting rheological properties. Collision of the two plates resulted in an initial subduction accretion process with the formation of many subduction zones affecting mainly the extended Armorican crust, which was an integral part of the Gondwana plate (Kroner and Romer, 2009; Kroner and Romer, 2013; Kroner *et al.*, 2016). Despite the differences, this model also considers the evolution of a belt characterized by indentation tectonics and transpressional deformation (Kroner and Romer, 2009; Kroner *et al*., 2016).

Major exposures of Variscan units occur in Central and Western Europe (fig. 3.2), parts of Morocco and Algeria and north of the West-African Craton.

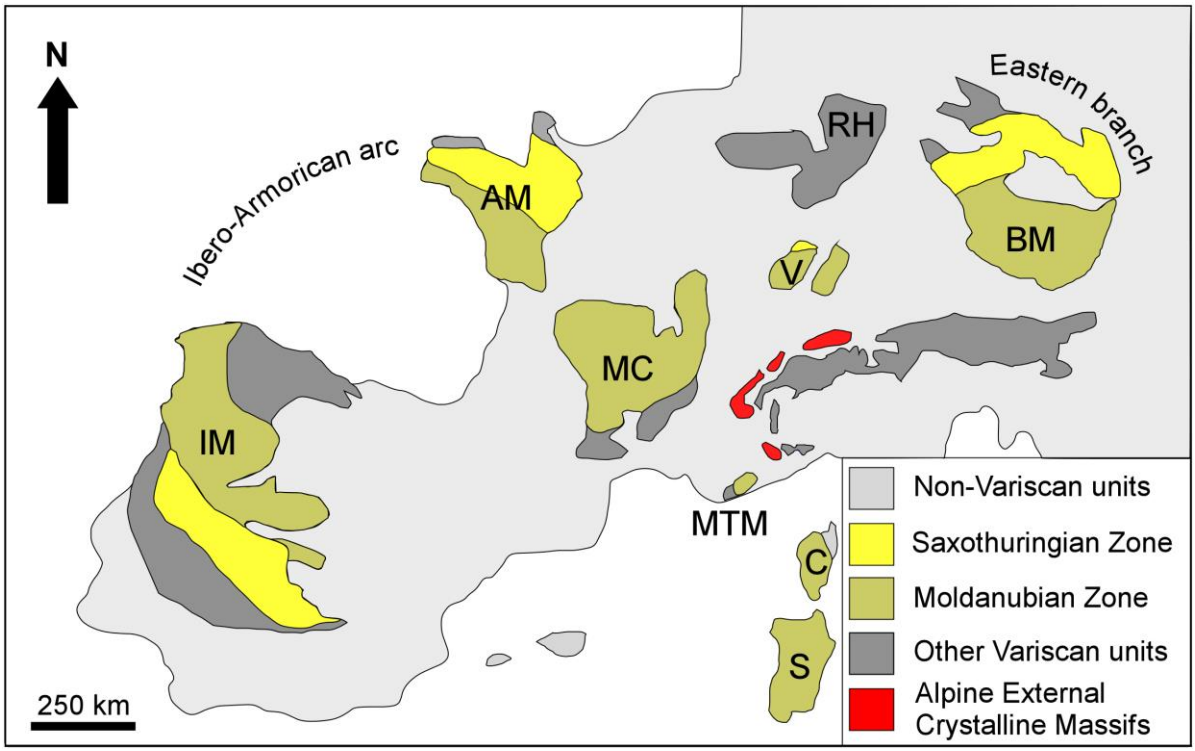

Figure 3.2 - Distribution of the Variscan units in Europe at the present day. S = Sardinia; C = Corsica; MTM = Maures-Tanneron Massif; MC = Massif Central; IM = Iberian Massif; AM = Armorican Massif; RH= Rheno-Hercynian; BM = Bohemian Massif; V = Vosges. Blue circle indicates the location of the Argentera Massif (modified after Compagnoni *et al.*, 2010)

The portion of the belt exposed in Central and Western Europe is known in the literature as the Variscides (figs. 3.2, 3.3). This is the sector that recorded the longest history of the whole belt (fig. 3.3). Here the architecture of the belt is well defined (Matte, 2001; Fluck *et al.*, 1991; Ballèvre *et al.*, 2009; Faure *et al.*, 2009; Skrzypek *et al.*, 2012): the Saxothuringian Zone (southwestern Iberian Massif, northern Armorican Massif, Vosges and Bohemian Massif) and the Moldanubian Zone (southern Iberian Massif, central and southern Vosges, Massif Central, southern Armorican Massif and southern Bohemian Massif) are recognized (fig. 3.2). The Moldanubian Zone is considered as the metamorphic root of the Variscan belt (Schulmann *et al*., 2009).

The Variscides are characterized by a composite orocline showing two large scale arcs (Matte, 1986b; Matte and Ribeiro, 1975): a western branch known as the Ibero–Armorican arc (Matte and Ribeiro, 1975; Brun and Burg, 1982; Dias and Ribeiro, 1995; Dias *et al.*, 2016; Fernández-Lozano *et al.*, 2016) and a smaller eastern branch (Matte, 2001; Bellot, 2005; Ballèvre *et al.*, 2018; Simonetti *et al.*, 2018; Simonetti *et al.*, submitted). The south-eastern sector of the Variscides underwent reworking and fragmentation during the Alpine Orogeny. Because of this, reconstruction of the southern European Variscan belt and the correlation between

the different fragments in the Mediterranean area is a matter of debate (Stampfli *et al.*, 2002; Rosenbaum *et al.*, 2002; Advokaat *et al.*, 2014). Key areas for understanding the evolution of the southern European Variscan Belt are the Maures-Tanneron Massif in southern France, the Corsica-Sardinia Block and the Alpine External Crystalline Massifs (fig. 3.2). Some authors proposed that, during Variscan time, the future Alpine External Crystalline Massifs were in lateral continuity with southern France and Corsica-Sardinia Block and all these sectors were affected by a transpressive regional-scale shear zone known as East Variscan Shear Zone (EVSZ; Matte, 2001; Corsini and Rolland, 2009; Carosi *et al.*, 2012; Simonetti *et al.*, 2018). Evidence for transpressional deformation is well-documented in northern Sardinia (Carosi and Palmeri, 2002; Frassi *et al.*, 2009; Iacopini *et al.*, 2008; Iacopini *et al.*, 2011; Carosi *et al.*, 2012) in the Maures Massif (Schneider *et al.*, 2014; Simonetti *et al*. Submitted) and in the Alpine External Crystalline Massifs (Carosi *et al.*, 2016; Simonetti *et al.*, 2018), in places were the Alpine metamorphic overprint is very weak.

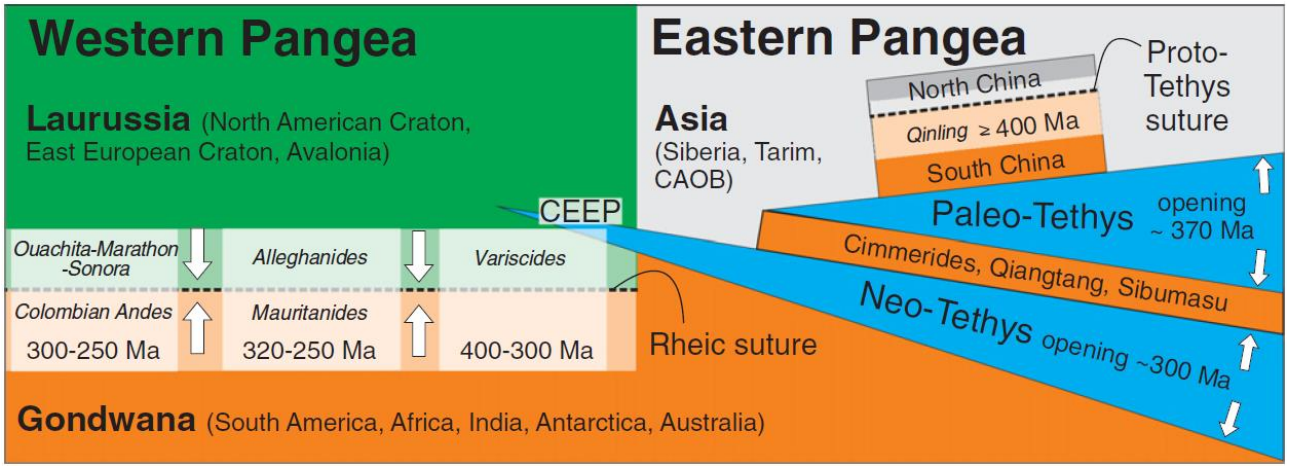

Figure 3.3 - Schematic illustration of the assembly of the supercontinent Pangea. Central Asian Orogenic Belt; CEEP — Central European Extensional Province (from Kroner *et al.*, 2016)

4. External Crystalline Massifs

The External Crystalline Massifs (ECM; Mont Blanc, Aiguilles Rouges, Belledonne, Pelvoux, Aar-Gothard and Argentera) crop out west of the Penninic front and belong to the Helvetic-Dauphinois domain of the Alps (fig. 4.1).

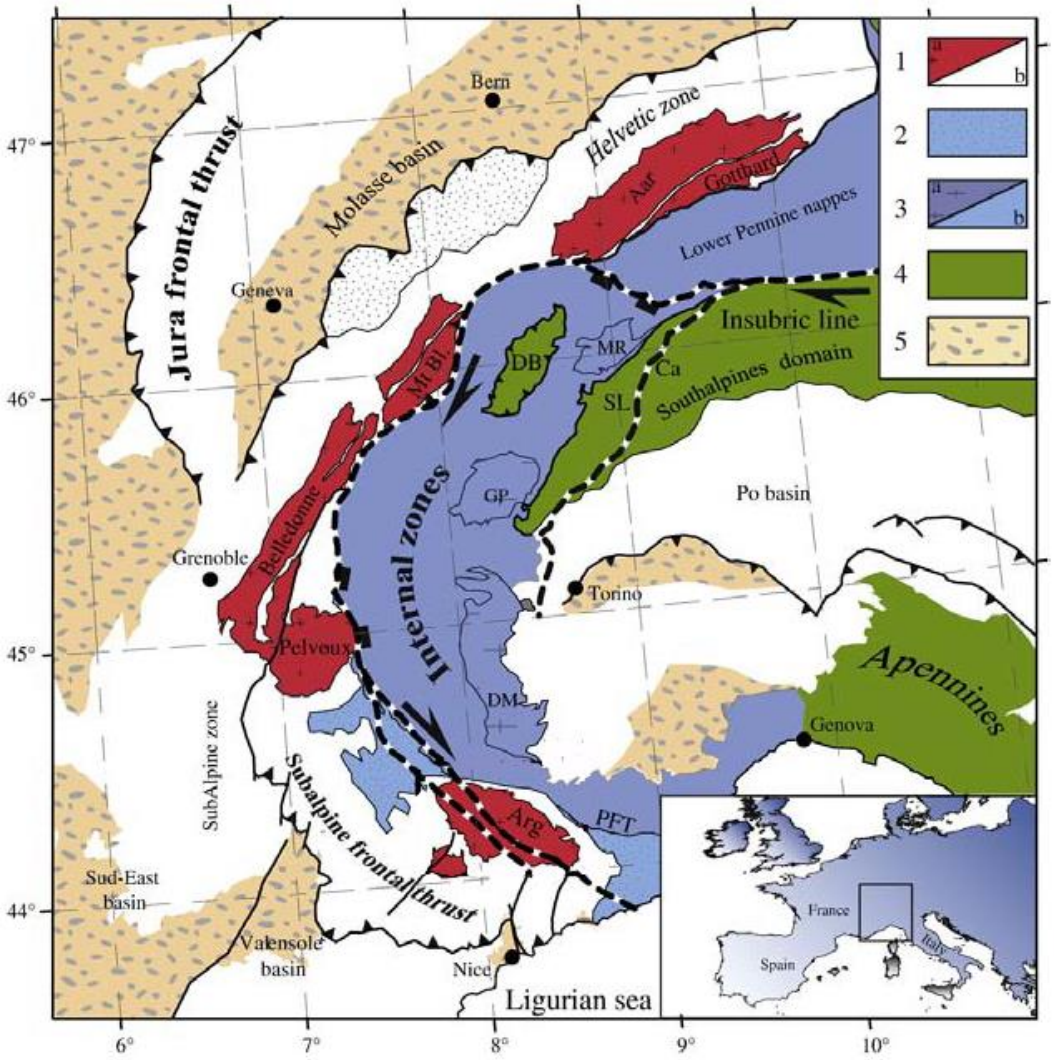

Figure 4.1 - Geological map of the Western Alps (modified after Bigi *et al*., 1990; Polino *et al*., 1990; Sanchez *et al*., 2011). 1 = Dauphinois zone, it comprises the External Crystalline Massifs (1a) and their Mesozoic (Trias-Cretaceous) sedimentary cover (1b); 2 = Upper Cretaceous Helminthoid flysch; 3 = Briançonnais and Piemontais zones: metamorphic rocks from the European passive continental margin (3a) and the Tethyan oceanic domain (3b); 4 = Austro-Alpine domain; 5 = Oligocene to Quaternary molasse basins. Black and white dashed lines represent main faults system. Mt Bl. = Mont Blanc; Arg = Argentera Massif; DM = Dora-Maira; GP = Grand Paradis; MR = Monte Rosa; PFT: Penninic Frontal Thrust; Ca: Canavese line; DB = Dent Blanche; SL = Sesia Lanzo zone

They represent fragments of the south-eastern sector of the Variscan belt with Gondwanian affinity. This sector of the Variscan belt was subsequently fragmented and partially overprinted by Alpine Orogenesis

during which the ECM represented the European basement. Because of this, the position of the ECM during Variscan time in relation to the other preserved fragments of the belt in the Meditrerranean area, is still a matter of debate. According to some authors they should have been in southward lateral continuity with the Maures-Tanneron Massif and with the Corsica-Sardinia Block (Rollet *et al.*, 2002; Rosenbaum *et al.*, 2002; Advokaat *et al.*, 2014), while according to Stampfli *et al.* (2002), Turco *et al.* (2012) and Von Raumer *et al.* (2013), the Corsica-Sardinia Block was located in a more westerly position connected to Iberia and therefore, away from southern France and the ECM.

The ECM are made by a high-to-medium grade metamorphic basement intruded by Permo-Carboniferous granoitoids (fig. 4.2).

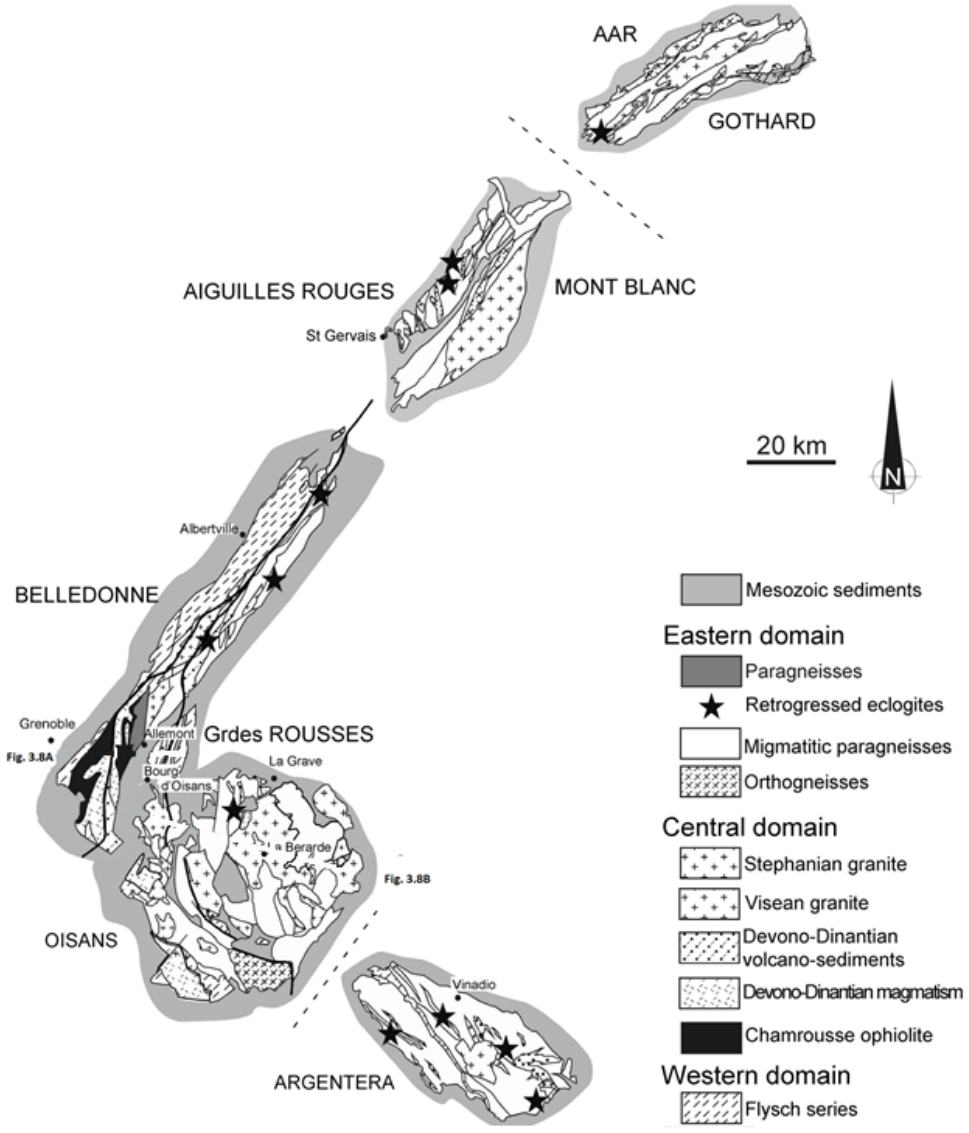

Figure 4.2 – Geological sketch maps of the External Crystalline Massifs (modified after Guillot *et al.*, 2009)

They are often cross-cut by km-scale shear zones (such as for example the Ferriere-Mollières shear zone in the Argentera Massif and the Angle Fault in the Aiguilles Rouge Massif) whose age of activity and deformation regime are not always well-constrained. It is also not clear whether these shear zones have been fully reactivated during the Alpine orogeny, or if evidence of Variscan deformation is still preserved.

However in these Massifs, the Alpine metamorphic overprint is generally weak and commonly limited to shear zones. In the Pelvoux Massif Fernandez *et al.* (2002) recognize an external migmatitic portion to the east and a western portion characterize by a low metamorphic grade. Migmatites are also present in the Mont Blanc, Aiguilles Rouge and Argentera Massifs, here anatexis is dated with U-Th-Pb method on monazite at ~320 Ma (Debon and Lemmet, 1999; Rubatto *et al.*, 2001; Compagnoni *et al.*, 2010).

Eclogitic relicts were found in the Belledonne Massif (fig. 4.2) and were dated at 390 ± 8 Ma (U-Pb on zircon; Paquette *et al*., 1989). In the Argentera Massif HP granulites and retrogressed eclogites (fig. 4.2) are present. U-Pb dating on zircons suggests protolith ages for the mafic intrusions ranging between 459 ± 4 Ma (Meris eclogite, Rubatto *et al*., 2001) and 486 ± 7 Ma (Laghi del Frisson, Rubatto *et al*., 2010). Retrogressed eclogites are also present in the Aiguilles Rouges Massif in the Val Bérard (fig. 4.2) and in the Aar and Pelvoux Massifs (fig. 4.2).

From the point of view of tectonics and deformation, Grandjean *et al*. (1996) recognized in the Belledonne Massif a transpression deformation regime dated at 324 ± 12 Ma (K-Ar on horneblende). In the same Massif Guillot *et al*. (2009) highlighted that most of the deformation is coupled with the emplacement of syn-kinematic granitoids along N-S oriented system of shear zones that can be followed along the Massif taking into account their position. A Variscan transpressional deformation regime is also recognized in the Argentera Massif (Compagnoni *et al*., 2010; Carosi *et al*., 2016; Simonetti *et al*., 2018) and in the Aiguilles Rouge (Von Raumer and Bussy, 2004; Compagnoni *et al*., 2010).

The southern part of the Western Alps, and therefore the southern ECM, suffered large counterclockwise rotations, up to 117° relative to stable Europe, since the Oligocene (Collombet *et al.*, 2002). The final exhumation of the External Crystalline Massifs initiated in the Miocene (Bigot-Cormier et al., 2006; Baietto *et al.*, 2009), at the end of the Alpine orogeny.

4.1 Argentera Massif

4.1.1 Introduction

In the present chapter we focus on the northern sector of the Ferriere-Mollières shear zone (FMSZ; Faure-Muret, 1955; Malaroda *et al*., 1970; Compagnoni *et al*., 2010), a km-scale shear zone located in the Argentera Massif close to the boundary between Italy and France (fig 4.3). This shear zone was studied where it reaches its maximum thickness, of nearly 2 km, between the Ferriere valley and the Ischiator valley.

Two structural-geological maps, based on the same legend, at the 1:10000 scale were produced: the first map falls between Ferriere valley to the North, and Piz valley to the south (appendix B); the second covers the area of the higher part of the Ischiator valley (appendix C). The topographic base is a vector topographic map (Carta Tecnica Regionale – Regione Piemonte).

The aim of this chapter is to clarify both the kinematics of flow and age of activity on the FMSZ.

Sample locations are reported in the sketch maps of figure 4.4. A list of only the samples used for analysis, with the relative position and results, is reported in appendix D.

The structural-geological map that covers the area between Ferriere valley and Piz valleys have been published in Journal of Maps (DOI: 10.1080/17445647.2016.1243491) with the title "*Geological map of the northwestern portion of the Ferriere-Mollieres shear zone, Argentera Massif, Italy*".

Furthermore, the structural analysis, the study of kinematic vorticity with the C' shear band method, the strain analysis and the petrochronological study with the LA-ICP-MS have been published in International Journal of Earth Science (DOI: 10.1007/s00531-018-1593-y) in a paper with the title "*kinematic and geochronological constraints on shear deformation in the ferriere-mollières shear zone (Argentera-Mercantour Massif, Western Alps): implications for the evolution of the Southern European Variscan Belt*".

A guide for a field trip with the aim to visit some key outcrops that allow to recognize the evolution and the features of both Variscan and Alpine deformation in the FMSZ is presented in the appendix E. The field guide is accepted for publication as a chapter of the volume "Structural Geology & Tectonics Field Guidebook (Springer)". A similar guide is published in the *Atti della Società Toscana di Scienze Naturali* (DOI: 10.2424/ASTSN.M.2017.25) with the title "*Variscan shear deformation in the Argentera Massif: a field guide to the excursion in the Pontebernardo Valley (CN, Italy)*".

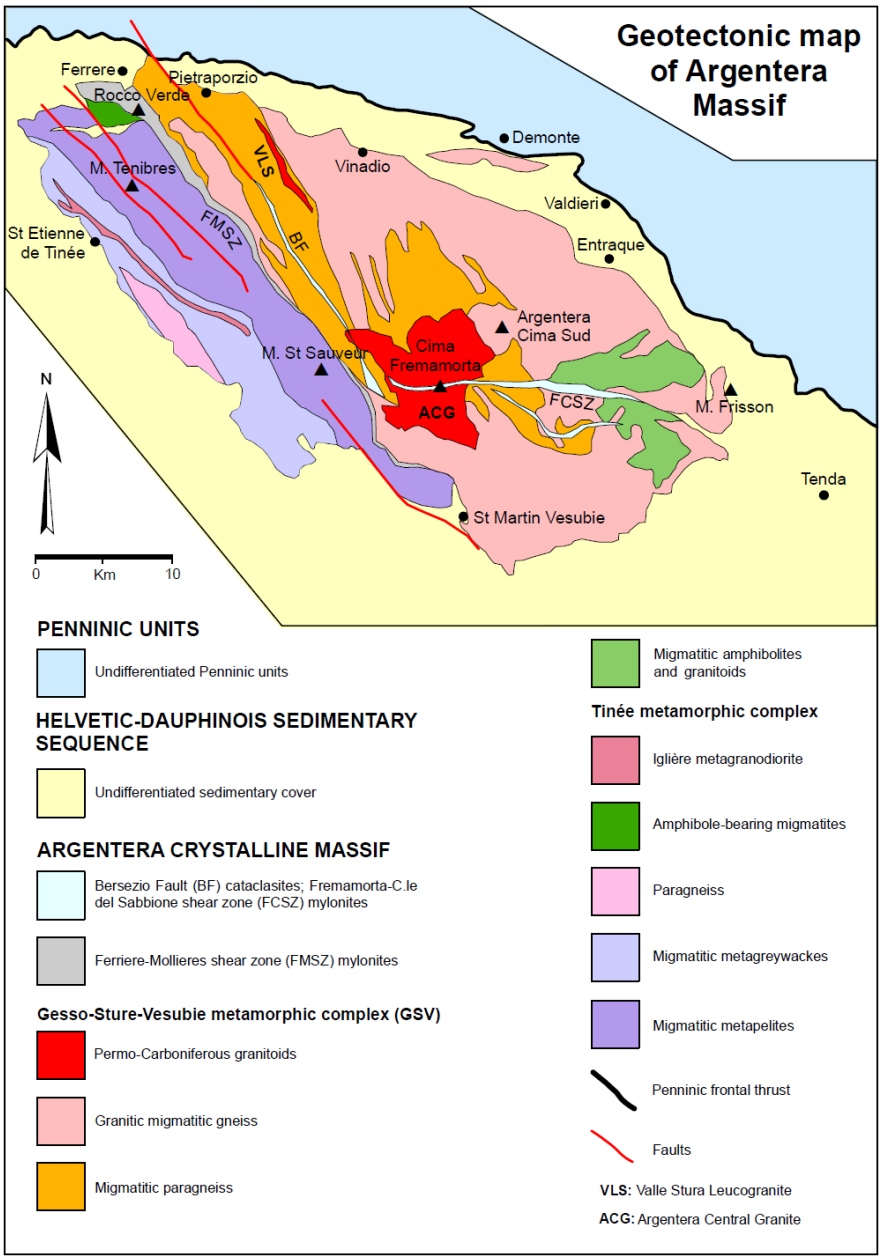

Figure 4.3 – Geological map of the Argentera Massifs (modified after Compagnoni *et al*., 2010)

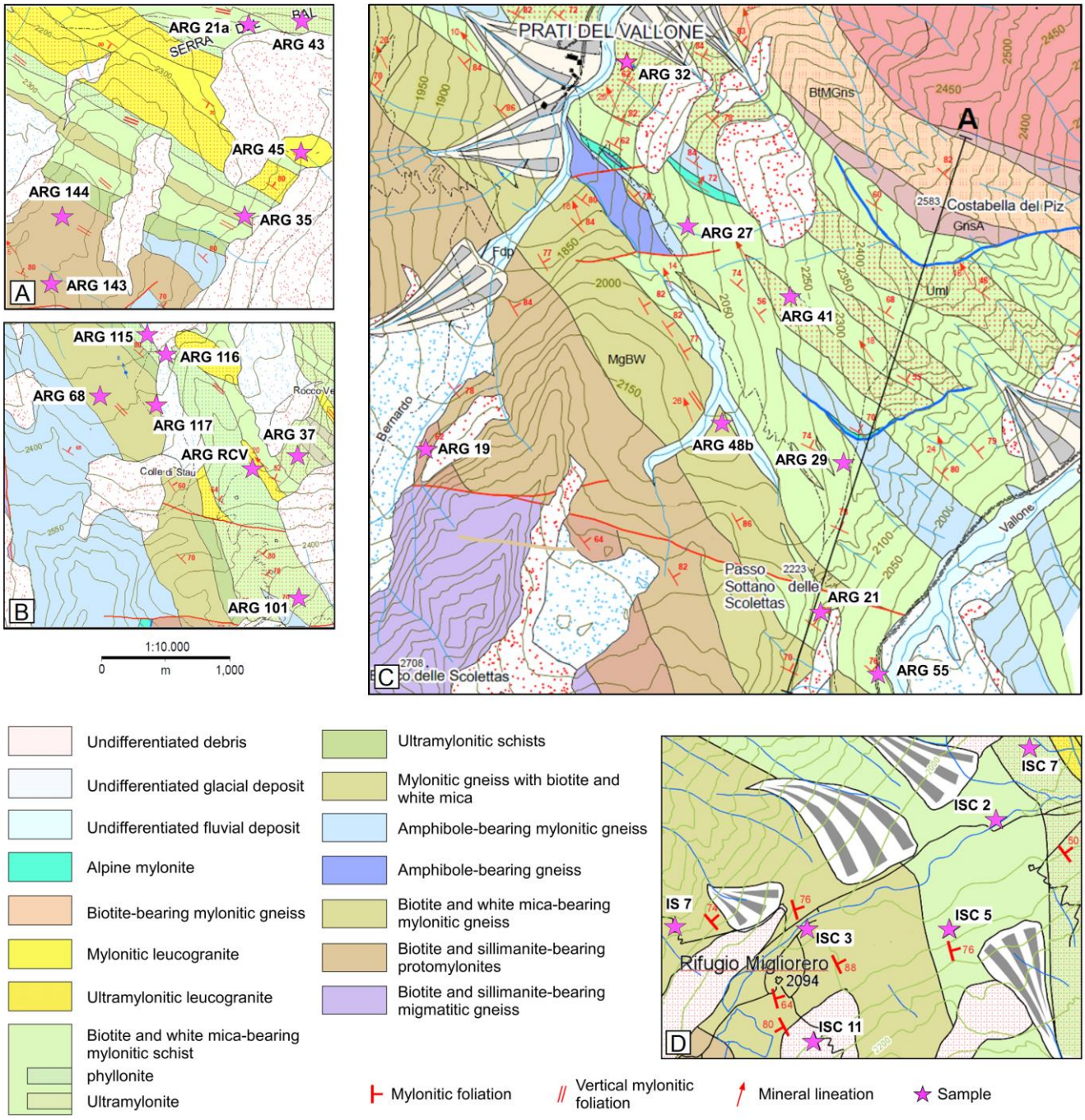

Figure 4.4 – Detailed geological maps of the main sampling locations of the FMSZ: A) Serra del Ball area in the Ferriere Valley; B) Colle di Stau area; C) Prati del Vallone area in the Pontebernardo Valley; D) Rifugio Migliorero area in the Ischiator Valley; cross-section A is reported in figure 4.10

4.1.2 Geological setting

The Argentera-Mercantour Massif is composed of the Gesso-Stura-Vésubie (GSV) and the Tinée (TMC) metamorphic complexes (Malaroda *et al*., 1970; Compagnoni *et al*., 2010) which are separated by the Ferriere-Mollières Shear Zone (FMSZ; fig. 4.3).

The GSV complex is made of migmatitic gneiss derived from Late Ordovician granitoids and migmatitic paragneiss. Ferrando *et al.* (2008) and Compagnoni *et al*. (2010) recognized a metamorphic evolution characterized by: 1) HP metamorphic peak; 2) initial decompression stage; 3) HT–MP amphibolite-facies metamorphism; 4) LT–LP amphibolite-facies metamorphism.

The TMC migmatites resulted from partial melting of metasediments. Eclogite relicts are reported by Faure-Muret (1955) and Malaroda *et al*. (1970). According to Compagnoni *et al*. (2010) the TMC has a smaller amount of melting than the migmatites of the GSV complex as testified by a smaller proportion of leucosomes. A greenschist facies imprint is mainly due to a system of ductile to brittle-ductile shear zones (Baietto *et al*., 2009) affecting the whole Argentera-Mercantour Massif (Corsini *et al.*, 2004; Sanchez *et al.*, 2011). The main Alpine faults of the Argentera-Mercantour Massif are the NW-SE Bersezio Fault Zone (fig. 4.3), in the central part, and the E-W Fremamorta-Colle Sabbione Shear Zone (fig. 4.3), in the southernmost part of the massif.

The FMSZ (also known as Valletta shear zone; Corsini *et al*., 2004) strikes NW–SE and extends for about 20 km with a thickness between 100 m to the south-east and more than 1000 m to the north-west. The fault rocks in the FMSZ resulted from the shearing of migmatites of the GSV and the TMC. The transition from non-sheared migmatites to protomylonites, mylonites and ultramylonites can be observed along a gradient of increasing deformation traced towards the center of the shear zone (fig. 4.5; Carosi *et al*., 2016).

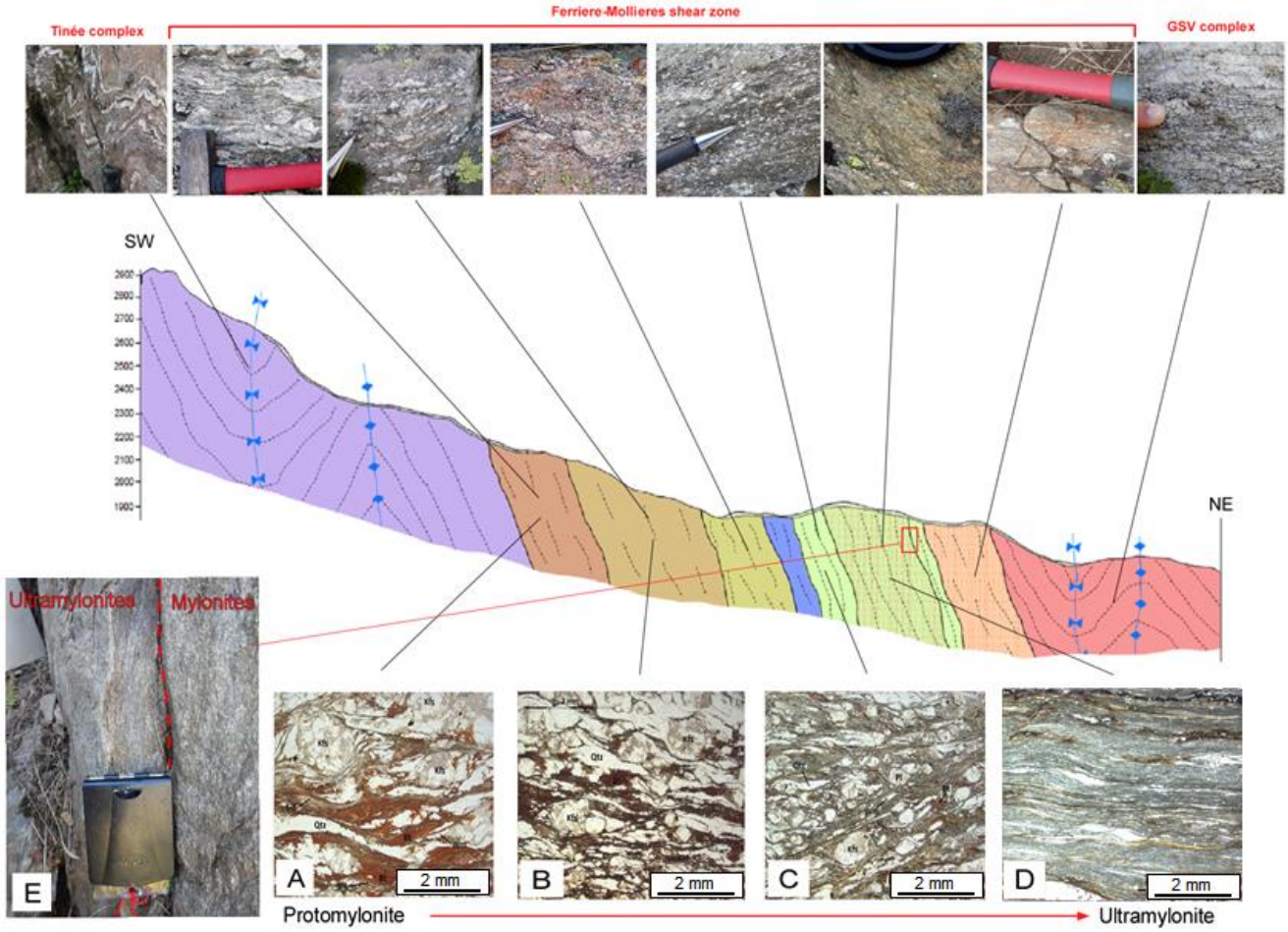

Figure 4.5 - Cross-section (section B, appendix B) of the FMSZ along the Pontebernardo valley (modified after Carosi *et al*., 2016). Legend is the same as in figure 3. Tinée migmatites are represented in violet and amphibole-bearing migmatitic gneiss are represented in blue. GSV migmatites are represented in red. With the various shades of brown, green, and orange are represented the different types of mylonites belonging to FMSZ. In both the metamorphic complexes axial planes of the syn-shear zone folds are represented in blue. The transition from unsheared lithotypes of the two metamorphic complexes to the FMSZ mylonites and ultramylonites is clearly visible both at the outcrop scale and in thin section. A) protomylonites (parallel nicols); B,C): mylonites (parallel nicols); D) ultramylonites (crossed nicols); E) contact between mylonites and ultramylonites

The rocks in the shear zone are medium-grained dark mylonitic schists with biotite and white mica ± garnet. Mylonites and ultramylonites with chlorite and white mica also occur in the central part of the shear zone while mylonites and protomylonites with biotite and sillimanite ± garnet are present in the margins of the shear zone. Because of the constant orientation of the mylonitic foliation, the mineral lineation and the sense of shear in all the rocks inside the FMSZ, Carosi *et al*. (2016) interpreted the paragenesis as being associated with progressive deformation in decreasing temperature conditions.

4.1.3 Structural and microstructural analysis

Ferrier-Mollières Shear Zone

The structural elements of the FMSZ and of the adjacent metamorphic complexes in relation to the deformation phase during which they have developed are shown in table 4.1.

The main structural elements in the FMSZ are a mylonitic foliation (Sm) defined by the preferred orientation of biotite + white mica and a protomylonitic foliation with biotite + sillimanite in the external part of the shear zone, both striking N100-140 and steeply dipping towards the northeast or the southwest (fig. 4.6a, b, c). A mineral lineation (Lm), defined by a preferred alignement of stretched quartz and feldspar, trends N110-130 and plunges at 20° towards the northwest (fig. 4.6a, b, c). Intrafolial isoclinal folds (Fm) are sometimes recognizable. The mylonitic foliation (Sm) underwent a post-shearing gentle folding (Fm+1) with sub-horizontal axial planes. Although this deformation event is not associated with a ductile pervasive axial plane foliation at the outcrop scale, a crenulation cleavage is sometimes exhibited.

	PRE-SHEAR ZONE DEFORMATION	SYN-SHEAR ZONE DEFORMATION	POST-SHEAR ZONE DEFORMATION
FMSZ	-	mylonitic foliation (Sm); lineation (Lm); syn-shear zone folds (Fm);	post-shearing gentle folding (Fm+1); alpine mylonitic foliation (Sa); alpine mineral lineation (La)
GSV complex	relict foliation (Sp-1)	axial plane foliation (Sp); tight folds (Fp);	alpine mylonitic foliation (Sa); alpine mineral lineation (La)
Tinée Complex	relict foliation (Sp-1)	axial plane foliation (Sp); tight folds (Fp);	alpine mylonitic foliation (Sa); alpine mineral lineation (La)

Table 4.1 - Structural elements of the FMSZ and of the adjacent metamorphic complexes in relation to the deformation phase during which they have developed (from Carosi *et al*., 2016)

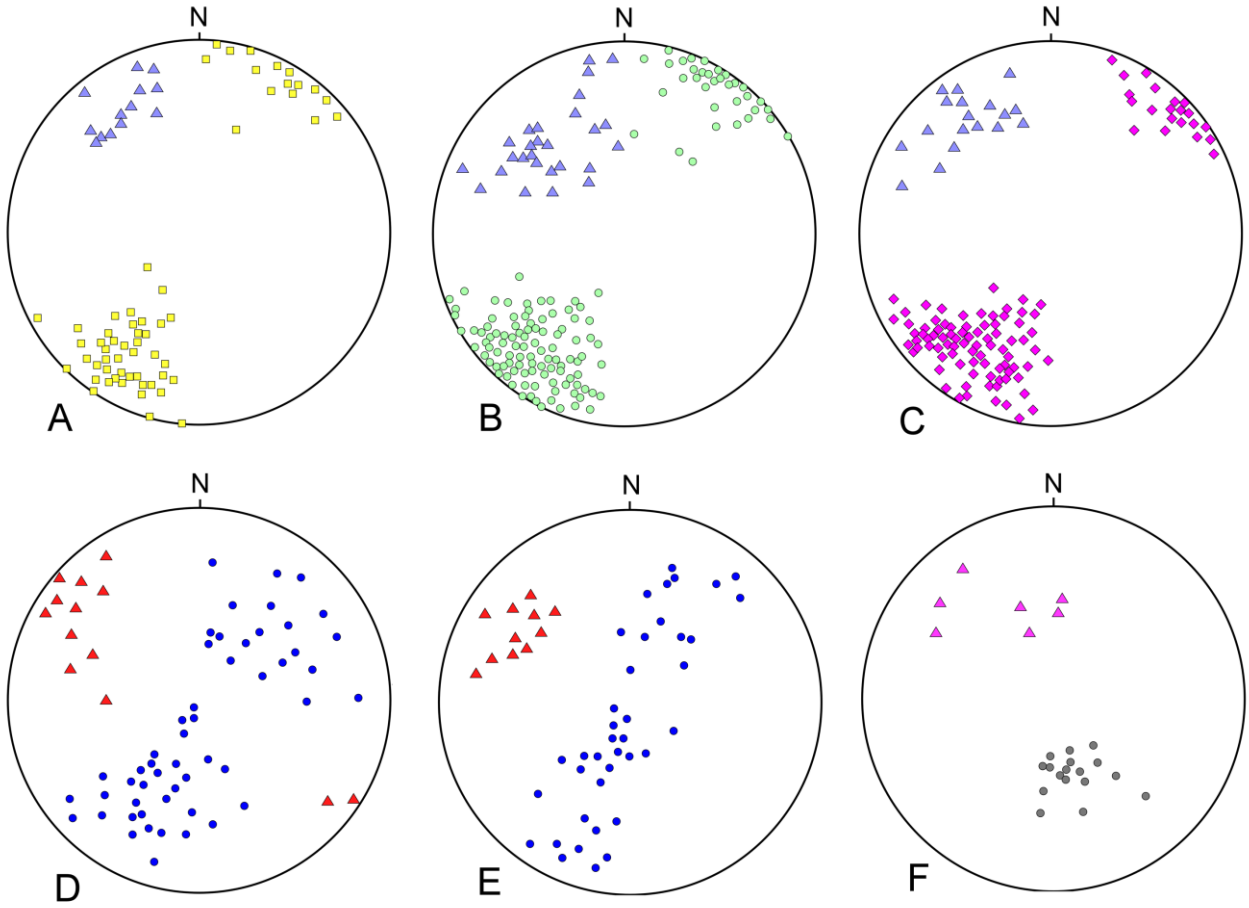

Figure 4.6 - Equal angle, lower hemisphere projections (modified from Carosi *et al*., 2016 and Simonetti *et al*., 2018): A) poles to Sm foliation (yellow squares, 60 data) and Lm mineral lineation (blue triangles, 13) in the ultramylonitic schists; B) poles to Sm foliation (green dots, 163 data) and Lm mineral lineation (blue triangles, 27 data) in the mylonitic schists; C) poles to Sm foliation (pink diamonds, 110 data) and Lm mineral lineation (blue triangles, 18 data) in the protomylonitic gneiss; D) poles to Sp-1 foliation (blue dots, 53 data) and fold axis (red triangles, 13 data) in the Tinèe complex; E) poles to Sp-1 foliation (blue dots, 39 data) and fold axis (red triangles, 11 data) in the Gesso-Stura-Vesubie complex; F) poles to Sa mylonitic foliation (grey dots, 17 data) and La mineral lination (pink triangles, 7 data) in the alpine shear zones

In protomylonites the foliation is an anastomosing disjunctive cleavage (Passchier and Trouw, 2005) formed by alternating coarse-grained layers of deformed quartz and feldspar and biotite- and sillimanite-rich layers (fig. 4.7a,b). Sillimanite occurs both in prismatic and fibrolitic habits. In the mylonites, a transition can be observed from a disjunctive cleavage with sub-parallel cleavage domains, formed by alternating layers of deformed quartz and biotite + white mica (fig. 4.7c,d), to a continuous cleavage in the most intensely deformed ultramylonites rich in phyllosilicates (fig. 4.7e, f). The mylonitic foliation underwent a later gentle folding of uncertain age with axial planes moderately dipping toward the SW and NW-SE trending axes. Kinematic indicators (S-C' fabric, micafish, mantled porphyroclasts and quartz oblique foliation) indicate a strike-slip component of movement with a minor reverse, top-to-the-SE, component where the foliation dips

northeast (fig. 4.8a,b,c) and with a minor normal component where it dips southwest. Quartz shows subgrain rotation recrystallization (Piazolo and Passchier, 2002; Stipp *et al.*, 2002) and only very minor effects of grain boundary migration in mylonites (fig. 4.8d) and ultramylonites. Quartz in protomylonites is mainly affected by grain boundary migration (Piazolo and Passchier, 2002; Stipp *et al*., 2002). Feldspar shows undulose extinction due to ductile deformation (fig. 4.8e) and does not show evidence of brittle deformation in the mylonites and protomylonites.

Sometimes in the ultramylonites and in the mylonites, is possible to observe extensional or hybrid fractures filled with quartz fibres (fig. 4.9a, b) and en echelon veins (fig. 4.9c). They are oriented NNE-SSW. At least two group of filled fractures were recognized: the first type cross-cut at high angle the main foliation (fig. 4.9a, d) and in some cases are subsequently shortened; the second type is transposed, rotated and stretched and strikes parallel to the main the main foliation forming quartz-rich domains of recrystallized grain with evidence of subgrain rotation recrystallization (fig 4.9e, f).

The thickness of the FMSZ progressively decreases from NW to SE. The maximum thickness of ~2 km is reached to the NW, in the Ferriere village area (fig. 4.4). Thickness variations of the different types of mylonites, at a local scale, were also reported (Carosi *et al*., 2016).

In the wall rocks of the FMSZ, in the GSV and TMC complex, Carosi *et al*. (2016) and Simonetti *et al.* (2017, 2018) recognized a relict foliation (Sp-1) that is deformed by outcrop-scale open to tight symmetric upright folds (Fp) with NW plunging axis (fig. 4.5d, e) in which the axial planar foliation (Sp) strikes NW-SE and is parallel to the mylonitic foliation (Sm).

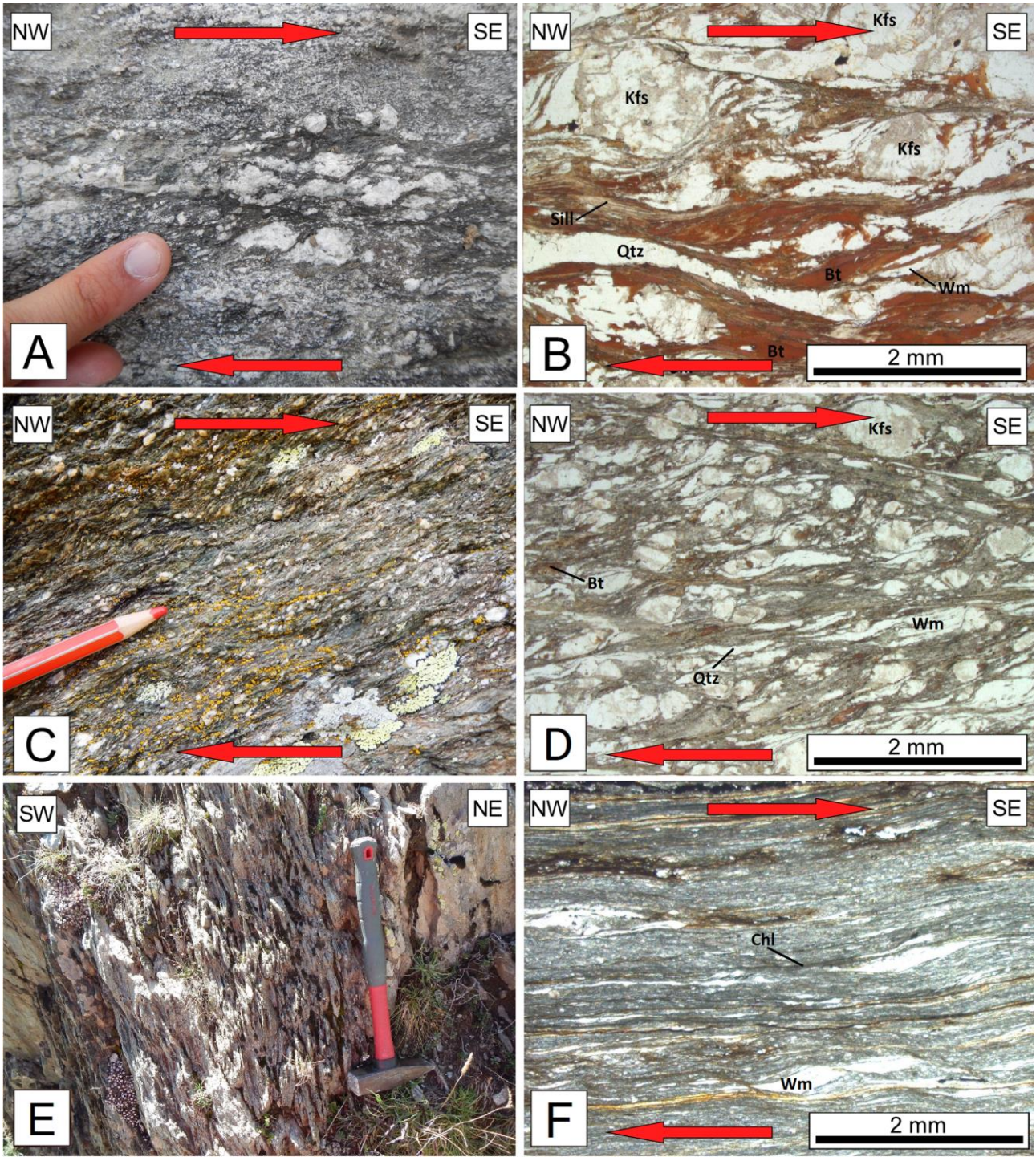

Figure 4.7 – FMSZ: A) protomylonites at the outcrop-scale; B) anastomosing disjunctive cleavage in protomylonites. It is possible to recognize K-feldspar, plagioclase and quartz in a medium grained biotite and sillimanite matrix with some white mica (plane-polarized light); C) mylonites at the outcrop-scale; D) disjunctive cleavage with sub-parallel cleavage domains in mylonites. Quartz, K-feldspar and plagioclase porphyroclasts in a fine grained biotite and white mica matrix are recognizable (plane-polarized light); E) ultramylonites at the outcrop-scale; F) continuous cleavage marked by white mica and chlorite in ultramylonites (plane-polarized light)

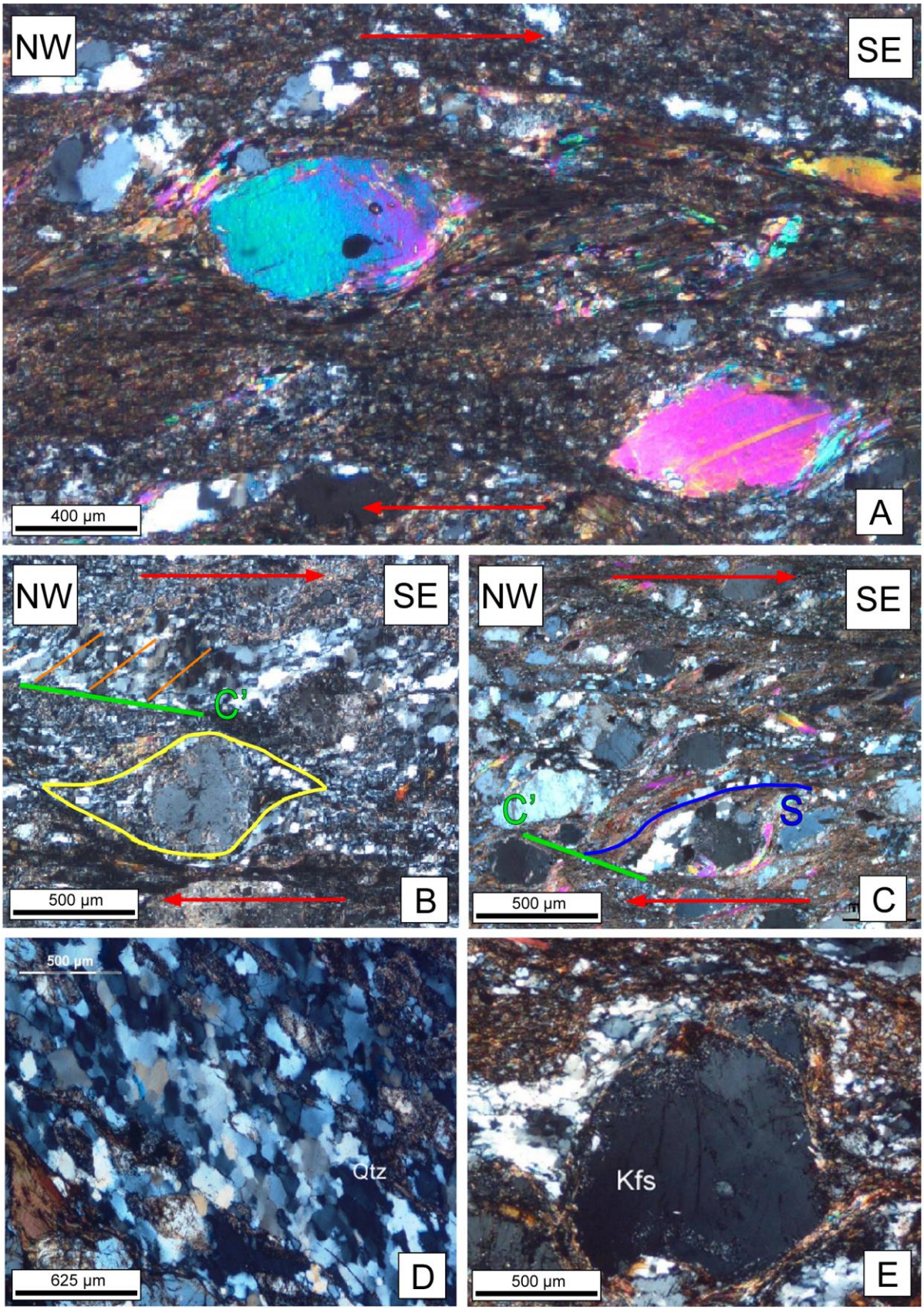

Figure 4.8 - Micrographs (crossed polars) of the kinematic indicators showing a top-to-the-SE sense of shear in the FMSZ. The short and the long borders of each micrograph are parallel to the Z and X axes of the strain ellipsoid, respectively. A) white mica fish and S-C' fabric; B) K-feldspar σ-type porphyroclast (yellow), C' plane (green) and oblique foliation (orange) in quartz level; C) S-C' fabric. D) Subgrain rotation and recrystallization in quartz (crossed polars); E) Undulose extinction in K-feldspar porphyroclasts (crossed polars)

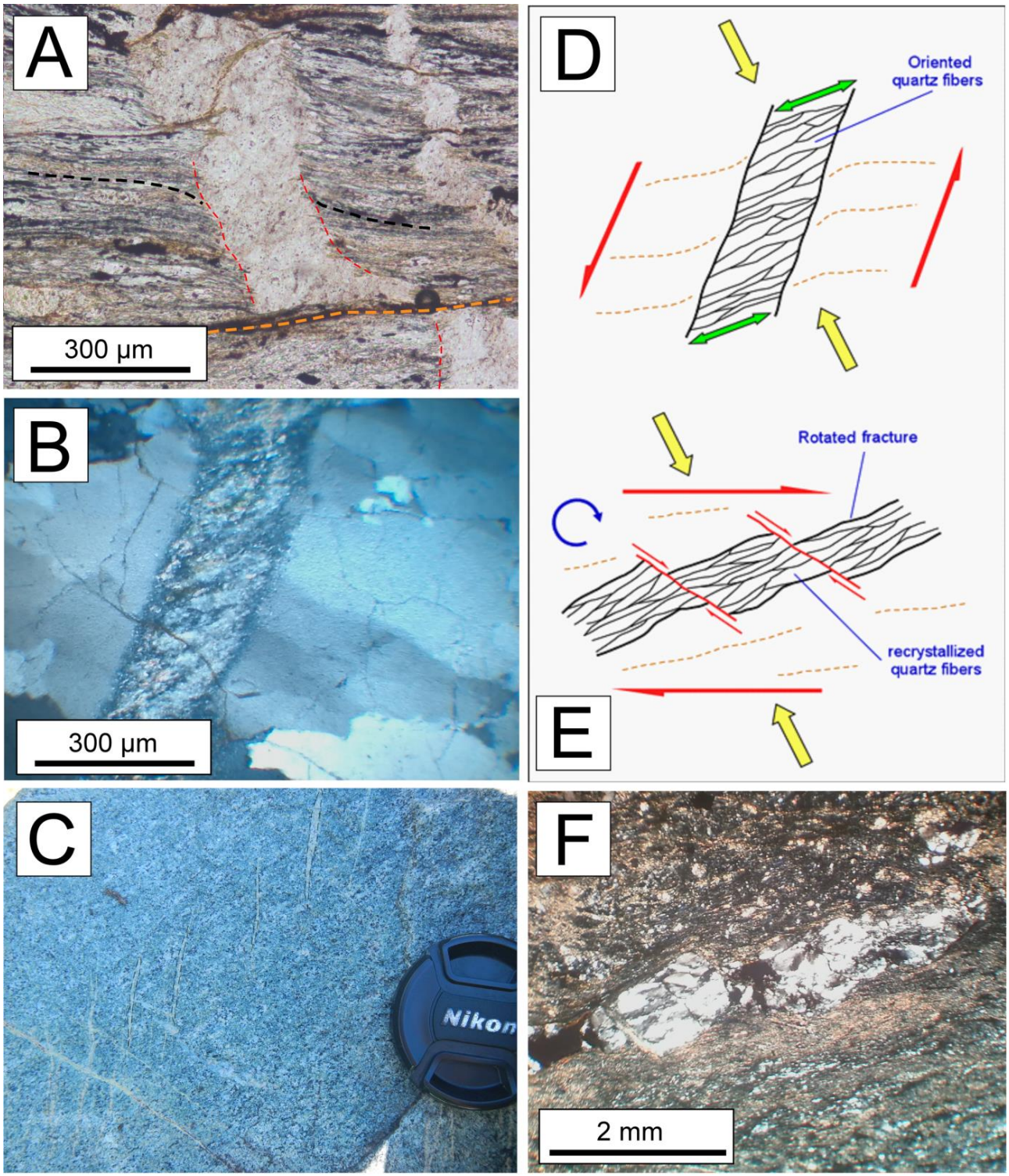

Figure 4.9 – A) hybrid fracture (red) crosscutting the main foliation (black) in a ultramylonite in the Rocco Verde area, the fracture is subsequently shortened or sheared along a plane sub-parallel to the main foliation (orange); B) quartz fibres within a fracture; C) en echelon vains (black) crosscutting the main foliation in the amphibole-bearing mylonitic gneiss; D) sketch of a hybrid fracture crosscutting the main foliation; E) sketch of a transposed and sheared fracture; F) sheared fracture with recrystallized quartz grains

Alpine shear zones and deformation

Shear zones cross-cutting the mylonites of the FMSZ and the migmatites of the two metamorphic complexes have been identified (fig. 4.10). These shear zones have metric to decametric thickness with lateral extents of up to several hundred meters.

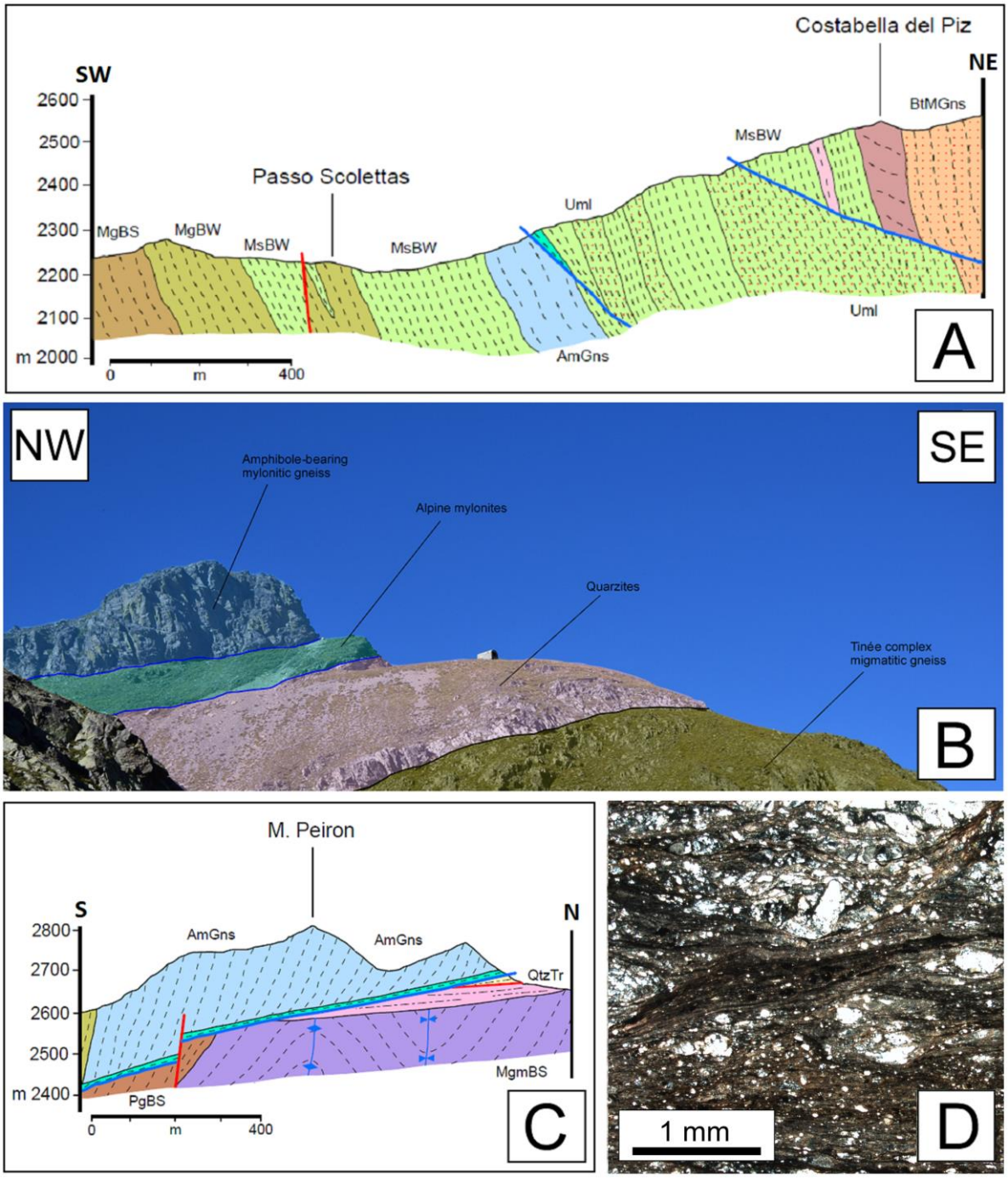

Figure 4.10 - A) cross-section (section A, appendix B) along the crest of the Costabella del Piz (modified after Carosi *et al*., 2016). Legend is the same as in appendix B. Alpine shear zone cross-cutting the mylonitic foliation of the FMSZ are in blue; B) Alpine mylonitic belt, delimited by blue lines, located near the Colle Panieris and M. Peiron (modified after Carosi *et al*., 2016); C) cross-section (part of section C, appendix B) showing the thrusting of basment rocks over the sedimentary cover of the Argentera Massif (modified after Carosi *et al*., 2016). Legend is the same as in appendix B; D) aspect in thin section of the mylonite of the Colle Panieris and Mt Peiron thrust (crossed nicols)

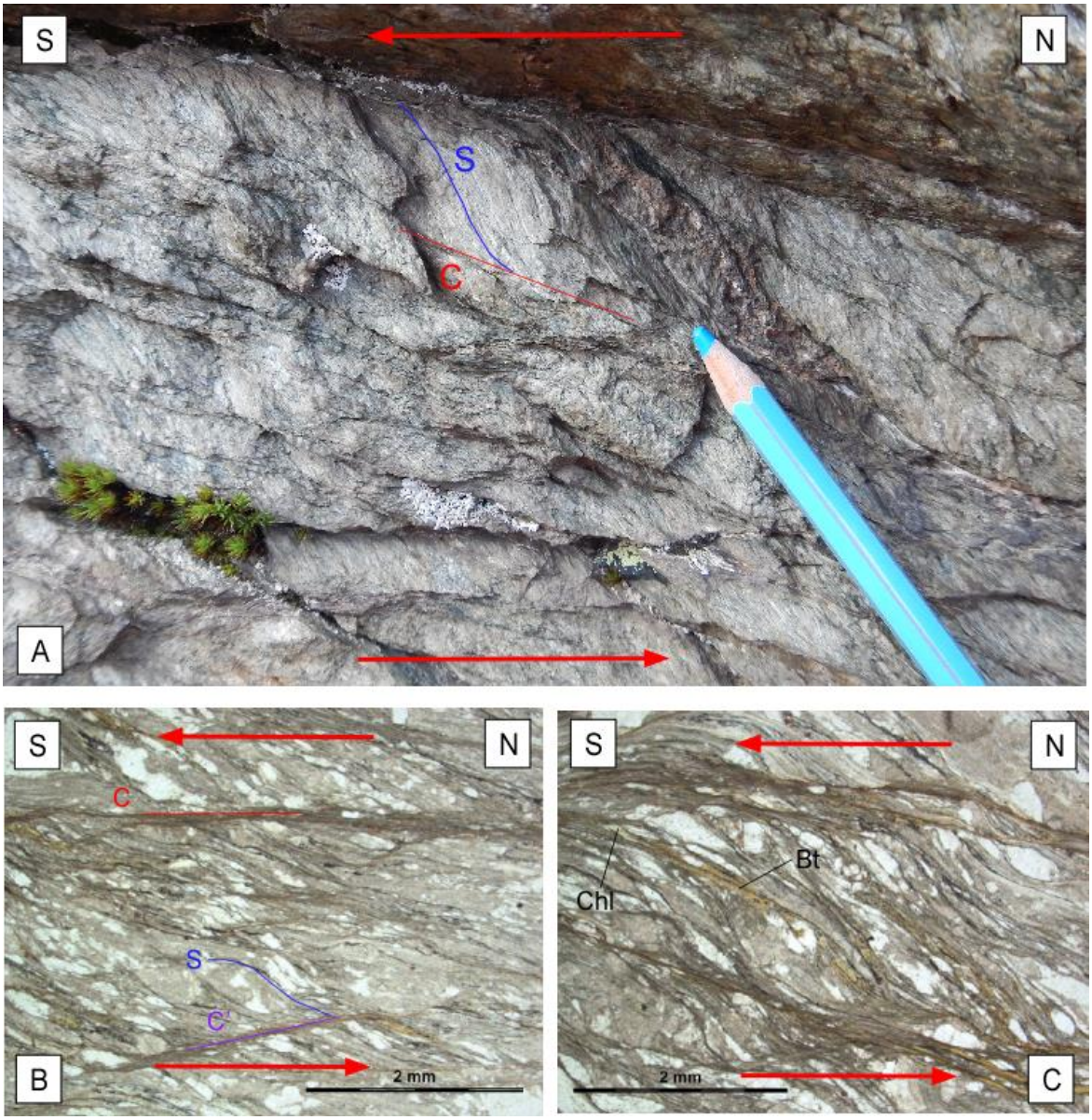

Figure 4.11 - Low-angle Alpine shear zones along the Costabella del Piz crest. A) S-C fabric at the outcrop scale; B) S-C and S-C' fabric in thin section (plane-polarized light); C) Deformed foliation with biotite relicts (plane-polarized light). The short and the long borders of each micrograph are parallel to the Z and X axes of the strain ellipsoid, respectively. All kinematic indicators show a reverse top-to-the-S sense of shear

The best examples of these shear zones are located along the Costabella del Piz crest and near the Colle Panieris and Mt Peiron, in the western part of the studied area (appendix B). The former shear zones cross-cut the sub-vertical mylonitic foliation of the Ferriere-Mollieres mylonites (fig. 4.10a); the latter is responsible for the overthrusting of the lithotypes of the FMSZ above the post-Variscan sediments of the Helvetic-Dauphinois sequence (fig. 4.10b, c, d). Those shear zones consist of fine-grained mylonites (fig. 4.11a) or phyllonites with quartz and feldspar porphyroclasts in a fine-grained chlorite + white mica matrix (fig. 4.11b, c). This paragenesis is indicative of greenschist-facies metamorphism. The proportion of matrix

relative to porphyroclasts is 65-75%. The foliation Sa strikes nearly E-W and dips at moderate to low angles toward the north with a north plunging mineral La lineation (fig. 4.6f).

The foliation is a spaced cleavage defined by the preferred orientation of chlorite and white mica. Kinematic indicators, mainly micafish and S-C and S-C' fabrics, indicate a top-to-the-S reverse sense of shear (fig. 4.11a, b). C and C’ planes are characterized by the presence of fine-grained chlorite. Along the S foliation biotite relicts are sometimes present (fig. 4.11c). Quartz shows undulose extinction, subgrains and new grains, the latter indicating subgrain rotation recrystallization (Piazolo and Passchier, 2002; Stipp *et al*., 2002) as the dominant deformation mechanism. Feldspar shows undulose extinction and deformation lamellae while some fractured porphyroclasts are also present.

Outside the FMSZ, the Tinée and GSV complexes are cross-cut by low-temperature ductile, brittle-ductile and brittle deformation. The main evidence is the presence of chlorite-rich brittle-ductile shear planes (fig. 4.12a) or metric-size shear zones (fig. 4.12b) made of mylonites cross-cutting Variscan foliation (fig. 4.12c). They are oriented N-S or E-W with a top-to-the-S sense of shear (fig. 4.12d) associated with a strike slip or reverse movement respectively. In the area of the St. Anna di Vinadio sanctuary, brittle shear planes of metric length and centimetric thickness are characterized by the presence of cataclasites (fig. 4.12e), formed at the expense of GSV migmatites, and by possible pseudotachilites. They appear as dark veins injected into the wall rock from the shear plane (fig. 4.12f). Unfortunately, despite the very characteristic shape, it was not possible to recognize in thin section evidence of quenched melt probably because of the effect of subsequent recrystallization, hydration and alteration that obliterated the primary texture.

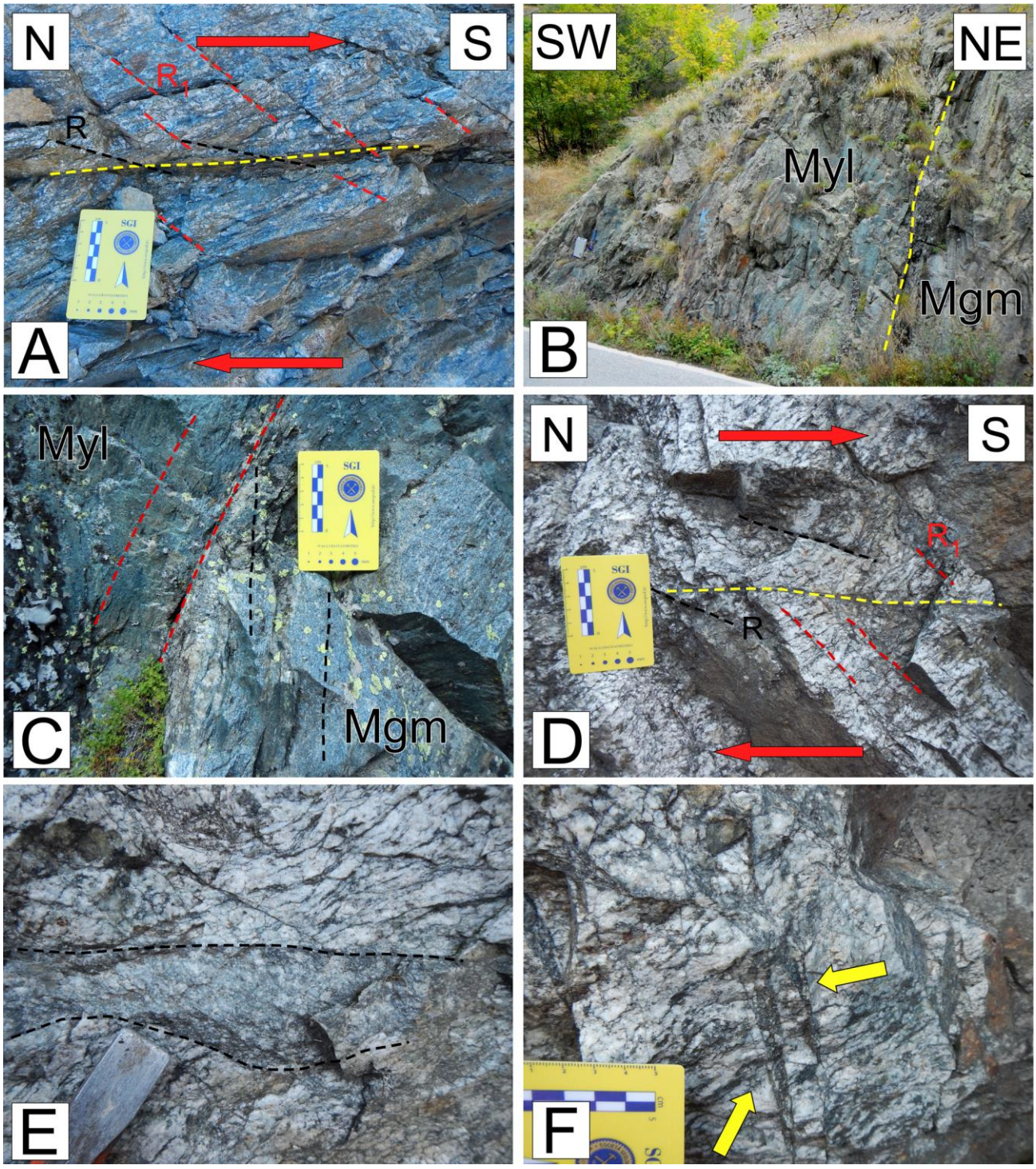

Figure 4.12 – A) chlorite-rich brittle-ductile shear plane with R and R_1 Ridel fractures indicative of a dextral top-to-the S sens of shear; B) mylonitic band (Myl) cross-cutting migmatites (Mgm) of the GSV; C) detail of the contact between alpine mylonites (Myl) and migmatites (Mgm) of the GSV; D) chlorite-rich shear plane cross-cutting the migmaties of the GSV with evident R and R_1 Ridel fractures indicative of a dextral top-to-the S sens of shear; E) cataclasite formed at the expense of migmatites of the GSV; F) possible pseudotachilites (yellow arrows), they appear as dark veins injected into the wall rock from the shear plane

4.1.4 Quartz microstructures, fabric analysis and deformation temperature

Quartz in protomylonites exhibits a large grain size and lobate grain boundaries indicative of grain boundary migration (fig.4.13a). In some cases subgrains and small new grains are present but it is still possibile to recognize the original lobed shape of the boundary (fig. 4.13b). These features are indicative of an incipient subgrain rotation recrystallization overprinting the GBM.

In mylonites it is possible to recognize quartz subgrains and new grains of smaller size around larger grains (fig. 4.13c) which generate a bimodal grainsize indicative of subrain rotation recrystallization as the main dynamic recrystallization mechanism. In ultramylonites, quartz shows subgrains and new grains of smaller size compared to the ones present in the mylonites. They are sometimes found around larger old grains. This is indicative of subgrain rotation recrystallization (fig. 4.13d). In cases where subgrain rotation recrystallization is prevalent it is possible to recognize orientation families (fig. 4.13e) and a strong crystallographic preferred orientation (fig. 4.13f)

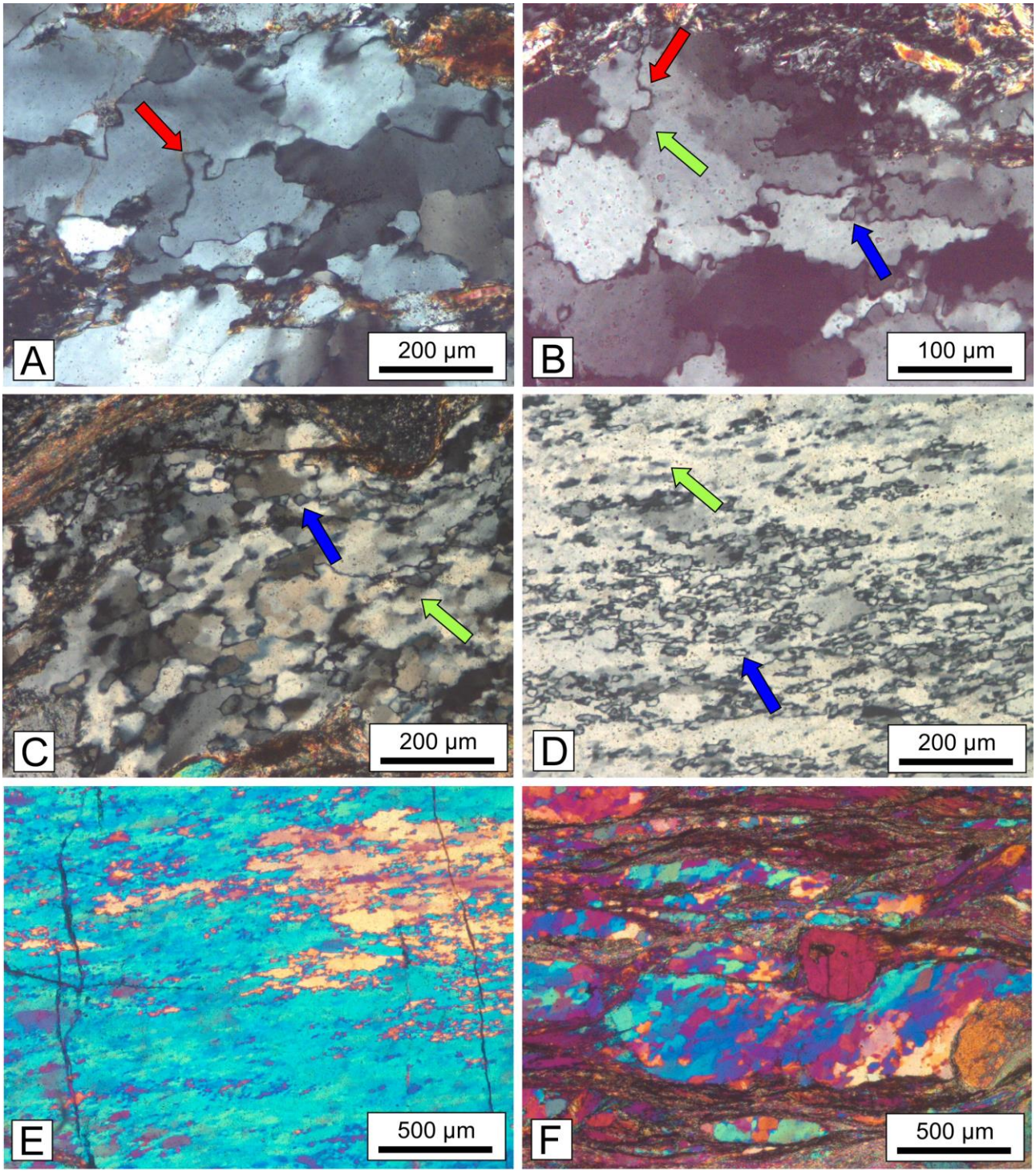

Figure 4.13 – Quartz microstructures in the mylonites of the FMSZ: A) quartz in a protomylonite showing big grain size and lobed boundary (red arrow) indicative of grain boundary migration; B) quartz showing lobate grain boundary (red arrow), indicative of grain boundary migration, partially overprinted by subgrain rotation recrystallization that forms subgrains (green arrow) and new grains (blue arrow) of smaller size; C) quartz dynamically recrystallized by subrain rotation recrystallization in a mylonite, subrains (green arrow) and new grains (blue arrow) can be recognized; D) subrains (green arrow) and new grains (blue arrow) indicative od subgrain rotation recrystallization in a ultramylonite; E) orientation families in a quartz domain recrystallized by subgrain rotation recrystallization in a ultramylonite; F) crystallographic preferred orientation of quartz in a mylonite

Quartz c-axis fabric were analysed for 12 rapresentative samples of protomylonites (ARG 19, ISC 3, ISC 11, IS 7; fig. 4.14), mylonites (ARG32, ARG 55, ISC 2, ISC 5; fig. 4.15) and ultramylonites (ARG RCV, ARG 37, ARG 43, ISC 7; fig. 4.16). A summary of the obtained data is reported in table 4.2.

	Sample	Dynamic recristallization mechanism	Opening angle	Temperature (°C)	β angle	α angle	Wk
Protomylonite	ARG 19	GBM	77°	608	15.45°	-	-
	ISC 3	GBM	74°	588	10.5°	-	-
	ISC 11	GBM	81°	634	5.70°	-	-
	IS 7	GBM	77°	610	11.55°	-	-
Mylonite	ARG 55	SRR	61°	482	5.20	14	0.62
	ISC 2	SRR overprintig GBM	67°	508	5.63°	18°	0.73
	ISC 5	GBM + incipient SRR	66°	528	8.38°	-	-
	ARG 32	SRR	61°	486	5.37°	17	0.70
Ultramylonite	ARG 37	SRR	52°	418	6.22°	27	0.91
	ARG RCV	SRR overprintig GBM	63°	500	5.47°	26	0.89
	ISC 7	SRR	55°	438	5.12°	24	0.85
	ARG 43	SRR	55°	436	4.75°	25°	0.86

Table 4.2 – Summary of data obtained by microstructural and c-axis fabric analysis of deformed quartz in protomylonites, mylonites, and ultramylonites

ARG 19, ISC 3, ISC 11and IS 7 show a type-II cross-girdle fabric (Lister, 1977) while ARG 55, ISC 2, ISC 5, ARG RCV and ISC 7 show a type-I fabric (Lister, 1977). Sample ARG 32 (mylonite) and samples ARG 37 and ARG 43 (ultramylonites) have fabrics intermediate between a type-I cross-girdle and a single girdle (Lister, 1977). All the obtained fabrics have weak asymmetry. This is evidence for non-coaxial shearing during deformation (Schmid and Casey, 1986; Law, 1990 and references therein) and is indicative of a dextral top-to-the-SW sense of shear in agreement with the observed kinematic indicators. The distribution of quartz c-axis suggest a deformation close to plane strain conditions (Lister and Hobbs, 1980).

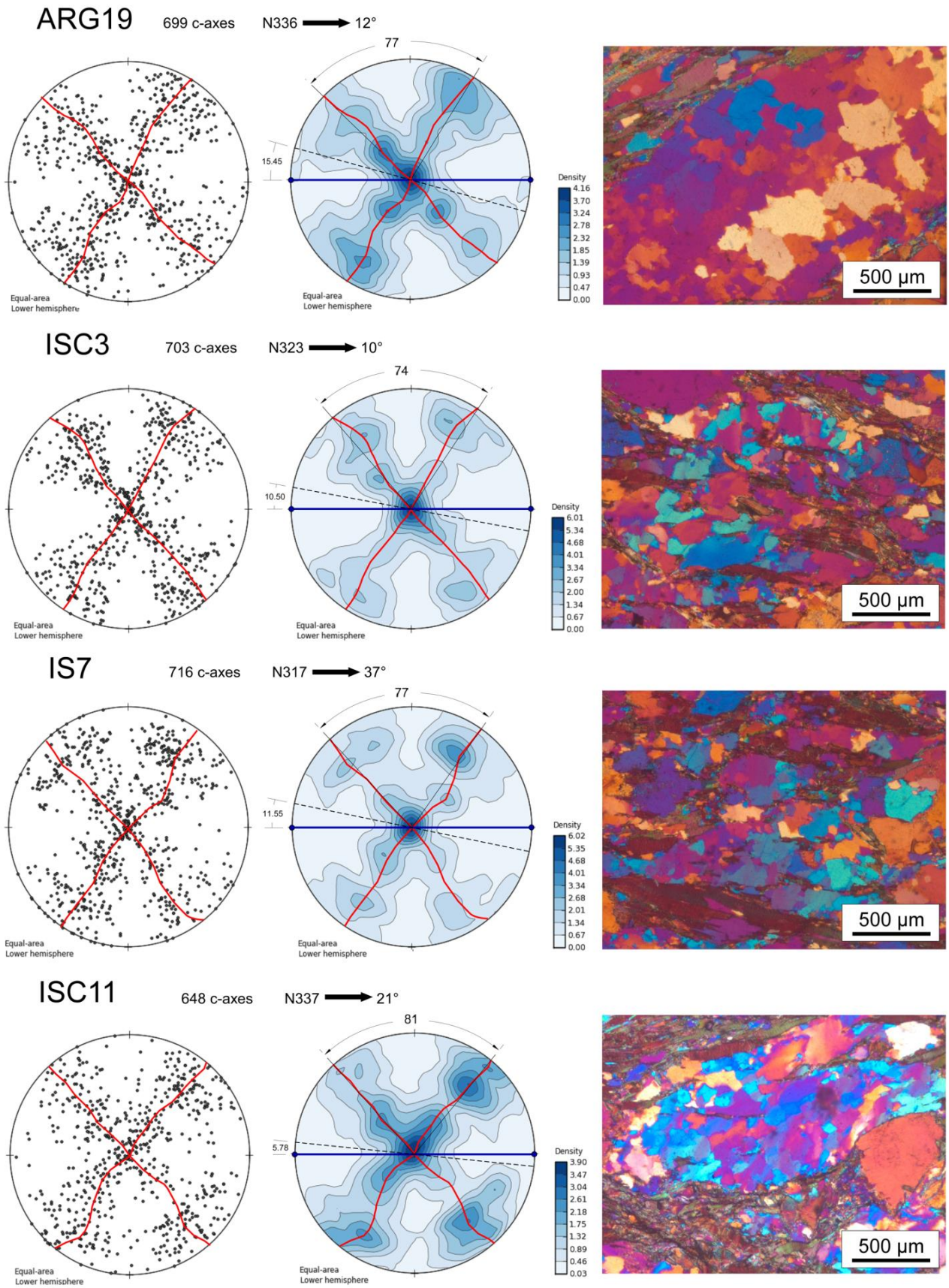

Figure 4.14 - Optically measured quartz c-axis fabrics for samples representative of protomylonites. All pole figures are oriented perpendicular to the foliation and parallel to the lineation. Dashed line is the shear plane; blue line is the main foliation and blue dots are the mineral lineation. Fabric asymmetries indicate a dextral top-to-the-SW sense of shear. Fabric opening angle and angle between the main foliation and the shear plane are reported

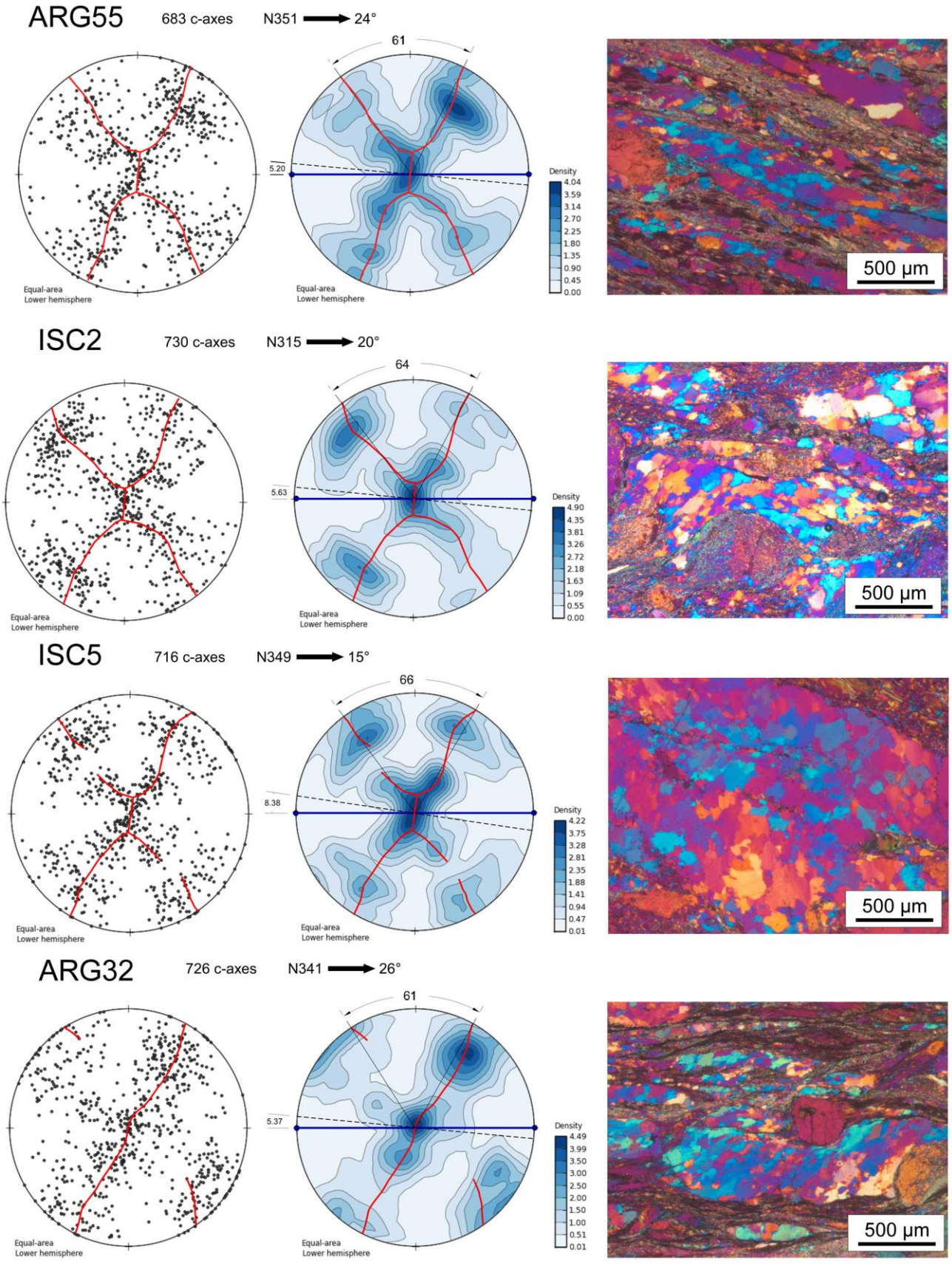

Figure 4.15 - Optically measured quartz c-axis fabrics for samples representative of mylonites. All pole figures are oriented perpendicular to the foliation and parallel to the lineation. Dashed line is the shear plane; blue line is the main foliation and blue dots are the mineral lineation. Fabric asymmetries indicate a dextral top-to-the-SW sense of shear. Fabric opening angle and angle between the main foliation and the shear plane are reported

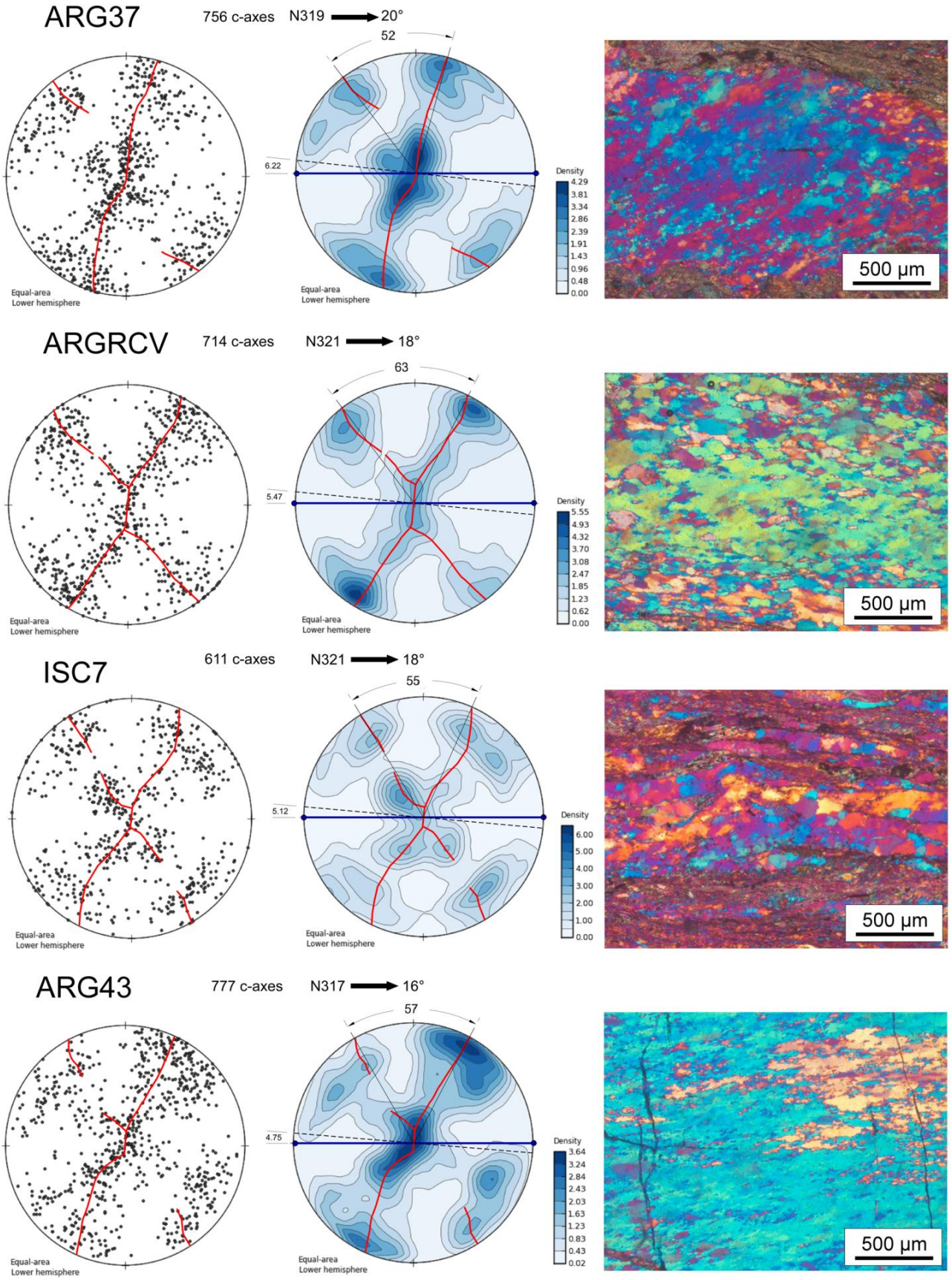

Figure 4.16 - Optically measured quartz c-axis fabrics for samples representative of ultramylonites. All pole figures are oriented perpendicular to the foliation and parallel to the lineation. Dashed line is the shear plane; blue line is the main foliation and blue dots are the mineral lineation. Fabric asymmetries indicate a dextral top-to-the-SW sense of shear. Fabric opening angle and angle between the main foliation and the shear plane are reported

Quartz microstructures (Stipp *et al*., 2002; Piazolo and Passchier, 2002) and the opening angles of quartz c-axis fabrics (Kruhl 1998; Law et al. 2004) have been used to estimate deformation temperatures. In particular we used the recent calibration of the thermometer proposed by Falerios *et al*. (2016).

The opening angles of c-axis fabrics in samples ARG 19, ISC 3, ISC11, IS7, representative of the protomylonites, are 77°, 74°, 81°, 77° respectively. According to the calibration of Falerios et al. (2016) those values are indicative of a deformation temperatures between 610° C and 588° C (fig. 4.17). In samples ARG32, ARG 55, ISC 2 and ISC 5 representative of the mylonites, the measured opening angle is 61°, 61°, 64°, 66° that are indicative of temperatures varying from 528° C and 482° C (fig. 4.17). In the ultramylonitic samples ARG RCV, ARG 37, ARG 43 and ISC 7 quartz opening angle is 63°, 52°, 57°, 55° respectively and therefore indicative of temperatures varying from 500° C and 418° C (fig. 4.17).

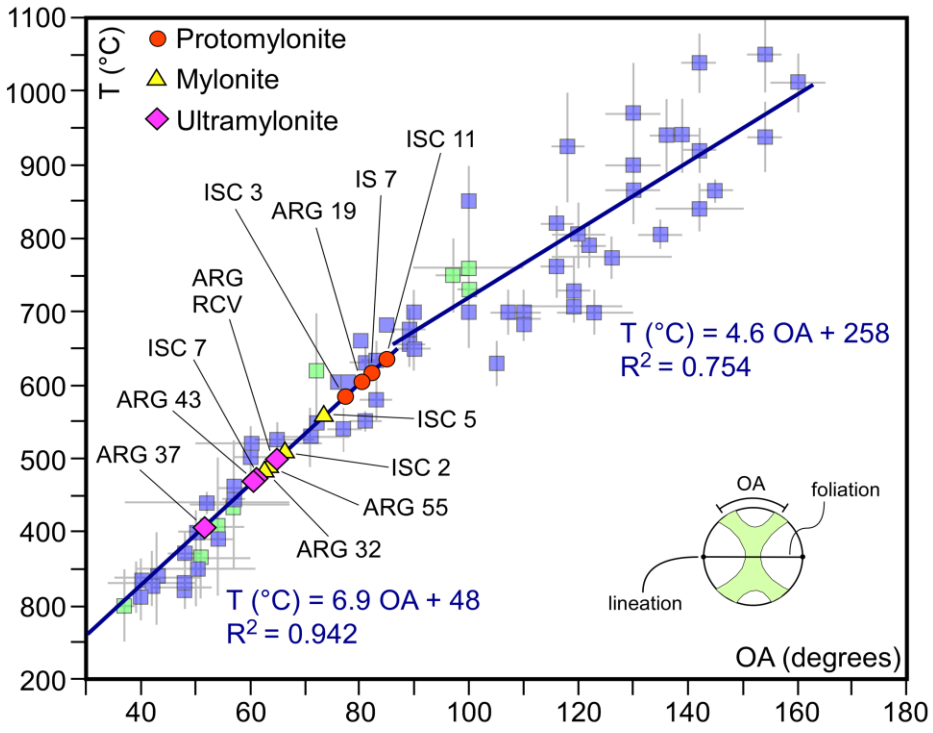

Figure 4.17 - Falerios *et al*. (2016) quartz c-axis fabric opening-angle thermometer in the range of 250 - 1050 °C, blue squares are data with pressure information used by Faleiros et al. (2016) to define their thermometer, while green squares are data used by Faleiros et al. (2016) that have no pressure information. Calibration was made after Khrul (1998), Morgan and Law (2004), Law (2014). Linear fits described by equation 1 and 2 are indicated

4.1.5 Quartz palaeopiezometry

Three samples from the core of the shear zone were selected for quartz-based palaeopiezometry. ARG 43 was collected in the Serra Del Bal area (fig. 4.4a), ARG RCV and ARG 37 were collected in the Rocco

Verde Area (fig. 4.4c). All the samples are ultramylonitic schists with white mica and chlorite along the main foliation. These rocks are generally depleted in quartz compared to the less sheared mylonites, however in those samples quartz-rich layer concordant with the main foliation are present. Here quartz is dynamically recrystallized by subgrain rotation rotation recrystallization. Quartz-filled fractures described in paragraph 4.1.3 are also present.

In sample ARG RCV, 892 grains were measured and the average grain size is 17.13 ± 4.4 μm (fig. 4.18a); in sample ARG 43, 641 grains were measured and the average grain size is 15.64 ± 4.5 μm (fig. 4.18b) and in sample ARG 37 the 995 measured grains give an average grain size of 12.54 ± 5.2 μm (fig. 4.18c). Grain boundary maps used for the analysis are reported in fig. 4.19 and fig. 4.20.

Those values are indicative of a differential stress of 51 ± 12 MPa, 55 ± 15 MPa and 65 ± 26 MPa respectively (fig. 4.18) according to the calibration of Holyoke and Kronenberg (2010). The original calibration of Stipp and Tullis (2003) gives differential stress of 70 ± 17 MPa for sample ARG RCV, 75 ± 4 MPa for sample ARG 43 and 89 ± 36 MPa for sample ARG 37. In order to apply the calibration of Shimizu (2008) we used deformation temperature measured with the opening angle termometer of quartz c-axis fabric (see paragraph 4.1.4), this relation provides the highest values of differential stress. Values of 104 ± 5 MPa, 128 ± 6 MPa and 160 ± 8 MPa for sample ARG RCV, ARG 43 and ARG 37 respectively were obtained. Despite the differences between the three calibrations, higher values are always obtained in sample ARG 37, intermediate values are obtained in sample ARG 43 and lower values are obtained in sample ARG RCV.

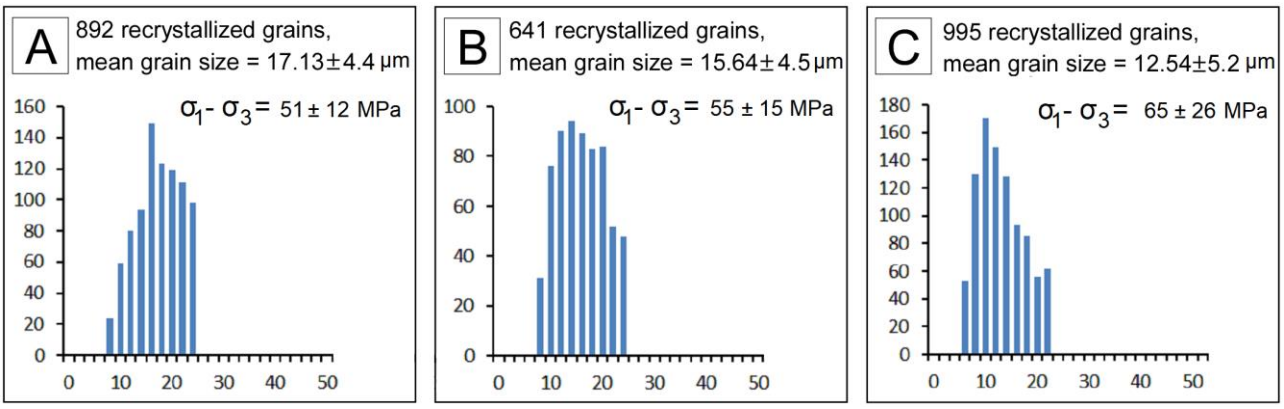

Figure 4.18 - Grain size distribution histograms with relative average value and obtained differential stress ($\sigma_1 - \sigma_2$; calibration of Holyoke and Kronenberg, 2010); A) sample ARG RCV; B) sample ARG 43; C) sample ARG 37

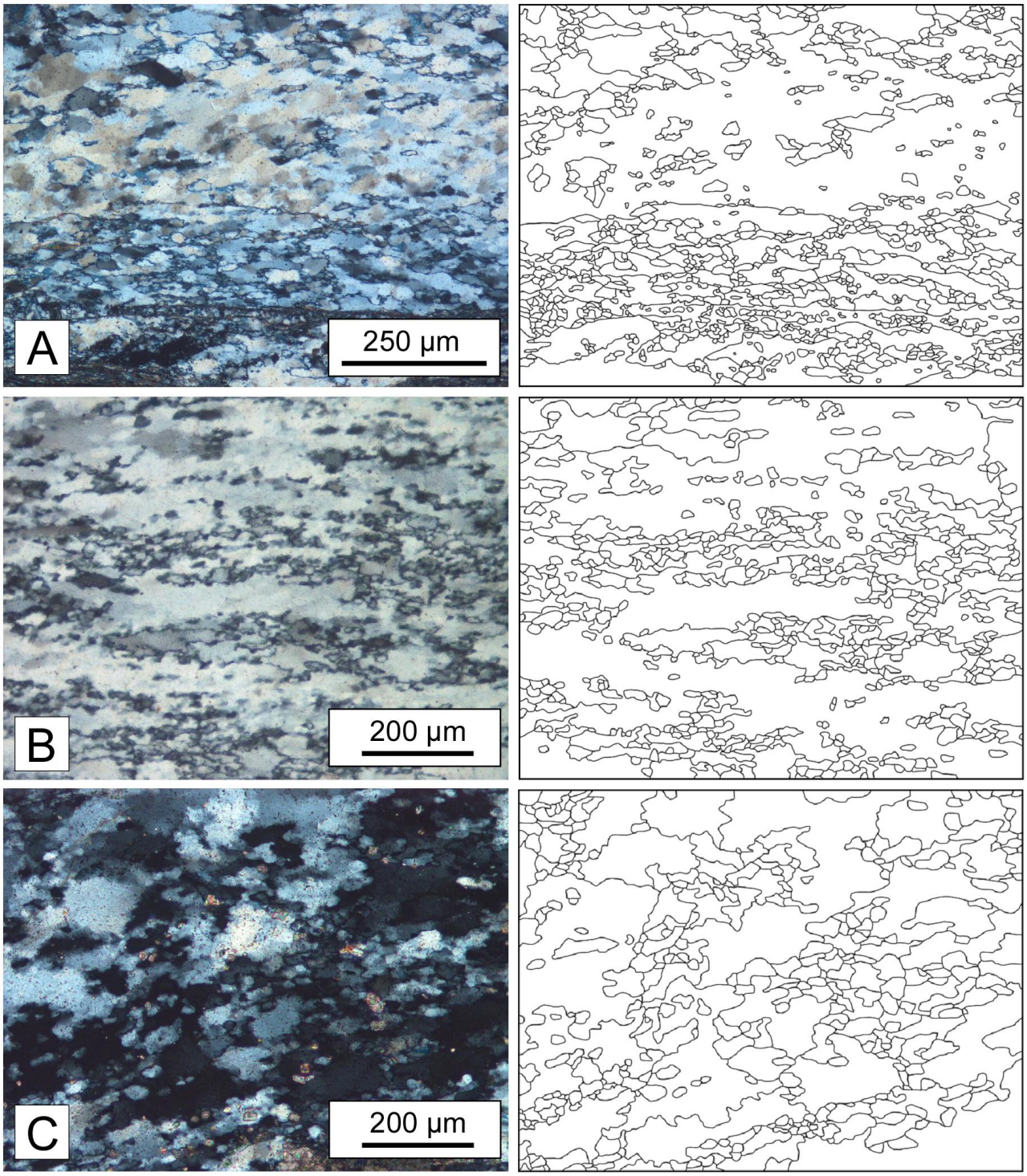

Figure 4.19 – First group of selected recrystallized areas and corresponding grain boundary maps; A) sample ARG RCV; B) sample ARG 43; C) sample ARG 37

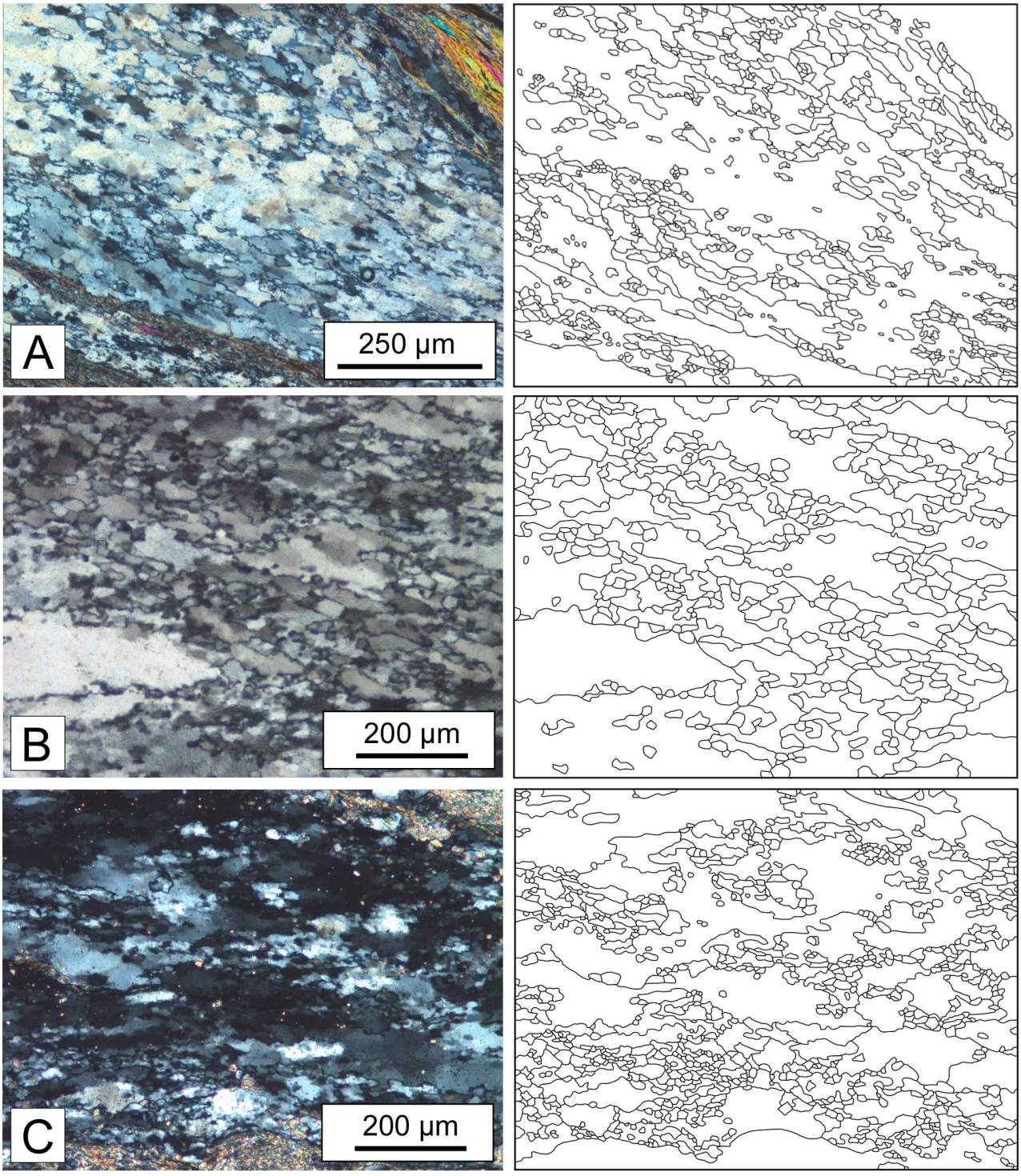

Figure 4.20 - Second group of selected recrystallized areas and corresponding grain boundary maps; A) sample ARG RCV; B) sample ARG 43; C) sample ARG 37

Strain rates were estimated by combining the values of differential stress and the quartz fabric-derived deformation temperature following the Gleason and Tullis (1995) flow law. Complete results are presented in table 4.3. In particular, estimated strain rates are in the range of 10^{-13} s^{-1} and 10^{-14} s^{-1} or in the range of 10^{-12} s^{-1} and 10^{-13} s^{-1} depending on the used pairs. Obtained strain rate-temperature pairs were plotted in a strain

rate-temperature recrystallization mechanism map for quartz (fig. 4.21; Hirth and Tullis, 1992; Dunlap *et al*., 1997; Hirth *et al*., 2001; Law, 2014). It should be noted that the obtained data fell in the field of subgrain rotation recrystallization, or are very close to its field, in agreement with the observed quartz microstructures.

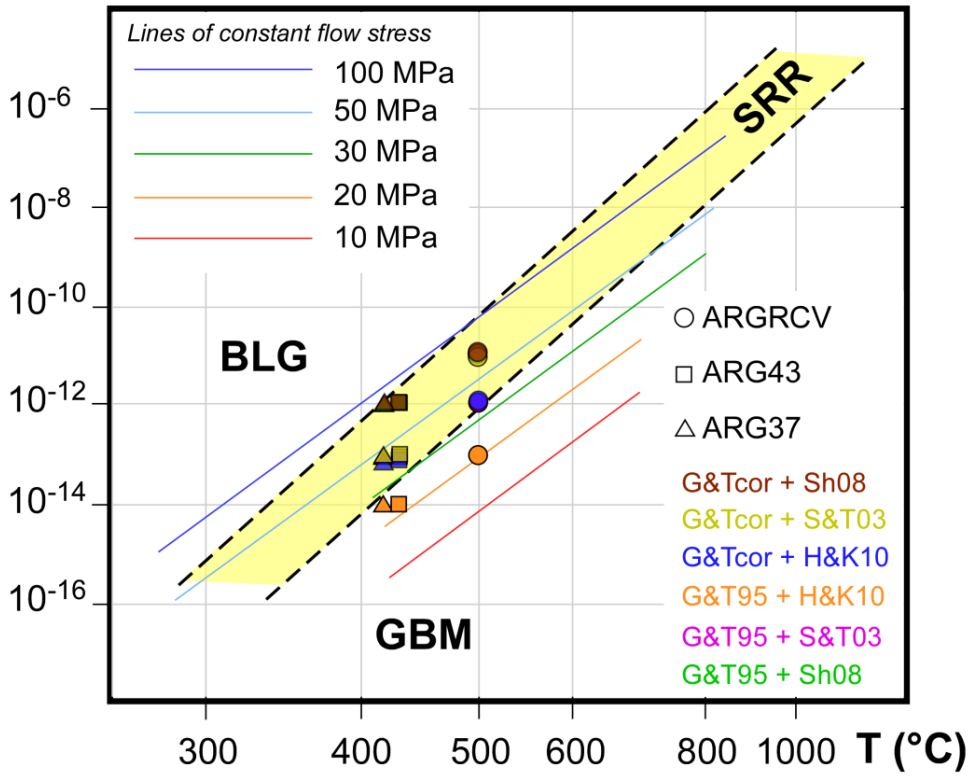

Figure 4.21 - Strain rate-temperature recrystallization mechanism map for quartz (modified after Hirth and Tullis, 1992; Dunlap et al., 1997; Hirth et al., 2001; Law, 2014); lines of constant flow stress are from Hirth *et al*. (2001); G&T95 = Gleason and Tullis (1995) wet quartzite flow low; G&Tcor = Gleason and Tullis (1995) wet quarzite flow low as corrected by Holyoke and Kronemberg (2010); H&K10 = Holyoke and Kronemberg (2010) calibration; S&T03 = Stipp and Tullis (2003) calibration; Sh08 = Shimizu (2008) calibration

SAMPLE	Strain rate (s^{-1})					
	G&T95			G&Tcor		
	H&K10	S&T03	Sh08	H&K10	S&T03	Sh08
ARG RCV	6.5×10^{-13}	2.3×10^{-12}	1.1×10^{-11}	3.0×10^{-12}	1.1×10^{-11}	5.1×10^{-11}
ARG 43	6.5×10^{-14}	1.3×10^{-13}	5.2×10^{-12}	1.4×10^{-13}	6.1×10^{-13}	5.1×10^{-12}
ARG 37	6.5×10^{-15}	1.0×10^{-13}	4.7×10^{-12}	1.3×10^{-13}	4.4×10^{-13}	4.6×10^{-12}

Table 4.3 – Summary of the obtained strain rates in the ultramylonites of the FMSZ; G&T95 = Gleason and Tullis (1995) wet quarzite flow low; G&Tcor = Gleason and Tullis (1995) wet quartzite flow low as corrected by Holyoke and Kronemberg (2010); H&K10 = Holyoke and Kronemberg (2010) calibration; S&T03 = Stipp and Tullis (2003) calibration; Sh08 = Shimizu (2008) calibration

4.1.6 Kinematic vorticity analysis

In order to characterize the type of flow and the deformation of the FMSZ, kinematic vorticity analyses were performed on mylonites collected perpendicular to the shear zone boundaries and parallel to the gradient of increasing deformation (fig. 4.4). The analyses were performed using the C' shear band method (Kurz and Northrup, 2008) and the quartz c-axis method (Platt and Behrmann, 1986; Law, 1990; Wallis, 1992, 1995). When possible both methods were applied on the same samples.

The first method (C' shear band; fig. 4.22 and fig. 4.23) highlighted that in protomylonites (samples: ARG 144, ARG 143, ARG 19, ISC 11, ISC 3, IS 7) Wk varies from 0.32 to 0.55; in mylonites (samples: ARG 45, ARG 21a, ARG 68, ARG 116, ARG 117, ARG 115, ARG 55, ARG 32, ISC 2, ISC 5) Wk varies between 0.37 and 0.72; In ultramylonites (samples: ARG 35, ARG 101, ARG 37, ARG RCV, ARG 41, ISC 7, ARG 43) Wk is variable between 0.69 and 0.89. The θ angle varies from 9° in protomylonites to 31° in ultramylonites.

The second method (quartz c-axis) highlighted that in mylonites (ARG 32, ARG 55, ISC 2) Wk varies between 0.62 and 0.73 while in ultramylonites (ARG 37, ARG RCV, ISC 7, ARG 43) Wk varies between 0.85 and 0.91. In order to check the accurancy of the angle between the mylonitic foliation and the shear plane obtained with the fabrics (figs. 4.14, 4.15, 4.16) we compared it with the angle between the mylonitic foliation and the shear zone margin observed in the field where the shear zone margin is well mapped (fig. 4.24) The results are very similar, and this strengthens the validity of our vorticity data obtained with this method. In cases where both methods were applied (sample ISC 2, ARG 55, ARG 32, ARG 37, ARG RCV, ISC 7, ARG 43), resultant Wk estimates are very similar (table 4.4).

Vorticity analysis revealed an increase in the value of Wk, that represents an increase in the simple shear component, along the deformation gradient toward the center of the shear zone. In particular: protomylonites show the lower Wk values that reflects a major component of pure shear; mylonites are characterized by intermediate values that are still indicative of prevalent pure shear but acting together with a slightly higher simple shear component; ultramylonites give Wk values indicative of a prevalent simple shear component.

SAMPLE	LITHOLOGY	Wk	
		C' shear band	Quartz c-axis
ISC2	Mylonite	0.72	0.73
ARG55	Mylonite	0.71	0.62
ARG32	Mylonite	0.69	0.7
ARG37	Ultramylonite	0.81	0.91
ARGRCV	Ultramylonite	0.83	0.89
ISC7	Ultramylonite	0.82	0.85
ARG43	Ultramylonite	0.82	0.86

Table 4.4 – Comparison between Wk values obtained with the C' shear band method and quartz c-axis method

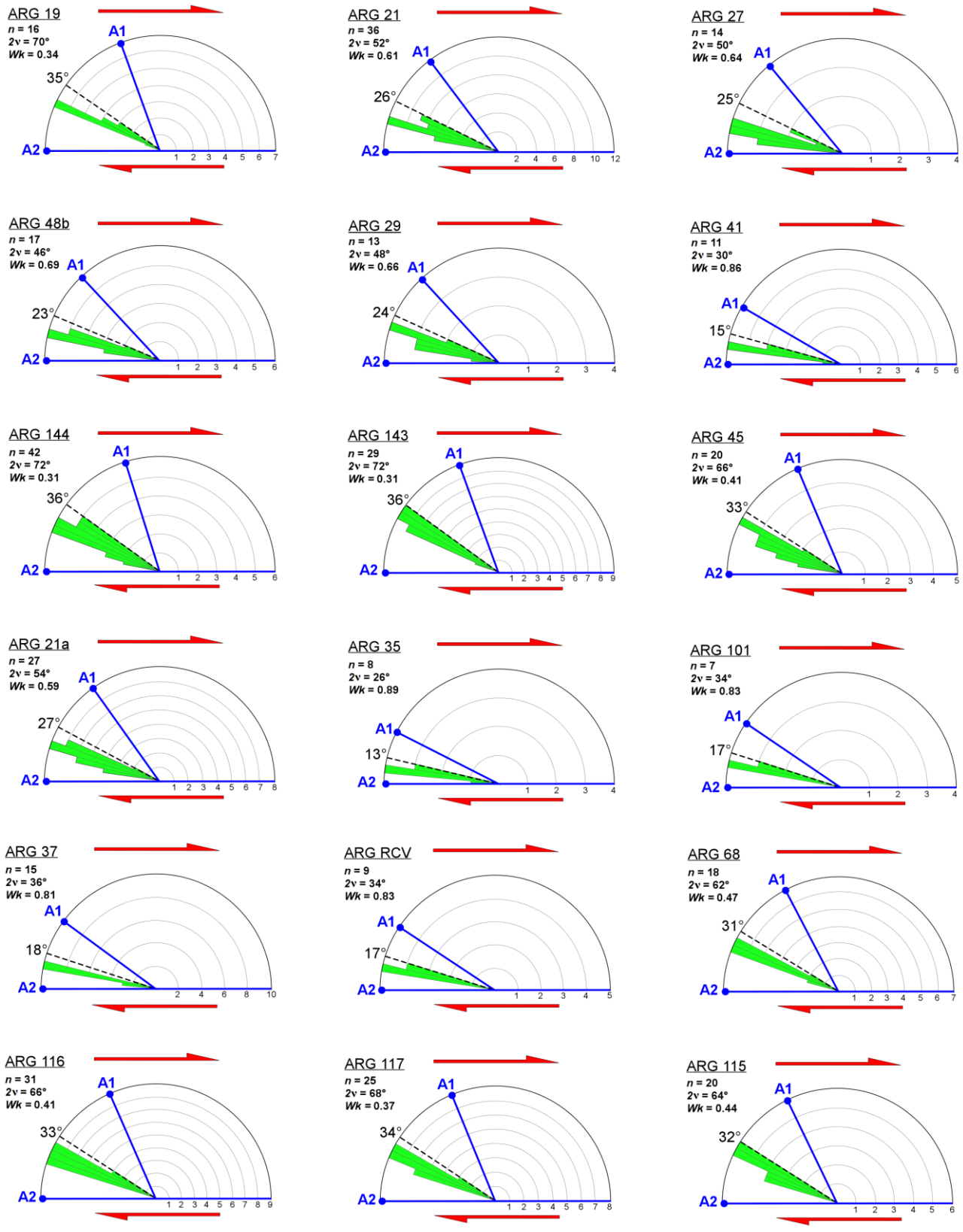

Figure 4.22 - Polar histograms used to derive the angle ν and to calculate kinematic vorticity with the C' shear band method (Kurz and Northrup, 2008) on field oriented samples. A1 = flow apophysis 1; A2 = flow apophysis 2. Dashed line represents the bisector of the angle between A1 and A2, green bars represent the number of data. All histograms are shown with the same sense of shear (red arrows)

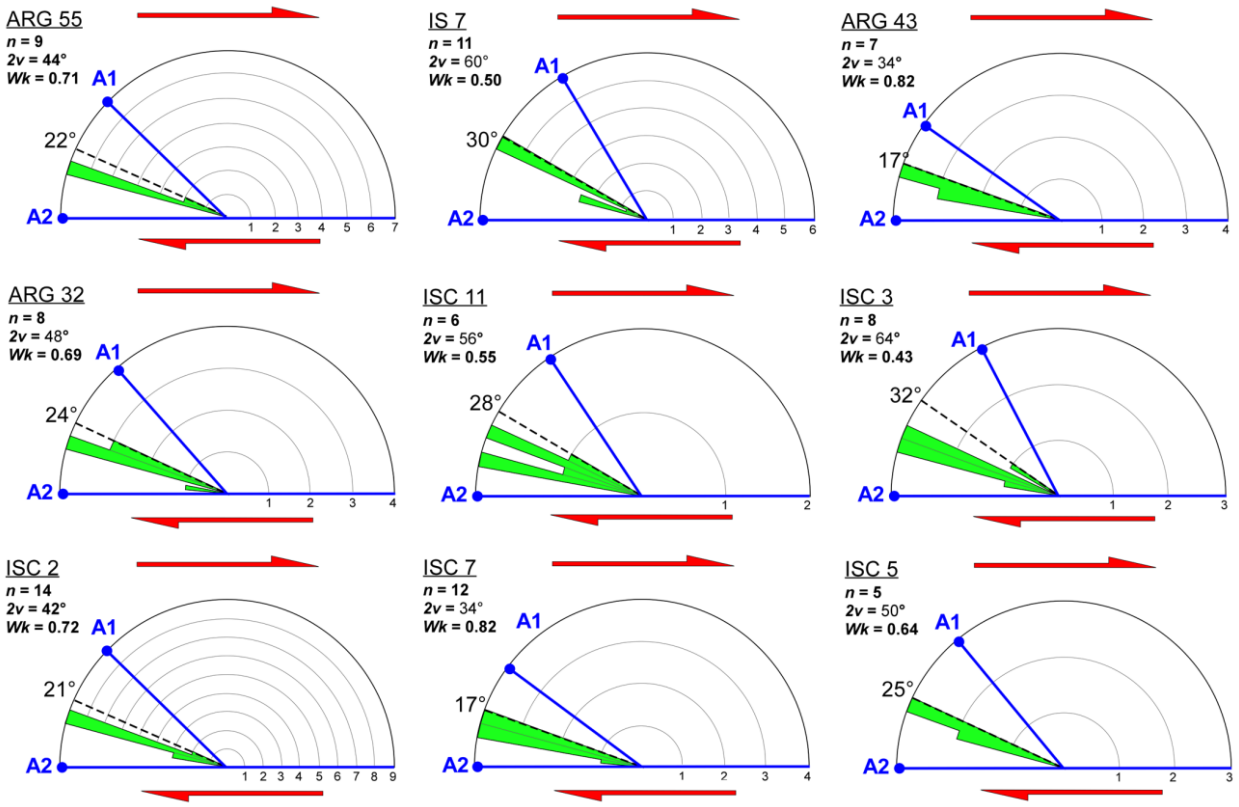

Figure 4.23 - Polar histograms used to derive the angle ν and to calculate kinematic vorticity with the C' shear band method (Kurz and Northrup, 2008) on field oriented samples. A1 = flow apophysis 1; A2 = flow apophysis 2. Dashed line represents the bisector of the angle between A1 and A2, green bars represent the number of data. All histograms are shown with the same sense of shear (red arrows)

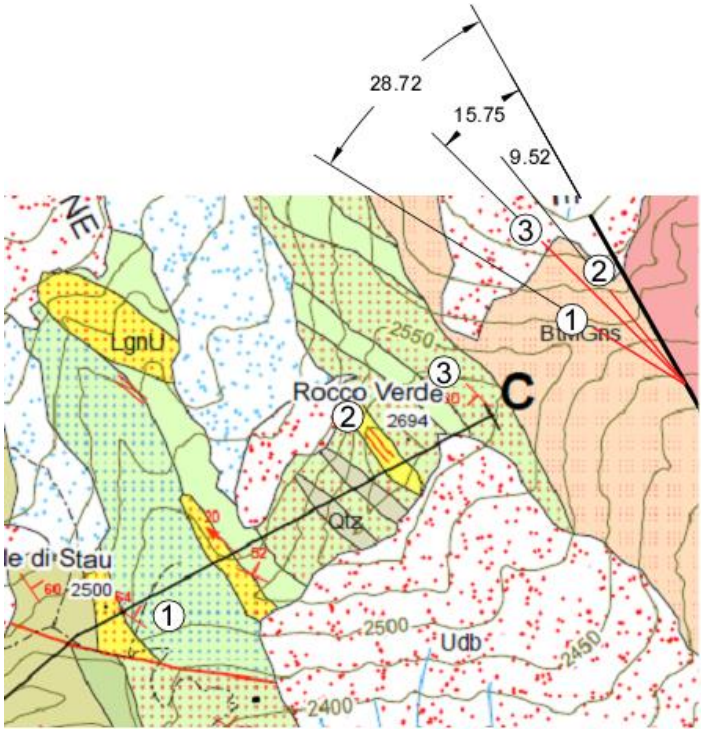

Figure 4.24 - Angle between the mylonitic foliation and the shear zone boundary estimated directly on the field in the Rocco Verde area (see appendix B)

4.1.7 Strain analysis

We performed a finite strain analysis in order to obtain the axial ratio of the finite strain ellipse (Rxz), which is indispensable for calculating the shortening perpendicular to the flow plane. Finite strain analyses have been performed on the XZ and YZ sections of oriented samples applying the center-to-center method (fig. 4.25 and fig. 4.26; Fry, 1979). The analyses were performed on samples in which an adequate number of feldspar porphyroclasts with a similar grain size were present. Feldspar porphyroclasts show a homogeneous distribution in the samples used for the analysis and therefore are in agreement with the fundamental assumption of the method (see Genier and Epard, 2007 for a critical review). The center-to-center analysis was carried out using the software EllipseFit 3.2 (Vollmer, 2005).

Finite deformation analysis revealed a general flattening deformation (fig. 4.27a). Combining the obtained values with Wk, we obtained shortening and stretching values quite concordant in all the studied samples (table 4.5). The correction of Law (2010) accounting for deviations from plane strain was applied when possible (fig. 4.27b), shortening varies from 19% to 37% with an average value of 27%; stretching ranges from 23% to 59% with an average value of 36%. We estimated a convergence angle between the wall-rocks for protomylonites, mylonites and ultramylonites of ~65°, ~52° and ~37° respectively.

SAMPLE	Rxz	Shortening (S)	Stretching (1/S)
ARG 144	1.88	0.74	1.35
ARG 143	1.99	0.72	1.38
ARG 21a	2.1	0.74	1.35
ARG 68	1.87	0.76	1.31
ARG 117	2.05	0.71	1.39
ARG 19	1.71	0.78	1.28
ARG 21	2.85	0.63	1.59
ARG 27	1.75	0.81	1.23
ARG 29	2.46	0.72	1.38

Table 4.5 – Axial ratio on the XZ section obtained with the center-to-center method and shortening and stretching values obtained combining finite strain data with vorticity data

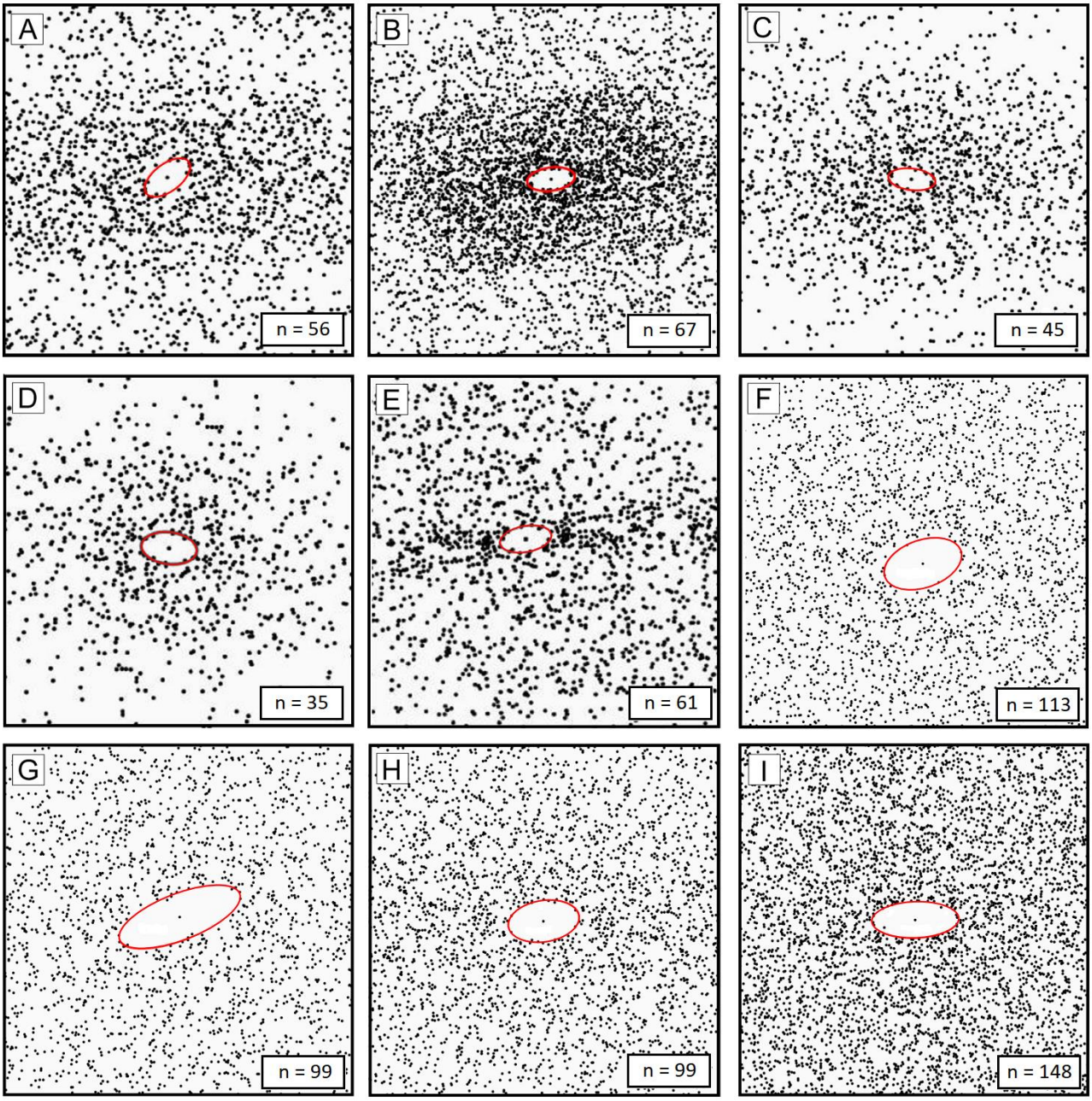

Figure 4.25 - Fry graphs used in the strain analysis obtained with the center-to-center method on the XZ sections; n = number of centers used for the Fry analysis. A) ARG 143; B) ARG 144; C) ARG 21a; D) ARG 68; E) ARG 117; F) ARG 19; G) ARG 21; H) ARG 27; I) ARG 29. Axial ratios Rxz are reported in table 4.4

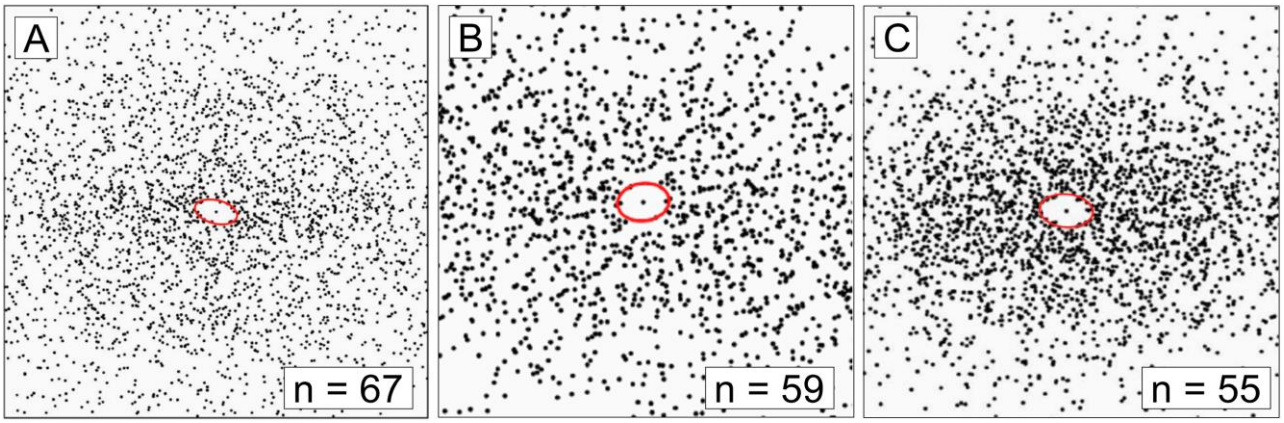

Figure 4.26 - Fry graphs used in the strain analysis obtained with the center-to-center method on the YZ section; n = number of centers used for the Fry analysis. A) ARG 21a; B) ARG 143; C) ARG 144

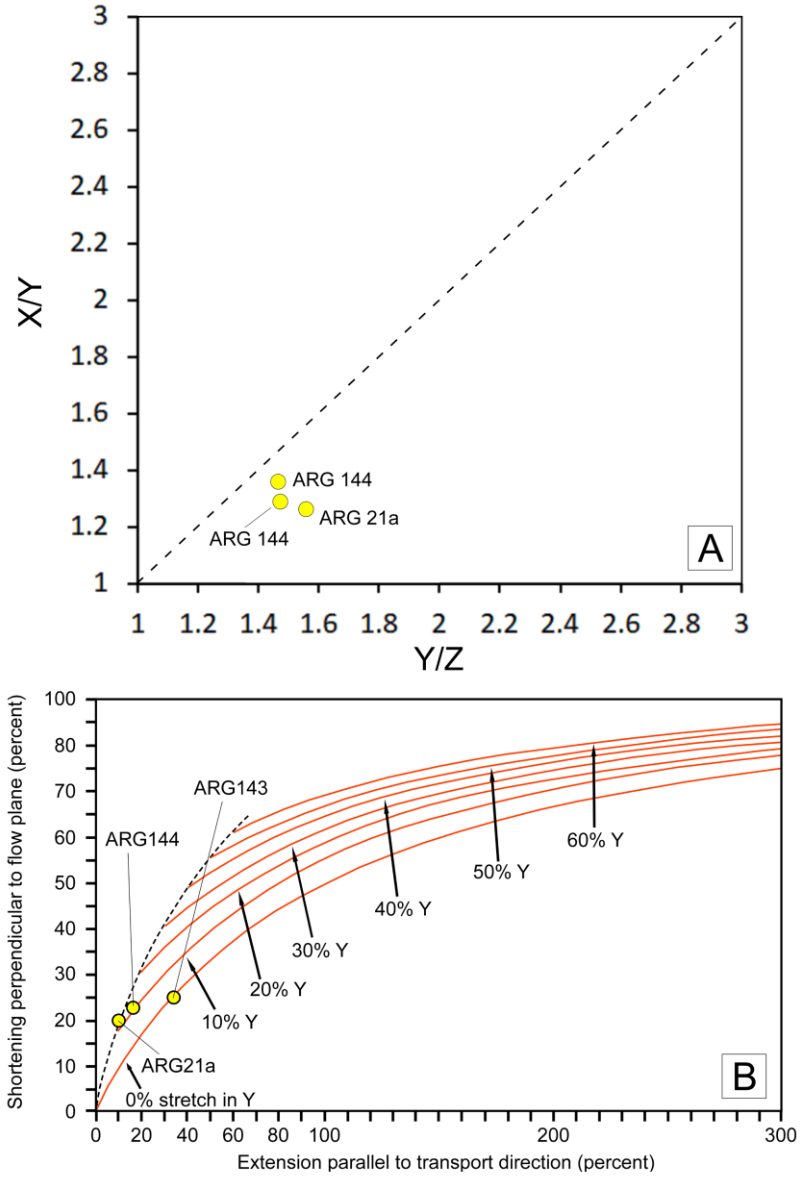

Figure 4.27 – A) Flinn diagram showing the position of the samples in the apparent flattening field (dots); B) curves representing the shortening perpendicular to flow plane versus extension in transport direction for general flattening with 0 – 60 % stretch along Y (modified from Law, 2010)

4.1.8 Petrochronology

In-situ U-Th-Pb analyses on monazite were performed in five samples (ARG 19, ARG 21, ARG 27, ARG 29, ARG 48b) collected along Pontebernardo valley with LA-ICP-MS and on three samples (ISC 3, ISC 5, ISC 2) collected in the Ischiator valley with LASS. All samples derive from biotite- and sillimanite-bearing migmatite but they differ in terms of intensity of the deformation, in particular: ARG 19 and ISC 11 are protomylonites while ARG21, ARG 27, ARG 29, ARG 48b, ISC 2 and ISC 5 are mylonites.

In both protomylonites and mylonites no xenotime crystals have been detected and cores of the monazites have often a lower Y content with respect to the rims (fig. 4.28). Some monazites have asymmetric shape coherent with the sense of shear. Monazites in mylonitic samples, sometimes, show irregular and frayed edges with asymmetric rims composed of allanite ± apatite often developed in extensional sites around the crystals. A total of 26 monazites grains, located in different microstructural position and with different chemical variability, were selected. Examples of monazite grains, with the relative Y compositional map, located in different structural positions are reported in figure 4.28. The complete dataset of selected monazite grains and the Y compositional maps are reported in appendix F together with the obtained age for every spot. Chemical analysis of all the monazite grains are reported in appendix G, spots are reported on BSE images in appendix F.

In samples analyzed with LA-ICP-MS (ARG 19, ARG 21, ARG 27, ARG 29, ARG 48b), U-Pb data (table 4.6) provide mainly discordant ages, with eight concordant U-Pb ages ranging from 348 to 297 Ma (fig. 4.29). In sample ARG 19 (protomylonite), $^{206}Pb/^{238}U$ and $^{208}Pb/^{232}Th$ data yield more concordant ages (table 4.6, fig. 4.29). Both $^{206}Pb/^{238}U$ and $^{208}Pb/^{232}Th$ ages range mainly from 340 to 320 Ma and define a broad rejuvenation trend from the least deformed sample (ARG 19 protomylonite) to highly sheared samples in the core of the shear zone (fig. 4.29; apppendix F).

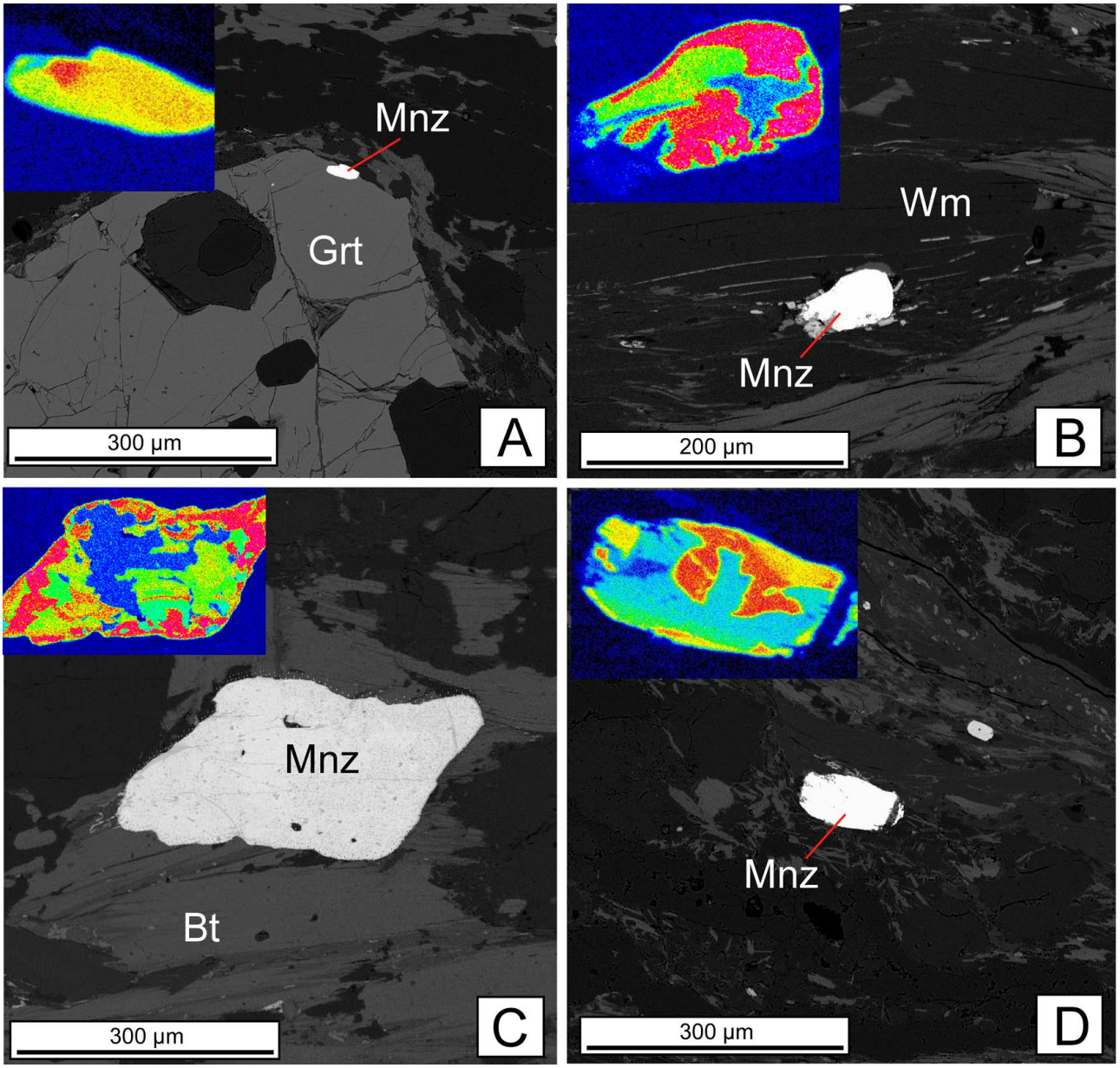

Figure 4.28 - Back-scattered electron pictures of monazite grains in different microstructural position with relative Y compositional map: A) Mnz 59, sample ARG 48b, included in garnet; B) Mnz 29, sample ARG 29, included in a white mica fish; C) Monazite with asymmetric shape along the main foliation marked by biotite within a protomylonte (Mnz 14, sample ARG19); D) Monazite along the main foliation in mylonite (Mnz 52, sample ARG 27)

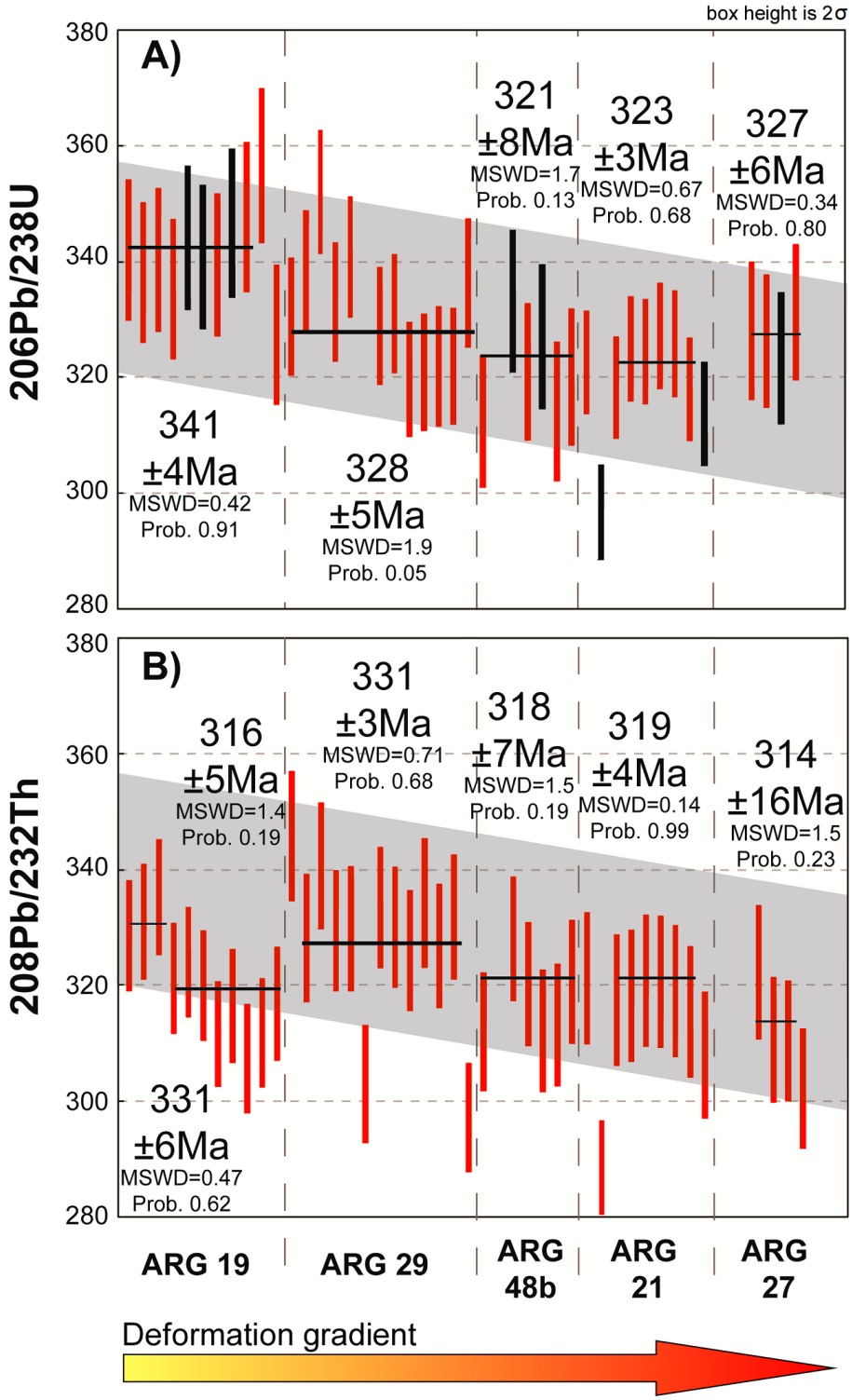

Figure 4.29 - Distribution of $^{206}Pb/^{238}U$ (A) and $^{208}Pb/^{232}Th$ (B) ages for different samples along the deformation gradient. Black vertical bars indicate concordant ages, black horizontal bar contains the averaged data (MSWD=Mean Square Weighted Deviates; prob.= probability). Geochronological data define a broad trend (grey area) reflecting the deformation gradient between samples analyzed

The oldest U-Th-Pb ages were obtained from a monazite grain included in garnet (>400 Ma; Mnz 59, sample ARG 48b) and a monazite grain included in a deformed white mica ($^{206}Pb/^{238}U$ age of 374 ± 6 Ma; Mnz 9,

ARG 29), suggesting a textural control and inheritance of the obtained ages. In samples collected in the Ponterbernardo valley we did not note a systematic correlation between ages and monazite chemical domains.

In samples analyzed with LASS (ISC 3, ISC 5, ISC 2), The $^{206}Pb/^{238}U$ and $^{208}Pb/^{232}Th$ ages are generally concordant, the full dataset is presented in table 4.7. In those samples, all the monazite grains are located along the main foliation. The average $^{206}Pb/^{238}U$ age for each sample is reported in figure 4.30, the relationships between age, Y content, Gd/Yb ratio and REE pattern normalized to chondrite (normalization values after McDonough and Sun 1995) of the compositional domains are reported in figure 4.31.

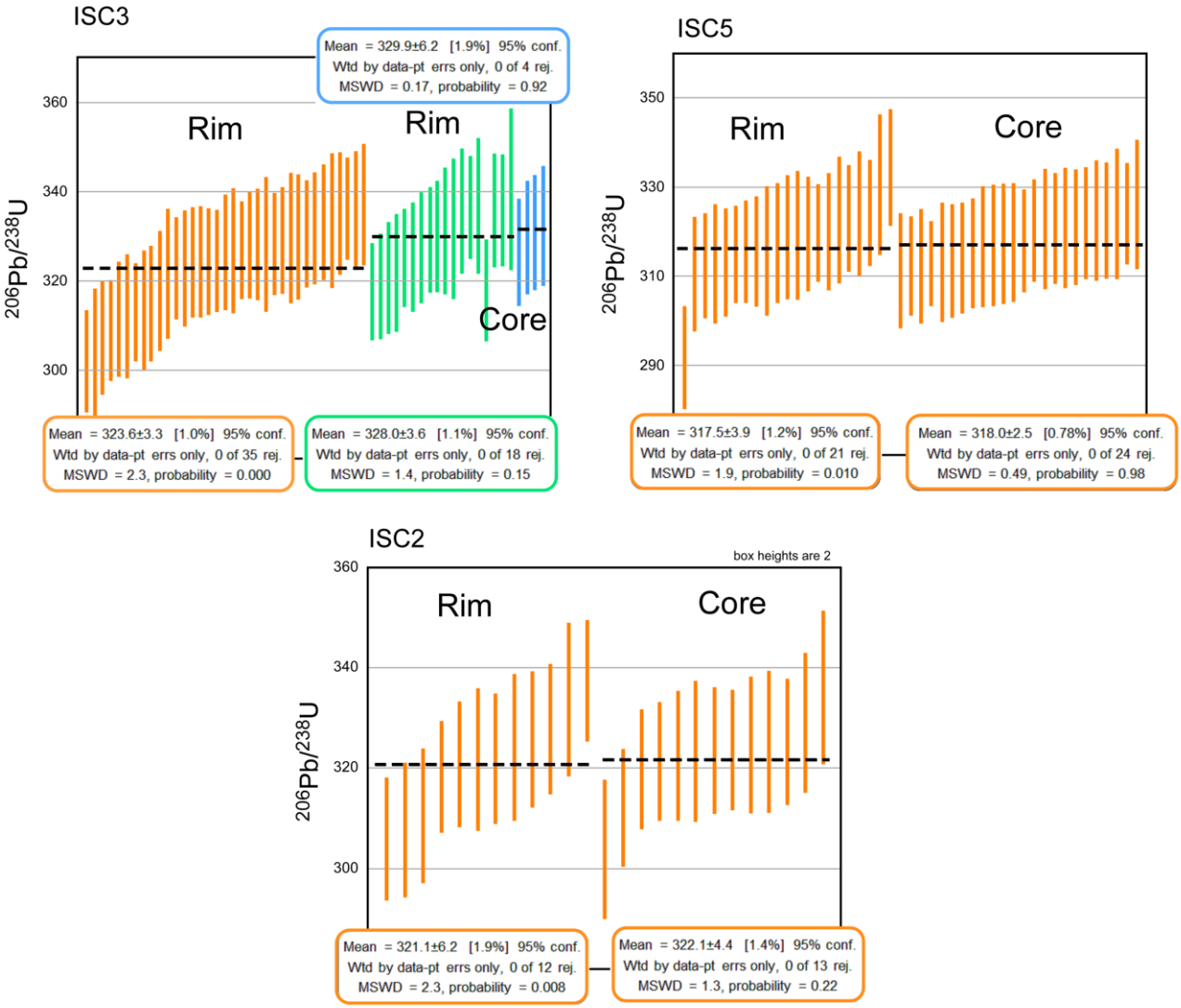

Figure 4.30 - Distribution of $^{206}Pb/^{238}U$ ages. Data are grouped according to the position of the spot within the grain and colors of the bars are organized according to the Y content: blue = low-Y domain in the core of the grain; green = medium-Y domain in the core of the grain or in an intermediate position between core and rim (mantle); orange = high-Y domain in the rim of the grain. MSWD = mean square weighted deviates

In sample ISC 3 (protomylonite) $^{206}Pb/^{238}U$ ages and $^{208}Pb/^{232}Th$ ages range from 329 Ma to 323 Ma. In samples ISC 2 and ISC 5 (mylonites) $^{206}Pb/^{238}U$ ages and $^{208}Pb/^{232}Th$ ages are very similar and range from 322 Ma to 317 Ma. The oldest U-Th-Pb ages were obtained from the low-Y and low-HREE cores of the monazites.

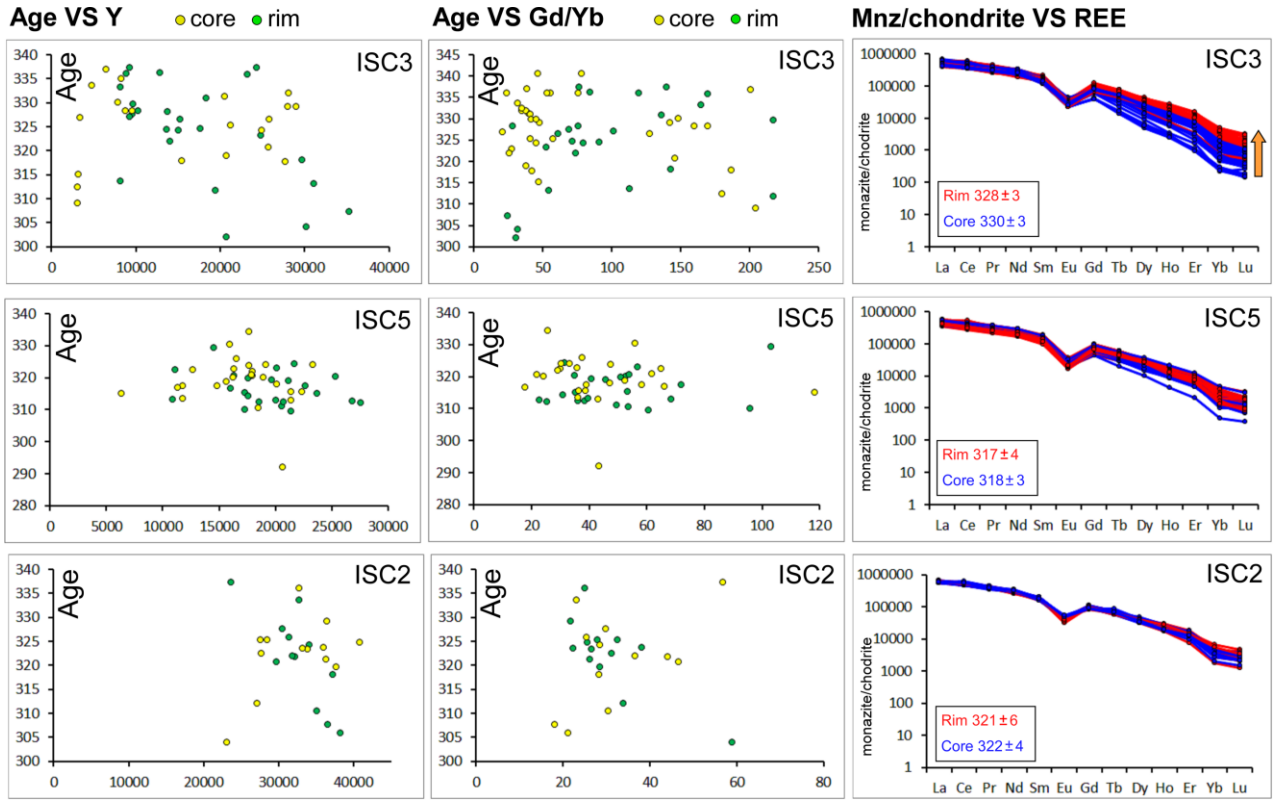

Figure 4.31 - Trace element characterization of the dated monazite crystals: in the left column the age vs Y content (ppm) is indicated; in the central column the age vs Gd/Yb ratio is given; on the right column chondrite normalized (based on values of McDonough and Sun, 1995) REE patterns of dated monazites are shown. Average age for rims and cores are also reported

							Data for Wetherill plot[3]						Ages[3]										U-Pb Concordant ages	
Sample	Mnz	Spot location	Zoning	$^{207}Pb/^{206}Pb$	1s abs	$^{207}Pb/^{235}U$	1s abs	$^{206}Pb/^{238}U$	1s abs	Rho	$^{208}Pb/^{232}Th$	1s abs	$^{207}Pb/^{206}Pb$	1s abs	$^{207}Pb/^{235}U$	1s abs	$^{206}Pb/^{238}U$	1s abs	$^{208}Pb/^{232}Th$	1s abs	% U-Pb disc[3]	% U-Th disc[4]		2s abs
ARG 19	Mnz14	core	low-Y	0.05060	0.00060	0.37949	0.00711	0.05446	0.00096	0.9	0.01639	0.00024	223	3	327	6	342	6	329	5	-4.6	3.9		
	Mnz14	core	int-Y	0.04850	0.00058	0.35984	0.00677	0.05384	0.00095	0.9	0.01651	0.00024	124	1	312	6	338	6	331	5	-8.3	2.1		
	Mnz14	rim	high-Y	0.04718	0.00054	0.35209	0.00655	0.05419	0.00097	1.0	0.01672	0.00025	58	1	306	6	340	6	335	5	-11.1	1.5		
	Mnz14	rim	high-Y	0.04719	0.00054	0.34671	0.00644	0.05337	0.00095	1.0	0.01602	0.00023	59	1	302	6	335	6	321	5	-10.9	4.2		
	Mnz14	rim	high-Y	0.05304	0.00063	0.39997	0.00750	0.05482	0.00098	0.9	0.01616	0.00023	331	4	342	6	344	6	324	5	-0.7	5.8	341	11
	Mnz14	core	low-Y	0.05362	0.00060	0.40053	0.00737	0.05427	0.00097	1.0	0.01596	0.00023	355	4	342	6	341	6	320	5	0.4	6.1	344	10
	Mnz6	rim	high-Y	0.04596	0.00053	0.34394	0.00640	0.05442	0.00098	1.0	0.01590	0.00023	-4	0	300	6	342	6	319	5	-13.8	6.7		
	Mnz6	rim	high-Y	0.04429	0.00049	0.32846	0.00606	0.05389	0.00097	1.0	0.01589	0.00023	-95	-1	288	5	338	6	319	5	-17.3	5.8		
	Mnz6	core	high-Y	0.04672	0.00052	0.34731	0.00641	0.05405	0.00097	1.0	0.01554	0.00022	35	0	303	6	339	6	312	4	-12.1	8.2		
	Mnz3	core	low-Y	0.05366	0.00075	0.40986	0.00859	0.05523	0.00101	0.9	0.01578	0.00024	357	5	349	7	347	6	316	5	0.6	8.7	348	12
	Mnz3	core	low-Y	0.05091	0.00074	0.38909	0.00823	0.05540	0.00102	0.9	0.01533	0.00023	237	3	334	7	348	6	308	5	-4.2	11.5		
	Mnz8	core	low-Y	0.05012	0.00073	0.39204	0.00837	0.05684	0.00105	0.9	0.01555	0.00023	201	3	336	7	356	7	312	5	-6.1	12.5		
	Mnz8	rim	high-Y	0.06046	0.00089	0.43421	0.00917	0.05209	0.00095	0.9	0.01580	0.00024	620	9	366	8	327	6	317	5	10.6	3.2		
ARG 29	Mnz5	core	high-Y	0.04671	0.00064	0.33727	0.00559	0.05260	0.00080	0.9	0.01725	0.00028	34	0	295	5	330	5	346	6	-12.0	-4.6		
	Mnz5	rim/core	low-Y	0.04793	0.00067	0.35617	0.00602	0.05387	0.00083	0.9	0.01637	0.00027	96	1	309	5	338	5	328	5	-9.3	3.0		
	Mnz2	core	low-Y	0.04709	0.00054	0.36473	0.00547	0.05610	0.00085	1.0	0.01699	0.00027	54	1	316	5	352	5	341	5	-11.4	3.2		
	Mnz2	core	high/int-Y	0.04631	0.00056	0.33850	0.00520	0.05301	0.00081	1.0	0.01643	0.00026	14	0	296	5	333	5	329	5	-12.5	1.1		
	Mnz9	rim	high-Y	0.04648	0.00061	0.34793	0.00565	0.05427	0.00083	0.9	0.01645	0.00026	23	0	303	5	341	5	330	5	-12.4	3.2		
	Mnz9	core	low-Y	0.18607	0.00259	1.52869	0.02448	0.05974	0.00093	1.0	0.01511	0.00025	2708	38	942	15	374	6	303	5	60.3	19.0		
	Mnz11	core	low-Y	0.04845	0.00058	0.34997	0.00538	0.05234	0.00080	1.0	0.01663	0.00026	121	1	305	5	329	5	333	5	-7.9	-1.4		
	Mnz11	core	low-Y	0.04926	0.00058	0.35799	0.00544	0.05268	0.00081	1.0	0.01646	0.00026	160	2	311	5	331	5	330	5	-6.5	0.3		
	Mnz11	rim	high-Y	0.05338	0.00064	0.37450	0.00578	0.05085	0.00078	1.0	0.01626	0.00026	345	4	323	5	320	5	326	5	1.0	-2.0		
	Mnz20	core	high-Y	0.04698	0.00072	0.33071	0.00590	0.05104	0.00080	0.9	0.01667	0.00027	48	1	290	5	321	5	334	5	-10.6	-4.1		
	Mnz20	rim	low-Y	0.04901	0.00074	0.34441	0.00616	0.05121	0.00082	0.9	0.01630	0.00026	148	2	301	5	322	5	327	5	-7.1	-1.5		
	Mnz24	core	high-Y	0.04687	0.00070	0.33064	0.00584	0.05121	0.00079	0.9	0.01655	0.00026	43	1	290	5	322	5	332	5	-11.0	-3.1		
	Mnz24	core	low-Y	0.05828	0.00114	0.43250	0.00934	0.05354	0.00088	0.8	0.01482	0.00023	540	11	365	8	336	5	297	5	7.9	11.6		
ARG 48b	Mnz58	Core	High-Y/low-Y	0.05115	0.00092	0.35022	0.00773	0.04967	0.00090	0.8	0.01556	0.00025	248	4	305	7	312	6	312	5	-2.5	0.1		
	Mnz59	Core	High-Y	0.05339	0.00112	0.54547	0.01353	0.07418	0.00138	0.7	0.02130	0.00035	345	7	442	11	461	9	426	7	-4.4	7.7		
	Mnz57	Core	High-Y/low-Y	0.05361	0.00100	0.39211	0.00893	0.05303	0.00096	0.8	0.01636	0.00026	355	7	336	8	333	6	328	5	0.8	1.5	334	12
	Mnz56	Core	Medium-Y	0.05584	0.00106	0.39324	0.00900	0.05105	0.00093	0.8	0.01597	0.00026	446	8	337	8	321	6	320	5	4.7	0.2		
	Mnz56	Core	Low-Y	0.05269	0.00115	0.37788	0.00964	0.05204	0.00098	0.7	0.01557	0.00026	315	7	325	8	327	6	312	5	-0.5	4.5	327	12
	Mnz55	Rim	Medium-Y	0.05513	0.00129	0.37930	0.01018	0.04995	0.00094	0.7	0.01562	0.00026	417	10	327	9	314	6	313	5	3.8	0.3		
	Mnz55	Core	Low-Y	0.04840	0.00093	0.33991	0.00792	0.05091	0.00093	0.8	0.01599	0.00026	119	2	297	7	320	6	321	5	-7.7	-0.2		
ARG21	Mnz55	Core	High-Y	0.05031	0.00085	0.35590	0.00626	0.05132	0.00070	0.8	0.01602	0.00028	209	4	309	5	323	4	321	6	-4.4	0.4		
	Mnz30	Core	High-Y	0.05196	0.00087	0.33730	0.00594	0.04713	0.00064	0.8	0.01430	0.00025	284	5	295	5	297	4	287	5	-0.6	3.3	297	8
	Mnz26	Core	High-Y	0.05001	0.00083	0.34893	0.00612	0.05062	0.00069	0.8	0.01583	0.00028	195	3	304	5	318	4	317	6	-4.7	0.3		
	Mnz7	Core	High-Y	0.04879	0.00081	0.34771	0.00610	0.05170	0.00071	0.8	0.01587	0.00028	138	2	303	5	325	4	318	6	-7.2	2.1		
	Mnz7	Core	High-Y	0.04893	0.00082	0.34800	0.00614	0.05161	0.00071	0.8	0.01600	0.00028	144	2	303	5	324	4	321	6	-7.0	1.1		
	Mnz16	Core	Medium-Y	0.05155	0.00087	0.36991	0.00661	0.05206	0.00072	0.8	0.01599	0.00028	266	4	320	6	327	5	321	6	-2.4	2.0		
	Mnz16	Rim	High-Y	0.04985	0.00085	0.35610	0.00638	0.05184	0.00072	0.8	0.01591	0.00028	188	3	309	6	326	5	319	6	-5.3	2.1		
	Mnz16	Rim	High-Y	0.04849	0.00081	0.33799	0.00598	0.05056	0.00070	0.8	0.01573	0.00028	123	2	296	5	318	4	315	6	-7.5	0.8		
	Mnz16	Core	High-Y	0.05254	0.00092	0.36114	0.00672	0.04988	0.00070	0.8	0.01536	0.00027	309	5	313	6	314	4	308	5	-0.2	1.8	314	9
ARG27	Mnz56	Core	High-Y	0.05027	0.00124	0.36285	0.00912	0.05220	0.00093	0.7	0.01609	0.00028	207	5	314	8	328	6	323	6	-4.4	1.6		
	Mnz58	Core	Low-Y	0.05897	0.00139	0.42181	0.01010	0.05192	0.00090	0.7	0.01551	0.00026	566	13	357	9	326	6	311	5	8.7	4.7		
	Mnz52	Rim-core	High-Y	0.05226	0.00123	0.37062	0.00886	0.05143	0.00089	0.7	0.01550	0.00026	297	7	320	8	323	6	311	5	-1.0	3.8	323	11
	mnz52	Rim	Low-Y	0.08657	0.00204	0.62877	0.01503	0.05273	0.00092	0.7	0.01509	0.00025	1351	32	495	12	331	6	303	5	33.1	8.6		
3 Discordance calculated as (1-(206Pb/238U age/207Pb/235U age))*100																								
4 Discordance calculated as (1-(208Pb/232Th age/206Pb/238U age))*100																								

Table 4.6 – Full dataset of LA-ICP-MS analysis on samples ARG 19, ARG 29, ARG48b ARG21 and ARG 27

															Age	1	Age	1	
sample	U ppm	Th ppm	$^{207}Pb/^{235}U$	2σ	$^{206}Pb/^{238}U$	2σ	rho	$^{238}U/^{206}Pb$	2σ	$^{207}Pb/^{206}Pb$	2σ	rho	$^{208}Pb/^{232}Th$	2σ	$^{208}Pb/^{232}Th$	2σ	7-corr	2σ	Concordance
ISC3_mnz8_5	9200	34000	0.385	0.013	0.05	0.00	0.97	20.00	0.69	0.056	0.001	-0.06	0.0157	0.0006	314	11	313	11	0.95
ISC3_mnz8_6	8300	36200	0.398	0.018	0.05	0.00	0.98	20.33	0.85	0.058	0.001	-0.15	0.0151	0.0007	302	13	307	13	0.91
ISC3_mnz8_7	8880	37300	0.382	0.015	0.05	0.00	0.95	20.70	0.80	0.057	0.001	-0.03	0.0150	0.0006	301	13	302	12	0.93
ISC3_mnz8_8	11360	35700	0.386	0.014	0.05	0.00	0.98	20.24	0.74	0.057	0.001	0.01	0.0155	0.0006	310	12	309	11	0.94
ISC3_mnz8_9	8700	44000	0.402	0.014	0.05	0.00	0.95	19.65	0.70	0.058	0.001	-0.02	0.0155	0.0006	312	11	318	11	0.93
ISC3_mnz8_10	8270	40800	0.388	0.017	0.05	0.00	0.97	19.88	0.82	0.056	0.001	0.03	0.0159	0.0007	319	13	315	13	0.95
ISC3_mnz8_12	8620	44600	0.391	0.016	0.05	0.00	0.97	20.49	0.82	0.059	0.001	0.08	0.0149	0.0006	299	13	305	12	0.92
ISC3_mnz8_13	9060	35300	0.376	0.016	0.05	0.00	0.98	20.96	0.82	0.057	0.001	-0.09	0.0145	0.0006	292	13	299	12	0.93
ISC3_mnz8_14	7210	36600	0.452	0.021	0.05	0.00	0.89	20.58	0.90	0.068	0.002	-0.16	0.0117	0.0005	236	11	300	13	0.81
ISC3_mnz8_15	11700	38600	0.386	0.017	0.05	0.00	0.98	20.04	0.90	0.056	0.001	0.02	0.0158	0.0007	317	14	312	14	0.95
ISC3_mnz8_16	8090	32600	0.391	0.017	0.05	0.00	0.98	19.96	0.86	0.056	0.001	0.03	0.0153	0.0007	307	14	314	13	0.94
ISC3_mnz13_1	6680	44200	0.385	0.016	0.05	0.00	0.98	20.08	0.83	0.056	0.001	-0.05	0.0152	0.0006	304	12	312	13	0.95
ISC3_mnz13_3	4251	35310	0.396	0.015	0.05	0.00	0.98	19.12	0.73	0.055	0.001	-0.15	0.0165	0.0007	332	13	328	12	0.97
ISC3_mnz13_5	5130	26080	0.413	0.015	0.05	0.00	0.95	18.59	0.64	0.055	0.001	-0.19	0.0166	0.0006	333	12	337	11	0.96
ISC3_mnz13_6	4820	23280	0.395	0.015	0.05	0.00	0.97	19.01	0.72	0.054	0.001	0.04	0.0171	0.0007	344	13	330	12	0.98
ISC3_mnz13_7	5140	22040	0.403	0.017	0.05	0.00	0.98	18.66	0.79	0.055	0.001	-0.06	0.0161	0.0007	324	14	336	14	0.98
ISC3_mnz13_8	6200	24160	0.381	0.015	0.05	0.00	0.99	19.57	0.76	0.054	0.001	-0.12	0.0165	0.0007	330	13	321	12	0.98
ISC3_mnz13_9	5920	24080	0.387	0.013	0.05	0.00	0.98	19.72	0.67	0.055	0.001	-0.08	0.0166	0.0006	334	12	318	11	0.96
ISC3_mnz13_11	5750	19920	0.386	0.015	0.05	0.00	0.98	19.34	0.74	0.054	0.001	0.16	0.0165	0.0007	331	13	324	12	0.98
ISC3_mnz13_12	5810	20140	0.392	0.014	0.05	0.00	0.98	19.05	0.69	0.054	0.001	-0.01	0.0167	0.0006	334	13	329	12	0.98
ISC3_mnz13_13	5430	21850	0.390	0.019	0.05	0.00	0.99	18.90	0.90	0.054	0.001	-0.15	0.0167	0.0008	335	17	332	16	0.99
ISC3_mnz13_15	6490	23370	0.393	0.015	0.05	0.00	0.99	19.65	0.73	0.055	0.001	0.04	0.0165	0.0007	331	13	319	12	0.95
ISC3_mnz13_16	6430	23520	0.388	0.016	0.05	0.00	0.98	18.94	0.81	0.054	0.001	-0.04	0.0168	0.0007	337	14	331	14	1.00
ISC3_mnz13_17	6640	24960	0.392	0.014	0.05	0.00	0.98	19.27	0.65	0.055	0.001	-0.02	0.0165	0.0006	331	12	325	11	0.97
ISC3_mnz13_18	6710	25260	0.388	0.013	0.05	0.00	0.96	19.42	0.69	0.054	0.001	0.05	0.0166	0.0006	334	13	323	11	0.97
ISC3_mnz13_19	5510	25540	0.393	0.014	0.05	0.00	0.98	19.31	0.68	0.055	0.001	0.05	0.0166	0.0006	332	13	325	11	0.97
ISC3_mnz13_20	3880	34610	0.406	0.018	0.05	0.00	0.98	18.59	0.85	0.055	0.001	0.06	0.0167	0.0008	335	15	337	15	0.98
ISC3_mnz13_21	6020	24610	0.392	0.015	0.05	0.00	0.98	18.90	0.72	0.054	0.001	0.15	0.0173	0.0007	346	14	332	12	0.99
ISC3_mnz13_22	4800	29750	0.391	0.015	0.05	0.00	0.98	19.19	0.77	0.055	0.001	0.06	0.0166	0.0007	333	14	327	13	0.98
ISC3_mnz13_23	3331	46300	0.408	0.017	0.05	0.00	0.97	18.83	0.77	0.055	0.001	0.05	0.0165	0.0007	330	14	333	13	0.96
ISC3_mnz13_24	3530	48000	0.405	0.016	0.05	0.00	0.97	18.90	0.75	0.056	0.001	-0.04	0.0164	0.0007	328	13	331	13	0.96
ISC3_mnz13_25	4053	42440	0.406	0.018	0.05	0.00	0.98	18.98	0.81	0.056	0.001	-0.01	0.0165	0.0007	331	15	330	14	0.96
ISC3_mnz13_26	3488	50500	0.407	0.017	0.05	0.00	0.96	18.98	0.72	0.056	0.001	-0.09	0.0164	0.0007	328	13	330	12	0.95
ISC3_mnz13_27	3498	50100	0.406	0.014	0.05	0.00	0.97	19.16	0.70	0.056	0.001	0.20	0.0162	0.0006	324	12	327	12	0.95
ISC3_mnz13_28	4960	32720	0.395	0.016	0.05	0.00	0.98	19.46	0.78	0.055	0.001	-0.12	0.0165	0.0007	331	14	322	13	0.96
ISC3_mnz13_29	5780	26790	0.395	0.016	0.05	0.00	0.98	19.27	0.74	0.055	0.001	0.16	0.0168	0.0007	337	14	325	12	0.96
ISC3_mnz5_1	3478	23960	0.431	0.019	0.05	0.00	0.97	19.57	0.83	0.060	0.001	0.07	0.0160	0.0007	321	14	318	13	0.88
ISC3_mnz5_2	4074	22370	0.426	0.016	0.05	0.00	0.98	19.27	0.77	0.060	0.001	0.04	0.0164	0.0007	328	13	323	13	0.91
ISC3_mnz5_3	3179	25370	0.413	0.015	0.05	0.00	0.93	19.05	0.66	0.056	0.001	0.13	0.0163	0.0006	326	12	328	11	0.94
ISC3_mnz5_5	3299	27270	0.409	0.016	0.05	0.00	0.95	19.05	0.72	0.057	0.001	-0.02	0.0164	0.0007	328	13	328	12	0.95
ISC3_mnz5_6	3163	28180	0.418	0.020	0.05	0.00	0.97	19.01	0.88	0.058	0.001	-0.17	0.0163	0.0008	327	16	328	15	0.93
ISC3_mnz5_7	3243	32320	0.413	0.016	0.05	0.00	0.94	19.27	0.74	0.057	0.001	0.01	0.0160	0.0006	320	12	324	12	0.93
ISC3_mnz5_10	3386	31440	0.418	0.015	0.05	0.00	0.95	18.98	0.69	0.057	0.001	-0.09	0.0162	0.0006	325	12	329	12	0.93
ISC3_mnz5_11	3053	29190	0.419	0.020	0.05	0.00	0.96	19.38	0.88	0.059	0.001	-0.02	0.0161	0.0007	322	15	322	14	0.91
ISC3_mnz5_12	3293	27200	0.407	0.017	0.05	0.00	0.97	19.12	0.83	0.057	0.001	0.08	0.0162	0.0007	324	14	327	14	0.95
ISC3_mnz5_13	3434	22940	0.417	0.016	0.05	0.00	0.94	19.23	0.71	0.058	0.001	-0.05	0.0162	0.0006	324	13	325	12	0.92
ISC3_mnz5_14	3405	22780	0.410	0.015	0.05	0.00	0.93	18.62	0.64	0.055	0.001	0.10	0.0166	0.0006	334	13	336	11	0.97
ISC3_mnz2_3	3197	25650	0.393	0.016	0.05	0.00	0.98	18.83	0.74	0.054	0.001	-0.15	0.0161	0.0006	323	13	333	13	0.99
ISC3_mnz2_4	3714	29270	0.395	0.019	0.05	0.00	0.99	19.01	0.85	0.054	0.001	-0.26	0.0162	0.0007	325	15	330	15	0.98
ISC3_mnz2_5	3955	28690	0.398	0.014	0.05	0.00	0.98	18.94	0.69	0.055	0.001	0.15	0.0164	0.0006	329	13	331	12	0.97
ISC3_mnz2_6	4560	25390	0.389	0.014	0.05	0.00	0.98	19.12	0.70	0.054	0.001	0.04	0.0161	0.0006	322	12	328	12	0.98
ISC3_mnz2_7	3814	25090	0.393	0.016	0.05	0.00	0.97	18.66	0.73	0.054	0.001	0.08	0.0164	0.0007	329	14	336	13	1.00
ISC3_mnz2_8	3196	27900	0.416	0.015	0.05	0.00	0.93	19.12	0.64	0.056	0.001	-0.14	0.0158	0.0006	316	11	327	11	0.93
ISC3_mnz2_9	3354	32150	0.399	0.019	0.05	0.00	0.99	18.80	0.86	0.054	0.001	0.19	0.0161	0.0007	324	15	334	15	0.98
ISC3_mnz2_10	3448	30640	0.395	0.016	0.05	0.00	0.97	18.73	0.76	0.053	0.001	0.18	0.0164	0.0007	329	14	335	13	0.99
ISC3_mnz2_11	3454	27940	0.393	0.015	0.05	0.00	0.97	18.69	0.70	0.053	0.001	0.01	0.0165	0.0006	331	13	336	12	1.00
ISC3_mnz2_12	3400	27250	0.401	0.022	0.05	0.00	0.99	18.42	0.99	0.054	0.001	0.01	0.0165	0.0009	331	17	341	18	1.00
ISC3_mnz2_13	3383	27650	0.401	0.016	0.05	0.00	0.98	18.59	0.75	0.054	0.001	0.21	0.0165	0.0006	331	13	337	13	0.99
ISC3_mnz2_14	3346	27040	0.389	0.015	0.05	0.00	0.97	18.69	0.70	0.053	0.001	-0.09	0.0164	0.0006	328	13	336	12	1.01

Table 4.7 – Full dataset of LASS analysis on samples ISC 2, ISC 3

ISC5_mnz7_1	7920	34780	0.412	0.015	0.05	0.00	0.98	19.76	0.71	0.059	0.001	-0.01	0.0157	0.0006	315	12	316	11	0.91
ISC5_mnz7_2	8450	40700	0.396	0.016	0.05	0.00	0.97	19.53	0.76	0.055	0.001	0.10	0.0162	0.0006	324	13	321	12	0.95
ISC5_mnz7_3	6400	29680	0.396	0.014	0.05	0.00	0.97	19.84	0.68	0.057	0.001	0.01	0.0161	0.0006	322	12	315	11	0.94
ISC5_mnz7_4	7560	28650	0.388	0.015	0.05	0.00	0.98	19.42	0.72	0.054	0.001	-0.12	0.0164	0.0006	330	13	323	12	0.97
ISC5_mnz7_5	7810	30320	0.396	0.017	0.05	0.00	0.99	20.08	0.83	0.058	0.001	0.04	0.0158	0.0007	316	13	311	13	0.92
ISC5_mnz7_7	7400	28600	0.397	0.017	0.05	0.00	0.98	19.53	0.82	0.056	0.001	0.00	0.0162	0.0007	326	14	321	13	0.95
ISC5_mnz7_8	6460	27920	0.462	0.020	0.05	0.00	0.98	19.49	0.82	0.065	0.001	0.07	0.0148	0.0007	297	13	318	13	0.84
ISC5_mnz7_10	3786	25510	0.443	0.019	0.05	0.00	0.94	18.90	0.81	0.060	0.001	0.08	0.0100	0.0004	201	9	329	14	0.89
ISC5_mnz7_12	4850	28510	0.462	0.018	0.05	0.00	0.91	19.92	0.72	0.066	0.002	-0.06	0.0110	0.0004	221	8	310	11	0.82
ISC5_mnz7_14	6700	27880	0.484	0.015	0.05	0.00	0.96	19.69	0.61	0.069	0.001	0.03	0.0150	0.0005	300	10	313	10	0.80
ISC5_mnz2_2	7280	29430	0.451	0.020	0.05	0.00	0.99	19.42	0.88	0.064	0.001	-0.01	0.0158	0.0007	317	14	319	14	0.86
ISC5_mnz2_3	6560	29570	0.452	0.016	0.05	0.00	0.88	19.38	0.65	0.064	0.002	0.05	0.0161	0.0005	323	11	320	11	0.86
ISC5_mnz2_5	6990	31570	0.451	0.019	0.05	0.00	0.99	19.80	0.84	0.064	0.001	-0.06	0.0159	0.0007	319	14	313	13	0.84
ISC5_mnz2_7	7530	26140	0.391	0.015	0.05	0.00	0.98	19.61	0.80	0.055	0.001	0.05	0.0163	0.0007	326	14	320	13	0.96
ISC5_mnz2_8	6560	26920	0.438	0.018	0.05	0.00	0.98	20.04	0.83	0.063	0.001	0.05	0.0142	0.0006	285	12	310	13	0.85
ISC5_mnz2_9	7370	26710	0.453	0.016	0.05	0.00	0.95	19.80	0.71	0.065	0.001	0.15	0.0156	0.0006	313	12	312	11	0.84
ISC5_mnz3_1	5370	22510	0.389	0.014	0.05	0.00	0.97	19.34	0.71	0.054	0.001	-0.13	0.0165	0.0006	332	12	324	12	0.97
ISC5_mnz3_2	5750	22230	0.391	0.015	0.05	0.00	0.98	20.04	0.76	0.056	0.001	-0.17	0.0160	0.0006	322	13	313	12	0.94
ISC5_mnz3_3	5830	23070	0.391	0.015	0.05	0.00	0.98	19.92	0.78	0.056	0.001	0.14	0.0162	0.0007	325	14	314	12	0.94
ISC5_mnz3_4	5490	22880	0.384	0.016	0.05	0.00	0.98	20.04	0.83	0.056	0.001	0.10	0.0161	0.0007	324	14	312	13	0.95
ISC5_mnz3_6	5800	26500	0.394	0.017	0.05	0.00	0.98	19.96	0.86	0.057	0.001	0.15	0.0161	0.0007	323	15	313	13	0.93
ISC5_mnz3_8	5060	23680	0.393	0.018	0.05	0.00	0.98	19.76	0.84	0.056	0.001	-0.26	0.0162	0.0007	324	14	317	13	0.95
ISC5_mnz3_9	5370	23230	0.396	0.017	0.05	0.00	0.99	19.42	0.81	0.056	0.001	-0.15	0.0164	0.0007	329	14	323	13	0.96
ISC5_mnz3_10	5750	23510	0.390	0.017	0.05	0.00	0.99	19.53	0.82	0.055	0.001	-0.18	0.0162	0.0007	326	14	321	13	0.96
ISC5_mnz3_11	4970	27160	0.399	0.014	0.05	0.00	0.99	19.53	0.69	0.056	0.001	-0.23	0.0162	0.0006	324	13	320	11	0.94
ISC5_mnz3_12	4990	24070	0.394	0.016	0.05	0.00	0.97	19.46	0.75	0.055	0.001	0.03	0.0165	0.0007	330	13	322	12	0.96
ISC5_mnz3_13	5160	25720	0.393	0.017	0.05	0.00	0.98	19.96	0.82	0.057	0.001	0.04	0.0164	0.0007	328	14	314	13	0.94
ISC5_mnz3_14	6590	23990	0.392	0.014	0.05	0.00	0.98	19.69	0.70	0.056	0.001	0.02	0.0165	0.0006	330	13	318	11	0.95
ISC5_mnz3_15	5630	20610	0.397	0.016	0.05	0.00	0.97	19.96	0.79	0.057	0.001	-0.05	0.0165	0.0007	330	13	313	12	0.93
ISC5_mnz3_17	5730	23320	0.392	0.017	0.05	0.00	0.99	19.72	0.84	0.056	0.001	0.11	0.0159	0.0007	319	14	318	13	0.95
ISC5_mnz3_19	6110	21810	0.426	0.019	0.05	0.00	0.98	19.23	0.83	0.059	0.001	-0.19	0.0169	0.0007	339	15	324	14	0.91
ISC5_mnz3_20	5920	22810	0.399	0.019	0.05	0.00	0.98	19.80	0.91	0.057	0.001	0.11	0.0160	0.0007	322	15	316	14	0.93
ISC5_mnz3_21	6480	24450	0.412	0.016	0.05	0.00	0.98	19.76	0.77	0.059	0.001	0.09	0.0163	0.0007	327	13	316	12	0.91
ISC5_mnz3_22	5940	22360	0.405	0.018	0.05	0.00	0.98	19.38	0.85	0.057	0.001	0.14	0.0165	0.0008	332	15	323	14	0.94
ISC5_mnz3_23	6050	24690	0.395	0.014	0.05	0.00	0.97	19.34	0.68	0.055	0.001	0.03	0.0163	0.0006	327	12	324	11	0.96
ISC5_mnz3_24	4740	24200	0.462	0.020	0.05	0.00	0.98	19.01	0.85	0.063	0.001	-0.08	0.0162	0.0007	325	14	326	14	0.86
ISC5_mnz3_25	5290	27400	0.464	0.018	0.05	0.00	0.98	19.61	0.76	0.066	0.001	-0.08	0.0158	0.0006	317	13	315	12	0.83
ISC5_mnz3_27	5470	22460	0.427	0.019	0.05	0.00	0.99	19.53	0.86	0.060	0.001	0.13	0.0162	0.0007	324	14	319	14	0.89
ISC5_mnz10_8	5580	23750	0.391	0.016	0.05	0.00	0.98	19.42	0.78	0.055	0.001	0.16	0.0166	0.0007	332	14	323	13	0.97
ISC5_mnz10_11	4810	16950	0.424	0.021	0.05	0.00	0.98	18.87	0.90	0.058	0.001	0.06	0.0173	0.0008	347	17	331	16	0.93
ISC5_mnz10_13	5290	19770	0.440	0.017	0.05	0.00	0.97	18.62	0.73	0.059	0.001	0.11	0.0172	0.0007	344	14	335	13	0.91
ISC5_mnz10_14	5750	20750	0.392	0.019	0.05	0.00	0.98	19.34	0.88	0.055	0.001	-0.02	0.0165	0.0008	332	16	324	14	0.97
ISC5_mnz10_16	5430	22290	0.472	0.020	0.05	0.00	0.97	19.46	0.82	0.066	0.001	-0.15	0.0161	0.0007	322	14	318	13	0.82
ISC5_mnz10_17	5470	20790	0.430	0.018	0.05	0.00	0.98	19.61	0.83	0.061	0.001	0.10	0.0162	0.0007	326	15	317	13	0.88
ISC5_mnz10_18	5300	20740	0.420	0.018	0.05	0.00	0.96	21.23	0.84	0.064	0.001	-0.22	0.0146	0.0005	292	11	292	11	0.83
ISC5_mnz10_20	5650	21660	0.411	0.017	0.05	0.00	0.97	20.08	0.83	0.059	0.001	-0.02	0.0152	0.0006	305	13	311	13	0.90
ISC5_mnz10_22	5590	20810	0.427	0.017	0.05	0.00	0.98	19.46	0.78	0.060	0.001	-0.05	0.0163	0.0007	327	13	320	13	0.89
ISC5_mnz10_23	6080	22320	0.387	0.016	0.05	0.00	0.98	19.53	0.79	0.054	0.001	-0.07	0.0166	0.0007	332	14	321	13	0.97

Table 4.7 – (continue) Full dataset of LASS analysis on samples ISC 5

4.1.9 Data discussion and interpretation

The FMSZ is a steeply dipping shear zone with a dominant right-lateral reverse top-to-the-SE sense of shear, whereas locally it shows a normal sense of shear, depending on the dip direction of the mylonitic foliation. The FMSZ developed under conditions of decreasing temperature. It initiated under HT amphibolite-facies conditions and evolved toward greenschist-facies condition as suggested by the change of the stable syn-kinematic assemblage: sillimanite + biotite, biotite + white mica and white mica + chlorite along the protomylonitic, mylonitic and ultramylonitic foliations, respectively. Deformation temperatures obtained with quartz c-axis thermometer confirm this interpretation and allow to identify temperature ranges of deformation: between 610° C – 588° C for the protomylonites, 538° C – 482° C for the mylonites, 500° C – 418° C for the ultramylonites.

The geometry of the foliation and mineral lineation, as well as the kinematic indicators, are concordant in the protomylonites and in the mylonites. Temperature during Alpine deformation was 375 ± 30 °C (greenschist facies metamorphism; Corsini *et al*., 2004; Sanchez *et al*., 2011) and, as a consequence, the amphibolite-facies metamorphism may be inferred to be pre-Alpine.

The results allowed us to define for the first time the deformation regime and the finite strain of the FMSZ.

The kinematic vorticity data obtained by the S-C' and quartz c-axis fabric methods allowed us to quantify the deformation, characterized by a non-coaxial flow, in terms of percentage of pure and simple shear components. Samples from the less deformed lithotypes, localized in the external portion of the shear zone, record a deformation dominated by pure shear. The amount of simple shear increases towards the center of the shear zone, from ~24 % in the protomylonites to ~ 62 % in the ultramylonites (fig. 4.32a).

Finite strain analysis yields average shortening and stretching values of 27% and 36%, measured parallel to the inferred flow plane (shear zone boundaries) and flow direction, respectively.

Taking into account the type of flow, the finite strain and the angles θ between the maximum horizontal ISA and the shear zone boundaries (fig. 4.32b), we can recognize a change from a pure shear dominated transpression to a simple shear dominated transpression (fig. 4.32c) according to the models proposed by Fossen and Tikoff (1993) and by Fossen *et al.* (1994).

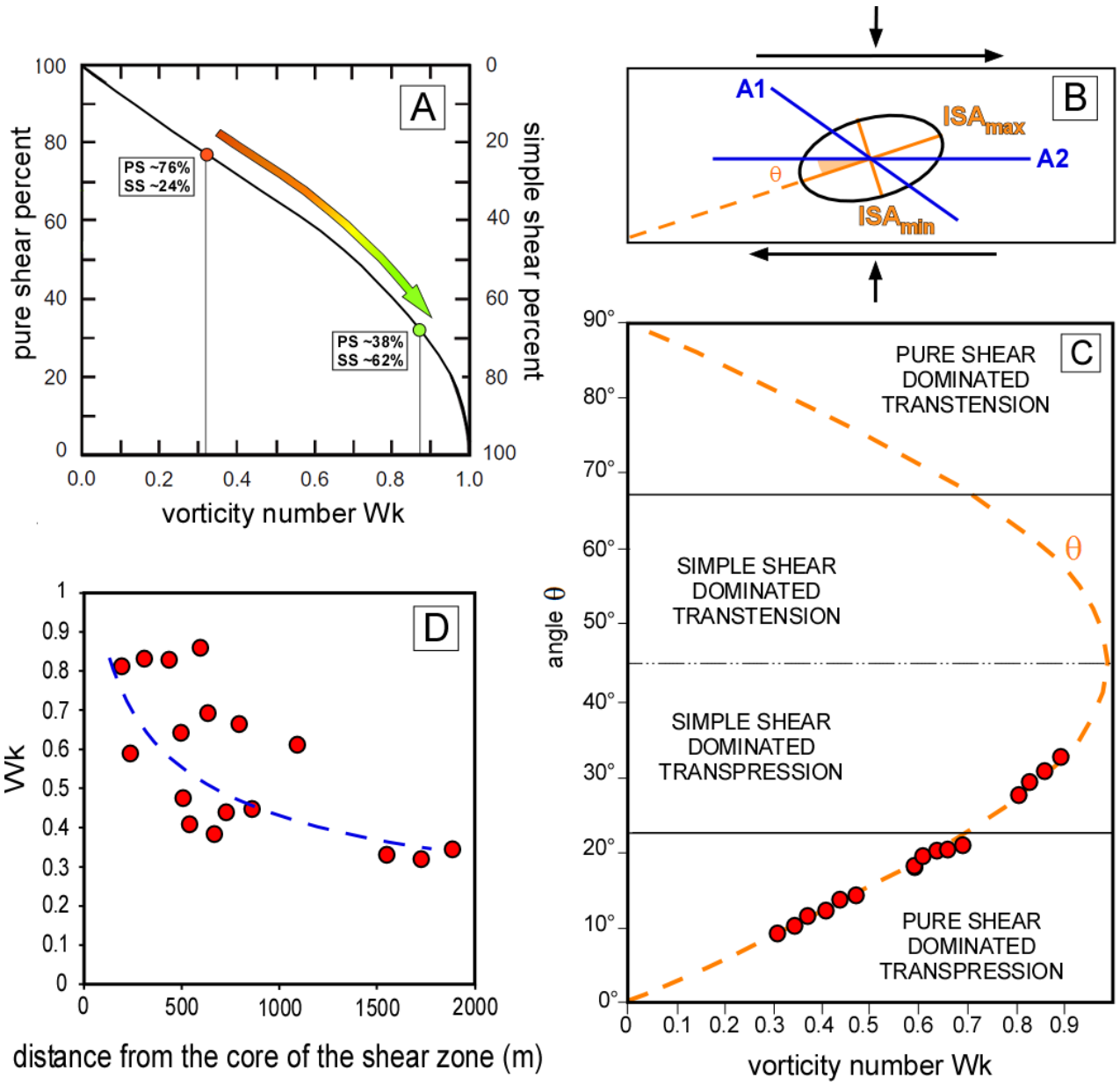

Figure 4.32 - A) Percentage of pure shear (PS) and simple shear (SS) in relation to the calculated maximum and minimum Wk values; B) simplified sketch showing orientation of the instantaneous flow elements and their angular relationships in a dextral shear zone with simultaneous pure shear and simple shear, θ is the angle between ISAmax and the shear zone boundary (modified after Xypolias, 2010); C) diagram showing relationship between the orientation of the maximum Istantaneous Stretching Axis (ISAmax) with respect to the shear zone boundary (angle θ) related to the kinematic vorticity number Wk (modified after Fossen and Tikoff, 1993; Fossen *et al.*, 1994) Wk value for which simple shear = pure shear is 0,71 according to Law *et al.*, 2004 and Xypolias, 2010. The distribution of the samples shows a variation from a pure shear dominated transpression to a simple shear dominated transpression linked to the increase of the vorticity number. Orange dashed line represents the theoretical trend of the angle θ. Note that the distribution of θ values in the studied samples is in good agreementt with the theoretical curve; D) variation of the vorticity number in relation with the distance of the sample from the center of the shear zone. The distribution of points shows increasing Wk values (i.e. increasing of simple shear component of deformation) toward the central part of the shear zone (trend: blue dashed line)

The orientation of the mylonitic foliation is sub-vertical along the 20 km length of the shear zone, in accordance with a transpressive shear zone setting (Fossen *et al.*, 1994; Fossen, 2016). In the case of transtensional deformation as suggested by Musumeci and Colombo (2002), the orientation of mylonitic

foliation is expected to be sub-horizontal due to the main sub-vertical shortening direction. Iacopini *et al.* (2008), discussing the orientations of the elongation lineation, suggest two kinds of transpressive shear zones: in the case of a sub-vertical lineation the shear zone was subjected to vertical extrusion while in the case of a sub-horizontal lineation extrusion was horizontal. The elongation lineation within the FMSZ is gently plunging, thus it would be compatible with a sub-horizontal direction of extrusion. Extrusion and shear zones with a component of pure shear are generally subjected to strain compatibility problems (Hudleston, 1999) and it is not trivial to explain how the flattening component of the deformation is accommodated.

To solve this problem Ramsay and Huber (1987) and Hudleston (1999) suggested that the flattening component can be obtained in a simple shear regime by volume loss in the deforming material. In this way the strain compatibility is maintained. However, this is not the case of the FMSZ because there is no evidence of structures suggesting major volume loss in the deformed rocks and the kinematic vorticity analysis revealed a major component of pure shear during deformation.

Anyway, Fossen (2016) have suggested that strain compatibility problems may also be overcome if the wall rocks are deformed by the same amount of coaxial strain as the shear zone. The wall rocks of the FMSZ, i.e. the GSV and the TMC complexes are deformed by open to tight upright folds with axial planes parallel to the mylonitic foliation in the FMSZ. According to Carosi *et al.* (2016) and Simonetti *et al.* (2017, 2018) these upright folds accommodate the component of shortening perpendicular to the FMSZ. Accordingly, the wall rocks and the shear zone could stretch together with no strain compatibility problems.

The Argentera-Mercantour Massif was involved in the Alpine orogeny at ~22 Ma (Corsini *et al.*, 2004, Sanchez *et al.*, 2011). Most of the Alpine deformation is concentrated in the sedimentary cover rocks, detached from the metamorphic basement along gypsum and limestone breccias levels (Malaroda *et al.*, 1970), in which several folding phases are recognizable (d'Atri *et al.*, 2016; Barale *et al.*, 2016). Evidence of Alpine deformation in the basement are brittle/ductile strike-slip faults and top-to-the-S reverse shear zones developed under greenschist facies conditions during the lower Miocene (Corsini *et al.*, 2004; Baietto *et al.*, 2009) cross-cutting both the FMSZ, in some sectors, and the GSV and Tinèe complexes. The kinematics of these Alpine shear zones is compatible with the transpressional regime that affects the Argentera Massif during the Lower Miocene (Baietto *et al.*, 2009). The presence of possible pseudotachylytes suggests seismic

activity associated with tectonically active structures, this hypothesis should be further tested by a detailed investigation of such structures. Variscan HT foliation and mylonitic foliation in the FMSZ all along its length are always subvertical and are not affected by strong subsequent folding.

U-Th-Pb petrochronology on monazites provides no Alpine ages demonstrating that the shear zone was not penetratively reactivated during the Alpine orogeny.

We interpret the obtained geochronological data combining textural observations, monazite chemistry and age distribution as follows. The occurrence of allanite ± apatite rims around some monazite grain in mylonites is indicative of the breakdown of monazite and is a further evidence of retrograde metamorphism. Since allanite and apatite grew asymmetrically in extensional sites around the monazite crystals, in agreement with the orientation of the instantaneous stretching axis during dextral shearing, it is possible to state that this reaction took place synkinematically during retrograde metamorphism (Gibson *et al*., 2004) and testifies to the decrease in temperature during a late stage of shearing. Further evidence supporting this interpretation include the high-Y, high-HREE content and low Gd/Yb ratio of syn-kinematic grains and/or rims that point to a growth during retro-metamorphism.

The oldest U-Th-Pb ages were obtained from monazite grains included in garnet and within a deformed white mica. These grains escaped subsequent deformation and other events perturbating the U-Th-Pb systematics. They can be interpreted as inherited ages from older tectono-metamorphic events as previously documented by other authors (Monié and Maluski, 1983; Rubatto *et al*., 2001; Corsini *et al*., 2004).

The $^{206}Pb/^{238}U$ and $^{208}Pb/^{232}Th$ ages range mainly from about 340 to 320 Ma. The oldest $^{206}Pb/^{238}U$ ages of this range were obtained in high-Y monazites along the protomylonitic foliation close to the margin of the shear zone and in asymmetric high-Y monazite rims in the same rocks (appendix F). This age, according to the syn-kinematic mineral assemblage and to the main deformation mechanism of quartz and feldspar, suggests that Variscan shear deformation in the Argentera Massif started at the metamorphic peak (dated at ~340 Ma in the GSV complex, Compagnoni *et al*., 2010; Rubatto *et al*., 2010) or shortly after it during the first partial melting event and triggered the exhumation of the GSV complex up to amphibolite-facies conditions.

Recently, Jouffray *et al*. (2020) dated at ~339 Ma ($^{40}Ar/^{39}Ar$ on amphiboles in textural equilibrium with plagioclase, ilmenite and garnet) the re-equilibration under amphibolite-facies conditions of eclogite relicts

embedded whithin migmatites of the GSV (outside of the FMSZ), thus conferming the time interval of ~340–330 Ma for initial retrogression and exhumation of the lower crust in the Argentera Massif in overall agreement with our findings.

Both $^{206}Pb/^{238}U$ and $^{208}Pb/^{232}Th$ ages become younger along the deformation gradient and monazite grains along the mylonitic foliation in the core of the shear zone have $^{206}Pb/^{238}U$ and $^{208}Pb/^{232}Th$ ages of ~320 ± 6 Ma. This broad correlation between ages and deformation gradient suggests a progressive concentration of deformation into the center of the shear zone. This approach also revealed long lasting activity on the FMSZ that continued for 20 million years under progressively changing high to low temperature conditions of metamorphism.

4.2 Aiguilles Rouge Massif

4.2.1 Introduction

In this chapter we focus on two areas of the Aiguilles Rouge Massif where rocks are strongly sheared along a thick belt of mylonites (Von Raumer and Bussy, 2004) and Alpine deformation is very weak and developed under brittle conditions (Pilloud, 1991; Dobmeier and Von Raumer, 1995). The aim of the chapter is to clarify both the kinematics of the flow and to directly constrain the age of the deformation in order to verify if they are similar to the ones proposed in the literature for the Argentera Massif and for the other fragments of the belt in the Mediterranean area.

Fieldwork and sample collection was based on previous work by Von Raumer and Bussy (2004).

We carried out a kinematic vorticity analysis and a U-Th-Pb petrochronological study on syn-kinematic monazites, combined with structural and microstructural analyses of sheared rocks already recognized by Von Raumer and Bussy (2004) and Genier *et al*. (2008). Sample locations are reported in figure 4.33. A list of the samples used for analysis, with the relative position and results, is reported in appendix D. All the data presented in this chapter were used to prepare a paper with the title "*Transpressive deformation in the Southern European Variscan Belt: new insights from the Aiguilles Rouges Massif (Western Alps)*" that was submitted to Tectonics.

4.2.2 Geological setting

The Aiguilles Rouges Massif is located on the boundary between Switzerland and France and belongs to the External Crystalline Massifs of the Western Alps (fig. 4.2) that represent fragments of the Moldanubian internal zone of the Variscan Belt that were caught up in the subsequent Alpine orogenesis. Here evidence for Carboniferous age evolution of the Variscan fragments are well-preserved due to a very weak Alpine overprint (Compagnoni *et al*., 2010).

Alpine metamorphism reached low-T greenschist-facies conditions as indicated by albite, stilpnomelane, green biotite, epidote and actinolite mineral assemblages (Von Raumer and Bussy, 2004). The Aiguilles

Rouges Massif is composed of multiply metamorphosed pelitic schist, paragneiss, orthogneiss and migmatite intruded by Carboniferous age granitoids (fig. 4.33; Von Raumer and Bussy, 2004).

Most of the Variscan tectono-metamorphic evolution of the Aiguilles Rouges Massif occurred during a time-span of ~ 25 Myr (Von Raumer *et al.*, 2003). A first stage of thrusting induced prograde Barrovian metamorphism (Von Raumer *et al.*, 1999) and nappe staking during collision and crustal thickening (Dobmeier, 1998). Subsequently the massif underwent strike-slip transpression deformation followed by gravitational collapse (Von Raumer and Bussy, 2004). Peak Variscan metamorphism in the Aiguilles Rouges Massif reached high amphibolite-facies. A U-Pb age on monazite of 327 ± 2 Ma is interpreted to date the near-peak conditions. Locally anatexis occurred at ~ 320 Ma during high T decompression (Bussy *et al.*, 2000; Genier *et al.*, 2008). The tectono-metmorphic evolution of the massif is also characterized by two magmatic pulses at ~ 330 Ma and ~ 307 Ma (Bussy *et al*., 2000; Von Raumer and Bussy, 2004). The first pulse is represented by high-K calc-alkaline to shoshonitic plutons that crop out in the southern part of the massif (Pormenaz monzonite and Montées Pélissier granite; Bussy *et al*., 2000); the second pulse was responsible for the syn-tectonic emplacement of sheet-like peraluminous granites (Vallorcine granite, Fully granodiorite, Montenverse granite; Bussy *et al*., 2000; Von Raumer and Bussy, 2004; Genier *et al*,. 2008).

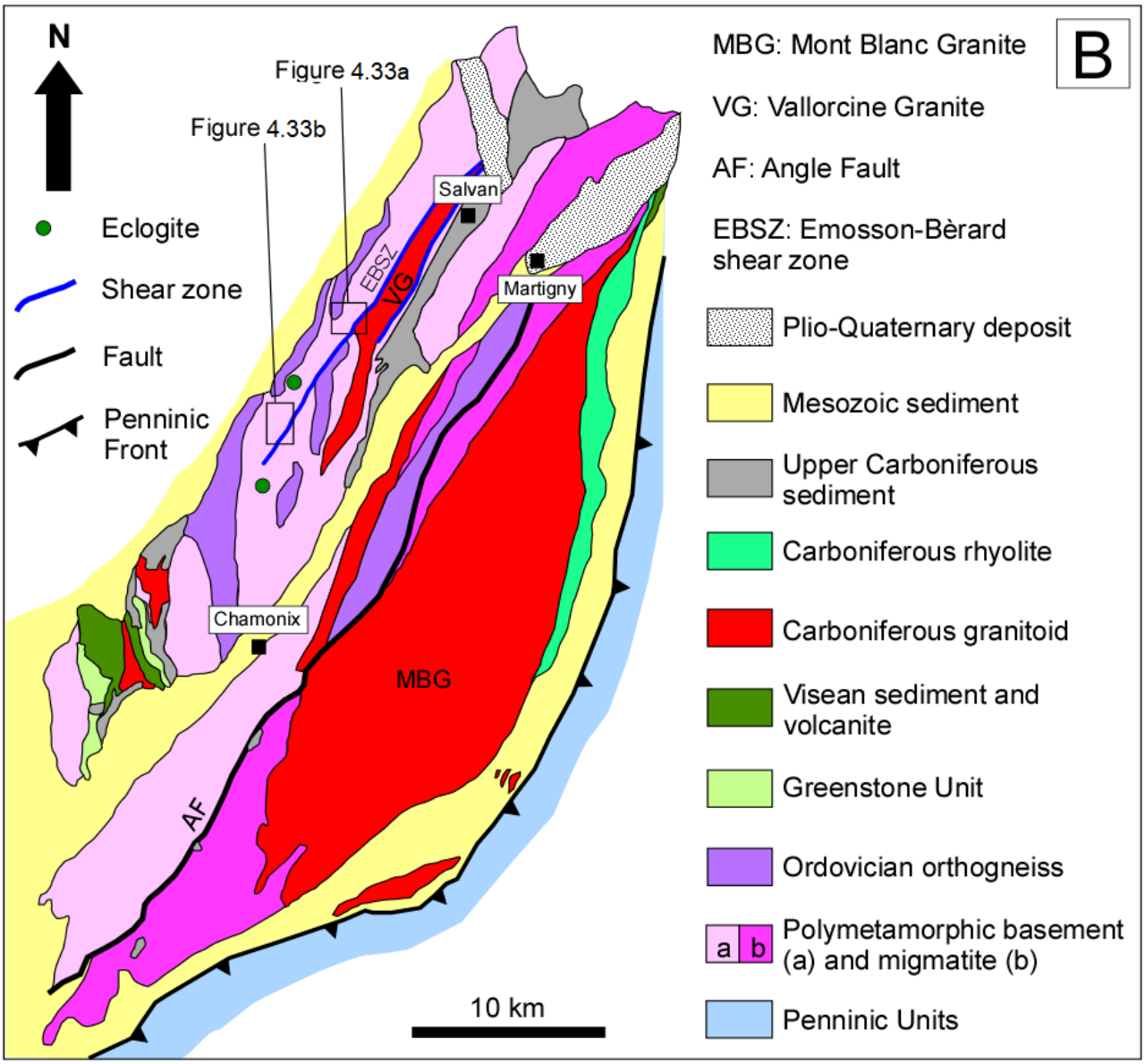

Figure 4.33 - Geological sketch map of the Aiguilles Rouges Massif (modified after Compagnoni *et al.*, 2010)

The crystalline basement rocks of the massif are overlain by Late Carboniferous coarse-grained clastic sedimentary rocks (fig. 4.33) deposited in a post-collisional strike-slip tectonic regime and affected by Alpine deformation (Capuzzo *et al.*, 2003). Volcanic deposits within those sediments occur and are dated to the Late Carboniferous (Capuzzo and Bussy, 2001), with an age of 308 ± 3 Ma for basal dacitic flows and of 295 ± 3 Ma for a tuff layer from the upper levels of the basin sequence. The Carboniferous rocks are overlain by a Mesozoic sedimentary sequence.

Shear deformation represents an important feature of Variscan basement in the Aiguilles Rouge.

The Angle Fault (fig. 4.33) is a major shear zone that divides the massif into two portions, each one with its own sedimentary cover: an internal portion, essentially granitic, located to the east, and a more composite external portion to the northwest (Epard, 1990). The Angle Fault probably developed as a shear zone during the late Variscan strike-slip shearing and was later brittly reactivated during the Alpine orogeny (Von Raumer and Bussy, 2004). In the northwest portion of the massif several steeply dipping mylonitic bands, striking NNE-SSW, and interpreted as strike-slip ductile shear zones, are present (Von Raumer and Bussy, 2004; Genier *et al*., 2008). Some of these shear zones were probably active during Late Carboniferous sedimentation and volcanism (Capuzzo and Bussy, 2001).

In the Emosson Lake area and along its SW extension, the Val Berard area, a ~500 m thick high-strain mylonitic zone developed in metasediment and orthogneiss (Von Raumer and Bussy, 2004; Genier *et al*., 2008). In the first area, mylonites truncate the late Variscan Vallorcine granite (fig. 4.33). The southeastern side of the same granite is truncated by another ductile shear zone (fig. 4.33) known as the Miéville Ultramilonite (Kerrich *et al*., 1980; Von Raumer and Bussy, 2004). Subvertical N-S to NE-SW oriented folds, with hinge planes oriented parallel to the main foliation of the high-strain zone, occur in the unsheared rocks (Von Raumer, 1983; Von Raumer and Schwander, 1985).

Partial melting at the expense of micaschists and metapelites within the shear zone is described by Von Raumer and Bussy (2004) and Genier *et al*. (2008) and interpreted to be induced by the addition of channeled external water.

4.2.3 Structural and microstructural analysis

Lake Emosson area

In the Lake Emosson area the high-strain zone is made of micaschist and metagreywake alternating with orthogneiss (fig. 4.34a). The main foliation Sp both in the metasediments and in the orthogneiss strikes NE-SW and is always subvertical (figs. 4.35a, b). In the metagreywake (fig. 4.36a) foliation is a fine-grained continuous cleavage (fig. 4.36b) defined mainly by white mica and chloritized biotite. The micaschist (fig. 4.36c) is characterized by a spaced foliation with zonal cleavage domains (fig. 4.36d) defined by chloritized biotite and fibrolitic sillimanite; microlithons are mainly made of quartz and feldspar.

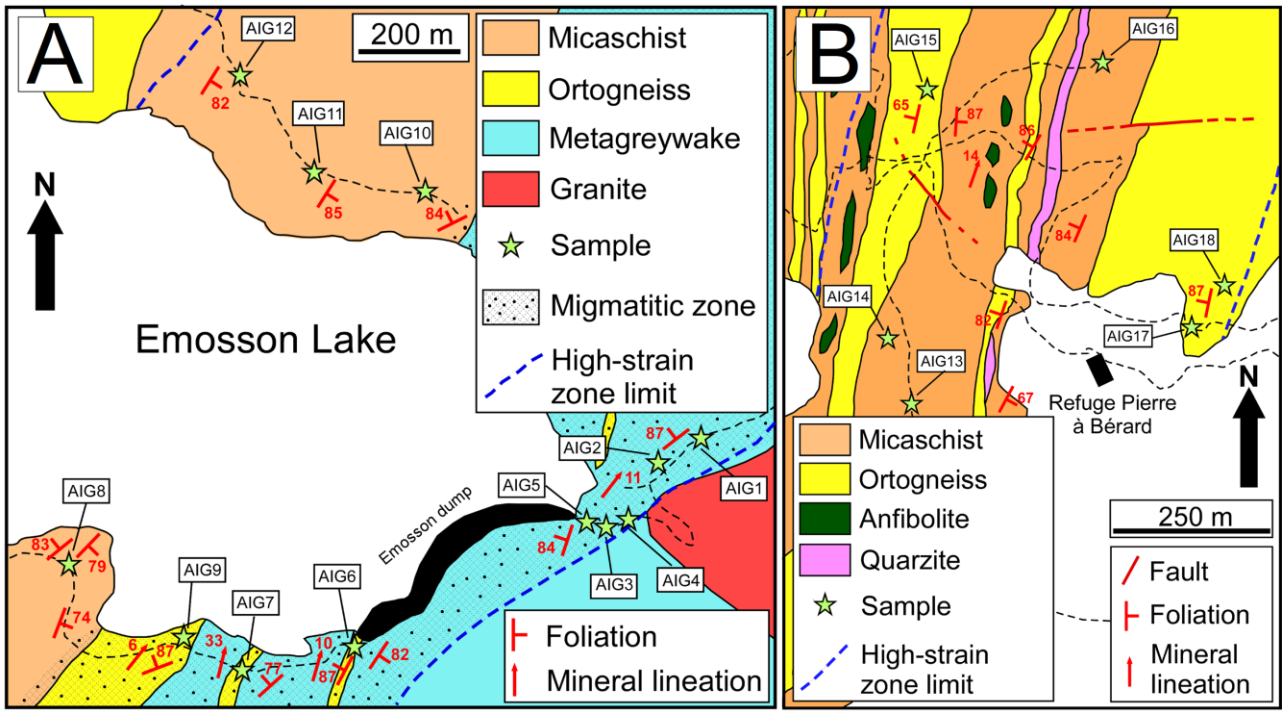

Figure 4.34 – Geological sketch maps of the two studied areas in the Aiguilles Rouges Massif (modified after Von Raumer and Bussy, 2004), their location is reported in figure 4.31: A) Emosson Lake area; B) Val Bèrard area

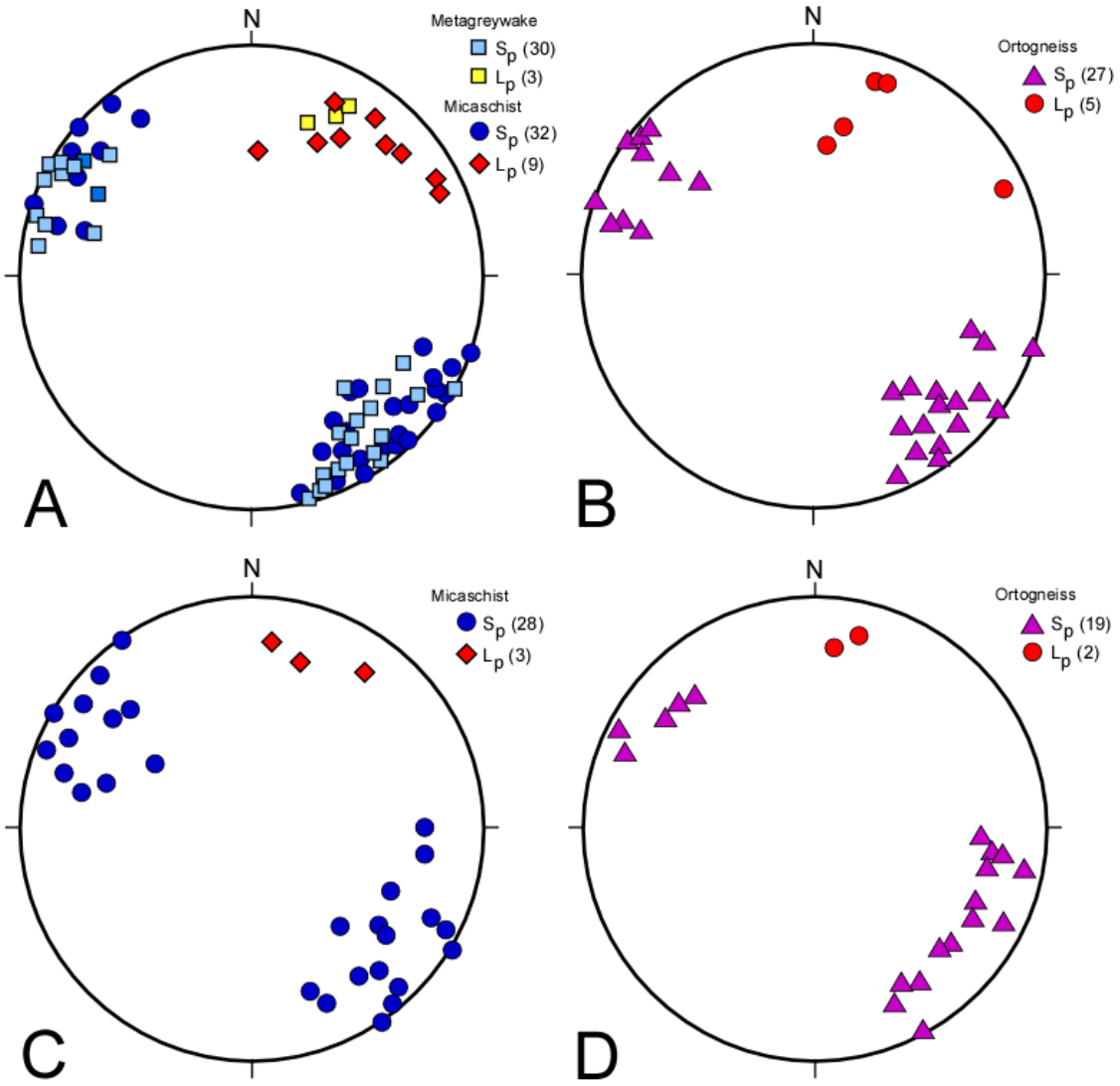

Figure 4.35 – Equal angle projection, lower hemisphere: A) poles to main foliation Sp in the micaschist (dots, 32 data) and in the metagraywake (squares, 30 data) and stretching lineation Lp in the micaschist (rombs, 9 data) and in the metagraywake (squares, 3 data) of the Emosson Lakes area; B) poles to main foliation Sp in the orthogneiss (triangles, 27 data) and stretching lineation Lp (dots, 5 data) in the Emosson Lake area; C) poles to main foliation Sp in the micaschist (dots, 28 data) and stretching lineation Lp (dots, 3 data) in the Val Bèrard area; D) poles to main foliation Sp in the orthogneiss (triangles, 19 data) and stretching lineation Lp (dots, 2 data) in the Val Bèrard area

Garnet porphyroclasts are also present. A mineral lineation Lp, plunging gently toward the NE (fig. 4.35a), occurs on the foliation and is made by aligned biotite and sillimanite crystals. In the orthogneiss (fig. 4.36e) an anastomosing disjunctive foliation (fig. 4.36f) defined by partially chloritized dark- brown biotite is observed. Microlithons are mainly made of quartz and feldspar. On this foliation a mineral lineation Lp made by elongated feldspar plunges gently towards the NE (fig. 4.35b).

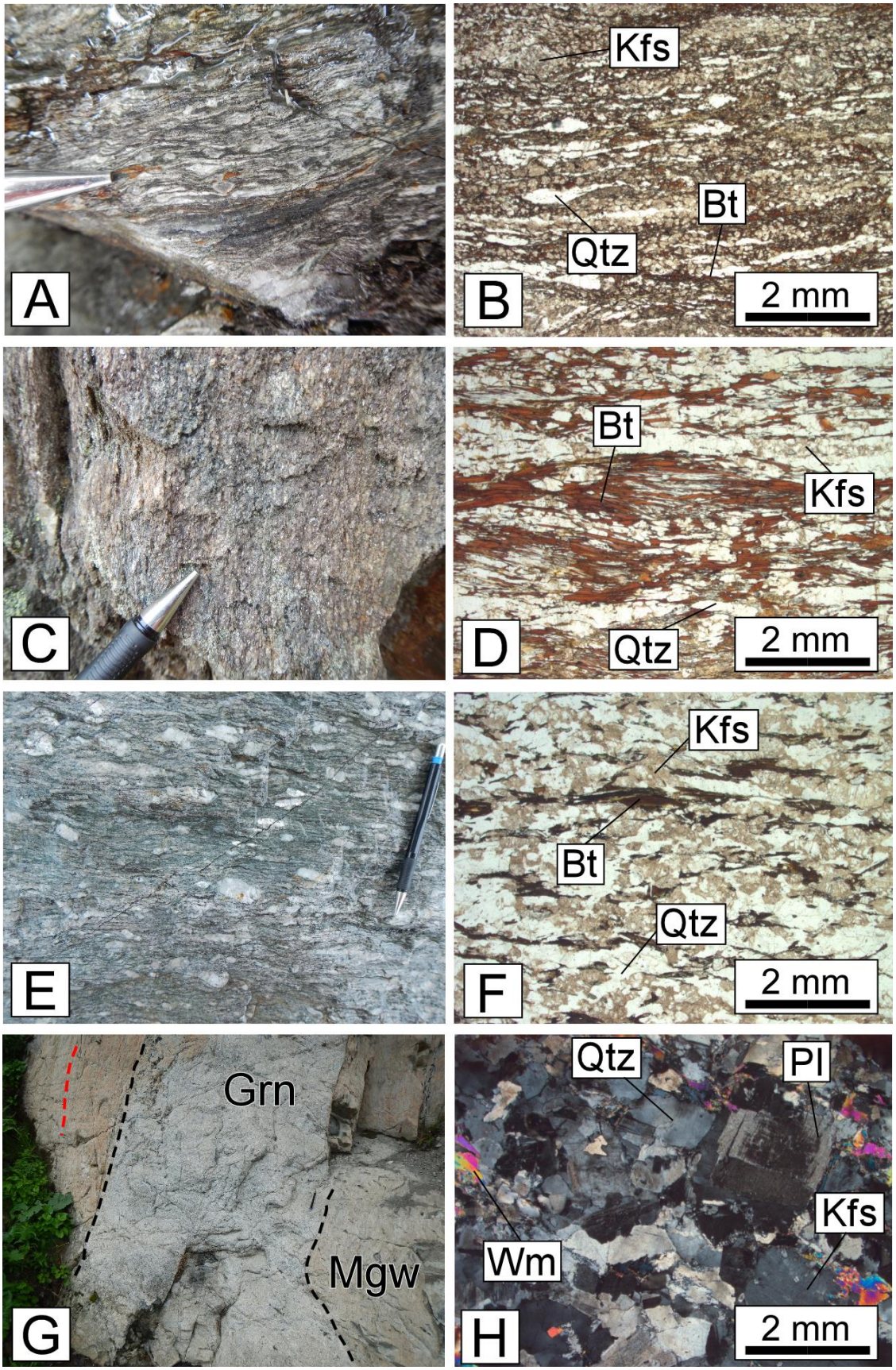

Figure 4.36 – A) Metagraywake of the Emosson Lake area at the outcrop scale; B) continuous cleavage in the metagraywake; C) micaschist of the Emosson Lake area at the outcrop scale; D) spaced foliation with zonal cleavage domains in the micaschist; E) orthogneiss of the Emosson Lake area at the outcrop scale; F) anastomosing disjunctive foliation in the orthogneiss; G) granitic dike intruded along the main foliation of the metagraywake; H) micrograph showing the minerals in the dike: quartz, plagioclase, feldspar and white mica

Close to the Vallorcine granite we recognized granitic dikes, composed of quartz, plagioclase, feldspar and white mica (fig.4.36h), that are intruded along the main foliation in the metagraywacke (fig. 4.36g) and cut by a poorly developed subvertical foliation striking nearly N-S.

Kinematic indicators such as S-C and S-C' fabric (figs. 4.37a, b), σ-type porphyroclasts (figs. 4.37c, d) and micafish (fig. 4.37e) in the metasediments and σ-type mantled porphyroclasts of K-feldspar in the orthogneiss indicate a dextral sense of sub-horizontal shear viewed geographically downwards.

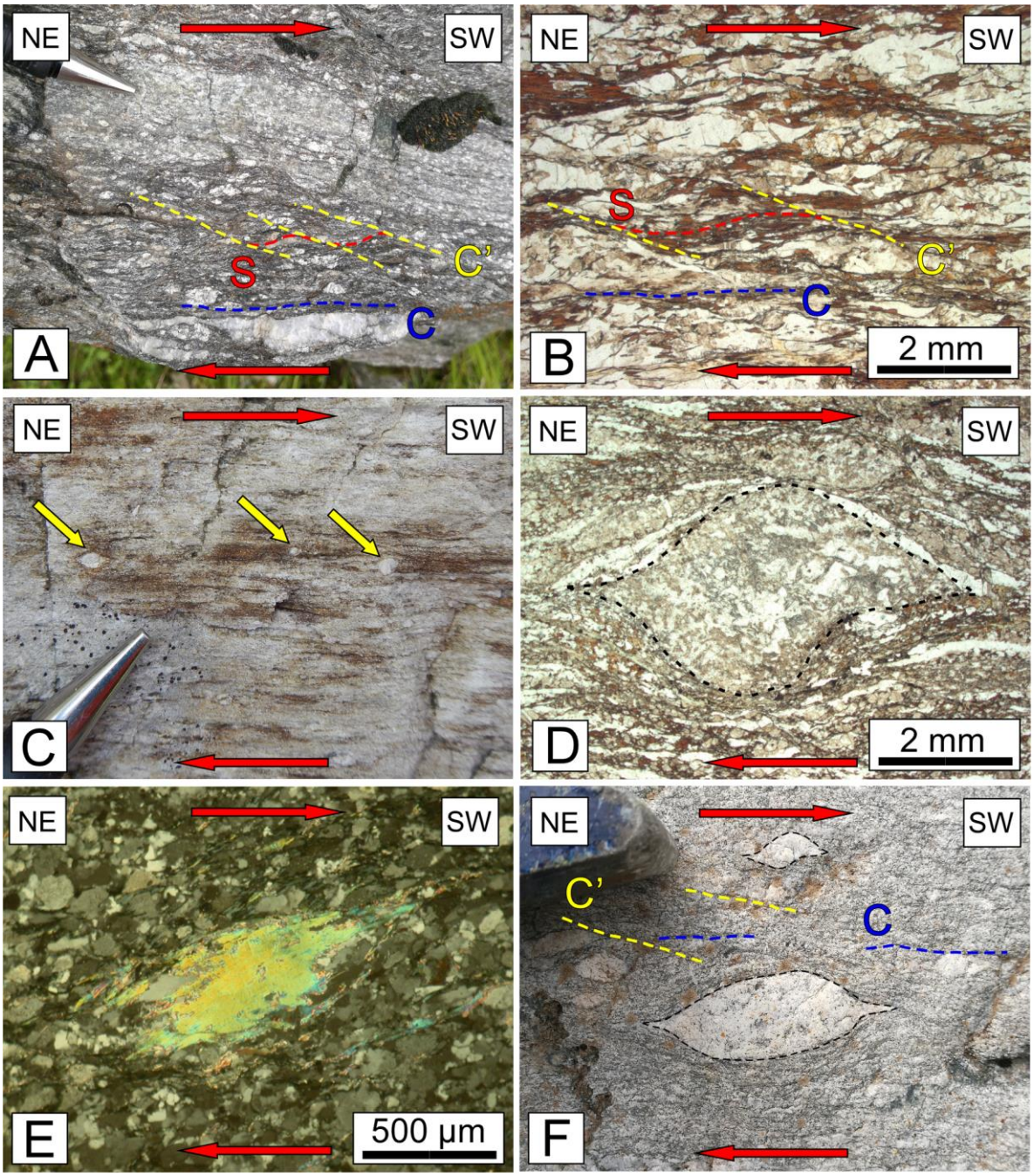

Figure 4.37 – Kinematic indicators at the outcrop scale and in thin section. A) S-C-C' fabric in the micaschist of the Val Bèrard area; B) S-C-C' fabric in the micaschist in thin section; C) σ-type porphyroclasts in the metagreywakes of the Emosson Lake area at the outcrop scale; D) K-feldspar σ-type porphyroclast in the metagreywakes; E) white mica micafish in the metagreywakes; F) S-C-C' fabric and σ-type K-feldspar porphyroclast at the outcrop scale in the orthogneiss of the Val Bèrard area

Val Bèrard area

Similarly to the Lake Emosson area, in the Val Bèrard area sheared garnet-bearing micaschist, interlayered with orthogneiss, occurs. Quarzite and amphibolite bodies embedded within the sheared micaschist are also present. The main foliation Sp in the micaschist and in the orthogneiss strikes NE-SW and it is always subvertical (fig. 4.35c, d). The micaschists (fig. 4.38a) are very similar to those observed in the Lake Emosson area. They are characterized by a spaced foliation with zonal cleavage domains defined by chloritized biotite and fibrolitic sillimanite (fig. 4.38b).

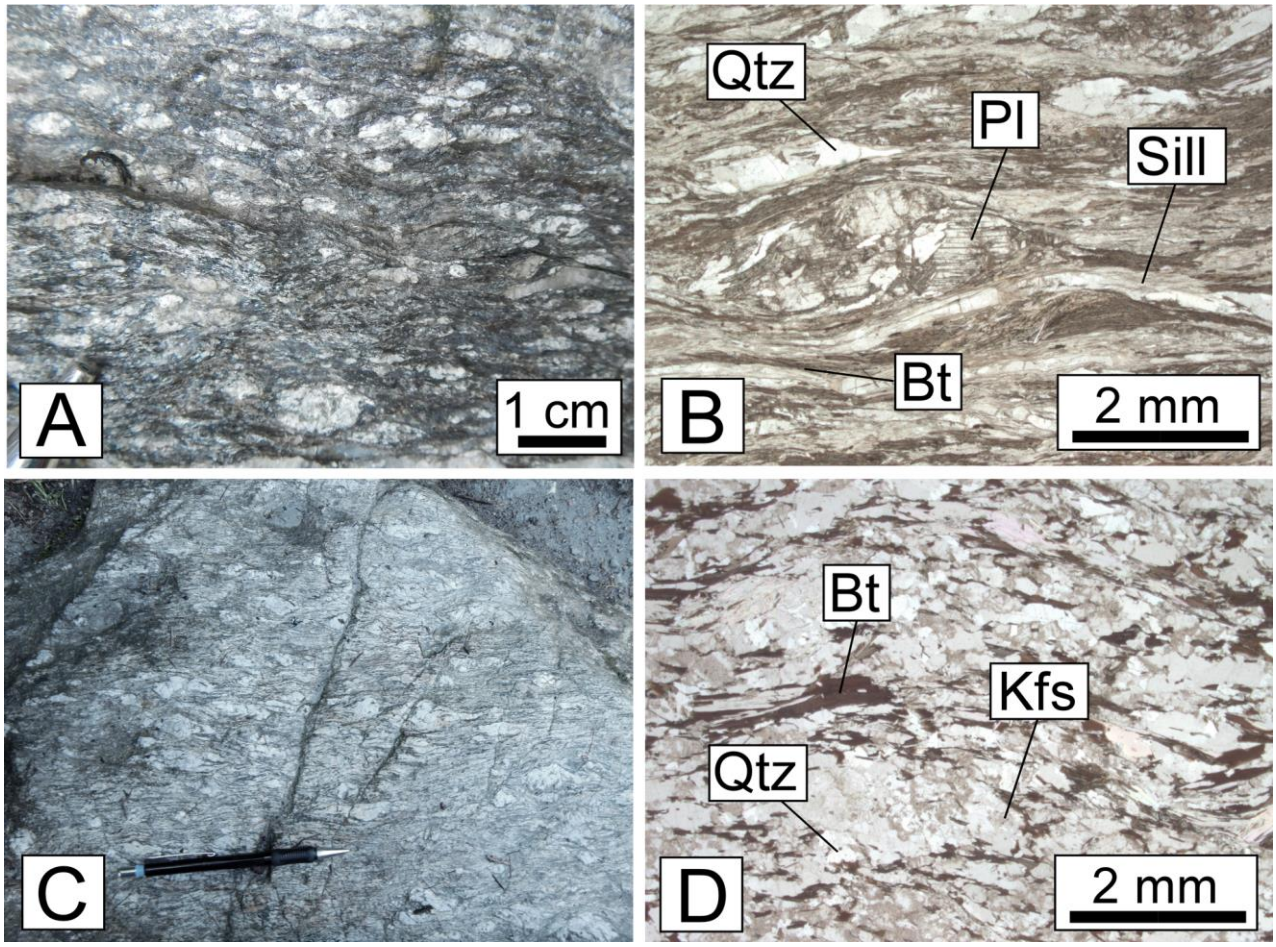

Figure 4.38 – A) micaschists of the Val Bèrard area at the outcrop scale; B) spaced foliation with zonal cleavage domains made by chloritized biotite and fibrolitic sillimanite in the micaschists; C) orthogneiss of the Val Bèrard at the outcrop scale; D) anastomosing disjunctive foliation made by biotite in the orthogneiss, microlithons are mainly made of quartz and feldspars

Microlithons defined by quartz and feldspars and garnet porphyroclasts are present. In the orthogneiss (fig. 4.38a) the main foliation is an anastomosing disjunctive foliation defined by biotite, while microlithons are mainly composed of quartz and feldspars (fig. 4.38b). A mineral lineation Lp, defined by biotite and elongated feldspars, plunges gently to the NE and is well recognizable in both lithotypes (fig. 4.35c, d). Kinematic indicators such as S-C and S-C' fabrics in the micaschists and σ-type cm-scale mantled K-feldspar porphyroclasts in the orthogneiss (fig. 4.37f) indicate a top-to-the-SW dextral sense of shear viewed geographically downwards.

4.2.4 Kinematic vorticity analysis

Kinematic vorticity was estimated using two independent kinematic vorticity gauges: the C' shear band method (Kurz and Northrup, 2008; Gillam *et al*., 2013) and the stable porphyroclast method (Passchier, 1987; Wallis *et al.*, 1993). In order to check the type of deformation we calculated the angles θ between the maximum Instantaneous Stretching Axis (ISA max) in the horizontal plane and the shear zone boundary.

The data obtained from the kinematic vorticity analysis with the C' shear band method and with the stable porphyroclast method are reported in table 4.8 and table 4.9 respectively.

SAMPLE	N	v max	2v	Wk	Angle θ	lithology	locality
AIG2	7	28	56	0.55	16.6	metagreywake	Emosson Lake
AIG4	9	25	50	0.64	19.8	metagreywake	Emosson Lake
AIG3	15	24	48	0.66	20.6	metagreywake	Emosson Lake
AIG6	13	35	70	0.34	9.3	orthogneiss	Emosson Lake
AIG9	22	33	66	0.4	11.7	orthogneiss	Emosson Lake
AIG8	10	28	56	0.55	16.6	micaschist	Emosson Lake
AIG12	6	34	68	0.52	15.6	micaschist	Emosson Lake
AIG14	9	27	54	0.58	17.7	micaschist	Val Bèrard
AIG15	7	32	64	0.43	12.7	orthogneiss	Val Bèrard
AIG16	16	26	52	0.61	18.7	micaschist	Val Bèrard
AIG17	11	33	66	0.4	11.7	orthogneiss	Val Bèrard
AIG18	16	31	62	0.46	13.6	orthogneiss	Val Bèrard

Table 4.8 – Table summarizing the data obtained with the C' shear band method: samples name, N = number of data, ν max angle, 2ν angle, Wk value and the value of the θ angle. Lithology of the samples and locality are also reported

SAMPLE	N	Rc_{min}	Rc_{max}	Rc_{mean}	Wm_{min}	Wm_{max}	Wm
A1	80	1.37	1.87	1.62	0.3	0.55	0.44
A2	231	1.8	1.88	1.84	0.52	0.55	0.54

Table 4.9 – Table summarizing the data obtained with the stable porphyroclasts method on outcrop A1 and A2. N = number of data, Rcmin = minimum critical axial ratio; Rcmax = maximum critical axial ratio; Rcmed = medium critical axial ratio; Wmmin = minimum vorticity number; Wmmax = maximum vorticity number; Wm = mean vorticity number

Polar histograms, used to derive the angle ν, are reported in figure 4.39. Examples of analyzed images for the stable porphyroclast method, preliminary Mulchrone test (Iacopini *et al.*, 2011) and graphs showing porphyroclasts distribution are reported in figure 4.40. From the compiled Mulchrone diagrams (fig. 4.40c, d) our data do not fit the theoretical curve calculated for a system in which slip between porphyroclasts and matrix occurs. Furthermore, selected feldspars are free to rotate in the matrix without mutual interference because the distance between porphyroclasts is larger than their maximum long axis. Vorticity analysis with the C' shear band method gives Wk values varying between 0.34 and 0.74 (fig. 4.39). In general Wk may vary according to the rock type in which it is measured but is quite constant for samples of the same rock type collected in our two study areas. Sample AIG8 and AIG12 (fig. 4.39), representative of the micaschists of the Emosson Lake area, yeld estimated Wk values of 0.55 and 0.52. Samples AIG2 and AIG3, representative of the metagreywakes from the same area, yield Wk value of Wk of 0.55 and 0.66 (fig. 4.39) respectively. Samples AIG14 and AIG16 (fig. 4.39) collected within the garnet-bearing micaschists of the Val Berard area yield Wk values of 0.58 and 0.61 respectively.

In contrast to the micaschist samples, Wk values from the orthogneisses are slightly lower: Samples AIG9 and AIG6, collected in the Emosson Lake area, yield Wk estimates of 0.40 and 0.34 respectively (fig. 4.39) while in samples AIG15, AIG17 and AIG18 (fig. 4.39) collected in the Val Berard area Wk values are estimated at 0.43, 0.40 and 0.46 respectively.

These Wk values are all indicative of a general shear deformation with synchronous components of both pure shear and a simple shear. The estimated percentage of pure shear component varies between 77 % and 53 %. In the orthogneiss the percentage of pure shear is always higher compared to the micaschists and the metagreywakes.

Vorticity analysis using the stable porphyroclasts method on the orthogneiss of the Emosson Lake area yield an estimated Wm value of 0.54 (fig. 4.40) whereas the Wm value obtained on the orthogneiss of the Val

Berard area is 0.44 (fig. 4.40). These values are indicative of a percentage of pure shear between 62 % and 70%. The datasets collected in the orthogneiss with the two methods are well comparable. Calculated θ angles between the maximum Instantaneous Stretching Axis (ISA max) in the horizontal plane and the shear zone boundary vary between ~ 20° and 9°.

These values, combined with the vorticity numbers estimated above, are indicative of a pure shear-dominated transpression (fig. 4.41).

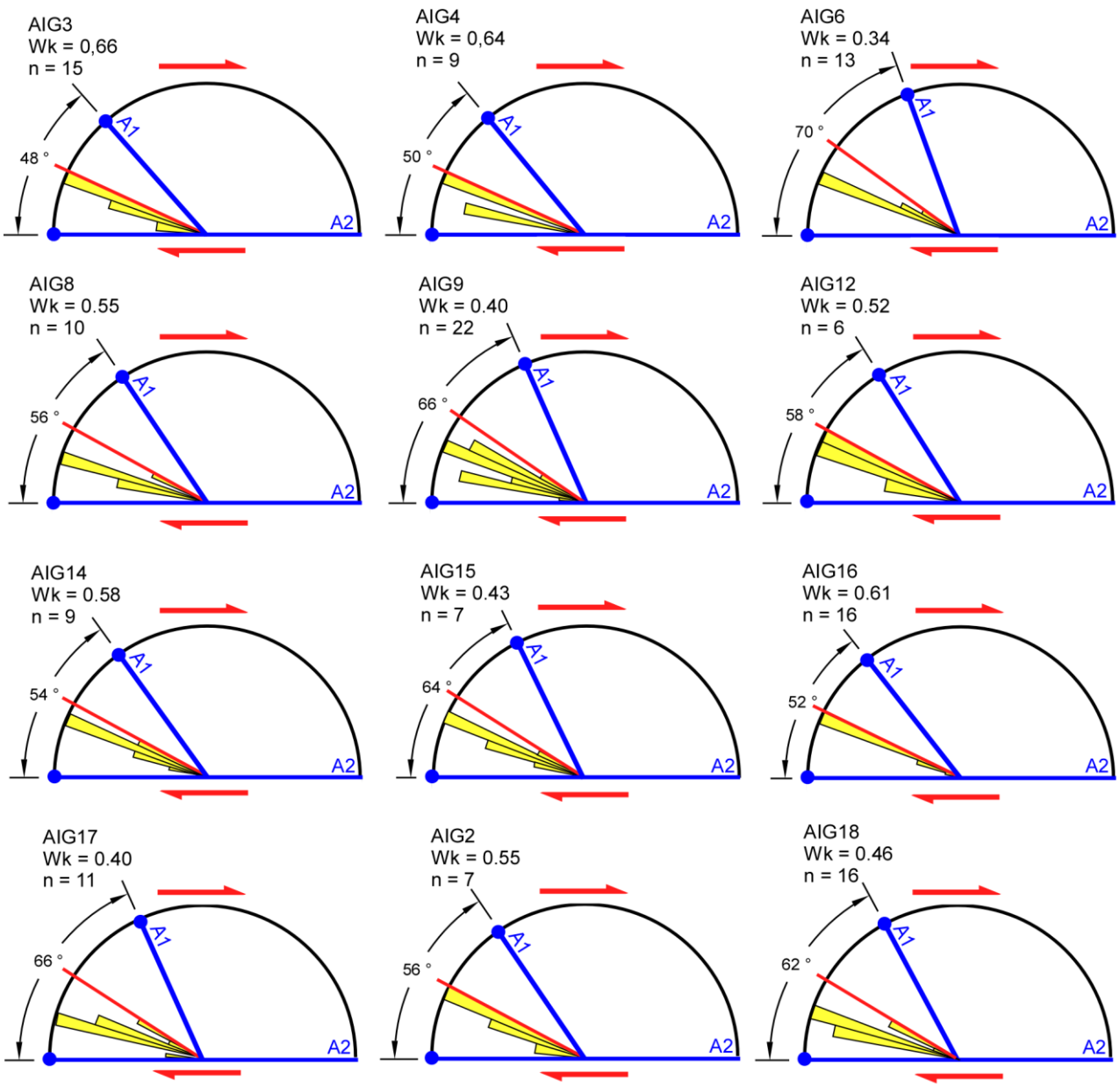

Figure 4.39 – Polar histograms used to derive the angle ν and to calculate kinematic vorticity with the S-C' method (Kurz and Northrup, 2008) on field oriented samples, Wk = vorticity number; n = number of data; A1 = flow apophysis 1; A2 = flow apophysis 2. Red line represent the bisector of the angle between A1 and A2, yellow bars represent the number of data. All histograms are shown with the same dextral sense of shear (red arrows)

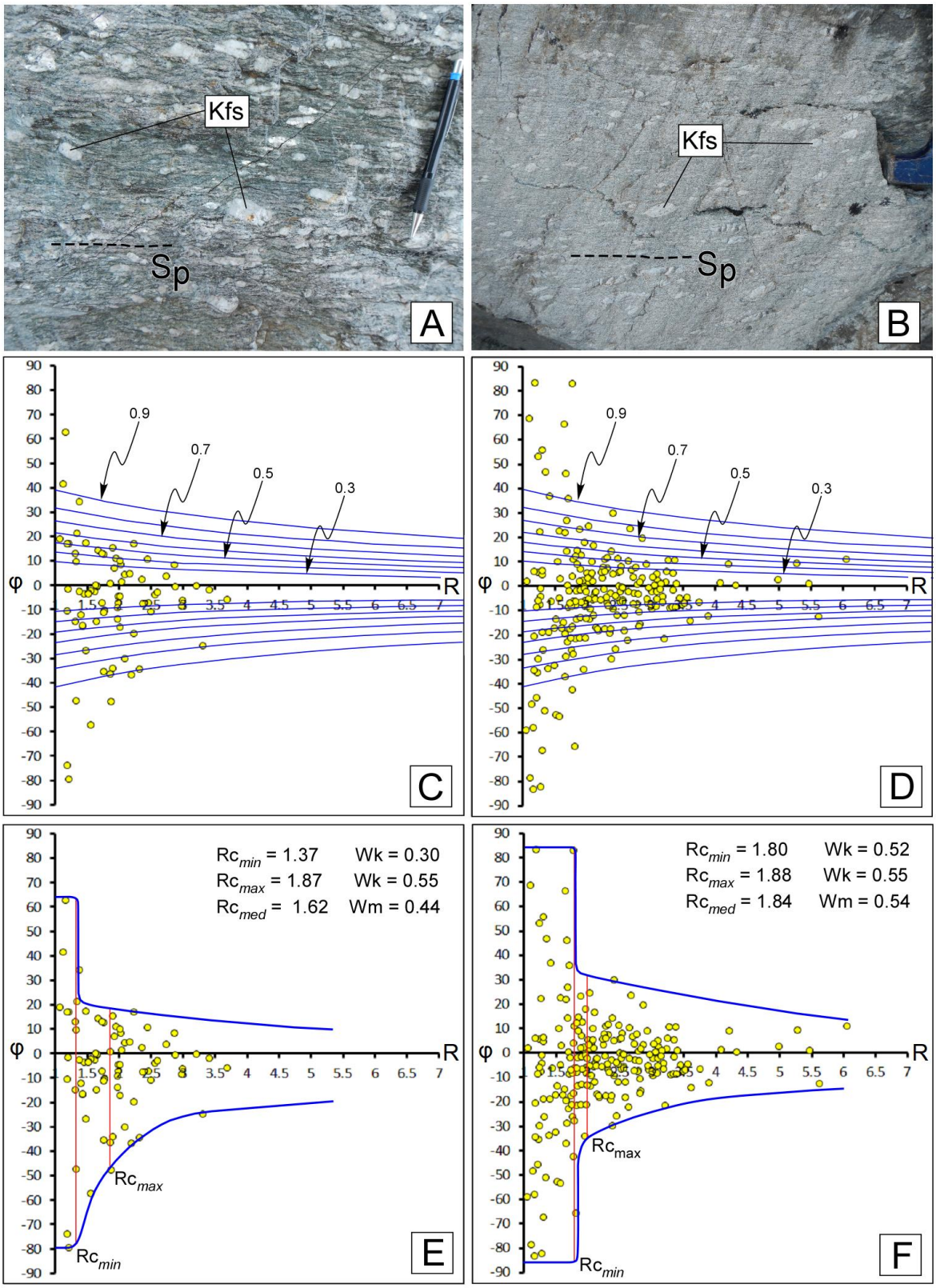

Figure 4.40 – A) orthogneiss of the Emosson Lake area at the outcrop scale; B) orthogneiss of the Val Berard area at the outcrop scale; C) Mulchrone test for the dataset collected in the outcrop A1, 80 data; D) Mulchrone test for the dataset collected in the outcrop A2, 231 data. Blue line represents the expected distribution of the data at different vorticity number in the presence of a clast/matrix slipping interface; E) graph used to determine the critical axial ratio in the outcrop A1; 80 data; F) graph used to determine the critical axial ratio in the outcrop A2; 231data. Rc_{min} = minimum critical axial ratio; Rc_{max} = maximum critical axial ratio; Rc_{med} = medium critical axial ratio; Wm = mean vorticity number. φ is the angle between the the major axis of the porphyroclast with respect to the mylonitic foliation; R is the aspect ratio

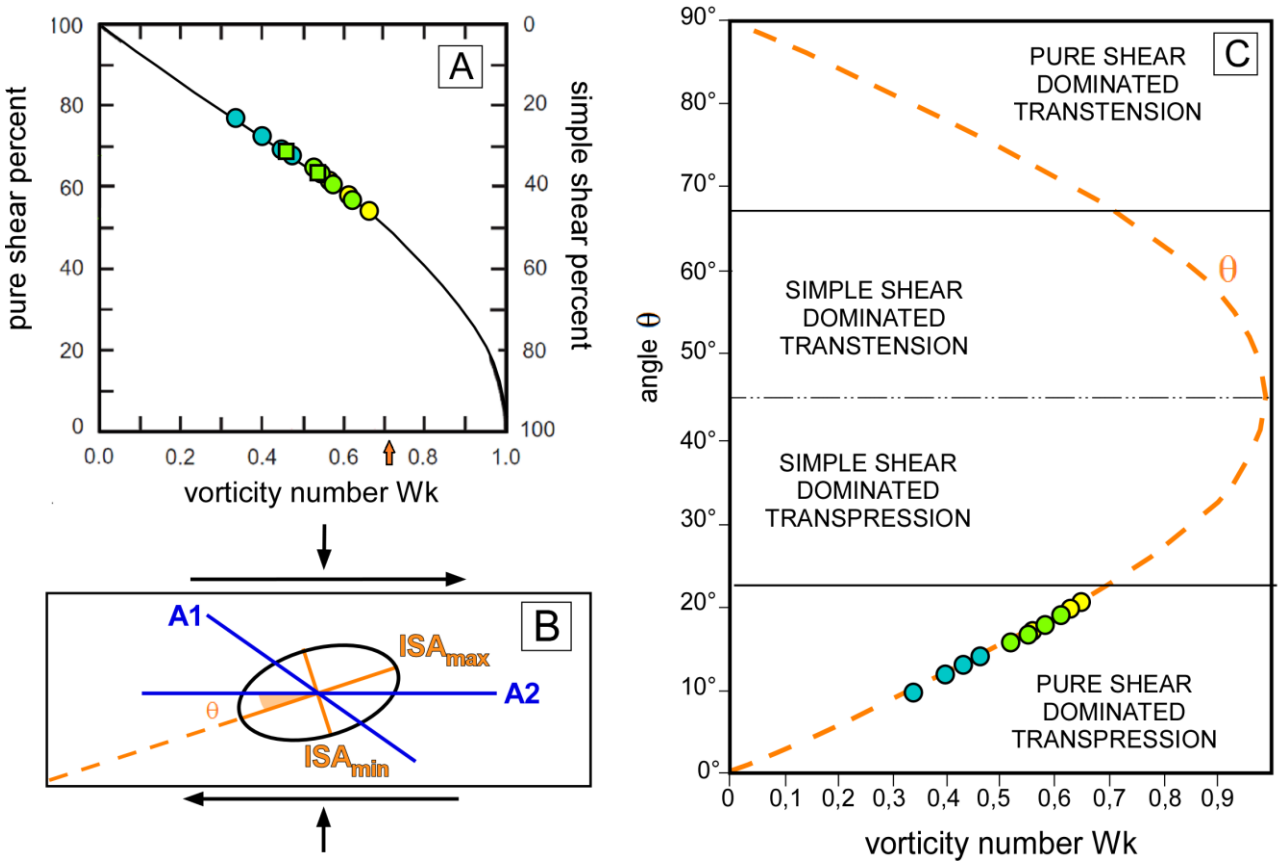

Figure 4.41 – Results of vorticity analysis (blue = orthogneiss; green = micaschist; yellow = metagreywake). A) percentage of pure shear and simple shear in relation to the calculated Wk values (dots = C' shear band methods; square = table porphyroclasts method). Arrow points Wk = 0.71 where equal contribution of simple shear and pure shear is realized (Law *et al.*, 2004; Xypolias, 2010); B) simplified sketch showing orientation of the instantaneous flow elements and their angular relationships in a dextral shear zone with simultaneous pure shear and simple shear. θ is the angle between ISAmax and the shear zone boundary (modified after Xypolias, 2010); C) Relationships between the orientation of the maximum Instantaneous Stretching Axis (ISAmax) with respect to the shear zone boundary (angle θ) related to the kinematic vorticity number Wk obtained with the C' shear band method (modified after Fossen and Tikoff, 1993; Fossen *et al*., 1994). All the study samples fall in the field of pure shear-dominated transpression

4.2.5 Strain analysis

We performed a finite strain analysis in order to obtain the axial ratio of the finite strain ellipse (Rxz), which is needed for calculating the shortening perpendicular to the flow plane. Because of the large grain size, finite strain analyses were performed on field oriented pictures of ortogneiss outcrops representative of the XZ section of the finite strain ellipse. Unfortunately it was not possible to clearly detect surfaces representative of the YZ sections at the outcrop scale. Because of this we limited the study to a 2D analysis. The center-to-center analysis (fig. 4.42) was carried out using the software EllipseFit 3.2 (Vollmer, 2005). Finite deformation analysis, combined with Wk values, allowed us to obtain shortening and stretching values : shortening is 32 %; stretching is 25 %. We estimated a convergence angle of ~57°.

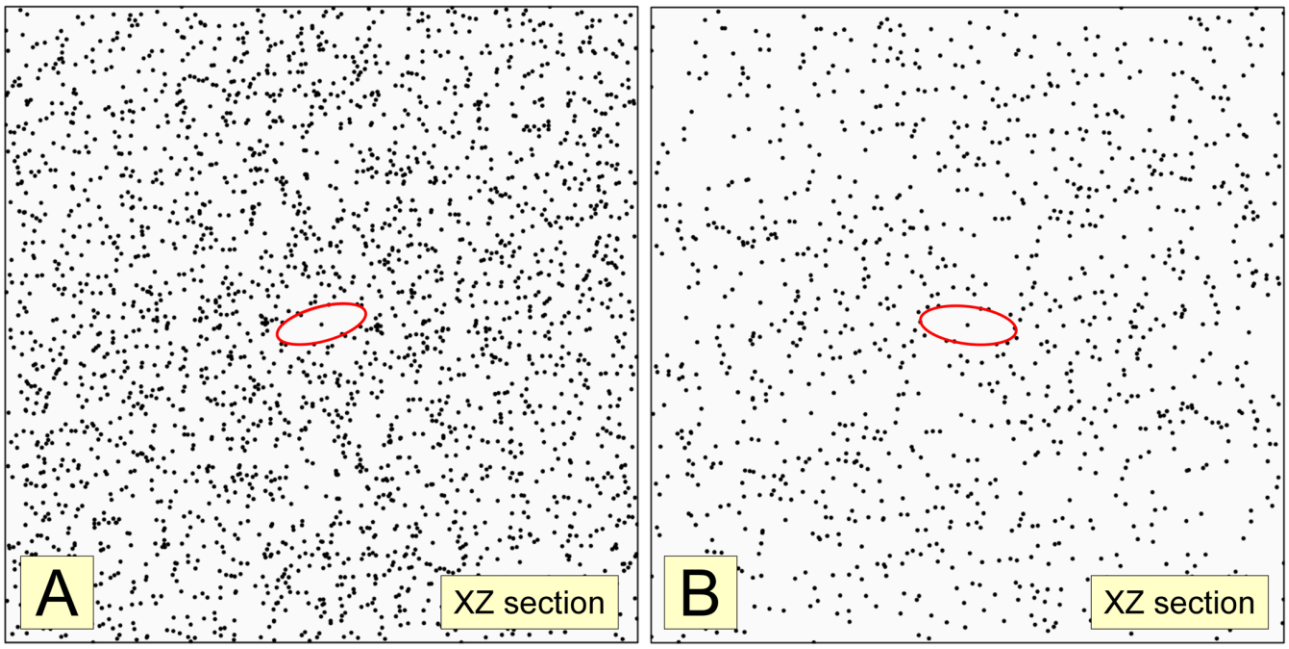

Figure 4.42 – Fry graphs used for strain analysis obtained with the center-to-center method: A) mylonitic orthogneiss of the Val Bèrard (96 data); B) mylonitic orthogneiss of the Lake Emosson area (77 data)

4.2.6 Quartz microstructures, fabric analysis and deformation temperature

In the analyzed samples, collected in both the orthogneiss and the metasedimentary rocks, quartz is generally coarse-grained with lobate boundaries (figs. 4.43a, b) and locally developed window structures (fig. 4.43c). These quartz microstructures indicate that grain boundary migration (GBM) is the dominant mechanism for dynamic recrystallization. Some grains are bounded by tilt walls (fig. 4.43d) and in few grains an incipient chessboard extiction is present (fig. 4.43e). Expecially in the metasedimentary rocks, quartz subgrains are also observed and new quartz grains of smaller size surround the larger grains (fig. 4.43f) forming a *'core and mantle structure'* (White, 1976) and generating a weakly bimodal grainsize. These microstructures are indicative of incipient subgrain rotation recrystallization (SGR) overprinting the GBM.

Quartz in the granitic dikes is also deformed, displaying undulose extinction and a weakly bimodal grainsize. A few grains have lobate grain boundaries (fig. 4.43g) while in most samples core and mantle microstructures defined by smaller dynamically recrystallized quartz grains surrounding larger grains are observed (fig. 4.43h). These microstructures are indicative of SGR as the main dymanic recrystallization mechanism. Quartz c-axis fabrics were measured in samples AIG3, AIG6, AIG7 and AIG8 (fig. 4.44), collected in the Lake Emosson area, and in samples AIG16, AIG17 and AIG18 (fig. 4.44), collected in the Val Berard area. Quartz c-axis fabrics were manually measured using a universal stage, with a minimum of

500 grains analyzed in each thin section. Samples AIG3, AIG6, AIG7, AIG8 and AIG16 are characterized by fabrics that are intermediate between Type-I and Type-II cross-girdles (Lister, 1977). Samples AIG17 and AIG18 are characterized by Type-II cross-girdle fabrics. All measured quartz fabrics have a weak external asymmetry with respect to foliation and lineation. All measured quartz fabrics have a weak external asymmetry with respect to foliation and lineation. This fabric asymmetry indicates a non-coaxial deformation (Schmid and Casey, 1986; Law, 1990 and references therein) associated with a dextral top-to-the-SW sense of shear in agreement with the observed microstructural kinematic indicators. The topology of the c-axis fabrics suggests that shearing occurred under close to plane strain conditions (Lister and Hobbs, 1980).

Quartz microstructures are indicative of GBM as the dominant recrystallization mechanisms in all the studied samples. This indicates a deformation temperature of 500° - 700° C.

Measured c-axis fabric opening angles in samples AIG3, AIG6, AIG7, AIG8 collected in the Emosson Lake area are 84°, 74°, 80°, 78°, respectively (fig. 4.43). These values indicate moderately high-temperature deformation conditions (fig. 4.45) ranging from ~ 550-630 °C, with opening angles in samples AIG3, AIG6, AIG7, AIG8 indicating temperatures of 629° C, 556° C, 602° C and 591° C, respectively.

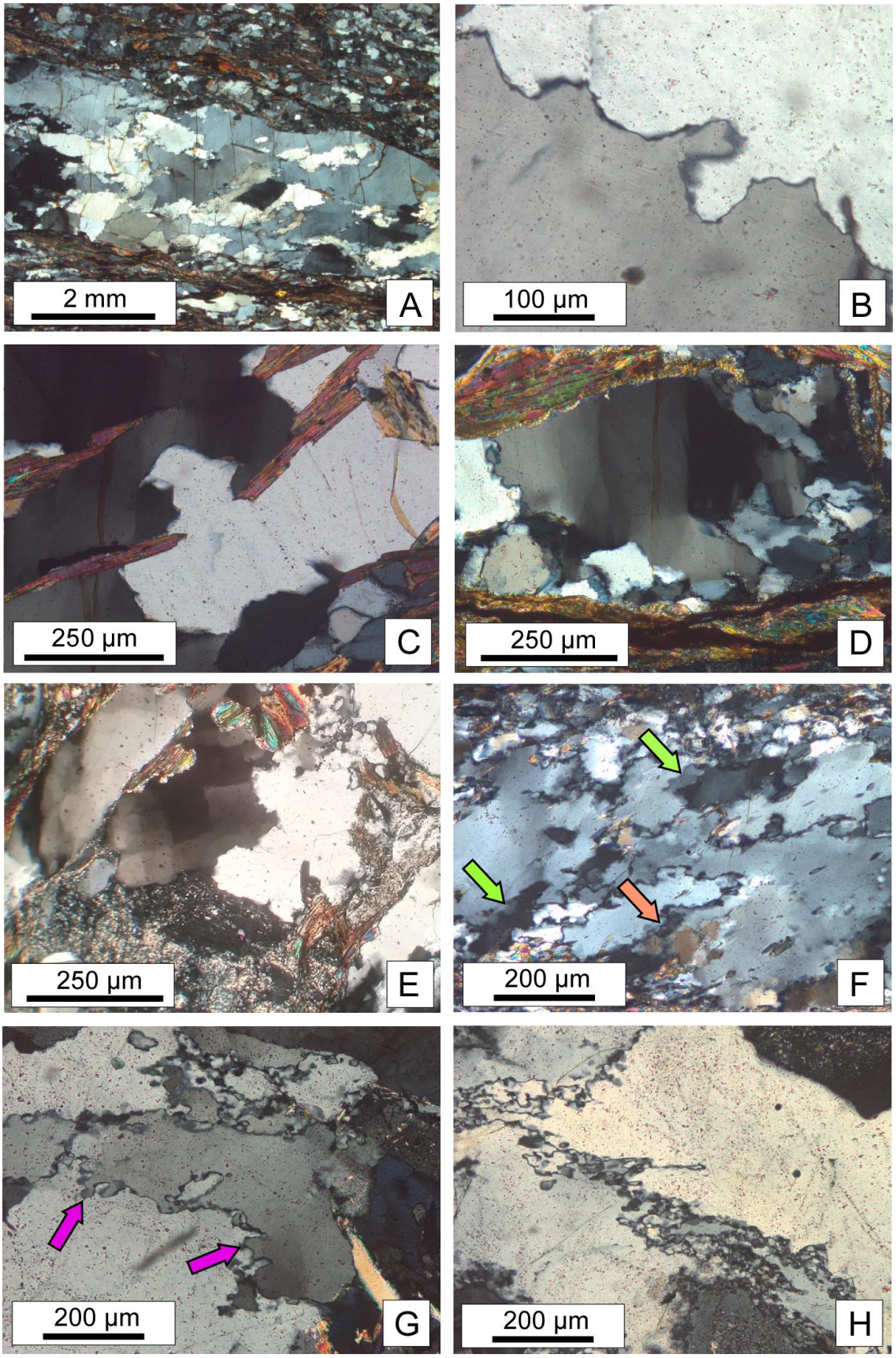

Figure 4.42 – A) coarse-grained quartz with lobate grain boundaries in the micaschists; B) detail of a lobate boundary; C) window structure; D) quartz grain showing tilt walls; E) quartz grain with incipient chessboard extinction; F) quartz subgrains (green arrow) and small new grains (pink arrow) around older coarse grains; G) quartz in the granitic dike with lobate grain boundary (violet arrows); H) bimodal grainsize of quartz in the granitic dike

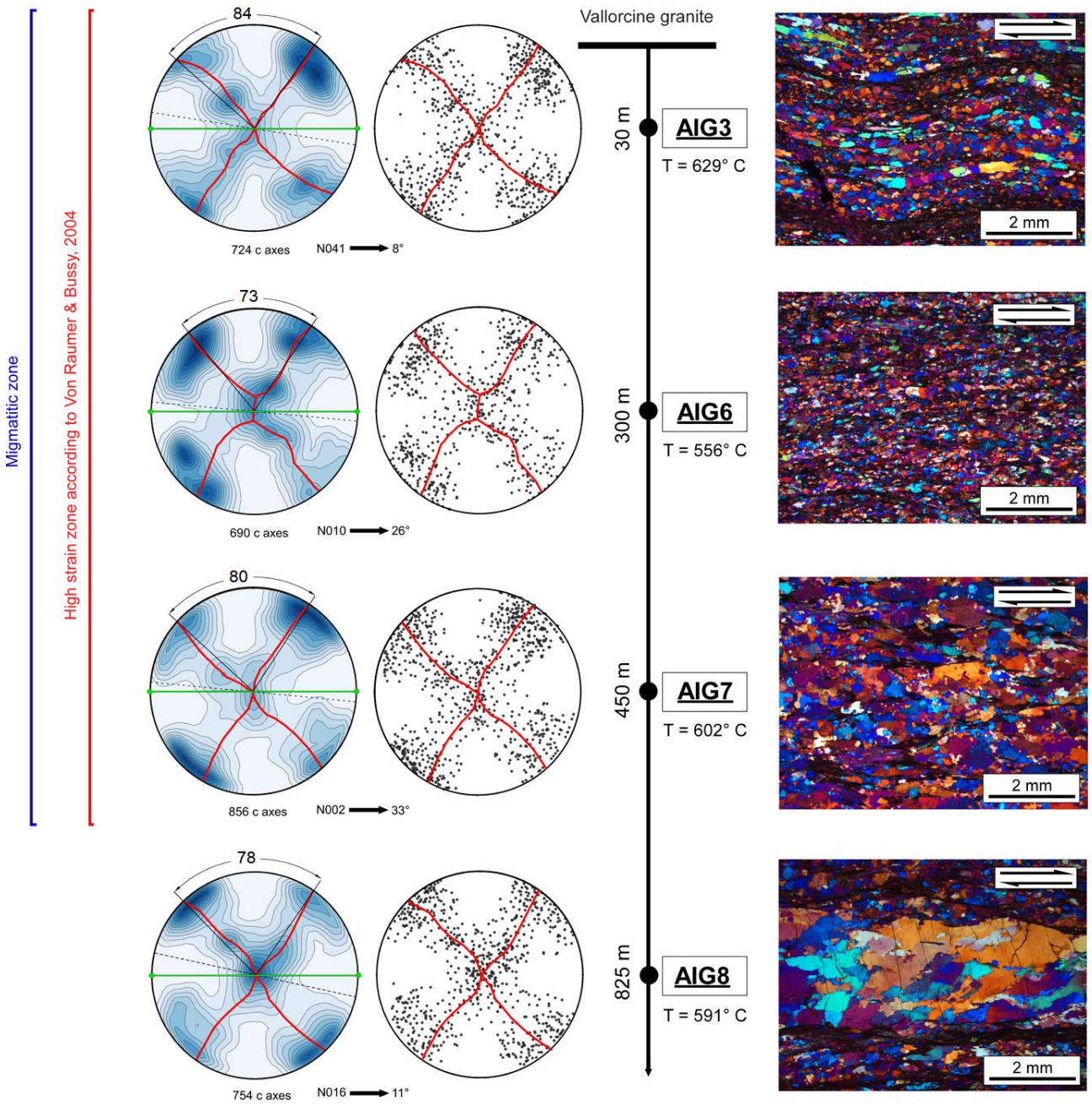

Figure 4.43 – Optically measured quartz c-axis fabrics (equal-area lower-hemisphere projections; 0, 0.70, 1.40, 2.10, 2.80, 3.50, 4.20 times uniform) and recrystallization microstructures for the samples collected in the Emosson Lake area. Samples are reported according to their distance from the Vallorcine granite that in the literature is considered as the SE limit of the high-strain zone in the Emosson Lake area (Von Raumer and Bussy, 2004; Genier *et al*., 2008). All pole figures and micrographs are oriented perpendicular to the foliation and parallel to the lineation. Dashed line is the shear plane; green line is the main foliation and green dots are the mineral lineation. Fabric asymmetries indicate a dextral top-to-the-SW sense of shear. Fabric opening angle and the related temperature and the angle between the main foliation and the shear plane are also reported

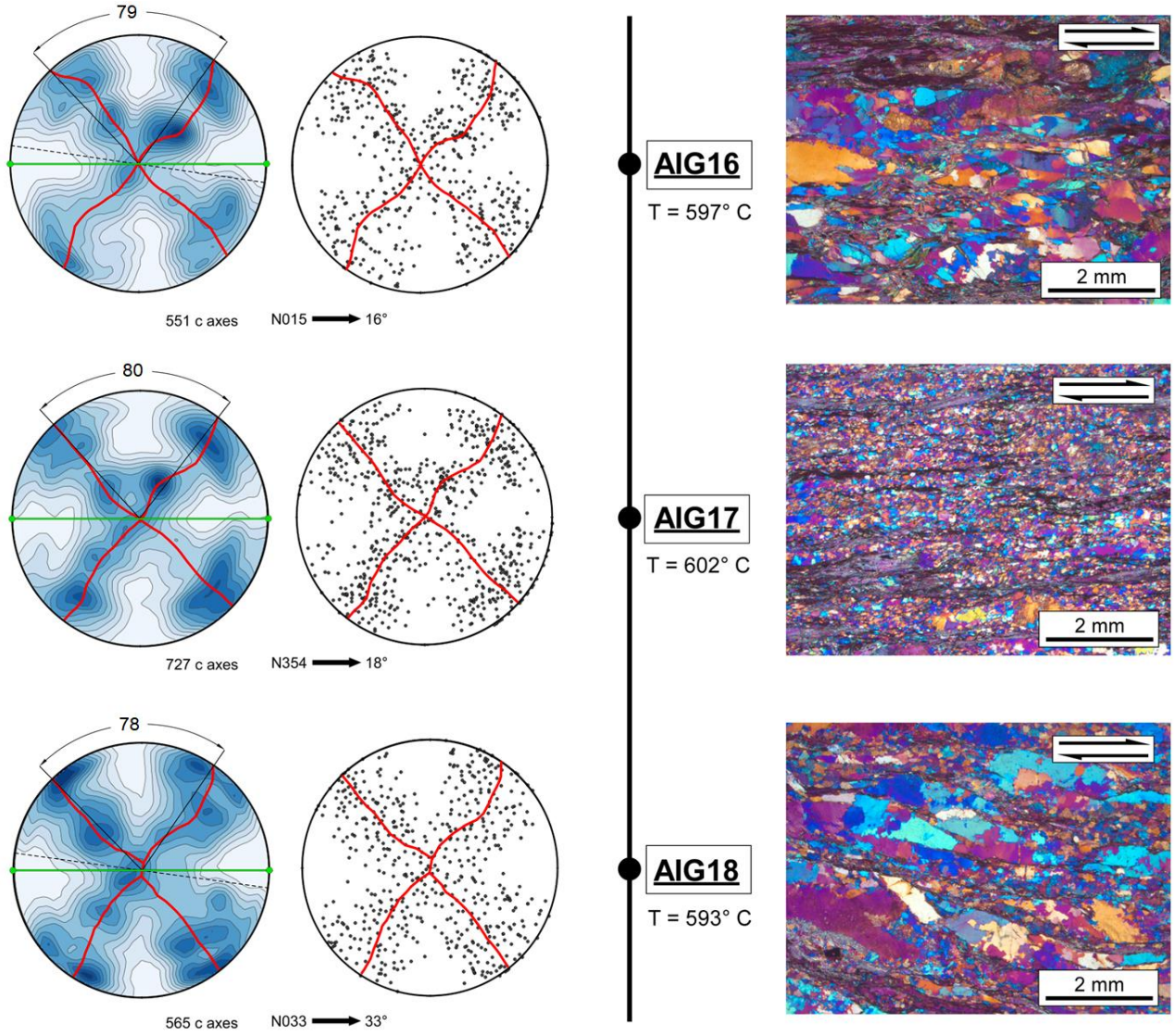

Figure 4.44 – Optically measured quartz c-axis fabrics (equal-area lower-hemisphere projections; 0, 0.70, 1.40, 2.10, 2.80, 3.50, 4.20 times uniform) and recrystallization microstructures for the samples collected in the Val Bèrard area. All pole figures and micrographs are oriented perpendicular to the foliation and parallel to the lineation. Dashed line is the shear plane; green line is the main foliation and green dots are the mineral lineation. Fabric asymmetries indicate a dextral top-to-the-SW. Fabric opening angle and the related temperature and the angle between the main foliation and the shear plane are also reported

Samples collected in the sector of the high-strain zone affected by partial melting exhibit the highest opening angle values and inferred deformation temperatures.. Both the opening angles and inferred deformation temperatures decrease slightly traced toward the NW, away from the migmatitic zone.

The opening angles of c-axis fabrics for samples AIG16, AIG17 and AIG18 collected in the Val Bèrard area are 80°, 80° and 79°, respectively (fig. 4.44). These opening angles are also indicative of moderately high deformation temperatures of ~ 593- 602°C. Quartz fabrics also provide insights on crystallographic slip system active in the deforming crystal, with fabric point maxima in the samples analysed indicating prism

[a], romb [a] and basal [a] slip in all the samples studied. We did not detect any fabric point maxima evidence for higher temperature (> ~630-650°C) prism [c] slip, although the presence of quartz chessboard extinction microstructures in some samples (AIG16 and AIG18; fig. 4.42e) indicates that prism [c] slip is at least locally important.

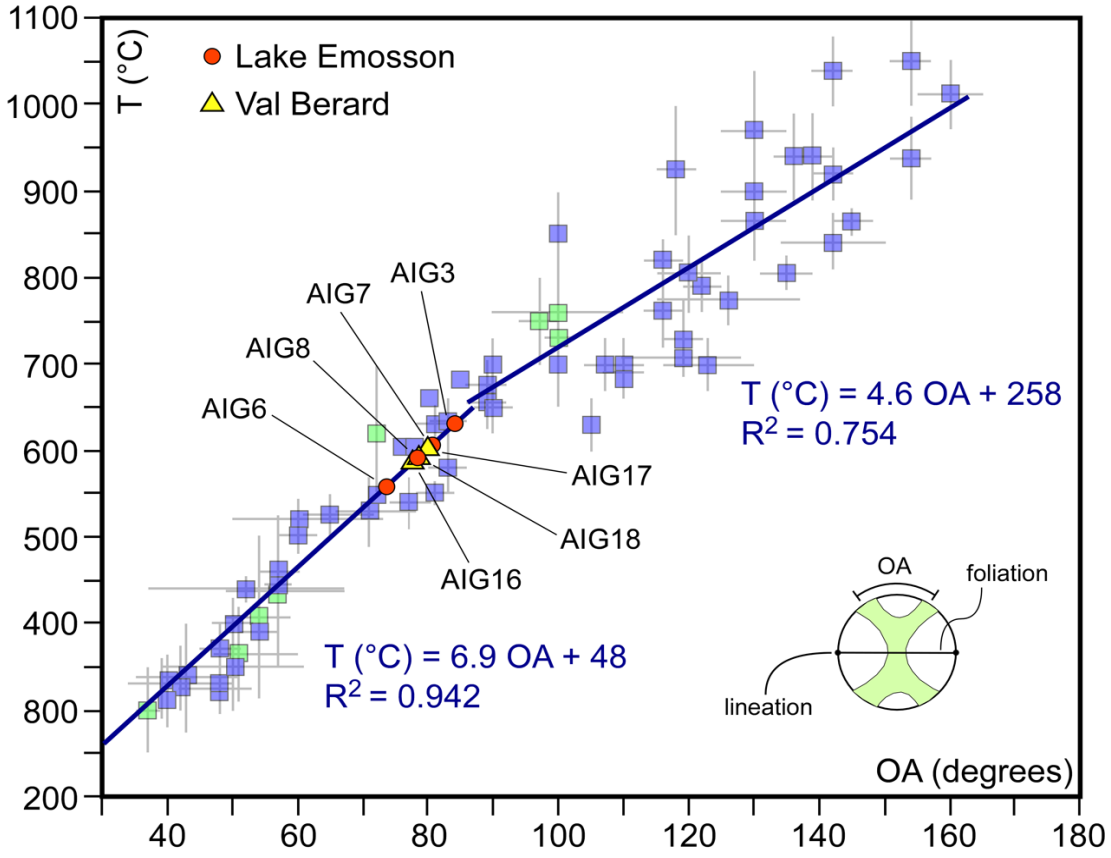

Figure 4.45 – Falerios *et al*. (2016) quartz c-axis fabric opening-angle thermometer in the range of 250 - 1050 °C, blue squares are data with pessure information used by Faleiros et al. (2016) to define their thermometer, while green squares are data used by Faleiros et al. (2016) that have no pressure information. Calibration was made after Khrul (1998), Morgan and Law (2004), Law (2014). Linear fits described by equation 1 and 2 are indicated

4.2.7 Petrochronology

In situ U–Th–Pb dating was performed on 8 monazites grains selected in 3 sheared samples of micaschist collected within the high-strain zones. 38 individual monazite spots were analysed on polished thin sections. Samples AIG8 and AIG11 were collected in the Emosson Lake area while sample AIG14 was collected in the Val Bèrard area.

In the studied samples, from the microstructural point of view, dated monazite grains may be broadly divided in two groups: a first group composed of grains included in garnet (Mnz10 in sample AIG11) or biotite

porphyroclasts (spot position Mnz34 in sample AIG11), and a second group composed of grains located within the main foliation (Mnz3, Mnz52, Mnz10, Mnz11 in sample AIG8; Mnz2 in sample AIG14; Mnz37 in sample AIG11). The two groups differ in terms of chemical characteristics. Chemical analysis obtained with the EPMA are reported in appendix G and the spots position is reported in appendix F.

Y content is low in monazite grains included in porphyroclasts (Y_2O_3 between ~0.11 and ~0.18 wt %), and is higher in grains located in the main foliation (Y_2O_3 between ~1.04 and ~2.74 wt %). Mnz37 in sample AIG11 and Mnz2 in sample AIG14, both in grains located within the main foliation, have a Y zoning with low-Y cores (Y_2O_3 between ~0.17 and ~0.72 wt %) and high-Y rims (Y_2O_3 between ~1.24 and ~1.82 wt %). Core-rim REE patterns (normalized to chondrite values of Mcdonough and Sun, 1995) from core to rim within monazites in different microstructural positions are reported in figure 4.46a. Monazite grains included in pre-tectonic porphyroclasts (Mnz10 and Mnz34 in sample AIG11) have a lower content in HREE (fig. 4.46a) with respect to the grains located in the main foliation (Mnz3, Mnz52, Mnz10, Mnz11 in sample AIG8; Mnz2 in sample AIG14). Monazites in the main foliation also have an anomaly in Eu content (fig. 4.46a). Relationship between Y content, age, microstructural position of the grain, and position of the spot are highlighted in figure 4.46b. The ages obtained with the U and Th systematics are generally well concordant. Ages from each spot are reported in appendix F on the compositional map of Y for each grain, and the full dataset is presented in table 4.10. The average age diagrams for the Th-Pb and U-Pb systematics and the probability density plots are reported in figure 4.47. Th-Pb ages ranges from ~333 ± 5 Ma to ~319 ± 3 Ma while U-Pb ages ranges from ~329 ± 13 Ma to ~318 ± 7 Ma. Taking into account the microstructural position of the grains, and the chemical composition of the dated domains, several age groups may be distinguished. Older ages (~340-330 Ma) were obtained in the low-Y grains included in the porphyroclasts and no significant age difference is recognized between core and rim of these grains. Younger ages (~ 320-310 Ma) were obtained from the high-Y grains located within the main foliation. In these grains a slight difference in age between cores and rims can be recognized.

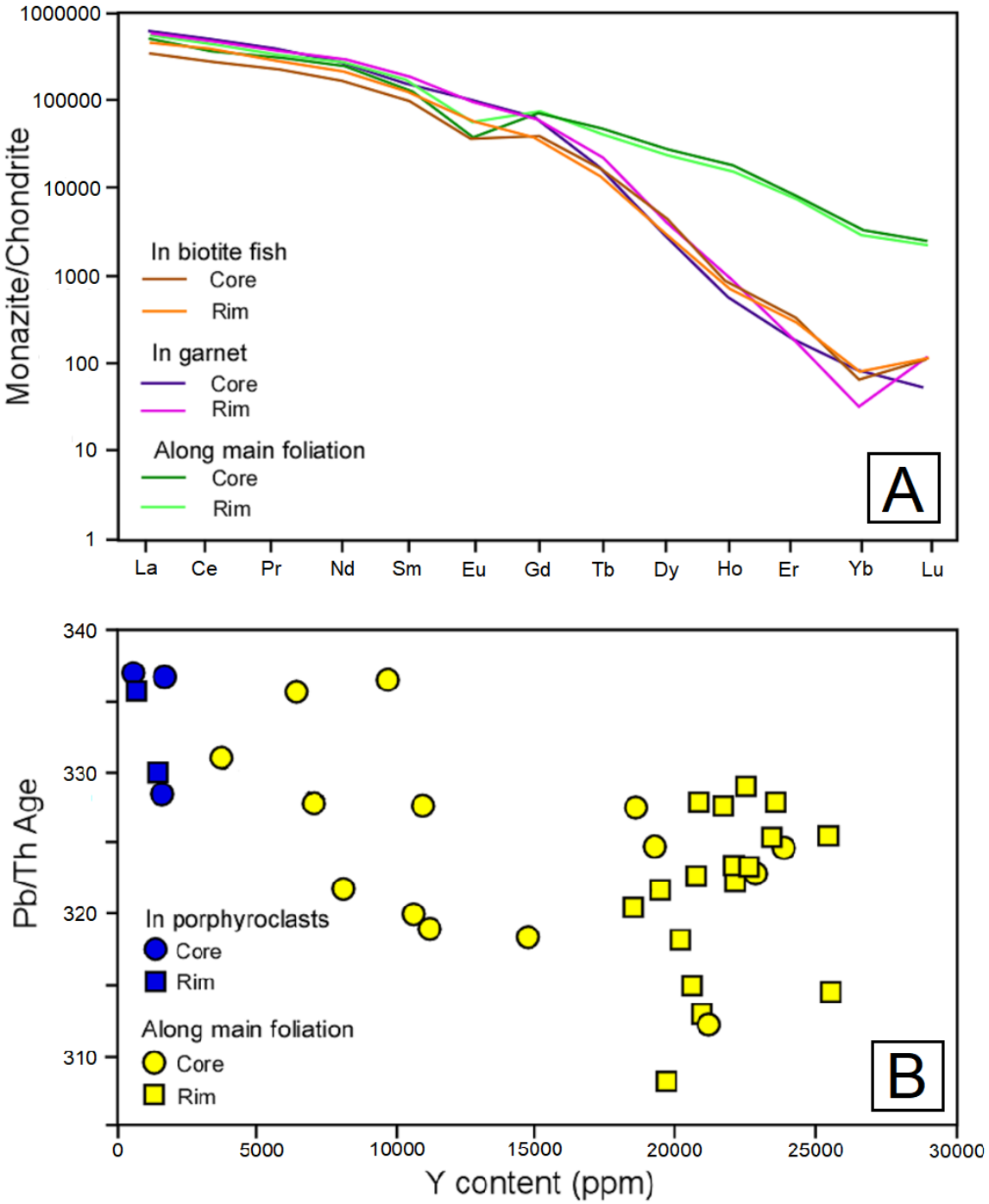

Figure 4.46 – Chemistry of the dated monazite crystals: A) REE distribution for core and rim of grains in different microstructural domains; B) age vs Y content (ppm) in core and rim of grains in different microstructural domains

													Age	1	Age	1	
SAMPLE	$^{207}Pb/^{235}U$	2σ	$^{206}Pb/^{238}U$	2σ	rho	$^{238}U/^{206}Pb$	2σ	$^{207}Pb/^{206}Pb$	2σ	rho	$^{208}Pb/^{232}Th$	2σ	$^{208}Pb/^{232}Th$	2σ	7-corr	2σ	Concordance
AIG11_mnz10_1	0.441	0.017	0.05	0.00	0.96	18.21	0.70	0.058	0.001	-0.04	0.0168	0.0007	337	14	342	13	0.93
AIG11_mnz10_2	0.452	0.016	0.06	0.00	0.97	18.08	0.61	0.059	0.001	-0.02	0.0168	0.0006	337	12	345	11	0.92
AIG11_mnz34_1	0.452	0.018	0.05	0.00	0.98	19.38	0.78	0.064	0.001	0.01	0.0165	0.0007	330	14	320	13	0.86
AIG11_mnz34_2	0.421	0.018	0.05	0.00	0.98	19.05	0.79	0.058	0.001	-0.07	0.0168	0.0007	337	14	328	13	0.92
AIG11_mnz34_3	0.406	0.015	0.05	0.00	0.96	19.69	0.73	0.058	0.001	-0.05	0.0164	0.0006	328	13	317	12	0.92
AIG11_mnz37_3	1.031	0.042	0.06	0.00	0.87	17.54	0.68	0.132	0.004	-0.08	0.0165	0.0007	331	13	322	13	0.50
AIG14_mnz2_1	0.414	0.018	0.05	0.00	0.98	19.53	0.82	0.059	0.001	-0.03	0.0160	0.0007	320	14	320	13	0.92
AIG14_mnz2_2	0.431	0.019	0.05	0.00	0.98	19.84	0.88	0.062	0.001	-0.15	0.0168	0.0007	337	15	313	14	0.87
AIG14_mnz2_3	0.405	0.017	0.05	0.00	0.99	19.46	0.78	0.056	0.001	-0.19	0.0164	0.0007	328	14	322	13	0.94
AIG8_mnz10_1	0.544	0.024	0.05	0.00	0.78	18.76	0.65	0.074	0.002	-0.10	0.0159	0.0006	319	12	326	11	0.76
AIG8_mnz10_2	0.383	0.015	0.05	0.00	0.99	19.65	0.76	0.054	0.001	-0.08	0.0160	0.0006	320	13	319	12	0.97
AIG8_mnz11_1	0.387	0.016	0.05	0.00	0.99	20.41	0.82	0.057	0.001	0.20	0.0159	0.0007	318	13	307	12	0.93
AIG8_mnz11_2	0.395	0.014	0.05	0.00	0.97	20.24	0.70	0.058	0.001	0.13	0.0163	0.0006	327	12	309	11	0.92
AIG8_mnz11_3	0.374	0.015	0.05	0.00	0.98	20.24	0.77	0.055	0.001	-0.12	0.0156	0.0006	313	12	310	12	0.96
AIG8_mnz11_4	0.381	0.015	0.05	0.00	0.99	19.65	0.76	0.055	0.001	-0.07	0.0162	0.0006	325	13	319	12	0.98
AIG8_mnz3_1	0.489	0.018	0.05	0.00	0.96	19.42	0.69	0.069	0.002	-0.17	0.0150	0.0006	300	12	317	11	0.80
AIG8_mnz3_10	0.426	0.018	0.05	0.00	0.98	19.88	0.82	0.061	0.001	0.09	0.0154	0.0007	308	13	313	13	0.88
AIG8_mnz3_11	0.429	0.015	0.05	0.00	0.97	19.57	0.73	0.061	0.001	-0.05	0.0156	0.0006	313	12	318	12	0.89
AIG8_mnz3_12	0.414	0.015	0.05	0.00	0.98	19.61	0.70	0.058	0.001	0.09	0.0161	0.0006	323	12	319	11	0.91
AIG8_mnz3_2	0.459	0.020	0.05	0.00	0.65	19.49	0.63	0.065	0.003	0.01	0.0151	0.0005	303	10	317	10	0.84
AIG8_mnz3_3	0.383	0.015	0.05	0.00	0.99	19.65	0.76	0.054	0.001	-0.06	0.0164	0.0007	328	13	319	12	0.97
AIG8_mnz3_4	0.437	0.021	0.05	0.00	0.99	19.08	0.92	0.061	0.001	0.29	0.0164	0.0008	328	16	326	15	0.89
AIG8_mnz3_5	0.443	0.018	0.05	0.00	0.98	19.42	0.75	0.063	0.001	-0.14	0.0159	0.0007	318	13	320	12	0.87
AIG8_mnz3_6	0.413	0.015	0.05	0.00	0.97	19.05	0.69	0.057	0.001	0.11	0.0163	0.0006	328	13	328	12	0.94
AIG8_mnz3_7	0.385	0.018	0.05	0.00	0.99	19.88	0.92	0.056	0.001	-0.02	0.0157	0.0007	315	14	315	14	0.96
AIG8_mnz3_8	0.388	0.014	0.05	0.00	0.97	19.27	0.71	0.054	0.001	0.07	0.0160	0.0006	322	12	326	12	0.98
AIG8_mnz3_9	0.387	0.015	0.05	0.00	0.98	19.61	0.76	0.055	0.001	0.10	0.0160	0.0006	320	13	320	12	0.97
AIG8_mnz52_1	0.403	0.014	0.05	0.00	0.94	19.80	0.71	0.058	0.001	-0.04	0.0157	0.0006	314	11	316	11	0.92
AIG8_mnz52_10	0.421	0.018	0.05	0.00	0.99	19.27	0.80	0.059	0.001	-0.19	0.0162	0.0007	325	14	324	13	0.91
AIG8_mnz52_11	0.392	0.014	0.05	0.00	0.98	19.27	0.68	0.055	0.001	0.06	0.0164	0.0006	328	13	326	11	0.97
AIG8_mnz52_2	0.387	0.014	0.05	0.00	0.98	19.31	0.71	0.054	0.001	-0.04	0.0162	0.0006	326	12	325	12	0.98
AIG8_mnz52_3	0.382	0.018	0.05	0.00	0.99	19.27	0.87	0.054	0.001	-0.12	0.0162	0.0007	325	15	326	14	0.99
AIG8_mnz52_4	0.385	0.017	0.05	0.00	0.99	19.34	0.78	0.054	0.001	-0.28	0.0163	0.0007	328	14	325	13	0.98
AIG8_mnz52_5	0.387	0.016	0.05	0.00	0.99	19.57	0.79	0.055	0.001	0.08	0.0161	0.0007	323	13	320	13	0.97
AIG8_mnz52_6	0.385	0.016	0.05	0.00	0.99	19.08	0.76	0.054	0.001	0.02	0.0164	0.0007	329	14	329	13	1.00
AIG8_mnz52_7	0.375	0.014	0.05	0.00	0.98	19.96	0.75	0.055	0.001	-0.11	0.0161	0.0007	323	13	314	12	0.97
AIG8_mnz52_8	0.382	0.015	0.05	0.00	0.98	19.57	0.76	0.054	0.001	0.12	0.0161	0.0007	324	13	321	12	0.98
AIG8_mnz52_9	0.381	0.016	0.05	0.00	0.99	19.76	0.84	0.054	0.001	-0.05	0.0161	0.0007	323	14	318	13	0.97

Table 4.10 – Full dataset of LASS analysis on monazite grains of the samples AIG8, AIG11, AIG14

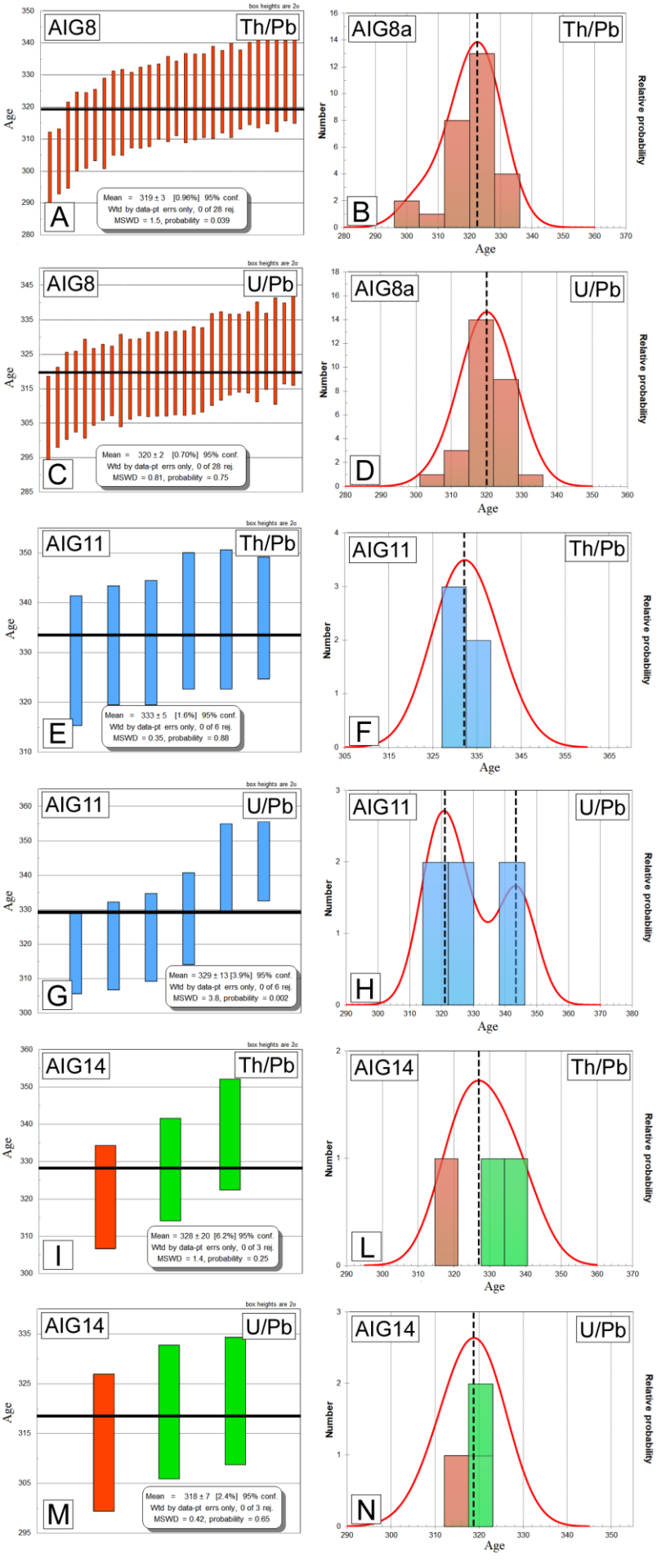
box heights are 2σ
AIG8
Th/Pb
Age
A
Mean = 319 ± 3 [0.96%] 95% conf.
Wtd by data-pt errs only, 0 of 28 rej.
MSWD = 1.5, probability = 0.039
AIG8a
Th/Pb
Number
Relative probability
B
Age
AIG8
U/Pb
C
Mean = 320 ± 2 [0.70%] 95% conf.
Wtd by data-pt errs only, 0 of 28 rej.
MSWD = 0.81, probability = 0.75
AIG8a
U/Pb
D
AIG11
Th/Pb
E
Mean = 333 ± 5 [1.6%] 95% conf.
Wtd by data-pt errs only, 0 of 6 rej.
MSWD = 0.35, probability = 0.88
AIG11
Th/Pb
F
AIG11
U/Pb
G
Mean = 329 ± 13 [3.9%] 95% conf.
Wtd by data-pt errs only, 0 of 6 rej.
MSWD = 3.8, probability = 0.002
AIG11
U/Pb
H
AIG14
Th/Pb
I
Mean = 328 ± 20 [6.2%] 95% conf.
Wtd by data-pt errs only, 0 of 3 rej.
MSWD = 1.4, probability = 0.25
AIG14
Th/Pb
L
AIG14
U/Pb
M
Mean = 318 ± 7 [2.4%] 95% conf.
Wtd by data-pt errs only, 0 of 3 rej.
MSWD = 0.42, probability = 0.65
AIG14
U/Pb
N

Figure 4.47 – Average age diagrams for the Th-Pb and U-Pb systematics (left column) and probability density plots for the Th-Pb and U-Pb systematics (right column) for the studied sample. Red bars represent data collected in the high Y domanins, green bars represent data collected in medium Y domains and blue bars represent data collected in low Y domains

4.2.8 Data discussion and interpretation

In the Emosson Lake and Val Bèrard areas metasedimentary rocks interlayered with orthogneiss are cut by a subvertical NE-SW striking foliation. Mineral lineations plunge gently toward the NE. In the Emosson Lake area granitic dikes were injected intruded along the main foliation and subsequently deformed, with microstructural and crystal fabric kinematic suggesting a top-to-the-SW dextral sense of shear.

In the Emosson Lake area Von Raumer and Bussy (2004) and Genier *et al*. (2008) described the studied high-strain zone as a mylonitic belt with a thickness of ~ 500 m and confined within a magmatic zone adjacent to the Vallorcine granite. Microstructural and quartz c-axis fabric analyses revealed that shear deformation also affects the adjacent non-migmatitic micaschist that previously were not thought to be caught up in this shear deformation (Von Raumer and Bussy, 2004). However, we detected evidence for shear deformation at up to ~ 800 m from the Vallorcine granite that has classically been considered as the southeastern limit of the shear zone (Von Raumer and Bussy, 2004; Genier *et al*. 2008). The shear zone in the Emosson Lake area is therefore wider than 500 m and it is not confined to the migamatitic rocks but also affects non-migmatitic litotypes, as also observed in the Val Bèrard area. Accordingly, the thickness of the high-strain zone ranges between ~ 800 m and ~ 650 m in the two study areas.

Kinematic vorticity analyses allow us to define, for the first time, the flow regime of the sheared rocks in the Aiguilles Rouges that involves a dominant component of pure shear acting together with simple shear. The estimated percentages of pure and simple shear, obtained with the C' shear band method, are variable between ~ 79 % and ~ 53 % and ~ 21 % and ~ 47 % respectively, while the stable porphyroclasts method indicates pure shear and simple shear of ~60 % and ~40 % respectively. Calculated θ angles range between ~ 20° and 9° and combined with the vorticity data indicate a transpressional deformation because the maximum ISA measured in the horizontal plane is oriented at an angle θ less than 45° to macroscopic shear zone boundary observed in the field. In particular those values indicate a pure shear-dominated transpression because the θ angle is less than 22.5° (Tikoff & Fossen 1995; Fossen 2010; Xypolias 2010). The orthogneisses always record a larger component of pure shear than the metasedimentary rocks, indicating a

partitioning of the deformation between the two lithotypes that is probably controlled by the differences in their rheological properties. Pre-existing structural weaknesses as rheological heterogeneities are one of the factors that can trigger deformation partition within a shear zone (Jones and Tanner, 1995).

2D strain analysis revealed a 32 % and a 25 % of stretching. Insights about 3D finite strain are given by the quartz fabrics, by comparing the topology of the measured fabrics with the fabrics predicted by Schmid and Casey (1986) for different strain paths. The measured fabrics are indicative of a deformation in conditions close to plain strain or slightly into the general flattening field.

The structural assets recognized in the field, the vorticity of the flow and insights about finite strain are all in good agreement with a pure shear-dominated transpression (Fossen and Tikoff, 1993; Fossen *et al.*, 1994; Fossen, 2016).

The syn-kinematic mineral assemblage associated with the mylonitic foliation in the study areas is indicative of amphibolite-facies conditions of metamorphism. In the Emosson Lake area, two superposed mineral assemblages in the metapelites have been described in the literature. Observed garnet zoning indicates early medium-high pressure conditions (8–10 kbar, 550 °C) followed by decompression and a thermal peak at 4–6 kbar, 630– 650 °C (Von Raumer, 1983; Von Raumer and Schwander, 1985). In the same area Genier *et al.* (2008) described a partial melting episode that was synchronous with shearing and occurred at P and T conditions close to the vapour-present minimum melting curve for granite (ca. 3.1 ± 1.1 kbar and 650 ± 20 °C). In the studied samples quartz microstructures indicate grain boundary migration as the dominant recrystallization mechanisms. Chessboard extinction was occassionaly recognized as an incipient microstructure but no direct corroborating evidence for high temperature prism [c] slip was recorded in the quartz c-axis fabrics measured in these samples. Local thin section scale microstructural domains characterized by subgrain rotation recrystallization partially overprinting these higher temperature microstructures are present, suggesting that shearing progressively evolved under decreasing ambient temperatures.

Opening angle of the measured quartz c-axis fabrics indicates deformation temperatures between 629° C and 556° C. These estimated temperatures are in agreement with likely temperature ranges indicated by both the syn-kinematic mineral assemblage and quartz microstructures, and are in good agreement with the results of previously published studies in the area (Bussy *et al.*, 2000; Von Raumer and Bussy, 2004; Genier *et al.*,

2008), suggesting that the measured fabrics were not strongly influenced by any lower temperature overprint. However the deformation temperatures indicated by the observed opening angles are regarded as minimum temperatures.

Quartz microstructures (dominanted by subgrain rotation) in the dikes injected along the main shear zone foliation suggest relatively low temperature deformation conditions. These dikes are very close to the Vallorcine granite, a syn-tectonic intrusion emplaced at 306.5 ± 1.5 Ma (Bussy *et al*., 2000), and the dikes can be structurally related to the Vallorcine granite . Our observation and interpretations are in agreement with previously published studies in the study areas, and indicate that shear deformation was still on-going under lower temperature conditions during granite intrusion.

Petrochronology allows us to constrain the age of transpression in the Aiguilles Rouges Massif. We recognized two groups of monazites: a first group composed of grains included in garnet or biotite porphyroclasts and a second group composed of grains within the main foliation. The two groups have chemical differences. Grains included in porphyroclasts have a lower content in HREE (heavy rare-earth element) relative to grains in the main foliation. The microstructural positions and the chemical compositions reveal that monazite grains of the first group grew before the shear episode, during prograde metamorphism, while monazite grains of the second group are syn-kinematic. Monazites in the main foliation have an anomaly in Eu content indicating synchronous growth with feldspar during partial melting (Braden *et al*. 2017; Rubatto *et al*. 2013) and suggesting that transpressional deformation occurred either at the same time or shortly after anatexis. Y content is lower in the monazite grains included in porphyroclast and higher in grains within the foliation, in agreement with the growth of syn-kinematic monazites during retrograde metamorphism and garnet breakdown. Two groups of monazite ages are distinguished: older ages of ~ 340-330 Ma, obtained in low-Y grains included in porphyroclasts and grown during prograde metamorphism under near peak amphibolite-facies conditions. Younger ages of ~ 320-310 Ma are obtained from the high-Y grains in the main foliation and are representative of the onset of transpressional deformation. Older ages are in agreement with the age of 327 ± 2 Ma (U-Pb method on monazite) obtained by Bussy *et al*. (2000), which is considered to date near peak temperature conditions of the amphibolite-facies metamorphism. Because the Vallorcine granite and its dikes are syn-tectonic intrusions emplaced at 306.5 ± 1.5 Ma (Bussy *et al*. 2000)

we can state that transpressive deformation in the Aiguilles Rouge Massif is a long lasting event of at least ~ 15 Myr.

The onset of transpression in the Aiguilles Rouge Massif at 320-310 Ma is younger than in the Argentera Massif where it is dated at ~ 340 Ma (Simonetti *et al*., 2018) but is similar to the ~ 323 Ma age for onset of transpression in both the Maures Massif of southern France (Simonetti *et al*., submitted) and in northern Sardinia ~ 320 Ma (Carosi *et al*., 2012).

5. Maures Massif

5.1 Introduction

In the present chapter we focus on the contact between internal and external zone of the Variscan belt in the Maures Massif in southern France (fig. 5.1; Buscail 2000; Bellot, 2005; Corsini and Rolland, 2009; Schneider *et al.*, 2014; Oliot *et al.*, 2015). It is marked by a km-scale shear zone known as Cavalaire Fault (CF; Schneider *et al,*. 2014; Oliot *et al*., 2015).

The aim of this chapter is to clarify the kinematics of the flow, the age of activity and the deformation temperature of the CF.

Sample locations are reported in the sketch maps of figures 5.2 and 5.3. A list of samples used for analysis, with the relative position and results, is reported in appendix D.

The structural analysis, the study of kinematic vorticity, the strain analysis and the petrochronological study were used to prepare a paper with the title "*Timing and kinematics of flow in a transpressive dextral shear zone, Maures Massif (Southern France)"* that was submitted to International Journal of Earth Science and is currently under review.

5.2 Geological setting

The MTM (fig. 5.1a) is the southernmost segment of the Variscan belt in France (Chabrier and Mascle, 1975; Matte, 2001). The MTM is composed of low- to high-grade metamorphic rocks, the latter intruded by Carboniferous granitoids (Crevola and Pupin, 1994). The Maures Massif is separated from the Tanneron Massif by the E-W trending Permian Esterel basin (fig. 5.1b).

The western domain of the MTM records Barrovian metamorphism increasing in grade from west to east (Buscail, 2000; Bellot, 2005; Corsini and Rolland, 2009; Schneider *et al*., 2014; Oliot *et al*., 2015). Several Variscan metamorphic units are distinguished (review in Schneider *et al*., 2014; fig. 5.1b). From W to E, the main units are: 1) the western metamorphic unit (fig. 5.1b) made by Early Paleozoic low-grade phyllite belonging to the chlorite zone; 2) the Collobrières unit (fig. 5.1b), included within the garnet-chlorite zone, consisting of iron-rich metasediments (quartzite, marble and gneiss) and metavolcanic rocks of the alkaline

leptyno-amphibolitic complex (Bard and Caruba 1981). The latter is interpreted as a volcano-sedimentary suite emplaced during Cambrian continental rifting (Briand *et al*. 2002; Innocent *et al.*, 2003); 3) the Bormes unit (fig. 5.1b), made up of the Bormes orthogneiss and associated metasediments, affected by Barrovian metamorphism from the biotite-staurolite zone up to the biotite-kyanite zone; 4) the La Garde-Freinet unit (fig. 5.1b) containing micaschist, migmatitic paragneiss and orthogneiss with acid, mafic and ultramafic lenses represented by an association of amphibolite and leptynite. Barrovian metamorphism is in the sillimanite-biotite zone; 5) the Eastern Gneiss and Tanneron units (fig. 5.1b), affected by metamorphism in the sillimanite-biotite zone, are made of migmatitic ortho- and paragneiss with associated mafic eclogite lenses showing a polyphase metamorphism. The La Garde-Freinet and Eastern Gneiss units are intruded by syn-kinematic calc-alkaline and peraluminous granitoids (fig. 5.1b): the Hermitan granite (in the La Garde-Freinet unit) and the Plan de la Tour granite (in the Eastern Gneiss unit), the last one cropping out in the core of a regional-scale N-S trending antiform (Rolland *et al.*, 2009). The La Garde-Freinet, Eastern Gneiss and Tanneron units are part of the internal zone (fig. 5.1b) characterized by widespread partial melting and syn-tectonic granitic intrusions (Schneider *et al*,. 2014).

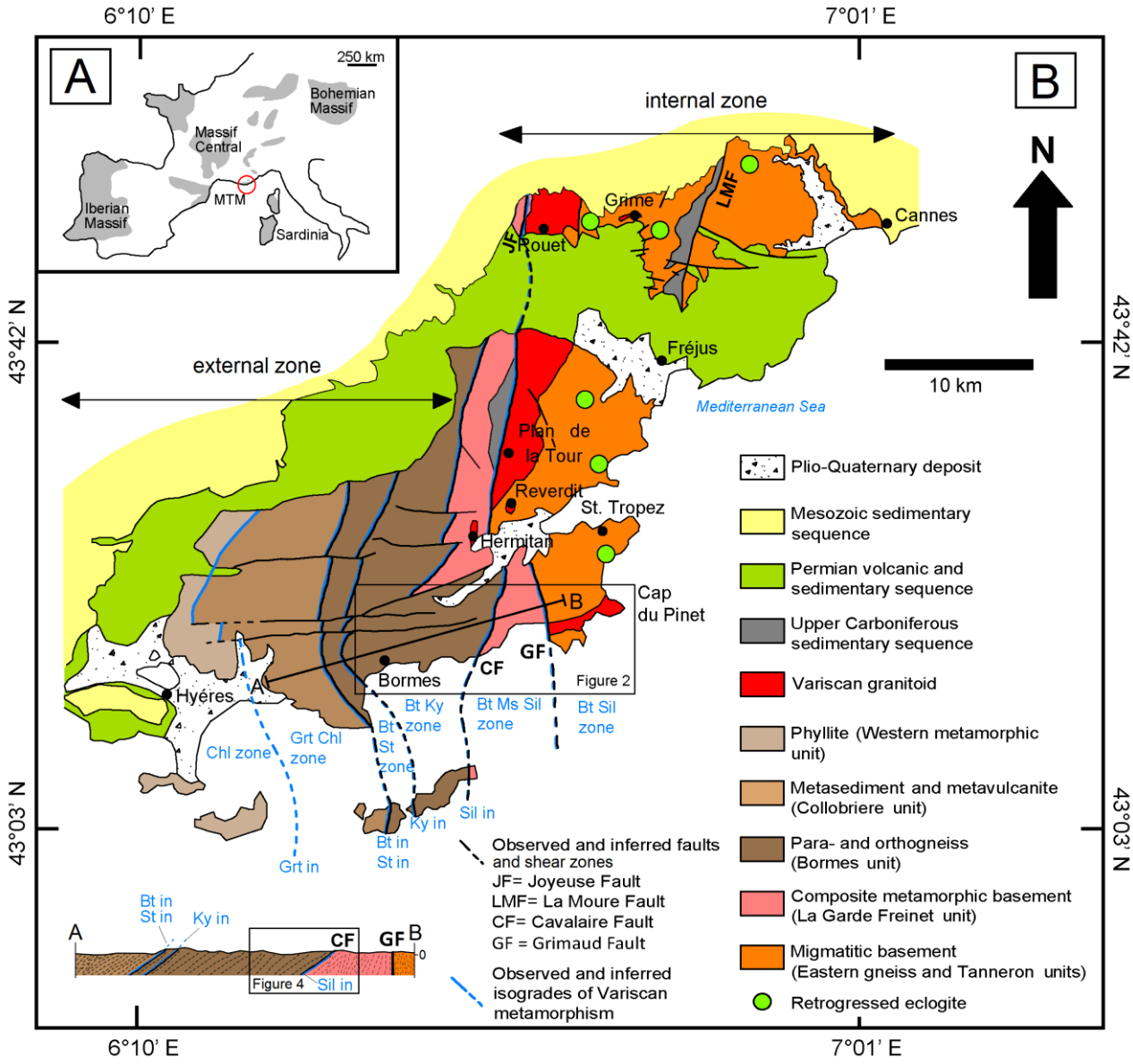

Figure 5.1 – A) Distribution of the Variscan basement in Europe and location of the Maures-Tanneron Massif (MTM); B) Geological and structural sketch map of the Variscan basement of the Maures-Tanneron Massif, metamorphic zonation is reported (modified after Compagnoni *et al*., 2010; Schneider *et al.*, 2014; Oliot *et al*., 2015)

Relicts of high pressure metamorphism in mafic rocks also occur in the internal zone. The Collobrières and Bormes units are part of the external zone (fig. 5.1b) characterized by a low-grade metamorphism and by the lack of high-pressure mafic relicts. The subdivision of the Maures Massif in two different tectonic-metamorphic zones, internal and external zones, was pointed out by Vauchez and Bufalo (1985, 1988) and Morillon *et al*. (2000) who described the presence of a high-temperature transcurrent shear zone, the Joyeuse–Grimaud Fault (fig. 5.1b), between the two zones. Recently, Schneider *et al.* (2014) recognized that the internal and external zones are separated by the CF (fig. 5.1b), interpreted as a major polyphase shear zone, rather than by the Joyeuse-Grimaud Fault located in the internal zone.

The CF was initially studied by Bellot *et al.* (2000, 2002). These Authors recognized an older period of top-to-the-E-SE thrusting on the shear zone during Early Carboniferous times, followed by reactivation as a normal fault during late Variscan phase, related to extensional tectonics, allowing a progressive thinning of a previously thickened crust. Recent studies (Schneider *et al*., 2014; Oliot *et al*., 2015;Gerbault *et al.*, 2016) are in agreement with the first top-to-the-E-SE thrust-sense movement, but recognized a later reactivation in a transpressional regime associated with exhumation of the mid- and lower crust between ~ 330 - 310 Ma.

In the MTM, Schneider *et al*. (2014) recognized several tectono-metamorphic stages. In the internal zone, relicts of eclogite-facies metamorphism (M_0) preserved in metabasic lenses, are related to an early stage of Siluro-Devonian subduction. A collisional stage, mostly preserved in the external zone, is marked by nappe stacking with top-to-the-west tectonic transport (D_1), followed by back-thrusting of the nappes towards the east (D_2). In the internal zone, exhumation of the tectonic units occurred in the context of a transpressive regime (D_3). Nappe stacking and back-thrusting were associated with typical Barrovian-type metamorphism M_1, progressively followed by LP-HT metamorphic stages, M_2 and M_3, during the Carboniferous.

We focused on two key areas of the Maures-Tanneron Massif (fig. 5.2) where the contact between internal and external zones is marked by a well-exposed high-strain zone, the CF. We performed mesoscale analyses combined with microstructural studies of field-oriented samples (fig. 5.2 and fig. 5.3) collected within the Bormes and La Garde Freinet units. The structural maps of the studied sector within the high-strain zone and the position of the collected samples are reported in figure 5.3.

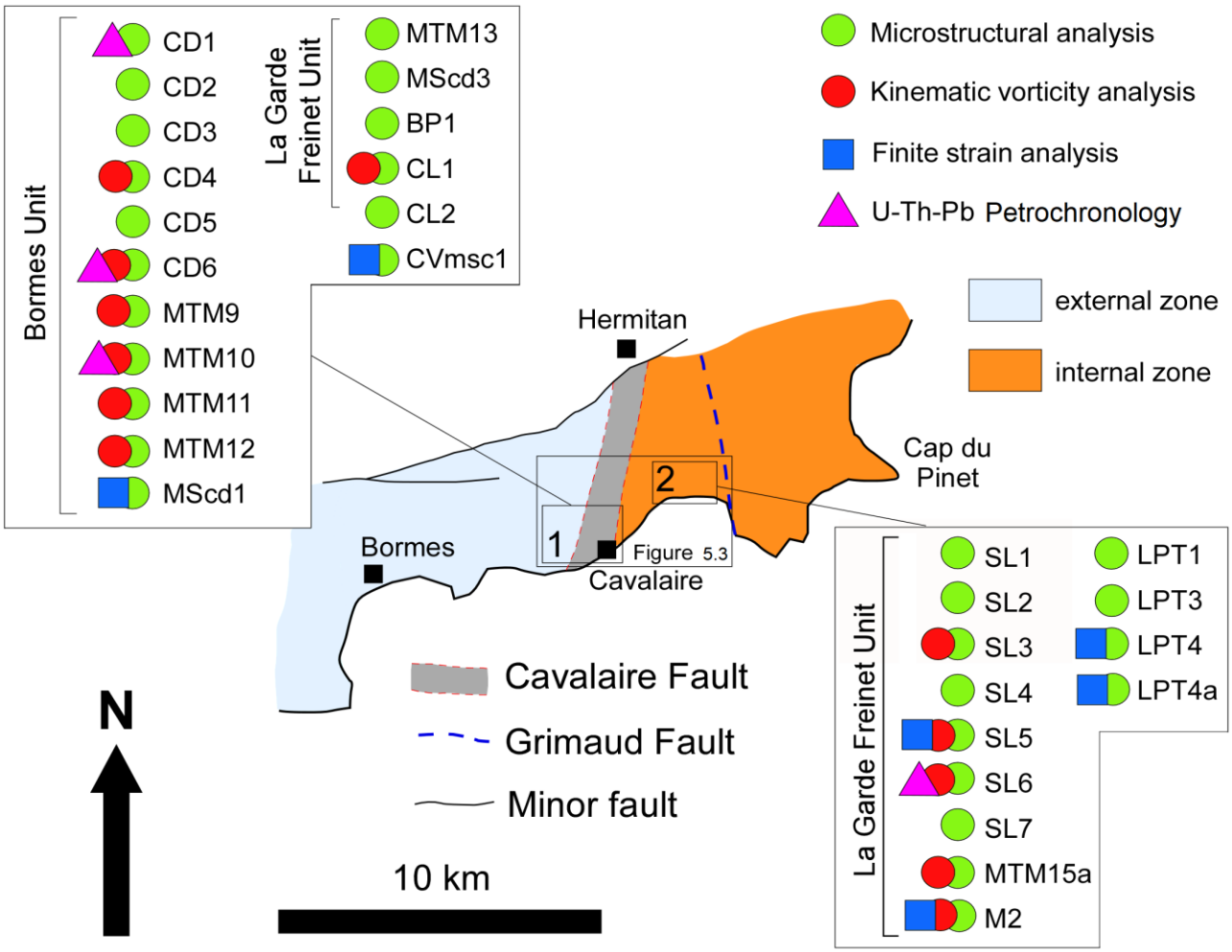

Figure 5.2 – Sketch with sample locations (1 and 2) of part of the Maures Massif. The samples location and the corresponding type of analysis are shown. Details of the selected study areas are given in fig. 5.3

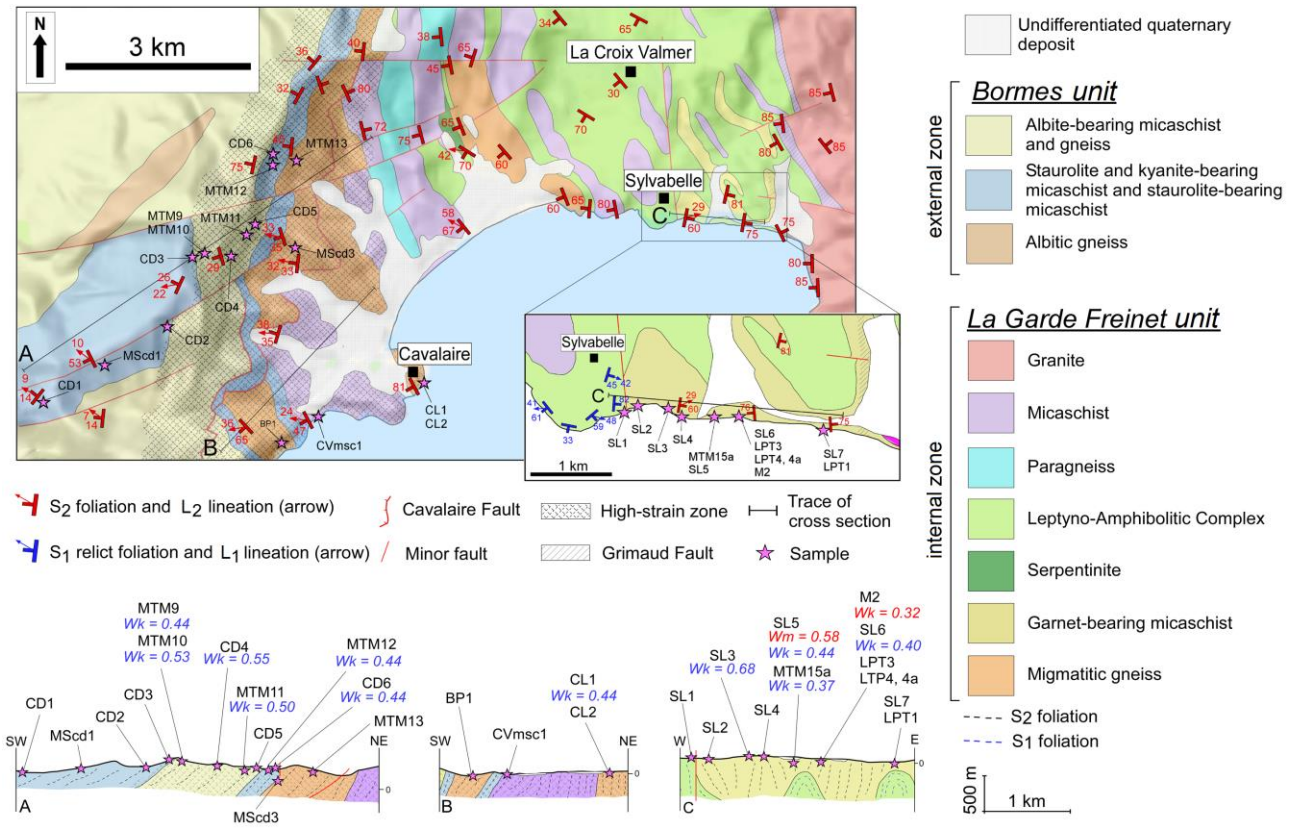

Figure 5.3 – Geological sketch maps of the study areas (location is reported in fig. 5.2) with samples locations (modified from geological map of Saint Tropez-Cap Lardier 1/50 000, editions BRGM; the limits of the high-strain zone of the Cavalaire Fault are modified after Bellot *et al*. 2002). Geological cross sections, with samples position and the relative vorticity number, are also reported

5.3 Structural and microstructural analysis

The CF, as testified by field observations, is characterized by a NE-SW trending km-thick high-strain zone, involving biotite-kyanite and biotite-muscovite-sillimanite zones (figs. 5.1, 5.3). West of the CF unsheared gneiss and micaschist of the Bormes unit (external zone) are present, whereas migmatite of the La Garde Freinet unit (internal zone) crops out on the eastern side of the CF (fig. 5.4). In the field, a deformation gradient is recognized toward the core of the CF high-strain zone (fig. 5.4). From west to east, within the high-strain zone, staurolite-kyanite-bearing micaschist and staurolite-bearing micaschist, belonging to the Bormes unit, have been mapped. They show a biotite + white mica continuous foliation, dipping to the NW, with a mineral lineation, defined by staurolite (fig. 5.5a), trending NW-SE and plunging to the NW. Shear planes dip towards W-NW at variable angles in the 14° and 53° range.

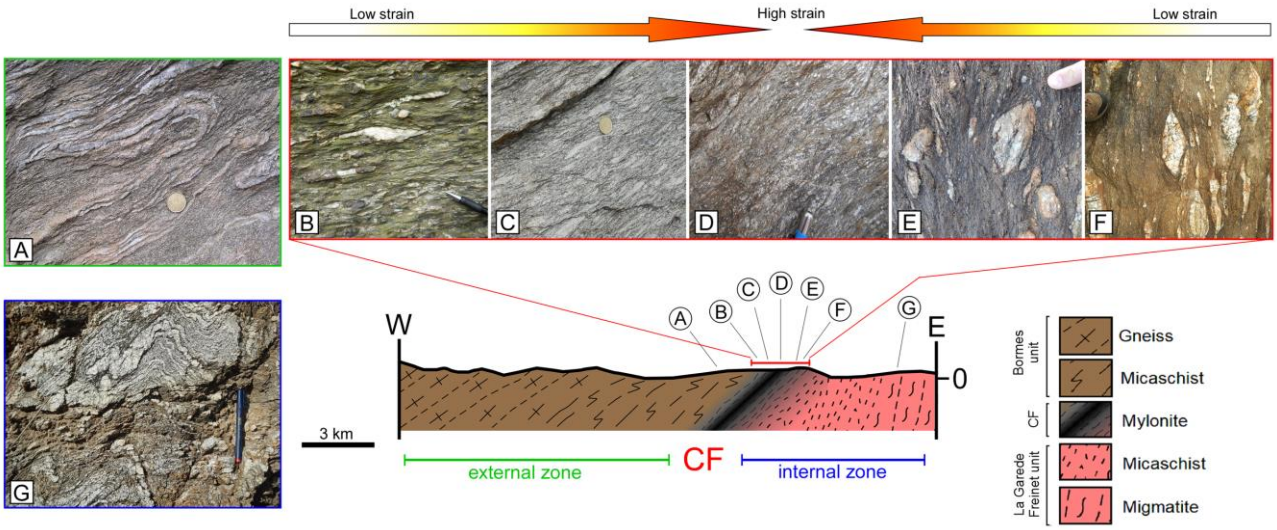

Figure 5.4 – Schematic cross-section across the contact between internal and external zones (location is reported in fig. 5.1) summarizing the main field-observed deformational features of the different structural domains. A) folded micaschist of the external zone (Bormes unit) cropping-out to the W of the CF; B) mylonite of the western side of the CF, developed at the expense of staurolite-bearing micaschist (Bormes unit); C) mylonite at the expense of paragneiss; D) mylonitic paragneiss in the core of the CF; E) mylonite at the expense of migmatite in the internal zone (La Garde Freinet unit); F) mylonite of the eastern limb of the CF affecting migmatite of the internal zone (La Garde Freinet unit); G) folded migmatite of the internal zone (La Garde Freinet unit; same outcrop described in Schneider *et al*. 2014)

Asymmetric strain fringes around staurolite porphyroclasts (fig. 5.6a) and C-S fabrics indicate a top-to-the-NW normal sense of shear. Boudins of quartz and feldspar rich-material, observed on both the XZ and YZ sections of the finite strain ellipsoid (fig. 5.6b), are often present. Folded boudins also occur (fig. 5.6c). The main foliation is deformed by a steeply dipping crenulation cleavage that is occasionally associated with dynamic recrystallization of chlorite (fig. 5.6d). Micaschist is in contact with the mylonitic gneiss and mylonitic micaschist of the CF and is cut by a penetrative mylonitic foliation steeply dipping to the W, and a mineral lineation plunging to the W-NW (fig. 5.5b). The sense of shear, highlighted by S-C and S-C' fabrics, is top-to-the-NW. In some sectors a sub-vertical crenulation cleavage, deforming the mylonitic foliation, is present. The La Garde Freinet unit, to the east of the mylonitic gneiss of the CF (figs.5.1, 5.3), is affected by non-coaxial deformation and folds. Sheared migmatite is cut by a sub-vertical foliation defined by biotite and sillimanite (fig. 5.5c). Both dextral and sinistral kinematic indicators occur in these rocks (fig. 5.6e). F_2 folds, confined within the high-strain zone, have been recognized in migmatite, amphibolite and garnet-bearing micaschist. F_2 folds have subvertical axes and axial planes (fig. .5.5d) parallel to the main foliation (fig. 5.6f).

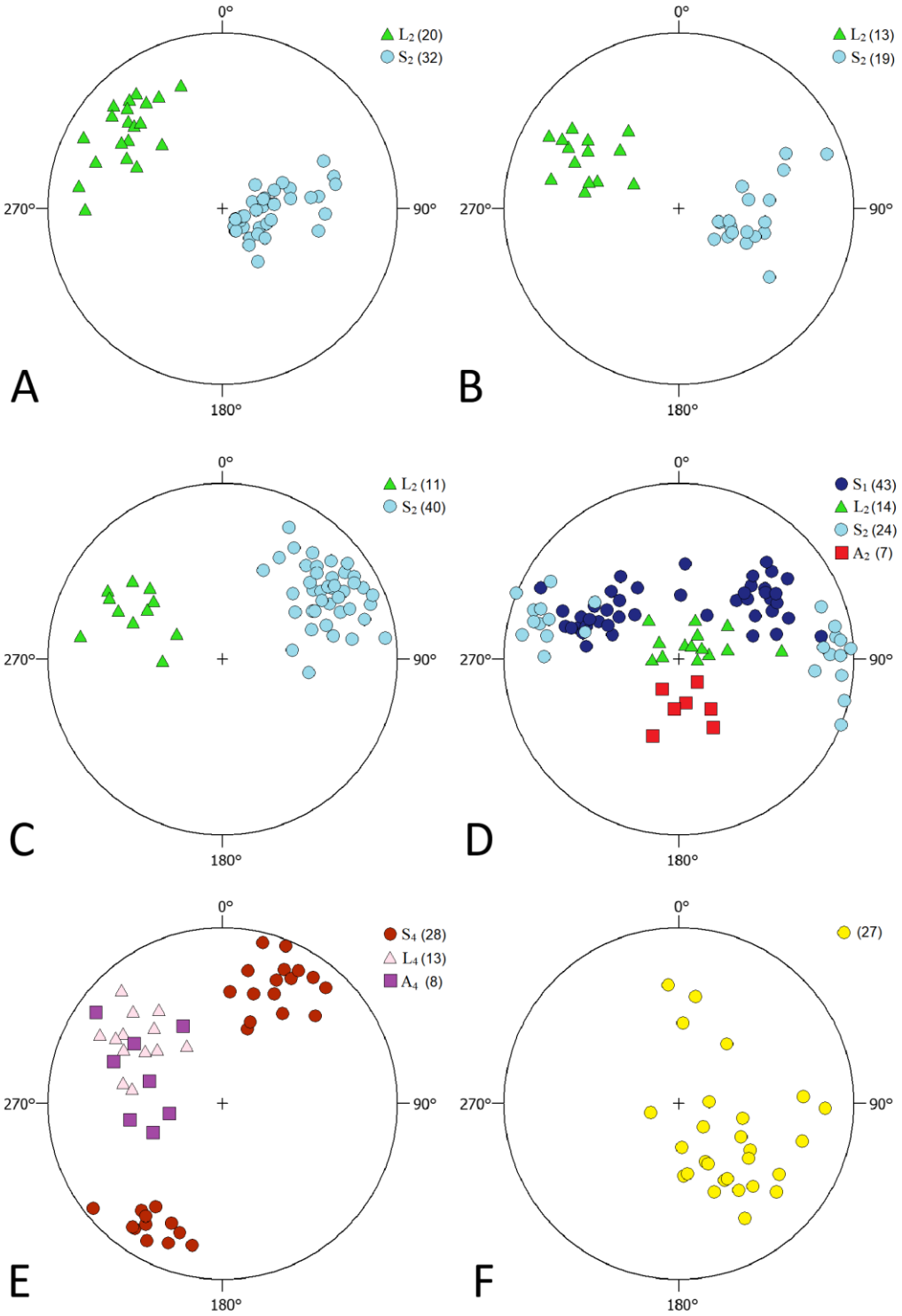

Figure 5.5 – Equal angle projection (lower hemisphere) of main structural elements: A) poles to S_2 foliation planes (dots, 32 data) and L_2 stretching lineation (triangles, 20 data) in the staurolite-bearing micaschist of the kyanite-biotite zone adjacent to the CF; B) poles to S_2 foliation planes (dots, 19 data) and stretching lineation L_2 (triangles, 13 data) in the mylonitic gneiss of the CF; C) poles to S_2 foliation planes (dots, 40 data) and L_2 stretching lineation (triangles, 11 data) in sheared migmatite of the Cavalaire Fault; D) structural elements of mylonite of the La Garde-Freinet unit east of the Cavalaire Fault. Poles to S_1 foliation planes in the amphibolite (dark dots, 43 data), poles to S_2 foliation planes in the garnet-bearing micaschist (light dots, 24 data) and L_2 stretching lineation (triangles, 14 data), A_2 fold axis (square, 7 data); E) structural elements associated to the crenulation cleavage measured in all the lithotypes of the contact zone. L_4 intersection lineation between the main foliation (S_2) and crenulation cleavage (S_4) planes (triangles, 13 data), poles to S_4 crenulation cleavage (dots, 28 data), A_4 fold axis of crenulation microfolds (square, 8 data); F) poles to brittle and brittle-ductile shear planes measured across the high-strain zone (dots, 27 data)

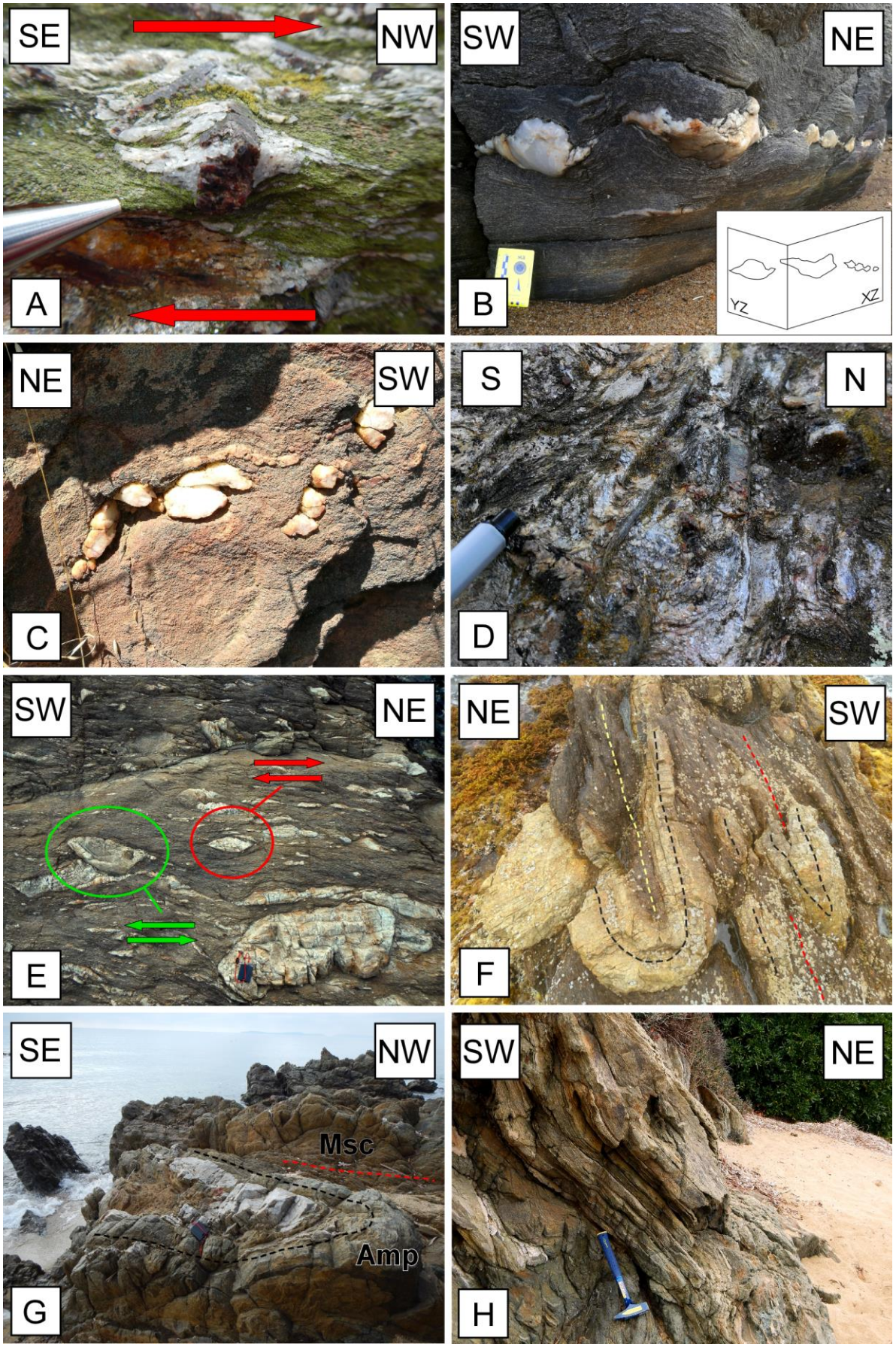
SE
NW
A
SW
NE
B
YZ
XZ
NE
SW
C
S
N
D
SW
NE
E
NE
SW
F
SE
NW
Msc
Amp
G
SW
NE
H

Figure 5.6 – A) Asymmetric quartz strain fringes around a staurolite porphyroclast in staurolite-bearing micaschist showing a top-to-the-NW sense of shear; B) boudins developed at the expense of quartz and feldspar rich levels recognizable both on the XZ and YZ section of the finite strain; C) folded boudins in sheared rocks of the Cavalaire Fault; D) steeply dipping S_4 cleavage defined by chlorite and deforming S_2 foliation in the staurolite-bearing micaschist (plan view); E) sheared migmatite showing both dextral and sinistral sense of shear; F) examples of F_2 syn-shear folds deforming quartz-rich domain in the garnet-bearing micaschist (black dashed line) with subvertical both axis and axial plane (yellow dashed line), parallel to the main S_2 foliation (red dashed line); G) syn-shear fold (F_2) deforming an older relict S_1 foliation (black dashed line) in the amphibolite (Amp). S_1 is preserved in the hinge zones of the fold, whereas it parallelized to the S_2 foliation of the garnet-bearing micaschist (Msc) in the limbs (red dashed line). Foliation in the micaschist and F_2 axial plane are parallel; H) late F_3 open folds with sub-horizontal axes and low angle axial planes deforming the S_2 foliation in garnet-bearing micaschist

Steeply dipping mineral lineations, L_2, have been observed on the main foliation (fig. 5.5d). An older S_1 foliation is preserved in the hinge zones of the folded amphibolite. This foliation is parallel to the S_2 foliation of the micaschist in the limbs of the F_2 folds (fig. 5.6g). Later open and reclined F_3 folds with axes and axial planes dipping at low angles to the SW, causes a variation in the dip angle and the dip direction of the mylonitic foliation (fig. 5.6h). A sub-vertical WNW-ESE S_4 crenulation cleavage occurs sporadically (fig. 5.5e), A_4 microfold axes plunge towards W-NW (fig. 5.5e) and an intersection lineation, between S_4 and S_2, plunges toward the NW (fig. 5.4e). Brittle and brittle-ductile shear planes affect the mylonitic foliation, striking NNE-SSW with variable dip (fig. 5.5f) and a top-to-the-WNW sense of shear.

Microstructural analyses were performed on sheared samples of the CF (figs. 5.2, 5.3). Foliations and kinematic indicators have been classified according to Passchier and Trouw (2005). Quartz microstructures, indicative of dynamic recrystallization, are defined according to Piazolo and Passchier (2002), Stipp *et al*. (2002) and Passchier and Trouw (2005).

Sheared staurolite-bearing micaschist, belonging to the Bormes unit, and involved in the CF, are characterized by a continuous foliation made of biotite + white mica. The foliation wraps around kyanite, staurolite and garnet porphyroclasts containing an internal foliation, mainly composed of elongate quartz. The internal foliation in the porphyroclasts is generally not continuous with the external foliation (fig. 5.7a), however in some staurolite crystals, an internal foliation at the grain rims is concordant with the external foliation (fig. 5.7b). These observations support the interpretation that staurolite growth predates, and is locally synchronous, with the development of the mylonitic foliation.

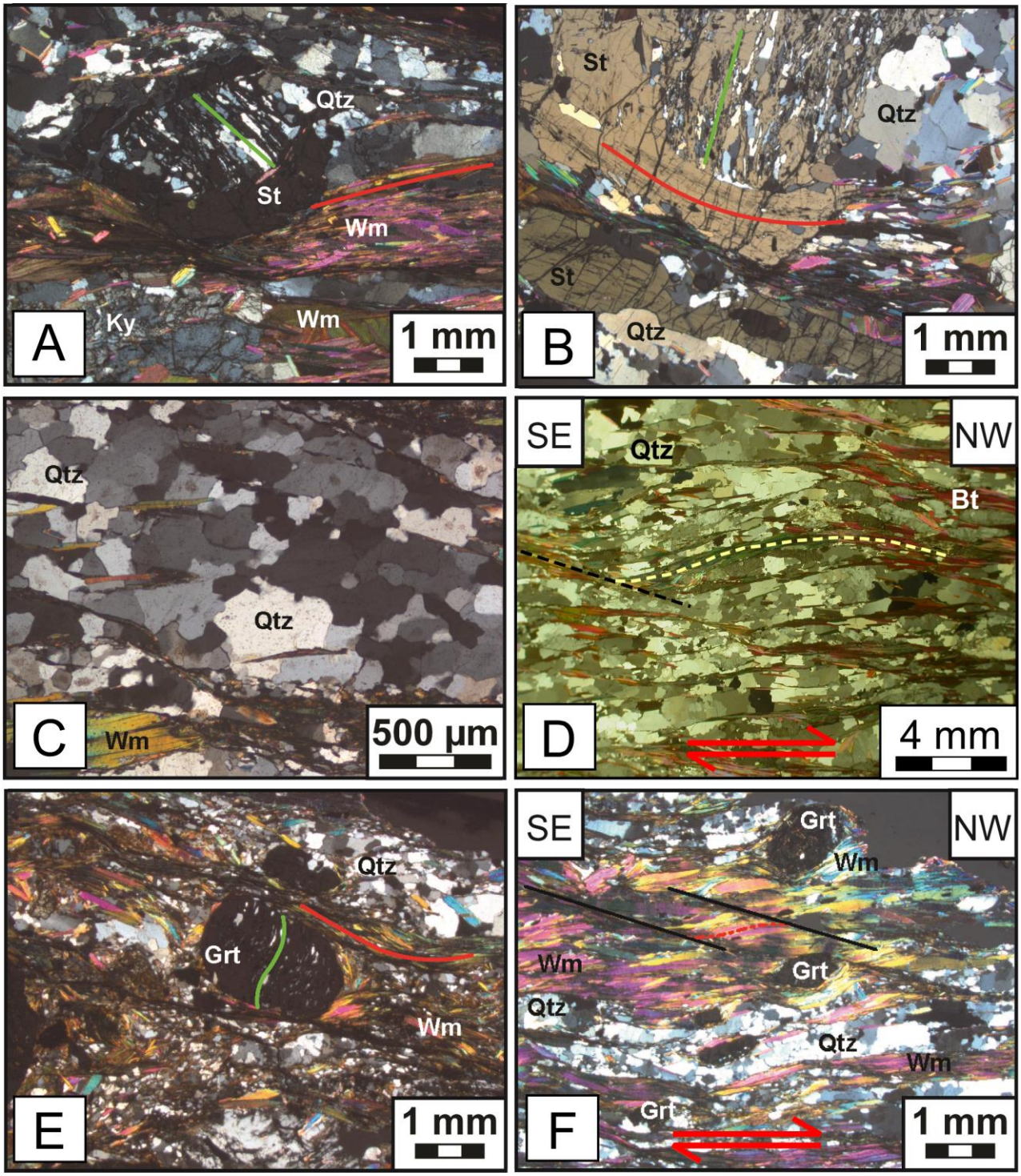

Figure 5.7 – A) Staurolite porphyroclast in kyanite-bearing micaschist with an internal foliation S_1 defined by quartz + white mica (green line). The porphyroclast is wrapped by the external foliation S_2 (red line) defined by quartz + white mica (XPL); B) staurolite porphyroblast, in staurolite-bearing micaschist, showing two stages of growth: an inter-tectonic core with an internal foliation S_1 (green line) and a syn-tectonic rim with an internal foliation S_2 (red line) in continuity with the external one (XPL); D) deformed quartz in staurolite-bearing micaschist showing lobed and irregular boundaries indicative of grain boundary migration; D) S-C' fabric in the mylonitic gneiss of the Cavalaire Fault showing a top-to-the-NW sense of shear (C' is marked by a black dashed line, S plane is marked by a yellow dashed line); F) garnet within garnet-bearing micaschist, showing an internal S_1 foliation defined by elongated quartz (green line), wrapped by an external S_2 foliation (red line) defined by quartz + white mica (XPL); F) S-C' fabric (S plane is marked by red dashed line, C' marked by black lines) pointing a top-to-the NW sense of shear in garnet-bearing micaschist (XPL)

A top-to-the-NW normal sense of shear is highlighted by the presence of asymmetric strain fringes around porphyroclasts of staurolite and garnet. Lobate and ameboid quartz grain boundaries suggest dynamic recrystallization by grain boundary migration (fig. 5.7c). The CF is associated with a mylonitic foliation overprinting previous structures developed in micaschist and gneiss of the Bormes unit (external zone) and in migmatite, amphibolite and micaschist of the La Garde-Freinet unit (internal zone). In the micaschist and gneiss of the Bormes unit, the mylonitic foliation is defined by biotite, white mica, ± fibrolitic sillimanite. Quartz grains have lobate grain boundaries suggesting dynamic recrystallization by grain boundary migration. However, in some sectors, incipient subgrain rotation recrystallization is recognized. K-feldspar sometimes shows mechanical twinning and undulose extinction and locally minor fractures at high-angle to the mylonitic foliation. S-C and S-C' fabrics indicate a top-to-the-NW normal sense of shear (fig. 5.7d). In the migmatite (La Garde-Freinet unit, internal zone), the mylonitic continuous foliation is defined by biotite and sillimanite. The mylonitic foliation wraps around sheared leucosomes consisting of quartz and feldspars. Folded amphibolite layers are composed of plagioclase and green amphibole-rich levels alternating with quartz + plagioclase and garnet bands. Garnet-bearing micaschist, occuring around amphibolite, contain a spaced schistosity with sharp and parallel cleavage domains defined by biotite + white mica. Garnet porphyroclasts contain an internal foliation marked by inclusions of elongated quartz, oriented at a high-angle with respect to the external foliation (fig. 5.7e). Quartz grains have lobate boundaries. Rotated porphyroclasts, S-C and S-C' fabric, point to a top-to-the-NW sense of shear (fig. 5.7f).

5.4 Kinematic vorticity analysis

Results of the vorticity analyses using both C' shear band and stable porphyroclast-methods, are reported in tables 5.1 and 5.2, respectively. Polar histograms used to derive the angle ν are provided in figure 5.8.

Sample	N	ν	Wk	θ
MTM10	19	32	0.44	13
CD4	4	28	0.55	17
MTM11	19	30	0.50	14
MTM12	29	32	0.44	13
CD6	6	32	0.44	13
CL1	9	32	0.44	12
SL3	6	23	0.68	21
MTM15a	33	32	0.44	13
M2	19	32	0.44	13
SL6	5	33	0.40	12
MTM9	23	29	0.53	16
SL5	27	34	0.37	11

Table 5.1 – Summary table of the vorticity data obtained with the C' shear band method: number of data (N), angle between C' planes and the shear zone boundary (ν), Wk value (Wk), angles between the maximum ISA in the horizontal plane and the shear zone boundary (θ)

Sample	N	Rc_{min}	Rc_{max}	Rc_m	Wk_{min}	Wk_{max}	Wm
M2	418	1.38	1.42	1.40	0.31	0.34	0.32
SL5	172	1.73	2.20	1.96	0.50	0.66	0.58

Table 5.2 – Summary table of the vorticity data obtained with the stable porphyroclasts method: number of data (N), minimum critical axial ratio (Rc_{min}), maximum critical axial ratio (Rc_{max}), mean critical axial ratio (Rc_m), minimum value of Wk (Wk_{min}), maximum value of Wk (Wk_{max}), mean value of Wk (Wm)

For the stable porphyroclasts method, preliminary Mulchrone tests are shown in figure 5.9a and 5.9b, whereas the porphyroclasts distributions are given in figure 5.9c and 5.9d. The twelve samples (see figure 5.3 for sample location) analysed by the C' shear band method give a vorticity number ranging from 0.40 to 0.68, with a mean of 0.47 and a mode of 0.44. These values indicate a flow regime characterized by an important contribution of pure shear, ranging between 52 % and 66% (fig. 5.10a).

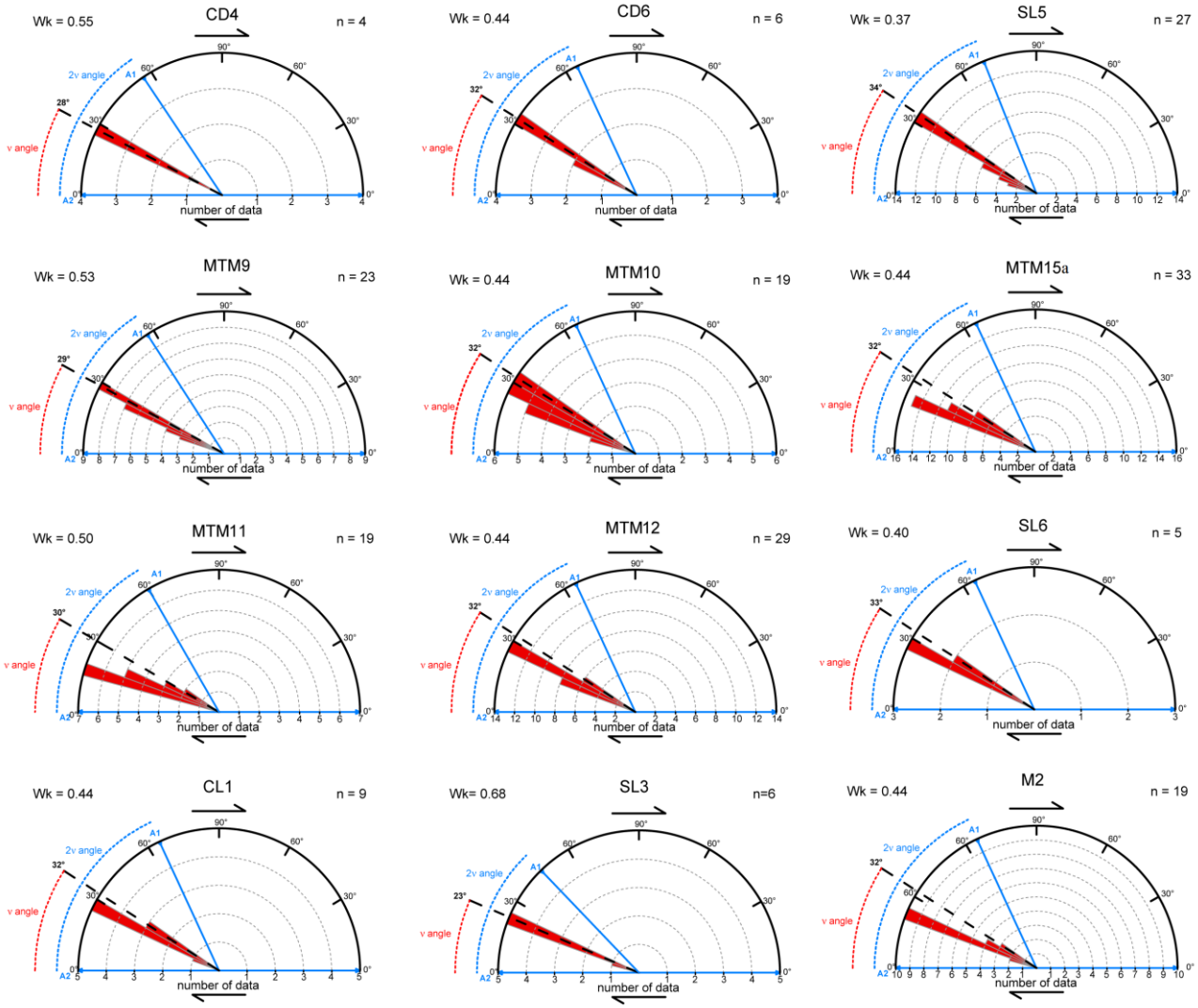

Figure 5.8 – Polar histograms used to derive the angle ν needed the calculation of kinematic vorticity. A1= flow apophysis 1; A2 = flow apophysis 2; n = total number of data; Wk = kinematic vorticity number. Dashed line represents the bisector of the angle between A1 and A2 apophyses

In sample M2 we detected, through the stable porphyroclast method, a minimum Rc of 1.38 and a maximum Rc of 1.42 corresponding to Wk values of 0.31 and 0.34, respectively. In sample SL5 minimum and maximum Rc values are 1.73 and 2.2 corresponding to Wk between 0.50 and 0.66. These values indicate a 55 - 75 % pure shear, in good agreement with the results based on C' shear band vorticity gauge.

Data obtained with the stable porphyroclast method are regarded as reliable since all the main assumptions (see above) of the method are satisfied. Indeed: garnet and feldspar porphyroclasts do not show significant internal deformation and are harder to deform compared to the mica-rich matrix; from the compiled Mulchrone diagrams (fig. 5.9) our data do not fit the theoretical curve calculated for a system in which slip between porphyroclasts and matrix occurs; the selected garnets and feldspars are free to rotate in the matrix

without mutual interference because the distance between porphyroclasts (~ 2 mm as average) is larger than their maximum long axis (~ 1.2 mm as average size).

According to the calculated θ angle, all samples plot in the field of pure shear-dominated transpression (Fig. 10b).

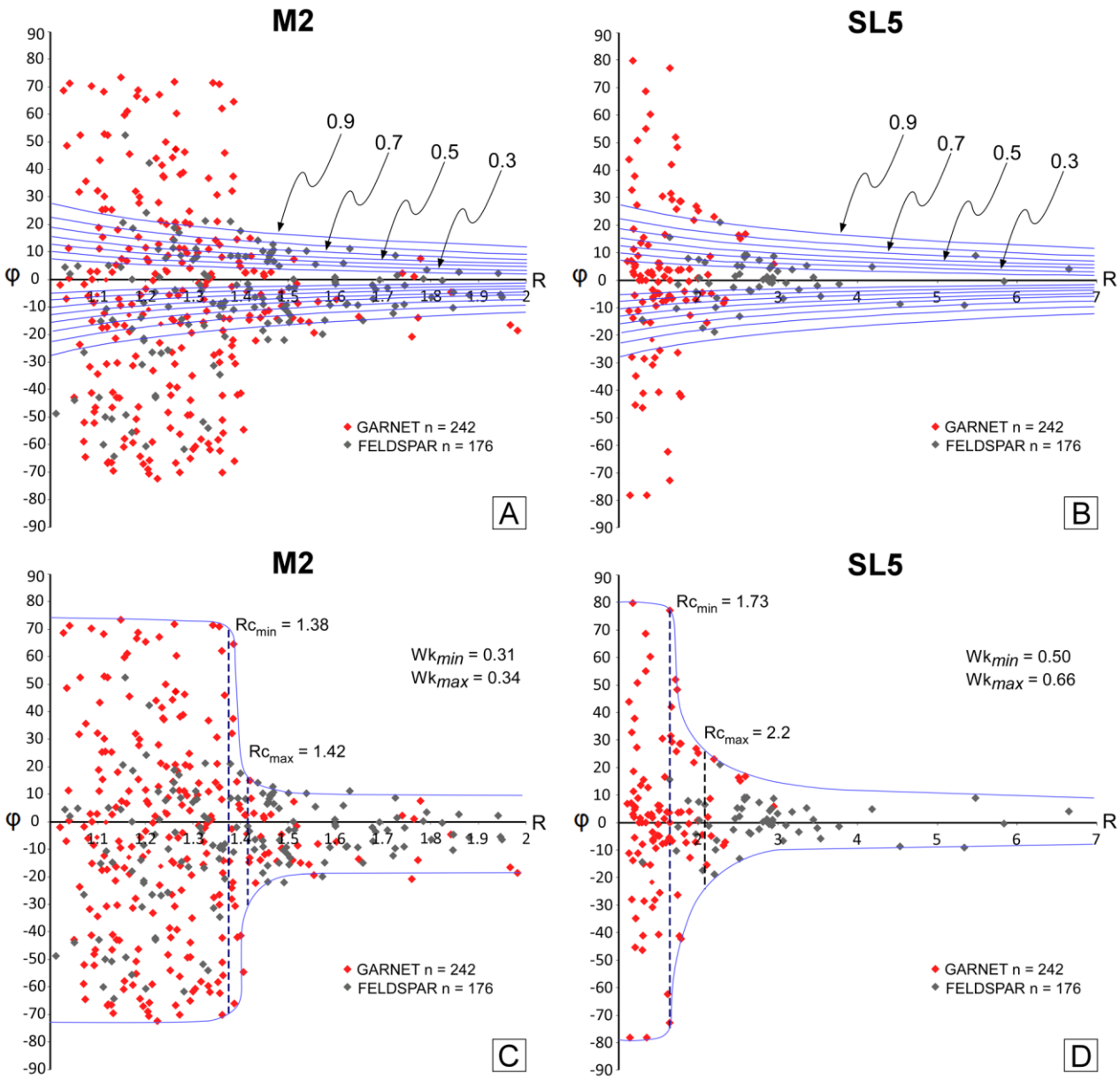

Figure 5.9 – A) Mulchrone test for sample M2; B) Mulchrone test for sample SL5. Blue curves represent the expected distribution of porphyroclasts, at different Wk values, reaching a stable position in the presence of a clast/matrix-slipping interface. In both samples the distribution of porphyroclasts does not fit these curves, revealing that no significant slip between porphyroclasts and matrix occurred. C) Graph used to determine the minimum and maximum critical axial ratio (Rc_{min} and Rc_{max} respectively) and the related Wk for sample M2; D) Graph used to determine the minimum and maximum critical axial ratio (Rc_{min} and Rc_{max} respectively) and the related Wk for sample SL5. R = aspect ratio of the porphyloclasts; φ = angle between the major axis of the porphyroclast and the mylonitic foliation

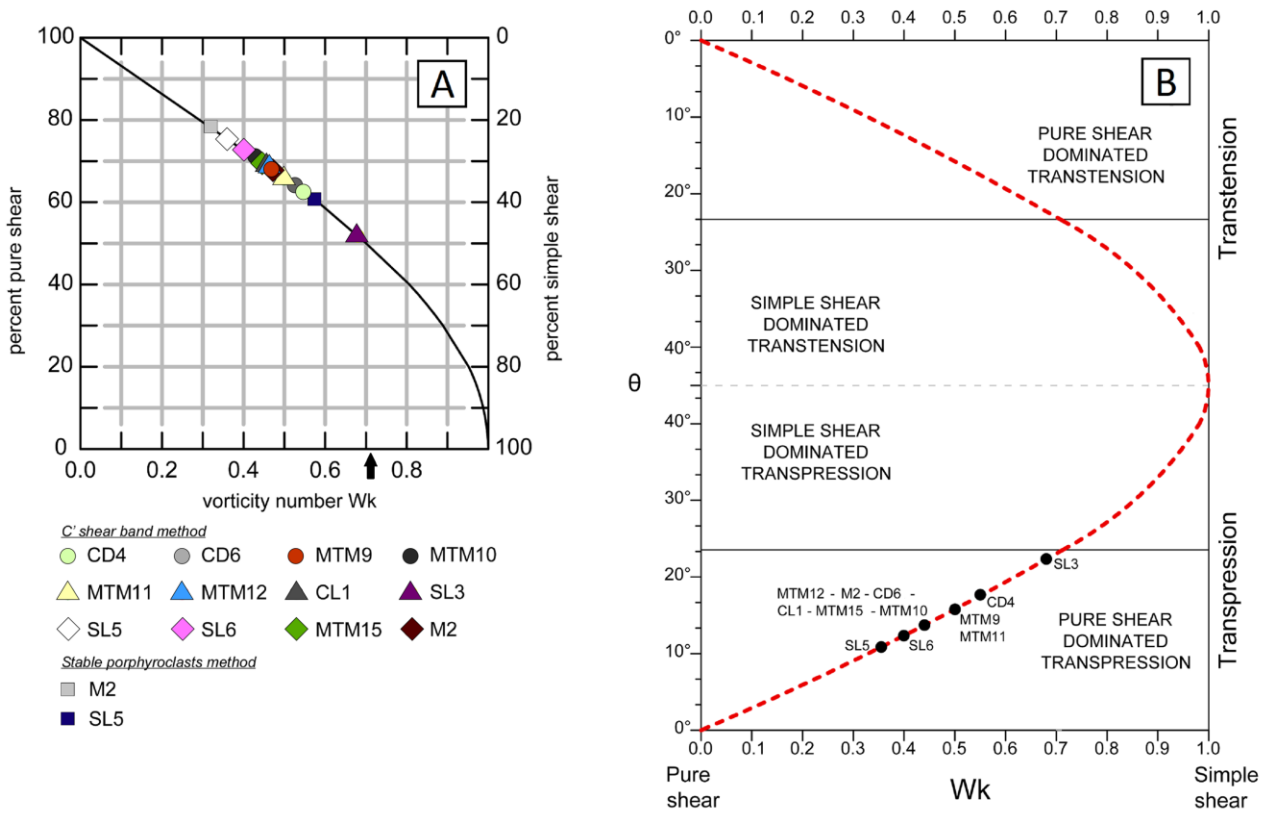

Figure 5.10 – A) Percentage of pure shear and simple shear in the study samples in relation to the calculated Wk values. Samples are highlighted with different colors and symbols: dots, triangles and rhombs are results of Wk based on C' shear band method (Kurz and Northrup 2008), whereas squares are the vorticity results based on the stable porphyroclasts method. Black arrow points to Wk=0.71 where equal contributions of simple shear and pure shear occur (see text); B) Relationships between the orientation of the maximum Instantaneous Stretching Axis (ISAmax) with respect to the shear zone boundary (angle θ) related to the kinematic vorticity number Wk (modified after Fossen and Tikoff 1993; Fossen et al. 1994). All the study samples fall in the pure shear-dominated transpression field

5.5 Strain analysis

The finite data set, obtained by the center-to-center method is reported in figure 5.11. Finite strain analyses indicate an axial ratio of 2.14, 2.56, 2.11, 2.23, 2.18 and 1.79 on the XZ sections and 1.47, 1.72, 1.66, 1.49, 1.44 and 1.77 on YZ sections of the finite strain ellipsoid for sample M2, SL5, CVmsc1, Lpt4a, MScd1 and Lpt4, respectively. The value of the shape parameter of the strain ellipsoid (K) is 0.95 for sample M2, 0.68 for sample SL5, 0.39 for sample CVmsc1, 1 for sample Lpt4a, 1 for sample MScd1 and 0.01 for sample Lpt4. In the Flinn diagram (Flinn, 1962), most of the samples fall in the general flattening field, whereas samples M2, Lpt4a and MScd1 are close to plane strain conditions (fig. 5.12a).

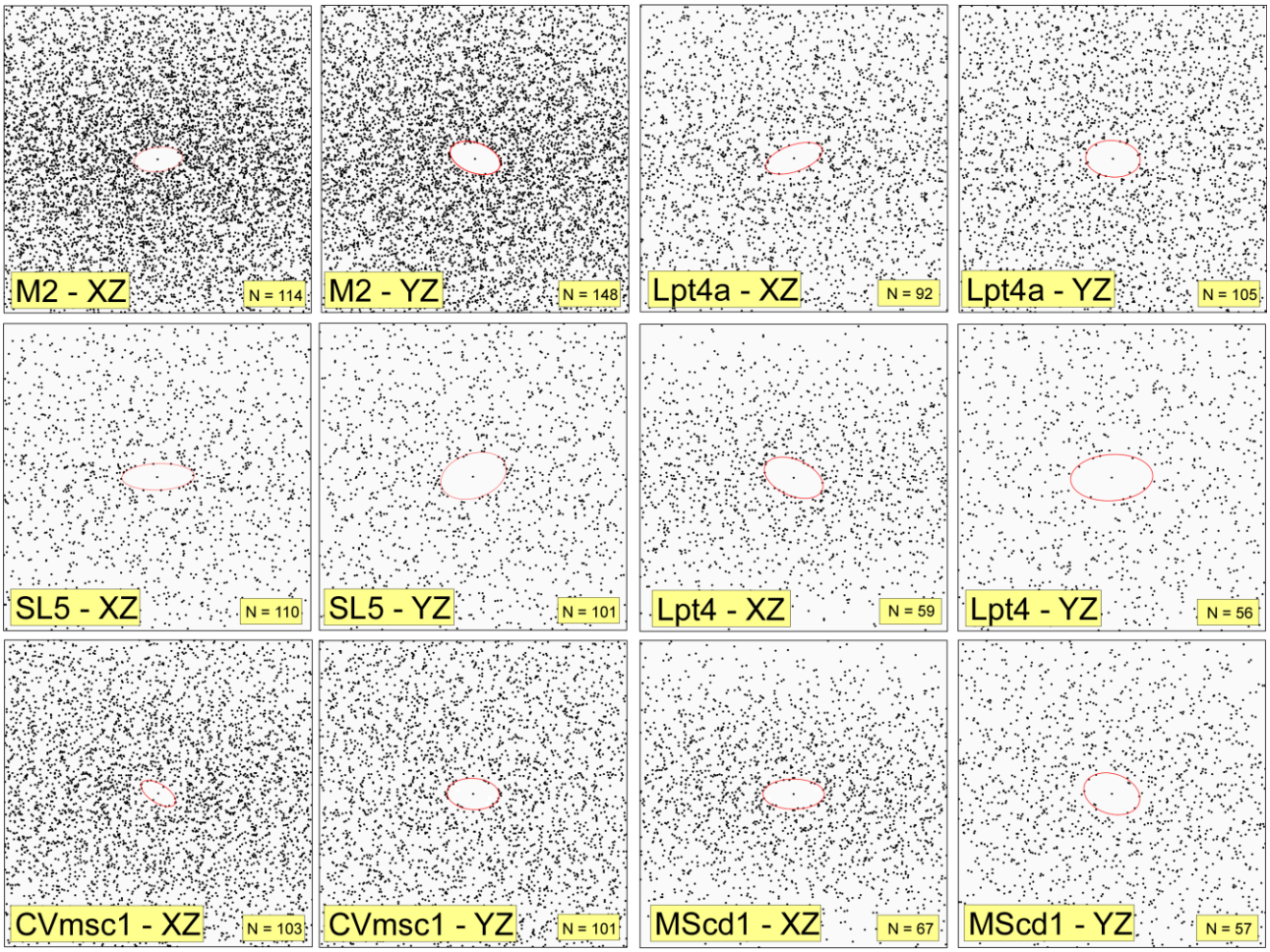

Figure 5.11 – Fry graphs used for the finite strain analysis and obtained with the center-to-center method on the XZ and YZ sections of the finite strain ellipsoid; n = number of used centers

Combining Wk values and finite strain estimates from the same sample, following Wallis *et al*. (1993) and Law *et al*. (2004), we calculate 30 % and 36 % shortening in sample M2 and SL5, respectively. This relation provides reliable stretching values only in the case of plane strain where, for a given amount of shortening, all of the elongation is transport-parallel and accommodated along the X axis of the strain ellipsoid (Law, 2010). Applying the correction of Law (2010) accounting for deviations from plane strain, stretching values parallel to the transport direction of 41 % and 40 % were obtained for M2 and SL5 samples (fig. 5.12b), respectively.

The estimated average convergence angle is ~61°.

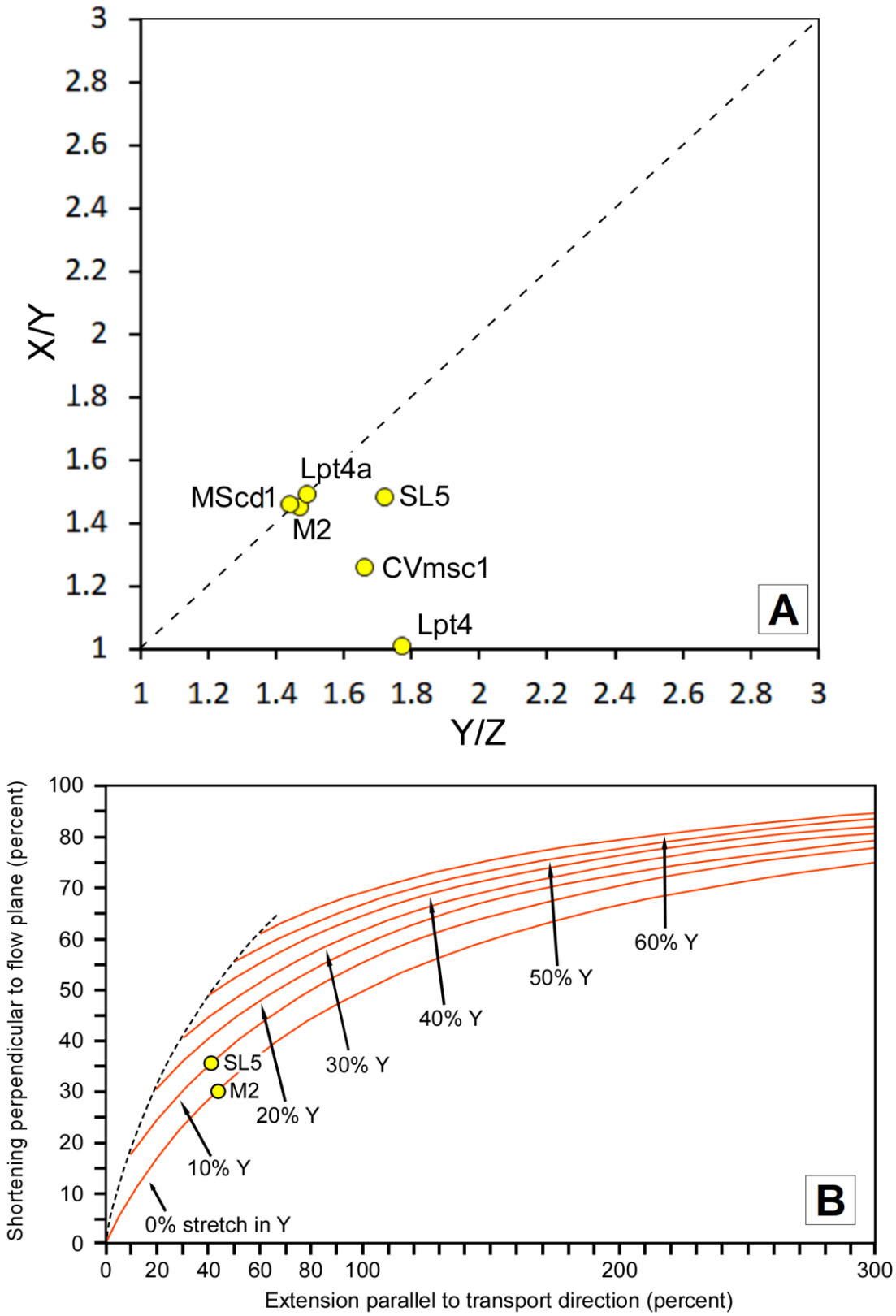

Figure 5.12 – A) Flinn diagram showing the position in the apparent flattening field of the study samples (dots); B) curves representing the shortening perpendicular to flow plane versus extension in the transport direction for general flattening with 0 – 60 % stretch along Y (modified from Law, 2010). Dots are samples M2 and SL5

5.6 Quartz fabric analysis and deformation temperature

In the analyzed samples, collected across the contact between external and internal zone, quartz is generally coarse-grained (fig. 5.13a) with lobate grain boundaries (fig. 5.13b) and it is possible to recognize window and pinning microstructures (fig. 5.13). This is indicative of grain boundary migration (GBM) as the main dynamic recrystallization mechanism. Quartz c-axis fabrics were analyzed in samples CD3, MTM10a, CD4, MTM12b, and CL1 (see fig. 5.2 and 5.3 for sample location).

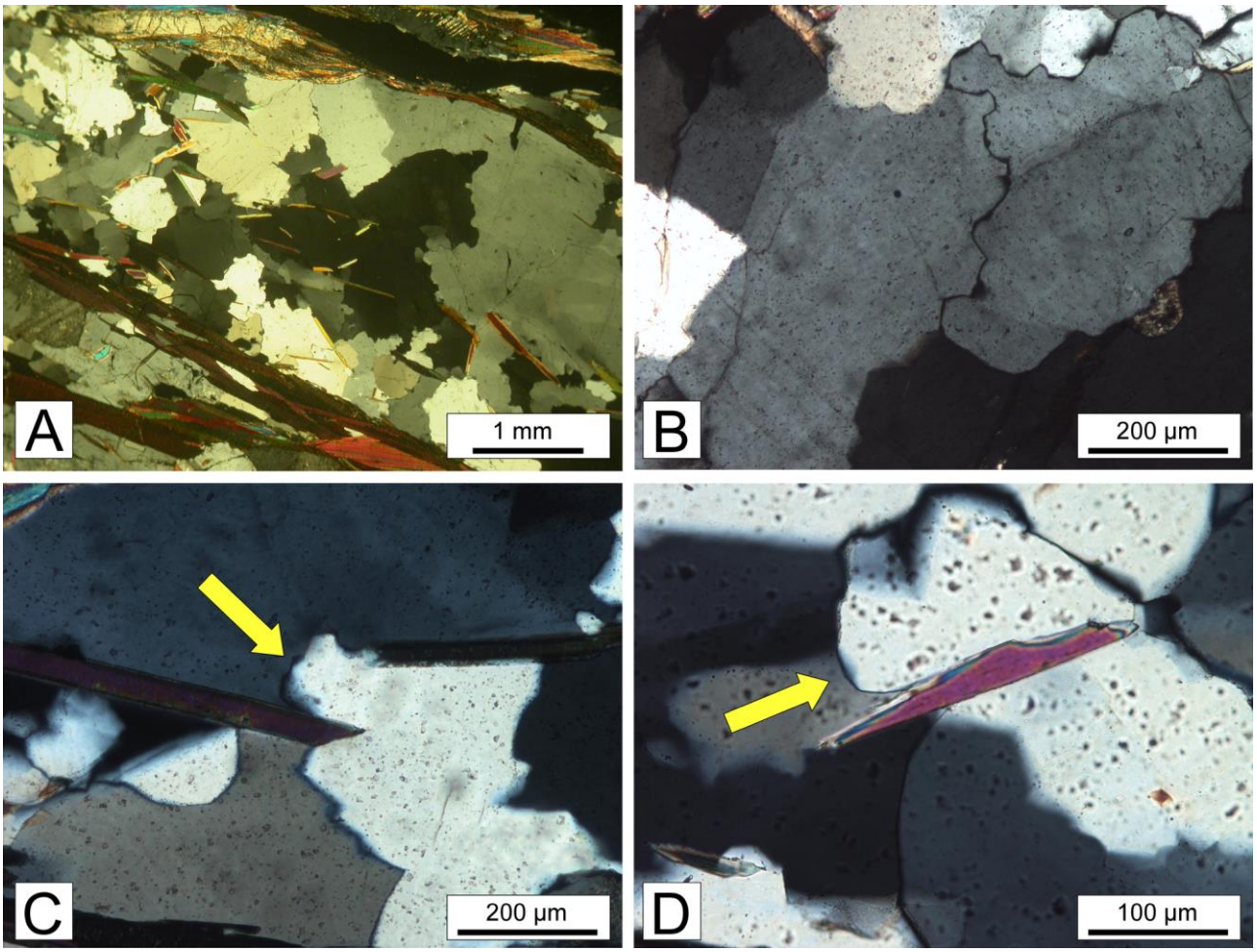

Figure 5.13 – A) coarse-grained quartz crystals with lobate grain boundaries; B) detail of a lobate grain boundary; C) window structure (yellow arrow); D) pinning structure (yellow arrow)

Fabrics were obtained by manual measurements with the universal stage of no less than 300 grains for each thin section.

All the fabrics (fig. 5.14) have a Type-II cross-girdle (Lister, 1977) shape and show a weak asymmetry. This indicate non-coaxial shearing (Schmid and Casey, 1986; Law, 1990 and references therein) and is indicative of a dextral top-to-the-NW sense of shear in agreement with the observed kinematic indicators.

The topology of the measured quartz c-axis fabrics suggests a deformation close to plane strain conditions (Lister and Hobbs, 1980).

A maximum concentration of c-axes along the Y direction is very well displayed in every fabric obtained (fig. 5.14). This fabric point maximum is indicative of crystal slip being dominated by activity on the prism <a> slip system in a temperature rage of 500-650° C (Lister and Dornisiepen, 1982; Law, 1990).

The opening angle of the fabrics (fig. 5.14) is 68°, 76 °, 80 °, 81 ° and 85 ° for samples CD3, MTM10a, CD4a, MTM12b and CL1 respectively. For these opening angles the Faleiros et al. (2016) opening angle thermometer indicates deformation temperatures of 518° C, 554° C, 603° C, 613° C and 638 ° C respectively (fig. 5.15). It is worth to note that samples collected close to the internal zone (such as MTM12b and CL1) give higher temperatures, while samples collected close to the external zone (such as CD3 and MTM10a) give lower temperatures.

EXTERNAL ZONE

~ 50 m

CD3
N = 376

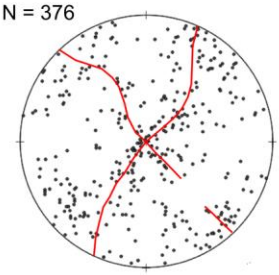

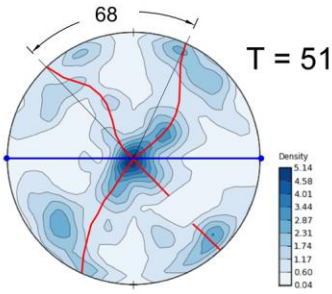

T = 518° C

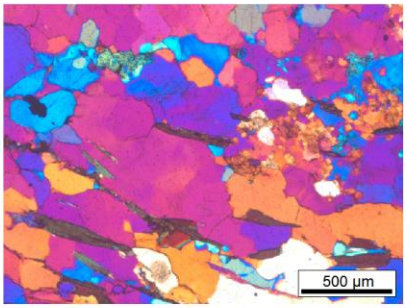

~ 250 m

MTM10a
N = 425

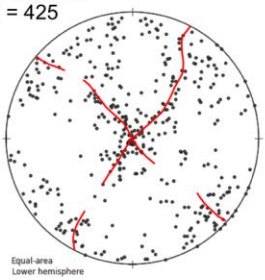

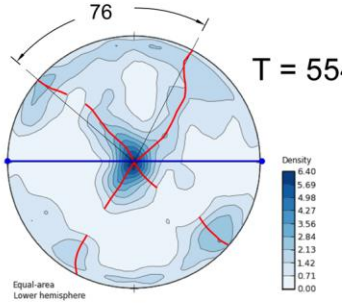

T = 554° C

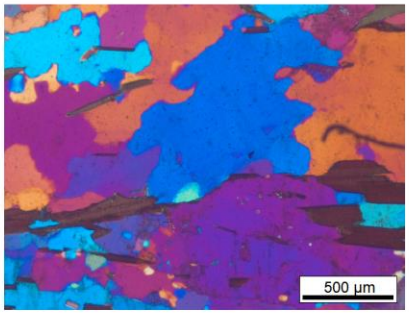

~ 600 m

CD4a
N = 453

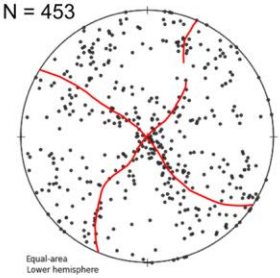

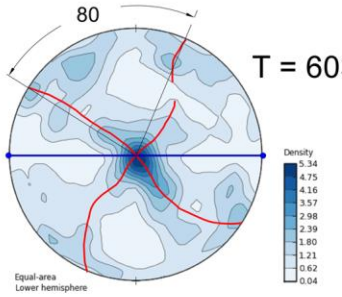

T = 603° C

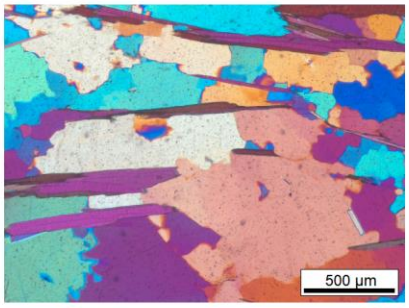

~ 800 m

MTM12b
N = 381

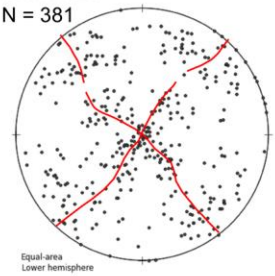

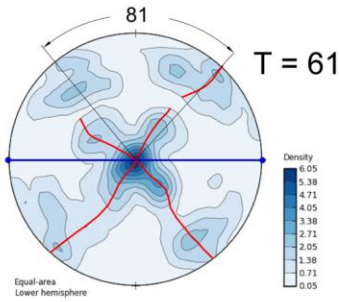

T = 613° C

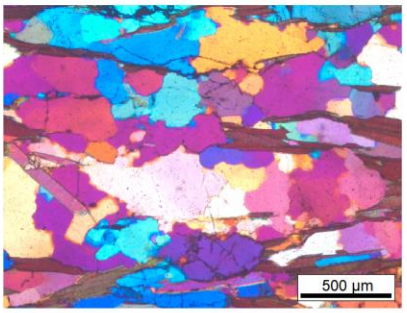

~ 2500 m

CL1
N = 504

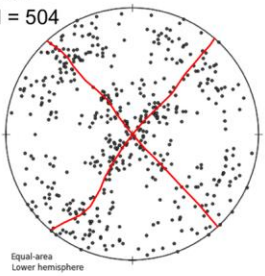

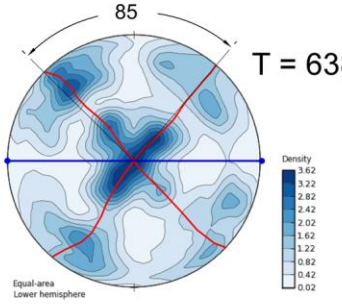

T = 638° C

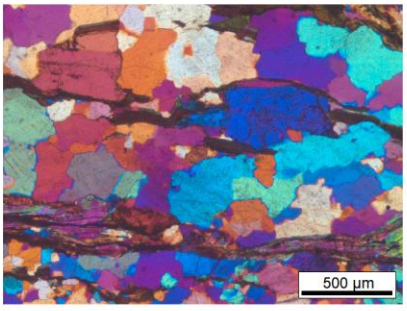

TRANSITION ZONE

INTERNAL ZONE

Figure 5.14 – Optically measured quartz c-axis for samples representative of mylonites. All pole figures are oriented perpendicular to the foliation and parallel to the lineation. Blue line is the main foliation and blue dots are the mineral lineation. Fabric asymmetries indicate a dextral top-to-the-NW sense of shear. Fabric opening angle is reported

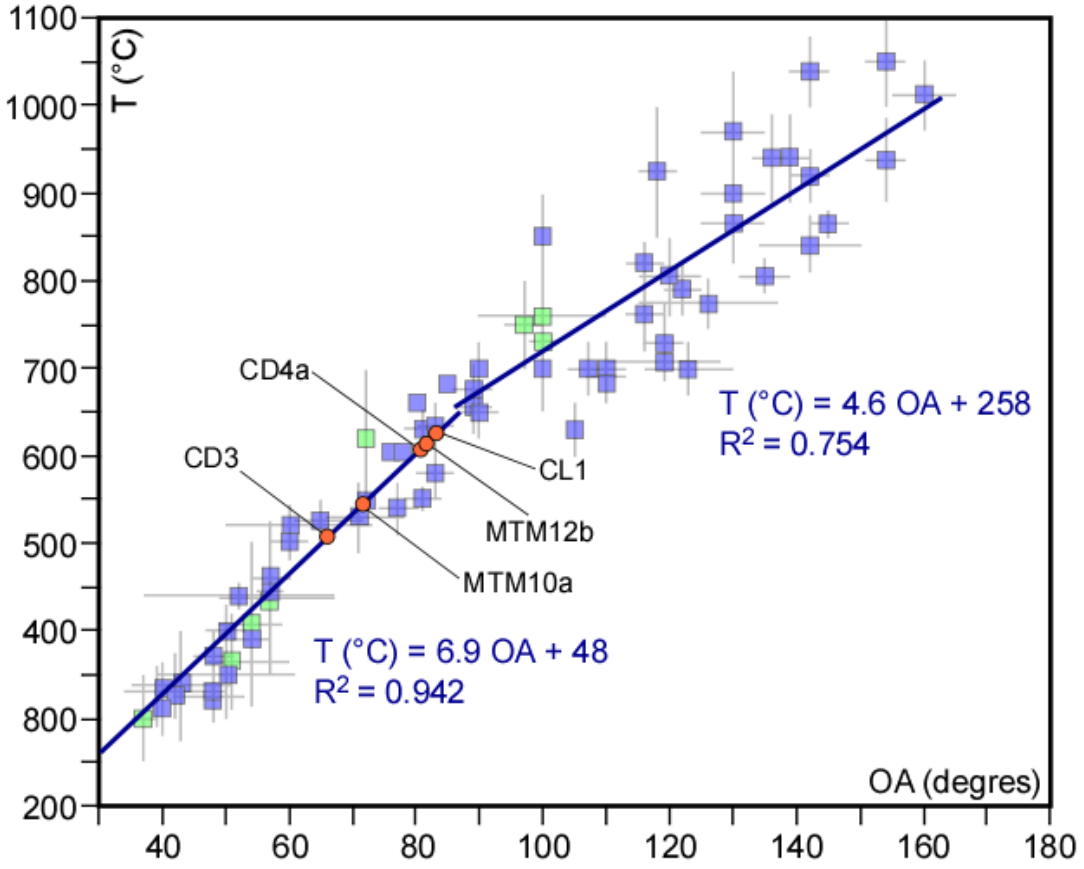

Figure 5.15 – Falerios *et al*. (2016) quartz c-axis fabric opening-angle thermometer in the range of 250 - 1050 °C, blue squares are data with pressure information used by Faleiros et al. (2016) to define their thermometer, while green square are data used by Faleiros et al. (2016) that have no pressure information. Calibration was made after Khrul (1998), Morgan and Law (2004), Law (2014). Linear fits described by equation 1 and 2 are indicated

5.7 Petrochronology

Four samples (fig. 5.2) were selected for *in-situ* microstructurally constrained monazite U-Th-Pb petrochronology. A total of 17 monazites grains, representative of the different microstructural position of monazite and of their chemical variability, were selected. Examples of the main features of selected monazite are reported in figure 5.16. In sample CD1, five grains (Mnz1, Mnz3, Mnz3b, Mnz4, Mnz5) lie along the S_2 foliation or are included within syn-kinematic biotite and white mica; one grain (Mnz6) is included in a plagioclase porphyroblast and one grain (Mnz7) is within a staurolite porphyroblast.

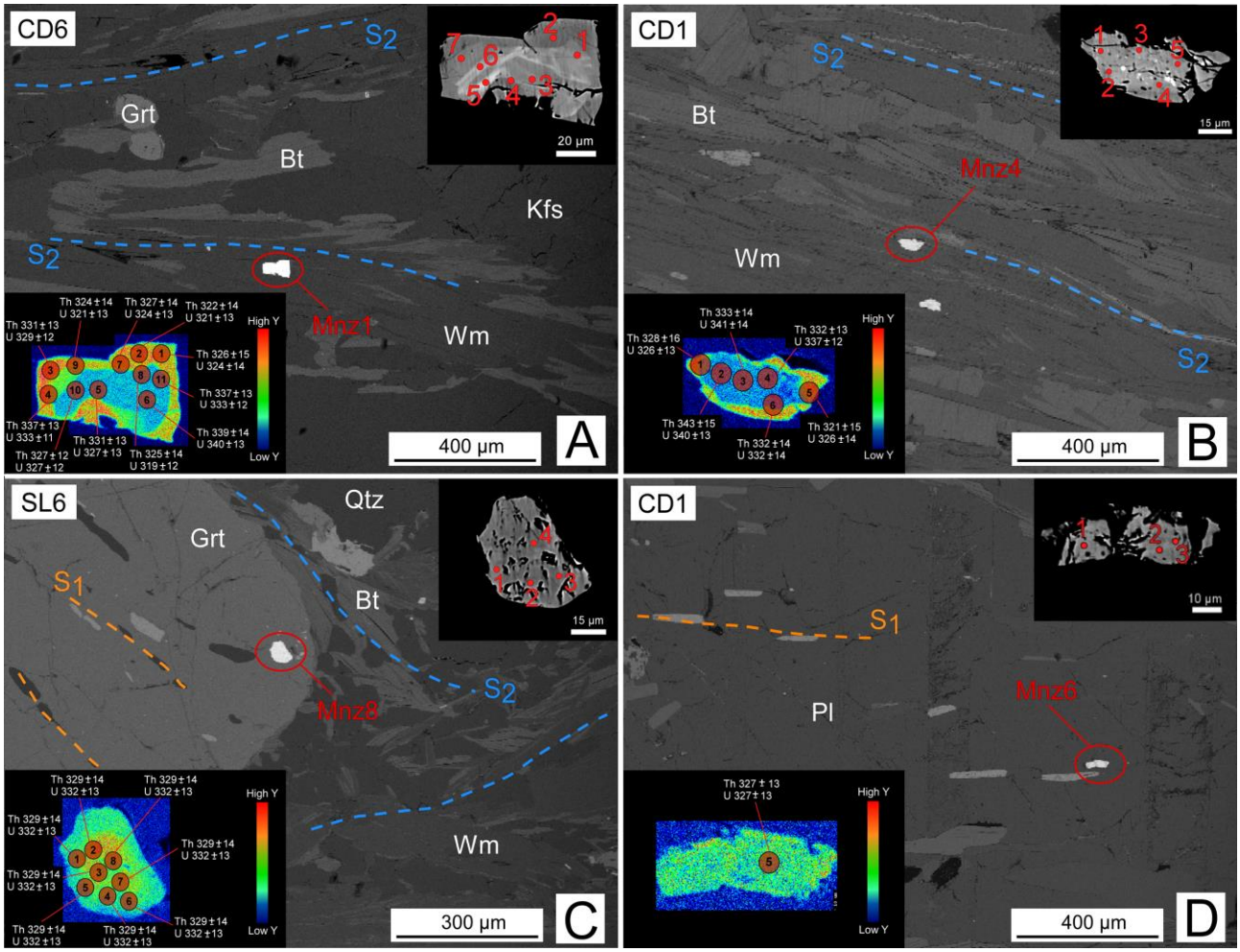

Figure 5.16 – Examples of textural position and zoning of monazite grains selected for *in situ* dating. Compositional map of Y shows the spot location and the corresponding $^{208}Pb/^{232}Th$ (Th) and 207-corrected $^{206}Pb/^{238}U$ (U) ages. In the BSE image of the grain, the position of the electron microprobe chemical analysis (red spots) is indicated. A) Mnz1 in sample CD6, laying along the main S_2 foliation; B) Mnz4 in sample CD1, located along the main S_2 foliation; C) Mnz8 in sample SL6, included in garnet porphyroclast; D) Mnz6 in sample CD1, included in plagioclase porphyroclast

In sample CD6a, four grains (Mnz1, Mnz9b, Mnz12, Mnz22) lie along the S_2 foliation. In sample MTM10, two grains (Mnz30, Mnz32) lie along the S_2 foliation and one grain (Mnz8) included in syn-kinematic biotite were chosen. In Sample SL6 we selected one grain (Mnz8) included in a garnet porphyroclast and two grains (Mnz9, Mnz10) included in syn-kinematic white mica on the S_2.

Within the samples analyzed monazite grains all show similar complex Y zoning as highlighted by microprobe chemical mapping (fig. 5.16 and appendix F). We recognize three main compositional domains: 1) high-medium Y cores (between ~0.7 and ~1.5 wt % of Y_2O_3); 2) low Y cores (between ~0.1 and ~0.5 wt % of Y_2O_3); 3) high Y rims (between ~1.3 and ~2.5 wt % of Y_2O_3). Monazites included in garnet (Mnz8, sample SL6), staurolite (Mnz7, sample CD1) and plagioclase (Mnz6, sample CD1) do not show high Y rims.

The Y content decreases from core to rim in these monazite grains, which are included within the Barrovian indicator minerals in the samples. Monazites along the main foliation, or included in syn-kinematic minerals, generally present all the three compositional domains described above (Mnz1, Mnz3, Mnz3b, Mnz4, Mnz5, sample CD1; Mnz1, Mnz9b, Mnz12, Mnz22, sample CD6a; Mnz9, Mnz10, sample SL6) or show an homogeneous high Y composition (Mnz8, Mnz30, Mnz32, sample MTM10) with Y_2O_3 content variable between ~1.9 and ~2.5 wt %, comparable with the amount of Y_2O_3 in the high Y rims.

Petrochronological data for all samples are reported in table 5.3. The relationships between age, Y content, Gd/Yb ratio and REE pattern normalized to chondrite (normalization values after McDonough and Sun 1995) of the different compositional domains are reported in figure 5.17. The $^{206}Pb/^{238}U$ and $^{208}Pb/^{232}Th$ ages are generally concordant. The average $^{206}Pb/^{238}U$ age for each sample is reported in figure 5.18. $^{208}Pb/^{232}Th$ ages ranges from 344 ± 5 Ma to 323 ± 4 Ma while $^{206}Pb/^{238}U$ ages ranges from 341 ± 4 Ma to 325 ± 5 Ma. Taking into account the microstructural position of the grains and the chemical composition of the dated domains, we distinguish groups/populations of ages. Ages older than ~ 340 Ma occur in both the high and low Y cores of the monazites included in the Barrovian minerals and in the matrix. Ages from high-Y and low-Y cores are quite similar. A second group of ages of ~ 333 Ma was obtained from a medium-low Y mantle. High Y rims, a feature observed in matrix grain, generally returned ages of ~ 323 Ma. There is a good correlation between ages and Y contents from cores to rims (fig. 5.17). Younger ages in the rims are coupled with low Gd/Yb ratios (fig. 5.17). In samples SL6, CD6 and CD1, we recognized an increase of the HREE content from the cores to the rims while in sample MTM10 there is no such variation (fig. 5.17). In samples MTM10 and CD6 the REE distribution highlight a negative Eu anomaly.

SAMPLE	$^{207}Pb/^{235}U$	2σ	$^{206}Pb/^{238}U$	2σ	rho	$^{238}U/^{206}Pb$	2σ	$^{207}Pb/^{206}Pb$	2σ	rho	$^{208}Pb/^{232}Th$	2σ	$^{208}Pb/^{232}Th$	Age 1 2σ	Age 7-corr	1 2σ	Concordan
SL6_mnz10_1	0.404	0.014	0.05	0.00	0.97	18.62	0.70	0.054	0.001	0.30	0.0167	0.0006	335	13	337	12	0.98
SL6_mnz10_2	0.412	0.017	0.05	0.00	0.97	18.32	0.76	0.054	0.001	0.20	0.0171	0.0007	342	15	342	14	0.98
SL6_mnz10_3	0.426	0.016	0.06	0.00	0.96	17.89	0.62	0.055	0.001	0.05	0.0173	0.0006	347	13	350	12	0.97
SL6_mnz10_4	0.420	0.016	0.05	0.00	0.97	18.28	0.70	0.055	0.001	-0.11	0.0171	0.0007	342	14	343	13	0.96
SL6_mnz10_5	0.406	0.015	0.05	0.00	0.98	18.62	0.67	0.055	0.001	-0.08	0.0171	0.0007	343	13	337	12	0.97
SL6_mnz9_1	0.397	0.017	0.05	0.00	0.99	18.73	0.80	0.054	0.001	-0.05	0.0174	0.0008	348	16	335	14	0.99
SL6_mnz9_2	0.406	0.014	0.05	0.00	0.96	18.76	0.65	0.055	0.001	0.08	0.0167	0.0006	334	12	334	11	0.97
SL6_mnz9_3	0.405	0.018	0.05	0.00	0.99	19.12	0.83	0.056	0.001	-0.21	0.0173	0.0008	347	15	327	14	0.95
SL6_mnz9_4	0.406	0.017	0.05	0.00	0.97	18.90	0.75	0.055	0.001	0.04	0.0169	0.0007	338	14	332	13	0.96
SL6_mnz9_5	0.424	0.016	0.05	0.00	0.96	18.38	0.71	0.057	0.001	0.15	0.0173	0.0007	346	14	340	13	0.95
SL6_mnz9_6	0.420	0.018	0.05	0.00	0.97	18.32	0.76	0.056	0.001	-0.15	0.0173	0.0008	347	15	342	14	0.96
SL6_mnz9_7	0.426	0.015	0.05	0.00	0.97	18.35	0.62	0.057	0.001	0.05	0.0172	0.0006	345	13	341	11	0.95
SL6_mnz9_8	0.415	0.017	0.05	0.00	0.97	18.45	0.74	0.056	0.001	-0.12	0.0171	0.0007	342	14	339	13	0.97
SL6_mnz9_9	0.413	0.018	0.05	0.00	0.96	18.83	0.77	0.056	0.001	-0.10	0.0169	0.0007	339	14	332	13	0.95
SL6_mnz9_10	0.419	0.015	0.06	0.00	0.98	18.05	0.69	0.055	0.001	0.00	0.0175	0.0007	351	14	347	13	0.98
SL6_mnz9_11	0.420	0.018	0.05	0.00	0.97	18.32	0.74	0.055	0.001	-0.16	0.0169	0.0007	339	13	342	14	0.96
SL6_mnz9_12	0.414	0.015	0.05	0.00	0.97	18.69	0.67	0.056	0.001	-0.03	0.0175	0.0007	351	13	335	12	0.96
SL6_mnz9_13	0.422	0.018	0.05	0.00	0.97	18.62	0.82	0.057	0.001	0.15	0.0170	0.0008	341	16	336	15	0.94
SL6_mnz9_14	0.432	0.017	0.06	0.00	0.99	17.92	0.71	0.056	0.001	-0.02	0.0172	0.0007	344	14	349	14	0.96
SL6_mnz9_15	0.400	0.016	0.05	0.00	0.97	19.05	0.76	0.055	0.001	0.09	0.0167	0.0007	334	14	329	13	0.97
SL6_mnz8_1	0.412	0.015	0.05	0.00	0.97	18.32	0.65	0.055	0.001	0.01	0.0171	0.0006	343	13	342	12	0.98
SL6_mnz8_2	0.401	0.016	0.05	0.00	0.98	18.69	0.73	0.054	0.001	-0.06	0.0163	0.0007	328	13	336	13	0.98
SL6_mnz8_3	0.421	0.017	0.06	0.00	0.98	17.89	0.73	0.054	0.001	0.11	0.0172	0.0007	346	14	350	14	0.98
SL6_mnz8_4	0.408	0.016	0.05	0.00	0.97	18.42	0.71	0.054	0.001	0.09	0.0170	0.0007	341	14	340	13	0.98
SL6_mnz8_5	0.419	0.016	0.05	0.00	0.97	18.42	0.74	0.055	0.001	0.04	0.0169	0.0007	339	14	340	13	0.96
SL6_mnz8_6	0.414	0.015	0.06	0.00	0.94	17.92	0.63	0.054	0.001	-0.01	0.0172	0.0007	345	13	350	12	1.00
SL6_mnz8_7	0.403	0.017	0.05	0.00	0.98	18.48	0.75	0.053	0.001	-0.06	0.0165	0.0007	331	14	340	14	0.99
SL6_mnz8_8	0.412	0.015	0.05	0.00	0.98	18.45	0.66	0.055	0.001	-0.05	0.0171	0.0006	342	13	340	12	0.97
CD6_mnz1_1	0.381	0.017	0.05	0.00	0.99	19.38	0.85	0.053	0.001	-0.02	0.0163	0.0007	326	15	324	14	0.99
CD6_mnz1_2	0.377	0.017	0.05	0.00	0.99	19.57	0.83	0.053	0.001	-0.06	0.0160	0.0007	322	14	321	13	0.99
CD6_mnz1_3	0.388	0.015	0.05	0.00	0.99	19.05	0.72	0.054	0.001	-0.15	0.0165	0.0007	331	13	329	12	0.99
CD6_mnz1_4	0.395	0.014	0.05	0.00	0.98	18.87	0.65	0.054	0.001	0.07	0.0168	0.0006	337	13	333	11	0.98
CD6_mnz1_5	0.394	0.016	0.05	0.00	0.98	19.19	0.80	0.055	0.001	0.09	0.0165	0.0007	331	13	327	13	0.97
CD6_mnz1_6	0.402	0.016	0.05	0.00	0.99	18.48	0.72	0.053	0.001	-0.19	0.0169	0.0007	339	14	340	13	0.99
CD6_mnz1_7	0.393	0.017	0.05	0.00	0.98	19.34	0.78	0.054	0.001	-0.10	0.0163	0.0007	327	14	324	13	0.97
CD6_mnz1_8	0.384	0.015	0.05	0.00	0.98	19.65	0.76	0.054	0.001	-0.05	0.0162	0.0007	325	14	319	12	0.97
CD6_mnz1_9	0.381	0.016	0.05	0.00	0.99	19.57	0.83	0.054	0.001	-0.06	0.0161	0.0007	324	14	321	13	0.98
CD6_mnz1_10	0.392	0.014	0.05	0.00	0.99	19.16	0.70	0.055	0.001	-0.03	0.0163	0.0006	327	12	327	12	0.98
CD6_mnz1_11	0.397	0.015	0.05	0.00	0.98	18.87	0.71	0.054	0.001	0.05	0.0168	0.0007	337	13	333	12	0.98
CD6_mnz9b_1	0.399	0.016	0.05	0.00	0.98	19.08	0.76	0.055	0.001	-0.09	0.0161	0.0007	323	13	328	13	0.97
CD6_mnz9b_2	0.389	0.014	0.05	0.00	0.98	19.12	0.70	0.054	0.001	0.12	0.0162	0.0006	324	12	328	12	0.98
CD6_mnz9b_3	0.396	0.014	0.05	0.00	0.97	18.55	0.69	0.054	0.001	0.05	0.0167	0.0007	334	13	338	12	1.00
CD6_mnz9b_4	0.410	0.016	0.06	0.00	0.98	18.08	0.69	0.053	0.001	-0.08	0.0167	0.0007	336	14	347	13	0.99
CD6_mnz9b_5	0.405	0.016	0.05	0.00	0.98	18.66	0.70	0.055	0.001	-0.05	0.0165	0.0007	331	13	336	12	0.97
CD6_mnz9b_6	0.408	0.016	0.05	0.00	0.98	19.08	0.73	0.056	0.001	-0.19	0.0161	0.0006	323	13	328	12	0.95
CD6_mnz9b_7	0.396	0.019	0.05	0.00	0.99	19.12	0.86	0.055	0.001	-0.07	0.0162	0.0007	325	15	328	14	0.97
CD6_mnz9b_8	0.392	0.014	0.05	0.00	0.98	18.90	0.69	0.054	0.001	0.03	0.0161	0.0006	322	13	332	12	0.99
CD6_mnz9b_9	0.399	0.015	0.05	0.00	0.98	18.48	0.69	0.053	0.001	-0.15	0.0169	0.0007	339	13	340	12	1.00
CD6_mnz9b_10	0.394	0.016	0.05	0.00	0.99	19.01	0.78	0.054	0.001	-0.05	0.0164	0.0007	329	14	330	13	0.98
CD6_mnz22_1	0.399	0.015	0.05	0.00	0.98	18.80	0.68	0.054	0.001	-0.10	0.0164	0.0006	329	13	334	12	0.98
CD6_mnz22_2	0.389	0.015	0.05	0.00	0.98	19.01	0.72	0.054	0.001	0.04	0.0163	0.0006	326	13	330	12	0.99
CD6_mnz22_4	0.394	0.016	0.05	0.00	0.99	18.94	0.75	0.054	0.001	-0.04	0.0164	0.0007	329	14	331	13	0.98
CD6_mnz22_5	0.399	0.014	0.05	0.00	0.98	18.28	0.65	0.053	0.001	-0.09	0.0168	0.0006	336	12	344	12	1.01
CD6_mnz22_6	0.401	0.016	0.05	0.00	0.99	18.38	0.74	0.053	0.001	-0.06	0.0165	0.0007	331	14	342	14	1.00
CD6_mnz22_7	0.388	0.015	0.05	0.00	0.99	19.16	0.73	0.054	0.001	-0.01	0.0160	0.0006	322	13	328	12	0.99
CD6_mnz12_1	0.406	0.012	0.05	0.00	0.95	19.01	0.55	0.056	0.001	0.16	0.0158	0.0005	317	9	329	9	0.95
CD6_mnz12_2	0.406	0.013	0.05	0.00	0.98	18.35	0.60	0.054	0.001	0.10	0.0159	0.0005	318	10	342	11	0.99
CD6_mnz12_3	0.383	0.013	0.05	0.00	0.97	19.57	0.63	0.054	0.001	-0.02	0.0160	0.0005	320	11	321	10	0.98

Table 5.3 – Full dataset of LASS analyses on monazite grains of the samples SL6, CD6, MTM10, CD1

MTM10_mnz32_1	0.395	0.016	0.05	0.00	0.97	18.76	0.74	0.054	0.001	0.01	0.0164	0.0007	330	13	335	13	0.99
MTM10_mnz32_2	0.397	0.015	0.05	0.00	0.96	18.21	0.73	0.053	0.001	0.13	0.0168	0.0007	338	14	345	14	1.01
MTM10_mnz32_3	0.397	0.015	0.05	0.00	0.97	18.42	0.68	0.053	0.001	0.18	0.0164	0.0006	329	13	341	12	1.00
MTM10_mnz32_4	0.403	0.019	0.06	0.00	0.98	18.05	0.80	0.053	0.001	-0.08	0.0169	0.0008	339	15	348	15	1.01
MTM10_mnz32_5	0.400	0.015	0.05	0.00	0.98	18.73	0.70	0.054	0.001	0.03	0.0165	0.0007	332	13	335	12	0.98
MTM10_mnz30_1	0.410	0.017	0.05	0.00	0.98	19.34	0.78	0.057	0.001	-0.17	0.0160	0.0006	322	13	323	13	0.93
MTM10_mnz30_2	0.398	0.015	0.05	0.00	0.97	19.31	0.74	0.056	0.001	-0.07	0.0165	0.0006	330	13	324	12	0.96
MTM10_mnz8_1	0.396	0.017	0.05	0.00	0.97	18.69	0.73	0.054	0.001	-0.18	0.0165	0.0006	331	13	335	13	0.99
MTM10_mnz8_2	0.393	0.014	0.05	0.00	0.98	18.94	0.72	0.054	0.001	-0.01	0.0163	0.0007	326	13	331	12	0.99
MTM10_mnz8_3	0.401	0.014	0.05	0.00	0.97	18.38	0.65	0.053	0.001	0.15	0.0167	0.0006	335	12	342	12	1.00
MTM10_mnz8_4	0.397	0.017	0.05	0.00	0.98	18.38	0.77	0.053	0.001	-0.09	0.0167	0.0007	335	14	342	14	1.01
CD1_mnz1_1	0.412	0.016	0.05	0.00	0.98	18.83	0.77	0.056	0.001	0.07	0.0164	0.0007	329	14	332	13	0.95
CD1_mnz1_2	0.439	0.022	0.06	0.00	0.99	18.15	0.90	0.058	0.001	0.19	0.0167	0.0008	336	16	344	17	0.94
CD1_mnz1_3	0.425	0.018	0.05	0.00	0.98	18.59	0.78	0.057	0.001	-0.05	0.0166	0.0007	333	14	336	14	0.94
CD1_mnz1_4	0.461	0.017	0.06	0.00	0.98	18.02	0.66	0.060	0.001	-0.06	0.0167	0.0006	335	12	345	12	0.90
CD1_mnz1_5	0.449	0.019	0.06	0.00	0.98	18.12	0.75	0.058	0.001	0.00	0.0168	0.0007	337	15	344	14	0.92
CD1_mnz1_6	0.456	0.019	0.05	0.00	0.98	18.62	0.79	0.062	0.001	-0.05	0.0172	0.0007	344	15	334	14	0.88
CD1_mnz1_7	0.434	0.018	0.05	0.00	0.98	18.80	0.77	0.059	0.001	0.03	0.0169	0.0007	340	14	332	13	0.91
CD1_mnz1_8	0.430	0.016	0.05	0.00	0.98	18.73	0.67	0.058	0.001	-0.02	0.0166	0.0006	333	13	333	12	0.92
CD1_mnz1_9	0.390	0.014	0.05	0.00	0.97	19.65	0.73	0.055	0.001	0.06	0.0168	0.0006	337	12	319	12	0.96
CD1_mnz3b_1	0.448	0.017	0.05	0.00	0.96	18.28	0.68	0.058	0.001	0.00	0.0173	0.0006	346	13	341	12	0.91
CD1_mnz3b_2	0.433	0.016	0.05	0.00	0.98	18.28	0.70	0.057	0.001	0.10	0.0172	0.0007	345	14	342	13	0.94
CD1_mnz3b_3	0.437	0.017	0.05	0.00	0.97	18.73	0.67	0.059	0.001	-0.13	0.0166	0.0006	332	12	333	12	0.91
CD1_mnz3b_4	0.453	0.017	0.05	0.00	0.97	18.83	0.74	0.061	0.001	0.25	0.0166	0.0006	333	13	330	13	0.88
CD1_mnz3b_5	0.410	0.016	0.05	0.00	0.99	18.73	0.76	0.055	0.001	-0.05	0.0171	0.0007	342	15	334	13	0.96
CD1_mnz3b_6	0.405	0.018	0.05	0.00	0.99	19.57	0.86	0.057	0.001	-0.14	0.0166	0.0007	332	14	319	14	0.93
CD1_mnz3b_7	0.393	0.015	0.05	0.00	0.98	19.38	0.72	0.055	0.001	-0.14	0.0167	0.0007	335	13	323	12	0.96
CD1_mnz5_1	0.394	0.015	0.05	0.00	0.98	19.61	0.73	0.056	0.001	0.17	0.0161	0.0007	323	13	319	12	0.95
CD1_mnz5_2	0.455	0.019	0.06	0.00	0.98	18.18	0.75	0.060	0.001	0.11	0.0165	0.0007	332	14	342	14	0.91
CD1_mnz5_3	0.451	0.017	0.05	0.00	0.97	18.45	0.66	0.061	0.001	-0.02	0.0167	0.0006	335	12	337	12	0.90
CD1_mnz5_4	0.443	0.019	0.05	0.00	0.98	18.69	0.82	0.060	0.001	0.12	0.0172	0.0008	344	15	333	14	0.90
CD1_mnz5_5	0.420	0.018	0.05	0.00	0.98	18.94	0.81	0.058	0.001	0.12	0.0168	0.0007	337	15	330	14	0.93
CD1_mnz4_1	0.403	0.017	0.05	0.00	0.99	19.23	0.77	0.056	0.001	-0.11	0.0164	0.0007	328	13	326	13	0.95
CD1_mnz4_2	0.431	0.018	0.05	0.00	0.98	18.38	0.74	0.057	0.001	0.07	0.0171	0.0007	343	15	340	13	0.94
CD1_mnz4_3	0.436	0.018	0.05	0.00	0.98	18.28	0.76	0.058	0.001	-0.02	0.0166	0.0007	333	14	341	14	0.93
CD1_mnz4_4	0.428	0.016	0.05	0.00	0.98	18.52	0.69	0.058	0.001	0.07	0.0165	0.0007	332	13	337	12	0.94
CD1_mnz4_5	0.405	0.018	0.05	0.00	0.99	19.19	0.86	0.056	0.001	0.08	0.0160	0.0007	321	15	326	14	0.95
CD1_mnz4_6	0.422	0.018	0.05	0.00	0.98	18.80	0.80	0.057	0.001	-0.09	0.0166	0.0007	332	14	332	14	0.93
CD1_mnz6_5	0.446	0.018	0.05	0.00	0.98	19.01	0.75	0.062	0.001	-0.06	0.0163	0.0007	327	13	327	13	0.88
CD1_mnz7_1	0.406	0.016	0.05	0.00	0.99	18.80	0.77	0.056	0.001	0.03	0.0170	0.0007	341	14	333	13	0.97
CD1_mnz7_2	0.444	0.018	0.05	0.00	0.98	19.05	0.76	0.061	0.001	-0.04	0.0162	0.0006	325	13	326	13	0.88
CD1_mnz7_3	0.453	0.017	0.06	0.00	0.96	18.18	0.64	0.059	0.001	0.07	0.0169	0.0006	339	12	342	12	0.91
CD1_mnz7_4	0.422	0.018	0.05	0.00	0.99	18.83	0.80	0.058	0.001	-0.04	0.0168	0.0007	336	14	332	14	0.93
CD1_mnz3_1	0.422	0.017	0.05	0.00	0.98	18.90	0.75	0.058	0.001	0.07	0.0166	0.0006	333	12	330	13	0.93
CD1_mnz3_2	0.460	0.019	0.05	0.00	0.98	18.45	0.74	0.061	0.001	0.00	0.0170	0.0007	340	14	337	13	0.89
CD1_mnz3_3	0.445	0.016	0.05	0.00	0.96	19.16	0.67	0.062	0.001	0.04	0.0161	0.0006	323	12	324	11	0.88
CD1_mnz3_4	0.452	0.017	0.05	0.00	0.98	18.80	0.68	0.062	0.001	0.09	0.0162	0.0006	324	13	330	12	0.88
CD1_mnz3_5	0.437	0.019	0.05	0.00	0.98	19.12	0.83	0.061	0.001	-0.01	0.0165	0.0007	331	15	325	14	0.89
CD1_mnz3_6	0.479	0.019	0.05	0.00	0.97	18.66	0.73	0.065	0.001	0.06	0.0161	0.0006	324	13	332	13	0.85

Table 5.3 – (continue) Full dataset of LASS analyses on monazite grains of the samples SL6, CD6, MTM10, CD1

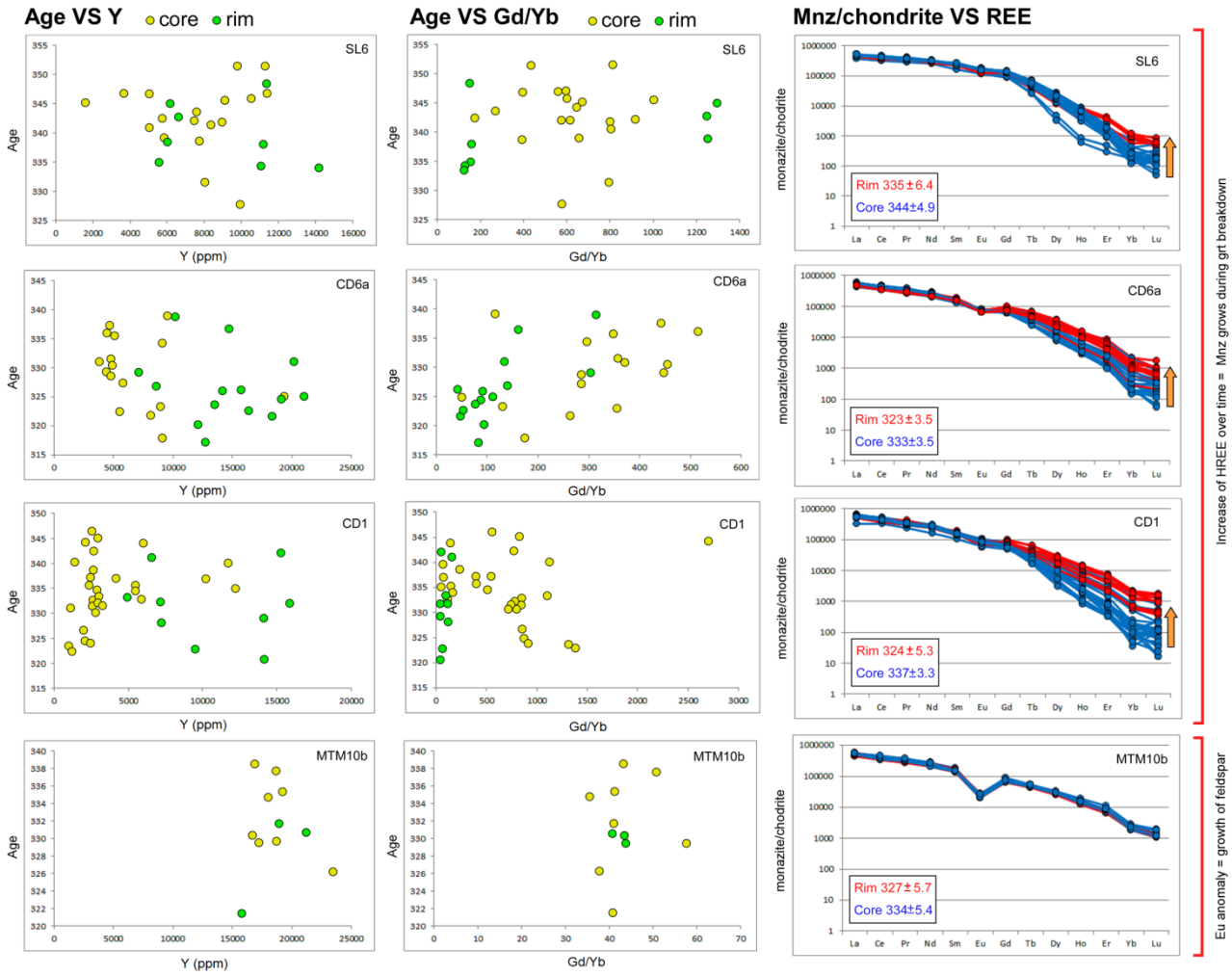

Figure 5.17 – Trace element characterization of the dated monazite crystals: in the left column the age vs Y content (ppm) is indicated; in the central column the age vs Gd/Yb ratio is given; on the right column chondrite normalized (based on values of McDonough and Sun, 1995) REE patterns of dated monazites are shown. Average age for rims and cores are also reported

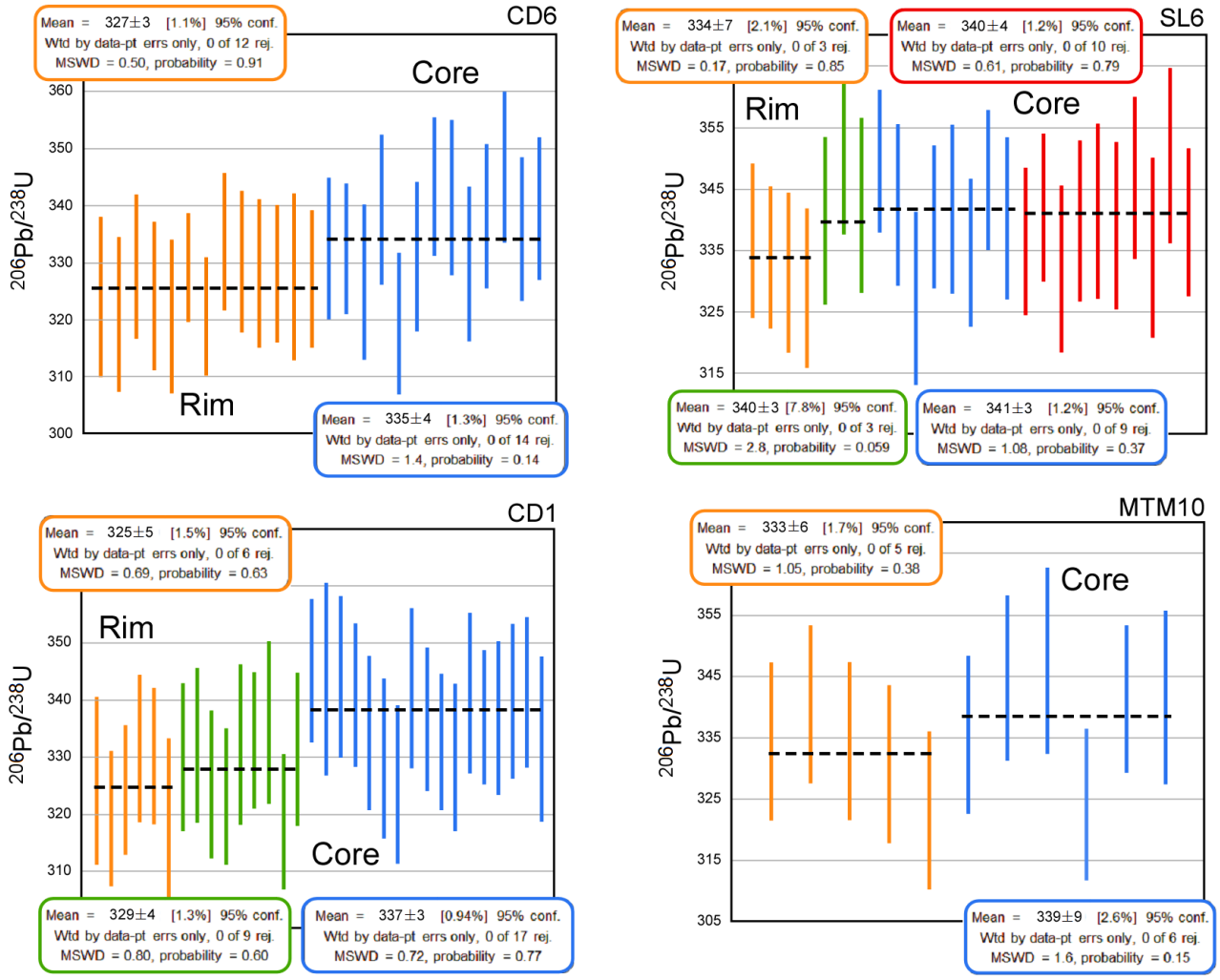

Figure 5.18 – Distribution of 207-corrected $^{206}Pb/^{238}U$ ages. Data are grouped according to the position of the spot within the grain and colors of the bars are organized according to the Y content: red = high-Y domain in the core of the grain; blue = low-Y domain in the core of the grain; green = medium-Y domain in the core of the grain or in an intermediate position between core and rim (mantle); orange = high-Y domain in the rim of the grain. MSWD = mean square weighted deviates

5.8 Data discussion and interpretation

The CF marks the boundary between external and internal zones, affecting both micaschist of the biotite-kyanite zone (Bormes unit) and migmatite (La Garde Freinet unit). In mylonites from the external zone (Bormes unit) syn-kinematic growth of biotite and white mica along the S_2 foliation is recognized. F_2 folds in the external zone and the mylonitic foliation developed during the same amphibolite-facies metamorphism (M_2 metamorphic stage of Schneider *et al*. 2014). Barrovian index minerals mainly grew between the collisional (D_1, M_1 metamorphism according to Schneider *et al*. 2014) and transpressional tectono-metamorphic event (M_2-M_3 metamorphism according to Schneider *et al*. 2014). However we recognized that

part of the staurolite growth is syn-kinematic during transpression. The observed blastesis-deformation relationships between Barrovian minerals and transpression-related non-coaxial shearing in the MTM are strikingly similar to that reported along the Posada Asinara Line in northern Sardinia (Carosi and Palmeri, 2002; Iacopini *et al*. 2008).

We find no evidence of previously reported top-to-the-E-SE thrusting as described by Bellot *et al*. (2002) and Schneider *et al*. (2014), because it is highly overprinted during transpression in the CF and within the internal zone. Hence, we do not describe three deformation phases (D_1 frontal collision, D_2 backthrust and D_3 transpression as in Schneider *et al*. 2014) and D_2 in this work (related to the transpression) corresponds to D_2-D_3 in Schneider *et al*. (2014). Kinematic indicators, both at the meso and microscale, point to a top-to-the-NW sense of shear in agreement with Schneider *et al*. (2014).

During transpression the internal zone was characterized by high-temperature metamorphism and widespread partial melting (Schneider *et al*. 2014). These metamorphic conditions are in agreement with the occurrence of grain boundary migration as the main dynamic recrystallization mechanism of quartz, indicative of a temperature range between 500° and 700° C. Quartz fabric analysis confirms this temperature range.

Feldspar in this zone shows evidence of ductile deformation, testifying to temperatures higher than ~ 450° C (Passchier and Trouw, 2005). However the occurrence of brittle fractures in feldspar could indicate decreasing temperature deformation, as suggested by Bellot *et al*. (2002), Bellot (2005) and Schneider *et al*. (2014), or a subsequent brittle overprint. The first hypothesis is supported by the observation that fractures are at a high-angle to the main foliation and are therefore compatible with the same shortening and stretching directions. Furthermore, local incipient subgrain rotation recrystallization, overprinting GBM in quartz has been recognized, supporting a lower temperature dynamic recrystallization mechanism.

Kinematic vorticity analyses have revealed that deformation along the CF occurred under general shear condition with a major component of pure shear acting together with simple shear. The presence of kinematic indicators pointing to both dextral and sinistral sense of shear in migmatite is in accordance with a high component of pure shear during deformation.

Finite strain data suggest a general flattening, in agreement with a pure shear-dominated transpression (Fossen and Tikoff, 1993; Fossen *et al*. 1994; Fossen, 2016), supported also by the presence of boudinage along both XZ and YZ sections of finite strain ellipsoid.

According to Schneider *et al*. (2014), the transpression event (their D_3 event) occurred during the doming of the internal zone. Schneider *et al*. (2014) hypothesized that the CF firstly developed as a back-thrust (their D_2 event) with a top-to-the-E-SE sense of shear.

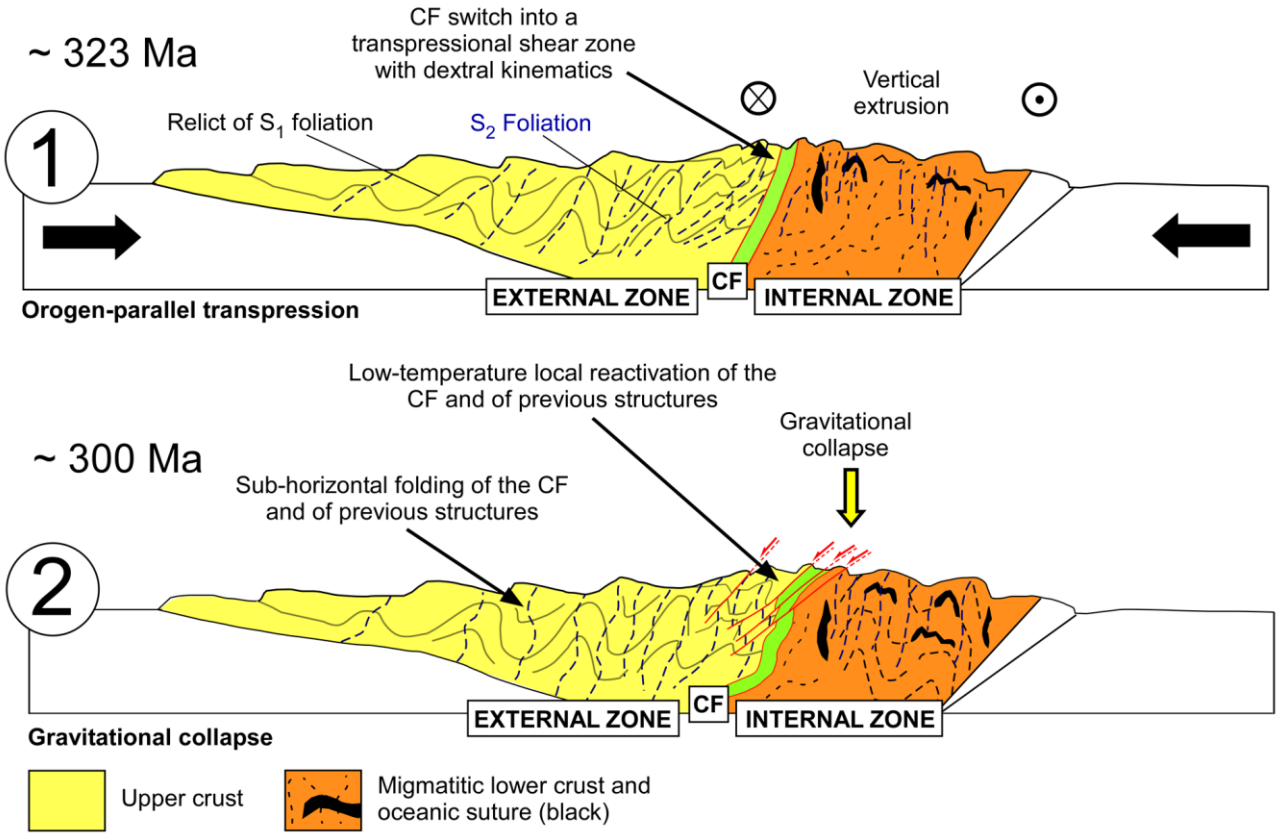

Figure 5.19 – Sketch of the structural evolution of the Cavalaire Fault located at the boundary between the internal and external zones of the Variscan belt in the MTM; 1) onset of orogen-parallel transpression with development of D_2 folds and associated S_2 foliation. Cavalaire Fault evolved into a transpressive shear zone during the retro-wedge building and, because of the high pure shear compoment, it suffered verticalization that allowed channelized vertical exhumation of the middle-lower crust; 2) gravitational collapse induced by vertical extrusion generate sub-horizontal open folds and partially reactivate the CF under low-temperature conditions

Our field and kinematic data are compatible with a reactivation of the CF as a transpressional shear zone further reoriented and finally reactivated as a normal sense shear zone (top-to-the W sense of shear). During transpression the CF acquired a steeply dipping attitude with a component of pure shear accommodating the exhumation of the internal zone (fig. 5.19, stage 1). This kinematic framework is in agreement with both the transpressional models proposed by Sanderson and Marchini (1984) and Fossen *et al*. (1994) and it could also account for the horizontal shortening pointed out by Schneider *et al*. (2014) during the building up of the orogen. In the two study areas the stretching lineation L_2 is steeply dipping, but in other sectors of the

Maures Massif L_2 is sub-horizontal or slightly plunging (Bellot *et al*. 2002). A similar structural setting was described in the Asinara Island (Sardinia) by Iacopini *et al*. (2008) in the northwesternmost outcrops of the Posada Asinara Line. In a transpressive system at a constant strain rate, the orientation of the stretching lineation is a function of time and vorticity number. The orientation of the stretching lineation can change over time during ongoing deformation and strain accumulation (see Iacopini *et al*. 2008 for a complete review). Iacopini *et al*. (2008), discussing this topic along the transpressive Posada-Asinara Line, argue that in the case of a sub-vertical lineation, the shear zone will be subjected to vertical extrusion.

The geometry and kinematics of the CF is in accordance with a nearly vertical dip of the shear zone developed in a transpressional regime within a collisional orogen, allowing the relative normal movement and exhumation of the surrounding rocks. Thompson *et al*. (1997) demonstrated that compressional forces could sustain the vertical channelized exhumation of the lower crust along sub-vertical shear zones. Therefore if the CF underwent internal vertical flow, the vertical extrusion could have triggered exhumation and later gravitational instability with development of late folds (F_3) and brittle-ductile reactivation with normal-sense kinematic (fig. 5.19, stage 2). At this stage, deformation took place at upper crustal levels in a prevalent brittle regime. Even so, preserved ductile features of sheared rocks acquired during the initial stage of transpression are still recognizable. The geometry of the structures in the study area is further complicated by a later, post-Variscan N-S shortening that resulted in sporadic formation of an S_4 crenulation cleavage. The present-day geometry is therefore the result of a complex and polyphase deformation history from late- to post-Variscan time.

A compilation of the existing U-(Th)-Pb time constraints related to the Variscan evolution of the Maures Massif is reported in table 5.4. Our new monazite petrochronology data, constrains the timing of shearing along the CF.

Zone	Unit	Rock type	Age (Ma)	Mineral	Method	Interpretation	Tectonic setting	Reference
External	Bormes	Paragneiss	367 ± 13	Monazite	EPMA in situ	Prograde metamorphism, underthrusting	Continental collision	Oliot et al., 2015
External	Bormes	Micaschist	352 ± 5	Monazite	EPMA in situ	Prograde metamorphism, nappes stacking	Continental collision	Oliot et al., 2015
External	Bormes	Othogneiss	345 ± 3	Monazite	TIMS	Age of deformation	Continental collision	Moussavou, 1998
External	Bormes	Othogneiss	344 ± 15	Zircon	TIMS	Age of deformation	Continental collision	Moussavou, 1998
External	Bormes	Othogneiss	339 ± 16	Zircon	TIMS	Age of deformation	Continental collision	Moussavou, 2000
External	Bormes	Paragneiss	335 ± 6	Monazite	EPMA in situ	Prograde metamorphism, backthrusting	Continental collision	Oliot et al., 2015
Transition	Bormes	Sheared micaschist	335 ± 4	Monazite	LASS in situ	Prograde metamorphism	Continental collision	This study
Transition	Bormes	Sheared micaschist	327 ± 3	Monazite	LASS in situ	Retrometamorphism	Transpression along the Cavalaire Fault	This study
Transition	La Garde-Freinet	Sheared micaschist	340 ± 4	Monazite	LASS in situ	Prograde metamorphism	Continental collision	This study
Transition	La Garde-Freinet	Sheared micaschist	340 ± 3	Monazite	LASS in situ	Prograde metamorphism	Continental collision	This study
Transition	La Garde-Freinet	Sheared micaschist	341 ± 4	Monazite	LASS in situ	Prograde metamorphism	Continental collision	This study
Transition	La Garde-Freinet	Sheared micaschist	334 ± 7	Monazite	LASS in situ	Prograde metamorphism	Continental collision	This study
Transition	Bormes	Sheared micaschist	337 ± 3	Monazite	LASS in situ	Prograde metamorphism	Continental collision	This study
Transition	Bormes	Sheared micaschist	329 ± 4	Monazite	LASS in situ	Prograde metamorphism	Continental collision	This study
Transition	Bormes	Sheared micaschist	325 ± 5	Monazite	LASS in situ	Retrometamorphism	Transpression along the Cavalaire Fault	This study
Transition	Bormes	Sheared paragneiss	339 ± 9	Monazite	LASS in situ	Progade metamorphism	Continental collision	This study
Transition	Bormes	Sheared paragneiss	333 ± 6	Monazite	LASS in situ	Progade metamorphism	Continental collision	This study
Internal	Eastern gneiss	Migmatitic paragneiss	382 ± 11	Monazite	EPMA in situ	Prograde metamorphism, underthrusting	Continental collision	Oliot et al., 2015
Internal	Eastern gneiss	Migmatitic paragneiss	344 ± 4	Zircon	EPMA in situ	Prograde metamorphism, nappes stacking	Continental collision	Oliot et al., 2015
Internal	Eastern gneiss	Migmatitic paragneiss	334 ± 3	Zircon	TIMS	Prograde metamorphism,	Continental collision	Moussavou, 1998
Internal	Eastern gneiss	Migmatitic paragneiss	333 ± 3	Monazite	TIMS	Prograde metamorphism	Continental collision	Moussavou, 1998
Internal	La Garde-Freinet	Diatexite	331 ± 5	Monazite	EPMA in situ	Prograde metamorphism, backthrusting	Continental collision	Oliot et al., 2015
Internal	Eastern gneiss	Plan-de-la-Tour granite	329 ± 3	Monazite	EPMA in situ	Plan-de-la-Tour granite emplacement	Variscan granitoid emplacement	Oliot et al., 2015
Internal	Eastern gneiss	Plan-de-la-Tour granite	324 ± 5	Zircon	TIMS	Plan-de-la-Tour granite emplacement	Variscan granitoid emplacement	Moussavou, 1998
Internal	Eastern gneiss	Migmatite leucosome	325 ± 8	Zircon	TIMS	Mineral growth during syn-shear melting	Post-collisional syn-shear Anatexis	Moussavou, 1998
Internal	Eastern gneiss	Migmatite leucosome	310 ± 10	Zircon	SHRIMP	Mineral growth during syn-shear melting	Post-collisional syn-shear Anatexis	Duchesne et al., 2013

Table 5.4 – Synthesis of the available U-(Th)-Pb time constraints, from this work and the literature, related to the Variscan evolution of the Maures Massif. EPMA = electron-probe micro-analyses; LASS = laser ablation split system; TIMS = thermal ionization mass spectrometry

Microstructural position, texture, zoning and chemical analyses, highlight a complex history of monazite growth during the tectono-metamorphic history. A first group of monazite (Mnz1) grew during prograde metamorphic conditions. This is supported by the decreasing Y content from cores to rims, by the low HREE content and by the high Gd/Yb ratio that are a consequence of garnet growth. A second group of monazite (Mnz2) shows high-Y, high-HREE content and low Gd/Yb ratio pointing to growth during retro-metamorphism and garnet breakdown. Mnz2 grows as tiny rims around Mnz1 when the last one is not included/shielded in Barrovian porphyroclasts or as a new grain along the main S_2 foliation with a homogeneous high-Y composition. Since prograde metamorphism is associated with the frontal collisional stage, whereas the retro-metamorphism is related to the transpressional deformation (Schneider *et al*. 2014; Oliot *et al*. 2015), the obtained ages for Mnz1 and Mnz2 allow us to constrain these two tectonic events. The REE patterns (fig. 5.17) highlight also the presence of an Eu anomaly in samples MTM10 and CD6, collected close to the internal zone. There is evidence for the growth of feldspar during partial melting that allows us to directly link the anatexis with the transpressional deformation (Schneider *et al*. 2014; Oliot *et al*. 2015). Ages from the Mnz2 indicate active deformation at ~ 323 Ma. Older ages, detected in the cores of monazite, range between ~ 340 Ma and ~ 333 Ma, are in agreement with the timing of the prograde metamorphism from 382 ± 11 Ma (Middle Devonian) to 331 ± 5 Ma (Late Visean) (table 5.4; Oliot *et al*. 2015). According to the evolution of a garnet-monazite system (Pyle and Spear, 1999; Pyle *et al.*, 2001; Williams *et al.*, 2007) during prograde metamorphism high-Y+HREE cores are expected to grow just before medium to low Y cores (Pyle and Spear, 1999), and therefore older ages are expected from the former. We detected little difference in the absolute ages of high- and low-Y cores (340 ± 4 Ma and 341 ± 3 Ma, respectively, fig. 5.18), this could reflect a rapid evolution of prograde metamorphism during ongoing collision.

6. Discussion

6.1 The Ferriere-Mollières Shear Zone (Argentera Massif)

The data presented in this work revealed a complex deformaton history for the FMSZ. It is a Variscan transpressional shear zone made up of different types of mylonite developed at the expense of migmatites. The shear zone has a vertical foliation, a sub-horizontal mineral lineation and a dextral top-to-the-SE sense of shear. It is characterized by a well-detectable increasing deformation gradient toward the center of the shear zone.

The presence of medium- to high-grade metamorphic mylonites associated with lower-grade ones, localized in the central part of the FMSZ, the strong deformation gradient and the changes in the deformation regime and age of deformation along the gradient are all evidence that the FMSZ evolved as a type II shear zone (Fossen, 2016) in which deformation localizes in the central part of the shear zone because of strain softening. Thus, the margins of the shear zone become inactive and preserve the features acquired during the early stages of shearing while the active central part gets progressively thinner (fig. 6.1) and records the final stages of shearing.

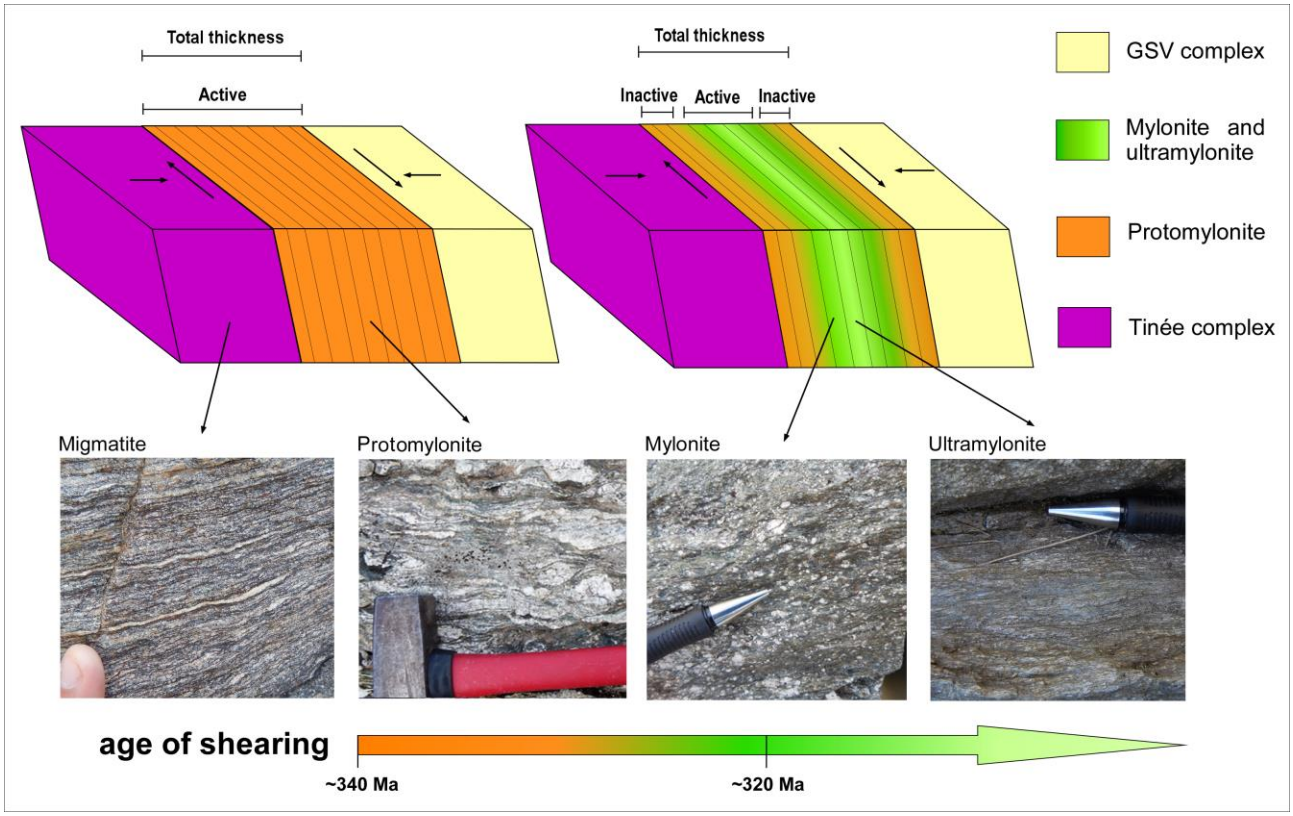

Figure 6.1 - Evolution of the Ferriere-Molliéres Shear Zone according to a type II growth model (Fossen, 2016) and relationship between deformation gradient and age of shear deformation: the margins become progressively inactive and preserve the features acquired during the older stages of shearing while the active part gets progressively thinner and records the younger stages of shear zone activity.

The result is a shear zone with a deformation gradient toward the central part along which, as in the case of the FMSZ, it is possible to observe variations in temperature, age of deformation and deformation regime. The main factors that are probably responsible for strain softening are the presence of fluids together with metamorphic reactions and grainsize reduction that are well-detectable both at the outcrop and at the micro scale. Supporting evidence for the first two factors is the breackdown of amphibolite-facies minerals such as sillimanite and biotite and consequent growth of white mica and chlorite in the most sheared rocks. Along the deformation gradient a reduction in the amount of quartz and feldspar in the rocks, accompanied by a concomitant increase in the amount of phyllosilicates, is evident. Protomylonites in the external part of the FMSZ preserve features acquired during the early stage of shear deformation (as testified by the older age of deformation) during high-temperature conditions whereas mylonites, in the internal part of the shear zone, record features acquired during younger stages of the deformation at lower temperature. These features are compatible with Type II shear zone evolution. Finally the ultramylonites preserve evidence of the final stage of activity of the shear zone. Three stages of development can be recognized (fig. 6.2), each one characterized by specific age, temperature and deformation regime. The first stage occurred between ~340 Ma and ~330 Ma under temperature range of ~610° C and ~590° C, protomylonites developed during this stage. The deformation regime was characterized by a prevalent component of pure shear. In the following stage, between ~330 Ma and ~320 Ma, deformation starts to concentrate toward the core of the shear zone leading to the formation of mylonites at temperatures between ~530° C and ~480° C.

A slight increase in the component of simple shear during the later stages of shear zone evolution. The last stage developed from ~ 320 Ma onwards under temperature conditions between ~500° C and ~420° C. This stage is recorded only in the core of the shear zone where the ultramylonites are present. It is characterized by a prevalent component of simple shear.

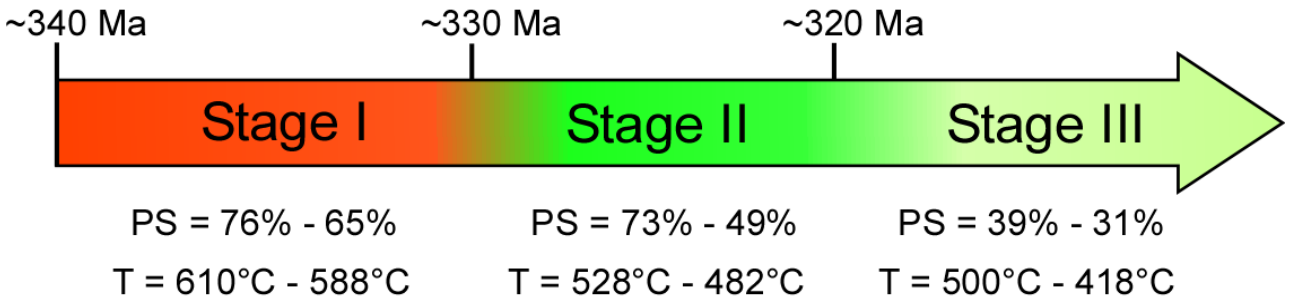

Figure 6.2 – Age, deformation regime and deformation temperature of the three stages of the evolution of the FMSZ

In agreement with the estimated temperature range, deformation in the ultramylonites is accompanied by retrograde greenschist-facies metamorphism. It is therefore likely that the deformation occurs in the presence of fluids channelized along the active core of the shear zone. Their presence enhances strain softening and is testified by the occurrence of metamorphic reactions involving fluid such as the growth of fillosilicates from anhydrous phases. The presence of fluids during deformation, influenced by the permeability of the shear zones, is a crucial parameter that can lead to the switching in deformation mode (from distributed to localized) and mechanisms (from viscous to frictional) and to a switch from ductile to brittle deformation mechanisms operating in the shear zone. Permeability enhancement can be associated with the development of extensional and hybrid vein arrays. In shear zones developed near the brittle-viscous transition, rock failure is mostly controlled by the evolution of stress state and fluid pressure states. Changes in those two parameters can lead to multiple cycles of alternating brittle-ductile deformation that allows concentration of deformation and activity of the shear zone.

In the case of the FMSZ the magnitudes of differential stress obtained in the ultramylonites with the Stipp and Tullis (2003) piezometer using the Holyoke and Kronenberg (2010) calibration are relatively low, and in agreement with the values of ~ 50 MPa predicted by Etheridge (1983) for producing extensional fractures and veins. Higher differential stress were obtained by applying the Shimizu (2008) calibration, as previously observed by Montomoli *et al*. (2018). These results should however be viewed with caution as the Shimizu (2008) calibration is very sensitive to changes in assumed deformation temperature, and input temperature values used here were derived from quartz c-axis fabric opening angles which may not reflect the precise temperature at which the measured recrystallized grains formed.

The presence of fluid and of both sheared and unsheared extentional and hybrid fractures suggests that during its very late stage, cycles of alternating brittle and ductile deformation driven by changes in fluid

pressure may have operated at least in the central part of the FMSZ. We suggest that fluid pressure may increase during deformation until it triggers brittle rock fracture. Fracturing in turn enhances permeability and fluid pressure then decreases while quartz precipitates in the newly opened fracture. New fluids are attracted and channelized in to the shear zone and finally ductile conditions are re-established (fig. 6.3). Subsequent ductile shear transposes the previously formed veins and filled fracture allowing the development of domains of recrystallyzed quartz.

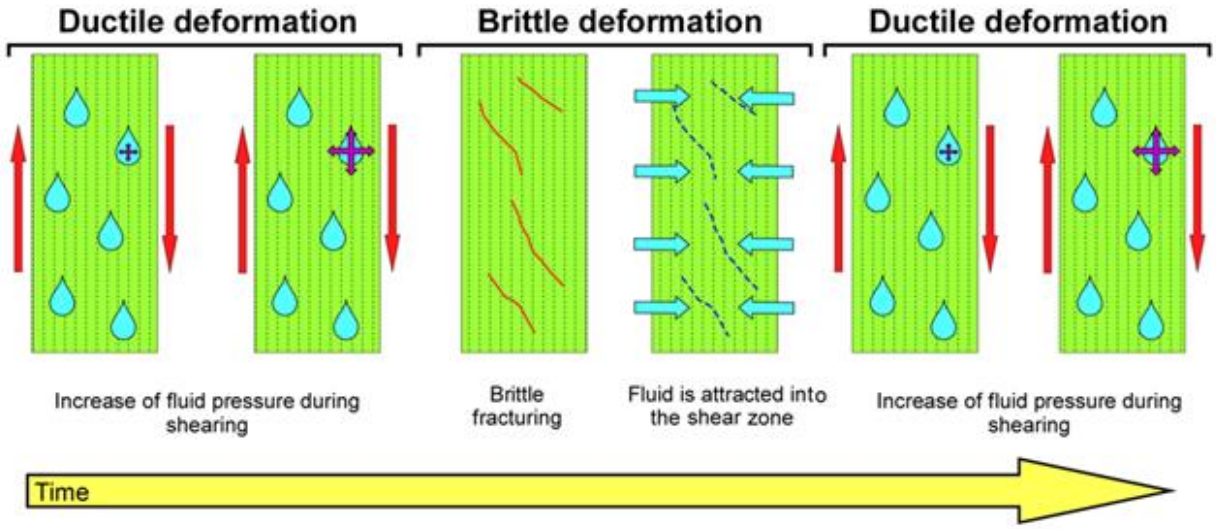

Figure 6.3 – Sketch of proposed model for alternating phases of ductile and brittle deformation during late stage activity on the FMSZ (viewed geographically downwards in map view)

Strain rate estimates obtained in the FMSZ ultramylonites range between 10^{-11} s^{-1} a 10^{-14} s^{-1} according to the different combination of paleopiezometry calibrations and flow laws.

Most of these estimates are within the "geologically typical" strain rates, in the range of 10^{-13} s^{-1} and 10^{-15} s^{-1} according to Pfiffner and Ramsay (1982) and Baxter and DePaolo (2004) and, if combined with temperature estimates, are in good agreement with the observed microstructures.

Because of the progressive decrease in the pure shear component we can infer that most of the horizontal shortening and exhumation due to motion on the FMSZ was accommodated during the first and second deformation stages. In the Alpine External Crystalline Massifs Variscan age shear deformation has not previously been quantified in terms of flow vorticity and its age, considered to be between ~320 Ma and ~300 Ma (Bussy and Von Raumer, 1993; Genier *et al*., 2008; Guillot *et al*., 2009) or Late Visean (Musumeci and Colombo, 2002), was always inferred relying on the age of emplacement of sin-kynematic granites.

Ages of ~340 and ~320 Ma obtained in this work are in agreement with the age proposed by Musumeci and Colombo (2002). Ages of ~320 Ma are consistent with both magmatic ages present in literature and ages of the dextral transpressional deformation in the Maures-Tanneron Massif (Schneider *et al*., 2014) and Corsica-Sardinia (Carosi and Palmeri, 2002; Di Vincenzo *et al*., 2004; Iacopini *et al*., 2008), dated at ~320-310 Ma (U-Th-Pb on monazites, Carosi *et al*., 2012), that affects migmatitic crust with strong tectono-metamorphic similarities to the migmatites cropping out in the Argentera-Mercantour Massif.

Our data support the suggestion that the FMSZ, because of its long-lasting activity, length and thickness, may have played a primary role in the exhumation of migmatitic rocks during Variscan time. Despite a similar structural evolution, characterized by strain localization during decreasing temperature, has been recently described in detail in the Yukon River shear zone (Northern Cordillera, Canada; Parsons *et al*., 2018). However other examples of regional scale strain softening shear zones are rare in the literature. The FMSZ should be considered as a new example of a strain-softening regional-scale shear zone, that can be useful to the community of structural geologists for future process-oriented investigations.

6.2 The Emosson-Berard Shear Zone (Aiguilles Rouge Massif)

The new data presented in this work demonstrate that the Aiguilles Rouges Massif was affected by dextral pure shear-dominated transpression occurred during Variscan times. Deformation started under high temperature conditions (between ~ 630 °C and 550 °C) and continued during decreasing temperature. The onset of transpression is dated at ~ 320 Ma and continued for at least ~ 15 Myr. The structural assets of the studied sectors and the age of deformation are in good agreement with those recognized in the Argentera Massif by Carosi *et al*. (2016) and Simonetti *et al*. (2017, 2018). Here the Ferriere Mollières Shear Zone, cross-cutting Variscan migmatites, is a steeply dipping dextral transpressional shear zone, with a prevalent pure shear component, active between ~ 340 Ma and ~ 320 Ma developed under decreasing temperature conditions from high amphibolite-facies to greenschist-facies.

The main difference is that, in the Ferriere-Mollieres Shear Zone, vorticity changed in time and space along a deformation gradient, with an increase in the simple shear component during later deformation stages (Simonetti *et al*., 2018). The Ferriere-Mollieres Shear Zone initiated earlier than the studied high-strain zone

in the Aiguilles Rouges Massif. However, vorticity analyses from both the Argentera and Aiguilles Rouge massifs indicate ~60% pure shear components at ~320 Ma. Vorticity analysis in the Maures Massif of southern France and in northern Sardinia also revealed a very similar deformation regime at ~320 Ma (Carosi and Palmeri, 2002; Carosi *et al*., 2012; Simonetti *et al*., submitted).

Ages of ~320 Ma are consistent with ages of transpressional deformation in the Maures-Tanneron Massif (Cavalaire Fault; Schneider *et al*. 2014; Simonetti et al. submitted) and northern Sardinia (Posada Asinara Shear Zone; Carosi and Palmeri, 2002; Di Vincenzo *et al*., 2004; Carosi *et al*., 2012), dated at ~323 Ma and 320-310 Ma respectively.

6.3 The Cavalaire Fault (Maures Massif)

The MTM shows striking similarities with the tectono-metamorphic evolution of the Variscan basement in northern Sardinia (Corsini and Rolland, 2009; Schneider *et al*., 2014).

Previous interpretations of the structural assets of the MTM considered the Joyeuse–Grimaud Fault as the suture zone and the major tectonic boundary in the massif (Vauchez and Bufalo 1985; 1988; Morillon *et al*., 2000; Bellot, 2005). A similar interpretation has been proposed for the Posada-Asinara Shear Zone in northern Sardinia (Cappelli *et al*., 1992; Carmignani *et al*., 1992, 1994). Accordingly, the two shear zones were regarded as being in continuity. The Posada-Asinara Shear Zone was later interpreted as an intracontinetal major late-Variscan sub-vertical transpressional shear zone separating two orogenic domains with different metamorphic imprints (Carosi and Palmeri, 2002; Carosi *et al*., 2012). Schneider *et al.* (2014) recognized that in the MTM the suture is located within the internal zone as a dismembered zone and that the Joyeuse–Grimaud Fault is a simple strike-slip shear zone confined within this zone. Therefore in the MTM, the Joyeuse–Grimaud Fault can no longer be considered the main boundary between the two orogenic domains.

The MTM and northern Sardinia both contain low-medium grade and magmatic complexes with granitic intrusions, separated by a ductile, transpressive shear zone. Vorticity analyses in the shear zone at both localities confirms the contemporaneous occurrence of simple and pure shear during deformation. In both Sardinia and MTM deformation linked to the collisional stage can be clearly recognized in the low- to medium- grade metamorphic domain and it is followed by a transpressive deformation. This transpressional

shear becomes more intense approaching the high-grade migmatitic zone, characterized by contemporary development of folds and shear zones (Carosi and Palmeri, 2002; Carosi *et al*., 2012). A progressive Barrovian metamorphism, approaching the transpressive zone, can be recognized both in Sardinia (from SW to NE; Carmignani *et al*., 1994) and in the MTM (from W to E; Corsini and Rolland, 2009; Schneider *et al*., 2014). In both sectors Barrovian minerals began to grow at the end of the collisional stage and continued to grow syn-kinematically during, at least, part of the subsequent transpressive stage.

In both shear zones transpressive deformation, associated with rocks decompression, developed from amphibolite-facies metamorphism up to greenschist facies. In both shear zones a general flow regime is observed with the coexistence of simple and pure shear, the latter with a shortening axis normal to the shear zone boundary. Moreover, our petrochronological data and available texturally-controlled geochronological information for northern Sardinia (Carosi *et al*., 2012; Di Vincenzo *et al*., 2004) indicate similar timing, both for the prograde and transpressive tectono-metamorphic histories. Finally, both the Posada-Asinara Shear Zone and the CF are affected by a later gravitational collapse of the belt (Carosi and Palmeri, 2002; Schneider *et al*., 2014) linked to the final exhumation of the mid- lower crust.

In summary, according to literature and our new data, the best correlation of shear zones in northern Sardinia and in the MTM can be made between the Posada-Asinara Shear Zone and the CF, because: a) they are two high-strain zones characterized by the presence of mylonites showing similar shear sense and kinematics (before Miocene rotation of the Corsica-Sardinia block); b) they affect Variscan para- and orthogneiss and migmatite; c) they underwent a similar polyphase deformation and tectono-metamorphic history leading to strikingly similar structural and metamorphic records and; d) they were active in the same time span at ~ 320 Ma.

Shear deformation recognized in northern Sardinia and MTM has been attributed to a network of dextral shear zones developed at the regional-scale referred in the literature as the East Variscan Shear Zone (EVSZ; Matte, 2001; Corsini and Rolland, 2009; Carosi *et al.*, 2012; Padovano *et al.* 2011; 2014; Schneider *et al.* 2014). Padovano *et al.* (2011) and Simonetti *et al*. (2017, 2018) highlighted that the EVSZ is not a unique shear zone, but a network of shear zones made by several branches with comparable tectono-metamorphic evolution affecting the Corsica-Sardinia block (Corsini and Rolland 2009; Carosi *et al*. 2012; Padovano *et al.*, 2011) and the External Crystalline Massifs in Western Alps (Carosi *et al.*, 2016; Simonetti *et al.*, 2017,

2018) in a comparable time span. According to our data the CF can be regarded as a branch of the EVSZ that was in close connection to northern Sardinia and the Western Alps. Our new structural data reinforce the model proposed by several authors (Arthaud and Matte, 1977; Ricci and Sabatini, 1978; Matte, 2001; Rollet *et al.*, 2002; Rosenbaum *et al.*, 2002; Elter and Pandeli, 2005; Bellot, 2005; Corsini and Rolland, 2009; Advokaat *et al.*, 2014; Edel *et al.*, 2014, 2018) in which the Corsica-Sardinia Block was connected to southern France. These new constraints reinforce a better correlation among the Late Carbonifeorus shear zones occurring in the fragments of the Variscan basement dispersed in the Mediterranean area and in the Western Alps. The new data fill a gap in the vorticity of the flow, deformation temperature, finite strain and timing of the southern sector of the EVSZ.

6.4 Extension, timing and evolution of the East Variscan Shear Zone

The External Crystalline Massifs, Maures-Tanneron Massif and Corsica-Sardinia Block show a striking similar tectono-metamorphic evolution during Variscan time (table 6.1). If the counterclockwise Oligo-Miocenic rotation of the Corsica-Sardinia block (Todesco and Vigliotti 1993; Advokaat et al. 2014) and of the Western Alps (Thomas *et al.*, 1999; Collombet *et al.*, 2002; Maffione *et al.*, 2008) is restored, all these sectors lie in lateral continuity.

In the Argentera Massif dextral shear deformation started at ~340 Ma under amphibolite-facies conditions. In the Maures-Tanneron Massif an anatectic post-collisional event is reported at ~340 Ma (Schneider *et al.*, 2014; Oliot *et a*l., 2015) while in northern Sardinia collision-related MP-MT metamorphism has been recognized at 344 ± 7 Ma (Rb-Sr method; Ferrara *et al*., 1978), although older ages of the thickening stage also occur in Sardinia and Corsica (between 380 and 340 Ma; Oliot *et al*., 2015).

Shear deformation recognized in northern Sardinia has been clearly characterized as a pure shear dominated transpression with an increasing component of simple shear traced towards the high strain zone.

The deformation regime recorded between ~340 Ma and ~320 Ma by the sher zones in the Argentera Massif, in the Aiguilles Rouge Massif and in the Maures Massif are all very similar (fig. 6.4).

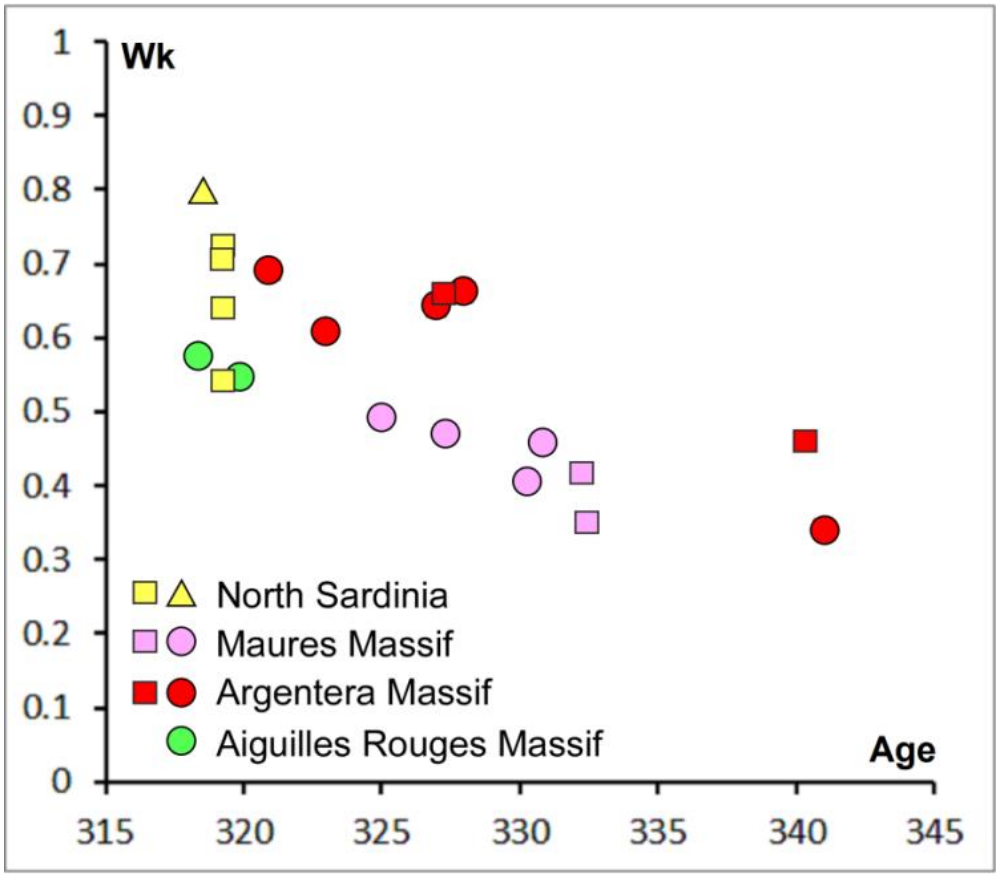

Figure 6.4 – Relation between vorticity number (dots: C'-shear band method; square: stable porphyroclasts method; triangles: quartz c-axis method) and age in the Argentera Massif (Simonetti *et al*. 2017, 2018), in the Aiguilles Rouge Massif (this work), in the Maures Massif (Simonetti *et al*., 2018, submitted) and in northern Sardinia (Carosi and Palmeri, 2002; Frassi *et al*., 2009; Carosi *et al*., 2012). All possible structural positions are represented with the age data.

		MAURES MASSIF	NORTH SARDINIA	ARGENTERA MASSIF	AIGUILLES ROUGES MASSIF
Main structure		Cavalaire Fault	Posada-Asinara shear zone	Ferriere-Mollières shear zone	Emosson-Bèrard shear zone
Involved lithotypes		Medium- to high-grade schist, gneiss and migmatite	Medium- to high-grade schist, gneiss and migmatite	Migmatite	Medium- to high-grade schist, gneiss and migmatite
Present-day sense of shear		top-to-the NW	top-to-the WNW	top-to-the SE	top-to-the-SW
Age of shearing		~ 323 Ma (U-Th-Pb on monazite)[1]	~325 - ~300 Ma (U-Th-Pb on monazite and zircon)[3]	~ 340 - ~320 Ma (U-Th-Pb on monazite)[6]	~ 320 Ma (U-Th-Pb on monazite)[12]
Syn-shear metamorphism		Retrometamorphism from Amphibolite-facies to greenschist-facies[1, 2]	Retrometamorphism from Amphibolite-facies to greenschist-facies[4]	Retrometamorphism from HT Amphibolite-facies to greenschist-facies[6]	Retrometamorphism from Amphibolite-facies to greenschist-facies[10, 11, 12]
Kinematic of the flow	**C' shear band method**	Pure shear-dominated transpression (p.s. 75% - 52%)1	-	Pure shear dominated transpression to simple shear dominated transpression (p.s. 86% - 33%)[6]	Pure shear-dominated transpression (p.s. 79% - 53%)[12]
	Stable porphiroclasts method	Pure shear-dominated transpression (p.s. 78% - 62%)[1]	Pure shear dominated transpression to simple shear dominated transpression (p.s. 64% - 48%)[4]	Pure shear-dominated transpression (p.s. 63% - 52%)[7]	Pure shear-dominated transpression (p.s. 65% - 60%)[12]
	Quartz c-axis method	-	simple shear dominated transpression (p.s 58% - 13%)[5]	-	-
Strain geometry		Plane strain to general flattening[1]	Nearly plane strain[5]	Plane strain to general flattening[6, 7, 8]	Nearly plane strain to general flattening [12]

1: Simonetti et al. submitted; 2: Schneider et al. 2014; 3: Carosi et al. 2012; 4: Carosi & Palmeri 2002; 5: Frassi et al. 2009; 6: Simonetti et al. 2018; 7: Simonetti et al. 2015; 8: Mammoliti 2015; 9: D'addario 2015; 10: Von Raumer & Bussy 2004 ; 11: Genier et al. 2008; 12: this work

Table 6.1 – Table summarizing the main features of the Emosson-Val Bèrard shear zone (Simonetti *et al.*, submitted), Cavalaire Fault (Simonetti *et al.*, submitted), Posada-Asinara shear zone (Carosi and Palmeri, 2002; Frassi *et al.* 2009; Carosi *et al.* 2012) and Ferriere-Mollières shear zone (Simonetti, 2015; Simonetti *et al.* 2018)

The shear zones in the Argentera, Aiguilles Rouges and Maures Massifs form part of a network of dextral shear zones belonging to the East Variscan Shear Zone (EVSZ; Corsini and Rolland, 2009; Carosi *et al*., 2012; Schneider *et al*., 2014).

The results obtained in this work support and strength, with new structural and geochronological data, the model proposed by Rosenbaum *et al*. (2002), Rollet *et al*. (2002), Advokaat *et al*. (2014) of the Corsica-Sardinia Block connected to southern France in continuity with the Western Alps and located along a major regional scale transpressive sher zone (fig. 6.5a).

The EVSZ is not a single shear zone but may be regarded as a network of interconnected transpressive shear zones developed progressively and recording a similar tectono-metamorphic history.

The Corsica-Sardinia Block, the Maures-Tanneron Massif and the future Alpine External Crystalline Massifs are cross-cutt by several shear zones (such as the Emosson-Berard shear zone, the Angle Fault, the Ferriere-Mollières shear zone, the Cavalaire Fault, the Grimaud Fault, the Posada-Asinara shear zone, the Barrabisa shear zone and the Porto Vecchio shear zone; fig. 6.5b) that, taking into account their position and their kinematics and if restored to their original orientation, can readily be interpreted as an interconnected structure belonging to the same network.

The various branches of the EVSV preserved in the various fragments of the belt have slightly different ages (fig. 6.5b). This can be explained by their progressive growth using a tectonic linkage model (Trudgill and Cartwright, 1994; Dawers and Anders, 1995; Walsh et al., 2002, 2003; Soliva and Benedicto, 2004; Soliva et al., 2006; Fossen and Cavalcante, 2017). Shear zones grow in length as they accumulate displacement, and tend to connect with adjacent structures to form composite systems or networks (fig. 6.6).

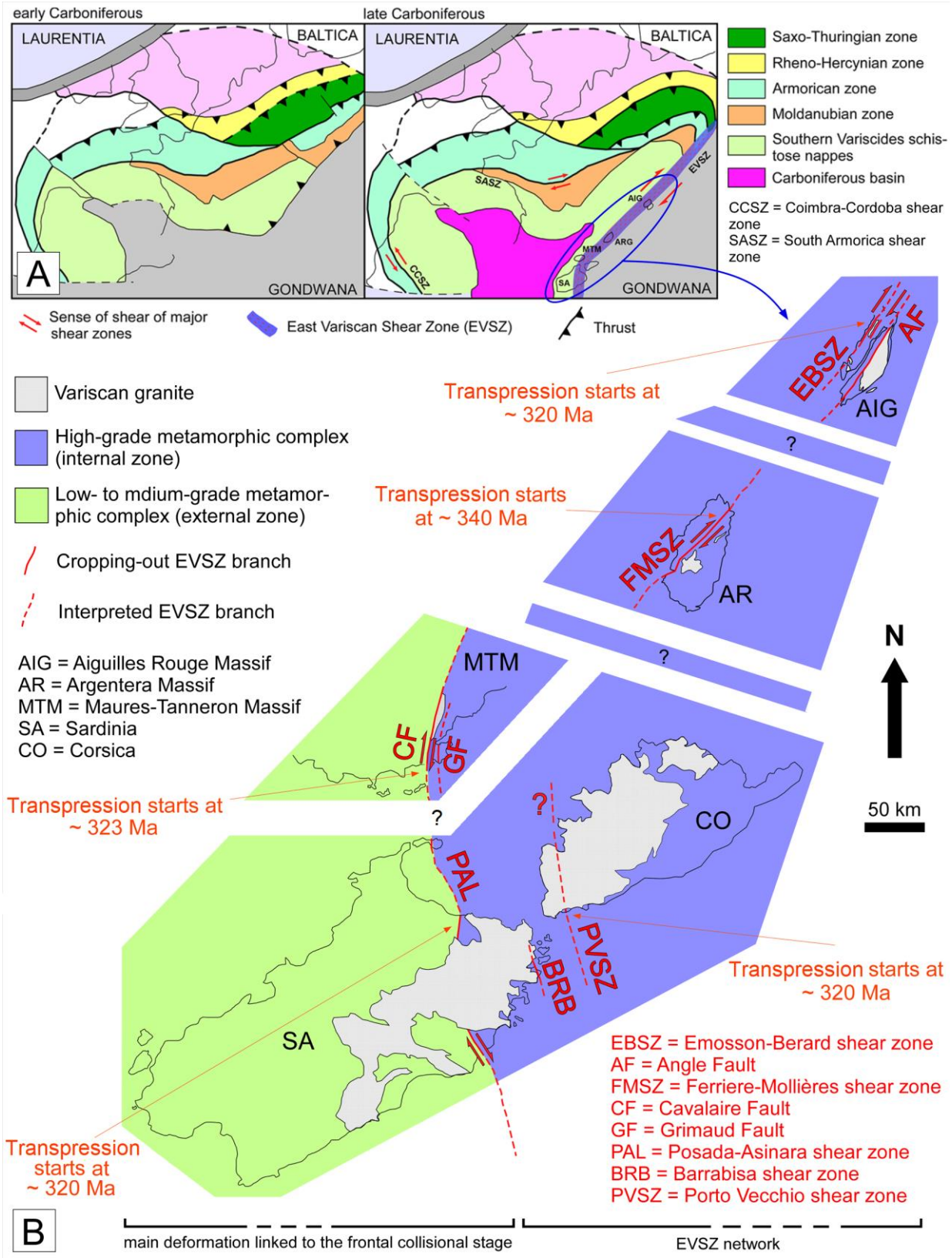

Figure 6.5 – A) Simplified sketch map of the European Variscides during early Carboniferous (modified after Faure *et al*., 2005; Guillot and Ménot, 2009; Žák *et al*., 2014) and during late Carboniferous after the onset of transpressional deformation (modified after Guillot and Ménot, 2009; Carosi *et al*., 2012; Simonetti *et al*., 2018). B) Detail of the inferred lateral relationship between the Corsica-Sardinia block, the Maures-Tanneron Massif, the Argentera Massif and the Aiguilles Rouges Massif. The main active shear zones are reported. Ages for of the onset of transpression are from: Simonetti *et al.* (2018) for the Argentera Massif; Simonetti *et al.* (submitted) for the Aiguilles Rouge Massif; Simonetti *et al.* (submitted) for the Maures-Tanneron Massif; Carosi *et al*. (2012) for the northern Sardinia

The result is that some of the branches are older, and were actived earlier than the others (fig. 6.5b) and record a longer deformation history (e.g the Ferriere Mollières Shear Zone in the Argentera Massif). On the other hand, younger branches record a shorter history (for example the Posada Asinara Shear Zone in northern Sardinia), but they are all compatible within the same tectono-metamorphic framework. Based on the age of transpression in the different fragments of the Belt affected by the EVSZ, we can identify at least two generations of branches: a first generation that initiated at around ~ 340-330 Ma and a second branch that initiated at ~ 320 Ma. Relations between the two generations are not completely clear and explainable with current data. A detailed investigation of other shear zones, potentially linked to the EVSZ, could reasonably lead to the recognition of other generations of branches and could clarify the relationship between them.

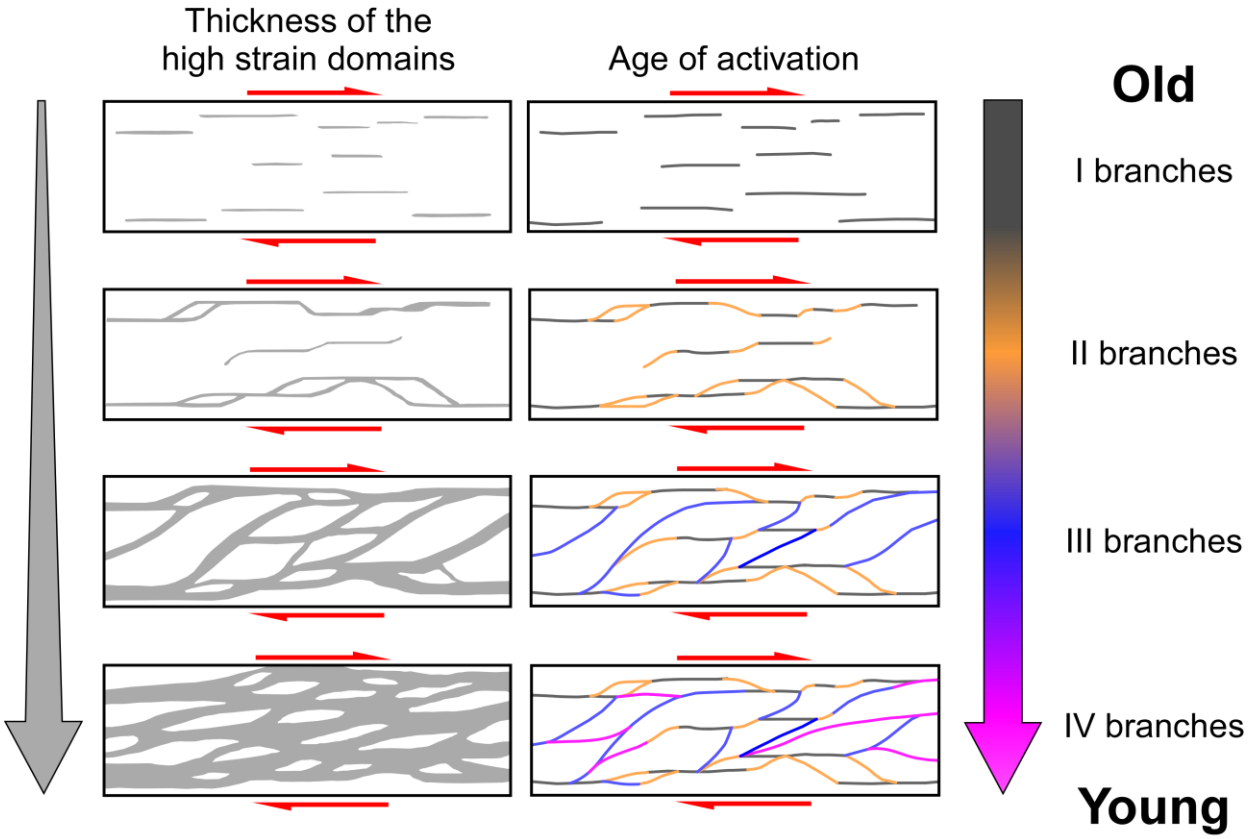

Figure 6.6 – Simplified sketch representing the evolution of a system of dextral shear zones based on progressive structural growth assumed in the fault linkage model (Trudgill and Cartwright, 1994; Dawers and Anders, 1995; Walsh *et al*., 2002, 2003; Soliva and Benedicto, 2004; Soliva *et al*., 2006; Fossen and Cavalcante, 2017). In the left column is reported the evolution of proportion of high strain domains within the shear zone over time; on the right, the different colors represent the age of activation of the different braches

It should be noted that the older branches, such as the Ferriere-Mollières Shear Zone in the Argentera Massif, unlike the younger ones, such as the shear zones in the Maures-Tanneron Massif, Aiguilles Rouges and northern Sardinia, developed fully within migmatitic crust. Variscan transpression is considered to be synchronous with anatexis, or to have initiate shortly after anatexis (Genier *et al*., 2008; Padovano *et al*., 2014; Simonetti *et al*., 2018, submitted). It is therefore possible that transpressional deformation along the EVSZ preferentially started to be accomodated in the lower crust which was easier to deform because of the ongoing anatexis, and later migrated into the non-migmatitic crust. Melt enhances deformation and strain localization (Rosenberg and Handy, 2005; Weinberg, 2016; Kellet *et al*., 2019). This is in agreement with the findings of Barboza and Bergantz (1998), Misra *et al.* (2014) and Diener and Fagereng (2014) who have demonstrated that partial melting in the lower crust causes a decrease in resistance of the rocks of nearly 30%. Rosenberg and Handy (2005) showed that an ~ 7 % of melt fraction is sufficient to lower the rocks strength by almost an order of magnitude.

Strike-slip transpression usually generates shear zones with subvertical dips (Fossen and Tikoff, 1998), this orientation is very effective in accommodating vertical movement. This is true even in cases where the transport direction is slightly inclined if the shear zone has a long lasting activity such as in the case of the EVSZ. The sub-horizontal component of pure shear that characterize transpressional shear zones is of great importance in increasing the effectiveness of exhumation because it can sustain vertical flow of the lower crust. Since all the branches of the EVSZ developed in transpressional regime it is possible to hypothesize that they have strongly favored the exhumation of the deep crust in the core of the network during transpression. The result is that some shear zones, especially those in a more marginal position within the network, juxtapose domains with different metamorphic imprint. These cases can be represented by the Cavalaire Fault in the Maures Massif or by the Posada Asinara Shear Zone in Sardinia (fig. 6.7). In this context the future Alpine External Crystalline Massifs should be regarded as being representative of the sheared and exhumed deep crust in the core of the EVSZ network (fig. 6.7).

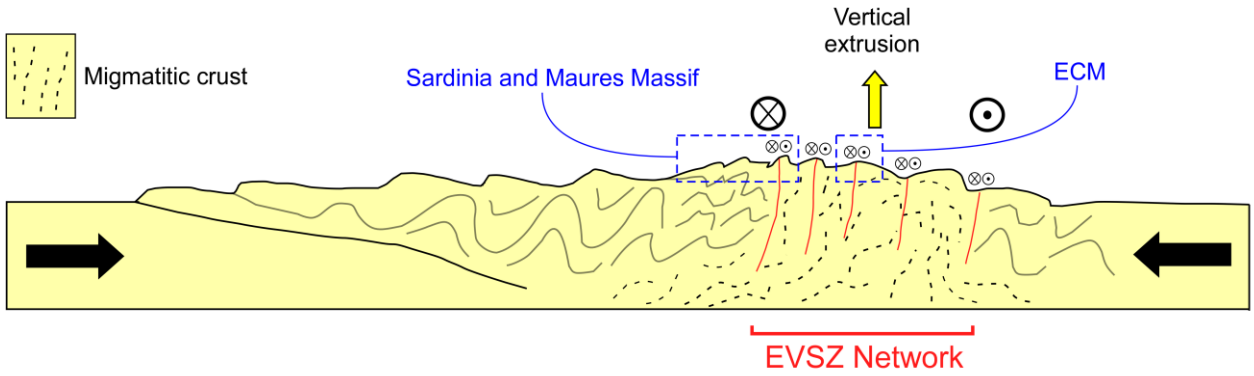

Figure 6.7 – Schematic cross section of the EVSZ network with location of Sardinia, Maures Massif and Alpine External Crystalline Massifs

A progressive increase in the simple shear component during transpressional deformation is recognized in the high-strain portions of the shear zones in both northern Sardinia (Carosi and Palmeri, 2002; Carosi *et al.*, 2009), and in the Argentera Massif (Simonetti *et al.*, 2018). In the Aiguilles Rouges Massif we did not detect this variation probably because of the lithology-controlled partitioning phenomena within the shear zone. A general increasing trend of simple shear during time, at the scale of the whole EVSZ, can be recognized by comparing vorticity data and ages of its branches (fig. 6.4). This reflects a change in the continent scale stress field which could be due to a change in the relative convergence angle between the wall rocks over time, to rotations of the active structures during ongoing collision or to a combination of the two factors. Evidence for the progressive change of the convergence angle was obtained in the FMSZ in the Argentera Massif. Here we detected a variation from 65° to 37° in convergence angle over a time span of nearly 20 Myr. In the other studied sectors, because of the different evolution of the shear zones, we do not detect such variation. It is worth to note that at ~320 Ma all the studied shear zones recorded a comparable convergence angle (52° in the FMSZ, 61° in the CF and 57° in the EBSZ).

The transpressional deformation regime, the high temperature of deformation and the late-Carboniferous age of shearing in the External Crystalline Massifs, all suggest that the activity on the EVSZ is not related to the post-Variscan deformation and a transition from Pangea B to Pangea A.

Our data therefore demonstrate that, at least in the Variscan fragments of the Western Alps, there is no geological and structural evidence that supports the dextral movement of Gondwana in Early Permian time along a more than 3000 km-long system of strike slip faults and shear zones crosscutting the whole Pangea.

This is in agreement with Pohl et al. (2018) who recognized that Carboniferous age transpressive dextral shear zones occur in the external part of the Alps, and are unrelated to the Early Permian basin formation and also to the Permian Pangea B to A transformation. Furthermore shear in the external part of Western Alps predates the deposition of the Early Permian rocks that yielded the paleomagnetic data (Muttoni *et al*., 2003) on which Pangea B is based.

Activation of the older branches of the EVSZ is coheval with the onset of sinistral transpressive deformation in the western sector of the Iberian Massif dated at ~ 340 Ma (U-Th-Pb on monazite and zircon; Pereira *et al*., 2008, 2010). Transpression in this sector of the Variscan belt is interpreted to be a consequence of a complex Devonian-Carboniferous polyphase indentation of a Gondwana promontory (Dias *et al*., 2016) and to orogenic syntaxial bending (Authemayou *et al*., 2019). According to Kroner *et al*. (2016) the European part of the Variscides decoupled from the Gondwana plate and the former convergent sector changed its mode to a dextral strike-slip zone starting at 340 Ma. The Ibero-Armorican Arc began to form with an open original curvature (Casas and Murphy, 2018) and was subsequently tightened during transpression (Dias *et al*., 2016). Kroner and Romer (2013) recognized during this phase a west-directed escape tectonics of the Iberian block contemporaneously with the eastward escape of an unspecified block to the east. Our data are in agreement with the onset of transpression at ~340 Ma and allows us to state that the EVSZ, may have contributed to this process during its early stages and subsequently facilitated formation of a second arc that characterizes the eastern sector of the Variscan Belt by allowing the eastward escape already hypothesized by Kroner and Romer (2013).

Our data are therefore in agreement with the composite orocline model proposed by Matte (1986b, 2001), Corsini and Rolland (2009), Guillot *et al*. (2009), Carosi *et al*. (2012) and Simonetti *et al*. (2018), and confirm that reconstruction of the European Variscan Belt should take into account the presence of an arc limited by the EVSZ located in the eastern part of the belt.

It is likely that the EVSZ also played a primary role as an inherited crustal discontinuity that influenced the evolution of new structures during post-Variscan and Alpine evolution (Bergomi *et al*., 2017; Ballèvre et al. 2018). Jammes and Lavier (2019) recently, with the use of numerical models, discussed the influence of strength variations from inherited crustal fabrics on the mechanism of rifting during the formation of magma-poor margins. They recognize the importance of the orientation of inherited heterogeneities: vertical fabrics

favor the initial formation of horst-and-graben structures whereas horizontal and shallowly dipping fabrics favor the formation of core complexes. During the Variscan transpressive deformation the development of vertical fabrics is predominant and therefore horst and graben formation would be facilitated during the initial stages of the post-Variscan extension and subsequent rifting. The presence of the EVSZ also has implications for the original position and provenance of the crustal blocks subsequently involved in the rifting, during Pangea break-up, and Alpine collision. As pointed out by Ballèvre *et al*. (2018), the Helvetic Alpine basement was separated from the Penninic Alpine basement by this shear zone during Carboniferous times and these basement blocks may have had contrasting geological histories during the initial stages of Variscan deformation. The juxtaposition of the basement of these two Alpine domains could have started during late-Carboniferous because of motion on the EVSZ.

Further studies are needed to recognize other potential sectors of the southern European Variscan Belt affected by branches of the EVSZ in order to better constrain the lateral extent of the EVSV, to formulate a more meaningful model for its evolution, and to better understand how the presence of this regional-scale discontinuity influenced post-Variscan tectonic evolution of western Europe.

7. Conclusions

The data obtained in this work allow us to establish that, during Variscan time, the Argentera Massif, the Aiguilles Rouges Massif and the Maures Massif were affected by pure-shear dominated transpression that started at ~340 Ma under high-temperature conditions and continued during retrograde metamorphism.

All the studied sectors were part of the same regional-scale dextral shear zone system known as the East Variscan Shear Zone. Its activity, constrained in three of its branches for the first time, is related to Carboniferous transpression and not to post Variscan deformation. Transpression starts to be accomodated in the weak migmaititc crust under high temperature conditions. The shear zone system remained active for a long time, triggering the exumation of the lower crust and evolving under decreasing temperature conditions. Because of this, several processes such as strain softening, strain localization, brittle-ductile cycles and progressive changes in the deformation regime occurred at a regional scale in the branches of the network.

The FMSZ, in the Argentera Massif should be considered as a new example of a strain-softening regional-scale shear zone forming at initially high temperatures and progressively evolving with decreasing temperature towards the brittle-ductile transition. In the Aiguilles Rouge Massif partitioning of pure and simple shear components during on-going deformation, have been detected in the EBSZ. The new data also allows us to better define the structural assets and evolution of the contact between the internal and external zones marked by the CF in the Maures Massif.

The EVSZ had a long-lasting history: it played a primary role during the polyphase indentation of Gondwana, in the shaping of the eastern sector of the belt during late-Variscan time and finally as an inherited discontinuity that influenced the post-Variscan and Alpine evolution.

Even if, at present day, just fragments of the EVSZ are visible and questions about its tectono-metarmophic evolution in orther fragments of the belt still remains to be clarified, such structures clearly represents an example for documenting the evolution of ductile deformation and associated metamorphism of large-scale intra-continental transpressional zones.

Our data demonstrate that a multidisciplinary approach is essential for obtaining useful results from the study of shear zones, especially at the regional scale. Different independent analytical methods for constraining temperature, absolute timing and deformation should always be systematically applied in different sectors of regional-scale structures in order to obtain data capable of addressing first order questions on regional/continent-scale tectonics and correlating between now widely separated fragments of once continuous orogenic belts.

8. References

Abramoff, M.D., Magalhaes, P.J. and Ram, S.J., 2004. Image processing with ImageJ: *Biophotonics Int*., 11, 7, 36-42.

Advokaat, E.L., van Hinsbergen, D.J.J., Maffione, M., Langereis, C.G., Vissers, R.L.M., Cherchi, A., Schroeder, R., Madani, H. and Columbu, S., 2014. Eocene rotation of Sardinia, and the paleogeography of the western Mediterranean region: *Earth and Planetary Science Letters*, **401**, p. 183–195, doi: 10.1016/j.epsl.2014.06.012.

Aleinikoff, J.N., Schenck, W.S., Plank, M.O., Srogi, L., Fanning, C.M., Kamo, S.L. and Bosbyshell, H., 2006. Deciphering igneous and metamorphic evens in high-grade rocks of the Wilmington Complex, Delaware: Morphology, cathodoluminescence and backscattered electron zoning, and SHRIMP U-Pb geochronology of zircon and monazite: *Geological Society of America Bulletin*, **118**, 39–64.

Amelin, Y. and Zaitsev, A.N., 2002. Precise geochronology of phoscorites and carbonatites: The critical role of U-series disequilibrium in age interpretations: *Geochim Cosmochim Acta*, **66**, 2399–2419.

Arthaud, F. and Matte, P., 1977. Late Paleozoic strikeslip faulting in southern Europe and northern Africa; result of a right-lateral shear zone between the Appalachians and the Urals: *Geological Society of America Bulletin*, **88**, p. 1305–1320.

Authemayou, C., Le Gall, B., Caroff, M. and Grosjean, D.B., 2019. Wrench-related dome formation and subsequent orogenic syntax bending in a hot orogen (Variscan Ibero-Armorican Arc, the Ouessant Island, France): *Tectonics*, doi: 10.1029/2018TC005189.

Baietto, A., Perello, P., Cadoppi, P. and Martinotti, G., 2009. Alpine tectonic evolution and thermal water circulations of the Argentera Massif (South-Western Alps): *Swiss Journal of Geosciences*, **102**, p. 223–245, doi: 10.1007/s00015-009-1313-5.

Bajolet, F., Replumaz, A., and Lainé, R., 2013. Orocline and syntaxes formation during subduction and collision: OROCLINE SYNTAXES IN CONVERGENT SETTINGS. *Tectonics*, **32**, 1529–1546, https://doi.org/10.1002/tect.20087.

Ballèvre, M., Bosse, V., Ducassou, C. and Pitra, P., 2009. Palaeozoic history of the Armorican Massif: Models for the tectonic evolution of the suture zones: *Comptes Rendus Geoscience*, **341**, p. 174–201, doi: 10.1016/j.crte.2008.11.009.

Ballèvre, M., Manzotti, P. and Dal Piaz, G.V., 2018. Pre-Alpine (Variscan) inheritance: a key for the location of the future Valaisan Basin (Western Alps).: Pre-Alpine (Variscan) inheritance: a key for the location of the future Valaisan Basin (Western Alps).: *Tectonics*,, doi: 10.1002/2017TC004633.

Barale, L., Bertok, C., d'Atri, A., Martire, L., Piana, F. and Domini, G., 2016. Geology of the Entracque–Colle di Tenda area (Maritime Alps, NW Italy): *Journal of Maps*, **12**, p. 359–370, doi: 10.1080/17445647.2015.1024293.

Barboza, S.A. and Bergantz, G.W., 1998. Rheological transitions and the progress of melting of crustal rocks: *Earth and Planetary Science Letters*, **158**, p. 19–29.

Baxter, E.F. and DePaolo, D.J., 2004. Can metamorphic reactions proceed faster than bulk strain?: Contributions to Mineralogy and Petrology, **146**, 657-670.

Bellot, J.-P., 2005. The Palaeozoic evolution of the Maures massif (France) and its potential correlation with others areas of the Variscan belt: a review: *Journal of the Virtual Explorer*, **19**, doi: 10.3809/jvirtex.2005.00116.

Bellot, J.-P., Bronner, G., Marchand, J., Laverne, C. and Triboulet, C., 2002. Chevauchement et détachement dans les Maures occidentales (Var, France): *Géologie de la France*, **1**, p. 21–37.

Bergomi, M.A., Dal Piaz, G.V., Malusà, M.G., Monopoli, B. and Tunesi, A., 2017. The Grand St Bernard-Briançonnais Nappe System and the Paleozoic Inheritance of the Western Alps Unraveled by Zircon U-Pb Dating: The Paleozoic Inheritance of the Alps: *Tectonics*, **36**, p. 2950–2972, doi: 10.1002/2017TC004621.

Bigi, G., Castellarin, A., Coli, M., Dal Piaz, G. V., Sartori, R., Scandone, P. and Vai, G. B., 1990. Structural Model of Italy 1:500.000, sheet 1. C.N.R., Progetto Finalizzato Geodinamica, SELCA Firenze.

Bigot-Cormier, F., Sosson, M., Poupeau, G., Stéphan, J.-F. and Labrin, E., 2006. The denudation history of the Argentera Alpine External Crystalline Massif (Western Alps, France– Italy): an overview from the analysis of fission tracks in apatites and zircons: *Geodinamica Acta*, **19**, 455–473.

Braden, Z., Godin, L. and Cottle J.M., 2017. Segmentation and rejuvenation of the Greater Himalayan sequence in western Nepal revealed by in situ U–Th/Pb monazite petrochronology: *Lithos, 285*, 751–765.

Briand, B., Bouchardon, J.L., Capiez, P. and Piboule, M., 2002. Felsic (A-Type)-Basic (Plume-Induced) Early Palaeozoic bimodal magmatism in the Maures massif (southeastern France): *Geol Mag*, **139**, 291-311.

Brun, J.P. and Burg, J.-P., 1982. Combined thrusting and wrenching in the Ibero-Armorican arc: A corner effect during continental collision: *Earth and Planetary Science Letters*, **61**, p. 319–332.

Buick, I.S., Hermann, J., Williams, I.S., Gibson, R.L. and Rubatto, D., 2006. A SHRIMP U–Pb and LA-ICP-MS trace element study of the petrogenesis of garnet–cordierite–orthoamphibole gneisses from the Central Zone of the Limpopo Belt, South Africa: *Lithos*, **88**, 150–172.

Burg, J.-P. and Matte, P., 1978. A cross section through the French Massif Central and the scope of its Variscan Geodynamic Evolution: *Zeitschrift der Deutschen Geologischen Gesellschaft*, **129**, p. 429–460.

Bussy, F. and Von Raumer, J.F., 1993. U–Pb dating of Paleozoic event in the Mont-Blanc crystalline massif, Western Alps: *Terra Nova*, **5**, 1, 382–383.

Bussy, F., Hernandez, J. and Von Raumer, J., 2000. Bimodal magmatism as a consequence of the post-collisional readjustment of the thickened Variscan continental lithosphere (Aiguilles Rouges-Mont Blanc Massifs, Western Alps): *Transactions of the Royal Society of Edinburgh: Earth Sciences*, **91**, p. 221–233, doi: 10.1017/S0263593300007392.

Capuzzo, N. and Bussy, F., 2001. Syn-sedimentary volcanism in the Late Carboniferous Salvan-Donrénaz basin (Western Alps): *Memorie Scienze Naturali Brescia*, **25**, p. 203–211.

Capuzzo, N., Handler, R., Neubauer, F. and Wetzel, A., 2003. Post-collisional rapid exhumation and erosion during continental sedimentation: the example of the late Variscan Salvan-Dorénaz basin (Western Alps): *International Journal of Earth Sciences*, **92**, 364-379.

Carosi, R., D'Addario, E., Mammoliti, E., Montomoli, C. and Simonetti, M., 2016. Geology of the northwestern portion of the Ferriere-Mollieres Shear Zone, Argentera Massif, Italy: *Journal of Maps*, **12**, p. 466–475, doi: 10.1080/17445647.2016.1243491.

Carosi, R., Frassi, C. and Montomoli, C., 2009. Deformation during exhumation of medium- and high-grade metamorphic rocks in the Variscan chain in northern Sardinia (Italy): *Geological Journal*, **44**, p. 280–305, doi: 10.1002/gj.1137.

Carosi, R., Montomoli, C., Tiepolo, M. and Frassi, C., 2012. Geochronological constraints on post-collisional shear zones in the Variscides of Sardinia (Italy): Post-collisional shear zones in the Variscides of Sardinia: *Terra Nova*, **24**, p. 42–51, doi: 10.1111/j.1365-3121.2011.01035.x.

Carosi, R. and Palmeri, R., 2002. Orogen-parallel tectonic transport in the Variscan belt of northeastern Sardinia (Italy): implications for the exhumation of medium-pressure metamorphic rocks: *Geological Magazine*, **139**, doi: 10.1017/S0016756802006763.

Carey, S.W., 1955. The orocline concept in geotectonics: *Papers and Proceedings of the Royal Society of Tasmania*, **89**, 255–288.

Casas, J.M. and Murphy, B.J., 2018. Unfolding the arc: The use of pre-orogenic constraints to assess the evolution of the Variscan belt in Western Europe: *Tectonophysics*, **736**, p. 47–61, doi: 10.1016/j.tecto.2018.04.012.

Chabrier, G. and Mascle, G., 1975. Comparaison des évolutions géologiques de la Provence et de la Sardaigne. *Revue de Géographie Pgysique ete de Géologie Dynamique*, **2**, XVII, 121-136.

Collombet, M., Thomas, J.C., Chauvin, A., Tricart, P., Bouillin, J.P. and Gratier, J.P., 2002. Counterclockwise rotation of the western Alps since the Oligocene: New insights from paleomagnetic data: TERTIARY ROTATION OF THE WESTERN ALPS: *Tectonics*, **21**, p. 14-1-14–15, doi: 10.1029/2001TC901016.

Compagnoni, R., Ferrando, S., Lombardo, B., Radulesco, N. and Rubatto, D., 2010. Paleo-European crust of the Italian Western Alps: Geological history of the Argentera Massif and comparison with Mont Blanc-Aiguilles Rouges and Maures-Tanneron Massifs: *Journal of the Virtual Explorer*, **36**, doi: 10.3809/jvirtex.2010.00228.

Corsini, M. and Rolland, Y., 2009. Late evolution of the southern European Variscan belt: Exhumation of the lower crust in a context of oblique convergence: *Comptes Rendus Geoscience*, **341**, p. 214–223, doi: 10.1016/j.crte.2008.12.002.

Corsini, M., Ruffet, G. and Caby, R., 2004. Alpine and late-hercynian geochronological constraints in the Argentera Massif (Western Alps): *Eclogae Geologicae Helvetiae*, **97**, p. 3–15, doi: 10.1007/s00015-004-1107-8.

Crevola, G., and Pupin, J.P., 1994. Crystalline provence: structure and Variscan evolution. in: Keppie, J.D. (Eds), Pre-Mesozoic geology in France and related areas, Springer Verlag, Berlin Heidelberg, 426–441.

Cruz, M.J., Cunha, J.C., Merlet, C. and Sabatè P., 1996. Datação pontual das monazitas da região de Itambé, Bahia, através da microssonda electronica: *XXXIX Congresso Brasileiro de Geologia*, *Bahià-Segipe*, **2**, 206–209.

D'Addario, E., 2015. Cartografia geologica, analisi strutturale e vorticità cinematica di una zona di taglio regionale: la "Ferriere-Mollères Shear Zone" tra i valloni Forneris e di Pontebernardo (Massiccio dell'Argentera, Alpi Occidentali): *Unpublished Thesis, Università degli Studi di Pisa (Italy)*, pp 203.

d'Atri, A., Piana, F., Barale, L., Bertok, C. and Martire, L., 2016. Geological setting of the southern termination of Western Alps: *International Journal of Earth Science (Geol Rundsch)*, **105**, 1831–1858, doi 10.1007/s00531-015-1277-9.

Davy, P. and Cobbold, P.R., 1988. Indentation tectonic in nature and experiment. 1. Experiments scaled for gravity: *Bullettin of the Geological Insititutions of Uppsala*, **14**, 129 – 141.

Dawers, N.H. and Anders, M.H., 1995. Displacement-length scaling and fault linkage: *J. Struct. Geol.*, **17**, 607–614.

Dell'Angelo, L.N. and Tullis, J., 1989. Fabric development in experimentally sheared quartzites: *Tectonophysics*, **169**, 1-21.

Debon, F., and Lemmet, M.,1999. Evolution of Mg/Fe Ratios in Late Variscan Pultonic Rocks from the External Crystalline Massif of the Alps (France, Italy, Switzerland): *J Petrol*, **40**, 1151– 1185.

Di Vincenzo, G., Carosi, R. and Palmeri, R., 2004. The Relationship between Tectono-metamorphic Evolution and Argon Isotope Records in White Mica: Constraints from in situ 40Ar-39Ar Laser Analysis of the Variscan Basement of Sardinia: *Journal of Petrology*, **45**, p. 1013–1043, doi: 10.1093/petrology/egh002.

Dias, R. and Ribeiro, A., 1995. The Ibero-Armorican Arc: A collision effect against an irregular continent? *Tectonophysics*, **246**, p. 113–128.

Dias, R., Ribeiro, A., Romão, J., Coke, C. and Moreira, N., 2016. A review of the arcuate structures in the Iberian Variscides; constraints and genetic models: *Tectonophysics*, **681**, p. 170–194, doi: 10.1016/j.tecto.2016.04.011.

Diener, J.F.A. and Fagereng, Å., 2014. The influence of melting and melt drainage on crustal rheology during orogenesis: *Journal of Geophysical Research: Solid Earth*, **119**, p. 6193–6210, doi: 10.1002/2014JB011088.

Dobmeier, C., 1998. Variscan P–T deformation paths from the southwestern Aiguilles Rouges massif (External massif, western Alps) and their implication for its tectonic evolution: *Geologische Rundschau*, **87**, p. 107–123.

Dobmeier, C. and von Raumer, J. F., 1995. Significance of latest-Variscan and Alpine deformation for the evolution of Montagne de Pormenaz (Southwestern Aiguilles Rouges massif, Western Alps): *Eclogae geol Helv*, **88**, 2, 267-279, doi:0012-9402/95/020267-13.

Doglioni, C., Gueguen, E., Harabaglia, P. and Mongelli F., 1999. On the origin of W-directed subduction zones and applications to the western Mediterranean. In Durand, B., Jolivet, L., Horvat, F., Seranne, M. (eds) The Mediterranean Basins: Teriary extension within the Alpine Orogen: *Geological Society, London, Special Publications*, **156**, 541 – 561.

Dunlap, W.J., Hirth, G. and Teyssier, C., 1997. Thermomechanical evolution of a ductile duplex: *Tectonics*, **16**, 983-1000.

Edel, J.B., Casini, L., Oggiano, G., Rossi, P., Schulmann, K., 2014. Early Permian 90° clockwise rotation of the Maures-Estérel-Corsica-Sardinia block confirmed by new palaeomagnetic data and followed by a Triassic 60° clockwise rotation: *Geol Soc Lond Spec Publ*, **405**, 1–29.

Edel, J.B., Schulmann, K., Lexa, O. and Lardeaux, J.M., 2018. Late Palaeozoic palaeomagnetic and tectonic constraints for amalgamation of Pangea supercontinent in the European Variscan belt: *Earth-Sci Rev*, **177**, 589–612.

Elter, F.M. and Pandeli, E., 2005. Structural-metamorphic correlations between three Variscan segments in southern Europe: Maures Massif (France), Corsica (France)-Sardinia (Italy), and Northern Appennines (Italy): *Journal of the Virtual Explorer*, **9**.

Engi, M., Lanari, P. and Kohn, M.J., 2017. Significant Ages - An Introduction to Petrochronology: Methods and Applications. In: Engi, M., Lanari, P. and Kohn, M.J. (Eds), Petrocronology: methods and applications: *Mineralogy and Geochemistry*, **83**. doi: 10.1515/9783110561890-002.

Etheridge, M.A., 1983, Differential stress magnitudes during regional deformation and metamorphism: Upper bound imposed by tensile fracturing: *Geology*, **11**, 4, 231-234.

Epard, J.L., 1990. La nappe de Morcles au sud-ouest du Mont-Blanc: *Mémoires de Géologie (Lausanne)*, 8, pp 165.

Faleiros, F.M., Moraes, R., Pavan, M. and Campanha, G.A.C., 2016. A new empirical calibration of the quartz c-axis fabric opening-angle deformation thermometer: *Tectonophysics*, **671**, p. 173–182, doi: 10.1016/j.tecto.2016.01.014.

Faure, M., Lardeaux, J.-M. and Ledru, P., 2009. A review of the pre-Permian geology of the Variscan French Massif Central: *Comptes Rendus Geosciences*, **341**, p. 202–213.

Faure-Muret, A., 1955. *Etudes géologiques sur le massif de l'Argentera-Mercantour et ses enveloppes sédimentaires*: Paris.

Fernandez, A., Guillot, S., Ménot, R.-P. and Ledru, P., 2002. Late Paleozoic polyphased tectonics in the SW Belledonne massif (external crystalline massifs, French Alps): *Geodinamica Acta*, **15**, p. 127–139, doi: 10.1080/09853111.2002.10510746.

Fernández-Lozano, J., Pastor-Galán, D., Gutiérrez-Alonso, G. and Franco, P., 2016. New kinematic constraints on the Cantabrian orocline: A paleomagnetic study from the Peñalba and Truchas synclines, NW Spain: *Tectonophysics*, **681**, p. 195–208, doi: 10.1016/j.tecto.2016.02.019.

Ferrando, S., Lombardo, B. and Compagnoni, R., 2008. Metamorphic history of HP mafic granulites from the Gesso-Stura Terrain (Argentera Massif, Western Alps, Italy): *European Journal of Mineralogy*, **20**, p. 777–790, doi: 10.1127/0935-1221/2008/0020-1891.

Ferrara, G., Ricci, C.A. and Rita, F., 1978. Isotopic ages and tectono-metamorphic history of the metamorphic basement of north-eastern Sardinia: *Contributions to Mineralogy and Petrology*, **68**, 99-106.

Flinn, D., 1962. On folding during three-dimensional progressive deformation: *QJ Geol Soc Lond*, **118**, 385 433.

Fluck, P., Piqué, A., Schneider, J.L. and Whitechurch, H., 1991. Le socle vosgien: *Sciences Géologiques*, **44**, p. 207–235.

Foster, G., Gibson, H.D., Parrish, R., Horstwood, M., Fraser, J. and Tindle, A., 2002. Textural, chemical and isotopic insights into the nature and behaviour of metamorphic monazite: *Chem Geol*, 191, 183–207.

Fossen, H., 2016. *Structural geology*: Cambridge University Press, Cambridge; New York.

Fossen, H., Basil, T. and Christian, T., 1994. Strain modeling of transpressional and transtensional deformation: *Norsk Geologisk Tidsskrift*, **74**, p. 134–145.

Fossen, H. and Cavalcante, G.C.G., 2017. Shear zones – A review: *Earth-Science Reviews*, **171**, p. 434–455, doi: 10.1016/j.earscirev.2017.05.002.

Fossen, H. and Tikoff, B., 1998. Extended models of transpression and transtension, and application to tectonic settings: *Geological Society, London, Special Publications*, **135**, p. 15–33.

Fossen, H. and Tikoff, B., 1993. The deformation matrix for simultaneous simple shearing, pure shearing and volume change, and its application to transpression-transtension tectonics: *Journal of Structural Geology*, **15**, p. 413–422, doi: 10.1016/0191-8141(93)90137-Y.

Franke, W., Robin, L. M. C. and Torsvik, T. H., 2017. The Palaeozoic Variscan Oceans Revisited: *Gondwana Research*, **48**, 257-284. doi: 10.1016/j.gr.2017.03.005.

Frassi, C., Carosi, R., Montomoli, C. and Law, R.D., 2009. Kinematics and vorticity of flow associated with post-collisional oblique transpression in the Variscan Inner Zone of northern Sardinia (Italy): *Journal of Structural Geology*, **31**, p. 1458–1471, doi: 10.1016/j.jsg.2009.10.001.

Fry, N., 1979. Random point distribution and strain measurement in rocks: *Tectonophysics*,, p. 89–105.

García-Navarro, E. and Fernández, C., 2004. Final stages of the Variscan orogeny at the southern Iberian massif: Lateral extrusion and rotation of continental blocks: VARISCAN ESCAPE TECTONICS, SW IBERIA: *Tectonics*, **23**, p. n/a-n/a, doi: 10.1029/2004TC001646.

Gasquet, D., Bertrand, J.M., Paquette, J.L., Lehmann, J., Ratzoy, G., De Ascencão Guedes, R., Tiepolo M., Boullier, A.M., Scaillet, S. and Nomade S., 2010. Miocene to Messinian deformation and hydrothermal activity in a pre-Alpine basement massif of the French western Alps: new U–Th–Pb and argon ages from the Lauzière massif: *Bulletin de la Société Géologique de France*, **181**, 227–241.

Genier, F. and Epard, J.L., 2007. The Fry method applied to an augen orthogneiss: problemsand results: *Journal of Structural Geology*, **29**, 209-224.

Genier, F., Bussy, F., Epard, J.-L. and Baumgartner, L., 2008. Water-assisted migmatization of metagraywackes in a Variscan shear zone, Aiguilles-Rouges massif, western Alps: *Lithos*, **102**, p. 575–597, doi: 10.1016/j.lithos.2007.07.024.

Gerbault, M., Schneider, J., Reverso-Peila, A. and Corsini, M., 2016. Crustal exhumation during ongoing compression in the Variscan Maures-Tanneron Massif, France-Geological and thermo-mechanical aspects: *Tectonophysics*,, doi: 10.1016/j.tecto.2016.12.019.

Ghosh, S., Bose, S., Mandal, N. and Dasgupta, S., 2016. Dynamic recrystallization mechanisms and their transition in the Daling Thrust (DT) zone, Darjeeling Himalaya: *Tectonophysics*, **674**, 166-181.

Gibson, H.D., Carr, S.C., Brown, R.L. and Hamilton, M.A., 2004. Correlations between chemical and age domains in monazite, and metamorphic reactions involving major pelitic phases: an integration of ID-TIMS and SHRIMP geochronology with Y–Th–U X-ray mapping: *Chemical Geology*, **211**, 237–260.

Gillam, B.G., Little, T.A., Smith, E. and Toy, V.G., 2013. Extensional shear band development on the outer margin of the Alpine mylonite zone, Tatare Stream, Southern Alps, New Zealand: *Journal of Structural Geology*, **54**, p. 1–20, doi: 10.1016/j.jsg.2013.06.010.

Glen, R. and Roberts, J., 2012. Formation of Oroclines in the New England Orogen, Eastern Australia. In: (Ed.) Johnston, S. and Rosenbaum, G., Oroclines, *Journal of the Virtual Explorer*, **43**, 3, doi:10.3809/jvirtex.2012.00305

Grandjean, V., Guillot, S. and Pecher, A., 1996. Un nouveau témoin de l'évolution métamorphique BP-HT post-orogénique hercynienne : l'unité de Peyre-Arguet (Haut-Dauphiné): *Comptes Rendus Académie Sci. Sér, Terre Planètes*, **322**, 2, 189–195.

Guillot, S., Di Paola, S., Ménot, R.-P., Ledru, P., Spalla, M.I., Gosso, G. and Schwartz, S., 2009. Suture zones and importance of strike-slip faulting for Variscan geodynamic reconstructions of the External Crystalline Massifs of the western Alps: *Bulletin de la Société géologique de France*, **180**, p. 483–500, doi: 10.2113/gssgfbull.180.6.483.

Hermann, J. and Rubatto, D., 2003. Relating zircon and monazite domains to garnet growth zones: age and duration of granulite facies metamorphism in the Val Malenco lower crust*: J Metamorph Geol*: **21**, 833–852.

Herwegh, M., and Handy, M.R., 1998. The origin of shape preferred orientations in mylonite: inferences from in-situ experiments on polycrystalline norcamphor: *Journal of Structural Geology*, **20**, 681-694.

Hirth, G. and Tullis, J., 1992. Dislocation creep regimes in quartz aggregates: Journal of Structural Geology, **14**, 149-159.

Hirth, G., Teyssier, C. and Dunlap, W.A., 2001. An evaluation of quartzite flow laws based on comparisons between experimentally and naturally deformed rocks: International Journal of Earth Sciences, **90**, 77-87.

Holyoke, C.W. and Kronenberg, A.K., 2010. Accurate differential stress measurement using the molten salt cell and solid salt assemblies in the Griggs apparatus with applications to strength, piezometers and rheology: *Tectonophysics*, **494**, p. 17–31, doi: 10.1016/j.tecto.2010.08.001.

Horstwood, M.S.A., Foster, G.L., Parrish, R.R., Noble, S.R. and Nowell G.M., 2003. Common-Pb corrected in situ U-Pb accessory mineral geochronology by LA-MCICP-MS: *Journal of Analytical Atomic Spectrometry*,**18**, 837–846.

Hudleston, P., 1999. Strain compatibility and shear zones: is there a problem? *Journal of Structural Geology*, **21**, p. 923–932.

Iaccarino, S., Montomoli, C., Carosi, R., Montemagni, C., Massonne, H.J., Langone, A., Jain, A.K.and Visonà, D., 2017. Pressure-Temperature-Deformation-Time Constraints on the South Tibetan Detachment System in the Garhwal Himalaya (NW India): *Tectonics*, 36, 2281–2304.

Iacopini, D., Carosi, R., Montomoli, C. and Passchier, C.W., 2008. Strain analysis and vorticity of flow in the Northern Sardinian Variscan Belt: Recognition of a partitioned oblique deformation event: *Tectonophysics*, **446**, p. 77–96, doi: 10.1016/j.tecto.2007.10.002.

Iacopini, D., Frassi, C., Carosi, R. and Montomoli, C., 2011. Biases in three-dimensional vorticity analysis using porphyroclast system: limits and application to natural examples: *Geological Society, London, Special Publications*, **360**, p. 301–318, doi: 10.1144/SP360.17.

Ildefonse, B., Launeau, P., Bouchez, J.L. and Fernandez, A., 1992. Effect of mechanical interactions on the development of shape preferred orientations: a twodimensional experimental approach: *Journal of Structural Geology*, **14**, 73–83.

Innocent, C., Michard, A., Guerrot, C. and Hamelin, B., 2003. U-Pb zircon age of 548 Ma for the leptynites (high-grade felsic rocks) of the central part of the Maures Massif. Geodynamic significance of the so-called leptyno-amphibolitic complexes of the Variscan belt of western Europe: *Bulletin de la Société Géologique de France*, **174**, p. 585–594.

Jeffery, G., 1922. The motion of ellipsoidal particles immersed in a viscous fluid. *Proceedings of the Royal Society London*, **122**, 161–179.

Jaffey, A.H., Flynn, K.F., Glendenin, L.E., Bentley, C.R. and Essling, A.M., 1971. Precision measurements of half-lives and specific activities of ^{235}U and ^{238}U: *Phys Rev C*, **4**, 1889–1906, doi:10.1103/PhysRevC.4.1889.

Jammes ,S. and Lavier, L.L., 2019. Effect of contrasting strength from inherited crustal fabrics on the development of rifting margins. *Geosphere*, **15**, 2, 1–16, doi.org/10.1130/GES01686.1.

Johnston, S.T., Weil, A.B. and Gutiérrez-Alonso, G., 2013. Oroclines: Thick and thin: *Bulletin*, **125**, p. 643–663.

Jones, R.R. and Tanner, G.P.W., 1995. Strain partitioning in transpression zones: *Journal of Structural Geology*, **17**, p. 793–802, doi: doi: 10.1016/0191-8141(94)00102-6.

Jouffray, F., Spalla, M.I., Lardeaux J.M., Filippi, M., Rebay, G., Corsini, M., Zanoni, D., Zucali, M., Gosso, G., 2020. Variscan eclogites from the Argentera–Mercantour Massif (External Crystalline Massifs, SW Alps): a dismembered cryptic suture zone. *International Journal of Earth Sciences*. doi: 10.1007/s00531-020-01848-2

Kellet, D.A., Cottle, J. M. and Larson, K.P., 2019. The South Tibetan Detachment System: history, advances, definition and future directions: *Geological Society of London Special Publications*, **483**, doi:10.1144/SP483.2.

Kerrich, R., Allison, I., Barnett, R.L., Moss, S. and Starkey, J., 1980. Microstructural and chemical transformations accompanying deformation of a granite in a shear zone at Mie´ville, Switzerland; with implications for stress corrosion cracking and superplastic flow: *Contrib. Mineral. Petrol*, **73**, 221– 242.

Kylander-Clark, A., Hacker, B., Cottle., J.M., 2013. Laser Ablation Split-Stream ICP Petrochronology: *Chemical Geology*, **345**, 99–112. doi: 10.1016/j.chemgeo.2013.02.019.

Kroner, U. and Romer, R.L., 2009. *The Saxo-Thuringian Zone – tip of the Armorican Spur and part of the Gondwana plate*: Schweizerbart, Stuttgart.

Kroner, U. and Romer, R.L., 2013. Two plates — Many subduction zones: The Variscan orogeny reconsidered: *Gondwana Research*, **24**, p. 298–329, doi: 10.1016/j.gr.2013.03.001.

Kroner, U., Roscher, M. and Romer, R.L., 2016. Ancient plate kinematics derived from the deformation pattern of continental crust: Paleo- and Neo-Tethys opening coeval with prolonged Gondwana–Laurussia convergence: *Tectonophysics*, **681**, p. 220–233, doi: 10.1016/j.tecto.2016.03.034.

Kruhl, J.H., 1998. Reply: prism- and basal-plane parallel subgrain boundaries in quartz: a microstructural geothermobarometer: *Journal of Metamorphic Petrology*, **16**, p. 142–146, doi: 10.1046/j.1525-1314.1996.00413.x.

Kurz, G.A. and Northrup, C.J., 2008. Structural analysis of mylonitic rocks in the Cougar Creek Complex, Oregon–Idaho using the porphyroclast hyperbolic distribution method, and potential use of SC′-type extensional shear bands as quantitative vorticity indicators: *Journal of Structural Geology*, **30**, p. 1005–1012, doi: 10.1016/j.jsg.2008.04.003.

Law, R.D., 1990. Crystallographic fabrics: a selective review of their applications to research in structural geology: *Geological Society, London, Special Publications*, **54**, p. 335–352, doi: 10.1144/GSL.SP.1990.054.01.30.

Law, R.D., 2010. Moine Thrust zone mylonites at the Stack of Glencoul: II - results of vorticity analyses and their tectonic significance: *Geological Society, London, Special Publications*, **335**, p. 579–602, doi: 10.1144/SP335.24.

Law, R.D., 2014. Deformation thermometry based on quartz c-axis fabrics and recrystallization microstructures: a review: *Journal of Structural Geology*. **66**, 129–161

Law, R.D., Searle, M.P. and Simpson, R.L., 2004. Strain, deformation temperatures and vorticity of flow at the top of the Greater Himalayan Slab, Everest Massif, Tibet: *Journal of the Geological Society*, **161**, p. 305–320.

Li, P. and Rosenbaum, G., 2014. Does the Manning Orocline exist? New structural evidence from the inner hinge of the Manning Orocline (eastern Australia): *Gondwana Research*, **25**, p. 1599–1613, doi: 10.1016/j.gr.2013.06.010.

Li, P., Rosenbaum, G. and Donchak, P.J.T., 2012. Structural evolution of the Texas Orocline, eastern Australia: *Gondwana Research*, **22**, p. 279–289, doi: 10.1016/j.gr.2011.09.009.

Lister, G.S., 1977. Crossed-girdle c-axis fabrics in quartzites plastically deformed by plane strain and progressive simple shear: *Tectonophysics*, **39**, p. 51–54, doi: 10.1016/0040-1951(77)90087-7.

Lister, G.S. and Dornisiepen, U.F., 1982. Fabric transitions in the Saxony granulite terrain: *Journal of Structural Geology*, **4**, p. 81–92, doi: 10.1016/0191-8141(82)90009-8.

Lister, G.S. and Hobbs, B.E., 1980. The simulation of fabric development during plastic deformation and its application to quartzite: The influence of deformation history: *Journal of Structural Geology*, **2**, p. 355–370, doi: 10.1016/0191-8141(80)90023-1.

Ludwig, K.R., 2003. *Isoplot/Ex Version: A Geochronological Toolkit for Microsoft Excel*:

Maffione, M., Speranza, F., Faccenna, C., Cascella, A., Vignaroli, G. and Sagnotti, L., 2008. A synchronous Alpine and Corsica-Sardinia rotation: *Journal of Geophysical Research*, **113**, doi: 10.1029/2007JB005214.

Malaroda, R., Carraro, F., Dal Piaz, G.V., Franceschetti, B., Sturani, C. and Zanella, E., 1970. Carta geologica del Massiccio dell'Argentera alla scala 1:50.000 e note illustrative: *Memorie della Società Geologica Italiana*, **9**, p. 557–663.

Mammoliti, E., 2015. La "Ferriere-Mollières Shear Zone" (Massiccio dell'Argentera, Alpi Occidentali): rilevamento, analisi strutturale e cinematica del flusso nella zona di Ferriere (Argentera, CN): Unpublished Thesis, Università degli Studi di Pisa (Italy), pp 217.

Matte, P., 1986a. La Chaîne varisque parmi les chaînes paléozoïques péri-atlantiques, modèle d'évolution et position des grands blocs continentaux au Permo-Carbonifère: *Bulletin de la Société géologique de France*, **8**, p. 4–24.

Matte, P., 1986b. Tectonics and plate tectonics model for the Variscan belt of Europe: *Tectonophysics*, **126**, p. 329–374.

Matte, P., 2001. The Variscan collage and orogeny (480–290 Ma) and the tectonic definition of the Armorica microplate: a review: *Terra nova*, **13**, p. 122–128.

Matte, P. and Ribeiro, A., 1975. Forme et orientation de l'ellipsoïde de déformation dans la virgation hercynienne de Galice. Relations avec le plissement et hypothèses sur la genèse de l'arc ibéro-armoricain: *CR Acad Sci Paris*, **280**, p. 2825–2828.

McDonough, W.F. and Sun, S.S., 1995. The composition of the Earth. *Chem Geol*, **120**, 223–253.

Mckinney, S.T., Cottle, J.M. and Lederer, G.W., 2015. Evaluating rare earth element (REE) mineralization mechanisms in Proterozoic gneiss, Music Valley, California: *Geological Society of America Bulletin*, **127**, 1135 – 1152.

Misra, S., Burg, J.-P., Vigneresse, J.-L. and Mainprice, D., 2014. Rheological transition during large strain deformation of melting and crystallizing metapelites: MELTING AND CRYSTALLIZING ROCK RHEOLOGY: *Journal of Geophysical Research: Solid Earth*, **119**, p. 3971–3985, doi: 10.1002/2013JB010777.

Monié, P. and Maluski, H., 1983. Données géochronologiques 39Ar/40Ar sur le socle ante Permien du massif de l'Argentera-Mercantour (Alpes-Maritimes, France): *Bull. Soc. Géol. France*, **7**, 247–257.

Montomoli, C., Iaccarino, S., Carosi, R., Langone, A. and Visonà, D., 2013. Tectonometamorphic discontinuities within the Greater Himalayan Sequence in Western Nepal (Central Himalaya): Insights on the exhumation of crystalline rocks: *Tectonophysics*, **608**, p. 1349–1370, doi: 10.1016/j.tecto.2013.06.006.

Montomoli, C., Iaccarino, S., Simonetti, M., Lezzerini, M. and Carosi, R., 2018. Structural setting, kinematics and metamorphism in a km-scale shear zone in the Inner Nappes of Sardinia (Italy): *Italian Journal of Geoscience*, **137**, 294-310.

Morgan, S.S. and Law, R.D., 2004. Unusual transition in quartzite dislocation creep regimes and crystal slip systems in the aureole of the Eureka Valley–Joshua Flat–Beer Creek plúton, California: a case for anhydrous conditions created by decarbonation reactions. *Tectonophysics*, **384**, 209–231.

Morillon, A.C., Féraud, G., Sosson, M., Ruffet, G., Crevola, G. and Lerouge, G., 2000. Diachronous cooling on both side of a major strike-slip fault in the Variscan Maures massif (SE France), as deduced from a detailed $^{40}Ar/^{39}Ar$ study: *Tectonophysics*, **321**, 103–126.

Moussavou, M., 1998. Contribution à l'histoire thermo-tectonique varisque du massif des Maures par la typologie du zircon et la géochronologie U/Pb sur minéraux accessoires: PhD Thesis, University of Montpellier, France, pp187.

Mulchrone, K.F., 2007a. An analytical solution in 2D for the motion of rigid elliptical particles with a slipping interface under a general deformation: *Journal of Structural Geology*, **29**, p. 950–960, doi: 10.1016/j.jsg.2007.03.008.

Mulchrone, K.F., 2007b. Shape fabrics in populations of rigid objects in 2D: Estimating finite strain and vorticity: *Journal of Structural Geology*, **29**, p. 1558–1570, doi: 10.1016/j.jsg.2007.06.006.

Musumeci, G. and Colombo, F., 2002. Late Visean mylonitic granitoids in the Argentera Massif (western Alps, Italy): age and kinematic constraints on the Ferrière–Mollières shear zone: *Comptes Rendus Geoscience*, **334**, p. 213–220.

Muttoni, G., Gaetani, M., Kent, D.V., Sciunnach, D., Angiolini, L., Berra, F., Garzanti, E., Mattei, M. and Zanchi, A., 2009. Opening of the Neo-Tethys Ocean and the Pangea B to Pangea A transformation during the Permian: *GeoArabia*, **14**, p. 17–48.

Muttoni, G., Kent, D.V., Garzanti, E., Brack, P., Abrahamsen, N. and Gaetani, M., 2003. Early Permian Pangea 'B' to Late Permian Pangea 'A'☆: *Earth and Planetary Science Letters*, **215**, p. 379–394, doi: 10.1016/S0012-821X(03)00452-7.

Oliot, E., Melleton, J., Schneider, J., Corsini, M., Gardien, V. and Rolland, Y., 2015. Variscan crustal thickening in the Maures-Tanneron massif (South Variscan belt, France): new in situ monazite U-Th-Pb chemical dating of high-grade rocks: *Bulletin de la Société géologique de France*, **186**, p. 145–169, doi: 10.2113/gssgfbull.186.2-3.145.

Padovano, M., Dörr, W., Elter, F.M. and Gerdes, A., 2014. The East Variscan Shear Zone: Geochronological constraints from the Capo Ferro area (NE Sardinia, Italy): *Lithos*, **196**–**197**, p. 27–41, doi: 10.1016/j.lithos.2014.01.015.

Padovano, M., Elter, F.M., Pandeli, E. and Franceschelli, M., 2012. The East Variscan Shear Zone: new insights into its role in the Late Carboniferous collision in southern Europe: *International Geology Review*, **54**, p. 957–970, doi: 10.1080/00206814.2011.626120.

Padovano, M., Elter, F.M., Pandeli, E. and Franceschelli, M., 2011. The East Varisican Shear Zone: new insights into its role in the Late Carboniferous collision in southern Europe: *Int Geol Rev*, **54**, 957-970.

Paquette, J.L. and Tiepolo M., 2007. High resolution (5 μm) U–Th–Pb isotope dating of monazite with excimer laser ablation (ELA)–ICPMS: *Chemical Geology*, **240**, 222–237.

Parsons, A.J., Coleman, M.J., Ryan, J.J., Zagorevski, A., Joyce, N.L., Gibson, H.D. and Larson, K.P., 2018. Structural evolution of a crustal-scale shear zone through a decreasing temperature regime: The Yukon River shear zone, Yukon-Tanana terrane, Northern Cordillera: *Lithosphere*,, doi: 10.1130/L724.1.

Passchier, C.W., 1987. Stable position of rigid objects in non-coaxial flow: a study in vorticity analysis: *Journal of Structural Geology*, **9**, p. 679–690.

Passchier, C.W., 1988. Analysis of deformation paths in shear zones: *Geologische Rundschau*, **77**, 309-318.

Passchier, C.W. and Trouw, R.A.J., 2005. *Microtectonics*: Springer, Berlin.

Pastor-Galán, D., Groenewegen, T., Brouwer, D., Krijgsman, W. and Dekkers, M.J., 2015a. One or two oroclines in the Variscan orogen of Iberia? Implications for Pangea amalgamation: *Geology*, **43**, p. 527–530, doi: 10.1130/G36701.1.

Pastor-Galán, D., Ursem, B., Meere, P.A. and Langereis, C., 2015b. Extending the Cantabrian Orocline to two continents (from Gondwana to Laurussia). Paleomagnetism from South Ireland: *Earth and Planetary Science Letters*, **432**, p. 223–231, doi: 10.1016/j.epsl.2015.10.019.

Paton, C., Woodhead, J.D., Hellstrom, J.C., Hergt, J.M., Greig, A. and Maa, R., 2010. Improved laser ablation U-Pb zircon geochronology through robust downhole fractionation correction: *Geochem Geophys Geosyst*, **11**, 3, 36, doi:10.1029/2009GC002618.

Paquette, J.L., Ménot, R.P. and Peucat, J.J., 1989. REE, Sm–Nd and U–Pb zircon study of eclogites from the Alpine external massifs (Western Alps): evidence for crustal contamination: *Earth and Planetary Science Letters*, **96**, 181–189.

Pereira, M.F., Apraiz, A., Silva, J.B. and Chichorro, M., 2008. Tectonothermal analysis of high-temperature mylonitization in the Coimbra–Córdoba shear zone (SW Iberian Massif, Ouguela tectonic unit, Portugal): Evidence of intra-continental transcurrent transport during the amalgamation of Pangea: *Tectonophysics*, **461**, p. 378–394, doi: 10.1016/j.tecto.2007.11.042.

Pereira, M.F., Silva, J.B., Drost, K., Chichorro, M. and Apraiz, A., 2010. Relative timing of transcurrent displacements in northern Gondwana: U–Pb laser ablation ICP-MS zircon and monazite geochronology of gneisses and sheared granites from the western Iberian Massif (Portugal): *Gondwana Research*, **17**, p. 461–481, doi: 10.1016/j.gr.2009.08.006.

Pfiffner, O.A. and Ramsay, J.G., 1982. Constraints on geological strain rates: Arguments from finite strain rates of naturally deformed rocks: *J. Geoph. Res. Solid Earth*, **87**, 311-321.

Piazolo, S. and Passchier, C.W., 2002. Experimental modeling of viscous inclusions in a circular high-strain shear rig: Implications for the interpretation of shape fabrics and deformed enclaves: EXPERIMENTAL MODELING OF VISCOUS INCLUSIONS: *Journal of Geophysical Research: Solid Earth*, **107**, p. ETG 11-1-ETG 11-15, doi: 10.1029/2000JB000030.

Pillaud, C. 1991. Structures de dèformation alpine dans le synclinal de permo-carbonifère de Salvan-Dorenaz (massif de Aiguilles Rouges): *Memoires de Géologie (Lausanne,)* **9**, 1-100.

Platt, J.P. and Vissers, R.L.M., 1980. Extensional structures in anisotropic rocks: *Journal of Structural Geology*, **2**, p. 397–410, doi: 10.1016/0191-8141(80)90002-4.

Platt, J.P. and Behrmann, J.H., 1986. Structures and fabrics in a crustal scale shear zone, Betic Cordilleras, S.E. Spain: *Journal of Structural Geology*, **8**, 15-34.

Pohl, F., Froitzheim, N., Obermüller, G., Tomaschek, F., Schröder, O., Nagel, T.J., Sciunnach, D. and Heuser, A., 2018. Kinematics and Age of Syn-Intrusive Detachment Faulting in the Southern Alps:

Evidence for Early Permian Crustal Extension and Implications for the Pangea A Versus B Controversy: *Tectonics*, **37**, p. 3668–3689, doi: 10.1029/2018TC004974.

Polino, R., Dal Piaz, G.V. and Gosso, G., 1990. Tectonic erosion at the Adria margin and accretionary processes for the Cretaceous orogeny of the Alps: *Mémoires de la Société Géologique de France*, **156**, 345–367.

Pyle, J.M. and Spear, F.S., 1999. Yttrium zoning in garnet: coupling of major and accessory phases during metamorphic reactions: *Geological Materials Research*, **1**, p. 1–49.

Pyle, J.M., Spear, F.S., Rudnick, R.L. and McDonough, W.F., 2001. Monazite–Xenotime–Garnet Equilibrium in Metapelites and a New Monazite–Garnet Thermometer: *Journal of Petrology*, **42**, p. 2083–2107.

Ramsay, J.G. and Huber, M.I., 1987. *The Techniques of Modern Structural Geology, Vol. 2: Folds and Fractures*: Academic Press, London.

Ree, J.H., 1991. An experimental steady-state foliation: *Journal of Structural Geology*,**13**, 1001-1011.

Vauchez, A. and Bufalo, M., 1985. La limite Maures occidentales–Maures orientales (Var, France): un décrochement ductile senestre majeur entre deux provinces structurales contrastées: *C R Acad Sci Paris série II*, **301**,14, 1059-1062.

Vauchez, A. and Bufalo, M., 1988. Charriage crustal, anatexie et décrochements ductiles dans les Maures orientales (Var, France) au cours de l'orogenèse varisque: *Geol Runds*, **77**, 1, 45-62

Ricci, C.A. and Sabatini, G., 1978. Petrogenetic affinity and geodynamic significance of metabasic rocks from Sardinia, Corsica and provence: *Neues Jahrbuch fur Geologie und Palaeontologie Monatschefte*, **1**, p. 23–38.

Rolland, Y., Corsini, M. and Demoux, A., 2009. Metamorphic and structural evolution of the Maures-Tanneron massif (SE Variscan chain): evidence of doming along a transpressional margin: *Bulletin de la Société géologique de France*, **180**, p. 217–230, doi: 10.2113/gssgfbull.180.3.217.

Rollet, N., Déverchère, J., Beslier, M.-O., Guennoc, P., Réhault, J.-P., Sosson, M. and Truffert, C., 2002. Back arc extension, tectonic inheritance, and volcanism in the Ligurian Sea, Western Mediterranean: LIGURIAN SEA BACK ARC STRUCTURE AND EVOLUTION: *Tectonics*, **21**, p. 6-1-6–23, doi: 10.1029/2001TC900027.

Rosenbaum, G., Lister, G.S. and Duboz, C., 2002. Reconstruction of the tectonic evolution of the western Mediterranean since the Oligocene: *Journal of the Virtual Explorer*, **08**, doi: 10.3809/jvirtex.2002.00053.

Rosenberg, C.L. and Handy, M.R., 2005. Experimental deformation of partially melted granite revisited: implications for the continental crust. J metamorphic Geol, 23, 19–28, doi:10.1111/j.15251314.2005.00555.x.

Rubatto, D., Hermann, J., Buick, I.S., 2006. Temperature and bulk composition control on the growth of monazite and zircon during low-pressure anatexis (Mount Stafford, central Australia): *J Petrol*, **47**, 1973–1996.

Rubatto, D., Ferrando, S., Compagnoni, R. and Lombardo, B., 2010. Carboniferous high-pressure metamorphism of Ordovician protoliths in the Argentera Massif (Italy), Southern European Variscan belt: *Lithos*, **116**, p. 65–76, doi: 10.1016/j.lithos.2009.12.013.

Rubatto, D., Chakraborty, S. and Dasgupta, S., 2013. Timescales of crustal melting in the Higher Himalayan Crystallines (Sikkim, Eastern Himalaya) inferred from trace element-constrained monazite and zircon chronology: *Contrib Mineral Petr*, 165, 2, 349-372.

Rubatto, D., Schaltegger, U., Lombardo, D., Colombo, F. and Compagnoni, R., 2001. Complex Paleozoic magmatic and metamorphic evolution in the Argentera massif (Western Alps), resolved with U-Pb dating: *Schweizerische mineralogische und petrographische Mitteilungen*, **81**, p. 213–228.

Rumelhart, P.E, Yin, A., Cowgill, E., Butler, R., Zhang, Q. and Wang, X.-F., 1999. Cenozoic vertical-axis rotation of the Altyn Tagh fault system: *Geology*, **27**, 819 – 822.

Sanchez, G., Rolland, Y., Schneider, J., Corsini, M., Oliot, E., Goncalves, P., Verati, C., Lardeaux, J.-M. and Marquer, D., 2011. Dating low-temperature deformation by 40Ar/39Ar on white mica, insights from the Argentera-Mercantour Massif (SW Alps): *Lithos*, **125**, p. 521–536, doi: 10.1016/j.lithos.2011.03.009.

Sanderson, D. and Marchini, R.D., 1984. Transpression: *Journal of Structural Geology*, **6**, 449-458.

Schmid, S.M. and Casey, M., 1986. Complete fabric analysis of some commonly observed quartz C-axis patterns. In: *Geophysical Monograph Series* (Hobbs, B.E., and Heard, H.C., eds.) American Geophysical Union, Washington, D. C., p. 263–286.

Schneider, J., Corsini, M., Reverso-Peila, A. and Lardeaux, J.-M., 2014. Thermal and mechanical evolution of an orogenic wedge during Variscan collision: an example in the Maures–Tanneron Massif (SE France): *Geological Society, London, Special Publications*, **405**, p. 313–331, doi: 10.1144/SP405.4.

Schulmann, K., Konopásek, J., Janoušek, V., Lexa, O., Lardeaux, J.-M., Edel, J.-B., Pavla Štípská, and Ulrich, S., 2009. An Andean type Palaeozoic convergence in the Bohemian Massif: *Comptes Rendus Geosci*, **341**, 266–286. doi:http://dx.doi.org/10.1016/j.crte.2008.12 .006.

Scotese, C.R. and McKerrow, W.S., 1990. Revised world maps and introduction. In: W.S. McKerrow and C.R.Scotese (eds), Palaezoic Palaegeography and Bio- geography*: Mem. Geol. Soc. London*, **12**, 1-21.

Seydoux-Guillaume, A.M., Paquette, J.L., Wiedenbeck, M., Montel, J.M. and Heinrich W., 2002a. Experimental resetting of the U–Th–Pb system in monazite: *Chemical Geology*, **191**, 165–181.

Seydoux-Guillaume, A.M., Wirth, R., Nasdala, L., Gottschalk, M., Montel ,J.M. and Heinrich W., 2002b. XRD, TEM and Raman study of experimental annealing of natural monazite: *Physics and Chemistry of Minerals*, **29**, 240–253.

Shaw, J. and Johnston, S., 2012. The Carpathian–Balkan bends: an oroclinal record of ongoing Arabian–Eurasian collision. In: (Ed.) Johnston, S. and Rosenbaum, G., Oroclines, *Journal of the Virtual Explorer*, **43**, 4, doi:10.3809/jvirtex.2012.00310.

Shimizu, I., 2008. Theories and applicability of grain size piezometers, the role of dynamic recrystallization mechanisms: *Journal of Structural Geology*, 30, 899-917, doi:10.1016/j.jsg.2008.03.004.

Simonetti, M., 2015. La 'Ferriere-Mollieres Shear Zone' (Massiccio dell' Argentera, Alpi Occidentali): rilevamento geologico, analisi strutturale e cinematica del flusso nella zona del Vallone di Pontebernardo (Pietraporzio, CN): Unpublished Thesis, Università degli Studi di Torino (Italy), pp 182.

Simonetti, M., Carosi, R. and Montomoli, C., 2017. Variscan shear deformation in the Argentera Massif: a field guide to the excursion in the Pontebernardo Valley (CN, Italy): *Atti della Società toScana di*

Scienze Naturali Residente in Pisa. Memorie. Serie a, **124**, p. 151–169, doi: 10.2424/ASTSN.M.2017.25.

Simonetti, M., Carosi, R., Montomoli, C., Langone, A., D'Addario, E. and Mammoliti, E., 2018. Kinematic and geochronological constraints on shear deformation in the Ferriere-Mollières shear zone (Argentera-Mercantour Massif, Western Alps): implications for the evolution of the Southern European Variscan Belt: *International Journal of Earth Sciences*,, doi: 10.1007/s00531-018-1593-y.

Simonetti, M., Carosi, R., Montomoli, C., Corsini, M., Petroccia, A., Cottle, J.M. and Iaccarino, S., submitted. Timing and kinematics of flow in a transpressive dextral shear zone, Maures Massif (Southern France). *International Journal of Earth Science*.

Simonetti, M., Carosi, R., Montomoli, C., Cottle, J.M. and Law, R.D, submitted. Transpressive deformation in the Southern European Variscan Belt: new insights from the Aiguilles Rouges Massif (Western Alps).*Tectonics*.

Simpson, C. and De Paor, D.G., 1993. Strain and kinematic analysis in general shear zones: *Journal of Structural Geology*, **15**, p. 1–20, doi: 10.1016/0191-8141(93)90075-L.

Skrzypek, E., Stìpskà, P. and Cocherie, A., 2012. The origin of zircon and the significance of U–Pb ages in high-grade metamorphic rocks: a case study from the Variscan orogenic root (Vosges Mountains, NE France): *). Contributions to Mineralogy and Petrology*, **164**, p. 935–957.

Soliva, R., Benedicto, A. and Maerten, L., 2006. Spacing and linkage of confined normal faults: importance of mechanical thickness*: J Geophys Res*, **111**, B1, doi. org/10.1029/2004JB003507.

Stampfli, G.M., Borel, G.D., Marchant, R. and Mosar, J., 2002. Western Alps geological constraints on western Tethyan reconstructions: *Journal of the Virtual Explorer*, **8**, p. 77.

Stahr, D.W. and Law, R.D., 2011. Effect of finite strain on clast-based vorticity gauges: *Journal of Structural Geology*, **33**, 1178–1192, doi.org/10.1016/j.jsg.2011.05.002.

Stipp, M., Stunitz, H., Heilbronner, R. and Schmid, S.M., 2002. The eastern Tonale fault zone: A 'natural laboratory' for crystal plastic deformation of quartz over a temperature range from 250 to 700°C: *Journal of Structural Geology*, **24**, p. 1864–1884.

Stipp, M. and Tullis, J., 2003. The recrystallized grain size piezometer for quartz: *Geophysical Research Letters*, **30**, doi: 10.1029/2003GL018444.

Stipp, M., Tullis, J. and Behrens, H., 2006. Effect of water on the dislocation creep microstructure and flow stress of quartz and implications for the recrystallized grain size piezometer: *J. Geoph. Res.*, **111**, B04201, doi:10.1029/2005JB003852.

Stipp, M., Tullis, J., Scherwath, M. and Behrmann, J.H., 2010. A new perspective on paleopiezometry: Dynamically recrystallized grain size distributions indicate mechanism changes: *Geology*, **38**, 8, 759-762, doi:10.1130/G31162.1.

Stipp, M., 2012. Stress Measurements in the Earth's Crust – Recrystallized Grain Size Piezometry Revisited. *Geoph. Res. Abstracts*, **14**, 13016.

Tapponnier, P. and Molnar, P.J., 1977. Active faulting and tectonics in China: *J Geophys Res*, **82**, 2905–2930.

Tapponnier, P., Peltzer, G., Le Dain, A.Y., Armijo, R. and Cobbold, P. 1982. Propagating extrusion tectonics in Asia: new insights from simple experiments with plasticine: *Geology*, **10**, 611–616.

Thomas, J.C., Claudel, M.E., Collombet, M., Tricart, P., Chauvin, A. and Dumont, T., 1999. First paleomagnetic data from the sedimentary cover of the French penninic Alps: Evidence for Tertiary counterclockwise rotations in the western Alps: *Earth and Planetary Science Letters*, **171**, p. 561–574.

Thompson, A.B., Schulmann, K. and Jezek, J., 1997. Thermal evolution and exhumation in obliquely convergent (transpressive) orogens: *Tectonophysics*, **280**, 171-184.

Tiepolo, M., 2003. In situ Pb geochronology of zircon with laser ablation–inductively coupled plasma-sector field mass spectrometry: *Chemical Geology*, **199**, 159–177.

Tikoff, B. and Fossen, H., 1995. The limitations of three-dimensional kinematic vorticity analysis: *Journal of Structural Geology*, **17**, p. 1771–1784.

Tollmann, A., 1982. Großraumiger variszischer Deckenbau im Moldanubikum und neue Gedanken zum Variszikum Europas: *Geotektonische Forschungen*, **64**, p. 1–91.

Trudgill, B. and Cartwright, J., 1994. Relay-ramp forms and normal-fault linkages, Canyonlands National Park, Utah: Geol. Soc. Am. Bull, 106, 1143–1157.

Tullis, J., Christie, J.M. and Griggs, D.T., 1973. Microstructures and preferred orientations of experimentally deformed quartzites: *Geological Society of America Bulletin*, **84**, p. 297–314.

Turco, E., Macchiavelli, C., Mazzoli, S., Schettino, A. and Pierantoni, P.P., 2012. Kinematic evolution of Alpine Corsica in the framework of Mediterranean mountain belts: *Tectonophysics*, **579**, p. 193–206, doi: 10.1016/j.tecto.2012.05.010.

Twiss, R.J., 1977. Theory and applicability of a recrystallized grain size paleopiezometer: *Pure and Applied Geophysics*, **115**, 227-244, doi:10.1007/BF01637105.

Van Actherbergh, E., Ryan, C. G., Jackson, S. E. and Griffin W., 2001. Data reduction software for LA–ICP–MS. In: Sylvester, P. (Ed.), Laser Ablation ICPMS in the Earth Sciences: *Mineralogical Association of Canada*, Short Course Series, **29**, 239 - 243.

Vollomer, F.W., 2015. *EllipseFit 3.2*: http://www.frederickvollmer.com/ellipsefit/.

Von Raumer, J.F., 1983. Die Metapelite von Emosson (Aiguilles- Rouges-Massiv) als Beispiel spätkaledonisch-frühvariszicher Metamorphose im Altkristallin des helvetischen Bereichs: *Schweizerische Mineralogische und Petrographische Mitteilungen*, **63**, p. 421–455.

Von Raumer, J.F. and Schwander, H.W., 1985. Garnet evolution in pre-Variscan pelitic rocks from the Lake Emosson area, Aiguilles Rouges Massif, Western Alps: *Journal of Metamorphic Geology*, **3**, p. 467–479.

Von Raumer, J., Abrecht, J., Bussy, F., Lombardo, B., Ménot, R.P. and Schaltegger, U., 1999. The Paleozoic metamorphic evolution of the Alpine external massifs: *Schweizerische Mineralogische und Petrographische Mitteilungen*, **79**, p. 5–22.

Von Raumer, J. and Bussy, F., 2004. Mont Blanc and Aiguilles Rouges geology of their polimetamorphic basement: *Mémoires de Géologie (Lausanne)*, 42, 210 pp.

Von Raumer, J., Dobmeier, C. and Bussy, F., 2003. Variscan structures in the Aiguilles Rouges-Mont Blanc areas (External Massifs, Alps): *Zentralblatt fur Geologie un Palaontologie*, **1**, p. 237–242.

Von Raumer, J.F., Bussy, F., Schaltegger, U., Schulz, B. and Stampfli, G.M., 2013. Pre-Mesozoic Alpine basements—Their place in the European Paleozoic framework: *Geological Society of America Bulletin*, **125**, p. 89–108, doi: 10.1130/B30654.1.

Wallis, S.R., Platt, J.P. and Knott, S.D., 1993. Recognition of syn-convergence extension in accretionary wedges with examples from Calabrian arc and the Eastern Alps: *American Journal of Sciences*, **293**, p. 463–495.

Wallis, S.R., 1995. Vorticity analysis and recognition of ductile extension in the Sanbagawa belt, SW Japan: *Journal of Structural Geology*, **17**, 1077-1093.

Walsh, J.J., Nicol, A. and Childs, C., 2002. An alternative model for the growth of faults: *Journal of Structural Geology*, **24**, 1669–1675.

Walsh, J.J., Bailey, W.R., Childs, C., Nicol, A. and Bonson, C.G., 2003. Formation of segmented normal faults: a 3-D perspective: *Journal of Structural Geology*, **25**, 1251–1262.

Weinberg, R.F., 2016. Himalayan leucogranites and migmatites: nature, timing and duration of anatexis: *Journal of Metamorphic Geology*, **34**, 821–843, doi:10.1111/jmg.12204.

Williams, M.L., Jercinovic, M.J. and Hetherington, C.J., 2007. Microprobe Monazite Geochronology: Understanding Geologic Processes by Integrating Composition and Chronology: *Annual Review of Earth and Planetary Sciences*, **35**, p. 137–175, doi: 10.1146/annurev.earth.35.031306.140228.

White, R. D., 1986. The effects of strain on the microstructures, fabrics, and deformation mechanisms in quartzites: *Philosophical Transactions Royal Society London*, **283**, 69–86.

Xypolias, P., 2010. Vorticity analysis in shear zones: A review of methods and applications: *Journal of Structural Geology*, **32**, 2072–2092, doi: 10.1016/j.jsg.2010.08.009.

	$^{207}Pb/^{206}Pb$			$^{207}Pb/^{235}U$			$^{206}Pb/^{238}U$			$^{208}Pb/^{232}Th$			Ages							
Identifier	Ratio	1s %	1s % (Prop	Ratio	1s %	1s % (Prop	Ratio	1s %	1s % (Prop	Ratio	1s %	1s % (Prop	$^{207}Pb/^{206}Pb$	1s abs	$^{207}Pb/^{235}U$	1s abs	$^{206}Pb/^{238}U$	1s abs	$^{208}Pb/^{232}Th$	1s abs
Ju08a001	0.05630	0.06%	0.10%	0.64227	0.77%	1.14%	0.08274	0.10%	0.11%	0.02538	0.04%	0.04%	464	8	504	9	512	7	507	9
Ju08a003	0.05708	0.06%	0.10%	0.65076	0.80%	1.18%	0.08270	0.11%	0.11%	0.02535	0.04%	0.04%	495	9	509	9	512	7	506	9
Ju08a004	0.05629	0.06%	0.10%	0.63652	0.78%	1.15%	0.08203	0.10%	0.11%	0.02501	0.04%	0.04%	464	8	500	9	508	7	499	9
Ju08a015	0.05790	0.06%	0.10%	0.65608	0.86%	1.22%	0.08220	0.11%	0.12%	0.02522	0.04%	0.04%	526	9	512	10	509	7	503	9
Ju08a016	0.05609	0.06%	0.10%	0.64304	0.85%	1.20%	0.08316	0.11%	0.12%	0.02493	0.04%	0.04%	456	8	504	9	515	7	498	9
Ju08a017	0.05580	0.06%	0.10%	0.63342	0.84%	1.19%	0.08234	0.11%	0.12%	0.02561	0.04%	0.04%	444	8	498	9	510	7	511	9
Ju08b001	0.05758	0.06%	0.14%	0.65908	0.87%	1.60%	0.08304	0.11%	0.14%	0.02527	0.04%	0.04%	514	12	514	12	514	9	504	9
Ju08b002	0.05519	0.06%	0.13%	0.63537	0.85%	1.54%	0.08352	0.11%	0.14%	0.02553	0.04%	0.04%	420	10	499	12	517	9	510	9
Ju08b003	0.05652	0.06%	0.14%	0.63603	0.85%	1.54%	0.08165	0.11%	0.14%	0.02510	0.04%	0.04%	473	11	500	12	506	9	501	8
Ju08b004	0.05674	0.07%	0.14%	0.64005	0.86%	1.56%	0.08185	0.11%	0.14%	0.02507	0.04%	0.04%	481	12	502	12	507	9	500	8
Ju08b013	0.05737	0.07%	0.14%	0.64299	0.91%	1.59%	0.08135	0.11%	0.14%	0.02499	0.03%	0.04%	506	12	504	12	504	9	499	8
Ju08b014	0.05797	0.07%	0.14%	0.66486	0.95%	1.65%	0.08325	0.11%	0.15%	0.02562	0.04%	0.04%	529	13	518	13	515	9	511	9
Ju08b015	0.05482	0.07%	0.13%	0.62971	0.91%	1.57%	0.08337	0.11%	0.15%	0.02516	0.03%	0.04%	405	10	496	12	516	9	502	8
Ju08c002	0.05705	0.06%	0.11%	0.64522	0.85%	1.45%	0.08209	0.11%	0.15%	0.02516	0.03%	0.04%	493	9	506	11	509	9	502	8
Ju08c003	0.05590	0.06%	0.10%	0.63972	0.84%	1.43%	0.08303	0.11%	0.15%	0.02523	0.03%	0.04%	448	8	502	11	514	9	504	8
Ju08c004	0.05766	0.07%	0.11%	0.65281	0.89%	1.48%	0.08217	0.11%	0.15%	0.02544	0.04%	0.04%	517	10	510	12	509	9	508	8
Ju08c013	0.05615	0.07%	0.11%	0.62536	0.88%	1.43%	0.08075	0.11%	0.15%	0.02484	0.03%	0.04%	458	9	493	11	501	9	496	8
Ju08c014	0.05742	0.07%	0.11%	0.65902	0.95%	1.53%	0.08325	0.11%	0.15%	0.02537	0.03%	0.04%	508	10	514	12	515	9	506	8
Ju08c015	0.05570	0.07%	0.11%	0.64087	0.93%	1.49%	0.08345	0.11%	0.15%	0.02541	0.04%	0.04%	440	9	503	12	517	9	507	8
No23a00	0.05641	0.06%	0.07%	0.64883	0.85%	1.22%	0.08347	0.11%	0.14%	0.02531	0.00032	0.00037	469	6	508	10	517	9	505	7
No23a00	0.05675	0.06%	0.07%	0.63471	0.85%	1.21%	0.08113	0.11%	0.14%	0.02501	0.00032	0.00037	482	6	499	10	503	9	499	7
No23a00	0.05671	0.06%	0.07%	0.65188	0.87%	1.24%	0.08336	0.12%	0.15%	0.02557	0.00032	0.00037	480	6	510	10	516	9	510	7
No23a00	0.0563	0.06%	0.07%	0.63964	0.86%	1.22%	0.08241	0.12%	0.15%	0.02515	0.00032	0.00037	464	6	502	10	510	9	502	7
No23a02	0.05692	0.06%	0.07%	0.65378	0.93%	1.29%	0.0833	0.12%	0.15%	0.02544	0.00032	0.00037	488	6	511	10	516	9	508	7
No23a02	0.057	0.06%	0.07%	0.65193	0.91%	1.27%	0.08295	0.12%	0.15%	0.02515	0.00032	0.00037	492	6	510	10	514	9	502	7
No23a02	0.05599	0.06%	0.07%	0.6331	0.89%	1.24%	0.082	0.12%	0.15%	0.02532	0.00032	0.00037	452	6	498	10	508	9	505	7
No23b00	0.05627	0.06%	0.07%	0.63949	0.93%	1.03%	0.08245	0.12%	0.12%	0.02519	0.00032	0.00039	463	6	502	8	511	8	503	8
No23b00	0.05716	0.06%	0.07%	0.64833	0.91%	1.02%	0.08229	0.12%	0.12%	0.0256	0.00033	0.0004	498	6	507	8	510	8	511	8
No23b00	0.05618	0.06%	0.07%	0.64229	0.91%	1.02%	0.08294	0.12%	0.12%	0.02499	0.00032	0.00039	459	6	504	8	514	8	499	8
No23b00	0.05676	0.06%	0.07%	0.64873	0.89%	1.01%	0.08291	0.12%	0.12%	0.02554	0.00032	0.00039	482	6	508	8	513	8	510	8
No23b02	0.05627	0.07%	0.08%	0.63878	0.95%	1.06%	0.08233	0.12%	0.13%	0.02532	0.00031	0.00038	463	6	502	8	510	8	505	8
No23b02	0.05664	0.06%	0.07%	0.64804	0.93%	1.04%	0.08297	0.12%	0.13%	0.02527	0.00031	0.00038	478	6	507	8	514	8	504	8

Appendix A: full dataset standards analyzed during dating with LA-ICP-MS

													Age	1	Age	1	
SAMPLE	$^{207}Pb/^{235}U$	2σ	$^{206}Pb/^{238}U$	2σ	rho	$^{238}U/^{206}Pb$	2σ	$^{207}Pb/^{206}Pb$	2σ	rho	$^{208}Pb/^{232}Th$	2σ	$^{208}Pb/^{232}Th$	2σ	7-corr	2σ	Concordance
554-1	0.186	0.032	0.01	0.00	0.27	102.46	5.73	0.142	0.024	0.05	0.0024	0.0001	48	1	55	4	0.36
554-10	0.121	0.023	0.01	0.00	0.22	195.69	10.70	0.181	0.033	0.09	0.0014	0.0000	28	1	27	2	0.28
554-11	0.164	0.026	0.01	0.00	0.20	97.37	5.39	0.122	0.019	0.15	0.0024	0.0001	48	2	60	4	0.43
554-11	0.151	0.026	0.01	0.00	0.16	112.36	5.99	0.126	0.021	0.10	0.0024	0.0001	48	1	51	3	0.40
554-12	0.134	0.025	0.01	0.00	0.21	106.72	5.24	0.103	0.018	-0.02	0.0024	0.0001	48	1	56	3	0.47
554-13	0.066	0.012	0.01	0.00	0.06	126.10	4.71	0.062	0.011	0.14	0.0021	0.0001	42	1	50	2	0.78
554-14	0.130	0.019	0.01	0.00	0.09	118.20	5.68	0.113	0.018	0.23	0.0024	0.0001	48	2	50	3	0.44
554-15	0.147	0.018	0.01	0.00	0.25	115.07	6.02	0.123	0.016	0.27	0.0024	0.0001	48	2	50	3	0.40
554-2	0.189	0.030	0.01	0.00	0.15	105.04	5.49	0.140	0.023	0.12	0.0024	0.0001	48	2	54	3	0.35
554-3	0.137	0.025	0.01	0.00	0.13	110.62	5.93	0.112	0.021	0.08	0.0023	0.0001	47	2	53	3	0.44
554-4	0.152	0.024	0.01	0.00	0.42	157.73	10.44	0.170	0.025	0.00	0.0018	0.0001	37	2	34	3	0.28
554-5	0.181	0.032	0.01	0.00	0.36	103.84	5.78	0.140	0.023	0.29	0.0023	0.0001	47	2	54	4	0.37
554-6	0.056	0.004	0.01	0.00	0.29	151.06	4.57	0.062	0.004	0.12	0.0021	0.0001	43	1	42	1	0.77
554-7	0.127	0.017	0.01	0.00	0.31	118.20	5.06	0.105	0.013	-0.04	0.0022	0.0001	44	1	50	2	0.45
554-8	0.078	0.018	0.01	0.00	-0.05	177.31	10.37	0.093	0.022	0.34	0.0016	0.0001	32	1	34	2	0.48
554-9	0.051	0.004	0.01	0.00	0.43	155.28	4.59	0.057	0.004	-0.04	0.0020	0.0001	39	1	41	1	0.82
FC-1	0.057	0.003	0.01	0.00	0.95	110.74	4.72	0.046	0.001	-0.05	0.0027	0.0001	55	2	58	2	1.02
FC-1	0.057	0.003	0.01	0.00	0.97	115.21	5.67	0.047	0.001	0.14	0.0026	0.0001	53	3	56	3	0.99
FC-1	0.059	0.003	0.01	0.00	0.94	107.76	4.81	0.047	0.001	0.05	0.0027	0.0001	55	2	60	3	1.02
FC-10	0.056	0.003	0.01	0.00	0.93	109.65	4.85	0.045	0.001	-0.07	0.0027	0.0001	55	2	59	3	1.05
FC-11	0.058	0.003	0.01	0.00	0.95	110.38	4.80	0.046	0.001	-0.02	0.0027	0.0001	55	2	58	3	1.02
FC-12	0.057	0.003	0.01	0.00	0.96	109.89	4.76	0.045	0.001	-0.02	0.0028	0.0001	56	2	59	3	1.03
FC-13	0.059	0.003	0.01	0.00	0.94	107.87	4.51	0.046	0.001	-0.02	0.0028	0.0001	57	2	60	2	1.02
FC-14	0.057	0.002	0.01	0.00	0.90	110.74	4.40	0.046	0.001	0.12	0.0028	0.0001	56	2	58	2	1.04
FC-15	0.058	0.002	0.01	0.00	0.96	110.86	4.52	0.046	0.001	0.00	0.0028	0.0001	56	2	58	2	1.02
FC-15	0.057	0.003	0.01	0.00	0.94	108.34	4.96	0.046	0.001	0.00	0.0028	0.0001	56	2	59	3	1.05
FC-2	0.058	0.003	0.01	0.00	0.95	111.48	5.00	0.047	0.001	-0.07	0.0027	0.0001	55	2	58	3	1.01
FC-2	0.057	0.002	0.01	0.00	0.93	111.36	3.62	0.046	0.001	-0.29	0.0027	0.0001	54	2	58	2	1.03
FC-3	0.056	0.002	0.01	0.00	0.88	113.64	3.44	0.046	0.001	0.03	0.0027	0.0001	54	2	57	2	1.02
FC-3	0.058	0.002	0.01	0.00	0.88	112.74	4.32	0.047	0.001	0.16	0.0027	0.0001	54	2	57	2	1.00
FC-4	0.057	0.002	0.01	0.00	0.93	112.74	4.65	0.047	0.001	0.04	0.0027	0.0001	54	2	57	2	1.01
FC-4	0.061	0.003	0.01	0.00	0.93	106.16	4.98	0.047	0.001	0.05	0.0027	0.0001	55	2	60	3	1.01
FC-5	0.056	0.003	0.01	0.00	0.95	112.49	5.31	0.046	0.001	0.11	0.0027	0.0001	54	3	57	3	1.03
FC-5	0.056	0.002	0.01	0.00	0.96	115.34	4.73	0.047	0.001	0.06	0.0026	0.0001	53	2	56	2	1.01
FC-6	0.056	0.002	0.01	0.00	0.95	112.87	4.77	0.046	0.001	0.19	0.0027	0.0001	54	2	57	2	1.02
FC-6	0.058	0.002	0.01	0.00	0.94	114.68	4.79	0.049	0.001	-0.02	0.0026	0.0001	52	2	56	2	0.97
FC-7	0.055	0.002	0.01	0.00	0.93	112.23	4.29	0.045	0.001	-0.10	0.0027	0.0001	55	2	57	2	1.06
FC-8	0.059	0.003	0.01	0.00	0.89	112.61	4.31	0.048	0.001	-0.13	0.0027	0.0001	55	2	57	2	0.99
FC-9	0.055	0.002	0.01	0.00	0.94	115.21	4.95	0.046	0.001	0.04	0.0027	0.0001	55	2	56	2	1.02
Manmon-	0.748	0.025	0.09	0.00	0.94	10.95	0.37	0.059	0.001	0.07	0.0279	0.0010	556	19	563	19	0.99
Manmon-	0.742	0.027	0.09	0.00	0.95	10.82	0.39	0.059	0.001	0.12	0.0284	0.0010	565	19	570	20	1.01
Manmon-	0.752	0.029	0.09	0.00	0.96	10.86	0.41	0.059	0.001	-0.03	0.0272	0.0010	543	20	568	21	1.00
Manmon-	0.753	0.027	0.09	0.00	0.94	10.99	0.38	0.059	0.001	-0.08	0.0284	0.0009	566	18	561	19	0.99
Manmon-	0.761	0.025	0.09	0.00	0.92	10.95	0.35	0.060	0.001	0.06	0.0280	0.0009	557	17	562	18	0.98
Manmon-	0.748	0.028	0.09	0.00	0.96	10.63	0.40	0.058	0.001	0.05	0.0288	0.0010	574	21	581	21	1.02
Manmon-	0.757	0.027	0.09	0.00	0.94	10.85	0.38	0.059	0.001	0.07	0.0283	0.0009	563	18	569	20	0.99
Manmon-	0.765	0.025	0.09	0.00	0.92	10.55	0.34	0.059	0.001	0.15	0.0286	0.0010	570	19	584	18	1.01
Manmon-	0.744	0.027	0.09	0.00	0.96	10.91	0.39	0.059	0.001	-0.17	0.0286	0.0010	570	21	566	20	1.00
Manmon-	0.742	0.027	0.09	0.00	0.96	11.29	0.41	0.061	0.001	0.00	0.0288	0.0010	574	20	546	19	0.97
Manmon-	0.754	0.027	0.09	0.00	0.97	10.57	0.38	0.057	0.001	0.12	0.0298	0.0010	594	21	584	20	1.02
Manmon-	0.757	0.026	0.09	0.00	0.97	10.71	0.37	0.059	0.001	0.13	0.0295	0.0010	587	20	576	19	1.01
Stern-1	0.656	0.024	0.08	0.00	0.98	12.14	0.44	0.057	0.001	-0.19	0.0254	0.0009	507	19	510	18	1.00
Stern-1	0.660	0.022	0.08	0.00	0.96	12.09	0.40	0.058	0.001	-0.04	0.0248	0.0009	495	17	512	17	1.00
Stern-1	0.661	0.027	0.08	0.00	0.99	12.06	0.51	0.057	0.001	0.15	0.0259	0.0011	517	22	514	21	1.00
Stern-10	0.648	0.024	0.08	0.00	0.98	11.99	0.44	0.056	0.001	0.08	0.0257	0.0010	513	19	517	19	1.02
Stern-10	0.640	0.025	0.08	0.00	0.98	12.50	0.46	0.057	0.001	-0.02	0.0253	0.0010	506	20	496	18	0.99
Stern-11	0.643	0.028	0.08	0.00	0.98	12.24	0.51	0.057	0.001	-0.07	0.0254	0.0011	507	22	507	21	1.00
Stern-11	0.661	0.023	0.08	0.00	0.98	11.90	0.42	0.057	0.001	0.16	0.0263	0.0010	525	20	521	18	1.01
Stern-12	0.645	0.026	0.08	0.00	0.98	12.47	0.50	0.058	0.001	0.12	0.0255	0.0011	508	21	497	20	0.98
Stern-12	0.653	0.031	0.08	0.00	0.99	12.08	0.56	0.057	0.001	0.14	0.0262	0.0013	522	25	513	23	1.00
Stern-13	0.653	0.026	0.08	0.00	0.98	12.15	0.48	0.057	0.001	0.00	0.0255	0.0010	510	20	510	20	1.00
Stern-13	0.644	0.027	0.08	0.00	0.98	12.15	0.49	0.057	0.001	-0.02	0.0258	0.0011	514	21	510	20	1.01
Stern-14	0.659	0.024	0.08	0.00	0.96	12.06	0.41	0.057	0.001	-0.03	0.0252	0.0009	503	18	514	17	1.00
Stern-14	0.657	0.027	0.08	0.00	0.98	12.17	0.51	0.058	0.001	0.05	0.0260	0.0012	519	23	509	21	0.99
Stern-15	0.634	0.023	0.08	0.00	0.98	12.39	0.44	0.057	0.001	0.19	0.0252	0.0009	502	18	500	18	1.00
Stern-15	0.649	0.031	0.08	0.00	0.98	12.18	0.56	0.057	0.001	-0.01	0.0257	0.0012	514	23	509	23	1.00
Stern-16	0.640	0.023	0.08	0.00	0.98	12.41	0.43	0.058	0.001	0.06	0.0254	0.0009	508	18	499	17	0.99
Stern-16	0.637	0.024	0.08	0.00	0.97	12.25	0.44	0.056	0.001	-0.08	0.0255	0.0009	508	18	506	18	1.01
Stern-17	0.644	0.030	0.08	0.00	0.98	12.44	0.57	0.058	0.001	0.14	0.0249	0.0011	497	22	498	22	0.99
Stern-17	0.643	0.028	0.08	0.00	0.99	12.18	0.53	0.057	0.001	-0.01	0.0256	0.0011	511	22	509	22	1.01
Stern-18	0.645	0.024	0.08	0.00	0.97	12.12	0.44	0.057	0.001	0.04	0.0256	0.0009	510	19	512	18	1.01
Stern-18	0.651	0.031	0.08	0.00	0.98	12.08	0.56	0.056	0.001	-0.15	0.0253	0.0012	505	23	514	23	1.01
Stern-19	0.650	0.026	0.08	0.00	0.98	12.06	0.49	0.057	0.001	-0.01	0.0258	0.0011	515	21	514	20	1.01
Stern-2	0.656	0.022	0.08	0.00	0.96	12.09	0.40	0.057	0.001	0.16	0.0257	0.0009	513	18	513	17	1.00
Stern-2	0.661	0.025	0.08	0.00	0.98	12.15	0.44	0.058	0.001	-0.20	0.0248	0.0010	495	19	510	18	0.99
Stern-2	0.655	0.027	0.08	0.00	0.98	12.27	0.51	0.058	0.001	0.01	0.0252	0.0011	503	21	505	21	0.99
Stern-20	0.650	0.026	0.08	0.00	0.98	12.18	0.47	0.057	0.001	0.07	0.0251	0.0010	501	19	509	19	1.00

Appendix A: full dataset standards analyzed during dating with LASS

Stern-21	0.654	0.027	0.08	0.00	0.99	12.11	0.50	0.057	0.001	-0.02	0.0259	0.0011	516	22	512	21	1.00
Stern-21	0.640	0.027	0.08	0.00	0.98	12.15	0.49	0.057	0.001	-0.02	0.0254	0.0011	506	22	510	20	1.01
Stern-22	0.654	0.024	0.08	0.00	0.98	12.17	0.46	0.057	0.001	0.17	0.0255	0.0010	509	20	509	19	1.00
Stern-23	0.658	0.027	0.08	0.00	0.98	11.86	0.50	0.057	0.001	0.11	0.0261	0.0011	520	21	522	21	1.02
Stern-24	0.654	0.023	0.08	0.00	0.97	12.12	0.42	0.057	0.001	-0.07	0.0259	0.0009	516	18	511	17	1.00
Stern-25	0.649	0.027	0.08	0.00	0.98	12.06	0.50	0.057	0.001	-0.03	0.0264	0.0011	526	23	514	21	1.01
Stern-26	0.663	0.027	0.08	0.00	0.97	11.88	0.49	0.057	0.001	-0.03	0.0261	0.0010	521	21	522	21	1.01
Stern-26	0.637	0.028	0.08	0.00	0.99	12.61	0.54	0.058	0.001	-0.09	0.0254	0.0011	507	22	491	21	0.98
Stern-27	0.670	0.028	0.09	0.00	0.98	11.76	0.48	0.057	0.001	0.02	0.0267	0.0011	533	22	526	21	1.01
Stern-27	0.637	0.027	0.08	0.00	0.99	12.42	0.51	0.057	0.001	-0.11	0.0259	0.0010	516	21	499	20	1.00
Stern-28	0.663	0.028	0.08	0.00	0.99	12.05	0.52	0.058	0.001	0.01	0.0261	0.0012	521	23	514	22	1.00
Stern-28	0.637	0.025	0.08	0.00	0.98	12.59	0.47	0.058	0.001	-0.05	0.0255	0.0010	509	19	492	18	0.98
Stern-29	0.672	0.028	0.08	0.00	0.98	11.99	0.51	0.058	0.001	0.02	0.0264	0.0011	526	21	516	21	0.99
Stern-29	0.638	0.021	0.08	0.00	0.96	12.35	0.42	0.058	0.001	0.28	0.0254	0.0009	507	18	502	17	1.00
Stern-29	0.650	0.026	0.08	0.00	0.99	12.02	0.50	0.057	0.001	0.16	0.0263	0.0011	525	22	515	21	1.01
Stern-3	0.665	0.025	0.08	0.00	0.98	11.96	0.44	0.057	0.001	-0.08	0.0261	0.0010	521	20	518	19	1.00
Stern-3	0.650	0.025	0.08	0.00	0.98	12.15	0.45	0.057	0.001	-0.10	0.0248	0.0010	496	19	510	19	1.00
Stern-3	0.666	0.032	0.08	0.00	0.98	11.92	0.55	0.057	0.001	-0.19	0.0257	0.0011	514	23	520	24	1.00
Stern-30	0.666	0.029	0.08	0.00	0.99	12.02	0.52	0.058	0.001	0.15	0.0259	0.0012	518	23	515	22	0.99
Stern-30	0.633	0.025	0.08	0.00	0.99	12.56	0.49	0.058	0.001	0.00	0.0256	0.0010	511	20	493	19	0.99
Stern-31	0.641	0.025	0.08	0.00	0.99	12.25	0.50	0.057	0.001	0.25	0.0263	0.0011	525	22	506	20	1.01
Stern-32	0.638	0.025	0.08	0.00	0.99	12.42	0.50	0.058	0.001	0.07	0.0259	0.0010	516	21	499	20	1.00
Stern-33	0.638	0.025	0.08	0.00	0.99	12.53	0.49	0.059	0.001	-0.02	0.0260	0.0010	519	21	494	19	0.99
Stern-34	0.651	0.028	0.08	0.00	0.99	12.18	0.53	0.058	0.001	0.00	0.0262	0.0011	522	22	508	22	1.00
Stern-35	0.647	0.029	0.08	0.00	0.99	12.09	0.55	0.057	0.001	0.27	0.0262	0.0012	522	24	512	23	1.01
Stern-36	0.643	0.022	0.08	0.00	0.98	12.14	0.42	0.057	0.001	-0.13	0.0260	0.0009	519	18	511	17	1.01
Stern-37	0.636	0.020	0.08	0.00	0.99	12.32	0.39	0.057	0.001	-0.12	0.0258	0.0009	516	17	504	16	1.01
Stern-38	0.656	0.030	0.08	0.00	0.99	12.06	0.55	0.057	0.001	0.12	0.0256	0.0011	512	23	514	23	1.00
Stern-39	0.654	0.027	0.08	0.00	0.99	11.98	0.49	0.056	0.001	-0.15	0.0262	0.0011	522	21	518	21	1.01
Stern-4	0.637	0.023	0.08	0.00	0.98	12.17	0.46	0.057	0.001	0.16	0.0251	0.0010	501	19	510	19	1.02
Stern-4	0.634	0.026	0.08	0.00	0.98	12.39	0.50	0.057	0.001	-0.08	0.0242	0.0010	484	20	500	20	1.00
Stern-4	0.649	0.026	0.08	0.00	0.99	12.18	0.49	0.057	0.001	0.06	0.0256	0.0011	510	21	509	20	1.00
Stern-40	0.648	0.025	0.08	0.00	0.99	11.96	0.45	0.056	0.001	0.05	0.0256	0.0010	511	19	519	19	1.02
Stern-41	0.714	0.031	0.09	0.00	0.98	10.96	0.47	0.057	0.001	-0.19	0.0251	0.0011	501	22	564	24	1.03
Stern-42	0.644	0.024	0.08	0.00	0.98	12.20	0.44	0.057	0.001	0.13	0.0258	0.0009	514	19	508	18	1.01
Stern-43	0.641	0.025	0.08	0.00	0.98	12.39	0.50	0.058	0.001	-0.03	0.0252	0.0010	503	20	500	20	0.99
Stern-44	0.649	0.027	0.08	0.00	0.98	11.82	0.49	0.056	0.001	0.02	0.0260	0.0011	520	21	525	21	1.03
Stern-45	0.667	0.027	0.09	0.00	0.98	11.55	0.47	0.057	0.001	0.09	0.0265	0.0011	528	21	536	22	1.03
Stern-46	0.694	0.029	0.09	0.00	0.98	11.31	0.45	0.057	0.001	-0.13	0.0259	0.0010	517	21	547	21	1.02
Stern-47	0.652	0.027	0.08	0.00	0.99	12.06	0.50	0.057	0.001	-0.11	0.0258	0.0011	514	21	514	21	1.01
Stern-48	0.663	0.023	0.08	0.00	0.98	11.81	0.42	0.057	0.001	-0.04	0.0259	0.0009	517	18	525	18	1.01
Stern-49	0.637	0.025	0.08	0.00	0.99	12.39	0.47	0.057	0.001	-0.13	0.0251	0.0010	501	20	500	19	1.00
Stern-5	0.648	0.023	0.08	0.00	0.97	12.18	0.42	0.058	0.001	0.02	0.0252	0.0009	504	18	509	17	1.00
Stern-5	0.629	0.027	0.08	0.00	0.99	12.52	0.57	0.057	0.001	0.28	0.0244	0.0011	487	22	495	22	1.00
Stern-5	0.654	0.027	0.08	0.00	0.98	12.08	0.49	0.057	0.001	-0.02	0.0258	0.0011	514	21	513	20	1.00
Stern-50	0.647	0.031	0.08	0.00	0.99	12.20	0.57	0.058	0.001	-0.04	0.0254	0.0012	508	24	508	23	1.00
Stern-51	0.648	0.026	0.08	0.00	0.99	11.88	0.49	0.056	0.001	-0.05	0.0256	0.0010	511	20	522	21	1.03
Stern-52	0.651	0.026	0.08	0.00	0.99	12.00	0.48	0.057	0.001	0.01	0.0255	0.0010	509	21	516	20	1.01
Stern-53	0.643	0.026	0.08	0.00	0.98	12.17	0.49	0.056	0.001	0.24	0.0256	0.0011	511	22	510	20	1.01
Stern-54	0.652	0.026	0.08	0.00	0.98	12.03	0.48	0.057	0.001	0.04	0.0254	0.0010	507	21	515	20	1.01
Stern-55	0.652	0.030	0.08	0.00	0.99	12.18	0.55	0.057	0.001	-0.13	0.0255	0.0011	509	23	509	22	1.00
Stern-56	0.650	0.029	0.08	0.00	0.99	12.09	0.51	0.056	0.001	-0.15	0.0253	0.0010	506	21	513	21	1.01
Stern-6	0.657	0.031	0.08	0.00	0.99	11.99	0.56	0.057	0.001	0.11	0.0255	0.0012	508	23	517	24	1.01
Stern-6	0.638	0.023	0.08	0.00	0.98	12.42	0.43	0.057	0.001	0.00	0.0250	0.0009	500	18	499	17	1.00
Stern-6	0.652	0.026	0.08	0.00	0.98	11.93	0.46	0.056	0.001	-0.10	0.0260	0.0010	519	21	520	20	1.02
Stern-7	0.648	0.026	0.08	0.00	0.98	12.32	0.50	0.058	0.001	0.04	0.0253	0.0011	504	21	503	20	0.99
Stern-7	0.638	0.027	0.08	0.00	0.97	12.61	0.54	0.059	0.001	0.18	0.0245	0.0011	488	21	491	21	0.98
Stern-7	0.649	0.027	0.08	0.00	0.98	12.18	0.51	0.057	0.001	0.18	0.0256	0.0011	512	21	509	21	1.00
Stern-8	0.657	0.025	0.08	0.00	0.97	11.85	0.41	0.057	0.001	-0.24	0.0253	0.0009	505	18	523	18	1.02
Stern-8	0.629	0.025	0.08	0.00	0.99	12.84	0.53	0.059	0.001	0.20	0.0241	0.0010	482	20	482	19	0.98
Stern-8	0.641	0.026	0.08	0.00	0.98	12.27	0.50	0.057	0.001	-0.11	0.0254	0.0010	507	20	505	20	1.00
Stern-9	0.633	0.021	0.08	0.00	0.96	12.22	0.41	0.056	0.001	0.07	0.0253	0.0009	504	18	508	17	1.02
Stern-9	0.634	0.024	0.08	0.00	0.98	12.71	0.46	0.058	0.001	0.02	0.0240	0.0009	479	18	488	17	0.98
Stern-9	0.648	0.024	0.08	0.00	0.98	12.18	0.43	0.057	0.001	-0.12	0.0260	0.0010	518	19	509	18	1.00

Appendix A: (continue) full dataset standards analyzed during dating with LASS

Treb-1	0.315	0.011	0.04	0.00	0.97	22.47	0.84	0.052	0.001	0.16	0.0137	0.0005	275	10	281	10	1.01
Treb-1	0.317	0.012	0.04	0.00	0.98	22.99	0.87	0.052	0.001	0.08	0.0131	0.0005	264	10	274	10	0.98
Treb-1	0.318	0.013	0.05	0.00	0.97	22.22	0.91	0.052	0.001	0.13	0.0130	0.0005	261	10	284	11	1.01
Treb-1	0.316	0.013	0.04	0.00	0.98	22.73	0.90	0.052	0.001	0.13	0.0132	0.0005	265	11	278	11	1.00
Treb-1	0.317	0.013	0.05	0.00	0.98	22.17	0.95	0.050	0.001	0.13	0.0133	0.0005	267	11	285	12	1.02
Treb-12	0.312	0.014	0.04	0.00	0.99	22.94	1.01	0.052	0.001	-0.07	0.0135	0.0006	270	11	275	12	1.00
Treb-13	0.310	0.014	0.04	0.00	0.99	23.09	1.02	0.052	0.001	0.08	0.0130	0.0006	261	11	273	12	1.00
Treb-14	0.313	0.014	0.04	0.00	0.98	22.94	0.96	0.052	0.001	-0.11	0.0130	0.0005	261	10	275	11	0.99
Treb-2	0.315	0.013	0.04	0.00	0.98	22.52	0.88	0.051	0.001	-0.09	0.0137	0.0005	275	11	280	11	1.01
Treb-2	0.320	0.014	0.05	0.00	0.98	21.83	1.01	0.050	0.001	-0.06	0.0137	0.0006	274	12	289	13	1.02
Treb-2	0.315	0.013	0.04	0.00	0.98	23.20	0.93	0.053	0.001	0.29	0.0126	0.0005	254	10	272	11	0.98
Treb-2	0.318	0.014	0.05	0.00	0.98	21.60	0.94	0.050	0.001	-0.01	0.0137	0.0006	274	12	292	13	1.04
Treb-3	0.312	0.014	0.04	0.00	0.98	22.99	1.06	0.052	0.001	0.16	0.0134	0.0006	270	12	274	12	1.00
Treb-3	0.316	0.012	0.04	0.00	0.98	22.27	0.83	0.051	0.001	0.08	0.0135	0.0005	271	10	283	10	1.02
Treb-3	0.315	0.012	0.04	0.00	0.98	22.68	0.81	0.052	0.001	-0.15	0.0127	0.0005	255	9	278	10	1.00
Treb-3	0.319	0.012	0.04	0.00	0.98	22.62	0.80	0.053	0.001	-0.13	0.0132	0.0005	266	9	279	10	0.99
Treb-4	0.318	0.011	0.04	0.00	0.97	22.52	0.76	0.052	0.001	-0.11	0.0137	0.0005	275	10	280	9	1.00
Treb-4	0.318	0.011	0.04	0.00	0.97	22.47	0.75	0.051	0.001	-0.02	0.0136	0.0005	272	10	281	9	1.00
Treb-4	0.318	0.014	0.04	0.00	0.98	22.88	0.95	0.052	0.001	0.02	0.0127	0.0005	255	11	275	11	0.98
Treb-4	0.317	0.014	0.04	0.00	0.99	22.32	1.00	0.051	0.001	-0.14	0.0138	0.0006	276	12	283	13	1.01
Treb-5	0.319	0.016	0.05	0.00	0.99	22.22	1.08	0.051	0.001	-0.14	0.0139	0.0007	279	13	284	14	1.01
Treb-5	0.312	0.011	0.04	0.00	0.97	22.52	0.84	0.052	0.001	-0.09	0.0137	0.0005	275	10	280	10	1.02
Treb-5	0.314	0.013	0.04	0.00	0.98	22.73	0.90	0.052	0.001	-0.01	0.0133	0.0005	266	11	278	11	1.00
Treb-5	0.308	0.013	0.04	0.00	0.98	22.94	0.91	0.051	0.001	-0.02	0.0135	0.0005	271	11	275	11	1.01
Treb-6	0.323	0.013	0.04	0.00	0.97	22.37	0.87	0.052	0.001	0.04	0.0138	0.0005	277	11	282	11	0.99
Treb-6	0.315	0.013	0.04	0.00	0.98	22.73	0.90	0.052	0.001	-0.08	0.0135	0.0005	272	11	277	11	1.00
Treb-6	0.310	0.012	0.04	0.00	0.98	23.15	0.93	0.052	0.001	0.05	0.0131	0.0005	264	11	272	11	0.99
Treb-6	0.305	0.011	0.04	0.00	0.99	24.04	0.89	0.053	0.001	0.02	0.0131	0.0005	263	10	262	10	0.97
Treb-7	0.316	0.014	0.04	0.00	0.98	22.42	0.92	0.051	0.001	-0.05	0.0138	0.0006	278	12	282	11	1.01
Treb-7	0.312	0.013	0.04	0.00	0.98	22.57	0.89	0.051	0.001	0.03	0.0137	0.0005	275	11	280	11	1.01
Treb-7	0.308	0.013	0.04	0.00	0.99	23.09	0.97	0.052	0.001	-0.06	0.0133	0.0005	267	11	273	11	1.00
Treb-8	0.308	0.013	0.04	0.00	0.98	23.58	1.01	0.053	0.001	0.17	0.0132	0.0006	265	11	267	11	0.98
Treb-9	0.307	0.013	0.04	0.00	0.99	23.42	0.99	0.052	0.001	-0.10	0.0127	0.0005	255	11	270	11	0.99

Appendix A: (continue) full dataset standards analyzed during dating with LASS

APPENDIX D: analyzed samples

Sample		Position			Vorticity			Finite strain		Age of Shear	
Name	*litotype*	*Locality*	*Coordinates*		*C' shear band*	*Stable porphyroclasts*	*quartz c-axis*	*Center-to-center method*	*Quartz c-axis*	$^{206}Pb/^{238}U$	$^{208}Pb/^{232}Th$
ARG45	Mylonite	Serra del Bal	44°19'28.1"N	006°59'21.7"E	0.41	-	-	Flattening	-	-	-
ARG 21a	Mylonite	Serra del Bal	44°21'03.5"N	006°56'42.9"E	0.59	0.55	-	Flattening	-	-	-
ARG 68	Mylonite	Comba del Pilone	44°20'16.4"N	006°57'19.2"E	0.47	0.61	-	Flattening	-	-	-
ARG 116	Mylonite	Comba del Pilone	44°20'22.0"N	006°57'37.0"E	0.41	-	-	Flattening	-	-	-
ARG 117	Mylonite	Comba del Pilone	44°20'09.1"N	006°57'38.5"E	0.37	0.51	-	Flattening	-	-	-
ARG 115	Mylonite	Comba del Pilone	44°20'23.9"N	006°57'35.6"E	0.44	0.53	-	Flattening	-	-	-
ARG 21	Mylonite	Passo Scolettas	44°18'23.9"N	00659'38.4"E	0.61	0.64	-	Flattening	-	323 ± 3	319 ± 4
ARG 27	Mylonite	Costabella del Piz	44°19'03.6"N	006°59'11.9"E	0.64	0.61	-	Plane strain	-	327 ± 6	314 ± 16
ARG 48B	Mylonite	Costabella del Piz	44°18'45.2"N	006°59'19.9"E	0.69	-	-	Flattening	-	321 ± 8	318 ± 7
ARG 29	Mylonite	Costabella del Piz	44°18'37.6"N	006°59'41.7"E	0.66	0.67	-	Flattening	-	328 ± 5	331 ± 3
ARG55	Mylonite	Piz Valley	44°18'15.9"N	006°59'45.7"E	0.71	-	0.62	-	Plane strain	-	-
ARG32	Mylonite	Prati del Vallone	44°19'15.0"N	006°59'02.9"E	0.69	-	0.70	-	Plane strain	-	-
ISC2	Mylonite	Ischiator Valley	44°17'13.9"N	007°01'39.2"E	0.72	-	0.73	-	Plane strain	322 ± 4	316 ± 3
ISC5	Mylonite	Ischiator Valley	44°17'06.6"N	007°01'31.4"E	0.64	-	-	-	Plane strain	318 ± 3	322 ± 3
IS7	Protomylonite	Ischiator Valley	44°11'35.9"N	007°07'59.8"E	0.50	-	-	-	Plane strain	-	-
ARG 143	Protomylonite	Rocca Reis	44°20'39.6"N	006°56'09.6"E	0.31	0.59	-	Flattening	-	-	-
ARG 144	Protomylonite	Rocca Reis	44°20'46.2"N	006°56'12.9"E	0.31	0.55	-	Flattening	-	-	-
ARG 19	Protomylonite	Vallone Sup. Pontebernardo	44°18'28.7"N	006°58'31.34"E	0.34	0.56	-	Flattening	Plane strain	341 ± 4	331 ± 6
ISC11	Protomylonite	Ischiator Valley	44°16'51.7"N	007°01'16.6"E	-	-	-	-	Plane strain	-	-
ISC3	Protomylonite	Ischiator Valley	44°16'59.5"N	007°01'07.5"E	0.43	-	-	-	Plane strain	328 ± 4	331 ± 3
ARG 35	Ultramylonite	Serra del Bal	44°20'46.9"N	006°56'37.2"E	0.89	-	-	Flattening	-	-	-
ARG 101	Ultramylonite	Colle di Stau	44°19'47.8"N	006°57'58.1"E	0.83	-	-	Flattening	-	-	-
ARG 37	Ultramylonite	Rocco Verde	44°20'01.8"N	006°58'06.3"E	0.81	-	0.91	Flattening	-	-	-
ARG RCV	Ultramylonite	Rocco Verde	44°19'58.9"N	006°58'02.0"E	0.83	-	0.89	Flattening	-	-	-
ARG 41	Ultramylonite	Serra del Bal	44°18'58.7"N	006°58'39.1"E	0.86	-	-	Flattening	-	-	-
ARG43	Ultramylonite	Serra del Bal	44°18'52.9"N	006°59'35.1"E	0.82	-	0.86	-	Plane strain	-	-
ISC7	Ultramylonite	Ischiator Valley	44°17'20.0"N	007°01'47.0"E	0.82	-	0.85	-	Plane strain	-	-

Appendix D: Samples of the Ferriere-Mollières Shear Zone used for analysis and relative results

Sample		Position			Vorticity	Finite strain	Age of shear		Other age		
Name	Litotype	Locality	Coordinates		C' shear band	Quartz c-axis	206Pb/238U	208Pb/232Th	206Pb/238U	208Pb/232Th	Interpretation
AIG1	Metagreywake	Emosson	46°04'08.0"N	006°56'15.0"E							
AIG2	Metagreywake	Emosson	46°04'06.0"N	006°56'12.0"E	0.55		-	-	-	-	-
AIG3a	Metagreywake	Emosson	46°04'02.0"N	006°56'07.0"E	0.66		-	-	-	-	-
AIG3b	Metagreywake	Emosson	46°04'02.0"N	006°56'07.0"E		Plane Strain	-	-	-	-	-
AIG3c	Metagreywake	Emosson	46°04'02.0"N	006°56'07.0"E			-	-	-	-	-
AIG4	Metagreywake	Emosson	46°04'02.0"N	006°56'07.0"E	0.64		-	-	-	-	
AIG5	Metagreywake	Emosson	46°04'02.0"N	006°56'06.0"E			-	-	-	-	-
AIG6a	Ortogneiss	Emosson	46°03'55.0"N	006°55'44.0"E	0.34		-	-	-	-	
AIG6b	Ortogneiss	Emosson	46°03'55.0"N	006°55'44.0"E		Plane Strain	-	-	-	-	-
AIG7	Ortogneiss	Emosson	46°03'56.0"N	006°55'39.0"E		Plane Strain	-	-	-	-	-
AIG8a	Micaschist	Emosson	46°04'01.0"N	006°55'20.0"E	0.55	Plane Strain	320 ± 2	319 ± 3	-	-	-
AIG8b	Micaschist	Emosson	46°04'01.0"N	006°55'20.0"E			-	-	-	-	-
AIG8c	Micaschist	Emosson	46°04'01.0"N	006°55'20.0"E			-	-	-	-	-
AIG9a	Ortogneiss	Emosson	46°03'55.0"N	006°55'30.0"E	0.40		-	-	-	-	-
AIG9b	Ortogneiss	Emosson	46°03'55.0"N	006°55'30.0"E			-	-	-	-	-
AIG10a	Micaschist	Emosson	46°04'23.0"N	006°55'49.0"E			-	-	-	-	-
AIG10b	Micaschist	Emosson	46°04'23.0"N	006°55'49.0"E			-	-	-	-	-
AIG11	Micaschist	Emosson	46°04'25.0"N	006°55'38.0"E			-	-	329 ± 13	333 ± 5	Prograde metamorphism
AIG12	Micaschist	Emosson	46°04'31.0"N	006°55'31.0"E	0.52		-	-	-	-	-
AIG13	Micaschist	Bèrard	46°00'07.0"N	006°52'03.0"E			-	-	-	-	-
AIG14	Micaschist	Bèrard	46°00'10.0"N	006°52'00.0"E	0.58		318 ± 7	328 ± 2	-	-	-
AIG15	Ortogneiss	Bèrard	46°00'20.0"N	006°51'57.0"E	0.43		-	-	-	-	-
AIG16	Micaschist	Bèrard	46°00'17.0"N	006°52'04.0"E	0.61	Plane Strain	-	-	-	-	
AIG17a	Ortogneiss	Bèrard	46°00'16.0"N	006°52'21.0"E	0.4		-	-	-	-	-
AIG17b	Ortogneiss	Bèrard	46°00'16.0"N	006°52'21.0"E		Plane Strain	-	-	-	-	-
AIG18	Ortogneiss	Bèrard	46°00'58.0"N	006°53'48.0"E	0.46	Plane Strain	-	-	-	-	-

Appendix D: Samples of the Emosson-Bèrard Shear Zone used for analysis and relative results

Sample		Position			Vorticity		Finite strain		Age of shear		Other age		
Name	Litotype	Locality	Coordinates		C' shear band	Stable porphyroclasts	Center-to-center method	Quartz c-axis	$^{206}Pb/^{238}U$	$^{208}Pb/^{232}Th$	$^{206}Pb/^{238}U$	$^{208}Pb/^{232}Th$	Interpretation
CD1	Mylonitic schist	Col du Canadel	43°10'09.0"N	006°28'29.0"E	-	-	-	-	325 ± 5	324 ± 5	337 ± 3	337 ± 3	prograde metamorphism
CD2	Mylonitic schist	Col du Canadel	43°11'02.1"N	006°29'54.8"E	-	-	-	-	-	-	-	-	-
CD3	Mylonitic schist	Col du Canadel	43°11'11.0"N	006°30'08.5"E	-	-	-	Nearly plane strain	-	-	-	-	-
CD4	Mylonitic schist	Col du Canadel	43°11'09.6"N	006°30'23.1"E	0.55	-	-	Nearly plane strain	-	-	-	-	-
CD5	Mylonitic schist	Col du Canadel	43°11'22.6"N	006°30'39.6"E	-	-	-	-	-	-	-	-	-
CD6	Mylonitic schist	Col du Canadel	43°11'50.4"N	006°30'55.1"E	0.44	-	-	-	327 ± 6	324 ± 4	335 ± 4	330 ± 3	prograde metamorphism
MTM9	Mylonitic schist	Col du Canadel	43°11'10.8"N	006°30'09.6"E	0.53	-	-	-	-	-	-	-	-
MTM10	Mylonitic schist	Col du Canadel	43°11'10.8"N	006°30'09.6"E	0.44	-	-	Nearly plane strain	-	-	339 ± 9	334 ± 5	progade metamorphism
MTM11	Mylonitic schist	Col du Canadel	43°11'16.2"N	006°30133.4"E	0.50	-	-	-	-	-	-	-	-
MTM12	Mylonitic schist	Col du Canadel	43°11'48.4"N	00630'55.6"E	0.44	-	-	Nearly plane strain	-	-	-	-	-
MTM13	Mylonitic schist	Col du Canadel	43°11'52.2"N	006°31'03.5"E	-	-	-	-	-	-	-	-	-
MScd1	Mylonitic schist	Col du Canadel	43°10'31.0"N	006°29'20.0"E	-	-	Plane strain	-	-	-	-	-	-
MScd3	Mylonitic schist	Col du Canadel	43°11'14.0"N	006°31'05.0"E	-	-	-	-	-	-	-	-	-
CVmsc1	Mylonitic schist	Plage de Bonporteau	43°09'53.0"N	006°31'13.0"E	-	-	General flattening	-	-	-	-	-	-
BP1	Micaschist	Bonporteau	43°09'46.0"N	006°30'59.0"E	-	-	-	-	-	-	-	-	-
CL1	Mylonitic migmatite	Cavalaire	43°10'08.4"N	006°32'23.7"E	0.44	-	-	Nearly plane strain	-	-	-	-	-
CL2	Mylonitic migmatite	Cavalaire	43°10'08.4"N	006°32'23.7"E	-	-	-	-	-	-	-	-	-
SL1	Anfibolite	Sylvabelle	43°11'12.6"N	006°34'51.3"E	-	-	-	-	-	-	-	-	-
SL2	Anfibolite	Sylvabelle	43°11'12.1"N	006°34'58.0"E	-	-	-	-	-	-	-	-	-
SL3	Micaschist	Sylvabelle	43°11'12.1"N	006°34'58.5"E	0.68	-	-	-	-	-	-	-	-
SL4	Micaschist	Sylvabelle	43°11'11.6"N	006°35'00.3"E	-	-	-	-	-	-	-	-	-
SL5	Garnet-braring micaschist	Sylvabelle	43°11'11.0"N	006°35'09.2"E	0.37	0.58	General flattening	-	-	-	-	-	-
SL6	Garnet-braring micaschist	Sylvabelle	43°11'11.2"N	006°35'11.5"E	0.40	-	-	-	-	-	340 ± 4	344 ± 9	Prograde metamorphism
SL7	Garnet-braring micaschist	Sylvabelle	43°11'09.4"N	006°35'27.6"E	-	-	-	-	-	-	-	-	-
MTM15a	Garnet-braring micaschist	Sylvabelle	43°11'10.9"N	006°35'09.2"E	0.44	-	-	-	-	-	-	-	-
M2	Garnet-braring micaschist	Sylvabelle	43°11'11.2"N	006°35'11.5"E	0.44	0.32	Plane strain	-	-	-	-	-	-
LPT1	Garnet-braring micaschist	Sylvabelle	43°11'08.0"N	006°35'28.0"E	-	-	-	-	-	-	-	-	-
LPT3	Garnet-braring micaschist	Sylvabelle	43°11'11.0"N	006°35'11.0"E	-	-	-	-	-	-	-	-	-
LPT4	Garnet-braring micaschist	Sylvabelle	43°11'11.0"N	006°35'11.0"E	-	-	flattening	-	-	-	-	-	-
LPT4a	Garnet-braring micaschist	Sylvabelle	43°11'11.0"N	006°35'11.0"E	-	-	Plane strain	-	-	-	-	-	-
ANF1	Anfibolite	Sylvabelle	43°11'13.0"N	006°34'50.0"E	-	-	-	-	-	-	-	-	-
MTM6	Metasediment	Bregancon	43°06'02.8"N	006°19'20.6"E	-	-	-	-	-	-	-	-	-
BO1	Bormes Micascist	St. Claire	43°08'20.8"N	006°22'51.6"E	-	-	-	-	-	-	-	-	-
BO2	Bormes Micascist and gneiss	St. Claire	43°08'21.0"N	006°22'52.6"E	-	-	-	-	-	-	-	-	-

Appendix D: Samples of the Cavalaire Fault used for analysis and relative results

APPENDIX E: field guide to the excursion in the Ferriere-Mollières shear zone (Argentera Massif, Western Alps, Italy)

In this appendx a field trip with the aim to visit some key outcrops that allow to recognize the evolution of the FMSZ and the features of bot Variscan and Alpine deformation in the Argentera Massif is presented.

The field trip develops entirely in the Valle Stura di Demonte (fig. 1; CN, Italy). The stops are organized in two days and located in the Ischiator (fig. 2) and Pontebernardo (fig. 3) valleys. Locations of the first day are reachable following the road SS21 that starts from Borgo San Dalmazzo (CN) village up to Bagni di Vinadio and from here travelling along the road for the locality of Besmorello where it is possible to park the car. From here all the stops can be reached by walking along the P26 marked trekking path. The itinerary develops in a high mountain environment and the overall altitude difference is about 750 m. Locations of the second day are reachable following the road SS21 up to the Pontebernardo village. The first stop is located along the road which leads to the locality of Prati del Vallone. From here the other stops can be reached by walking along the GTA marked trekking path and then following directions to Colle Panieris along a minor path. The itinerary develops in a high mountain environment and the overall altitude difference is about 1000 m.

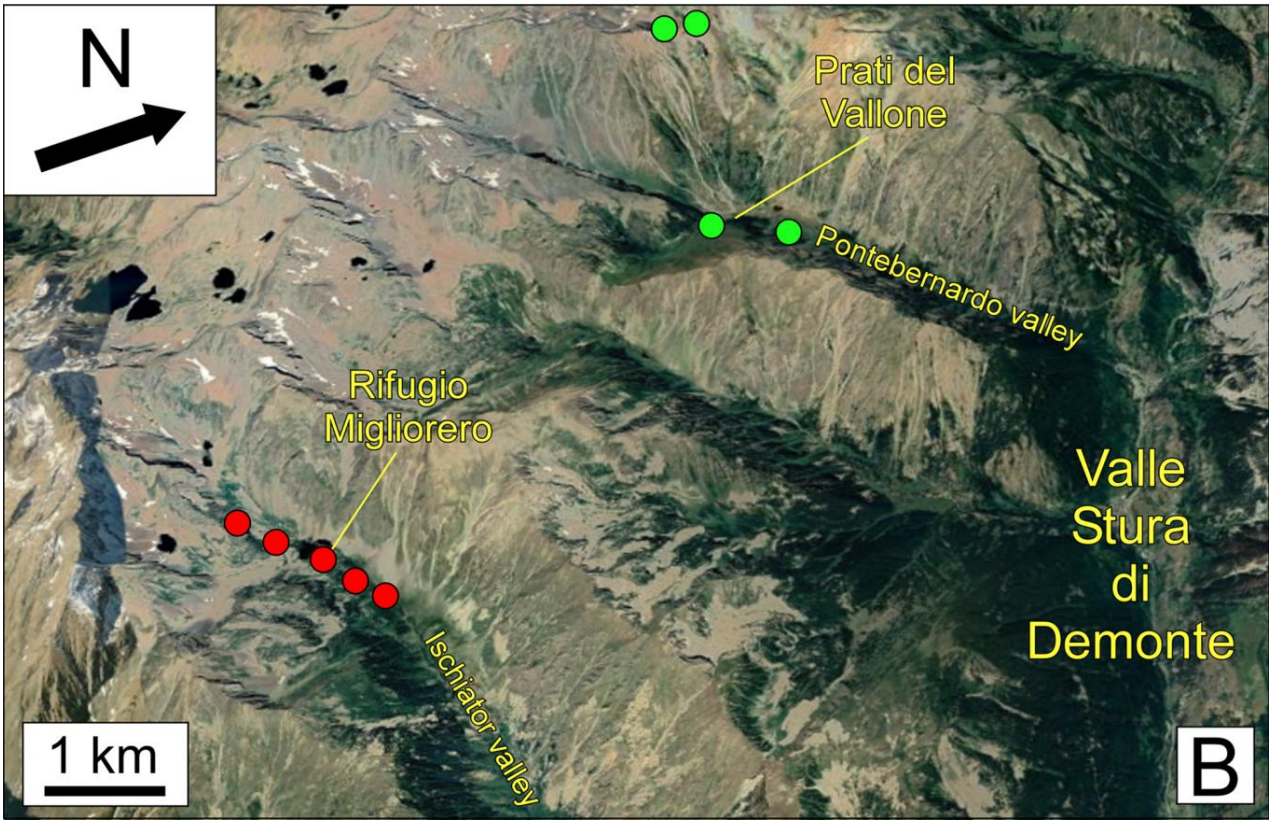

Fig. 1 - Satellite view (from Google Earth) of the Ischiator and Pontebernardo Valley. Circles indicate the location of the stops of the field trip (red = stops of day 1; green = stops of day 2).

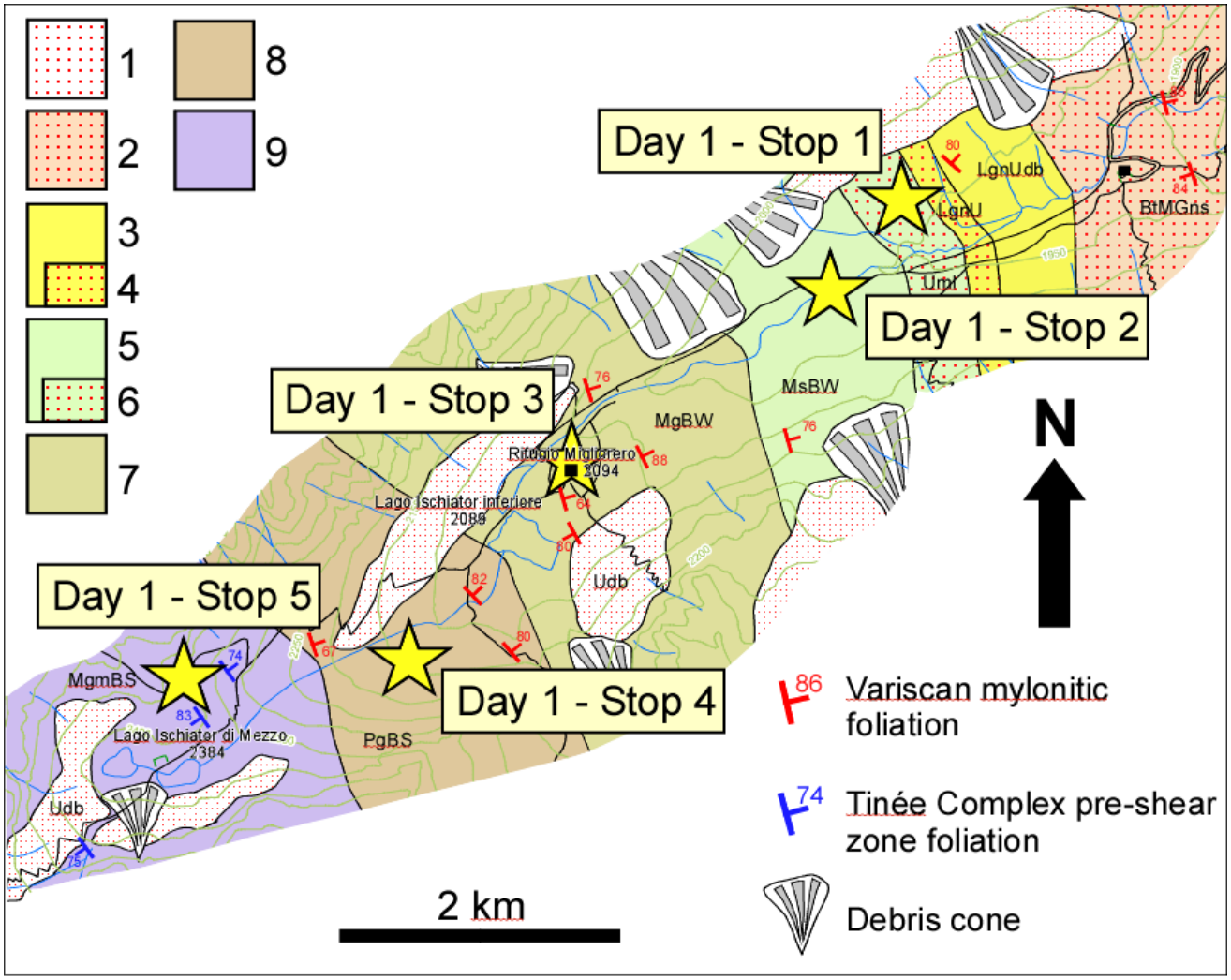

Fig. 2 - Structural-geological map (1:10000 scale) of the Ischiator Valley (fig. 2). 1: undifferentiated debris (udb); 2: biotite-bearing mylonitic gneiss (BtMGns); 3: leucogranite (lgn); 4: ultramylonitic leucogranite (lgnU); 5: mylonitic schist (MsBW); 6: ultramylonite (Uml); 7: mylonitic gneiss with biotite and white mica (MgBW); 8: protomylonitic gneiss with biotite and sillimanite (PgBS); 9: migmatitic gneiss of the Tinée complex (MgmBS).

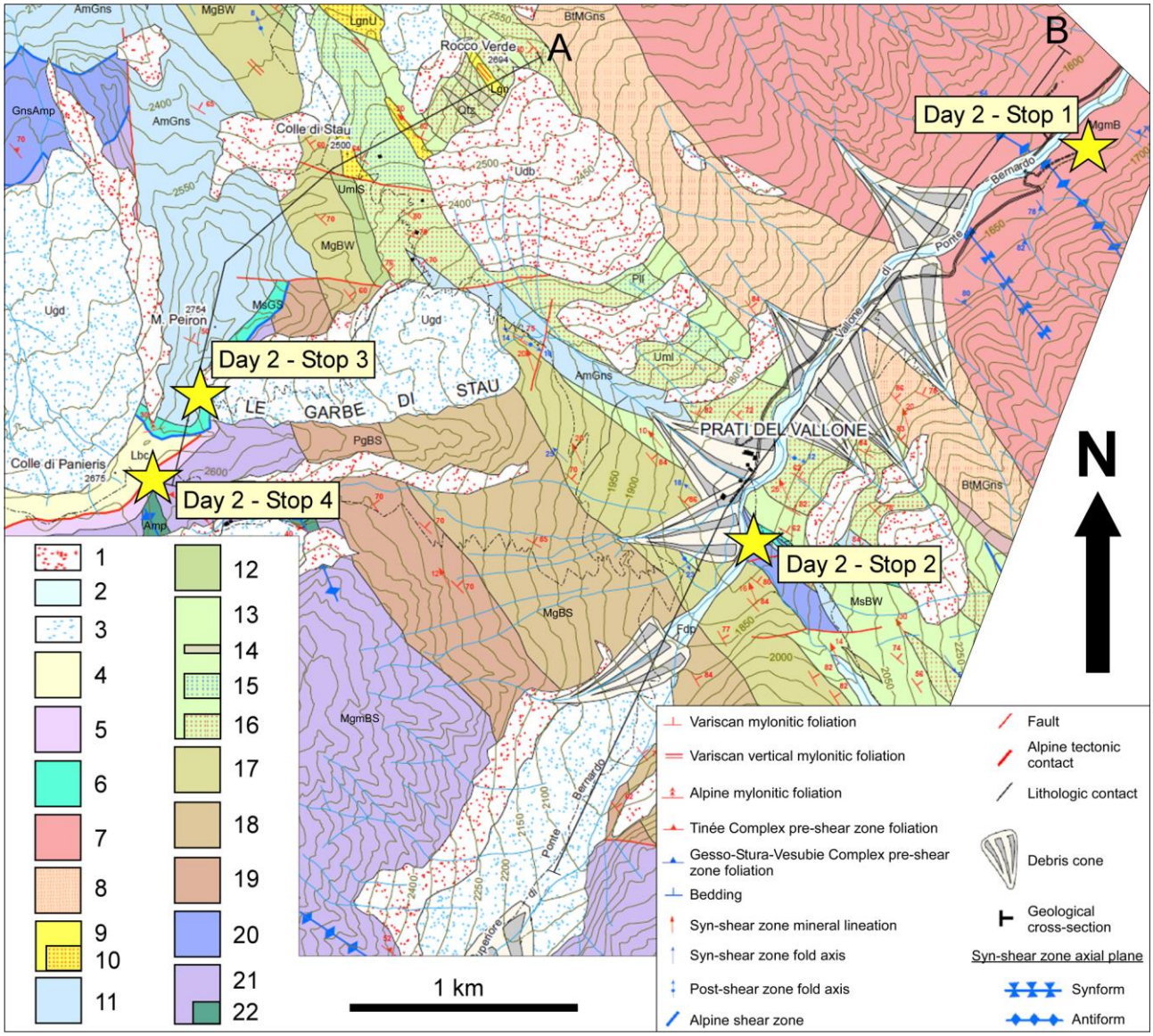

Fig. 3 - Structural-geological map (1:10000 scale) of the Pontebernardo Valley (fig. 2; modified after Carosi et al., 2016). 1: undifferentiated debris (Udb); 2: fluvial deposit (Fdp); 3: undifferentiated glacial deposit (Ugd); 4: limestone breccia (Lbc); 5: triassic quarzite (QtzTr); 6: alpine mylonitic schist with chlorite and white mica (MsGS); 7: migmatitic gneiss of the GSV complex (MgmB); 8: biotite-bearing mylonitic gneiss (BtMGns); 9: mylonitic leucogranite (Lgn); 10: ultramylonitic leucogranite (LgnU); 11: amphibole-bearing mylonitic gneiss (AmGns); 12: ultramylonitic schist (UmlS); 13: mylonitic schist (MsBW); 14: quarzite (Qtz); 15: phyllonite (Pll); 16: ultramylonite (Uml); 17: mylonitic gneiss with biotite and white mica (MgBW); 18: mylonitic gneiss with biotite and sillimanite (MgBS); 19: protomylonitic gneiss with biotite and sillimanite (PgBS); 20: amphibole-bearing migmatitic gneiss (GnsAmp); 21: migmatitic gneiss of the Tinée complex (MgmBS); 21: amphibolite (Amp). Yellow stars show the stops of the itinerary.

Day 1 - stop 1: ultramylonitic schist (coord. 44°17'20.9"N; 07°01'20.6"E)

In the first stop (fig. 2) we can observe the most sheared rocks of the FMSZ that crop out in the lower part of the Ischiator valley (fig. 1). They are ultramylonites (fig. 4a) with >90% matrix. They show a continuous cleavage (fig. 4b) made by white mica and chlorite striking NW-SE dipping steeply toward the NE (fig. 5a). This mineral assemblage is indicative of a greenschist-facies metamorphism. Mineral lineation, plunges at shallow angle toward the NW. In agreement with the syn-kinematic mineral assemblage, quartz is recrystallized by subgrain rotation (fig. 4c) (Piazolo & Passchier 2002; Stipp et al. 2002). This indicate temperature of deformation of nearly 400° C. An S-C-C' fabric, associated to a dextral top-to-the SW sense of shear, well-detectable both at the meso and micro scale (fig. 4a) and in thin section (fig. 4d). Flow analysis performed by Simonetti et al. (2018) with the C' shear band method (Kurtz & Northrup, 2008) highlights a general shear with a component of simple shear of nearly 60% (fig. 6).

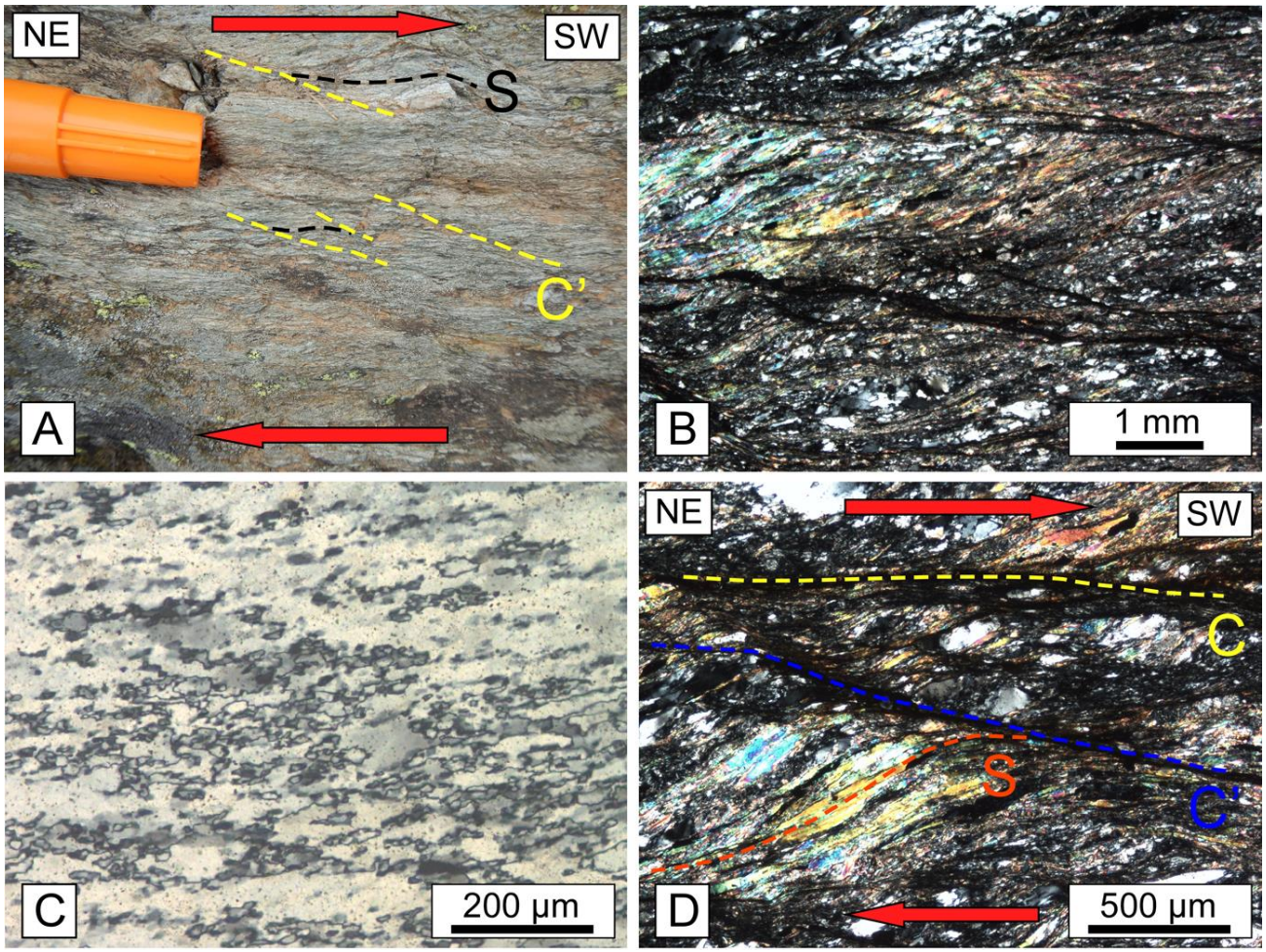

Fig. 4 – A) ultramylonite at the outcrop-scale, an S-C' fabric is indicative of a top-to-the SW sense of shear; B) continuous cleavage made by white mica and chlorite. Amount of matrix is over 90% (crossed nicols); C) quartz in the ultramylonite with bimodal grainsize, subgrains and new grains indicative of a subgrain rotation recrystallyzation (crossed nicols); D) S-C-C' fabric in the ultramylonite pointing a top-to-the SW sense of shear (crossed nicols).

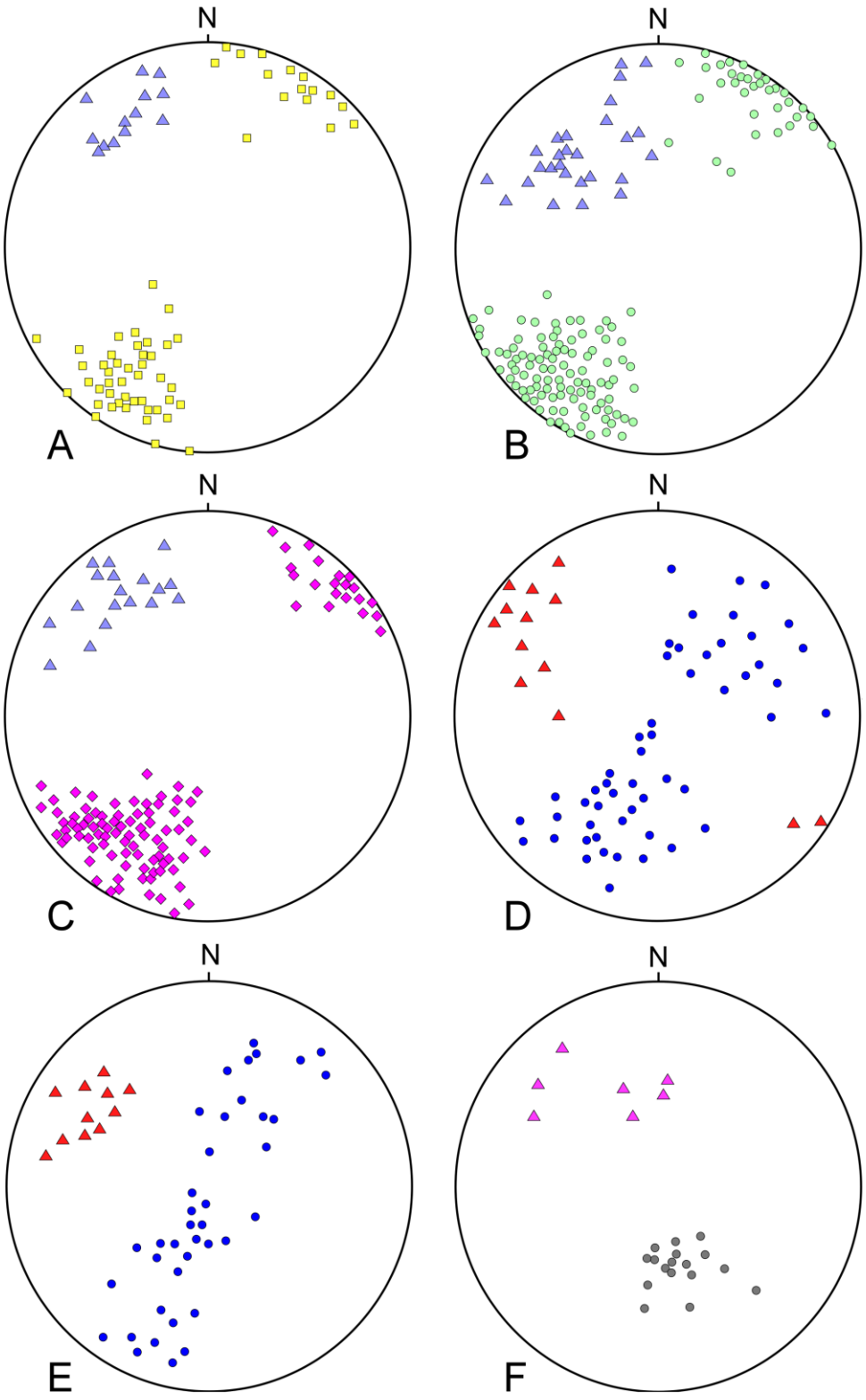

Fig. 5 – Equal angle, lower hemisphere projections: A) poles to foliation (yellow squares, 60 data) and mineral lineation (blue triangles, 13) in the ultramylonitic schists; B) poles to foliation (green dots, 163 data) and mineral lineation (blue triangles, 27 data) in the mylonitic schists; C) poles to foliation (pink diamonds, 110 data) and mineral lineation (blue triangles, 18 data) in the protomylonitic gneiss; D) poles to foliation (blue dots, 53 data) and fold axis (red triangles, 13 data) in the Tinèe complex; E) poles to foliation (blue dots, 39 data) and fold axis (red triangles, 11 data) in the Gesso-Stura-Vesubie complex; F) poles to mylonitic foliation (grey dots, 17 data) and mineral lineation (pink triangles, 7 data) in the Colle Panieris-Mt Peiron alpine thrust.

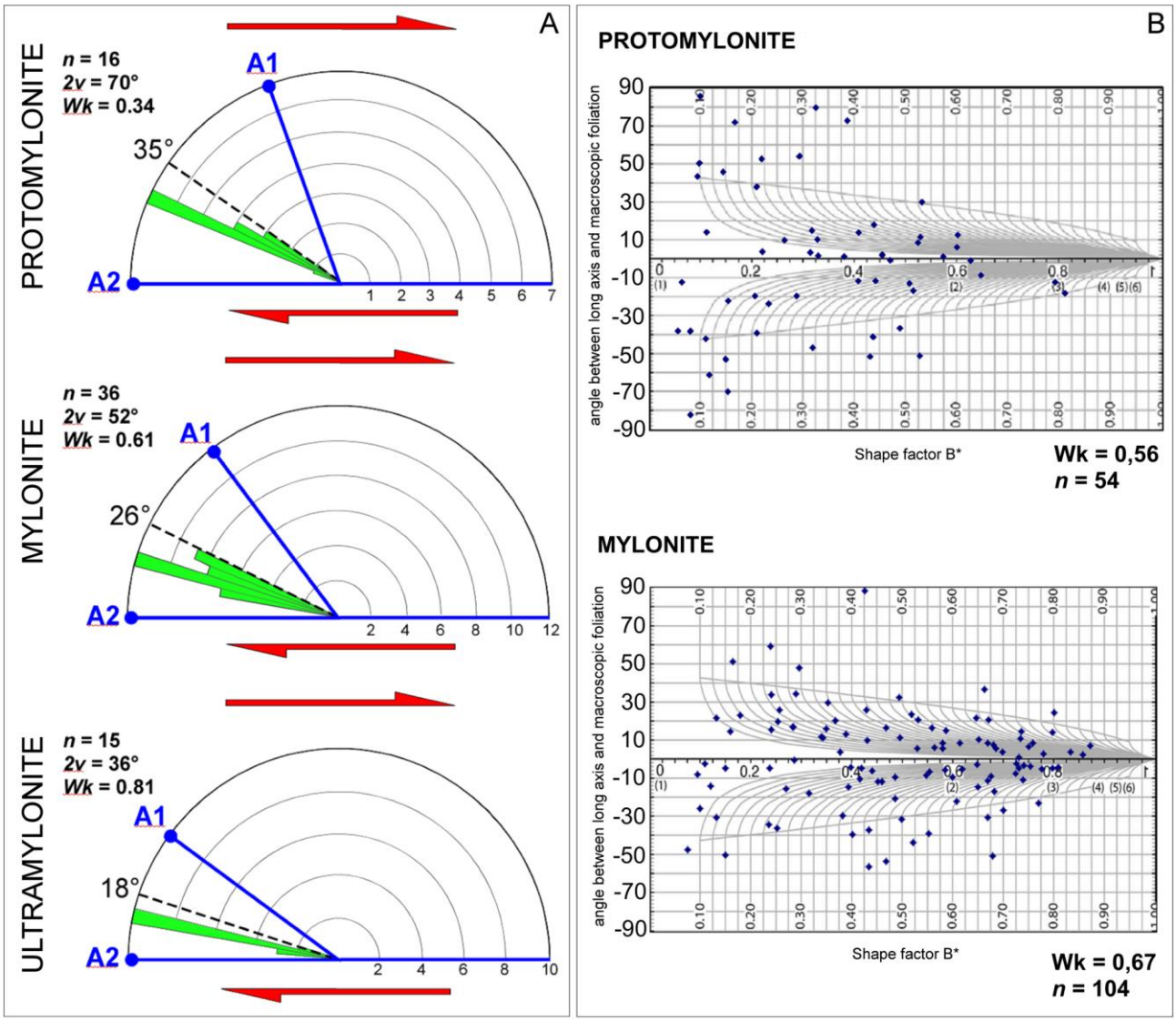

Fig. 6 - A) polar istograms used for calculating kinematic vorticity number (Wk) with the C' shear band method (Kurz & Northrup, 2008) for a protomylonite (Wk = 0.34), a mylonite (Wk = 0.61) and a ultramylonite(Wk = 0.81); B) results of kinematic vorticity analysis with stable porphyroclasts method (Passchier, 1987; Wallis et al., 1993; Law et al., 2004) for a protomylonitic sample and a mylonitic sample. Data are represented with Rigid Grain Net graphs (Jessup et al., 2007) that show Wk values of 0.56 and 0.67 respectively for protomylonite and mylonite. These values indicate a pure shear-dominated deformation but it is possible to see an increase of the simple shear component in the mylonite.

Day 1 - stop 2: mylonitic schist (coord. 44°17'14.1"N; 07°01'39.7"E)

In this stop is possible to observe the most classical mylonites of the FMSZ. They are medium grained dark-green mylonitic schist (fig. 7a) made of quartz, K-feldspar and plagioclase porphyroclasts in a fine grained biotite and white mica matrix (fig. 7b). The amount of matrix is nearly 75%.

Foliation strikes NW-SE and is steeply-dipping toward the NE or SW with a mineral lineation that plunges at low angle toward the NW (fig. 5b). The orientation of the main foliation is perfectly concordant with the one observed in the ultramylonitic schist at stop 1. Foliation is a penetrative disjunctive cleavage with smooth and parallel cleavage domain (fig. 7b) that are made by biotite and white mica. Both at the meso and micro scale kinematic indicators are well recognizable. They are mainly represented by rotated porphiroclasts, quarter mats (fig. 7c), S-C' fabric (fig. 7c), micafish (fig. 7d) and quartz oblique foliation and show a dextral top-to-the SW or top-to-the-SE sense of shear, depending on the dip direction of the foliation. Quartz is characterized by the presence of bigger grains with irregular boundaries and new grains of smaller size. Subrains are also present (fig. 7e). These features suggest subgrain rotation and recrystallization (Piazolo & Passchier 2002; Stipp et al. 2002) as the main dynamic rechrystallization mechanism overprinting a previous grain boundary migration. In some domains effects of grain boundary migration can be still recognized (fig. 7f). This indicates a deformation compatible between the transition of the two recrystallization mechanisms at ~500° C.

Kinematic vorticity analysis (fig. 6) in these rocks was investigated by Simonetti et al. (2018) and revealed a general flow with a dominant component of pure shear between ~70% and ~55% (C' shear band method and Stable porphyroclasts method). *In situ* U-Th-Pb petrochronology on syn-kinematic monazites (fig. 8) constrain the age of shearing in these rocks at ~320 Ma (Simonetti et al. 2018).

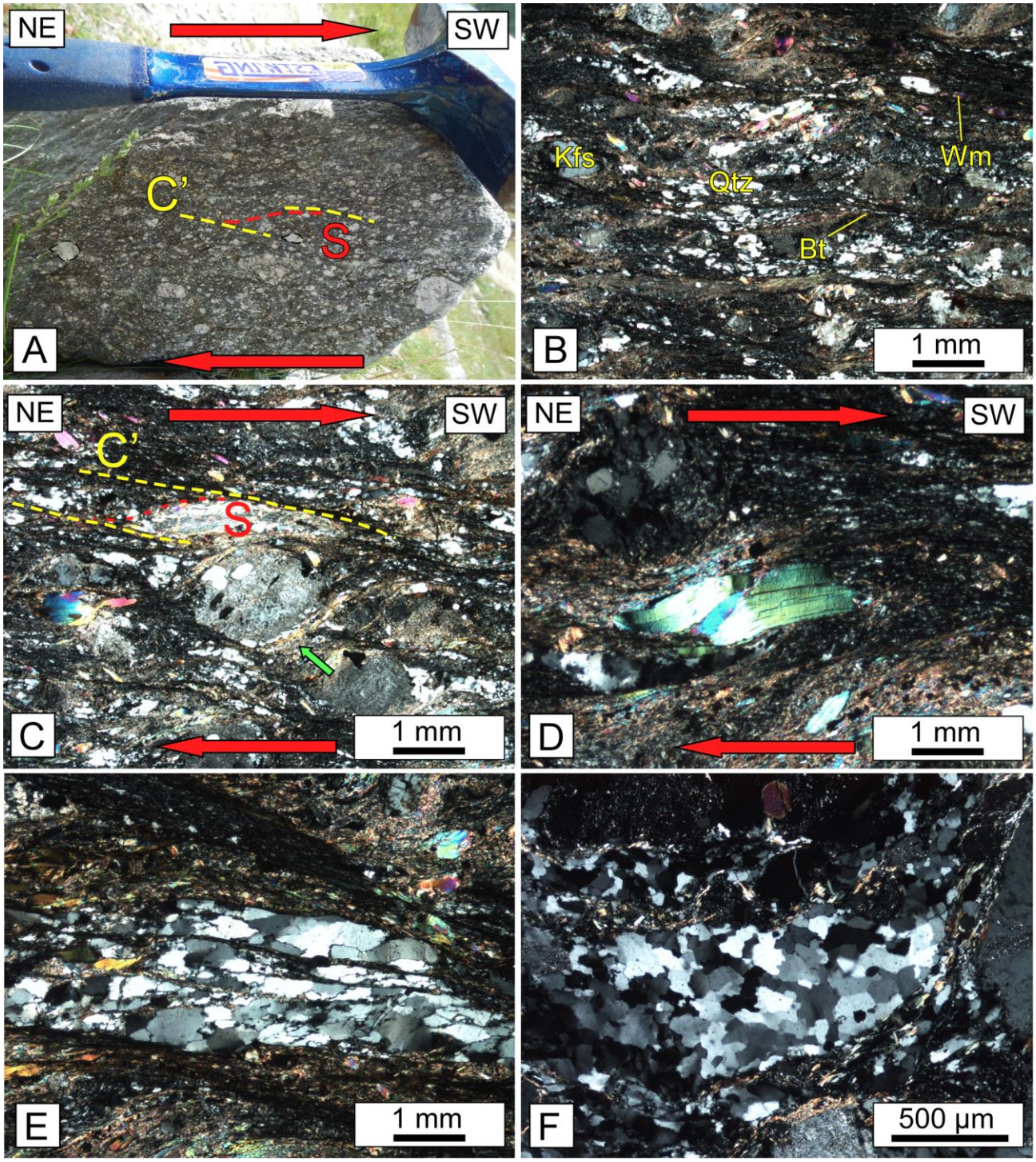

Fig. 7 - A) medium grained dark-green mylonitic schist at the outcrop scale with S-C' fabric pointing to a top-to-the SW sense of shear is well-detectable B) feldspar porphyroclasts in a finer matrix (nearly 75%), foliation is a penetrative disjunctive cleavage with smooth and parallel cleavage domain made by biotite and white mica (crossed nicols); C) S-C' fabric and white mica quarter mats (green arrow) around a feldpsar porphyroclast, both kinematic indicators are consistent with a top-to-the SW sense of shear (crossed nicols); D) micafish made of white mica showing a top-to-the SW sense of shear (crossed nicols); E) Quartz Big quartz grains with irregular boundaries and new grains of smaller size, subgrains are also present (crossed nicols); F) quartz with lobate grain boundaries in a domain where grain boundary migration effcts are still preserved (crossed nicols).

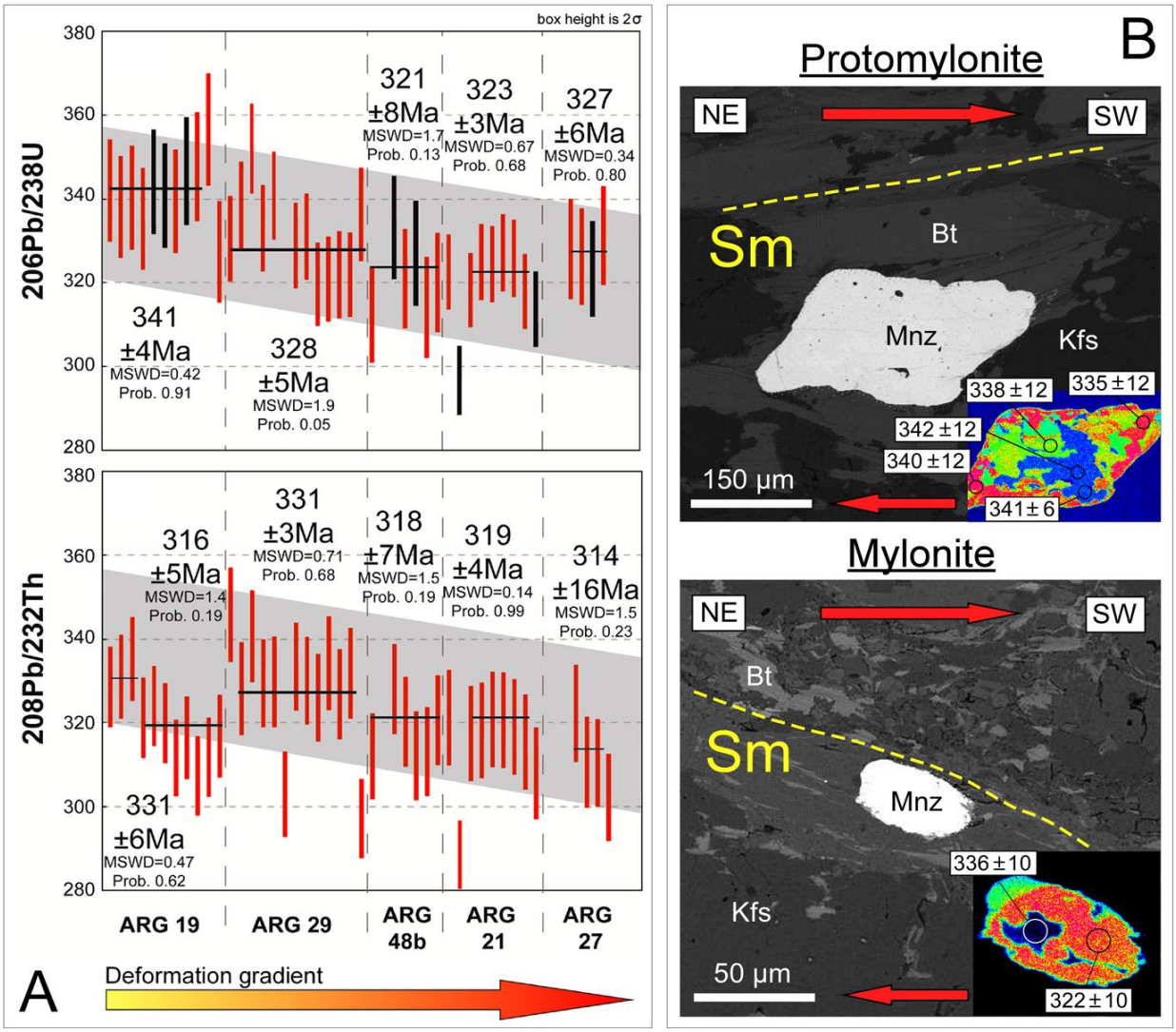

Fig. 8 - A) age of shear deformation along the deformation gradient (U-Th-Pb on monazite; Simonetti et al., 2018); B) Examples of textural position and zoning of monazite grains selected for in situ dating in a protomylonite and a mylonite. Compositional map of Y shows the spot location and the corresponding $^{206}Pb/^{238}U$ age (modified from Simonetti et al., 2018).

Day 1 - stop 3: mylonitic gneiss with biotite and white mica (coord. 44°16'58.1"N; 07°01'09.2"E)

Following the P26 path we reach Rifugio Migliorero (fig. 1) in the middle of Ischiator valley (fig. 2). Here beautiful outcrops of protomylonitic gneiss crop-out (fig. 9a). These rocks are made of K-feldspar, plagioclase, and quartz porphyroclasts in a fine-grained biotite and white mica matrix (fig. 10b). The amount of matrix is nearly 50%. The foliation is oriented NW-SE and dips at high-angle toward the NE (fig. 5c), this is very similar to what was observed in the previous stops. Foliation is a penetrative disjunctive cleavage with smooth and parallel cleavage domain (fig. 9b). Quartz shows lobate grain boundaries (fig. 9c) indicating that the main dynamic recrystallization mechanism is grain boundary migration. Incipient subgrain rotation recrystallization is locally recogized. The mineral assemblage indicative of amphibolite-facies conditions, and quartz microstructures reveal higher deformation temperature, estimated to be higher than 500°C (Piazolo & Passchier, 2002); Stipp et al., 2002; Passchier & Trouw, 2005), compared to the mylonitic schist of stop 2.

At the outcrop scale asymmetric and stretched leucosomes are recognizable. In thin section rotated

porphyroclasts and porphyroclasts with asimmetric strain shadows (fig. 9d), mica fish, C and C' shear band occurr. Kinematic indicators point to a dextral top-to-the SW sense of shear. Vorticity estimation (fig. 7) in these rocks revealed a deformation with a prevalent component of pure shear (~70%; Simonetti et al., 2018).

Recent U-Th-Pb *in situ* petrochronology on syn-kinematic monazites, revealed a deformation age of ~328 Ma (fig. 8; Simonetti er al., 2018), older than the age of shear in the Mylonitic schist of stop 2.

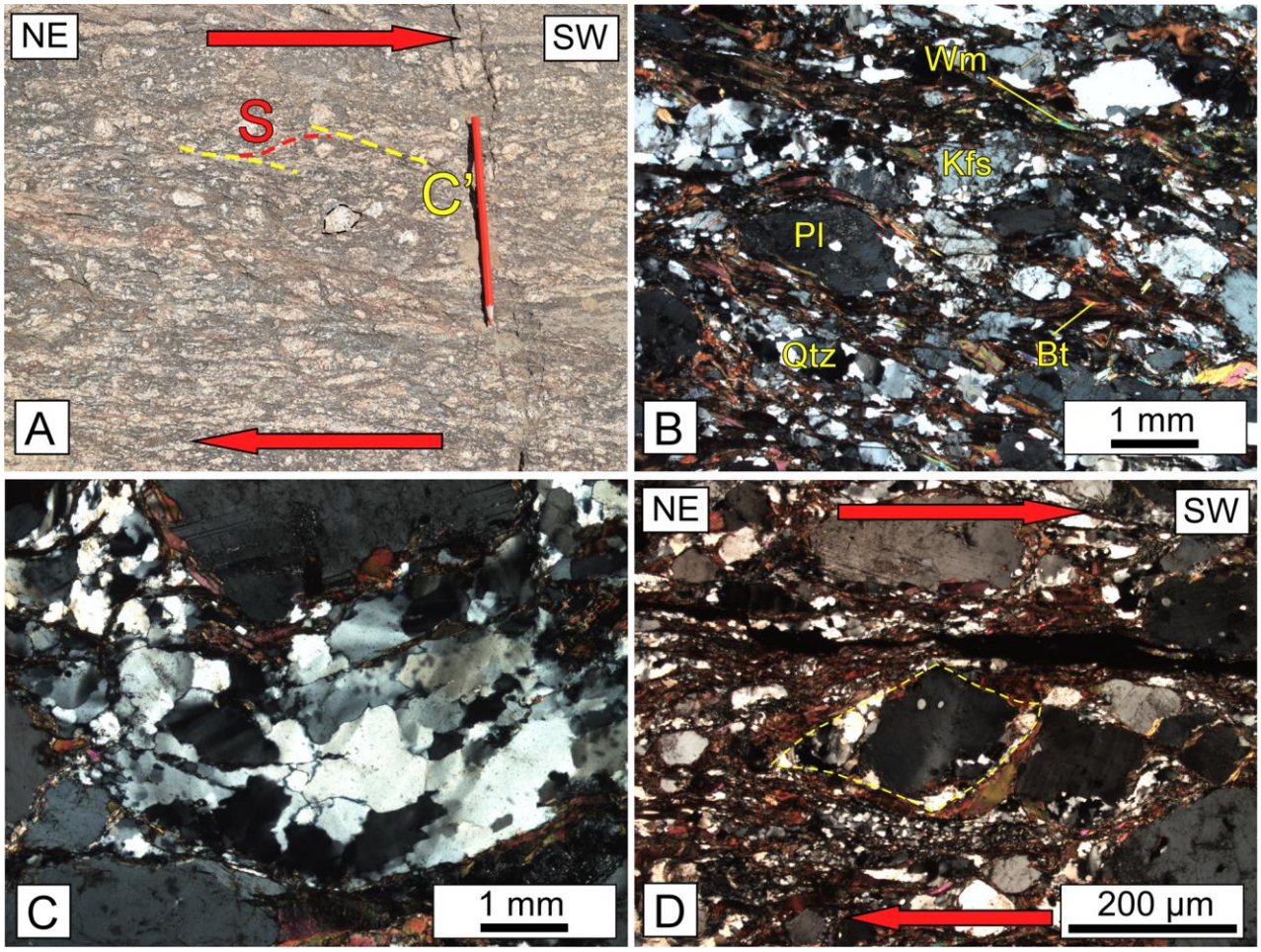

Fig. 9 - A) protomylonitic gneiss cropping out near the Migliorero hut, an S-C' fabric pointing to a dextral top-to-the SW sense of shear is present; B) penetrative disjunctive cleavage with smooth and parallel cleavage domain in the protomylonitic gneiss (crossed nicols); C) quartz showing lobate grain boundaries indicative of grain boundary migration (crossed nicols); D) feldspar porphyroclasts with asimmetric strain shadows indicative of a dextral top-to-the SW sense of shear (crossed nicols).

Day 1 - stop 4: protomylonitic gneiss with biotite and sillimanite (coord. 44°16'46.8"N; 07°00'59.1"E)

In this stop we can observe protomylonitic gneiss with biotite and sillimanite located at the boundary of the FMSZ (fig. 10a). At the outcrop scale this lithotype is very similar to the mylonitic gneiss of stop 3, the main difference is the presence of sillimanite and the lower abundance of white mica (Carosi et al., 2016). Asimmetric and stretched leucosomes are recognizable (fig. 10a). The amount of matrix in this lithotype is about 40% which testifies the less intense deformation of these rocks compared to those visited in stops 1, 2, 3 and 4. The main foliation, oriented NW-SE and dipping at high angle toward the NE, is a penetrative disjunctive cleavage (fig. 10b) with smooth and

anastomozed cleavage domains rich in biotites and prismatic or fibrolitic sillimanite (fig. 10b). The orientation of the main foliation is perfectly concordant with the orientation observed in the more sheared rocks. At the microscale kinematic indicators, such as porphyroclasts with asymmetric strain shadows, micafish and C-C' shear bands are present (fig. 10c). All of them point to a top-to-the SW sense of shear. Quartz is dynamically recrystallized by grain boudary migration (fig. 10d). Deformation temperature above 500°C is in agreement with syn-kinematic biotite+sillimanite assemblage and quartz microstructures. The age of shear deformation, obtained with *in situ* U-Th-Pb petrochronology on syn-kinematic monazites (Simonetti et al., 2018) is ~340 Ma (fig. 8). Deformation is therefore older compared to the age of shear deformation obtained in the mylonitic schist (stop 2) and in the mylonitic gneiss (stop 3).

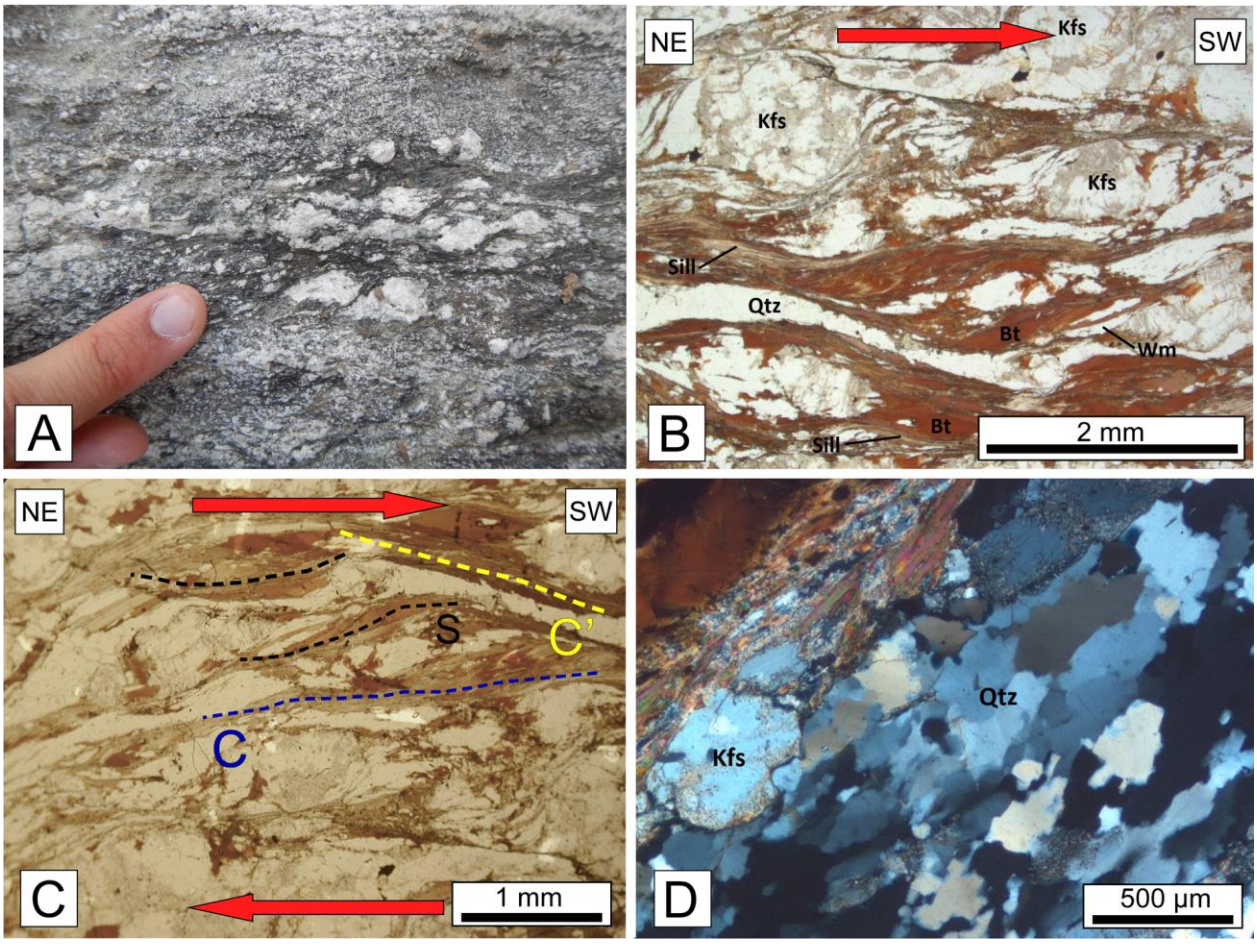

Fig. 10 - A) protomylonitic gneiss with biotite and sillimanite at the outcrop scale; B) disjunctive cleavage with smooth and anastomized cleavage domain rich in biotites and sillimanite, rotated porphyroclasts show a a dextral top-to-the SW sense of shear (parallel nicols); C) S-C-C' fabric indicative of dextral top-to-the SW sense of shear (parallel nicols); D) quartz showing lobate grain boundaries indicative of grain boundary migration (crossed nicols).

Day 1 - stop 5: migmatitic gneiss of the Tinèe Complex (coord. 44°16'39.2"N; 07°00'29.3"E)

In the area near the Laghi dell'Ischiator (fig. 2), migmatitic gneiss with biotite and sillimanite ('Rabuons Formation' in the literature; Faure-Muret, 1955; Malaroda et al., 1970), belonging to the Tinèe Complex crops out (fig. 11a). These rocks are unaffected by shear of the FMSZ. Migmatites resulted from partial melting of metasediments (Malaroda et al.,

1970; Ferrando et al., 2008; Compagnoni et al., 2010) and are not affected by shear deformation of the FMSZ. Leucosomes show variable thickness. These rocks show a disjunctive foliation (fig. 11b) oriented NW-SE and variably dipping to NE or SW (fig. 5d). Quartz present a big grainsize and lobated margins in accordance with grain boundary migration (fig. 11c) deformation mechanism. Open to tight symmetric folds with subvertical axial plane oriented NW-SE and sub-horizontal axis are present (fig. 11e). Fold axial plane is parallel to the mylonitic foliation within the FMSZ so that the folding event occurred in a strain regime compatible with the shearing deformation in the FMSZ (Simonetti et al., 2018). Folds contributed to accomodate the nearly horizontal shortening resulted from the pure shear component acting during transpression.

Transpressional deformation is generally subjected to strain compatibility problems (Hudleston, 1999) because it is not easy to explain how the flattening component of the deformation is accomodated.

The presence of syn-shear folds in the unsheared migmatites testifies that the Tinée Complex and the shear zone could have been stretched together during transpression and therefore no strain compatibility problems are present.

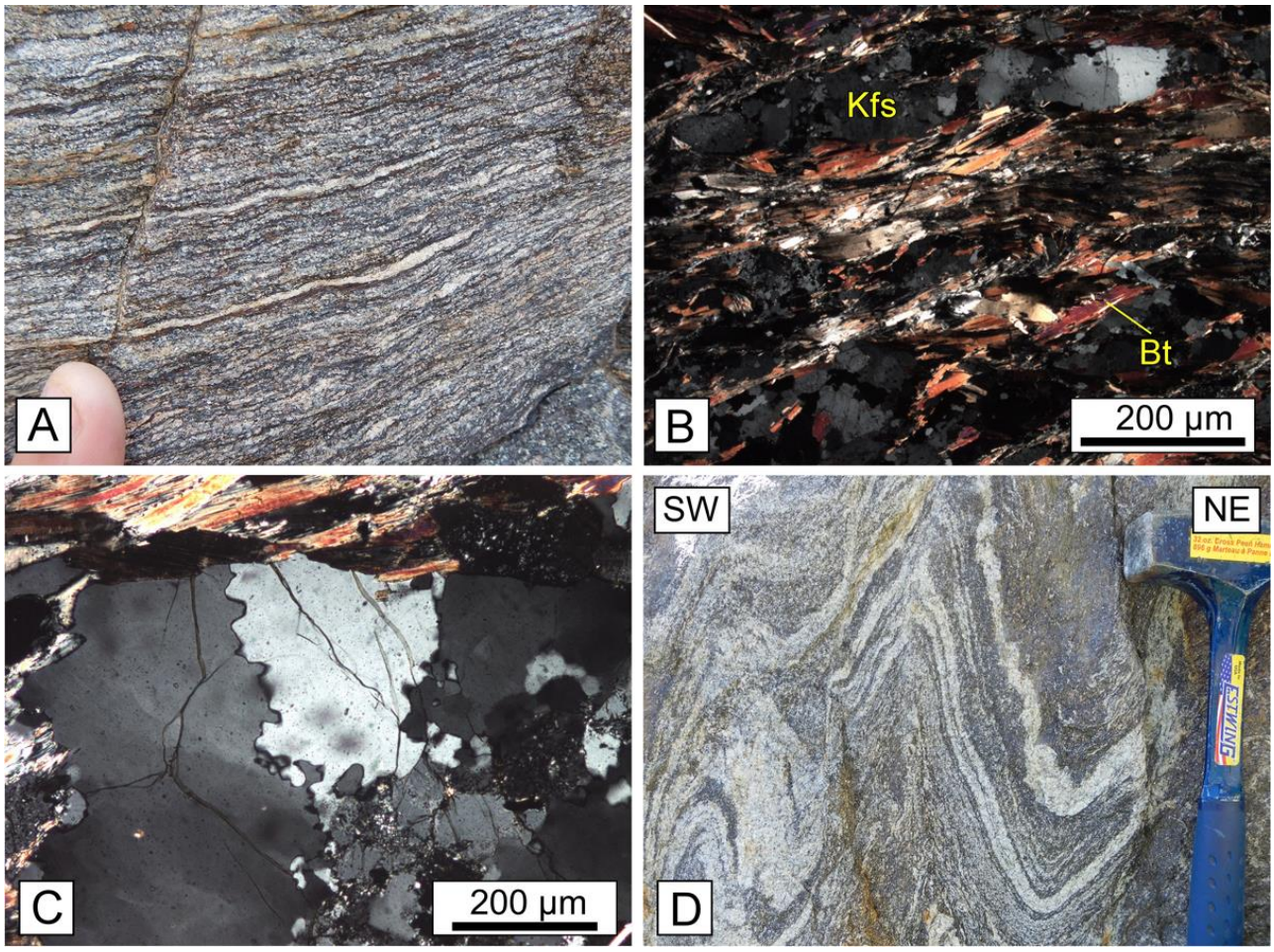

Fig. 12 - A) migmtitic gneiss of the Tinée complex at the outcrop scale; B) disjunctive foliation of the migmatitic gneiss (crossed nicols); C) quartz showing big grainsize and lobated margins idnicative of grain boundary migration (crossed nicols); D) symmetric folds with subvertical axial plane oriented NW-SE in the migmatitic gneiss.

Day 2 - stop 1: migmatites of the Gesso-Stura-Vesubie Complex (Coord. 44°20'00.8"N; 06°59'54.6"E)

From Pontebernardo we follow the road towards the locality Prati del Vallone (fig. 1; fig. 3). Halfway down the road it is possible to leave the car and follow a footpath up to a small abandoned technical building where we can reach the first outcrop of the day. Here migmatites of the Gesso-Stura-Vesubie Complex, formed at the expense of metasedimentary rocks, can be observed (fig. 12a). These rocks are medium-grained migmatitic gneiss with a quartz-plagioclase (An_{20-30})-biotite-fibrolitic sillimanite-cordierite assemblage with few K-feldspar and muscovite (fig. 12b). Relict kyanite and garnet rarely included in plagioclase suggest that these rocks reached P-T conditions of the upper amphibolite-facies (650–700°C; 0.6–0.8 GPa) and subsequently suffered a decompression from the kyanite to the sillimanite stability field (Compagnoni et al., 2010).

Meter-thick leucocratic portions with less biotite locally occur. About 10-20 Ma after the Carboniferous HP metamorphism, the Argentera Massif underwent amphibolite-facies metamorphism with extensive development of migmatites at 323 ± 12 Ma (Rubatto et al., 2001). Older ages for the anatectic event are reported from other Variscan migmatites in different fragments of the Variscan chain (Compagnoni et al., 2010; Oliot et al., 2015; Schneider et al., 2014) suggesting that several melting events may have succeeded one to each other in a complex anatectic history.

From the structural point of view the migmatites shows a disjucntive foliation that is affected by open to tight symmetric folds (figs. 12c, 12d), with fold axes gently plunging toward the NW and subvertical NW-SE striking axial planes (fig. 5e) (Carosi et al., 2016). Axial planes are parallel to the mylonitic foliation of the FMSZ (fig. 13a). Similarly to the structural framework observed in stop 5 of day 1, folding event occurred in a strain regime compatible with shear in the FMSZ (fig. 14b; Carosi et al., 2016; Simonetti et al., 2018) and contributed to accomodate a nearly horizontal shortening. We come back on the road and we reach the locality Prati del Vallone where we can leave the car.

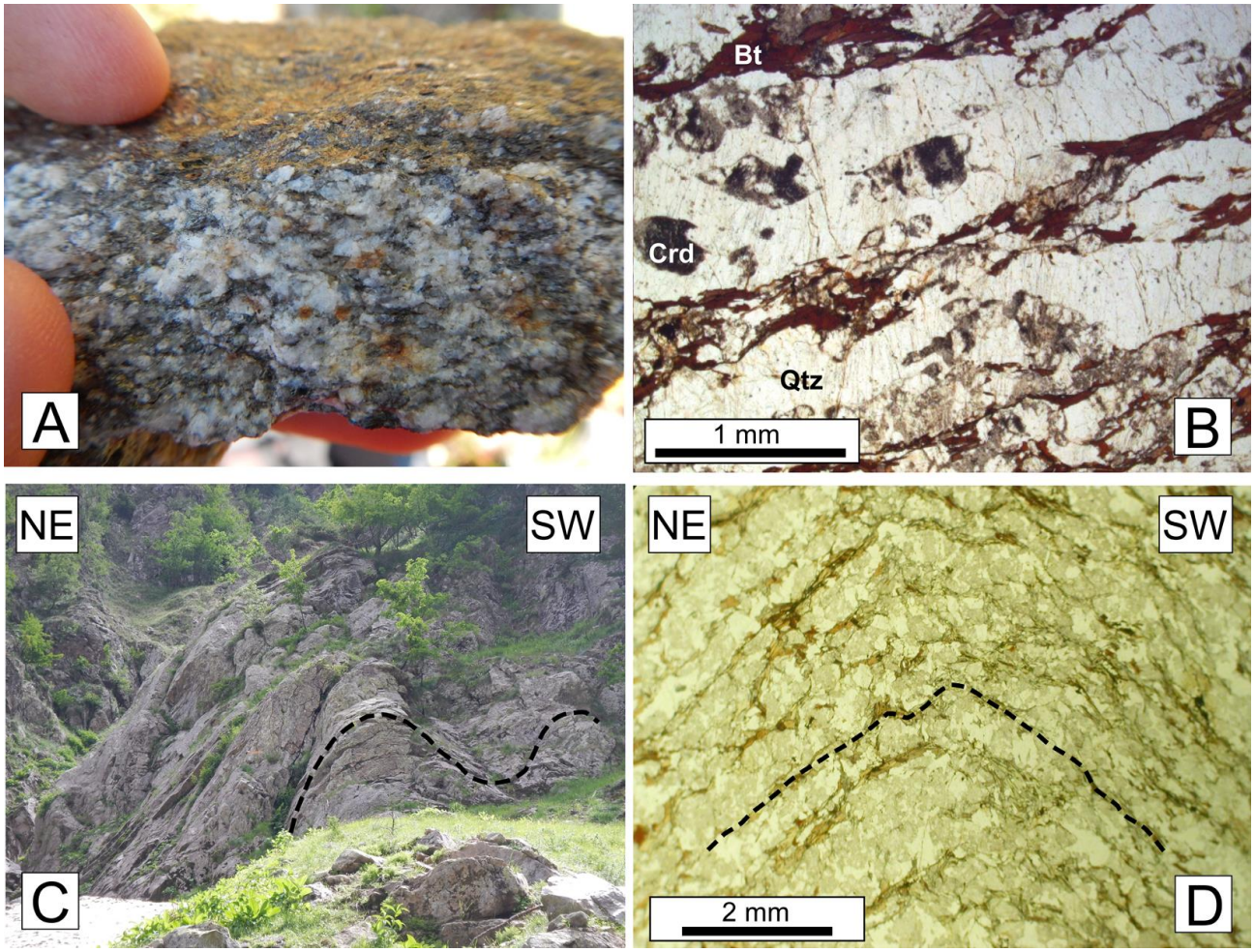

Fig. 12 - A) para-derived migmatites belonging to the Gesso-Stura-Vesubie Complex; B) alternating levels of red biotite and quartz + cordierite domains that materialize a gneissic foliation (parallel nicols); C) folds affecting the gneissic foliation of the GSV migmatites; D) gneissic foliation folded in thin section (parallel nicols).

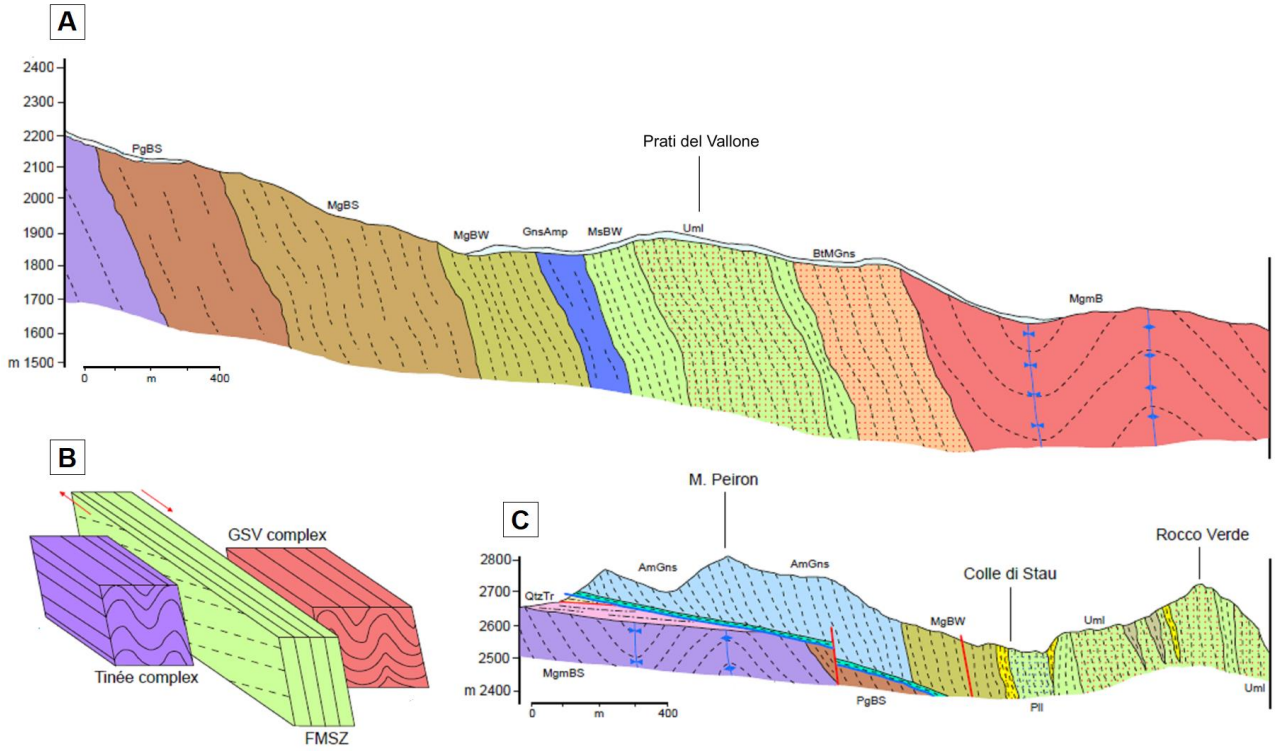

Fig. 13 - geological cross-section of the FMSZ (legend is the same as in figure 4, modified after Carosi et al., 2016): A) section across the Pontebernardo Valley (section A, figure 3); B) relationship between the mylonitic foliation in the FMSZ and the folds observed both in the GSV and Tinée complexes (Carosi et al., 2016); C) section across the Mt Peiron-Colle di Stau-Rocco Verde (section B, figure 3).

Day 2 - stop 2: sheared amphibole-bearing gneiss (coord. 44°19'06.7"N; 06°59'01.5"E)

In this stop we can observe a decameter-sized lense of amphibole-bearing gneiss (fig. 3) within the FMSZ ("*Embrechiti ed anatessiti anfiboliche*" according to Malaroda et al., 1970). These are light-colored gneiss made of amphibole (horneblende), quartz, biotite and plagioclase (An 50-60%) generally with a massive appearance (fig. 14a) or only weakly foliated (fig. 14b). When present foliation is a disjunctive cleavage (fig. 14c). The gneiss belongs to the Tinée complex and extensively crops out in the north-western sector of the crystalline basement of the Argentera Massif (fig. 4; Carosi et al., 2016). According to Compagnoni et al. (2010) the protolith of the gneiss is an intermediate igneous rock. Several lenses of this lithotype (fig. 14d), showing different amount of deformation, are present within the FMSZ (Carosi et al., 2016). Sometimes deformation is very strong that the original structure of the rock is nearly unrecognizable (fig. 14e) and the percentage of matrix in higher than 65%. Because of the position of this lense, very close to the central part of the shear zone, it is possible to observe sheared portions with evident S-C-C' fabric indicative of a top-to-the-SE sense of shear (fig. 14f).

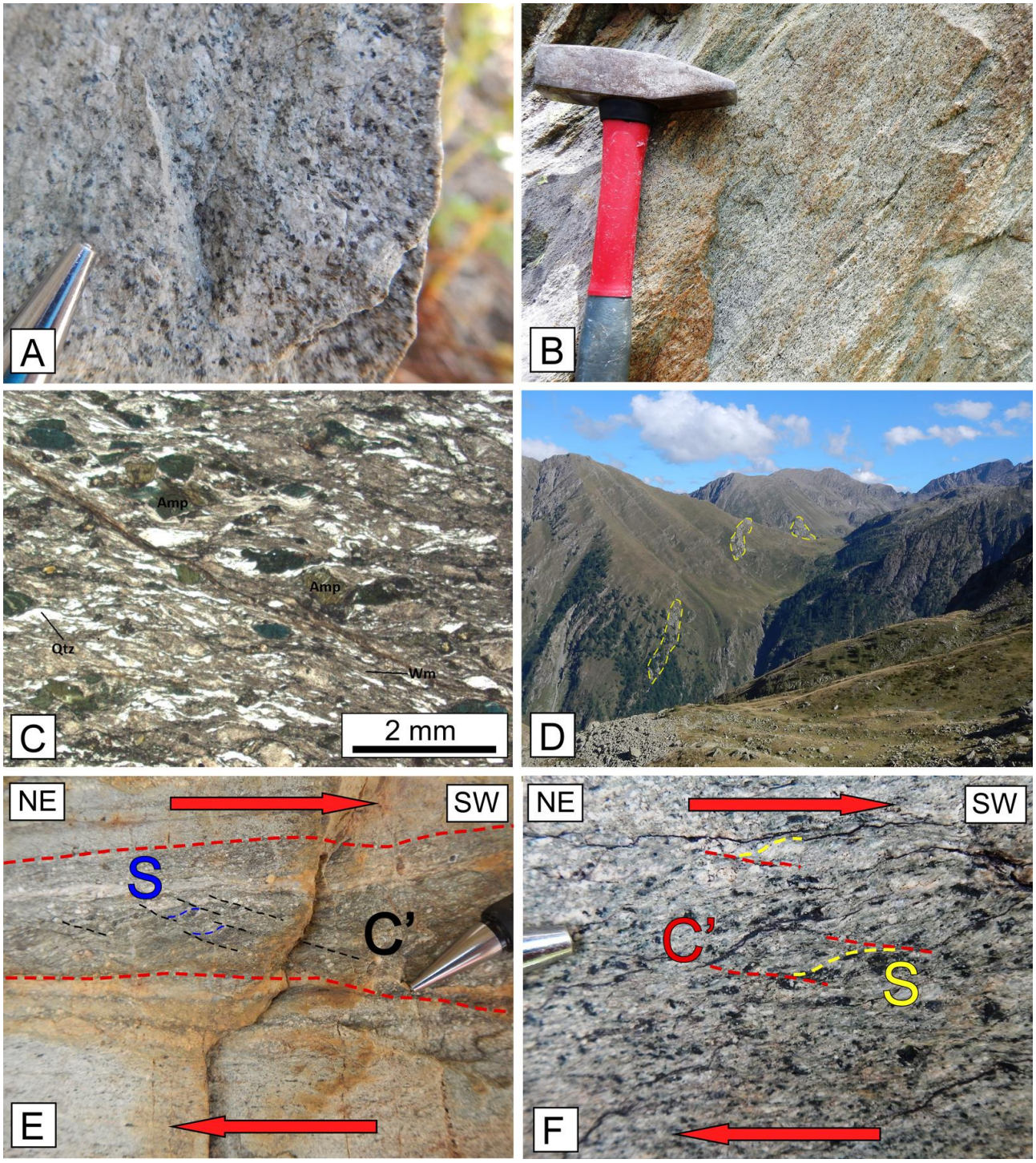

Fig. 14 - A) amphibole-bearing gneiss with massive aspect; B) foliated amphibole-bearing gneiss; C) amphibole-bearing gneiss in thin section, the disjunctive foliation can be recognized (parallel nicols); D) decametric lenses of amphibole-bearing gneiss (highlighted in yellow) within the FMSZ; E) low strain domain and strongly sheared domain with S-C' fabric in the amphibole bearing gneiss, sense of shear is dextral top-to-the SW; F) S-C' fabric at the outcrop scale, dextral top-to-the SW sense of shear.

Day 2 - stop 3: Mt Peiron-Colle Panieris alpine thrust (coord. 44°19'31.6"N; 06°57'24.6"E)

From Prati del Vallone we follow the GTA path and then we go toward the Colle Panieris on a minor path. Below the Mt Peiron we can observe evidence of Alpine deformation in the basament of the Argentera Massif.

In the Mt Peiron-Colle Panieris area, a mylonitic belt with metric thickness (fig. 3) thrusts Amphibole-bearing mylonitic gneiss of the FMSZ above Permo-Triassic sedimentary cover of the Argentera Massif (fig. 15a; fig. 13c), represented by light colored quarzite. Mylonitic foliation strikes nearly E-W and gently dips toward the N with a NNW plunging mineral lineation (fig. 5f). Mylonite are made of quartz and feldspar porphyroclasts in a fine-grained chlorite + white mica matrix (fig. 15b). The amount of matrix variable between 65% and 75%. The mineral assemblage indicates greenschist-facies metamorphism. Foliation varies from a continous cleavage in the most deformed part to a disjunctive cleavage with zonal and parallel cleavage domains. An S-C frabric is well recognizable both at the outcrop scale (fig. 15c) and in thin section and is indicative of an inverse top-to-the-SSE sense of shear. Quartz is dynamically recristallized by subgrain rotation recrystallization and feldspar porphyroclasts are fractured suggesting temperature of deformation in agreement with the syn-kinemtic mineral assemblage.

The Argentera Massif was involved in the Alpine orogeny at ~22 Ma (Corsini et al., 2004; Sanchez et al., 2011). Most of the deformation is concentrated in the sedimentary covers (Malaroda et al., 1970; Barale et al., 2016; d'Atri et al., 2016) that are detached from the metamorphic basement along evaporites and limestone breccias levels. Alpline overprint in the basament is limited and concentrated along ductile and brittle ductile shear zones (Compagnoni et al., 2010; Carosi et al., 2016; Simonetti et al., 2017, 2018), the Mt Peiron-Colle Panieris thrust can be considered as one of shuch shear zones.

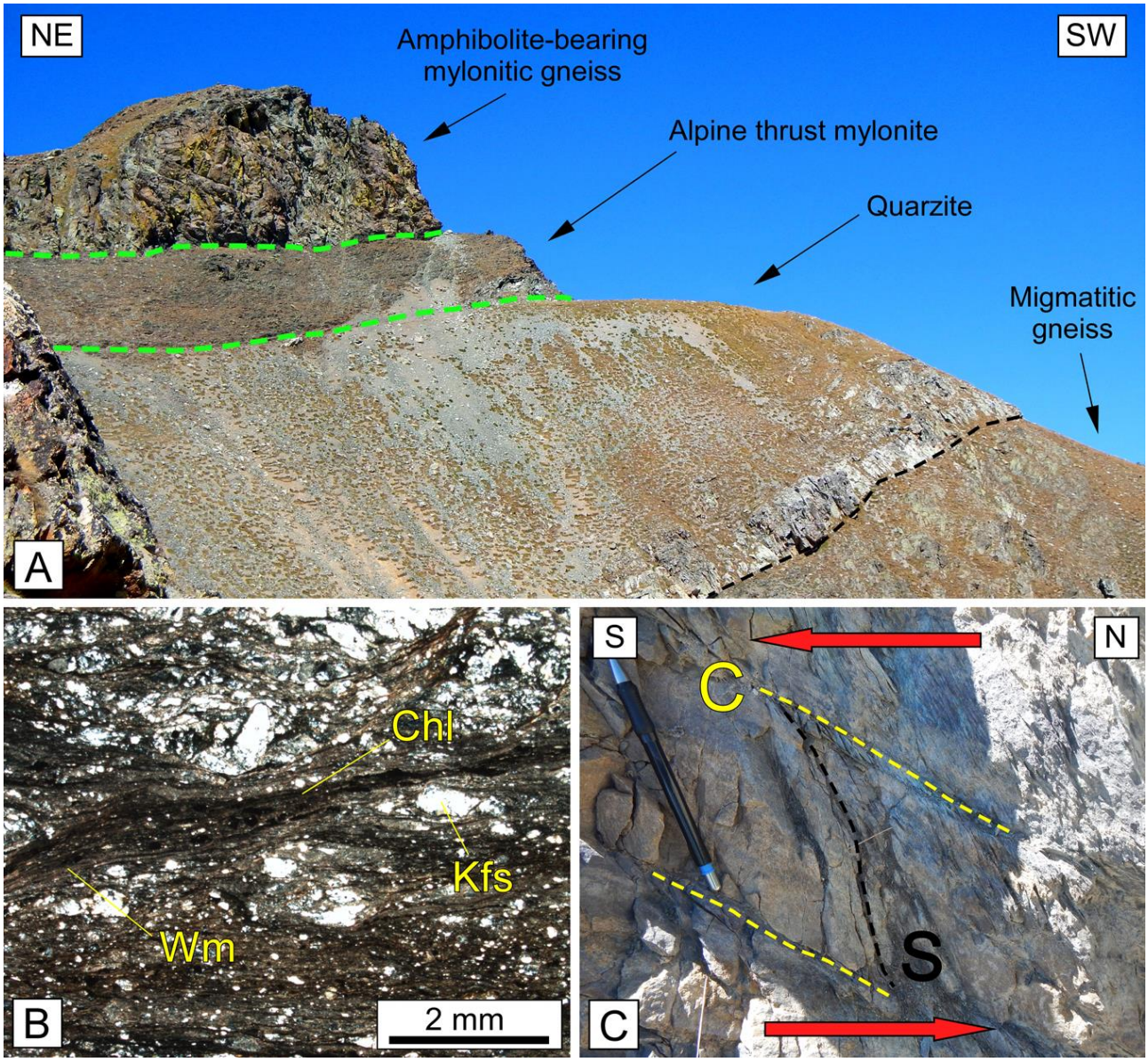

Fig. 15 - A) mylonitic belt with metric thickness thrusting Amphibole-bearing mylonitic gneiss of the FMSZ above Permo-Triassic sedimentary cover of the Argentera Massif in the Mt Peiron-Colle Panieris area; B) mylonite of the Mt Peiron-Colle Panieris thrust in thin section, quartz and feldspar porphyroclasts in a fine-grained chlorite + white mica matrix can be recognized (crossed nicols); C) S-C fabric at the outcrop scale showing a top-to-the S sense of shear.

Day 2 - stop 4: undeformed Permo-Triassic quarzite (coord. 44°19'18.8"N; 06°57'12.8"E)

Not far from stop 2, following a small path toward the SW for nearly 450 m, white-grey quarzites of Permo-Triassic age (Barale et al., 2015) crops out and lay in angular unconformity directly above the migmatitic basement (fig. 16a). They are made of quartz and very few white mica (fig. 16b), ripple marks are often well recognizable (fig. 16c).

Above the quarzites tectonic carbonatic breccias known as '*Formazione delle Carniole'* (Malaroda et al., 1970) with both gypsum and dolomitic limestone clasts, occurs (fig. 3). These are interpreted as weak horizons along which the detachment of the sedimentary succession occurs.

The presence of undeformed Permo-Triassic sediments directly above the basement is a good constrain for the age of Variscan transpression.

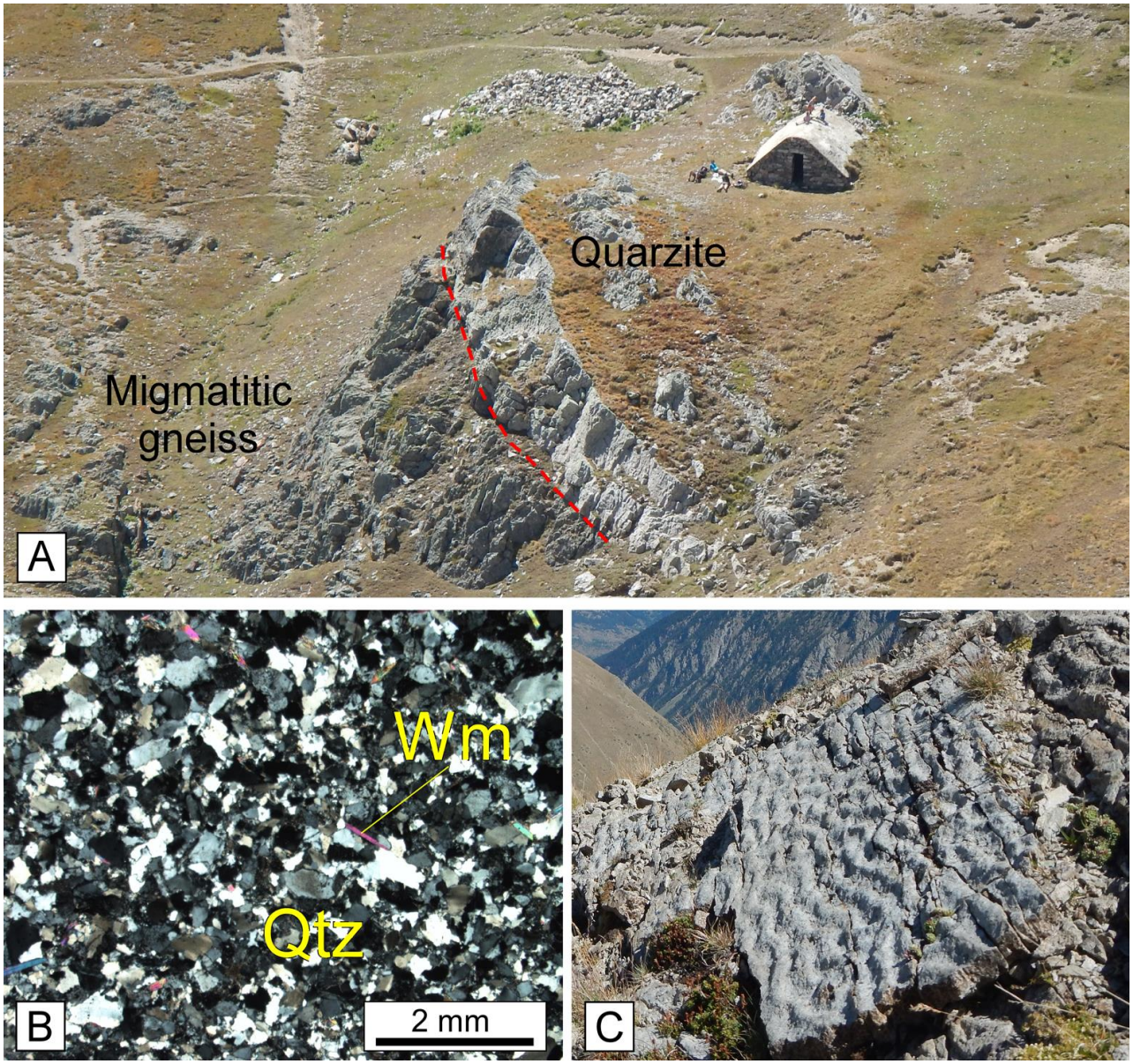

Fig. 17 - A) quarzites of Permo-Triassic age in angular unconformity directly above the migmatitic basement in the Colle Panieris area; B) fine grained white mica in the quarzite (crossed nicols); C) strata surface with ripple marks.

5 – DISCUSSION

The features observed in the outcrops of the field trip highlight a complex evolution of the FMSZ. Kinematic vorticity analysis (Simonetti et al., 2018) highlighs a transpressional deformation (fig. 17a) with a variable component of simple shear (fig. 17b) icreasing along the deformation gradient from the wall-rocks to the high-strain zone in the central part of the FMSZ (fig. 17c). This is in agreement with the structural asset of the FMSZ in the field where it is possible to recognize a subvertical mylonitic foliation, with constant orientation in all the lithotypes. This is in agreement with the model of transpressional deformation (Fossen et al., 1994). Folds with subvertical axial plane parallel to the mylonitic foliation in the GSV Complex and Tinèe Complex are another evidence of horizontal shortening attributed to the component of pure shear. Because the two walls of the FMSZ (the GSV and the Tinèe Complex) can deform togheter with the shear zone no strain compatibility problems are present (Simonetti et al., 2018).

In situ petrochronology (combining U-Th-Pb ages with textural observations and monazite chemistry) revealed that the Variscan transpression in the Argentera Massif started at the metamorphic peak of the GSV complex (dated at ~340 Ma; Compagnoni et al., 2010; Rubatto et al., 2010) or shortly after it and triggered its exhumation (Simonetti et al., 2018). This approach also revealed a long-lasting activity of the FMSZ that activated for at least 20 Ma under changing metamorphic conditions from high-temperature to low temperature.

The presence of medium- to high-grade metamorphic mylonites associated with lower-grade ones, localized in the central part of the FMSZ, the strong deformation gradient and the changes in the deformation regime and age of deformation along the gradient are evidence that the FMSZ evolved as a strain softening type II shear zone (fig. 18; Fossen, 2016). In this type of shear zone, deformation progressively concentrates in the central part because of strain softening (due to the presence of channeled fluids, metamorphic reactions and grain size reduction) leaving the external parts of the structure progressively inactive (fig. 18). Because of this the active thickness decreases whereas the total thickness remains constant (fig. 18). Strain softening can be enhanced by the presence of fluids joined with metamorphic reactions and grainsize reduction, well detectable both at the meso and micro scale. Evidence of the first two factors is the breackdown of amphibolite-facies minerals such as sillimanite and biotite and consequent growth of white mica and chlorite in the most sheared rocks. Along the deformation gradient a reduction in the amount of quartz and feldspar in the rocks in favour of the amount of phillosilicates is evident.

Because of the type II evolution, protomylonites in the external part of the FMSZ preserve features acquired during the early stage of shear (testified by the older age of deformation) during high-temperature condition whereas mylonites, in the internal part of the shear zone, record features acquired during younger deformation stages of the deformation at lower temperature. Finally the ultramylonites preserve evidence of the final stage of activity of the shear zone. Despite a similar evolution, characterized by strain localization during decreasing temperature, has been recently described in detail in the Yukon River shear zone (Northern Cordillera, Canada; Parsons et al., 2018), other well-described examples of regional-scale strain softening shear zones are not so common in literature up to now. The FMSZ should be considered as a new example of a strain-softening regional-scale shear zone, that can be useful to the community of structural geologists for future process-oriented investigations.

Furthermore, the described data are yet another example that, as pointed out by Fossen & Cavalcante (2017) and Oriolo et al. (2018), a multidisciplinary approach is strictly necessary to obtain meaningful results to address unsolved problems in modern structural geology and in the study of shear zones, were complexity arises from the coupling between long-lasting progressive and/or polyphasic deformation, metamorphism and fluid-rock interaction.

Detailed field work and meso-structural analysis should always be combined with microstructural observations, with moderne tecniques for vorticity analysis, with deformation temperature estimation and with detailed petrochronology in order to unreveal the fundamental steps of the tectono-metamorphic history of shear zones.

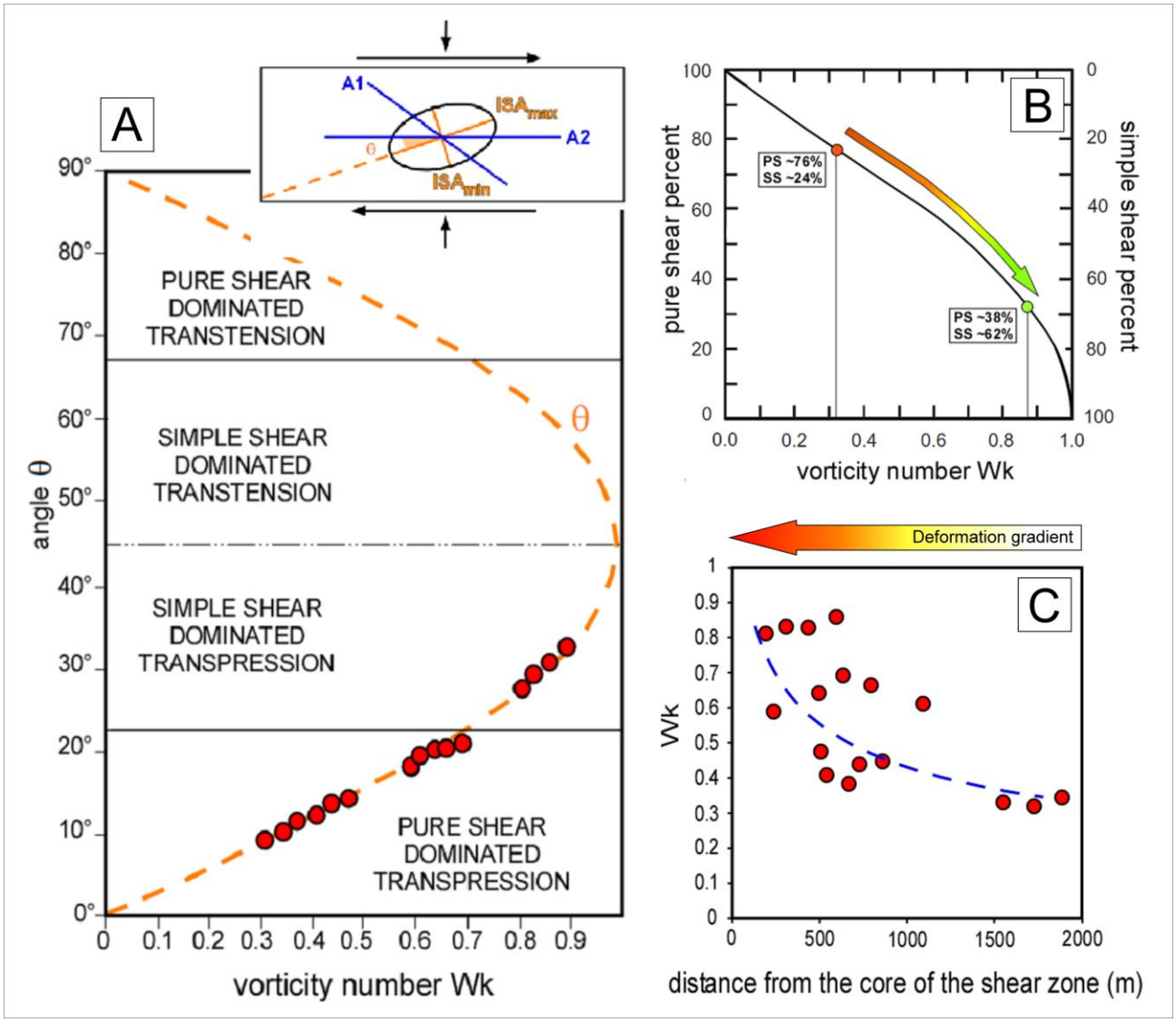

Fig. 17 - A) diagram showing relationship between the orientation of the maximum Instantaneous Stretching Axis (ISAmax) with respect to the shear zone boundary (angle θ) related to the kinematic vorticity number Wk (modified after Fossen & Tikoff 1993; Fossen et al., 1994). Wk value for which simple shear = pure shear is 0.71 according to Law et al. (2004) and Xypolias (2010). The distribution of the samples shows a variation from a pure shear dominated transpression to a simple shear dominated transpression linked to the increase of the vorticity number. Orange dashed line represents the theoretical trend of the angle θ in relation to Wk; B) Percentage of pure shear (PS) and simple shear (SS) in relation to the calculated maximum and minimum Wk values; C) variation of the vorticity number in relation with the distance of the sample from the center of the shear zone. The distribution of points shows increasing Wk values (i.e., increasing of simple shear component of deformation) toward the central part of the shear zone (trend: blue dashed line).

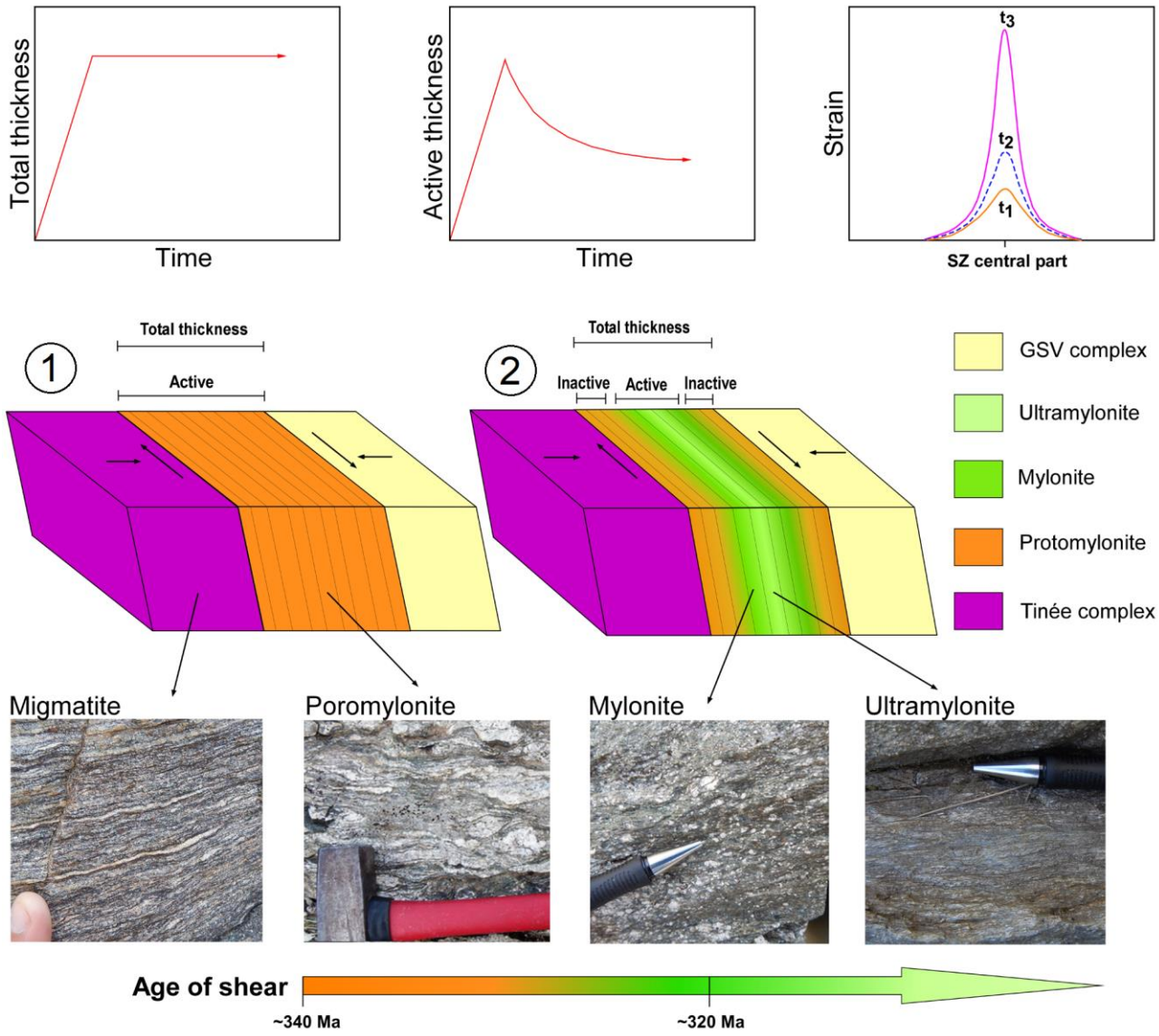

Fig. 18 -sketch summarizing the evolution of the Ferriere-Mollières Shear Zone according to the type II growth model (Fossen, 2016). Graphs show the theoretical variation of total and active thickess during time and the amount of strain within the shear zone.

6 – CONCLUSIVE REMARKS

- A deformation gradient, marked by a transition from protomylonites to mylonites and to ultramylonites, is recognizable from the marginal part of the FMSZ shear zone toward the central part;
- Foliation of the FMSZ shows a constant trend of orientation in all the different type of mylonites;
- Fold axial planes the GSV complex and Tinèe complex are subparallel to the mylonitic foliation;
- Vorticity analysis constrained a transpressional deformation with a prevalent component of pure shear acting toghether with simple shear. Simple shear component increase along the deformation gradient;
- syn-kinematic mineral assemblage along the deformation gradient highlight a syn-shear retro-metamorphism from high-temperature amphibolite-facies to greenschist-facies. Quartz microstructures also highlight a temperature decrease during deformation;
- Because of strain softening phenomena, deformation in the FMSZ starts to concentrate in its central part leaving the margin inactive according to a type II evolution;
- Across the deformation gradient is possible to observe different stage of formation of the FMSZ;
- *In situ* U-Th-Pb petrochronology on monazite revealed a long-lasting activity of the FMSZ (between ~340 Ma and ~320 Ma) and constrained the different strain-softening evolution stages;
- The FMSZ is a very good case study of strain-softening shear zone that can be a good case of study, at regional scale, for future process-oriented investigations;

References

Advokaat E.L., van Hinsbergen D.J.J., Maffione M., Langereis C.G., Vissers R.L.M., Cherchi A., Schroeder R., Madani H., Columbus S., 2014, Eocene rotation of Sardinia, and the paleogeography of the western Mediterranean region. Earth Planet Sc Lett, 401, 183–195.

Arthaud F., Matte P., 1977, Late Paleozoic strikeslip faulting in southern Europe and northern Africa; result of a right-lateral shear zone between the Appalachians and the Urals. Geological Society of America Bulletin 88:1305–1320.

Baietto A., Perello P., Cadoppi P., Martinotti G., 2009, Alpine tectonic evolution and thermal water circulations of the Argentera Massif (South-Western Alps). Swiss Journal of Geosciences 102 (2), 223 - 245.

Barale L., Bertok C., D'atri A., Martire L., Piana F., Domini G., 2016, Geology of the Entracque–Colle di Tenda area (Maritime Alps, NW Italy). Journal of Maps, 12, 359–370.

Burg J-P., Matte P., 1978, A cross section through the French Massif Central and the scope of its Variscan Geodynamic Evolution. Zeitschrift der Deutschen Geologischen Gesellschaft 129:429–460

Carosi R., Palmeri R., 2002, Orogen-parallel tectonics transport in the Variscan belt of northeastern Sadinia (Italy): implications for the exhumation of medium-pressure metamorphic rocks. Geol Mag, 139, 497-511

Carosi R., Montomoli C., Tiepolo M., Frassi C., 2012, Geochronological constraints on post-collisional shear zones in the Variscides of Sardinia (Italy), Terra Nova, 24, 42 - 51.

Carosi R., D'addario E., Mammoliti E., Montomoli C., Simonetti M., 2016, Geological map of the northwestern portion of the Ferriere-Mollieres shear zone, Argentera Massif, Italy. Journal of Maps, 12, 466-475.

Carosi R., Frassi C., Iacopini D., Montomoli C., 2005, Post collisional transpressive tectonics in northern Sardinia (Italy). Journal Virtual Explorer, 19, 3, 1-18.

Carosi R., Montomoli C., Iaccarino S., Visonà D., 2018, Structural evolution, metamorphism and melting in the Greater Himalayan Sequence in central-western Nepal. In: (Eds.) Treloar P. J., and Searle M. P., 2019, Himalayan Tectonics: A Modern Synthesis. Geological Society, London, Special Publications, 483, 305–323.

Compagnoni R., Ferrando S., Lombardo B., Radulesco N., Rubatto D., 2010, Paleo-European crust of the Italian Western Alps: Geological history of the Argentera Massif and comparison with Mont Blanc-Aiguilles Rouges and Maures-Tanneron Massifs. In: (Eds.) M. Beltrando, A. Peccerillo, M. Mattei, S. Conticelli & C. Doglioni, Journal of the Virtual Explorer, volume 36, paper 4, doi: 10.3809/jvirtex.2009.00228

Corsini M., Ruffet G., Caby R., 2004, Alpine and late Hercynian geochronological constraints in the Argentera Massif (Western Alps). Eclogae geologicae Helvetiae, 97, 3 - 15.

Corsini M., Rolland Y., 2009, Late evolution of the southern European Variscan belt: exhumation of the lower crust in a context of oblique convergence. Comptes Rendus Geosciences 341 (2–3), 214–223.

Cottle J.M., Searle M.P., Jessup M.J., Crowley J.L., Law R.D., 2015, Rongbuk Re-visited: Geochronology of Leucogranites in the Footwall of the South Tibetan Detachment System, Everest Region, Southern Tibet. Lithos, 227, 94 - 106.

Cruciani G., Montomoli C., Carosi R., Franceschelli M., Puxeddu M., 2015, Continental collision from two perspectives: A review of Variscan metamorphism and deformation in northern Sardinia. Periodico di mineralogia, 84, 3, 657-699.

d'Atri A., Piana F., Barale L., Bertok C., Martire L., 2016, Geological setting of the southern termination of Western Alps. Int J Earth Sci (Geol Rundsch), 105, 1831–1858. DOI 10.1007/s00531-015-1277-9.

Dias R., Ribeiro A., 1995, The Ibero-Armorican Arc: A collision effect against an irregular continent? Tectonophysics, 246, 113–128.

Dias R., Ribeiro A., Romão J., Coke C., Moreira N., 2016, A review of the arcuate structures in the Iberian Variscides; constraints and genetic models. Tectonophysics, 681, 170–194. doi: 10.1016/j.tecto.2016.04.011

Di Vincenzo G., Carosi R., Palmeri R., 2004, The relationship between tectono-metamorphic evolution and argon isotope records in white mica: constraints from in situ 40Ar–39Ar laser analysis of the Variscan basement of Sardinia. Journal of Petrology 45, 5, 1013-1043.

Faure-Muret A., 1955, Etudes géologiques sur le massif de l'Argentera-Mercantour et ses enveloppes sédimentaires. Mémoires pour servir à l'explication de la Carte géologique détaillée de la France, Paris, Imprimerie Nationale, France, with «Esquisse Géologique du Massif de l'Argentera-Mercantour et de sa Bordure Sédimentaire (Versant français) » at the 1/100.000 scale., pp 336.

Fernández-Lozano J., Pastor-Galán D., Gutiérrez-Alonso G., Franco P., 2016, New kinematic constraints on the Cantabrian orocline: A paleomagnetic study from the Peñalba and Truchas synclines, NW Spain. Tectonophysics, 681, 195–208. doi: 10.1016/j.tecto.2016.02.019

Ferrando S., Lombardo B., Compagnoni R., 2008, Metamorphic history of HP mafic granulites from the Gesso-Stura Terrain (Argentera Massif, Western Alps, Italy). European Journal of Mineralogy, 20, 777 - 790.

Ferrara G., Malaroda R., 1969, Radiometric age of granitic rocks from the Argentera Massif (Maritime Alps). Bollettino della Società Geologica Italiana, 88, 311-320.

Fossen H., Tikoff B., 1993, The deformation matrix for simultaneous simple shearing, pure shearing and volume change, and its application to transpression-transtension tectonics. Journal of Structural Geology, 15, 413-422, DOI: 10.1016/0191-8141(93)90137-Y.

Fossen H., Tikoff B., Teyssier C., 1994, Strain modeling of transpressional and transtensional deformation. Norsk Geol. Tidsskr. 74, 134-145.

Fossen H., 2016, Structural Geology. Cambridge University Press, p 510.

Fossen H., Cavalcante G. C. G., 2017, Shear zones – A review. Earth-Science Reviews, 171, 434–455.

Fossen H., Rotevatn A., 2016, Fault linkage and relay structures in extensional settings—a review. Earth Sci. Rev. 154, 14–28. http://dx.doi.org/10.1016/j.earscirev

Fossen H., Tikoff B., Teyssier C., 1994, Strain modeling of transpressional and transtensional deformation. Norsk Geol. Tidsskr. 74, 134-145.

Frassi C., Carosi R., Montomoli C., Law R.D., 2009, Kinematics and vorticity of flow associated with post-collisional oblique transpression in the Variscan Inner Zone of northern Sardinia (Italy). J Struct Geol, 31, 1458-1471.

Hudleston P., 1999, Strain compatibility and shear zones: is there a problem? Journal of Structural Geology, 21, 923–932.

Iaccarino S., Montomoli C., Carosi R., Massonne H.-J., Langone A., Visonà D., 2015, Pressure-temperature-time-deformation path of kyanite-bearing migmatitic paragneiss in the Kali Gandaki valley (central Nepal): Investigation of late Eocene–early Oligocene melting processes: Lithos, 231, 103–121. doi: 10.1016 /j .lithos .2015.06 .005

Iacopini D., Carosi R., Montomoli C., Passchier C. W., 2008, Strain analysis of flow in the Northern Sardinian Varisican Belt: recognition of a partitioned oblique deformation event. Tectonophysics, 221, 345 - 359.

Jessup M.J., Law R.D., Frassi C., 2007, The Rigid Grain Net (RGN): An alternative method for estimating mean kinematic vorticity number (Wm). Journal of Structural Geology 29, 411–421.

Kurz G.A., Northrup C.J., 2008, Structural analysis of mylonitic fault rocks in the Cougar Creek Complex, OregoneIdaho using the porphyroclast hyperbolic distribution method, and potential use of SC'-type extensional shear bands as quantitative vorticity indicators. Journal of Structural Geology 30, 1005-1012.

Law R. D., Searle M. P., Simpson R. L., 2004, Strain, deformation temperatures and vorticity of flow at the top of the Greater Himalayan Slab, Everest Massif, Tibet. Journal of the Geological Society, London, 161, 305-320

Malaroda R., Carraro F., Dal Piaz G. V., Franceschetti B., Sturani C., Zanella E., 1970, Carta geologica del Massiccio dell'Argentera alla scala 1:50.000 e note illustrative. Memorie della Società Geologica Italiana. Volume 9, 557 - 663.

Matte P., Ribeiro A., 1975, Forme et orientation de l'ellipsoïde de déformation dans la virgation hercynienne de Galice. Relations avec le plissement et hypothèses sur la genèse de l'arc ibéro-armoricain. CR Acad Sci Paris, 280, 2825–2828.

Matte P., 1986, Tectonics and plate tectonics model for the Variscan belt of Europe. Tectonophysics, 126, 329 - 374.

Matte P., 2001, The Variscan collage and orogeny (480–290 Ma) and the tectonic definition of the Armorica microplate: a review: Terra nova, 13, p. 122–128.

Montomoli C., Iaccarino S., Carosi R., Langone A., Visonà D., 2013, Tectonometamorphic discontinuities within the Greater Himalayan Sequence in western Nepal (central Himalaya): Insights on the exhumation of crystalline rocks. Tectonophysics, 608, 1349 - 1370.

Montomoli C., Carosi R., Iaccarino S., 2015, Tectonometamorphic discontinuities in the Greater Himalayan Sequence: A local or a regional feature? In Mukherjee, S., Carosi, R., van der Beek, P.A., Mukherjee, B.K., and Robinson, D.M., eds., Tectonics of the Himalaya: Geological Society of London Special Publication, 412, 25 - 41, doi: 10 .1144 /SP412.3

Musumeci G., Colombo F., 2002, Late Visean mylonitic granitoids in the Argentera Massif (Western Alps): age and kinematic constraints on the Ferrière-Mollières shear zone. Comptes Rendus de l'Académie des Sciences Serie II 334, 213 - 220.

Oliot E., Melleton J., Schneider J., Corsini M., Gardien V., Rolland, Y., 2015, Variscan crustal thickening in the Maures-Tanneron massif (South Variscan belt, France): new in situ monazite U-Th-Pb chemical dating of high-grade rocks. Bulletin de la Société géologique de France, 186, p. 145–169, doi: 10.2113/gssgfbull.186.2-3.145.

Oriolo S., Wemmer K., Oyhantcabal P., Fossen H., Schulz B., Siegesmund S., 2018, Geochronology of shear zones – A review. Earth-Science Reviews, 185, 665–683.

Parson A.J., Coleman M.J., Ryan J.J., Zagorevski A., Joyce N.L., Gibson H.D., Larson K.P., 2018, Structural evolution of a crustal-scale shear zone through a decreasing temperature regime: The Yukon River shear zone, Yukon-Tanana terrane, Northern Cordillera. Lithosphere, 10, 6, 760–782.

Passchier C.W., 1987, Stable position of rigid objects in non-coaxial flow: a study in vorticity analysis. Journal of Structural Geology, 9, n° 5/6, pp 679-690.

Passchier C.W., Trouw R.A.J., 2005, Microtectonics, Springer-Verlag Berlin Heidelberg, p 101.

Peacock D.C.P., Sanderson D.J., 1991, Displacements, segment linkage and relay ramps in normal fault zones. J. Struct. Geol. 13, 721–733.

Piazolo S., Passchier C. W., 2002, experimental modelling of viscous inclusions in a circular high-strain ring: implication for the interpretation of shape fabrics and deformed enclaves. J Geophy Res, 107, B10, 2242, ETG 11: 1 - 15.

Ramsay J.G., 1980, Shear zone geometry: a review. J. Struct. Geol., 2, 83–99.

Rosenbaum G., Lister G.S., Duboz C., 2002, Reconstruction of the tectonic evolution of the western Mediterranean since the Oligocene. In: Rosenbaum G, Lister GS (Eds), Reconstruction of the Alpine-Himalayan Orogen. Journal of the Virtual Explorer, 8, 107-126.

Rubatto D., Schaltegger U., Lombardo B., Colombo F., Compagnoni R., 2001, Complex Paleozoic magmatic and metamorphic evolution in the Argentera Massif (Western Alps) resolved with U–Pb dating. Schweizerische mineralogische und petrographische Mitteilungen, 81, 213–228.

Sanchez G., Rolland Y., Schneider J., Corsini M., Oliot E., Goncalves P., Verati C., Lardeaux J.M., Marquer D., 2011, Dating low-temperature deformation by 40Ar/39Ar on white mica, insights from the Argentera-Mercantour Massif (SW Alps). Lithos 125, 521 - 536.

Schneider J., Corsini M., Reverso-Peila A., Lardeaux J. M., 2014, Thermal and mechanical evolution of an orogenic wedge during Variscan collision: an example in the Maures-Tanneron massif (SE France). Geol. Soc., London, spec. publ., 405, 313-331.

Sibson R. H., 1977, Fault rocks and fault mechanisms. J. Geol. Soc. Cond. 133, 191-213.

Simonetti M., Carosi R., Montomoli C., 2017, Variscan shear deformation in the Argentera Massif: a field guide to the excursion in the Pontebernardo Valley (CN, Italy). Atti della Società Toscana di Scienze Naturali Memorie, Serie A, 124, doi: 10.2424/ASTSN.M.2017.02.

Simonetti M., Carosi R., Montomoli C., Langone A., D'Addario E., Mammoliti E., 2018, kinematic and geochronological constraints on shear deformation in the ferriere-mollières shear zone (Argentera-Mercantour Massif, Western Alps): implications for the evolution of the Southern European Variscan Belt. Int J Earth Sci, 107, 6, 2163-2189. doi: 10.1007/s00531-018-1593-y

Simonetti M., Carosi R., Montomoli C., Corsini M., Petroccia A., Cottle J. M., Iaccarino S., submitted, Timing and kinematics of flow in a transpressive dextral shear zone, Maures Massif (Southern France): implications for the evolution of the Southern European Variscan belt. Int J Earth Sci.

Soliva R., Benedicto A., 2004, A linkage criterion for segmented normal faults. J. Struct. Geol. 26, 2251–2267. http://dx.doi.org/10.1016/j.jsg.2004.06.008

Stampfli G.M., von Raumer L.F., Borel G.D., 2002, Paleozoic evolution of pre-Variscan terranes: from Gondwana to the Variscan collision. Geol S Am S, 364, 263-280.

Stipp M., Stunitz H., Heilbronner R., Schmid S. M., 2002, The eastern Tonale fault zone: a "natural laboratory" for crystal plastic deformation of quartz over a temperature range from 250 to 700° C, J Struct Geol, 24, 1861-1884.

Tollmann A., 1982, Großraumiger variszischer Deckenbau im Moldanubikum und neue Gedanken zum Variszikum Europas. Geotektonische Forschungen 64, 1–91.

Viegas L.G.F., Archanjo C.J., Hollanda M.H.B.M., Vauchez A., 2014, Microfabrics and zircon U–Pb (SHRIMP) chronology of mylonites fromthe Patos shear zone (Borborema Province, NE Brazil). Precambrian Research, 243, 1–17.

Wallis S. R., Platt J. P., Knott S. D., 1993, Recognition of syn-convergence extension in accretionary wedges with examples from Calabrian arc and the Eastern Alps. American Journal of Sciences ,293, 463-495.

Xypolias P., 2010, Vorticity analysis in shear zones: A review of methods and applications. Journal of Structural Geology, 32, 2072 – 2092.

APPENDIX F: BSE images and Y compositional maps of collected monazite for petrochronology

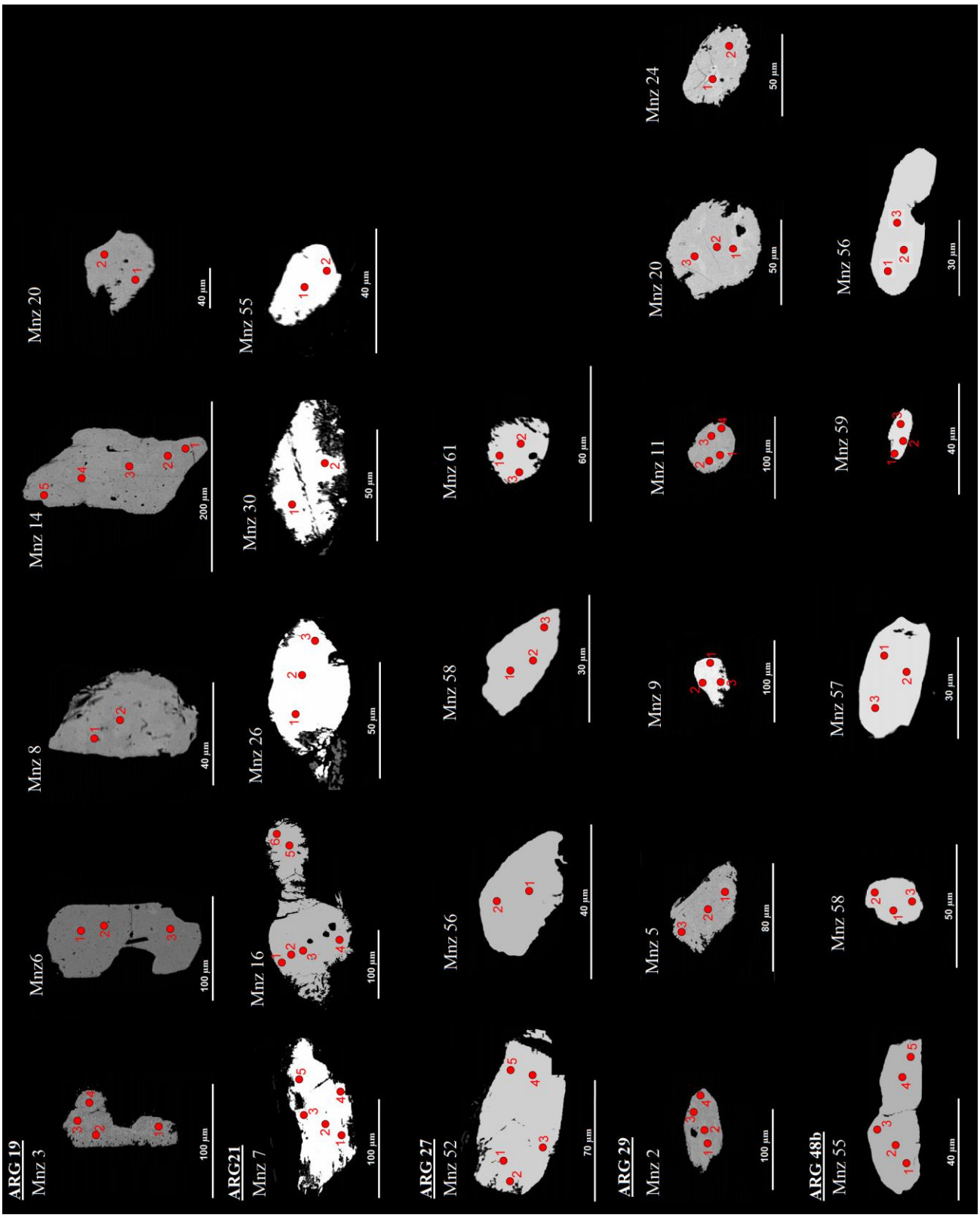

Appendix F: study monazite grains collected in the samples from the Ferriere-Mollières Shear Zone between the Ferriere Valley and Piz Valley. Spots of the EPMA analysis are reported

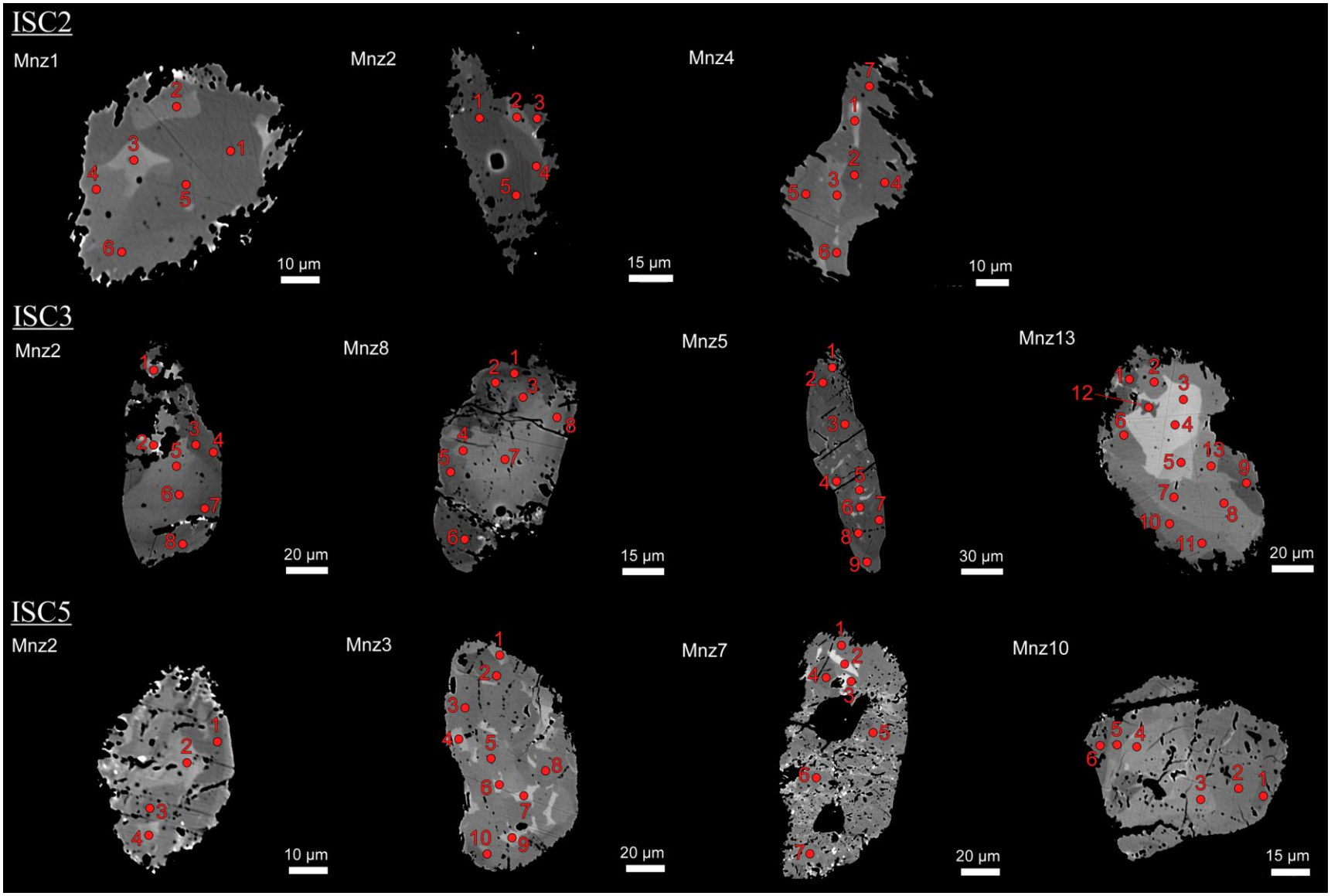

Appendix F: study monazite grains collected in the samples from the Ferriere-Mollières Shear Zone in the Ischiator Valley. Spots of the EPMA analysis are reported.

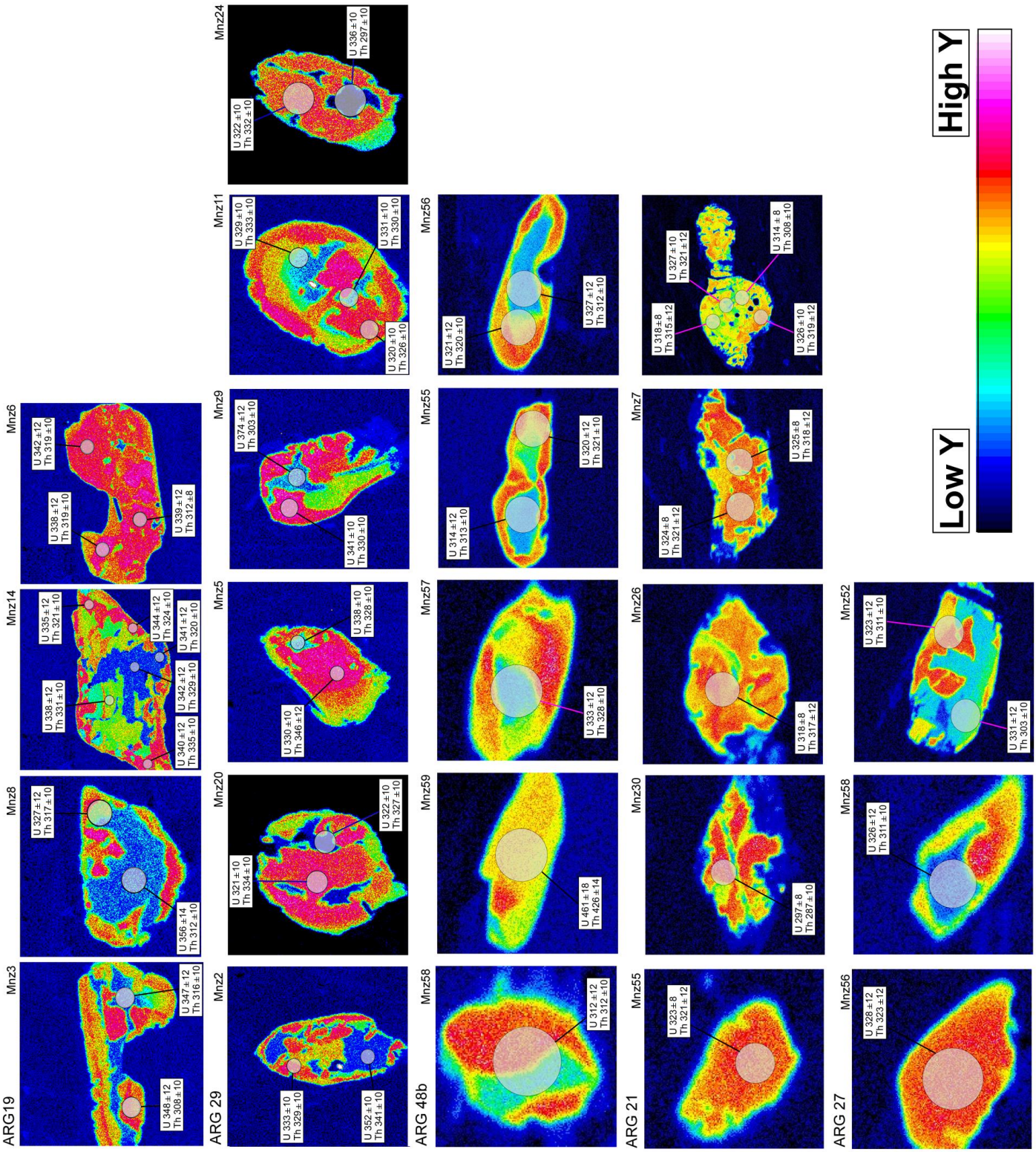

Appendix F: compositional maps of Y of the monazite grains collected in the samples from the Ferriere-Mollières Shear Zone between the Ferriere Valley and Piz Valley. Spots of the LA-ICP-MS and relative ages are reported; U = $^{206}Pb/^{238}U$ systematic; Th = $^{208}Pb/^{232}Th$ systematic

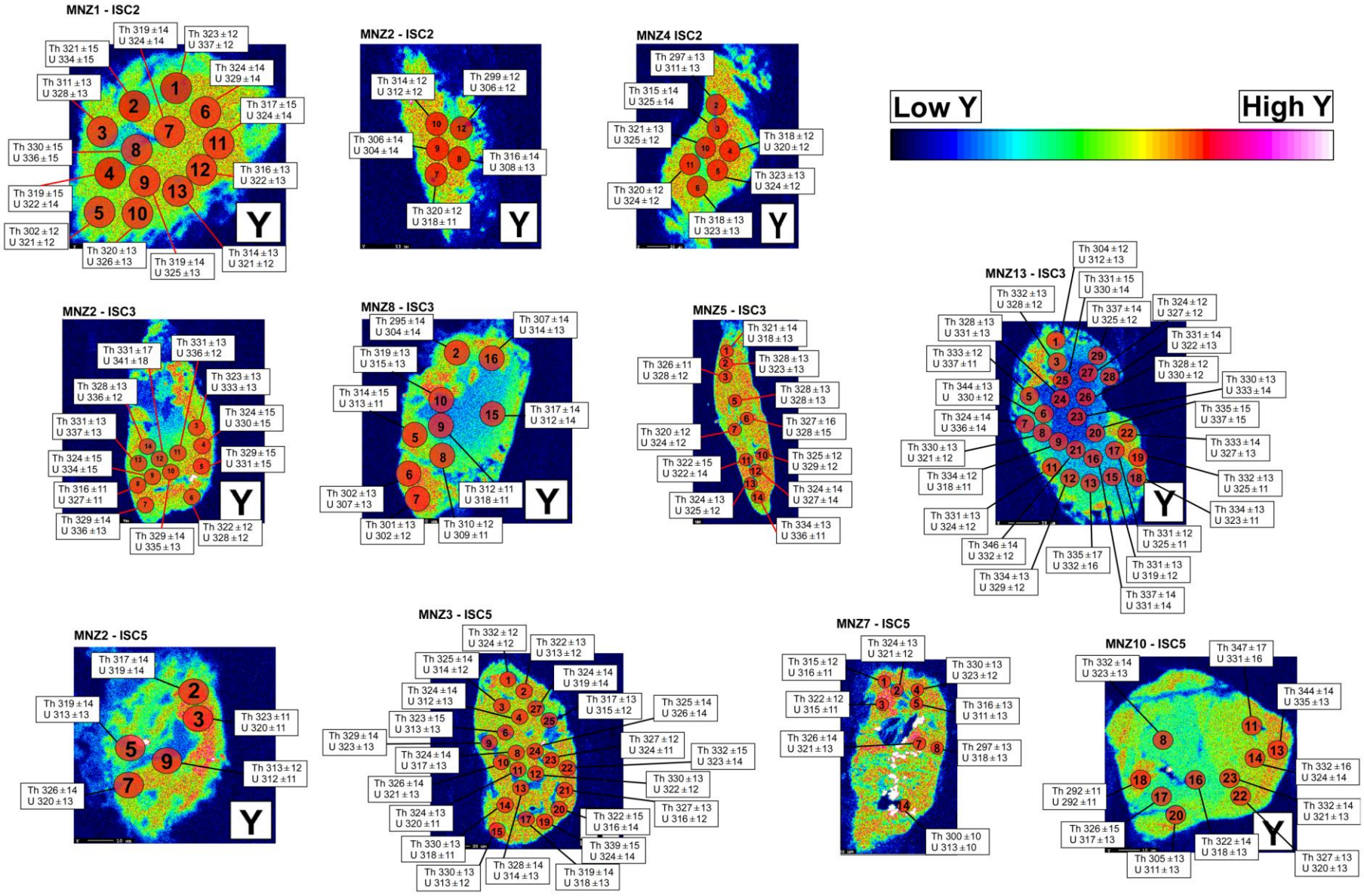

Appendix F: compositional maps of Y of the monazite grains collected in the Ferriere-Mollères Shear Zone in the Ischiator Valley. Spots of the LASS and relative ages are reported; U = $^{206}Pb/^{238}U$ systematic; Th = $^{208}Pb/^{232}Th$ systematic

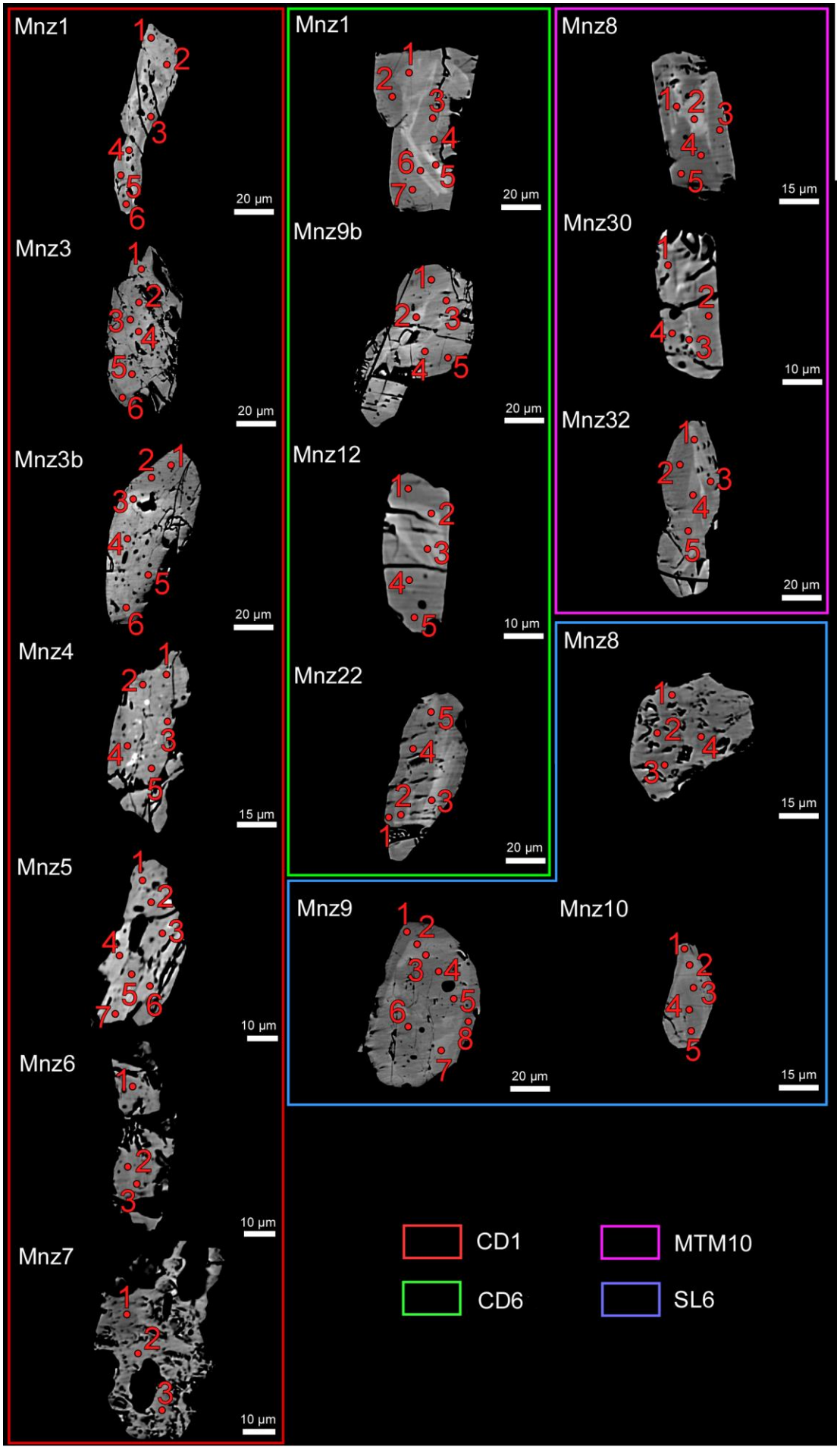

Appendix F: study monazite grains collected in the samples from the Cavalaire Fault. Spot of the EPMA analysis are reported.

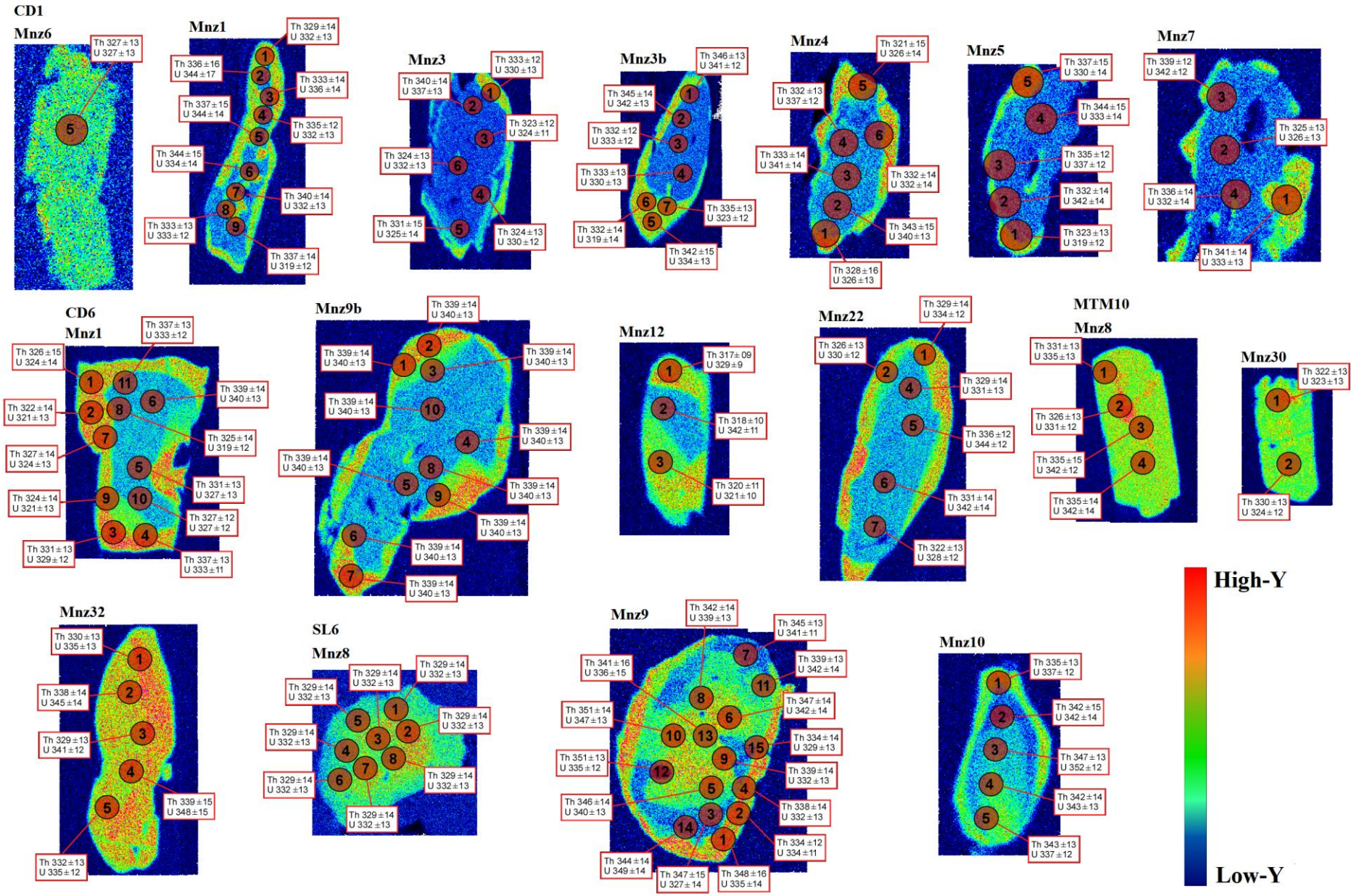

Appendix F: compositional maps of Y of the monazite grains collected in the Cavalaire Fault. Ages of the LASS spots are reported; U = $^{206}Pb/^{238}U$ systematic; Th = $^{208}Pb/^{232}Th$ systematic

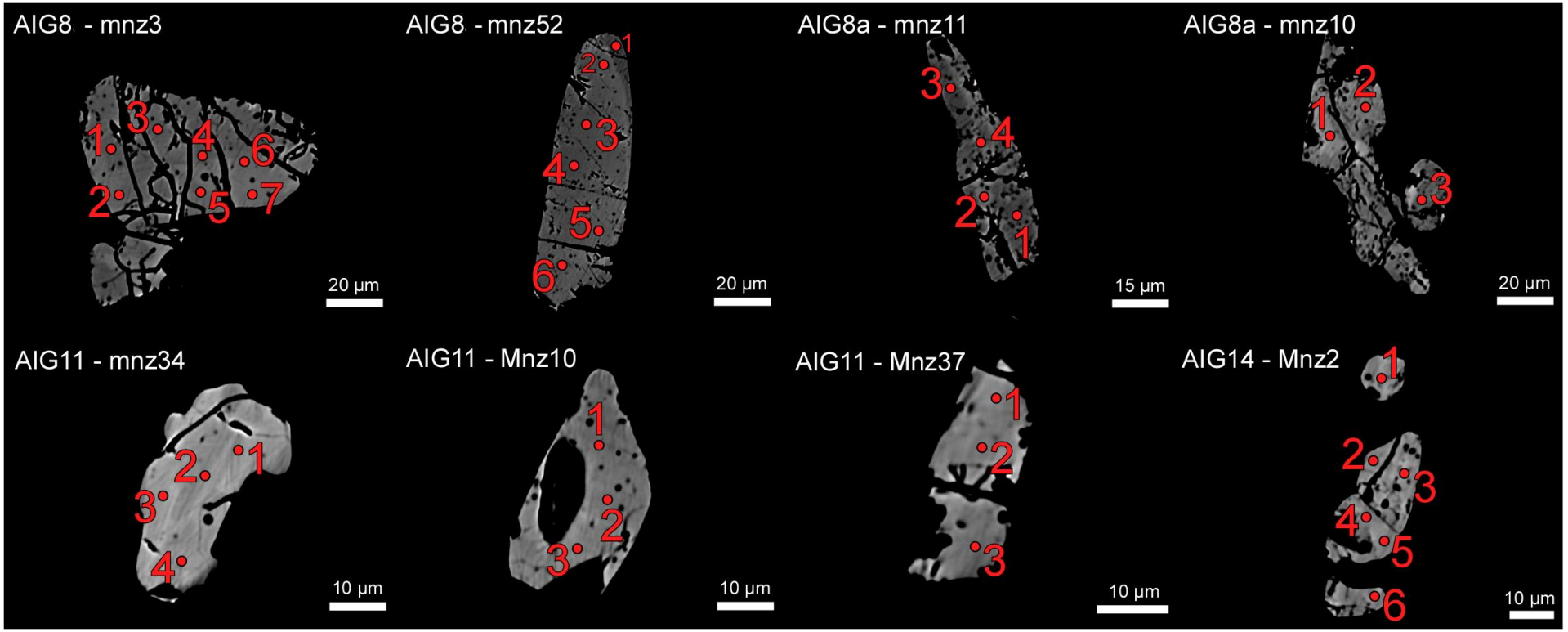

Appendix F: monazite grains collected in the samples from the Emosson-Berard Shear Zone. Spot of the EPMA analysis are reported

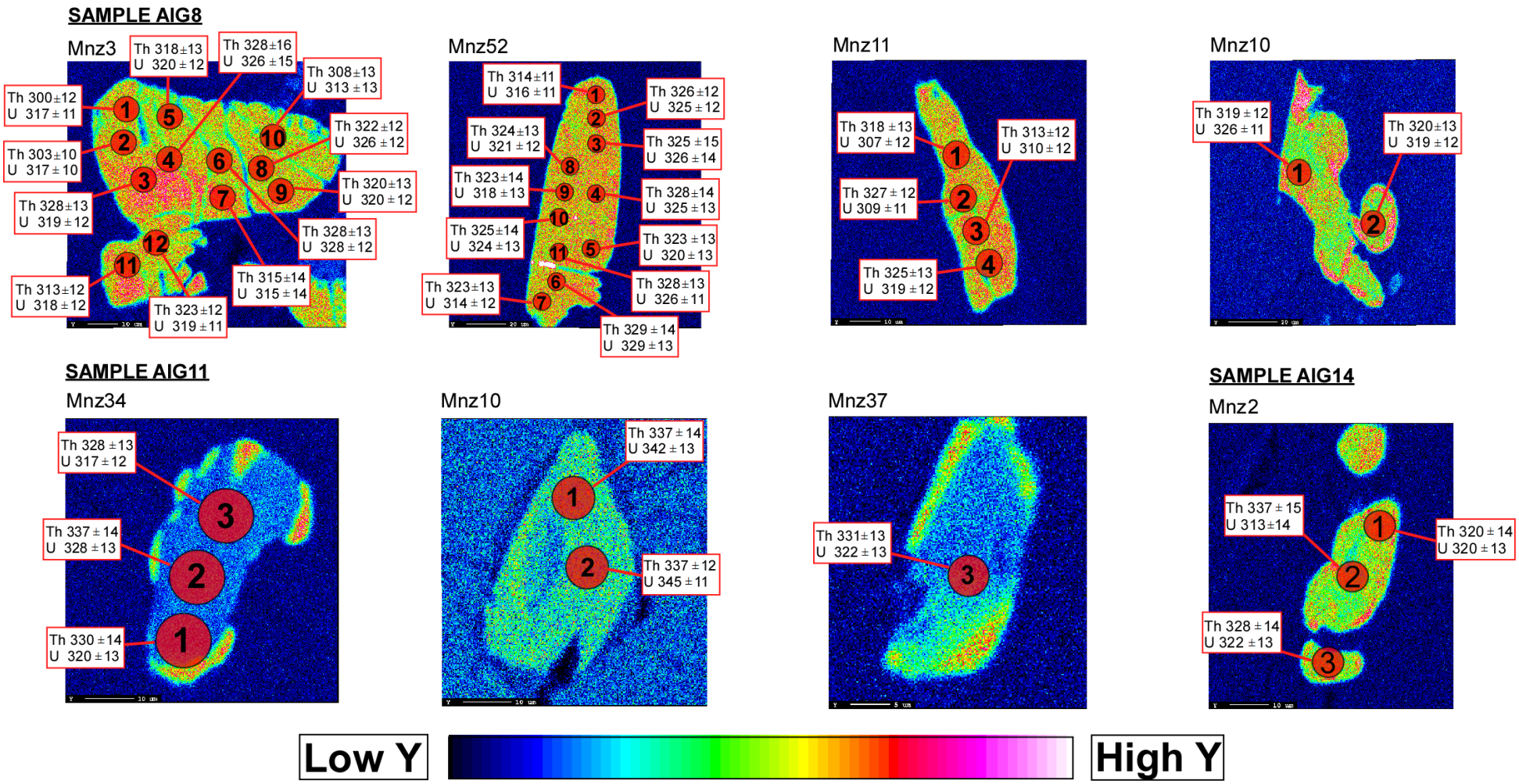

Appendix F: Compositional maps of Y of the monazite grains collected in the Emosson-Berard Shear Zone. Ages of the LASS spots are reported; U = $^{206}Pb/^{238}U$ systematic; Th = $^{208}Pb/^{232}Th$ systematic

APPENDIX G: chemical analyses of the dated monazites

wt%	ARG 29 - M2 - 1	ARG 29 - M2 - 2	ARG 29 - M2 - 3	ARG 29 - M2 - 4	ARG 29 - M5 - 1	ARG 29 - M5 - 2	ARG 29 - M5 - 3	ARG 29 - M9 - 1
SiO2	0.103	0.002	0.095	0.446	0.215	0.031	0.051	0.311
P2O5	29.790	29.410	29.960	29.490	29.710	29.730	29.800	29.750
CaO	0.989	1.022	0.944	0.921	0.921	1.007	1.030	0.936
Y2O3	2.100	2.350	3.480	0.130	0.838	3.200	2.320	0.287
La2O3	13.380	13.180	12.100	13.860	13.670	12.960	13.400	14.200
Ce2O3	29.270	29.180	26.460	30.610	29.230	27.970	28.180	29.860
Pr2O3	3.230	3.330	3.390	3.720	3.260	3.460	3.240	3.100
Nd2O3	11.170	10.990	11.660	11.970	12.730	11.640	11.930	12.570
Sm2O3	1.730	1.570	2.160	1.690	2.090	1.600	1.950	1.880
Eu2O3	0.000	0.000	0.000	0.000	0.000	0.000	0.000	0.000
Gd2O3	1.480	1.460	1.820	1.061	1.580	1.720	1.400	1.037
ThO2	3.860	3.850	3.890	4.620	4.230	3.820	3.940	4.320
UO2	0.688	0.612	0.537	0.534	0.680	0.795	0.768	0.447
Sum	97.789	96.956	96.496	99.051	99.154	97.933	98.009	98.698
Cationi								
Si	0.004	0.000	0.004	0.018	0.009	0.001	0.002	0.012
P	1.002	1.000	1.009	0.990	0.995	0.998	1.001	0.998
Ca	0.042	0.044	0.040	0.039	0.039	0.043	0.044	0.040
Y	0.044	0.050	0.074	0.003	0.018	0.068	0.049	0.006
La	0.196	0.195	0.178	0.203	0.200	0.190	0.196	0.208
Ce	0.426	0.429	0.385	0.445	0.424	0.406	0.409	0.433
Pr	0.047	0.049	0.049	0.054	0.047	0.050	0.047	0.045
Nd	0.158	0.158	0.166	0.170	0.180	0.165	0.169	0.178
Sm	0.024	0.022	0.030	0.023	0.029	0.022	0.027	0.026
Eu	0.000	0.000	0.000	0.000	0.000	0.000	0.000	0.000
Gd	0.019	0.019	0.024	0.014	0.021	0.023	0.018	0.014
Th	0.031	0.031	0.031	0.037	0.034	0.031	0.032	0.035
U	0.006	0.005	0.005	0.005	0.006	0.007	0.007	0.004
sum	2.00	2.00	1.99	2.00	2.00	2.00	2.00	2.00

Appendix G: chemical analyses of the dated monazites in samples from the Argentera Massif

ARG 29 - M9 - 2	ARG 29 - M9 - 3	ARG 29 - M11 - 1	ARG 29 - M11 - 2	ARG 29 - M11 - 3	ARG 29 - M11 - 4	ARG 29 - M20 - 1	ARG 29 - M20 - 2	ARG 29 - M20 - 3	ARG 29 - M24 - 1
0.222	0.120	0.061	0.849	0.207	0.075	0.392	0.126	0.441	0.413
30.280	30.710	30.030	29.270	30.930	29.560	30.020	30.430	29.830	30.040
1.004	1.135	1.135	1.215	1.083	1.133	0.960	1.052	0.968	1.099
1.550	2.730	3.120	0.336	1.940	2.560	0.257	3.060	0.346	0.404
11.990	12.720	12.580	13.790	12.830	12.770	13.850	13.140	14.130	14.350
27.820	27.220	26.720	28.790	27.150	27.900	28.890	27.790	29.440	29.770
3.640	3.370	3.300	3.280	3.490	3.410	3.770	3.390	3.290	3.160
13.410	11.790	11.030	10.790	11.700	11.410	12.080	11.780	12.340	11.740
2.320	1.940	1.820	1.480	2.250	1.920	1.730	2.060	1.870	1.690
0.000	0.000	0.000	0.000	0.000	0.000	0.000	0.000	0.000	0.000
1.870	1.570	1.970	0.711	1.790	1.300	1.138	1.340	1.560	1.380
4.400	4.770	4.920	7.700	4.650	4.230	4.730	4.610	4.960	5.220
0.256	0.338	0.622	0.564	0.684	0.900	0.665	0.535	0.763	0.816
98.762	98.412	97.308	98.774	98.704	97.168	98.482	99.312	99.938	100.081
0.009	0.005	0.002	0.034	0.008	0.003	0.015	0.005	0.017	0.016
1.006	1.013	1.008	0.984	1.017	1.000	1.004	1.003	0.992	0.995
0.042	0.047	0.048	0.052	0.045	0.049	0.041	0.044	0.041	0.046
0.032	0.057	0.066	0.007	0.040	0.054	0.005	0.063	0.007	0.008
0.174	0.183	0.184	0.202	0.184	0.188	0.202	0.189	0.205	0.207
0.400	0.388	0.388	0.419	0.386	0.408	0.418	0.396	0.423	0.426
0.052	0.048	0.048	0.047	0.049	0.050	0.054	0.048	0.047	0.045
0.188	0.164	0.156	0.153	0.162	0.163	0.170	0.164	0.173	0.164
0.031	0.026	0.025	0.020	0.030	0.026	0.024	0.028	0.025	0.023
0.000	0.000	0.000	0.000	0.000	0.000	0.000	0.000	0.000	0.000
0.024	0.020	0.026	0.009	0.023	0.017	0.015	0.017	0.020	0.018
0.035	0.038	0.040	0.062	0.037	0.034	0.038	0.036	0.040	0.041
0.002	0.003	0.005	0.005	0.006	0.008	0.006	0.005	0.007	0.007
1.99	1.99	2.00	1.99	1.99	2.00	1.99	2.00	2.00	2.00

Appendix G: chemical analyses of the dated monazites in samples from the Argentera Massif

ARG 29 - M24 - 2	ARG 19 - M3 - 1	ARG 19 - M3 - 2	ARG 19 - M3 - 3	ARG 19 - M3 - 4	ARG 19 - M6 - 1	ARG 19 - M6 - 2	ARG 19 - M6 - 3	ARG 19 - M8 - 1	ARG 19 - M8 - 2
0.034	0.015	0.073	0.396	0.101	0.081	0.097	0.040	0.169	0.350
30.820	30.570	31.230	30.010	29.550	28.500	30.940	29.760	30.760	29.900
1.120	0.991	0.926	0.841	0.910	1.058	1.170	1.920	0.819	0.998
3.070	2.890	3.230	0.247	1.660	0.262	2.820	3.050	2.060	0.161
13.410	12.180	12.430	14.610	12.750	14.060	12.920	12.020	12.050	14.420
28.200	28.230	27.250	30.360	28.730	28.850	26.290	25.960	27.180	29.850
3.630	3.310	3.270	3.740	3.610	3.210	3.030	3.360	3.830	3.590
11.530	12.390	12.090	11.800	12.990	10.820	11.780	12.250	12.810	11.140
2.010	2.340	2.320	1.630	2.380	1.220	1.890	2.270	2.200	1.490
0.000	0.000	0.000	0.000	0.000	0.000	0.000	0.000	0.000	0.000
1.330	1.970	1.910	1.160	2.240	1.054	1.810	2.040	1.980	0.649
4.470	4.060	3.620	3.970	3.610	7.160	4.680	4.240	3.090	4.510
0.612	0.418	0.439	0.471	0.536	0.526	0.521	0.760	0.494	0.751
100.236	99.364	98.788	99.234	99.067	96.800	97.947	97.670	97.442	97.809
0.001	0.001	0.003	0.016	0.004	0.003	0.004	0.002	0.007	0.014
1.005	1.007	1.019	0.999	0.992	0.992	1.020	0.997	1.020	1.005
0.046	0.041	0.038	0.035	0.039	0.047	0.049	0.081	0.034	0.042
0.063	0.060	0.066	0.005	0.035	0.006	0.058	0.064	0.043	0.003
0.191	0.175	0.177	0.212	0.187	0.213	0.186	0.175	0.174	0.211
0.398	0.402	0.385	0.437	0.417	0.434	0.375	0.376	0.390	0.434
0.051	0.047	0.046	0.054	0.052	0.048	0.043	0.048	0.055	0.052
0.159	0.172	0.167	0.166	0.184	0.159	0.164	0.173	0.179	0.158
0.027	0.031	0.031	0.022	0.033	0.017	0.025	0.031	0.030	0.020
0.000	0.000	0.000	0.000	0.000	0.000	0.000	0.000	0.000	0.000
0.017	0.025	0.024	0.015	0.029	0.014	0.023	0.027	0.026	0.009
0.035	0.032	0.028	0.032	0.029	0.060	0.037	0.034	0.025	0.036
0.005	0.004	0.004	0.004	0.005	0.005	0.005	0.007	0.004	0.007
2.00	2.00	1.99	2.00	2.01	2.00	1.99	2.02	1.99	1.99

Appendix G: chemical analyses of the dated monazites in samples from the Argentera Massif

ARG 19 - M14 - 1	ARG 19 - M14 - 2	ARG 19 - M14 - 3	ARG 19 - M14 - 4	ARG 19 - M14 - 5	ARG 19 - M20 - 1	ARG 19 - M20 - 2	ARG 21 - M26 - 1	ARG 21 - M26- 2
0.056	0.487	0.709	0.105	0.068	0.074	0.017	0.0408	0.0347
29.790	29.730	28.830	29.800	30.300	29.710	29.420	29.6	29.83
0.973	1.187	1.280	1.289	1.089	1.045	0.986	1.0185	1.0442
3.010	0.229	0.230	1.860	1.960	2.440	2.570	2.92	2.55
12.860	14.620	14.070	14.050	13.300	12.460	12.250	12.34	12.43
26.670	29.200	28.590	27.860	28.120	27.450	27.000	27.89	27.44
3.100	3.440	3.660	3.230	3.260	3.520	3.120	3.7	3.7
11.450	10.610	10.330	10.440	11.330	11.800	12.020	12.01	12.06
2.080	1.270	1.250	1.260	1.690	1.800	2.210	2.27	1.99
0.000	0.000	0.000	0.000	0.000	0.000	0.000	0.000	0.000
1.930	0.763	0.775	1.121	1.430	1.640	2.000	1.61	1.76
4.040	6.590	7.650	5.660	4.670	3.980	3.620	3.73	4.33
0.271	0.530	0.719	0.309	0.665	0.808	0.769	0.6613	0.5336
96.230	98.655	98.093	96.985	97.882	96.727	95.982	97.791	97.703
0.002	0.019	0.028	0.004	0.003	0.003	0.001	0.002	0.001
1.009	0.997	0.981	1.007	1.012	1.006	1.005	0.997	1.003
0.042	0.050	0.055	0.055	0.046	0.045	0.043	0.043	0.044
0.064	0.005	0.005	0.040	0.041	0.052	0.055	0.062	0.054
0.190	0.214	0.209	0.207	0.193	0.184	0.182	0.181	0.182
0.391	0.423	0.421	0.407	0.406	0.402	0.399	0.406	0.399
0.045	0.050	0.054	0.047	0.047	0.051	0.046	0.054	0.054
0.164	0.150	0.148	0.149	0.160	0.169	0.173	0.171	0.171
0.029	0.017	0.017	0.017	0.023	0.025	0.031	0.031	0.027
0.000	0.000	0.000	0.000	0.000	0.000	0.000	0.000	0.000
0.026	0.010	0.010	0.015	0.019	0.022	0.027	0.021	0.023
0.033	0.053	0.062	0.046	0.037	0.032	0.030	0.030	0.035
0.002	0.005	0.006	0.003	0.006	0.007	0.007	0.006	0.005
2.00	1.99	2.00	2.00	1.99	2.00	2.00	2.00	2.00

Appendix G: chemical analyses of the dated monazites in samples from the Argentera Massif

ARG 21 - M26 - 3	ARG 21 - M16 - 1	ARG 21 - M16 - 2	ARG 21 - M16 - 3	ARG 21 - M16 - 4	ARG 21 - M16 - 5	ARG 21 - M16 - 6	ARG 21 - M30 - 1	ARG 21 - M30 - 2
0.0641	0.0439	0.0274	0	0.0222	0.0159	0.1145	0.059	0
30.11	28.88	29.55	29.11	29.95	29.67	29.21	29.85	29.76
1.0283	1.008	1.0952	1.1628	0.941	1.129	1.2013	1.0798	1.1004
2.75	2.38	2.19	2.17	3.75	3.31	3.16	1.45	2.85
12.21	12.75	14.03	14.02	12.13	12.4	12.65	12.78	11.78
27.47	26.86	27.42	26.97	26.36	25.41	25.98	28.09	26.62
3.89	3.84	3.64	3.55	3.53	3.37	3.92	3.6	3.68
11.73	12.14	10.54	10.74	11.88	11.53	11.25	12.03	12.48
2.01	2.05	1.43	1.51	2.26	1.98	2.01	1.83	2.2
0.000	0.000	0.000	0.000	0.000	0.000	0.000	0.000	0.000
1.73	1.73	1.1433	1.149	1.89	2	1.36	1.6	1.4
3.76	3.65	4.74	4.66	3.46	4.5	4.94	3.97	3.31
0.5145	0.7352	0.3929	0.5781	0.6051	0.4357	0.4734	0.9105	0.7709
97.267	96.067	96.199	95.620	96.778	95.751	96.269	97.249	95.951
0.003	0.002	0.001	0.000	0.001	0.001	0.005	0.002	0.000
1.009	0.995	1.007	1.002	1.007	1.009	0.997	1.008	1.010
0.044	0.044	0.047	0.051	0.040	0.049	0.052	0.046	0.047
0.058	0.052	0.047	0.047	0.079	0.071	0.068	0.031	0.061
0.178	0.191	0.208	0.210	0.178	0.184	0.188	0.188	0.174
0.398	0.400	0.404	0.402	0.383	0.374	0.383	0.410	0.391
0.056	0.057	0.053	0.053	0.051	0.049	0.058	0.052	0.054
0.166	0.176	0.152	0.156	0.169	0.165	0.162	0.171	0.179
0.027	0.029	0.020	0.021	0.031	0.027	0.028	0.025	0.030
0.000	0.000	0.000	0.000	0.000	0.000	0.000	0.000	0.000
0.023	0.023	0.015	0.015	0.025	0.027	0.018	0.021	0.019
0.030	0.030	0.039	0.038	0.028	0.037	0.040	0.032	0.027
0.005	0.007	0.004	0.005	0.005	0.004	0.004	0.008	0.007
2.00	2.01	2.00	2.00	2.00	2.00	2.00	2.00	2.00

Appendix G: chemical analyses of the dated monazites in samples from the Argentera Massif

ARG 21 - M55 - 1	ARG 21 - M55 - 2	ARG 21 - M7 - 1	ARG 21 - M7 - 2	ARG 21 - M7 - 3	ARG 21 - M7 - 4	ARG 21 - M7 - 5	ARG 27 - M56 - 1	ARG 27 - M56 - 2
0.1388	0.0853	0.3168	0.0463	0.0606	0.0072	0.1512	0.0701	0.0817
30.25	29.86	29.81	29.2	29.04	29.44	29.69	30.04	29.45
0.9051	1.0349	1.027	0.96	1.1083	0.9459	1.4	0.9628	0.9436
2.54	2.26	0.6275	2.97	2.56	3	2.35	2.78	2.84
12.52	12.57	15.41	12.34	12.17	12.88	12.64	12.05	11.73
28.23	27.96	29.95	26.93	27.47	28.06	27.22	26.92	27.18
3.78	3.82	3.83	3.5	3.76	3.92	3.88	4.19	3.86
12.27	12.55	11	11.81	11.54	11.46	12.26	12.26	12.19
2.12	2.2	1.51	2.19	1.97	1.95	2.02	2.07	2.1
0.000	0.000	0.000	0.000	0.000	0.000	0.000	0.000	0.000
1.78	1.74	0.6932	1.45	1.57	1.69	1.6	1.65	1.77
3.33	4.03	3.8	3.79	3.62	3.62	3.47	3.87	3.65
0.6317	0.8079	0.663	0.5744	1.045	0.5758	1.19	0.4103	0.509
98.496	98.918	98.638	95.761	95.914	97.549	97.871	97.273	96.304
0.005	0.003	0.013	0.002	0.002	0.000	0.006	0.003	0.003
1.004	0.997	0.997	1.001	0.997	0.996	0.996	1.008	1.002
0.038	0.044	0.043	0.042	0.048	0.040	0.059	0.041	0.041
0.053	0.047	0.013	0.064	0.055	0.064	0.050	0.059	0.061
0.181	0.183	0.225	0.184	0.182	0.190	0.185	0.176	0.174
0.405	0.404	0.433	0.399	0.408	0.410	0.395	0.391	0.400
0.054	0.055	0.055	0.052	0.056	0.057	0.056	0.061	0.057
0.172	0.177	0.155	0.171	0.167	0.164	0.174	0.174	0.175
0.029	0.030	0.021	0.031	0.028	0.027	0.028	0.028	0.029
0.000	0.000	0.000	0.000	0.000	0.000	0.000	0.000	0.000
0.023	0.023	0.009	0.019	0.021	0.022	0.021	0.022	0.024
0.027	0.032	0.030	0.031	0.030	0.029	0.028	0.031	0.030
0.006	0.007	0.006	0.005	0.009	0.005	0.010	0.004	0.005
2.00	2.00	2.00	2.00	2.00	2.00	2.01	2.00	2.00

Appendix G: chemical analyses of the dated monazites in samples from the Argentera Massif

ARG 27 - M61 - 1	ARG 27 - M61 - 2	ARG 27 - M61 - 3	ARG 27 - M52 - 1	ARG 27 - M52 - 2	ARG 27 - M52 - 3	ARG 27 - M52 - 4	ARG 27 - M52 - 5	ARG 27 - M58 - 1
0.0909	0.0047	0.1156	1.0216	0.1595	0.076	0.0219	0	0.1835
29.58	29.64	29.18	28.61	29.4	29.2	29.52	29	28.96
1.044	0.9812	1.1014	1.3587	1.043	1.0671	1.1532	1.0439	0.9846
2.09	2.8	2.15	0.1663	0.5901	0.9676	3	2.89	1.2403
12.42	12.01	12.17	14.62	14.3	13.37	12.53	12.45	14.22
27.53	26.65	27.52	29.32	29.68	28.82	27.07	27.22	29.55
3.69	4.03	3.88	3.62	3.9	3.85	4.16	3.85	3.66
12.62	11.68	12	10.09	11.1	12.43	10.96	11.42	11.25
2.05	2.13	2.08	1.0652	1.54	2.06	1.98	2.04	2.02
0.000	0.000	0.000	0.000	0.000	0.000	0.000	0.000	0.000
1.8	1.96	1.57	0.8575	0.9134	1.51	1.74	1.43	1.58
3.33	3.45	3.51	7.68	4.63	3.83	4.51	4.09	4.18
0.6797	0.6417	0.9289	0.4138	0.4494	0.9953	0.6424	0.705	0.6413
96.925	95.978	96.206	98.823	97.705	98.176	97.288	96.139	98.470
0.004	0.000	0.005	0.041	0.006	0.003	0.001	0.000	0.007
1.002	1.008	0.998	0.968	0.998	0.992	0.999	0.996	0.984
0.045	0.042	0.048	0.058	0.045	0.046	0.049	0.045	0.042
0.045	0.060	0.046	0.004	0.013	0.021	0.064	0.062	0.027
0.183	0.178	0.181	0.216	0.212	0.198	0.185	0.186	0.211
0.403	0.392	0.407	0.429	0.436	0.423	0.396	0.404	0.434
0.054	0.059	0.057	0.053	0.057	0.056	0.061	0.057	0.054
0.180	0.168	0.173	0.144	0.159	0.178	0.156	0.165	0.161
0.028	0.030	0.029	0.015	0.021	0.028	0.027	0.029	0.028
0.000	0.000	0.000	0.000	0.000	0.000	0.000	0.000	0.000
0.024	0.026	0.021	0.011	0.012	0.020	0.023	0.019	0.021
0.027	0.028	0.029	0.062	0.038	0.031	0.037	0.034	0.034
0.006	0.006	0.008	0.004	0.004	0.009	0.006	0.006	0.006
2.00	2.00	2.00	2.00	2.00	2.01	2.00	2.00	2.01

Appendix G: chemical analyses of the dated monazites in samples from the Argentera Massif

ARG 27 - M58 - 2	ARG 27 - M58 - 3	ARG 48B - M55 - 1	ARG 48B - M55 - 2	ARG 48B - M55 - 3	ARG 48B - M55 - 4	ARG 48B - M55 - 5	ARG 48B - M56 - 1	ARG 48B - M56 - 2
0.3118	0.1356	3.18	2.74	1.171	0.7525	0.2774	0.1818	0.2275
28.7	29.52	24.56	26.73	27.29	29.26	28.49	29.55	28.19
1.0521	1.1038	0.4876	0.4257	0.5601	0.9337	1.233	1.1568	1.1244
0.2858	2.24	0.4049	0.4928	0.5245	0.9374	1.84	2.45	1.99
14.28	13.37	13.04	13.58	14.68	14.2	13.22	13.01	12.74
29.73	27.86	25.63	27.14	29.32	28.97	27.42	26.83	27.2
3.73	3.61	3.48	3.35	3.84	3.63	3.6	3.37	3.84
11.15	10.73	10.13	10.67	11.2	11.02	11.17	11.19	11.23
1.43	1.58	1.42	1.27	1.26	1.35	1.78	1.91	1.89
0.000	0.000	0.000	0.000	0.000	0.000	0.000	0.000	0.000
1.0721	1.1375	0.6012	0.686	0.9371	1.0137	1.34	1.5	1.95
4.91	4.69	13.58	11.42	6.34	6.34	5.91	4.69	5.21
0.7162	0.6934	0.3975	0.3269	0.1854	0.2599	0.467	0.3317	0.4195
97.368	96.670	96.911	98.831	97.308	98.667	96.747	96.170	96.011
0.013	0.005	0.135	0.111	0.048	0.030	0.011	0.007	0.009
0.986	1.002	0.880	0.918	0.951	0.984	0.983	1.004	0.981
0.046	0.047	0.022	0.018	0.025	0.040	0.054	0.050	0.050
0.006	0.048	0.009	0.011	0.011	0.020	0.040	0.052	0.044
0.214	0.198	0.204	0.203	0.223	0.208	0.199	0.193	0.193
0.442	0.409	0.397	0.403	0.442	0.421	0.409	0.394	0.410
0.055	0.053	0.054	0.049	0.058	0.053	0.053	0.049	0.058
0.162	0.154	0.153	0.155	0.165	0.156	0.163	0.160	0.165
0.020	0.022	0.021	0.018	0.018	0.018	0.025	0.026	0.027
0.000	0.000	0.000	0.000	0.000	0.000	0.000	0.000	0.000
0.014	0.015	0.008	0.009	0.013	0.013	0.018	0.020	0.027
0.040	0.038	0.117	0.094	0.053	0.051	0.049	0.038	0.043
0.006	0.006	0.004	0.003	0.002	0.002	0.004	0.003	0.004
2.00	2.00	2.00	1.99	2.01	2.00	2.01	2.00	2.01

Appendix G: chemical analyses of the dated monazites in samples from the Argentera Massif

ARG 48B - M56 - 3	ARG 48B - M58 - 1	ARG 48B - M58 - 2	ARG 48B - M58 - 3	ARG 48B - M59 - 1	ARG 48B - M59 - 2	ARG 48B - M59 - 3	ARG 48B - M57 - 1	ARG 48B - M57 - 2	ARG 48B - M57 - 3
0.9249	0.7983	0.352	2.6	1.5125	0.7917	0.5389	0.4407	0.8034	0.1253
28	27.47	28.79	24.78	27.67	27.12	27.86	28.2	27.35	28.09
0.6595	1.3617	1.1996	0.893	0.9548	0.8921	0.8071	0.9465	0.8788	1.0132
0.3896	2.25	2.21	0.7778	0.791	1.76	2.28	1.1962	0.5989	2.88
14.37	12.42	12.78	12.25	13.29	13.12	12.89	13.32	13.77	12.35
28.91	27.1	27.37	24.75	27.46	27.62	27.51	28.33	27.95	26.49
3.98	3.46	3.82	2.96	3.49	3.8	3.93	4.03	4.23	3.48
11.2	10.29	10.4	10.77	10.84	10.66	11.19	11.34	11.63	11.3
1.56	1.46	1.9	1.57	1.61	1.7	1.66	1.62	1.55	2.14
0.000	0.000	0.000	0.000	0.000	0.000	0.000	0.000	0.000	0.000
0.6751	1.45	1.56	1.23	1.37	1.67	1.59	1.37	1.0234	1.65
6.03	5.44	5.28	12.93	8.12	5.62	5.11	4.93	5.97	4.27
0.2446	0.3328	0.459	0.8369	0.403	0.4668	0.3012	0.3319	0.6274	0.5125
96.944	93.833	96.121	96.348	97.511	95.221	95.667	96.055	96.382	94.301
0.038	0.033	0.014	0.111	0.061	0.033	0.022	0.018	0.033	0.005
0.969	0.969	0.989	0.892	0.952	0.959	0.973	0.980	0.960	0.988
0.029	0.061	0.052	0.041	0.042	0.040	0.036	0.042	0.039	0.045
0.008	0.050	0.048	0.018	0.017	0.039	0.050	0.026	0.013	0.064
0.217	0.191	0.191	0.192	0.199	0.202	0.196	0.202	0.211	0.189
0.433	0.414	0.407	0.386	0.409	0.422	0.415	0.426	0.424	0.403
0.059	0.053	0.056	0.046	0.052	0.058	0.059	0.060	0.064	0.053
0.164	0.153	0.151	0.164	0.157	0.159	0.165	0.166	0.172	0.168
0.022	0.021	0.027	0.023	0.023	0.024	0.024	0.023	0.022	0.031
0.000	0.000	0.000	0.000	0.000	0.000	0.000	0.000	0.000	0.000
0.009	0.020	0.021	0.017	0.018	0.023	0.022	0.019	0.014	0.023
0.050	0.046	0.043	0.112	0.067	0.048	0.043	0.041	0.050	0.036
0.002	0.003	0.004	0.008	0.004	0.004	0.003	0.003	0.006	0.005
2.00	2.01	2.00	2.01	2.00	2.01	2.01	2.01	2.01	2.01

Appendix G: chemical analyses of the dated monazites in samples from the Argentera Massif

wt%	ISC2-MNZ1-1	ISC2-MNZ1-2	ISC2-MNZ1-3	ISC2-MNZ1-4	ISC2-MNZ1-5	ISC2-MNZ1-6	ISC2-MNZ2-1	ISC2-MNZ2-2
SiO2	0.0881	0.1078	0.1291	0.1288	0.1064	0.1369	0.1237	0.0949
P2O5	31.31	31.11	31.05	31.17	31.18	31.18	30.87	31.02
CaO	1.0564	1.0368	0.933	1.1335	1.0267	0.9662	0.9886	1.0342
Y2O3	3.37	1.95	1.42	3.01	3.32	3.18	1.5	2.68
La2O3	12.98	13.03	13.12	12.7	12.76	12.16	13.49	13.3
Ce2O3	28.72	29.63	29.95	28.27	28.28	27.83	29.44	28.69
Pr2O3	3.24	3.43	3.56	3.37	3.35	3.36	3.52	3.39
Nd2O3	11.49	12.48	12.76	11.75	11.73	12.17	12.57	11.77
Sm2O3	2.1	2.38	2.36	2.23	2.16	2.35	2.36	2.12
Eu2O3	0.000	0.000	0.000	0.000	0.000	0.000	0.000	0.000
Gd2O3	1.91	1.93	1.8	2.02	1.95	2	1.94	1.89
ThO2	4.07	4.24	3.87	4.4	3.92	3.88	3.7	3.82
UO2	0.8898	0.6394	0.7343	0.9762	0.927	0.6754	0.6428	0.8842
Sum	101.224	101.964	101.686	101.159	100.710	99.889	101.145	100.693
Cationi								
Si	0.003	0.004	0.005	0.005	0.004	0.005	0.005	0.004
P	1.008	1.004	1.005	1.006	1.008	1.012	1.004	1.007
Ca	0.043	0.042	0.038	0.046	0.042	0.040	0.041	0.042
Y	0.068	0.040	0.029	0.061	0.067	0.065	0.031	0.055
La	0.182	0.183	0.185	0.179	0.180	0.172	0.191	0.188
Ce	0.400	0.413	0.419	0.395	0.395	0.391	0.414	0.403
Pr	0.045	0.048	0.050	0.047	0.047	0.047	0.049	0.047
Nd	0.156	0.170	0.174	0.160	0.160	0.167	0.173	0.161
Sm	0.028	0.031	0.031	0.029	0.028	0.031	0.031	0.028
Eu	0.000	0.000	0.000	0.000	0.000	0.000	0.000	0.000
Gd	0.024	0.024	0.023	0.026	0.025	0.025	0.025	0.024
Th	0.031	0.033	0.030	0.034	0.030	0.030	0.029	0.030
U	0.008	0.005	0.006	0.008	0.008	0.006	0.005	0.008
sum	2.00	2.00	2.00	2.00	1.99	1.99	2.00	2.00

Appendig G: chemical analyses of the dated monazites in samples from the Argentera Massif

ISC2-MNZ2-3	ISC2-MNZ2-4	ISC2-MNZ2-5	ISC2-MNZ10-1	ISC2-MNZ10-2	ISC2-MNZ10-3	ISC2-MNZ10-4	ISC2-MNZ10-5	ISC2-MNZ10-6
0.0987	0.0802	0.0887	0.4176	0.0773	0.5459	0.536	0.0841	0.0835
30.97	30.96	31.22	30.48	30.97	30.19	29.95	31.15	30.86
1.0581	1.038	1.0522	1.1954	1.1411	1.1901	1.166	0.9474	0.9906
2.7	3.39	3.42	1.47	3.05	0.2048	0.2913	2.98	2.42
13.08	12.57	12.56	13.2	12.45	14.8	13.5	12.43	13.22
28.22	28.13	28.17	28.96	27.78	30.55	29.53	28.22	29.1
3.42	3.34	3.34	3.28	3.3	3.36	3.45	3.42	3.46
11.55	11.76	11.85	11.97	12.21	11.49	12.09	12.75	12.09
2.1	2.12	2.14	2	2.26	1.65	1.84	2.36	2.02
0.000	0.000	0.000	0.000	0.000	0.000	0.000	0.000	0.000
1.78	1.78	1.85	1.42	1.81	0.9489	1.0063	1.89	1.54
3.8	3.89	3.9	5.98	4.76	5.89	6.26	3.79	4.25
0.874	0.9255	0.9192	0.6533	0.4967	0.5948	0.7124	0.3253	0.4088
99.651	99.984	100.510	101.026	100.305	101.415	100.332	100.347	100.443
0.004	0.003	0.003	0.016	0.003	0.021	0.021	0.003	0.003
1.011	1.008	1.010	0.996	1.008	0.989	0.991	1.010	1.006
0.044	0.043	0.043	0.049	0.047	0.049	0.049	0.039	0.041
0.055	0.069	0.070	0.030	0.062	0.004	0.006	0.061	0.050
0.186	0.178	0.177	0.188	0.177	0.211	0.195	0.176	0.188
0.398	0.396	0.394	0.409	0.391	0.433	0.423	0.396	0.410
0.048	0.047	0.046	0.046	0.046	0.047	0.049	0.048	0.049
0.159	0.162	0.162	0.165	0.168	0.159	0.169	0.174	0.166
0.028	0.028	0.028	0.027	0.030	0.022	0.025	0.031	0.027
0.000	0.000	0.000	0.000	0.000	0.000	0.000	0.000	0.000
0.023	0.023	0.023	0.018	0.023	0.012	0.013	0.024	0.020
0.030	0.030	0.030	0.047	0.037	0.046	0.050	0.029	0.033
0.008	0.008	0.008	0.006	0.004	0.005	0.006	0.003	0.004
1.99	2.00	1.99	2.00	2.00	2.00	2.00	1.99	2.00

Appendix G: chemical analyses of the dated monazites in samples from the Argentera Massif

ISC2-MNZ10-7	ISC2-MNZ10-8	ISC2-MNZ10-9	ISC2-MNZ4-1	ISC2-MNZ4-2	ISC2-MNZ4-3	ISC2-MNZ4-4	ISC2-MNZ4-5	ISC2-MNZ4-6
0.0901	0.0808	0.1124	0.1845	0.1041	0.1369	0.0946	0.1038	0.1293
31.02	31.11	31.06	30.64	30.97	30.76	30.88	30.5	30.75
1.0029	0.9714	0.9846	0.9528	1.0335	0.9574	1.1167	1.0979	1.168
2.9	3.03	3.57	1.2608	3.41	1.82	3.34	3.01	2.96
12.84	12.4	12.2	13.55	12.57	13.35	12.67	12.85	12.49
28.27	28.1	27.7	30.5	28.37	30.08	28.11	28.66	28.14
3.39	3.4	3.32	3.42	3.31	3.39	3.29	3.21	3.26
12.24	12.62	12.25	12.28	11.51	12.28	11.15	11.58	11.73
2.24	2.33	2.28	2.1	2.08	2.19	1.97	2.12	2.17
0.000	0.000	0.000	0.000	0.000	0.000	0.000	0.000	0.000
1.86	1.92	1.84	1.55	1.77	1.73	1.74	1.88	1.88
4.14	4.03	3.66	4	3.88	3.88	4.47	4.14	4.55
0.507	0.3679	0.6636	0.5595	0.8527	0.6166	0.773	0.8843	0.8384
100.500	100.360	99.641	100.998	99.860	101.191	99.604	100.036	100.066
0.003	0.003	0.004	0.007	0.004	0.005	0.004	0.004	0.005
1.008	1.010	1.011	1.001	1.008	1.001	1.009	1.000	1.005
0.041	0.040	0.041	0.039	0.043	0.039	0.046	0.046	0.048
0.059	0.062	0.073	0.026	0.070	0.037	0.069	0.062	0.061
0.182	0.175	0.173	0.193	0.178	0.189	0.180	0.184	0.178
0.397	0.394	0.390	0.431	0.399	0.423	0.397	0.407	0.398
0.047	0.047	0.046	0.048	0.046	0.047	0.046	0.045	0.046
0.168	0.173	0.168	0.169	0.158	0.169	0.154	0.160	0.162
0.030	0.031	0.030	0.028	0.028	0.029	0.026	0.028	0.029
0.000	0.000	0.000	0.000	0.000	0.000	0.000	0.000	0.000
0.024	0.024	0.023	0.020	0.023	0.022	0.022	0.024	0.024
0.032	0.031	0.029	0.031	0.030	0.030	0.035	0.033	0.036
0.004	0.003	0.006	0.005	0.007	0.005	0.007	0.008	0.007
2.00	1.99	1.99	2.00	1.99	2.00	1.99	2.00	2.00

Appendix G: chemical analyses of the dated monazites in samples from the Argentera Massif

ISC2-MNZ4-7	ISC3-MNZ8-1	ISC3-MNZ8-2	ISC3-MNZ8-3	ISC3-MNZ8-4	ISC3-MNZ8-5	ISC3-MNZ8-6	ISC3-MNZ8-7	ISC3-MNZ8-8
0.085	0.0606	0.05	0.1354	0.1682	0.0551	0.0844	0.1634	0.1343
30.99	30.68	30.94	30.66	30.61	30.84	30.81	30.61	30.69
1.153	0.8572	0.8462	0.7814	0.9136	0.8446	1.0073	0.8801	0.7813
3.14	2.58	2.55	1.1824	0.7076	2.77	3.58	0.8823	1.39
13.02	13.67	12.86	13.61	14.3	12.72	12.75	13.7	12.9
28.62	29.34	28.74	30.37	31.18	28.6	27.69	30.86	29.75
3.24	3.4	3.45	3.56	3.58	3.43	3.28	3.53	3.67
11.35	11.81	12.75	12.78	12.4	12.82	11.5	12.78	13.07
2.03	2.18	2.52	2.39	2.08	2.58	2.09	2.22	2.44
0.000	0.000	0.000	0.000	0.000	0.000	0.000	0.000	0.000
1.8	1.79	2.26	1.8	1.52	2.31	2	1.68	1.87
3.93	2.79	2.82	2.9	3.8	2.98	3.81	3.75	2.84
0.8325	0.4926	0.6558	0.7006	0.6108	0.7284	0.5885	0.6678	0.7992
100.191	99.650	100.442	100.870	101.870	100.678	99.190	101.724	100.335
0.003	0.002	0.002	0.005	0.006	0.002	0.003	0.006	0.005
1.007	1.006	1.007	1.003	0.997	1.004	1.009	0.998	1.006
0.047	0.036	0.035	0.032	0.038	0.035	0.042	0.036	0.032
0.064	0.053	0.052	0.024	0.014	0.057	0.074	0.018	0.029
0.184	0.195	0.182	0.194	0.203	0.180	0.182	0.195	0.184
0.402	0.416	0.405	0.429	0.439	0.403	0.392	0.435	0.422
0.045	0.048	0.048	0.050	0.050	0.048	0.046	0.050	0.052
0.156	0.163	0.175	0.176	0.170	0.176	0.159	0.176	0.181
0.027	0.029	0.033	0.032	0.028	0.034	0.028	0.029	0.033
0.000	0.000	0.000	0.000	0.000	0.000	0.000	0.000	0.000
0.023	0.023	0.029	0.023	0.019	0.029	0.026	0.021	0.024
0.031	0.022	0.022	0.023	0.030	0.023	0.030	0.029	0.022
0.007	0.004	0.006	0.006	0.005	0.006	0.005	0.006	0.007
2.00	2.00	2.00	2.00	2.00	2.00	2.00	2.00	2.00

Appendix G: chemical analyses of the dated monazites in samples from the Argentera Massif

ISC3-MNZ13-1	ISC3-MNZ13-2	ISC3-MNZ13-3	ISC3-MNZ13-4	ISC3-MNZ13-5	ISC3-MNZ13-6	ISC3-MNZ13-7	ISC3-MNZ13-8	ISC3-MNZ13-9
0.0453	0.11	0.6995	0.7186	0.5525	0.0838	0.1138	0.1117	0.0731
30.44	30.37	29.56	29.58	29.66	30.24	30.43	30.76	30.8
1.0239	1.1578	0.9143	0.9246	0.7561	0.7173	0.8242	0.7905	0.8509
3.16	1.67	0.2797	0.2975	0.2808	1.45	0.9692	0.9684	3.25
12.61	13.21	14.56	14.3	15.04	13.04	13.48	13.48	12.39
27.7	28.45	29.93	30.09	31.04	29.86	30.4	30.43	27.47
3.3	3.38	3.48	3.46	3.61	3.59	3.59	3.55	3.35
11.77	11.84	11.58	11.66	11.64	13.36	12.9	12.97	12.14
2.14	2.03	1.47	1.6	1.48	2.47	2.28	2.27	2.39
0.000	0.000	0.000	0.000	0.000	0.000	0.000	0.000	0.000
1.87	1.64	0.8447	0.9151	0.8274	1.99	1.69	1.59	2.15
4.11	5.25	6.36	6.57	5.09	2.91	3.39	3.17	3.44
0.5327	0.3944	0.2737	0.3371	0.2319	0.4688	0.586	0.5774	0.5503
98.702	99.502	99.952	100.453	100.209	100.180	100.653	100.668	98.854
0.002	0.004	0.028	0.028	0.022	0.003	0.004	0.004	0.003
1.007	1.005	0.985	0.983	0.986	0.999	1.001	1.006	1.012
0.043	0.048	0.039	0.039	0.032	0.030	0.034	0.033	0.035
0.066	0.035	0.006	0.006	0.006	0.030	0.020	0.020	0.067
0.182	0.190	0.211	0.207	0.218	0.188	0.193	0.192	0.177
0.396	0.407	0.431	0.432	0.446	0.427	0.432	0.431	0.390
0.047	0.048	0.050	0.049	0.052	0.051	0.051	0.050	0.047
0.164	0.165	0.163	0.163	0.163	0.186	0.179	0.179	0.168
0.029	0.027	0.020	0.022	0.020	0.033	0.031	0.030	0.032
0.000	0.000	0.000	0.000	0.000	0.000	0.000	0.000	0.000
0.024	0.021	0.011	0.012	0.011	0.026	0.022	0.020	0.028
0.033	0.042	0.051	0.052	0.041	0.023	0.027	0.025	0.027
0.005	0.003	0.002	0.003	0.002	0.004	0.005	0.005	0.005
2.00	2.00	2.00	2.00	2.00	2.00	2.00	2.00	1.99

Appendix G: chemical analyses of the dated monazites in samples from the Argentera Massif

ISC3-MNZ13-10	ISC3-MNZ13-11	ISC3-MNZ13-12	ISC3-MNZ13-13	ISC3-MNZ5-1	ISC3-MNZ5-2	ISC3-MNZ5-3	ISC3-MNZ5-4	ISC3-MNZ5-5
0.1059	0.1136	0.0608	0.1681	0.1987	0.0627	0.0674	0.0974	0.3691
30.38	30.51	30.62	30.61	30.7	31.04	30.86	30.96	30.45
0.7175	0.7304	1.0995	0.8832	0.8219	0.8825	1.023	1.2116	1.005
1.62	1.56	3.06	0.7715	0.9387	3.55	3.45	2.7	1.32
12.9	12.9	12.7	13.82	13.7	12.63	12.73	13.7	14.03
29.45	29.53	27.64	29.98	30.26	27.8	27.18	28.47	29.49
3.58	3.53	3.35	3.49	3.58	3.3	3.27	3.27	3.44
13.13	13.03	11.55	12.2	12.84	12.04	11.56	11.33	11.87
2.48	2.53	2.02	2.05	2.23	2.33	2.18	1.87	1.84
0.000	0.000	0.000	0.000	0.000	0.000	0.000	0.000	0.000
1.95	1.94	1.66	1.39	1.68	2.26	2.02	1.51	1.33
2.67	2.81	4.73	4.06	3.58	3.58	4.49	5.48	5.28
0.5545	0.5836	0.4502	0.4692	0.3626	0.4867	0.4034	0.2201	0.2508
99.538	99.768	98.941	99.892	100.892	99.962	99.234	100.819	100.675
0.004	0.004	0.002	0.007	0.008	0.002	0.003	0.004	0.014
1.004	1.005	1.009	1.008	1.003	1.010	1.011	1.005	0.997
0.030	0.030	0.046	0.037	0.034	0.036	0.042	0.050	0.042
0.034	0.032	0.063	0.016	0.019	0.073	0.071	0.055	0.027
0.186	0.185	0.182	0.198	0.195	0.179	0.182	0.194	0.200
0.421	0.421	0.394	0.427	0.428	0.391	0.385	0.400	0.418
0.051	0.050	0.048	0.049	0.050	0.046	0.046	0.046	0.048
0.183	0.181	0.161	0.169	0.177	0.165	0.160	0.155	0.164
0.033	0.034	0.027	0.027	0.030	0.031	0.029	0.025	0.025
0.000	0.000	0.000	0.000	0.000	0.000	0.000	0.000	0.000
0.025	0.025	0.021	0.018	0.021	0.029	0.026	0.019	0.017
0.021	0.022	0.037	0.032	0.028	0.028	0.035	0.043	0.041
0.005	0.005	0.004	0.004	0.003	0.004	0.003	0.002	0.002
2.00	2.00	1.99	1.99	2.00	1.99	1.99	2.00	2.00

Appendix G: chemical analyses of the dated monazites in samples from the Argentera Massif

ISC3-MNZ5-6	ISC3-MNZ5-7	ISC3-MNZ5-8	ISC3-MNZ5-9	ISC3-MNZ2-1	ISC3-MNZ2-2	ISC3-MNZ2-3	ISC3-MNZ2-4	ISC3-MNZ2-5
0.0915	0.0987	0.1013	0.1499	0.1603	0.2678	0.0667	0.0985	0.156
31	31.06	31.02	30.73	30.8	30.28	30.89	30.76	30.54
1.0871	0.9223	0.8705	0.9788	1.1072	0.9589	0.971	0.9274	1.0081
2.52	3.59	3.52	2.73	1.31	0.539	3.46	2.6	0.922
13.31	12.55	12.63	12.95	12.96	14.16	12.9	13.1	13.53
28.47	27.25	27.65	27.85	28.75	30.55	27.98	28.23	29.87
3.41	3.4	3.43	3.41	3.49	3.62	3.36	3.44	3.53
11.81	11.85	12.04	11.87	12.67	12.25	11.76	12.1	12.62
2.14	2.27	2.34	2.19	2.27	1.93	2.07	2.13	2.13
0.000	0.000	0.000	0.000	0.000	0.000	0.000	0.000	0.000
1.7	2.08	2.18	1.68	1.71	1.2	1.93	1.74	1.49
4.91	3.88	3.55	3.99	4.36	4.5	3.93	3.77	4.31
0.2364	0.3697	0.4108	0.4218	0.3484	0.3155	0.3551	0.4186	0.3554
100.685	99.321	99.743	98.951	99.936	100.571	99.673	99.315	100.462
0.004	0.004	0.004	0.006	0.006	0.010	0.003	0.004	0.006
1.007	1.013	1.010	1.010	1.009	0.997	1.008	1.010	1.003
0.045	0.038	0.036	0.041	0.046	0.040	0.040	0.039	0.042
0.051	0.074	0.072	0.056	0.027	0.011	0.071	0.054	0.019
0.188	0.178	0.179	0.185	0.185	0.203	0.183	0.187	0.194
0.400	0.384	0.389	0.396	0.407	0.435	0.395	0.401	0.424
0.048	0.048	0.048	0.048	0.049	0.051	0.047	0.049	0.050
0.162	0.163	0.165	0.165	0.175	0.170	0.162	0.168	0.175
0.028	0.030	0.031	0.029	0.030	0.026	0.028	0.028	0.028
0.000	0.000	0.000	0.000	0.000	0.000	0.000	0.000	0.000
0.022	0.027	0.028	0.022	0.022	0.015	0.025	0.022	0.019
0.038	0.030	0.028	0.031	0.034	0.036	0.031	0.030	0.034
0.002	0.003	0.004	0.004	0.003	0.003	0.003	0.004	0.003
2.00	1.99	1.99	1.99	1.99	2.00	2.00	1.99	2.00

Appendix G: chemical analyses of the dated monazites in samples from the Argentera Massif

ISC3-MNZ2-6	ISC3-MNZ2-7	ISC3-MNZ2-8	ISC5-MNZ10-1	ISC5-MNZ10-2	ISC5-MNZ10-3	ISC5-MNZ10-4	ISC5-MNZ10-5	ISC5-MNZ10-6
0.1107	0.1033	0.0966	0.1103	0.1064	0.1417	0.1265	0.0871	0.0511
30.66	30.66	30.67	31.31	31.16	31	30.66	30.56	30.53
1.0217	1.1845	1.0615	0.9943	0.9769	0.9311	1.0429	1.0258	0.9729
1.82	2.57	3.32	3.24	2.75	1.81	1.87	2.45	2.84
12.94	12.38	12.46	12.75	12.84	12.35	12.41	12.94	12.69
28.69	27.33	27.18	28.16	27.78	29.16	28.9	28.52	28.42
3.47	3.33	3.24	3.33	3.47	3.73	3.52	3.41	3.47
12.66	12.06	11.64	11.84	11.79	13.07	12.86	11.91	12.21
2.38	2.19	2.19	2.16	2.15	2.39	2.34	2.16	2.25
0.000	0.000	0.000	0.000	0.000	0.000	0.000	0.000	0.000
1.99	1.84	1.96	1.92	1.87	1.88	1.87	1.97	1.81
4.38	5.11	4.5	3.74	3.82	3.82	4.42	3.96	3.43
0.3529	0.3576	0.4284	0.7443	0.7646	0.7309	0.7161	0.7478	0.6818
100.475	99.115	98.747	100.299	99.478	101.014	100.736	99.741	99.356
0.004	0.004	0.004	0.004	0.004	0.005	0.005	0.003	0.002
1.004	1.010	1.010	1.012	1.015	1.007	1.003	1.005	1.005
0.042	0.049	0.044	0.041	0.040	0.038	0.043	0.043	0.041
0.037	0.053	0.069	0.066	0.056	0.037	0.038	0.051	0.059
0.185	0.178	0.179	0.180	0.182	0.175	0.177	0.185	0.182
0.406	0.389	0.387	0.394	0.392	0.410	0.409	0.405	0.405
0.049	0.047	0.046	0.046	0.049	0.052	0.050	0.048	0.049
0.175	0.168	0.162	0.161	0.162	0.179	0.177	0.165	0.170
0.032	0.029	0.029	0.028	0.029	0.032	0.031	0.029	0.030
0.000	0.000	0.000	0.000	0.000	0.000	0.000	0.000	0.000
0.026	0.024	0.025	0.024	0.024	0.024	0.024	0.025	0.023
0.034	0.040	0.036	0.029	0.030	0.030	0.035	0.031	0.027
0.003	0.003	0.004	0.006	0.007	0.006	0.006	0.006	0.006
2.00	1.99	1.99	1.99	1.99	1.99	2.00	2.00	2.00

Appendix G: chemical analyses of the dated monazites in samples from the Argentera Massif

ISC5-MNZ3-1	ISC5-MNZ3-2	ISC5-MNZ3-3	ISC5-MNZ3-4	ISC5-MNZ3-5	ISC5-MNZ3-6	ISC5-MNZ3-7	ISC5-MNZ3-8	ISC5-MNZ3-9
0.121	0.0423	0.0682	0.2502	0.0471	0.0693	0.3123	0.0721	0.0365
30.66	30.93	30.76	30.21	30.89	30.95	30.53	31.17	30.96
0.802	0.96	0.966	0.9311	0.9825	1.0753	0.8863	1.0278	1.0038
1.35	2.73	2.64	0.4383	2.43	2.01	0.385	3.06	2.81
12.61	13.42	13.25	14.38	13.61	13.7	14.67	13.2	13.37
29.39	28.61	28.16	30.43	29.03	28.9	30.74	28.13	28.53
3.65	3.36	3.34	3.52	3.3	3.36	3.5	3.28	3.35
13.29	11.4	11.67	11.89	11.58	11.36	11.74	11.58	11.34
2.4	1.89	2.1	1.8	1.95	1.8	1.76	1.99	1.98
0.000	0.000	0.000	0.000	0.000	0.000	0.000	0.000	0.000
1.91	1.6	1.79	1.0354	1.58	1.26	1.0545	1.72	1.69
3.01	3.81	3.76	4	4.08	4.61	4.5	4.12	4.03
0.5924	0.6502	0.7366	0.6473	0.6131	0.6019	0.6214	0.6949	0.6174
99.785	99.403	99.241	99.532	100.093	99.697	100.700	100.045	99.718
0.005	0.002	0.003	0.010	0.002	0.003	0.012	0.003	0.001
1.008	1.013	1.010	1.002	1.009	1.013	1.001	1.012	1.011
0.033	0.040	0.040	0.039	0.041	0.045	0.037	0.042	0.041
0.028	0.056	0.055	0.009	0.050	0.041	0.008	0.062	0.058
0.181	0.191	0.190	0.208	0.194	0.195	0.210	0.187	0.190
0.418	0.405	0.400	0.436	0.410	0.409	0.436	0.395	0.403
0.052	0.047	0.047	0.050	0.046	0.047	0.049	0.046	0.047
0.184	0.157	0.162	0.166	0.160	0.157	0.162	0.159	0.156
0.032	0.025	0.028	0.024	0.026	0.024	0.024	0.026	0.026
0.000	0.000	0.000	0.000	0.000	0.000	0.000	0.000	0.000
0.025	0.021	0.023	0.013	0.020	0.016	0.014	0.022	0.022
0.024	0.030	0.030	0.032	0.032	0.036	0.035	0.032	0.032
0.005	0.006	0.006	0.006	0.005	0.005	0.005	0.006	0.005
1.99	1.99	1.99	2.00	1.99	1.99	1.99	1.99	1.99

Appendix G: chemical analyses of the dated monazites in samples from the Argentera Massif

ISC5-MNZ3-10	ISC5-MNZ2-1	ISC5-MNZ2-2	ISC5-MNZ2-3	ISC5-MNZ2-4	ISC5-MNZ7-1	ISC5-MNZ7-2	ISC5-MNZ7-3	ISC5-MNZ7-4	ISC5-MNZ7-5	ISC5-MNZ7-6	ISC5-MNZ7-7
0.0944	0.1008	0.3151	0.1245	0.2532	0.0946	0.5148	0.5275	0.0622	0.0889	0.0892	0.1505
30.89	30.94	30.69	31.05	30.56	30.47	29.97	29.04	30.7	30.8	30.74	30.85
1.0589	0.9062	0.681	0.8691	0.7491	1.0759	1.51	1.47	1.0192	1.0475	1.0069	1.1683
2.88	3.32	0.3398	2.8	1.2035	2.54	0.3244	0.2754	2.88	2.49	2.58	2.46
12.92	12.67	15.52	13.01	13.6	12.98	13.17	13.52	12.75	13.08	13.02	12.97
28.21	27.89	32.05	28.84	29.69	28.22	28.22	29.05	28.24	28.1	28.56	28.3
3.27	3.36	3.59	3.48	3.58	3.29	3.28	3.33	3.38	3.34	3.31	3.24
11.74	11.8	12.02	12.36	12.7	11.87	11.62	11.74	11.83	11.58	12.01	11.76
2.16	2.16	1.72	2.18	2.17	2.26	1.74	1.79	2.19	2.15	2.18	2.22
0.000	0.000	0.000	0.000	0.000	0.000	0.000	0.000	0.000	0.000	0.000	0.000
1.97	1.94	0.9741	1.73	1.64	1.93	0.9421	0.8851	1.89	1.92	1.92	1.95
4.12	3.55	3.33	3.34	3.16	4.1	7.48	7.11	4.08	4.1	4.07	4.71
0.8044	0.6776	0.4357	0.6976	0.6213	0.7747	1.0355	0.964	0.5814	0.8155	0.7343	0.7765
100.118	99.315	101.666	100.481	99.927	99.605	99.807	99.702	99.603	99.512	100.220	100.555
0.004	0.004	0.012	0.005	0.010	0.004	0.020	0.021	0.002	0.003	0.003	0.006
1.007	1.011	0.998	1.008	1.004	1.003	0.995	0.978	1.007	1.010	1.005	1.005
0.044	0.037	0.028	0.036	0.031	0.045	0.063	0.063	0.042	0.043	0.042	0.048
0.059	0.068	0.007	0.057	0.025	0.053	0.007	0.006	0.059	0.051	0.053	0.050
0.184	0.180	0.220	0.184	0.195	0.186	0.190	0.198	0.182	0.187	0.185	0.184
0.398	0.394	0.451	0.405	0.422	0.402	0.405	0.423	0.401	0.399	0.404	0.399
0.046	0.047	0.050	0.049	0.051	0.047	0.047	0.048	0.048	0.047	0.047	0.045
0.162	0.163	0.165	0.169	0.176	0.165	0.163	0.167	0.164	0.160	0.166	0.162
0.029	0.029	0.023	0.029	0.029	0.030	0.024	0.025	0.029	0.029	0.029	0.029
0.000	0.000	0.000	0.000	0.000	0.000	0.000	0.000	0.000	0.000	0.000	0.000
0.025	0.025	0.012	0.022	0.021	0.025	0.012	0.012	0.024	0.025	0.025	0.025
0.032	0.028	0.026	0.026	0.025	0.032	0.060	0.057	0.032	0.032	0.032	0.037
0.007	0.006	0.004	0.006	0.005	0.007	0.009	0.009	0.005	0.007	0.006	0.007
2.00	1.99	2.00	1.99	1.99	2.00	1.99	2.01	2.00	1.99	2.00	2.00

Appendix G: chemical analyses of the dated monazites in samples from the Argentera Massif

wt%	AIG8-MNZ11-1	AIG8-MNZ11-2	AIG8-MNZ11-3	AIG8-MNZ11-4	AIG8-MNZ52-1	AIG8-MNZ52-2	AIG8-MNZ52-3	AIG8-MNZ52-4
SiO2	0.3096	0.5054	0.317	0.3748	2.45	0.4667	0.3059	0.2534
P2O5	30.1	29.83	30.17	30.61	30.84	30.95	31.12	30.97
CaO	0.8706	1.2585	0.8056	0.9752	1.1001	1.1159	0.8359	0.8041
Y2O3	2.09	2.2	1.98	2.07	2.24	2.23	2.19	2.16
La2O3	13.2	12.51	13.45	13.1	13.09	13.03	13.61	13.61
Ce2O3	29.72	27.93	29.94	29.21	29	28.85	30.16	30.32
Pr2O3	3.75	3.52	3.77	3.66	3.74	3.66	3.7	3.7
Nd2O3	12.6	11.82	12.47	12.37	11.78	11.98	12.32	12.25
Sm2O3	2.22	2.15	2.22	2.14	1.9	2.12	2.09	2.02
Eu2O3	0.000	0.000	0.000	0.000	0.000	0.000	0.000	0.000
Gd2O3	1.85	1.77	1.76	1.74	1.55	1.82	1.81	1.74
ThO2	3.48	6.16	3.27	4.5	3.6	4.95	3.44	3.16
UO2	0.7653	0.9666	0.7428	0.7627	0.6515	0.7211	0.762	0.7496
Sum	100.956	100.621	100.895	101.513	101.942	101.894	102.344	101.737
Cationi								
Si	0.012	0.020	0.012	0.014	0.091	0.018	0.012	0.010
P	0.988	0.984	0.990	0.994	0.965	0.996	0.998	0.999
Ca	0.036	0.053	0.033	0.040	0.044	0.045	0.034	0.033
Y	0.043	0.046	0.041	0.042	0.044	0.045	0.044	0.044
La	0.189	0.180	0.192	0.185	0.179	0.183	0.190	0.191
Ce	0.422	0.398	0.425	0.410	0.393	0.402	0.418	0.423
Pr	0.053	0.050	0.053	0.051	0.050	0.051	0.051	0.051
Nd	0.174	0.164	0.173	0.169	0.156	0.163	0.167	0.167
Sm	0.030	0.029	0.030	0.028	0.024	0.028	0.027	0.027
Eu	0.000	0.000	0.000	0.000	0.000	0.000	0.000	0.000
Gd	0.024	0.023	0.023	0.022	0.019	0.023	0.023	0.022
Th	0.027	0.049	0.026	0.035	0.027	0.038	0.026	0.024
U	0.007	0.008	0.006	0.007	0.005	0.006	0.006	0.006
sum	2.00	2.00	2.00	2.00	2.00	2.00	2.00	2.00

Appendix G: chemical analyses of the dated monazites in samples from the Aiguilles Rouge Massif

AIG8-MNZ52-5	AIG8-MNZ52-6	AIG8-MNZ3-1	AIG8-MNZ3-2	AIG8-MNZ3-3	AIG8-MNZ3-4	AIG8-MNZ3-5	AIG8-MNZ3-6	AIG8-MNZ3-7	AIG8-MNZ10-1
0.3443	0.4148	0.2691	0.2647	0.2454	4.6	0.2281	0.2851	0.3117	0.411
31.14	31.18	30.88	30.61	30.54	26.61	30.57	30.32	30.22	29.74
0.8958	0.7709	0.6763	0.7446	0.7087	0.6893	0.7567	0.7831	0.8745	1.0009
2.15	2.24	2.26	2.31	2.05	1.7	2.74	2.06	2.02	1.0425
13.37	13.6	13.73	13.85	13.97	12.07	13.62	14.43	14.04	13.53
29.74	30.12	30.42	29.76	30.64	26.66	29.47	30.44	30.09	30.03
3.65	3.67	3.72	3.62	3.71	3.72	3.56	3.58	3.6	3.66
12.29	12.24	12.26	12.32	12.46	10.75	12.35	11.78	11.72	12.28
2.06	2.11	1.98	2.04	1.99	1.74	2.1	1.82	1.88	2.08
0.000	0.000	0.000	0.000	0.000	0.000	0.000	0.000	0.000	0.000
1.8	1.74	1.77	1.8	1.68	1.4	1.95	1.7	1.69	1.66
3.88	3.19	3.07	3.2	3.24	2.8	2.88	3.52	4.25	4.62
0.6985	0.7696	0.5542	0.8571	0.4584	0.4293	0.9091	0.5161	0.5474	1.1232
102.019	102.045	101.590	101.376	101.693	93.169	101.134	101.234	101.244	101.178
0.013	0.016	0.010	0.010	0.009	0.185	0.009	0.011	0.012	0.016
1.000	0.999	0.999	0.995	0.993	0.904	0.995	0.991	0.989	0.982
0.036	0.031	0.028	0.031	0.029	0.030	0.031	0.032	0.036	0.042
0.043	0.045	0.046	0.047	0.042	0.036	0.056	0.042	0.042	0.022
0.187	0.190	0.193	0.196	0.198	0.179	0.193	0.205	0.200	0.195
0.413	0.417	0.425	0.418	0.431	0.392	0.415	0.430	0.426	0.429
0.050	0.051	0.052	0.051	0.052	0.054	0.050	0.050	0.051	0.052
0.167	0.166	0.167	0.169	0.171	0.154	0.170	0.162	0.162	0.171
0.027	0.028	0.026	0.027	0.026	0.024	0.028	0.024	0.025	0.028
0.000	0.000	0.000	0.000	0.000	0.000	0.000	0.000	0.000	0.000
0.023	0.022	0.022	0.023	0.021	0.019	0.025	0.022	0.022	0.021
0.030	0.025	0.024	0.025	0.025	0.023	0.022	0.028	0.033	0.037
0.006	0.006	0.005	0.007	0.004	0.004	0.008	0.004	0.005	0.010
2.00	2.00	2.00	2.00	2.00	2.00	2.00	2.00	2.00	2.00

Appendix G: chemical analyses of the dated monazites in samples from the Aiguilles Rouge Massif

AIG8-MNZ10-2	AIG8-MNZ10-3	AIG11-MNZ10-1	AIG11-MNZ10-2	AIG11-MNZ10-3	AIG11-MNZ37-1	AIG11-MNZ37-2	AIG11-MNZ37-3	AIG11-MNZ34-1	AIG11-MNZ34-2
0.3157	0.4343	0.3834	0.4554	0.463	0.512	0.4834	0.3664	0.3591	0.3835
30.64	30.46	30.56	30.11	30.23	29.22	28.96	29.45	29.66	29.36
1.1727	0.8949	0.7313	0.9781	0.9539	1.0587	1.0332	1.114	0.9073	1.0382
1.38	1.28	0.0047	0	0	0.1705	0.2116	0.7206	0.1769	0.1132
13.52	13.57	14.78	14.63	14.69	14.09	14.32	14.29	15.19	14.27
29.98	30.28	31.49	30.91	31.12	30.16	30.19	30.23	30.72	30.65
3.62	3.7	3.83	3.68	3.75	3.68	3.78	3.73	3.73	3.89
12.21	12.49	12.6	12.36	12.26	12.34	12.31	12.14	12.43	12.7
2.09	2.17	2.13	2.11	2	2.12	2.13	2.05	2.16	2.15
0.000	0.000	0.000	0.000	0.000	0.000	0.000	0.000	0.000	0.000
1.74	1.77	1.47	1.29	1.18	1.28	1.38	1.29	1.59	1.27
3.95	3.66	3.76	5.1	5.17	5.57	5.44	4.97	4.12	4.93
1.0334	0.843	0.185	0.3047	0.3065	0.4034	0.4304	0.5164	0.4424	0.4373
101.652	101.552	101.924	101.928	102.123	100.605	100.669	100.867	101.486	101.192
0.012	0.017	0.015	0.018	0.018	0.020	0.019	0.014	0.014	0.015
0.995	0.992	0.995	0.987	0.988	0.977	0.972	0.979	0.981	0.978
0.048	0.037	0.030	0.041	0.039	0.045	0.044	0.047	0.038	0.044
0.028	0.026	0.000	0.000	0.000	0.004	0.004	0.015	0.004	0.002
0.191	0.192	0.210	0.209	0.209	0.205	0.209	0.207	0.219	0.207
0.421	0.426	0.443	0.438	0.440	0.436	0.438	0.435	0.440	0.441
0.051	0.052	0.054	0.052	0.053	0.053	0.055	0.053	0.053	0.056
0.167	0.172	0.173	0.171	0.169	0.174	0.174	0.170	0.173	0.178
0.028	0.029	0.028	0.028	0.027	0.029	0.029	0.028	0.029	0.029
0.000	0.000	0.000	0.000	0.000	0.000	0.000	0.000	0.000	0.000
0.022	0.023	0.019	0.017	0.015	0.017	0.018	0.017	0.021	0.017
0.031	0.029	0.029	0.040	0.041	0.045	0.044	0.040	0.033	0.039
0.009	0.007	0.002	0.003	0.003	0.004	0.004	0.005	0.004	0.004
2.00	2.00	2.00	2.00	2.00	2.01	2.01	2.01	2.01	2.01

Appendix G: chemical analyses of the dated monazites in samples from the Aiguilles Rouge Massif

AIG11-MNZ34-3	AIG11-MNZ34-4	AIG14-MNZ2-1	AIG14-MNZ2-2	AIG14-MNZ2-3	AIG14-MNZ2-4	AIG14-MNZ2-5	AIG14-MNZ2-6
0.4115	0.3673	0.6167	0.6962	0.743	0.5465	0.5787	4.69
29.6	30.24	30.25	29.66	29.58	29.33	29.55	29.27
1.0691	0.8771	1.2367	0.9891	1.78	1.1023	1.0389	1.0582
0.1835	0.1437	1.82	1.71	1.76	1.68	1.2475	1.42
14.2	14.58	13.49	14.06	13.1	13.89	14.35	13.34
30.13	31.01	28.19	29.66	27.55	29.35	30.04	27.77
3.88	3.97	3.64	3.74	3.21	3.63	3.67	3.8
12.29	12.77	11.53	11.86	11.29	12	11.96	11.57
2.16	2.2	1.93	1.94	1.97	2.02	1.96	1.92
0.000	0.000	0.000	0.000	0.000	0.000	0.000	0.000
1.31	1.37	1.66	1.65	1.68	1.67	1.45	1.55
5.4	4.3	6.09	4.52	7.64	4.91	4.82	4.41
0.5262	0.446	0.9376	0.635	0.8001	0.6475	0.5654	0.6988
101.160	102.274	101.391	101.120	101.103	100.776	101.231	101.497
0.016	0.014	0.024	0.027	0.029	0.021	0.023	0.173
0.982	0.988	0.986	0.975	0.973	0.973	0.975	0.915
0.045	0.036	0.051	0.041	0.074	0.046	0.043	0.042
0.004	0.003	0.037	0.035	0.036	0.035	0.026	0.028
0.205	0.208	0.192	0.201	0.188	0.201	0.206	0.182
0.432	0.438	0.398	0.422	0.392	0.421	0.429	0.375
0.055	0.056	0.051	0.053	0.045	0.052	0.052	0.051
0.172	0.176	0.159	0.165	0.157	0.168	0.167	0.153
0.029	0.029	0.026	0.026	0.026	0.027	0.026	0.024
0.000	0.000	0.000	0.000	0.000	0.000	0.000	0.000
0.017	0.018	0.021	0.021	0.022	0.022	0.019	0.019
0.043	0.034	0.048	0.036	0.060	0.039	0.038	0.033
0.005	0.004	0.008	0.005	0.007	0.006	0.005	0.006
2.01	2.00	2.00	2.01	2.01	2.01	2.01	2.00

Appendix G: chemical analyses of the dated monazites in samples from the Aiguilles Rouge Massif

wt%	SL6-MNZ10-1	SL6-MNZ10-2	SL6-MNZ10-3	SL6-MNZ10-4	SL6-MNZ10-5	SL6-MNZ9-1	SL6-MNZ9-2	SL6-MNZ9-3
SiO2	0.273	0.336	0.316	0.293	0.294	0.252	0.233	0.185
P2O5	30.460	30.270	30.310	30.600	30.920	29.960	30.130	30.400
CaO	0.556	0.522	0.446	0.344	0.415	0.559	0.684	0.840
Y2O3	1.290	0.139	0.476	0.535	0.791	1.710	0.197	0.206
La2O3	12.530	12.630	12.450	12.590	12.610	12.080	12.660	12.600
Ce2O3	28.150	28.640	28.460	28.800	28.360	27.430	29.260	29.290
Pr2O3	3.970	4.110	4.040	4.000	3.910	3.750	3.960	3.900
Nd2O3	14.600	15.290	14.880	15.140	14.710	14.490	14.790	14.990
Sm2O3	3.180	3.250	3.280	3.320	3.260	3.220	3.080	3.070
Eu2O3	0.000	0.000	0.000	0.000	0.000	0.000	0.000	0.000
Gd2O3	2.730	2.460	2.920	3.020	2.980	2.900	2.150	2.050
ThO2	2.130	2.140	1.880	1.290	1.440	2.000	2.490	2.410
UO2	0.615	0.493	0.246	0.302	0.481	0.684	0.794	1.540
Sum	100.483	100.280	99.705	100.235	100.171	99.035	100.427	101.482
Cations								
Si	0.011	0.013	0.012	0.011	0.011	0.010	0.009	0.007
P	1.000	1.000	1.003	1.005	1.010	0.998	0.997	0.997
Ca	0.023	0.022	0.019	0.014	0.017	0.024	0.029	0.035
Y	0.027	0.003	0.010	0.011	0.016	0.036	0.004	0.004
La	0.179	0.182	0.179	0.180	0.180	0.175	0.183	0.180
Ce	0.400	0.409	0.407	0.409	0.401	0.395	0.419	0.415
Pr	0.056	0.058	0.058	0.057	0.055	0.054	0.056	0.055
Nd	0.202	0.213	0.208	0.210	0.203	0.204	0.207	0.207
Sm	0.042	0.044	0.044	0.044	0.043	0.044	0.041	0.041
Eu	0.000	0.000	0.000	0.000	0.000	0.000	0.000	0.000
Gd	0.035	0.032	0.038	0.039	0.038	0.038	0.028	0.026
Th	0.017	0.017	0.015	0.010	0.011	0.016	0.020	0.019
U	0.005	0.004	0.002	0.003	0.004	0.006	0.007	0.013
Sum	2.00	2.00	1.99	1.99	1.99	2.00	2.00	2.00

Appendix G: chemical analyses of the dated monazites in samples from the Maures Massif

SL6-MNZ9-4	SL6-MNZ9-5	SL6-MNZ9-6	SL6-MNZ9-7	SL6-MNZ9-8	SL6-MNZ8-1	SL6-MNZ8-2	SL6-MNZ8-3	SL6-MNZ8-4	CD6-MNZ9b-1
0.170	0.169	0.126	0.226	0.185	0.268	0.212	0.237	0.258	0.336
30.670	30.680	30.350	30.970	31.060	30.700	31.780	31.140	30.760	30.420
0.336	0.387	0.382	0.609	0.537	0.419	0.345	0.406	0.419	1.040
0.730	1.225	1.460	0.186	1.660	0.491	0.843	1.105	1.113	2.110
12.480	12.700	12.420	12.740	12.320	12.510	12.910	12.580	12.780	12.690
29.250	28.930	28.440	29.300	28.020	28.600	29.040	28.310	28.460	28.960
4.050	3.750	3.820	4.010	3.810	4.020	4.000	4.020	3.950	3.520
15.010	14.890	14.890	15.000	14.770	14.980	15.150	14.880	15.000	12.470
3.230	3.240	3.370	3.070	3.190	3.240	3.220	3.360	3.300	2.200
0.000	0.000	0.000	0.000	0.000	0.000	0.000	0.000	0.000	0.000
3.040	3.010	3.260	2.150	2.910	3.000	2.890	3.010	2.890	1.910
1.570	1.480	1.430	2.290	1.930	1.900	1.200	1.670	1.470	4.040
0.232	0.413	0.511	0.829	0.598	0.257	0.369	0.561	0.606	0.868
100.768	100.875	100.460	101.380	100.991	100.385	101.958	101.278	101.006	100.564
0.007	0.007	0.005	0.009	0.007	0.010	0.008	0.009	0.010	0.013
1.005	1.003	1.000	1.007	1.008	1.007	1.016	1.009	1.003	0.995
0.014	0.016	0.016	0.025	0.022	0.017	0.014	0.017	0.017	0.043
0.015	0.025	0.030	0.004	0.034	0.010	0.017	0.022	0.023	0.043
0.178	0.181	0.178	0.181	0.174	0.179	0.180	0.178	0.182	0.181
0.415	0.409	0.405	0.412	0.393	0.406	0.402	0.397	0.401	0.410
0.057	0.053	0.054	0.056	0.053	0.057	0.055	0.056	0.055	0.050
0.208	0.205	0.207	0.206	0.202	0.207	0.204	0.203	0.206	0.172
0.043	0.043	0.045	0.041	0.042	0.043	0.042	0.044	0.044	0.029
0.000	0.000	0.000	0.000	0.000	0.000	0.000	0.000	0.000	0.000
0.039	0.039	0.042	0.027	0.037	0.039	0.036	0.038	0.037	0.024
0.012	0.012	0.011	0.018	0.015	0.015	0.009	0.013	0.011	0.032
0.002	0.004	0.004	0.007	0.005	0.002	0.003	0.005	0.005	0.007
1.99	2.00	2.00	1.99	1.99	1.99	1.99	1.99	1.99	2.00

Appendix G: chemical analyses of the dated monazites in samples from the Maures Massif

CD6-MNZ9b-2	CD6-MNZ9b-3	CD6-MNZ9b-4	CD6-MNZ9b-5	CD6-MNZ1-1	CD6-MNZ1-2	CD6-MNZ1-3	CD6-MNZ1-4	CD6-MNZ1-5	CD6-MNZ1-6
0.286	0.318	0.293	0.251	0.230	0.457	0.319	0.299	0.881	0.633
30.250	30.710	30.450	30.870	30.870	30.420	30.980	30.820	30.670	30.100
0.867	0.824	0.759	0.949	1.087	0.961	0.753	0.735	1.460	1.135
0.467	0.408	0.402	1.700	2.110	0.504	0.448	0.491	0.473	0.470
14.500	15.360	14.920	13.050	12.940	14.060	14.420	13.920	12.990	13.390
31.440	31.350	31.360	29.300	29.020	30.880	31.920	31.610	28.760	30.050
3.670	3.870	3.840	3.650	3.630	3.810	3.820	3.960	3.550	3.690
12.710	11.790	12.090	12.460	11.900	12.040	12.610	12.750	11.630	12.050
2.100	1.810	1.940	2.250	2.260	2.030	2.080	2.190	1.910	2.000
0.000	0.000	0.000	0.000	0.000	0.000	0.000	0.000	0.000	0.000
1.530	1.290	1.370	2.160	2.010	1.570	1.460	1.610	1.490	1.490
3.540	3.630	3.580	3.720	4.370	4.900	3.490	3.610	8.630	6.050
0.613	0.660	0.550	0.753	0.806	0.736	0.568	0.597	0.877	0.814
101.973	102.018	101.553	101.113	101.233	102.367	102.868	102.592	103.320	101.871
0.011	0.012	0.011	0.010	0.009	0.018	0.012	0.011	0.033	0.024
0.989	0.997	0.995	1.002	1.001	0.989	0.997	0.997	0.985	0.984
0.036	0.034	0.031	0.039	0.045	0.040	0.031	0.030	0.059	0.047
0.010	0.008	0.008	0.035	0.043	0.010	0.009	0.010	0.010	0.010
0.207	0.217	0.212	0.185	0.183	0.199	0.202	0.196	0.182	0.191
0.445	0.440	0.443	0.412	0.407	0.434	0.444	0.442	0.400	0.425
0.052	0.054	0.054	0.051	0.051	0.053	0.053	0.055	0.049	0.052
0.175	0.161	0.167	0.171	0.163	0.165	0.171	0.174	0.158	0.166
0.028	0.024	0.026	0.030	0.030	0.027	0.027	0.029	0.025	0.027
0.000	0.000	0.000	0.000	0.000	0.000	0.000	0.000	0.000	0.000
0.020	0.016	0.018	0.027	0.026	0.020	0.018	0.020	0.019	0.019
0.028	0.028	0.028	0.029	0.034	0.038	0.027	0.028	0.066	0.047
0.005	0.006	0.005	0.006	0.007	0.006	0.005	0.005	0.007	0.007
2.00	2.00	2.00	2.00	2.00	2.00	2.00	2.00	1.99	2.00

Appendix G: chemical analyses of the dated monazites in samples from the Maures Massif

CD6-MNZ1-7	CD6-MNZ22-1	CD6-MNZ22-2	CD6-MNZ22-3	CD6-MNZ22-4	CD6-MNZ22-5	CD6-MNZ12-1	CD6-MNZ12-2	CD6-MNZ12-3
0.357	0.246	0.372	0.488	0.334	0.368	0.334	0.605	0.612
30.670	30.690	30.490	30.390	30.260	30.330	31.100	30.750	30.860
1.085	1.050	0.733	1.145	0.706	0.859	1.035	0.991	0.994
1.360	2.070	0.467	0.427	0.443	0.670	2.550	0.591	0.537
13.200	13.010	14.080	13.990	14.320	13.890	12.300	13.580	13.760
29.300	29.170	31.710	30.380	32.010	30.900	28.230	30.340	30.590
3.700	3.670	3.840	3.620	3.890	3.800	3.740	3.720	3.730
12.340	12.160	12.770	12.010	12.680	12.460	12.220	12.230	12.250
2.190	2.180	2.060	1.940	2.090	2.070	2.360	2.040	2.010
0.000	0.000	0.000	0.000	0.000	0.000	0.000	0.000	0.000
2.010	1.770	1.490	1.390	1.470	1.520	2.230	1.530	1.540
4.690	4.220	3.400	5.350	3.310	4.030	3.750	4.870	4.920
0.873	0.813	0.536	0.659	0.560	0.694	0.985	0.853	0.726
101.775	101.048	101.949	101.789	102.073	101.591	100.834	102.099	102.528
0.014	0.009	0.014	0.019	0.013	0.014	0.013	0.023	0.023
0.996	0.999	0.993	0.991	0.989	0.992	1.005	0.994	0.994
0.045	0.043	0.030	0.047	0.029	0.036	0.042	0.041	0.041
0.028	0.042	0.010	0.009	0.009	0.014	0.052	0.012	0.011
0.187	0.184	0.200	0.199	0.204	0.198	0.173	0.191	0.193
0.411	0.411	0.447	0.428	0.452	0.437	0.394	0.424	0.426
0.052	0.051	0.054	0.051	0.055	0.053	0.052	0.052	0.052
0.169	0.167	0.175	0.165	0.175	0.172	0.167	0.167	0.166
0.029	0.029	0.027	0.026	0.028	0.028	0.031	0.027	0.026
0.000	0.000	0.000	0.000	0.000	0.000	0.000	0.000	0.000
0.026	0.023	0.019	0.018	0.019	0.019	0.028	0.019	0.019
0.037	0.033	0.027	0.042	0.026	0.032	0.029	0.038	0.038
0.007	0.007	0.005	0.006	0.005	0.006	0.008	0.007	0.006
2.00	2.00	2.00	2.00	2.00	2.00	1.99	1.99	2.00

Appendix G: chemical analyses of the dated monazites in samples from the Maures Massif

CD6-MNZ12-4	CD6-MNZ12-5	MTM10-MNZ8-1	MTM10-MNZ8-2	MTM10-MNZ8-3	MTM10-MNZ8-4	MTM10-MNZ8-5	MTM10-MNZ32-1	MTM10-MNZ32-2
0.419	0.266	1.320	1.112	0.658	0.600	0.603	0.881	0.574
30.910	31.190	29.070	29.310	30.230	29.870	29.590	29.300	29.760
1.073	0.854	1.339	1.182	0.722	0.665	0.815	1.022	0.637
1.580	1.690	2.410	2.110	2.060	2.080	1.980	2.430	2.070
12.960	12.700	12.470	13.180	13.620	13.370	13.170	12.100	13.220
29.170	29.750	27.500	28.630	30.370	30.680	30.260	28.010	30.510
3.600	3.770	3.260	3.350	3.570	3.650	3.510	3.570	3.760
12.340	13.210	10.990	11.240	11.850	12.270	12.210	11.530	12.190
2.230	2.330	1.980	1.940	2.030	2.170	2.160	2.180	2.160
0.000	0.000	0.000	0.000	0.000	0.000	0.000	0.000	0.000
2.010	1.770	1.710	1.720	1.720	1.740	1.760	1.890	1.800
4.520	2.980	8.730	7.140	4.510	4.090	4.550	6.780	4.020
0.814	0.815	0.690	0.627	0.375	0.365	0.378	0.599	0.327
101.626	101.325	101.469	101.541	101.715	101.551	100.986	100.292	101.028
0.016	0.010	0.051	0.043	0.025	0.023	0.024	0.035	0.022
0.999	1.006	0.956	0.963	0.983	0.978	0.976	0.972	0.979
0.044	0.035	0.056	0.049	0.030	0.028	0.034	0.043	0.027
0.032	0.034	0.050	0.044	0.042	0.043	0.041	0.051	0.043
0.182	0.179	0.179	0.189	0.193	0.191	0.189	0.175	0.190
0.408	0.415	0.391	0.407	0.427	0.434	0.432	0.402	0.434
0.050	0.052	0.046	0.047	0.050	0.051	0.050	0.051	0.053
0.168	0.180	0.153	0.156	0.163	0.170	0.170	0.161	0.169
0.029	0.031	0.027	0.026	0.027	0.029	0.029	0.029	0.029
0.000	0.000	0.000	0.000	0.000	0.000	0.000	0.000	0.000
0.025	0.022	0.022	0.022	0.022	0.022	0.023	0.025	0.023
0.035	0.023	0.069	0.056	0.035	0.032	0.036	0.054	0.032
0.007	0.007	0.006	0.005	0.003	0.003	0.003	0.005	0.003
2.00	1.99	2.01	2.01	2.00	2.00	2.01	2.00	2.00

Appendix G: chemical analyses of the dated monazites in samples from the Maures Massif

MTM10-MNZ32-3	MTM10-MNZ32-4	MTM10-MNZ32-5	MTM10-MNZ30-1	MTM10-MNZ30-2	MTM10-MNZ30-3	MTM10-MNZ30-4	CD1-MNZ1-1	CD1-MNZ1-2
0.715	0.569	0.747	0.879	0.581	0.730	0.623	0.2154	0.3194
29.780	30.150	30.140	29.880	31.060	30.260	30.290	30.03	30.36
0.742	0.649	0.874	0.996	0.715	0.901	0.716	0.7833	0.8368
2.000	2.110	2.480	2.570	2.270	2.340	2.150	0.2722	0.2458
13.340	13.160	12.470	12.410	13.060	13.080	13.120	14.02	13.68
29.810	30.010	28.800	28.350	30.190	29.330	29.940	29.6	29.25
3.610	3.780	3.700	3.630	3.740	3.780	3.810	3.42	3.39
11.960	12.310	11.910	11.720	12.460	11.600	12.170	11.98	11.9
2.130	2.290	2.260	2.180	2.270	2.100	2.190	2.22	2.05
0.000	0.000	0.000	0.000	0.000	0.000	0.000	0.000	0.000
1.800	1.890	1.920	1.850	1.910	1.760	1.830	1.65	1.46
5.110	4.080	5.840	6.560	4.340	5.690	4.430	3.94	4.77
0.344	0.326	0.542	0.731	0.323	0.488	0.348	0.4693	0.3757
101.341	101.324	101.683	101.755	102.919	102.059	101.617	98.600	98.638
0.028	0.022	0.029	0.034	0.022	0.028	0.024	0.009	0.013
0.977	0.985	0.981	0.974	0.992	0.981	0.985	1.006	1.011
0.031	0.027	0.036	0.041	0.029	0.037	0.029	0.033	0.035
0.041	0.043	0.051	0.053	0.046	0.048	0.044	0.006	0.005
0.191	0.187	0.177	0.176	0.182	0.185	0.186	0.205	0.198
0.423	0.424	0.405	0.400	0.417	0.411	0.421	0.429	0.421
0.051	0.053	0.052	0.051	0.051	0.053	0.053	0.049	0.049
0.166	0.170	0.164	0.161	0.168	0.159	0.167	0.169	0.167
0.028	0.030	0.030	0.029	0.030	0.028	0.029	0.030	0.028
0.000	0.000	0.000	0.000	0.000	0.000	0.000	0.000	0.000
0.023	0.024	0.024	0.024	0.024	0.022	0.023	0.022	0.019
0.040	0.032	0.046	0.051	0.033	0.044	0.035	0.032	0.038
0.003	0.003	0.005	0.006	0.003	0.004	0.003	0.004	0.003
2.00	2.00	2.00	2.00	2.00	2.00	2.00	1.99	1.99

Appendix G: chemical analyses of the dated monazites in samples from the Maures Massif

CD1-MNZ1-3	CD1-MNZ1-4	CD1-MNZ1-5	CD1-MNZ1-6	CD1-MNZ3-1	CD1-MNZ3-2	CD1-MNZ3-3	CD1-MNZ3-4	CD1-MNZ3-5
0.0502	0.3764	0.1133	0.0567	0.3882	0.4361	0.2234	0.5643	0.2987
31.22	30.52	30.57	31.07	29.88	29.88	30.09	29.56	29.86
0.8875	1.0753	0.7811	0.8615	0.9514	1.0164	0.7211	1.1693	1.0589
1.63	0.2886	1.2416	1.48	0.0943	0.0934	0.0704	0.0785	0.0923
13.22	13.09	13.3	13.27	13.63	13.38	13.89	13.12	13.69
28.81	28.33	28.78	28.8	29.16	29.17	30.08	27.85	28.94
3.44	3.38	3.5	3.47	3.46	3.45	3.54	3.29	3.38
11.78	11.92	11.92	11.94	11.73	11.92	12.2	11.59	11.69
2.03	2.17	2.23	2.12	1.94	2.11	2.01	1.95	1.99
0.000	0.000	0.000	0.000	0.000	0.000	0.000	0.000	0.000
1.55	1.67	1.84	1.67	1.39	1.36	1.38	1.25	1.29
3.68	6.02	3.34	3.56	5.58	6.1	3.87	7.35	5.56
0.6048	0.4173	0.6403	0.636	0.3534	0.3197	0.3157	0.3167	0.4706
98.903	99.258	98.256	98.934	98.557	99.236	98.391	98.089	98.321
0.002	0.015	0.004	0.002	0.015	0.017	0.009	0.022	0.012
1.023	1.010	1.016	1.021	1.002	0.998	1.008	0.998	1.004
0.037	0.045	0.033	0.036	0.040	0.043	0.031	0.050	0.045
0.034	0.006	0.026	0.031	0.002	0.002	0.001	0.002	0.002
0.189	0.189	0.193	0.190	0.199	0.195	0.203	0.193	0.201
0.408	0.405	0.414	0.409	0.423	0.421	0.436	0.407	0.421
0.049	0.048	0.050	0.049	0.050	0.050	0.051	0.048	0.049
0.163	0.166	0.167	0.165	0.166	0.168	0.172	0.165	0.166
0.027	0.029	0.030	0.028	0.026	0.029	0.027	0.027	0.027
0.000	0.000	0.000	0.000	0.000	0.000	0.000	0.000	0.000
0.020	0.022	0.024	0.021	0.018	0.018	0.018	0.017	0.017
0.029	0.048	0.027	0.028	0.045	0.049	0.031	0.059	0.045
0.005	0.004	0.006	0.005	0.003	0.003	0.003	0.003	0.004
1.98	1.99	1.99	1.99	1.99	1.99	1.99	1.99	1.99

Appendix G: chemical analyses of the dated monazites in samples from the Maures Massif

CD1-MNZ3-6	CD1-MNZ3B-1	CD1-MNZ3B-2	CD1-MNZ3B-3	CD1-MNZ3B-4	CD1-MNZ3B-5	CD1-MNZ3B-6	CD1-MNZ4-1	CD1-MNZ4-2
0.0702	0.0532	0.0477	0.2493	0.2752	0.2341	0.2025	0.1901	0.2285
30.64	30.34	30.27	29.85	29.89	30.14	29.95	30.15	29.93
1.0017	0.9179	0.8929	0.8052	0.8789	0.8191	0.7013	0.6686	0.7835
1.93	1.83	1.82	0.218	0.2344	0.2643	0.2505	0.2427	0.2519
12.87	12.98	12.92	13.81	13.65	13.59	13.93	14.37	13.92
27.81	28.19	28.28	29.46	29.07	29.46	29.72	30.42	29.43
3.29	3.41	3.32	3.39	3.36	3.45	3.48	3.46	3.38
11.51	11.77	11.89	12.29	12.09	12.07	12.07	11.95	11.89
2.03	2.13	2.31	2.18	2.18	2.21	2.09	2.11	2.06
0.000	0.000	0.000	0.000	0.000	0.000	0.000	0.000	0.000
1.78	1.82	1.93	1.61	1.68	1.65	1.57	1.51	1.58
3.96	3.63	3.45	4.34	4.71	4.34	3.52	3.28	4.21
0.7963	0.7836	0.8568	0.2922	0.3428	0.3624	0.3347	0.3668	0.4004
97.688	97.855	97.987	98.495	98.361	98.590	97.819	98.718	98.064
0.003	0.002	0.002	0.010	0.011	0.009	0.008	0.007	0.009
1.019	1.013	1.011	1.003	1.004	1.008	1.008	1.007	1.007
0.042	0.039	0.038	0.034	0.037	0.035	0.030	0.028	0.033
0.040	0.038	0.038	0.005	0.005	0.006	0.005	0.005	0.005
0.186	0.189	0.188	0.202	0.200	0.198	0.204	0.209	0.204
0.400	0.407	0.409	0.428	0.422	0.426	0.433	0.439	0.428
0.047	0.049	0.048	0.049	0.049	0.050	0.050	0.050	0.049
0.161	0.166	0.168	0.174	0.171	0.170	0.171	0.168	0.169
0.027	0.029	0.031	0.030	0.030	0.030	0.029	0.029	0.028
0.000	0.000	0.000	0.000	0.000	0.000	0.000	0.000	0.000
0.023	0.024	0.025	0.021	0.022	0.022	0.021	0.020	0.021
0.032	0.029	0.028	0.035	0.038	0.035	0.028	0.026	0.034
0.007	0.007	0.008	0.003	0.003	0.003	0.003	0.003	0.004
1.99	1.99	1.99	1.99	1.99	1.99	1.99	1.99	1.99

Appendix G: chemical analyses of the dated monazites in samples from the Maures Massif

CD1-MNZ4-3	CD1-MNZ4-4	CD1-MNZ4-5	CD1-MNZ5-1	CD1-MNZ5-2	CD1-MNZ5-3	CD1-MNZ5-4	CD1-MNZ5-5	CD1-MNZ5-6
0.2347	0.1935	0.1499	0.3065	0.2779	0.3099	0.2998	0.2493	0.282
30.43	30.19	30.23	29.84	29.99	29.72	29.91	29.72	29.61
0.7546	0.6353	0.6684	0.8148	0.7709	0.8136	0.9207	0.6805	0.8648
0.268	0.225	0.2032	0.2381	0.2741	0.2252	0.2929	0.1964	0.273
13.72	14.08	14.18	13.77	13.69	13.97	13.5	15.23	13.58
29.48	30.19	30.04	29.41	29.68	28.81	28.61	29.52	28.98
3.42	3.46	3.38	3.43	3.42	3.46	3.43	3.23	3.45
12.1	12.26	11.96	11.63	12.29	12.15	12.03	12.23	11.94
2.16	2.18	2.01	2.05	2.18	2.12	2.15	2.07	2.19
0.000	0.000	0.000	0.000	0.000	0.000	0.000	0.000	0.000
1.66	1.63	1.41	1.54	1.71	1.51	1.65	1.57	1.58
4.01	3.18	3.1	4.55	4.27	4.43	4.86	3.58	4.62
0.2921	0.331	0.5672	0.3494	0.3418	0.3285	0.3951	0.3809	0.3631
98.529	98.555	97.899	97.929	98.895	97.847	98.049	98.657	97.733
0.009	0.008	0.006	0.012	0.011	0.012	0.012	0.010	0.011
1.013	1.009	1.013	1.005	1.003	1.003	1.006	0.999	1.002
0.032	0.027	0.028	0.035	0.033	0.035	0.039	0.029	0.037
0.006	0.005	0.004	0.005	0.006	0.005	0.006	0.004	0.006
0.199	0.205	0.207	0.202	0.199	0.205	0.198	0.223	0.200
0.424	0.436	0.436	0.428	0.429	0.421	0.416	0.429	0.424
0.049	0.050	0.049	0.050	0.049	0.050	0.050	0.047	0.050
0.170	0.173	0.169	0.165	0.173	0.173	0.171	0.173	0.171
0.029	0.030	0.027	0.028	0.030	0.029	0.029	0.028	0.030
0.000	0.000	0.000	0.000	0.000	0.000	0.000	0.000	0.000
0.022	0.021	0.019	0.020	0.022	0.020	0.022	0.021	0.021
0.032	0.025	0.025	0.037	0.034	0.036	0.039	0.029	0.037
0.003	0.003	0.005	0.003	0.003	0.003	0.003	0.003	0.003
1.99	1.99	1.99	1.99	1.99	1.99	1.99	2.00	1.99

Appendix G: chemical analyses of the dated monazites in samples from the Maures Massif

CD1-MNZ5-7	CD1-MNZ6-1	CD1-MNZ6-2	CD1-MNZ6-3	CD1-MNZ7-1	CD1-MNZ7-2	CD1-MNZ7-3
0.3149	0.3536	0.2355	0.3666	0.0672	0.3564	0.261
29.55	28.9	29.4	28.97	30.62	29.7	30.87
0.7747	0.7927	0.8861	0.7445	0.8388	0.9197	0.7127
0.1991	0.1403	0.3391	0.189	1.69	0.2293	0.2465
13.77	13.78	13.66	13.95	12.96	13.22	14.16
29.43	29.4	29.59	30.2	28.29	28.38	30
3.46	3.24	3.38	3.42	3.35	3.38	3.49
11.82	11.68	12	11.97	12.07	11.96	12.04
2.05	2.08	2.14	2.11	2.29	2.12	2.05
0.000	0.000	0.000	0.000	0.000	0.000	0.000
1.52	1.45	1.42	1.48	1.93	1.49	1.65
4.18	4.25	3.67	3.84	3.47	5.33	3.76
0.3556	0.3206	0.7153	0.3561	0.7629	0.3197	0.3434
97.424	96.387	97.436	97.596	98.339	97.405	99.584
0.013	0.014	0.009	0.015	0.003	0.014	0.010
1.002	0.996	0.999	0.990	1.016	1.005	1.014
0.033	0.035	0.038	0.032	0.035	0.039	0.030
0.004	0.003	0.007	0.004	0.035	0.005	0.005
0.204	0.207	0.202	0.208	0.187	0.195	0.203
0.432	0.438	0.435	0.446	0.406	0.415	0.426
0.051	0.048	0.049	0.050	0.048	0.049	0.049
0.169	0.170	0.172	0.173	0.169	0.171	0.167
0.028	0.029	0.030	0.029	0.031	0.029	0.027
0.000	0.000	0.000	0.000	0.000	0.000	0.000
0.020	0.020	0.019	0.020	0.025	0.020	0.021
0.034	0.035	0.030	0.031	0.028	0.043	0.030
0.003	0.003	0.006	0.003	0.007	0.003	0.003
1.99	2.00	2.00	2.00	1.99	1.99	1.99

Appendix G: chemical analyses of the dated monazites in samples from the Maures Massif